AN ABSTRACT OF THE DISSERTATION OF

Jason R. Patton for the degree of Doctor of Philosophy in Oceanography presented on January 9, 2014
Title: A Sedimentary and Geophysical Investigation Offshore of Sumatra: Subduction Zone Earthquakes, Ground Motions, and Submarine Landslides.

Abstract approved:_____
Chris Goldfinger

Abstract text: Subduction zone earthquake and tsunami hazards affect tens of millions worldwide and the recurrence of these disasters can be evaluated with paleoseismic techniques, because earthquake cycles (and their supercycles) typically span many millennia. In these three chapters, I discuss a suite of analyses I use to evaluate the sedimentary record of earthquakes as sampled in cores collected by the authors on the R/V Roger Revelle in 2007 offshore Sumatra, cruise RR0705, aka KNOX05RR. In the first chapter I discuss the mid- to late-Holocene recurrence of earthquakes in the region of the 2004 Sumatra-Andaman subduction zone earthquake. I estimate that the early Holocene to historic recurrence of turbidity current triggering earthquakes in the region of the 2004 Sumatra-Andaman subduction zone earthquake to be 260 ± 160 calendar years. I identify the uppermost turbidite in fifteen cores to have been deposited as a result of strong ground shaking from this 2004 earthquake. In the second chapter I compare and contrast the physiographic control of seismoturbidite deposition along the continental margins of the Sumatra-Andaman and Cascadia subduction zones. Cascadia's margin is dominated by glacial cycle constructed pathways which promote turbidity current flows for large distances. Sumatra margin pathways do not inherit analogous sedimentary systems, so turbidity currents and their deposits are more localized. Finally, I discuss slope stability and earthquake ground motions along the continental margin offshore the coast of Sumatra. In this third chapter I relate the potential for slope instability with core stratigraphy in slope basin cores along the Sumatra-Andaman subduction zone, both for generic earthquakes and for the 2004 earthquake. Using 2-D profile factor of safety analyses, I estimate that slopes become unstable when a seismic load of <0.2 g is imparted. Using infinite slope factor of safety analyses, I conclude that turbidity currents are triggered by earthquakes of at least magnitude M = 7. For the 2004 Sumatra-Andaman subduction zone earthquake, I find that the shaking intensity from ground motion does not explain the thickness of turbidites, which must be explained by other factors like site effects, site geomorphology, or source proximity.

A Sedimentary and Geophysical Investigation Offshore of Sumatra: Subduction Zone Earthquakes, Ground Motions, and Submarine Landslides

by
Jason R. Patton

A DISSERTATION
submitted to
Oregon State University

in partial fulfillment of
the requirements for the
degree of

Doctor of Philosophy

Presented January 9, 2014
Commencement June, 2014

Doctor of Philosophy dissertation of Jason R. Patton presented on January 9, 2014.

APPROVED:

_____
Major Professor, representing Oceanography

_____
Dean of the College of Earth, Ocean, and Atmospheric Sciences

_____
Dean of the Graduate School

I understand that my dissertation will become part of the permanent collection of Oregon State University libraries. My signature below authorizes release of my dissertation to any reader upon request.

_____
Jason R. Patton, Author

ACKNOWLEDGEMENTS

The author expresses sincere appreciation to the following (in no particular order, except for the first three):

Sandra G. Patton, my mother. Her support of me has been infinite.

Robert W. Patton, my father R.I.P., who provided endless challenges in my youth.

Matthew R. Patton, my brother who always has loved and supported me.

Thomas H. Leroy, who helped inspire me to do field work in the mid 1990's (and the man with 3 first names, maybe 4).

Chicken my cat, who acts like a dog and is happy to see me every day, regardless of how stressed I am.

Gary Carver, who inspired me to begin studying evidence of past earthquakes.

Chris Goldfinger, who recognized and utilized many of the methods that I inherit and use in my research.

Ann E. Morey, who helped me cope with grad school and afflicted me with my foram picking skills (more like a curse).

Chris Romsos, who's institutional wisdom made those tough days that much easier.

My fellow lab mates, Jeff Beeson, Brandi Black, Amy M. Garrett, Morgan Erhardt, and Timothy Kane for being the group white board for discussing our observations.

Brian Atwater, who has always given me the best advice when I needed it.

Mrs. Ohlinder, my 7th grade science teacher, who gave me a B on my research paper because I included humor in the report. She summarily read it to her husband who had shingles and he laughed in pain listening to my report.

Bob Brigham, my high school stage crew teacher for training me to think on my feet and to manage teams of workers while under stressful conditions.

Morgan Salisbury, a fellow Ph.D. student at OSU, for living in his van in my driveway to remind me of what really matters in life.

Robert Allan and Lori Hartline, who have provided me with the essential support to complete this degree.

CONTRIBUTION OF AUTHORS

Chapter 2. Dr. Chris Goldfinger for providing editorial comments on the text and figures; Ann Morey, Dr. Ken Ikehara, Dr. Joseph Stoner, and Chris Romsos for conducting field work and lab analyses; and Yusuf Djadjadihardja, Eddy Zulkarnaen Gaffar, and Udrekh for assisting in field work.

Chapter 3. Dr. Chris Goldfinger for providing editorial comments on the text and figures; Brandi Black for the Cascadia seismic data and processing (along with suggestions on processing the Sumatra seismic data); Ann Morey, Brandi Black, Ken Ikehara, and Chris Romsos for conducting field work and lab analyses; and Yusuf Djadjadihardja and Udrekh Udrekh for assisting in field work.

Chapter 4. Dr. Chris Goldfinger for providing editorial comments on analytical strategies, along with editorial comments on the text and figures; and Yusuf Djadjadihardja and Udrekh for assisting in field work.

TABLE OF CONTENTS

TABLE OF CONTENTS (Continued)

TABLE OF CONTENTS (Continued)

LIST OF FIGURES

LIST OF FIGURES (continued)

LIST OF FIGURES (continued)

LIST OF TABLES

LIST OF TABLES (continued)

LIST OF APPENDICES

LIST OF APPENDIX FIGURES

LIST OF APPENDIX TABLES

DEDICATION

The author dedicates this document to the honor of my parents, Sandra G. Patton and Robert W. Patton. With their support I have developed into the person that I am.

A Sedimentary and Geophysical Investigation Offshore of Sumatra: Subduction Zone Earthquakes, Ground Motions, and Submarine Landslides

Chapter 1: Abstract

The temporal and spatial distribution of great earthquakes along subduction zone faults drive the geologic hazard in coastal regions and contribute significantly to risk estimates. Recent earthquakes have broken basic principles held to be true about fault zone properties and recurrence of subduction zone earthquakes, calling into question our theories of seismogenesis and what controls fault rupture through time. Submarine paleoseismology is one strategy that allows one to view these earthquake patterns through time and space. Historic and prehistoric earthquakes associated with the Sunda subduction zone offshore Sumatra provide us with a natural laboratory for our investigations.

In the first chapter, I evaluate patterns of past earthquakes offshore northern Sumatra, using sediment core, seismic reflection, and multibeam bathymetric data. I use stratigraphic correlation methods as a basis to attribute a seismogenic landslide triggering mechanism for turbidity currents offshore Sumatra. I do this by ruling out alternative landslide triggering mechanisms. I use core geophysical and seismic reflection data to correlate sedimentary deposits as a strategy to establish the spatial extent of earthquakes. I use radiometric ages to constrain the timing of sedimentary deposition with the use of age models. Finally I make estimates of recurrence for earthquakes on the megathrust in the region of the 2004 Sumatra-Andaman subduction zone (SASZ) earthquake.

In the second chapter, I use sediment core stratigraphy to interpret the turbidity current depositional systems and compare the systems offshore Sumatra with those offshore Cascadia. Slope basin sedimentary systems are similar along both margins, but channel systems in the trench are a strong indicator of the spatial extent of coarse grained turbidites. Sumatra lacks modern extensive axial trench channel systems, so the coarse fraction of turbidity currents appears to be more localized.

In the final chapter, I conduct slope stability analyses and use modeled earthquake ground motion intensities as a seismic load to these slope stability models. I also compare static slope stability analyses with these pseudostatic (seismic) results. I

take results from the 2004 slip model, along with intensities modeled for generic earthquakes, to base interpretations about what are the driving factors for deposition of turbidites in the slopes offshore northern Sumatra.

While there is still more work to be done with these cores, I find that the sedimentary geologic evidence for earthquakes is convincing. Recurrence of great subduction zone earthquakes in the region of the 2004 SASZ earthquake is 260 ± 160 years. It is highly likely that we cored a turbidite triggered by the 2004 earthquake, based on ^{14}C and ^{210}Pb age data and the correlation between core geophysical data and seismologic observations of the earthquake. Seismic reflection data collected offshore Sumatra shows that these earthquake records found in the cores may be used to extend back in time the recurrence of seismic cycling, from the Holocene into the latest Pleistocene. Landslide triggering appears to be highly sensitive to the regions of higher slip during megathrust earthquakes, but the sedimentary record may be biased depending on the sedimentary setting.

Chapter 2 – A 7,500 year earthquake history in the region of the 2004 Sumatra-Andaman Earthquake

Historic ruptures of the subduction zone fault off shore Sumatra have spatially and temporally spanned the entire length of the subduction zone. Different earthquakes have filled all the space, along strike, from the southern tip of Sumatra to the northernmost extent of the 2004 earthquake slip region. These Sumatra-length coeval ruptures have been documented for various sections of the fault (Sieh et al., 2008; Meltzner et al., 2010, 2012) and may rupture in unison (over months to decades). Twenty-first century ruptures have not yet filled in the entire fault length, along strike, off shore of Sumatra. We may expect more earthquakes in the southern Sumatra margin given the slip deficit measured by Chlieh et al., (2008) in the region of the earthquakes that occurred there in 1797, 1833, 2007, and 2009 (Chlieh et al., 2008; Prawirodirdjo et al., 2010; Philibosian et al., 2012).

We collected 144 piston, gravity, Kasten, and multi- cores in accretionary prism piggy back basins and subduction zone trench settings in order to test our ideas about studying earthquakes by using turbidites. We collected multibeam bathymetry and shallow seismic reflection data to locate our coring sites in places likely to be depocenters for these turbidite systems. Our sediment cores extend the paleoseismic

record into the early Holocene. Our seismic reflection data may extend the paleoseismic record into the latest Pleistocene.

There are many potential triggers for submarine landslides and one of the principal strategies to evaluate each as a likely trigger is based on stratigraphic correlation of these turbidites. Most all non-earthquake trigger mechanisms act upon either site-specific spatial extent (e.g. methane hydrate destabilization or hyperpycnal flow from high river flow) or other regionally limited areas. Alternative triggers that do act upon regions as equally extensive as earthquakes are rarer (e.g. bolide impacts) or more frequent (e.g. tsunamis) than the deposits found in our cores. If deposits can be correlated from sites that have unique sediment sources and the core sites extend over large lateral distances, it is reasonable to interpret them as seismoturbidites (turbidites deposited from seismogenically triggered turbidity currents). I use geophysical properties from the cores, along with the basic laws of stratigraphic superposition, to help me correlate the deposits.

Each paleoseismic method has limitations that impart some filter to their ability to record earthquakes. This depends upon, at least, earthquake magnitude. Coral micro-atoll paleoseismology is limited temporally to ~800 years and in an elevation restricted region near the coast. Tsunami deposits are sensitive to spatial proximity to the ocean and therefore relative sea-level (Dura et al., 2011), in addition to taphonomic/ bioturbation problems in the tropical coastal regions. Turbidites are sedimentary records and are indirect, or secondary evidence of earthquakes. Each of these data sets has limitations in their application to the number and/or aliasing of seismic cycles along the subduction zone (Natawidjaja et al., 2004; Briggs et al., 2006; Natawidjaja et al., 2006; Meltzner et al., 2010, 2012). We need to include all these evidences to obtain a full catalog of large magnitude earthquakes on any given subduction zone.

Using 120 ^{14}C ages, we constrain the timing of seismoturbidites and conclude with a recurrence interval of 260 $\pm$ 160 years for earthquakes in the 2004 SASZ earthquake region. Planktic foraminiferid tests provide organic material for our radiocarbon age determinations. Slope cores are the only cores shallower than the carbonate compensation depth, so are the only cores that have ^{14}C based age control. None of the trench cores have ^{14}C based age control. We use radiocarbon age models to better constrain the timing of deposition for the turbidites in our cores.

I also investigate sedimentological characteristics and use measures of relative and radiometric age for the uppermost turbidite in cores collected near the 2004 SASZ earthquake region. I interpret the uppermost turbidite in 15 cores to have been deposited as a result of the Mw 9.2 26 December 2004 Sumatra-Andaman subduction zone earthquake. ^{210}Pb and ^{14}C age determinations support this interpretation.

Chapter 3 – Seismoturbidite Record as Preserved at Core Sites along the Cascadia and Sumatra-Andaman Subduction Zone

Turbidite paleoseismology has been a successful tool in regions where an understanding of the flow systems and pathways can be developed in order to maximize the potential for successful core site selection (sites that have good stratigraphic records). I evaluate the turbidity current pathways in the Sumatra and Cascadia margins to help me interpret the stratigraphy cored offshore Sumatra. Source proximity, basin effects, turbidity current flow path, earthquake rupture patterns (both temporal and spatial), hydrodynamics, and topography all likely play roles in the deposition of the turbidites as evidenced by the vertical structure of the final deposit. Channel systems tend to promote low-frequency components of the content of the current over longer distances, while more proximal slope basins and base-of-slope apron fan settings result in a turbidite structure that is likely influenced by local physiography and other factors

The sedimentary systems of the continental slope and abyssal plain offshore Sumatra and Cascadia are controlled by the tectonics of the accretionary prism and by the glacial history of the regional and local sources of terrestrial sediment (Stow, 1990; Underwood, 2005). There is a wide range of sedimentary settings in both margins. While Cascadia has a local source of sediment, especially during low sea-level stands and during glacial periods of increased sediment supply, Sumatra has mostly the sediments that are uplifted into the accretionary prism originally sourced from the Bengal and Nicobar fans. Because of this difference in sediment supply, Cascadia has large turbidity current channel systems that tend to promote turbidity current propulsion (Goldfinger et al., 2012, 2013). These active channel systems are absent along the trench offshore Sumatra (Patton 2013), so turbidity currents may not travel great distances and turbidites may be more proximal in nature (making them more difficult to correlate).

Chapter 4 – Slope Stability: Factor of Safety along the Seismically Active Continental Slope Offshore Sumatra

In order to test the hypothesis that slopes along the Sumatra margin are susceptible to seismic loading, we conduct slope stability Factor of Safety (FOS) analyses for seafloor surfaces imaged with multibeam bathymetry. I first model static slope stability and then apply a seismic load for a pseudostatic stability analysis. I evaluate ground motion prediction equations and select two empirical forms to derive seismic loads for these FOS analyses. I estimate Arias Intensity and Peak Ground Acceleration for submarine slopes from earthquakes of magnitudes M = 6, 7, 8, and 9.

Balancing driving forces with resisting forces, we conduct regional analysis using infinite slope Newmark displacement techniques (Newmark, 1965) for translational style landslides. First we use static conditions to test that slopes are stable under static conditions. Then we apply a seismic load for this same regional analysis for a pseudostatic FOS analysis. Secondly we conduct a series of site-specific Morgenstern-Price type Method of Slices (Morgenstern and Price, 1965; Morgenstern, 1967) static and pseudostatic analyses for slopes immediately upslope of our core sites. I iterate seismic loads to determine the critical seismic acceleration required to induce slope failures along these 2-D profiles.

Based on the regions that drain to some core sites in the region of the 2004 SASZ earthquake, I evaluate the possible seismic contribution to slopes that deliver to those core sites. These core sites have sedimentary source areas that sample different distances to the fault, similar ranges of slopes, and, in the case of the 2004 earthquake, different distances to the heterogeneous slip patch. Sedimentary evidence probably from the 2004 SASZ earthquake supports our interpretation that depositional setting (geomorphology) can be a major factor controlling turbidite deposition.

All slope and trench sites are statically stable (FOS < 1) and sensitive to ground motions generated by earthquakes of magnitude greater than 7. We conclude that for earthquakes of magnitude 6 to 9, PGA of 0.4-0.6 to 1.4-2.5 g would be expected, respectively, from existing GMPE's. However, saturation of accelerations in the accretionary wedge may limit actual accelerations to less than 1 g (Skarlatoudis and C. B. Papazacho, 2012; Stewart et al., 2013). Arias intensities of 0.4-1.7 to 7.9-33 m/s are estimated for the M = 6 and M = 9 events, respectively, are expected in the

source regions of piggyback basins for local slope failures. Typical sites have mean Dn displacements of 0.1, 1.6, 7.7, and 16 cm for earthquakes of M = 6, 7, 8, and 9; suggested thresholds for displacement range between 5 and 10 cm. Thus the observed turbidite stratigraphy in the Sumatra piggyback basins can be explained by local ground motions during earthquakes with magnitude greater than ~7, given the static stability. Ground shaking along the continental slope offshore Sumatra is a function of distance to the fault ("Rdist") for generic earthquakes and for the 2004 SASZ earthquake (Sorensen et al., 2007). Landslide dimensions may relate to Mw and Rdist, but possibly dominated by site conditions. Estimates of ground motion depend upon the rate of attenuation with distance (i.e. the shape of the attenuation curve; PGA vs. AI).

Conclusion

The combination of the methods described in these three chapters provides independent ways of evaluating the sedimentary record of earthquakes along the subduction zone offshore Sumatra. Geophysical and stratigraphic based correlations of sedimentary deposits are supported by ^{14}C analyses, seismic reflection records, and tephrologic analyses. Core site isolation from terrigenous sources, and from each other, further support our interpretations. The antecedent sedimentary pathways present in Cascadia are absent in Sumatra, explaining the proximal nature of sedimentary deposits cored in the trench. Seismic slope stability analyses, at the regional- and site-scale, also support the hypothesis that earthquakes may trigger landslides along the accretionary prism offshore Sumatra, Indonesia. Core site selection is vital and some favorable factors include: high relief sedimentary source areas, close distance to the fault and slip patches, locations away from segment boundaries, and channelized turbidite systems.

A 6,500 year earthquake history in the region of the 2004 Sumatra-Andaman Earthquake

Jason R. Patton[1], Chris Goldfinger[1], Ann E. Morey[1], Ken Ikehara[2], Chris Romsos[1], Joseph Stoner[1], Yusuf Djadjadihardja[3], Udrekh[3], Eddy Zulkarnaen Gaffar[4].

1. College of Oceanic and Atmospheric Sciences, Oregon State University, Corvallis, OR 97331 USA. 2. National Institute of Advanced Industrial Science and Technology. 3. Bandan Penghajian Dan Penerapan Teknologi BPPT 2nd Building, 19th Floor, Jl.MH. Thamrin 8, Jakarta, 10340 Indonesia, 4. Geotechnology LIPI Bandung.

Chapter 2 Abstract

In order to investigate the possibility of a long term paleoseismic record from offshore sedimentary records in Sumatra, we collected 144 deep sea sediment cores in the trench and in lower slope piggyback basins of the Sumatra accretionary prism. We used multibeam bathymetry and seismic reflection data to develop an understanding of catchment basins, turbidity current pathways, and depositional styles, as well as to precisely locate our gravity, piston, Kasten, and multi- cores. We use detailed physical property data, including Computed Tomographic X-Ray- (CT) and Gamma-density, magnetic susceptibility, and CT imagery to evaluate the turbidite stratigraphy at each site, and to test for potential correlations between isolated sites in piggyback basins and the trench. We use radiocarbon age control for most piggyback basin sites above the Carbonate Compensation Depth (CCD), and use ^{210}Pb and ^{137}Cs to evaluate the timing of the most recent sedimentary deposits.

Along the northern Sumatra margin, we find evidence for very young turbidites, most likely emplaced within the past few decades, at the seafloor in both the 2004 and 2005 earthquake rupture zones with no overlying hemipelagic sediment. We observe rapid die-out of these deposits with distance from the slip zones, from local sources of sediment supply, and in the segment boundary between the slip zones. The likely 2004 turbidite has a distinctive stacked structure of three major fining upward sequences observed at several basin and trench sites. Many individual turbidites show strong similarities between isolated sites, as well as having similar emplacement times. The correlated beds at slope sites do not appear to extend south of the 2004 rupture area, but may do so in the trench. The most probable explanation for the similarity of timing and individual turbidite structure in isolated basin and trench stratigraphic sequences is a seismogenic origin.

Based on these observations and radiocarbon based age control, our lithostratigraphic correlations between isolated basin and trench core sites supports the interpretation that 28 turbidites can be linked spatially over a distance of 350 km within the southern portion of the 2004 Sumatra-Andaman subduction zone earthquake rupture zone. The mean interseismic time, or recurrence Interval (RI) estimate, for probable strong to great (magnitude > 6) earthquakes in the 2004 rupture region for the last 6.5 ± 0.06 ka is 260 ± 160 years. The ages of eight of the eleven uppermost beds are consistent with the terrestrial paleoseismic/tsunami records in Thailand, Sumatra, and the Andaman Islands. We interpret the uppermost turbidite in 15 cores to have been deposited as a result of the Mw 9.2 26 December 2004 Sumatra-Andaman subduction zone earthquake. ^{210}Pb and ^{14}C age determinations support our interpretation.

2-1.0 Introduction

Following the Mw 9.2 26 December 2004 Sumatra-Andaman and 11 March 2011 Tohoku-Oki subduction zone earthquakes and tsunamis, earthquake geologists have been re-evaluating global models of subduction zone earthquake recurrence (i.e. Ruff and Kanamori, 1980; Shimazaki and Nakata, 1980). Given the short record of historic earthquakes (a few centuries) and the knowledge that many subduction zones have great (M > 8) earthquake return periods that span multiple centuries, it has been difficult to properly document, characterize, and develop new models of their recurrence (Wesnousky, 1994; Murray and Segal, 2002; Satake and Atwater, 2007; Stein and Okal, 2007; Hindle and Mackey, 2011; Schlagenhauf et al., 2011; Colela et al., 2012; Kagan, 2012; Parsons, 2012; Parsons et al., 2012; Béjar-Pizarro et al., 2013; Davis et al., 2013; Goldfinger et al., 2013; Heki and Mitsui, 2013; Ide, 2013; Kopp, 2013; Ninis et al., 2013). Many aspects of subduction zone seismogenesis have been evaluated to understand the likelihood of size or timing of future earthquakes (Chlieh et al., 2008; Ruff and Kanamori, 1980; and Wiseman and Bürgmann 2011); parameters include: lower plate age, convergence rate, fault coupling ratio, seismicity, geodesy, etc. Paleoseismology can reveal the behavior of a fault through multiple earthquake cycles by using longer time spans than possible with historical and instrumental records (McCalpin, 1996; Goldfinger et al., 2012). Proxies for earthquake magnitude found in the paleoseismic record may eventually provide some measure of the cycling of plate convergence rates through time (Goldfinger et al., 2012 a, 2013 a). Submarine (and sublacustrine) paleoseismology is benefitted because the sedimentary record, while it comprises secondary evidence for earthquakes (McCalpin,

2009), can commonly be well preserved for long time scales.

Strong ground shaking from earthquake rupture has been inferred to trigger turbidity currents that potentially deposit a very long record of past earthquakes in the form of turbidites (Dallimore et al., 2005; Enkin et al., 2013; Goldfinger et al., 2003, 2008, 2012 a; Inouchi et al., 1996; Karlin et al., 2007; Noda 2008; Rajendran et al., 2008; Shiki 2000; Nakajima and Kanai, 2000; St-Onge et al., 2004, 2012). The combined evidence from sedimentology, tests of synchroneity, stratigraphic correlation, and analysis of non-earthquake triggers can be used to develop a reliable earthquake record for submarine fault zones, in some cases (Adams, 1990; Karlin and Abella, 1992, 1996; Karlin et al., 2004; Moernaut et al., 2007; Drab et al., 2012; Goldfinger et al., 2012; Gràcia et al., 2012; Pouderoux et al., 2012; Barnes et al., 2013; Smith et al., 2013).

In this paper, we describe our initial results from a submarine paleoseismic investigation conducted offshore of Sumatra in the region of the 26 December 2004 Mw 9.2 earthquake (Ishii et al., 2005; Subarya et al., 2006; Chlieh et al., 2007; Stein and Okal, 2007). We introduce the geologic setting and our rationale for examining the stratigraphic record for evidence of earthquakes, or the lack thereof. Building on an initial examination of styles of sediment transport (Patton et al., 2013), we closely examine the marine turbidite stratigraphy and event timing to test for the possibility of regional synchronous deposition during earthquakes.

2-1.1 Sumatra Andaman Subduction Zone Plate Boundary Seismicity

The December 26, 2004, Mw ~9.2 earthquake that struck Sumatra and the Andaman - Nicobar Islands (e.g., Park et al., 2005), resulted in a tsunami that inundated coastal communities around the Indian Ocean, killing over 220,000 people. This earthquake was followed by the Mw 8.7 Nias earthquake in March, 2005 (e.g., Hsu et al., 2006; Briggs et al., 2006), and by further earthquakes in 2007 (e.g., Konca et al., 2008) and 2010 (Newman et al., 2011). These earthquakes all ruptured sections of the megathrust between the subducting India-Australia plate and the overriding Burma-Sunda microplate (**Fig. 2-1**), and they appear to constitute a repeating rupture series (Sieh et al. 2008). The 2004 and 2005 events were the first great subduction earthquakes in this region to be analyzed using advanced seismological and geodetic techniques.

Historic SASZ earthquakes in the 2004 rupture zone (Chhibber, H. 1934; Bilham, 2005; Malik et al., 2011: 1679, 1762, 1847, 1881, and 1941) were much smaller (magnitude <

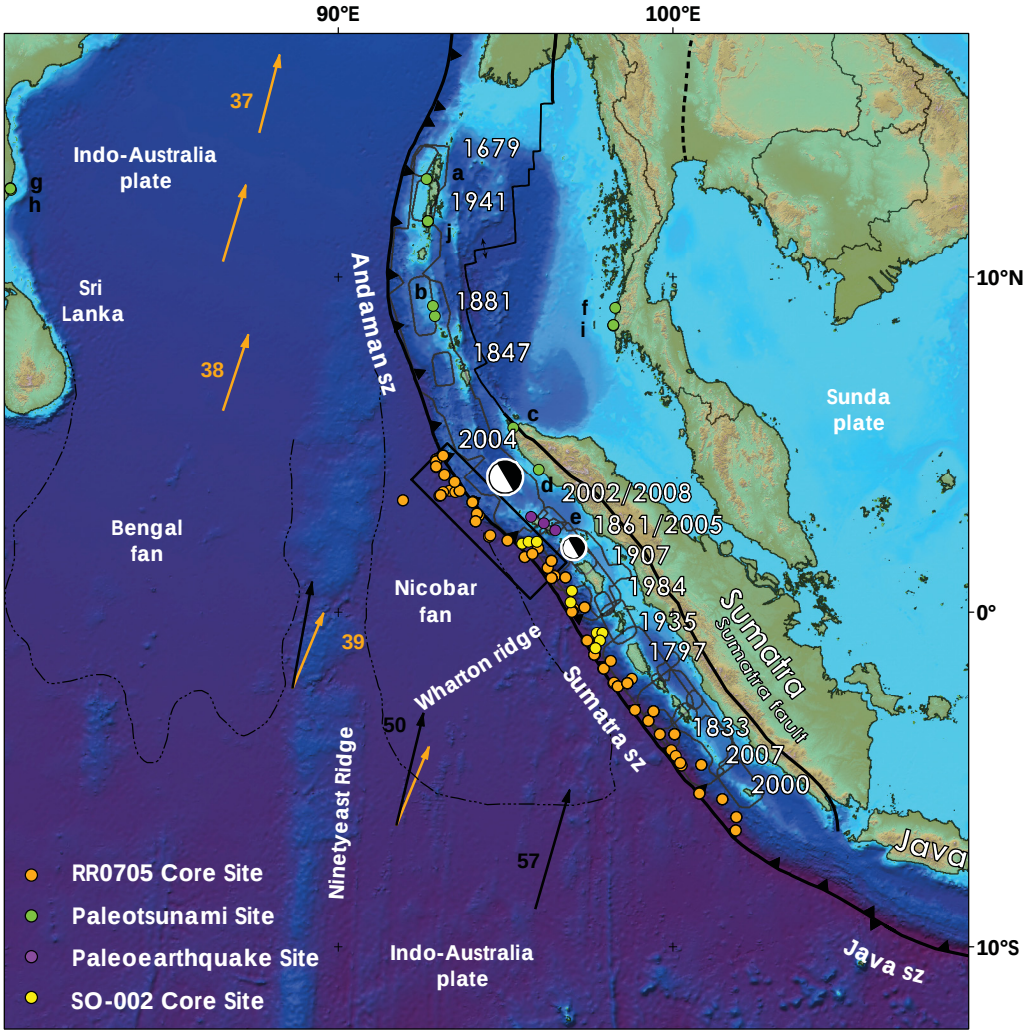

Figure 2-1. Plate-Tectonic Setting. SRTM bathymetry and topography is in shaded relief and colored vs. elevation (Smith and Sandwell, 1997).The India-Australia plate subducts northeastwardly beneath the Sunda plate (part of Eurasia) at modern rates (GPS velocity based on Nuvel-1A; Bock et al., 2003; Subarya et al., 2006): India/Australia are black vectors and Australia/Asia are orange vectors. Historic ruptures (Bilham, 2005; Malik et al., 2011) are plotted in grey, with years of rupture in white. Paleotsunami and paleoearthquake sites are plotted in green and labeled with a letter: a (Rajendran et al., 2007), b (Rajendran et al., 2007), c (Grand-Pre et al., 2008), d (Monecke wet al., 2008), e in purple (Meltzner et al., 2010), f (Jankaew et al., 2008), g (Rajendran et al., 2008), h (Nair et al, 2010), I (Rhodes et al., 2011), j (Malik et al., 2011). RR0705 cores are plotted in orange, SO-002 cores are plotted in yellow (Sumner et al., 2013). The location of **Fig. 2-3** and **Fig. S 2-2** is shown as a black rectangle. Bengal and Nicobar fans cover structures of the India-Australia plate in the northern part of the map, are delimited on their southern boundary with dashed black lines (Stow et al., 1990).The 2004 and 2005 earthquake epicenters are plotted.

8.0) than the 2004 earthquake (**Fig. 2-1**). Historic earthquakes further south along the margin were also generally of smaller magnitude, north to south: 2002 M = 7.3, 1861 M = 8.6, 1907 M = 7.6, 1984 M = 7.9, 1935 M = 7.7, 1797 M = ~8.6, 1833 M = ~9; 2000 M = 7.9; 2007 M = 8.4, 7.9; 2009 M = 7.5; 2010 M = 7.8 (Newcomb and McCann, 1987; Rivera et al., 2002; Abercrombie et al., 2003; Natawidjaja et al., 2006; Konca et al., 2008; Bothara, 2010; Kanamori et al., 2010; Philibosian et al., 2012). Recent investigations of secondary evidence left behind by tsunami as sand sheets in northern Sumatra (Monecke et al, 2007), Thailand (Jankaew et al., 2008), and the Andaman-Nicobar (A-N) Islands (Rajendran et al., 2008), along with coral microatoll evidence (Meltzner et al., 2010; 2012; Philibosian et al., 2012) suggest the penultimate subduction zone earthquake most likely occurred 500-700 years ago, and an ante-penultimate earthquake/tsunami in Sumatra (Monecke et al, 2007; Rajendran et al., 2008), the Andaman and Nicobar Islands (Rajendran et al., 2008), and India (Rajendran, 2007) likely occurred ~ 900-1,200 years ago. These initial studies suggested that recurrence of Mw>8 earthquakes is about half a millennia within the past 1,200 years.

The southern 2004 rupture was centered beneath a ~150 km-wide forearc plateau which contrasts with the typical wedge structure of many accretionary margins (Moore and Karig 1980; Henstock et al., 2006; Fisher et al., 2007). The rupture initiated near Simeulue Island, and propagated up-dip and northwestward at 2-2.5 km/sec (e.g., Ammon et al., 2005; Ishii et al., 2005; Chlieh et al., 2007; their Figs. 1, 3). Moment release appears to have been concentrated in three main patches that were captured in nearly all inversion models (Ni et al., 2005; Tolstoy and Bohnenstiehl, 2006; Ishi et al., 2008; Chlieh et al., 2007). Offshore N Sumatra, the location of the greatest seismic moment release (e.g., Ammon et al., 2005), the rupture propagated relatively far seaward beneath a large part of the forearc plateau/prism, and was not focused beneath the forearc basins as suggested by some recent models (Wells et al., 2003; Song and Simons, 2003). In contrast, slip during the 2005 rupture was concentrated beneath the forearc islands and did not propagate co-seismically beneath the seaward-tapered wedge. Velocity strengthening slip occurred up- and down-dip post-seismically over the next few months (Hsu et al., 2006).

2-1.2 Physiography of the Sumatra Andaman Subduction Zone

The Sumatra Andaman subduction zone (SASZ) is formed by the Indo-Australia plate subducting 50-70 mm per year at ~N30E beneath the Burma microplate of Eurasia (**Fig. 2-1**; Bock et al., 2003; Subarya et al., 2007). Continental margin morphology in western

Sumatra is dominated by the upper plate structure of a Tertiary and Quaternary accretionary prism with structural highs and forearc basins (Karig et al., 1980; Fisher et al., 2007). Fold and thrust belt topography forms longitudinal, discontinuously linked basins that can be either isolated, or drain to the trench. Canyon systems tend to be short and drainage catchments are relatively small, limiting the potential areal extent of source areas for turbidity currents (Graindorge et al., 2008).

The absence of trench-parallel channel systems offshore Sumatra is likely due to the low late-Pleistocene sedimentation rate and the interruption of the trench by subducting features. Southward transport in the trench is thought to be cut-off from Himalaya derived sediment by a large landslide at 14° north (Moore et al., 1976) and the intersection of the ninety-east ridge with the subduction zone trench (**Fig. 2-1**). The outer forearc is isolated from northern Sumatra terrestrial sediment sources by the broad, unfilled Aceh forearc basin (Matson and Moore, 1992).

The trench deepens southward from 4.5 km to 6.5 km, from 5° N to 7° S, and is filled with sediment several km thick in the north from the Nicobar fan, partially burying lower plate structures that trend across the trench (Dean et al., 2008; Graindorge et al., 2008). The outer forearc is sedimentologically isolated from northern Sumatra by the longitudinal forearc basin, which is comprised of the Aceh, Simeulue, Nias, Pini, Siberut, and Bengkulu Neogene forearc sub-basins (Sieh et al., 2000; Susilohadi et al., 2005). Sediment input from the offshore islands of Simeulue, Nias, and Siberut Island is possible for some basins in the central and southern Sumatra outer margin. Lack of input from the forearc basin and from northern sediment sources results in recent sediment starvation, thus the abyssal seafloor topography is dominated by trench sub-parallel bending moment normal faults and north-striking fracture zones. Topography is controlled largely by the blocks of sediment up to 4 km thick (Bandopadhyay and Bandopadhyay, 1999; Fisher et al., 2007) uplifted from the Indo-Australia plate (likely by duplexing of the accretionary complex) to form the upper part of the accretionary prism and marginal plateau (Fisher et al., 2007; Mosher et al., 2008; Gulick et al., 2011). Through-going submarine canyon systems are absent, but short canyon systems linking some basins in short paths through the outer slope to the trench exist (Patton et al., 2013, their Fig. 1). Many basins do not drain to the trench and have an expanded Holocene section (e.g. Lamb et al., 2006). Outer forearc canyon systems have channels only on the flanks of the lower slope

and these channels die out in the trench, trending to the south, within ten's of km from the canyon mouths. This morphology controls turbidite channel flow within the trench, which is possibly unmixed and dominated by proximal sedimentary processes (Patton et al., 2013).

2-1.3 Turbidite Paleoseismology and Rationale as Applied to the Northern Sumatran Margin

Paleoseismology is the study of evidence for past earthquakes. Primary evidence of past earthquakes generally involves the identification of sedimentary deposits (including soils) that have been offset by fault rupture, typically found in an excavation of ground across the fault (McCalpin, 2009). Secondary evidence of past earthquakes is interpreted from sedimentary deposits that contain evidence of the fault motion from an earthquake (Atwater and Hemphill-Haley, 1997; Goldfinger, 2009). The paleoseismology of subduction zone faults is primarily based on secondary evidence because the subduction zone fault is located in the submarine setting, where fault trenching is not yet possible. Examples of secondary evidence for subduction zone earthquakes include tsunami deposits (Hemphill-Haley, 1995), buried marsh soils (Atwater, 1987), landslides (Wilson and Keefer, 1985; Schulz et al., 2012)), and turbidites (Goldfinger et al, 2003).

Paleoseismicity in lacustrine and marine environments has been tested and applied in numerous localities globally, under a variety of conditions of climate, sedimentation rate, subaqueous setting: Lake Baikal (Lees et al., 1998 a, b), Ecuador (Ratzov, et al., 2010), Iberian margin (Gràcia et al., 2010), Chile (Moernaut et al., 2007), Kumano trough, Japan (Shirai et al., 2010), Lake Washington, Washington (Karlin et al., 1992, 1996, 2004), Lake Tahoe, California (Karlin et al., 2004), Okinawa trough, Japan (Huh et al., 2004, 2006), central Switzerland (Monecke et al., 2006), Saguenay Fiord, Canada (Syvitski et al., 1996; St-Onge et al., 2004), Canadian arctic (Grantz et al., 1996), Kuril trench (Noda et al, 2008), Lake Biwa, Japan (Shiki 2000), southern margin Japan (Abdeldayem et al., 2008), Cascadia (Goldfinger et al., 2003; 2012; Pastor et al., 2009, 2012; Enkin et al., 2013; Blaise-Stevens et al., 2011), the Northern San Andreas fault in California (Goldfinger et al., 2003; 2008); south and south-central Chile (Moernaut et al, 2007; Van Daele et al., 2013), Gulf of California (Gonzalez-Yajimovich et al., 2007), the Santa Barbara basin (Gorsline et al., 2000), Lake Biwa (Inouchi et al., 1996), eastern Japan Sea (Nakajima, 2000), and Marmara Sea (Sari and Çağatay, 2006).

Earthquakes are well known as subaerial landslide triggers, with a possible minimum triggering earthquake magnitude of M ~ 5 (Keeper, 1984). Landslide density is found to be greater in areas of stronger ground acceleration (Meunier et al, 2007). Earthquake magnitude thresholds for submarine landslides are less well constrained than subaerial landslides (M~ 7.1 in Cascadia, Goldfinger et al., 2012, 2013 a; M = 7.4 in Japan, Nakajima and Kanai, 2000; M = 7.3 in northern California/Cascadia, Wilson and Keefer, 1985; Rollins and Stein, 2010; M = 5.2 in Venezuela, Lorenzoni et al, 2012), probably because the evidence of minimum values is largely lacking. Earthquakes are posed as one of the dominant submarine landslide triggers (Ross, 1971; Almagor and Wiseman, 1977; Hampton et al., 1978, 1996; Masson et al., 2006), with most historic examples attributed to ground accelerations from earthquakes (Mosher et al., 2010).

Submarine landslides may transform into turbidity currents that leave behind deposits called turbidites (Morgenstern, 1967; Stow and Bowen, 1980; Felix and Peakall, 2006); known as seismoturbidites or seismites when earthquake triggered. Turbidity currents are turbulence driven (autosuspension) sediment rich gravity flows (Bouma, 1962; Middleton, 1967; Kneller and Buckee, 2000). The sedimentary sequence of an individual deposit reflects the time-history of deposition from the turbidity current as it passes a sedimentary depositional setting (Baas et al., 2004). In other words, the vertical structure of a turbidite is a sampling of the longitudinal velocity and density structure of the causal turbidity current (Lowe, 1982; Kneller and McCaffrey, 2003). Early assumptions were that turbidity currents are the result of a single impulse of sediment into the system, and that multiple fining upward sequences were due to erosion of later currents into younger ones (Ericson, 1952; Kneller and McCaffrey, 2003). More recent studies have revealed that sometimes the input of sediment into the turbidity current was not singular, but was likely formed from a heterogeneous (with time) flux of sediment (Lowe, 1982; Piper et al., 1999; Nakajima and Kanai, 2000, Kneller and McCaffrey, 2003; Goldfinger et al., 2008; 2012 a; Pastor et al., 2012). For this and other reasons, it is difficult to interpret the physical components of a turbidite based on a single or a few cores without having core data sampled from upstream and downstream within the same channel system (Kneller, 1995), and within multiple systems in the case of regionally triggered multiple currents.

Adams (1990) and Goldfinger et al. (2003, 2012 a) suggest eight plausible triggering mechanisms for turbidity currents: 1) storm wave loads, 2) earthquake loads, 3) tsunami wave loads (local or distant), 4) sediment loads, 5) hyperpycnal flows, 6) volcanic

explosions, 7) submarine landslides, and 8) bolide impacts. In addition to these triggers, tidal bottom currents may be included in this list (Thomson et al., 2010). Of the possible landslide triggers listed by Adams (1990), Sultan et al. (2004), and Goldfinger et al. (2010, 2012 a), only bolide impacts, hyperpycnal flows, tides, wave loads, gas hydrate destabilization, and earthquakes can directly trigger submarine landslides, as other phenomena may simply precondition the slope for failure (Goldfinger et al., 2012 a). This subset of triggers can be evaluated in terms of plausibility, expected frequency, sedimentology, aerial extent, and correspondence to other evidence onshore, and other factors. Some suggest turbidite structure is evidence that autocyclic forcing dominates turbidite deposition (Kneller and McCaffrey, 2003; Dennielou et al., 2006), but they do not consider a longitudinal change in sediment flux within the turbidity current. Others suggest that the allocyclic forcing of turbidity currents is preserved in the turbidite structure because the current flows were triggered by a shared source, possibly due to earthquakes (Morey and Goldfinger, 2004; Garret et al., 2011, Goldfinger et al., 2011, 2012 b). Amalgamation is posed as an indicator that the turbidites were deposited from multiple turbidity currents, merging and forming a longitudinal structure reflected in the deposit (Nakajima and Kanai, 2000), possibly from multiple slides on slopes. In Lake Biwa, Nakajima and Kanai (2000) conclude these multiple pulses are the results of synchronous triggering of multiple parts of the canyon system. It is likely a combination of multiple factors. The turbidite correlations in Sumatra are in some part based on the correlation of shared turbidite structures between cores (Goldfinger et al., 2012 a; Patton et al., 2013). Goldfinger et al. (2003, 2007, 2008, 2012 a) and Morey and Goldfinger (2004) attribute a seismogenic trigger to Cascadia turbidity currents through stratigraphic correlation of turbidites with shared sedimentary structures (i.e. “fingerprints”), supported by a framework of depositionally constrained radiocarbon ages and relative age tests, demonstrating that they represent synchronous deposition (Goldfinger et al., 2012; 2013 b).

The study of turbidite paleoseismology is the most well developed for the Cascadia subduction zone (CSZ; Goldfinger et al., 2012 a, 2013 a). The seminal work of Adams (1990) used a tephra datum (Mazama Ash, approx. 7.7 ka; Bacon, 1983; Zdanowicz et al., 1999; Klug et al., 2002; Bacon and 2006) and a confluence of separate channels to constrain the number of turbidites above the tephra in each core (confluence test; Adams, 1990), and is in part the basis of the original case for seismogenic triggering of these turbidity currents. What also contributed to the success of the work in Cascadia was the extensive research done on both the turbidite systems offshore, and the terrestrial paleoseismol-

ogy in the region, which provided a chronologic framework with which to compare with the submarine results. While others inferred that the CSZ was seismogenic (Adams, 1984), Atwater (1987) found the first evidence of paleodeformation related to subduction zone earthquakes along the CSZ in the form of sand sheets overlying coseismically subsided intertidal deposits. Thereafter, more evidence of paleodeformation, paleotsunami, and paleoliquefaction was found and compiled into a large catalog of paleoseismic events that had variations in space and time (Petersen and Madin, 1997; Obermeier et al., 2000; Kelsey et al., 2002; Leonard et al., 2004; Kelsey et al., 2005; Nelson et al., 2006; Goldfinger et al., 2008; 2012). Onshore, it was not possible to directly correlate stratigraphic evidence from site-to-site because the terrestrial sedimentary evidence was discontinuous between sites north to south (Nelson et al., 2006). It was not until the submarine record was developed that the spatiotemporal linkages could be made between offshore sites, and with less certainty, to the existing terrestrial records (Goldfinger et al., 2008, 2012 a; Witter et al., 2011, 2013). Unfortunately such an extensive terrestrial record for past earthquakes is not well developed for the SASZ.

In this paper we test the plausibility of a seismogenic trigger as a source for the observed turbidite stratigraphy in northern Sumatra primarily by 1) using tests for synchronous triggering of sedimentologically isolated turbidite systems and 2) using sedimentologic characteristics (e.g. structure) of the turbidites. We apply both tests to aid in discrimination between seismic and non-seismic trigger sources. Radiocarbon age estimates provide constraints to help link turbidite stratigraphy between multiple sites and provide independent tests of our correlations. Our rationale was to seek sites that were sedimentologically isolated from terrestrial sediment sources and from each other, reducing the list of potential turbidity current triggers to just earthquakes and self-failures. With the problem reduced to this simpler case, if turbidites can be correlated between sites separated by a large distance or that are isolated from each other, synchronous triggering can be inferred. Individual linkages are commonly subject to the uncertainties in radiometric age control and interpretation, thus a large number of sites is preferred in order to help overcome these problems and construct tests for synchroneity. While secondary evidence, if synchronous deposition over a wide areal extent is supported by the suite of temporal and spatial criteria, and most or all other triggering mechanisms are unlikely, then seismogenic origin is the most likely mechanism (Goldfinger et al., 2003, 2008, 2012; Shiki, 2000; Gorsline et al., 2000; Nakajima, 2000; Shiki et al., 2000).

2-2.0 Methods

We used primarily 10 cm piston and gravity coring as the primary methods to collect turbidite stratigraphy, supplemented with Kasten-, box-, and multi-cores (the latter two are used to sample the sediment-water interface and the upper-most units with minimal disturbance). 20 cm square Kasten cores are useful as they provide a larger volume of sediment from which volume restricted age samples ($CaCO_3$ foraminiferid tests) are collected.

2-2.1 Site Selection and Coring

As in all geologic and paleoseismic investigations, selecting the best sites is critical. We use continental margin physiography to narrow the selection of sites to those most likely to preserve seismoturbidites, while excluding as many other sources as possible. We located core sites that would be most likely to preserve stratigraphy with deposits that have the greatest dynamic range in particle size (texture) above the background sediment particle size or density. With a large dynamic range in texture, the distinction between hemipelagic mud and turbidite sediment is enhanced, important for calculating background sedimentation rates and sampling for age control. A large dynamic range in texture also helps with stratigraphic correlation, discussed below. Core sites that are too distal have turbidites with very little variation in density and particle size (Kneller and McCaffrey, 2003), making it difficult to characterize the structure of any given deposit. Distal sites in an un-channelized setting may fade very rapidly from local sources (Nelson et al., 1986; Baas et al., 2004, 2005; Johnson et al., 2005; Goldfinger et al., 2012 a; Patton et al., 2013). Conversely, core sites that are too proximal are commonly dominated by a series of amalgamated debrites (Bouma, 2004), making interpretation problematic.

Our rationale for selecting core sites also considers issues of age control, sedimentary isolation, and geospatial relevance to historic and prehistoric fault segments. We select core sites in slope basins due to the absence of usable radiocarbon material in cores collected in the trench. Another benefit of these slope basin core sites is that they typically have isolated submarine landslide source areas. On the other hand, this is a disadvantage for paleoseismology as most coring sites are therefore more proximal to their source which may result in noisier and less distinguishable sedimentary structure that is more difficult to compare from site to site.

We attempt to correlate strata between slope basin and trench cores in order to provide age control to the trench stratigraphy. Initially we focus our correlations on the basin-basin correlations since the radiocarbon is one of the most powerful independent tests of our correlations. The absence of long trench-parallel channel systems in Sumatra however, lends to the potential that a given turbidity current will not travel a sufficient distance along the trench axis, and thus confound its association with a given earthquake by its spatial extent and position alone.

We are not only interested in developing a chronology of earthquakes along this subduction zone, but we are also interested in investigating the spatial limits to past earthquake ruptures. Because recent earthquakes exhibit segmentation, we adopt these segments to help us locate core sites, allowing us to test the idea that there may be some permanence to them. While this premise was untested in 2007, it has subsequently been supported by onshore paleoseismic work (Jankaew et al., 2008; Monecke et al., 2008; Sieh et al., 2008; Fujino et al., 2009; Meltzner et al., 2010, 2012; Dura et al., 2011; Philibosian et al., 2012). We choose core sites that are within these historic and recent prehistoric segments, as well as at the segment boundaries. Since the effects of earthquakes taper rapidly with distance from the fault slip (deformation: Natawidjaja et al., 2004, 2006; Meltzner et al., 2006, 2010, 2012; Sieh et al., 2008; Philibosian et al. 2012; ground shaking: Arias, 1970; Keefer, 1984; Wilson and Keefer, 1985; Wilson, 1993; Campbell, 1997; Kayen et al., 1997; Youngs et al., 1997; Atkinson and Boore, 2003, 2011; Travasarou et al., 2003; Sorensen et al., 2007; Boore and Atkinson, 2008; Zhao et al., 2012), the sedimentary evidences of these earthquakes may also be spatially limited. Sites that receive sedimentary input that has been transported in the trench would violate the spatial limit premise. But in some cases, with sites that have basements with higher underlying seismic velocities, may not taper so rapidly (Jibson and Harp, 2012). Cores that are near segment boundaries may be difficult to correlate because they may either have diminished sedimentary records (deposits with lower dynamic range of density or lesser developed structure) or have records from the overlapping fault segments (possibly for larger magnitude earthquakes). Trench cores are more likely to include records from adjacent slip regions since the trench may transport these turbidity currents, while the slope cores are less likely due to their smaller source areas and shorter transport paths parallel to the margin. Our initial correlations have been focused on cores within each of these fault segments and this is the first paper in a series; focusing primarily on evidence in the region of the 2004 SASZ earthquake in this paper.

Multibeam mapping was essential to evaluate the physiographic setting for the relevant sedimentary systems. Multibeam bathymetry and backscatter data were collected with the Kongsberg EM-120 system on the R/V *Roger Revelle*, and edited on board using "MB-System" so that coring sites could be chosen in real-time (RR0705 Superquakes07 Cruise Report http://www.activetectonics.coas.oregonstate.edu/sumatra/report/index.html). Prior to the cruise, existing bathymetric data were compiled. Sumatra bathymetry was collected by expeditions lead by: Japanese (R/V Natsushima: Japan Agency for Marine Earth-Science and Technology, Jamstec), United Kingdom (HMS Scott: UK Royal Navy and Southampton Oceanography Centre, NOCS), French (R/V Marion Dufresne: Ifremer), and German (R/V Sonne: Federal Institute for Geosciences and Natural Resources, BGR) ships and shared utilizing a cooperative agreement with these international institutions and the Indonesian Government (Agency for the Assessment and Application of Technology, BPPT), without which, our coring study would not have been possible (Henstock et al., 2006; Ladage et al., 2006). The EM 120 has a depth resolution of 10, 20, and 40 cm, for pulse lengths of 2, 5, and 15 milliseconds, and covers depth ranges from 20 to 11,000 meters. After editing the raw data, we visualized and rendered the bathymetric data using Fledermaus and ArcGIS software applications in order to plan for potential core sites.

We extensively used 3.5 kHz Compressed High Intensity Radar Pulse (CHIRP) seismic profiles of the shallow sub-bottom to survey Holocene turbidites stratigraphy in trench and slope basins to aid in core site selection. We used a Knudsen 320BR, (FM CHIRP mode typically sweeping 2 to 6 kHz) at full bandwidth and data rate. These lines were heave-corrected in real time using the ships PosMV320. We post-processed the data using Sioseis (http://sioseis.ucsd.edu/sioseis.html; Henkart, 2011) using band pass filtering, muting, and a heave filtering algorithm. Digital correlation processing of the CHIRP signal reduces the effective frequency, improving the signal to noise ratio and boosting the effective vertical resolution to ~25 cm, degraded somewhat by off-axis "scatterers," vessel motion, and the water column. In addition to the utility of developing a potential core site, these seismic reflection data can reveal the continuity (or lack thereof) of repeated local turbidite sedimentation, local faulting, and mass wasting deposits both within and between sites.

After we selected a core site, we typically deployed a 6.66 cm diameter gravity corer. This core was used as a reconnaissance tool due to the higher velocity that the core can be deployed to the sea floor (100 meters per minute, versus 40 meters per minute for larger diameter cores). For sites where good turbidite stratigraphy was found, we then deployed a 10.14 cm diameter Piston-Trigger core pair. Due to equipment failures

(sheave bearings below deck were incapacitated due to high temperatures near the equator), piston cores were mostly deployed on a rail-road track constructed from spare parts, from the stern deck with the stern A-frame. This configuration limited the length of the piston corer to two core sections (2 X 10'), with a maximum coring depth of 6.09 m (20'). Trigger cores had a maximum coring depth of 3.05 m (10'). The 1,000 to 2,200 kg weight stand (attached to the piston corer) drives the piston core into the seafloor with greater velocity than the trigger corer (possibly eroding surface sediment from the sea floor), thus some core tops are lost from the piston, but not the trigger nor multi-cores. Kasten and Box cores tend to collect the uppermost sediments because of their large aerial extent.

All cores were scanned for geophysical properties (multi sensor core logging (MCSL) including: gamma density, low resolution magnetic susceptibility (MS) using a loop sensor, p-wave velocity, and resistivity) and then split lengthwise and imaged with a Geo-Tek high-resolution line-scan camera, and finally described on lithostratigraphic data sheets. Subsequently, high-resolution point magnetic susceptibility data were collected from each core using a point sensor (Bartington MS2E high-resolution surface sensor) at 0.5 or 1 cm intervals. Following the cruise, cores were then scanned with Computed Tomographic X-ray techniques (CT scans) using a Toshiba Aquilion 64-slice Computed Tomography (CT) unit at 0.5 mm voxel resolution. CT data also provide densostratigraphic information (down-core variation in density) when CT imagery is used for down-core line-scan analysis. CT data permit a refined view of the strata and the effect of core disturbance, while gamma and magnetic data reflect signals that average these effects over a vertical distance related to the amount that the sediment is disturbed vertically. Grain size analysis was done using laser diffraction particle size measurements using a Beckman-Coulter LS 13 -320 laser counter (Blott and Pye, 2006) with a Fraunhofer based Polarization Intensity Differential Scattering (PIDS) optical model. Particle size analyses are limited to a size range of 0.040 μm to 2,000 μm. In a limited number of cores we collected down-core X-ray Fluorescence (XRF) measurements and superconducting rock magnetometer measurements of remnant magnetization. ^{210}Pb and ^{137}Cs isotopic analyses, and Accelerator Mass Spectrometry (AMS) ^{14}C radiocarbon analyses were performed for age control. We also conducted Neutron Activation Analysis (NAA) on a Multi Core, seeking evidence of short-lived radionuclides and isotope chemistry. Core geophysical methods and radiometric age analyses are further summarized in **Appendix S 2-1**.

2-2.2 Age Control

Age control for stratigraphy is provided by Accelerator Mass Spectrometer (AMS) ^{14}C, ^{137}Cs, and ^{210}Pb radiometric techniques. ^{14}C data is based on decay with a half-life of 5,730 years and is useful for strata up to ~50,000 years old (Stuiver and Polach, 1977; Stuiver and Braziunas, 1993; Hughen et al., 2004; Fairbanks et al., 2005; Reimer et al., 2009, 2013). ^{210}Pb data, based on a shorter half-life of 22.3 years (Noller, 2000; Faure and Mensing, 2005), provides information about sedimentary deposition for the past ~150 years. ^{137}Cs data, based on the half-life of 30.17 years (Faure and Mensing, 2005), but may have a shorter effective half -life closer to a decade (Robinson et al., 2003). ^{137}Cs age data can reveal the timing of sedimentation after 1954 (Robbins et al, 1978). We use ^{210}Pb and ^{137}Cs age data to constrain the timing of deposition for the most recently deposited sediments. While ^{210}Pb and ^{137}Cs have similar half-lives, ^{210}Pb input is continuous, while ^{137}Cs input was episodic (Faure and Mensing, 2005). The peak input for ^{137}Cs was during 1962/1963 as a result of fallout from above-ground nuclear testing. Nuclear accidents, like Chernobyl, are an additional source of ^{137}Cs (Faure and Mensing, 2005). ^{137}Cs has been detected in seawater (Alam et l., 1996) and sediments (Michels et al, 2003) in the northern Bay of Bengal.

In order to evaluate the timing of the possible 2004 turbidite with radiometric techniques, we collected sediment samples below the turbidite at 1 cm spacing. ^{210}Pb samples were prepared and analyzed using methods developed by Guillaume St. Onge at Institut des sciences de la mer de Rimouski (Flynn, 1968; St. Onge, 2004; Levesque et al., 2006). ^{137}Cs samples were prepared and analyzed using methods developed by Robert Wheatcroft at Oregon State University (Gilmore and Hemingway, 1995; Wheatcroft and Summerfield, 2005).

To estimate ages of the turbidites using radiocarbon, we extract the calcium carbonate tests of planktic foraminifers preserved in the hemipelagic sediment below each turbidite to provide a maximum limiting age. We utilize planktic foraminiferid species as they most closely represent the age of the youngest sea water, the surface water that is most closely in ^{14}C equilibrium with the atmosphere. We sample below each turbidite because this is the sediment closest in age to the turbidite. We typically do not use the age of the sediment above the turbidite because the boundary between the top of the turbidite tail and the overlying hemipelagic sediment is difficult to identify reliably, and bioturbation

is also concentrated at this boundary. These methods are also outlined in Goldfinger et al. (2012 a).

Sources of sampling error include basal erosion, sediment deformation from coring, differences in stratigraphic thickness between cores, bioturbation, etc. Some of these factors cannot be evaluated readily because of the coring induced deformation of stratigraphic thickness and sedimentary structure (aleatory uncertainty: how well do the sediment cores represent the real sedimentary thicknesses). Bioturbation is difficult to evaluate as a factor controlling age estimates because we do not have multiple cores in a single location that have both bioturbated sedimentary section and non bioturbated sedimentary section. Erosion can be estimated in some cases (Goldfinger et al., 2012), but the tests require multiple cores at a site, and thus we are unable to test this factor due to the lack of multiple cores at most sites. We attempted to estimate erosion, but the cores that were collected in close proximity (<10 km) were not good candidates because some cores had poor turbidite structure, highly bioturbated sediment, or extensive coring deformation. These confounding factors made it difficult to distinguish hemipelagic sediment from turbiditic sediment, to interpret the stratigraphic contacts/boundaries between these deposit types, and to estimate stratigraphic thicknesses for more than one core at any core site.

Other sources of uncertainty include factors that affect some of our assumptions regarding how well the sediment age actually represents the time of deposition for the turbidite. Sources of this type of epistemic uncertainty include changes in the age of the surficial sea water at the time of deposition, changes in carbon export to the seafloor (rate of foraminiferid sedimentation), changes in species distribution through time, etc. Changes of the age of seawater can be affected by upwelling, bringing older water to the surface, making the sediment appear older in radiocarbon years. If carbon flux to the seafloor increases during the time the sample represents, the age determination would be biased to an age representing the higher carbon flux (this would change the concentration of forams per unit volume of sediment, biasing the age towards the time that had a higher concentration of foraminiferid tests). If the species distribution changes through time, if deeper shallow water species might dominate, the age of the sediment would be older. We do not have sufficient data to evaluate nor test these sources of aleatoric uncertainty.

Sediment samples were removed from the cores while avoiding the 0.5 cm of material nearest the core walls to avoid visible or undetected deformation and friction drag along the core walls. In some cases, highly irregular turbidite bases resulted in sampling an interval below the basal irregularities. We corrected these ages by subtracting the time represented by the sediment "gap." Hemipelagic sediment samples were freeze dried to separate clay particles to improve rinsing through a sieve, washed in a dilute Calgon^{tm} (sodium hexametaphosphate) solution to keep the fine particles in suspension, sieved through a 125 µm stainless steel sieve, then dried in a warm oven. Typically 25-50 individual planktic foraminifers (depending on size and mass) are identified and removed from this dried > 125 µm size fraction using a fine sable brush moistened with distilled water. Foraminiferal sample ages are determined using Accelerator Mass Spectrometry (AMS) methods at the Keck AMS facility at University of California, Irvine in collaboration with John Southon.

Radiocarbon age reporting follows a set of standards (Stuiver and Polach, 1977). "Lab" radiocarbon ages are reported in years before present (BP, measured from 1950) with a two standard deviation lab error (Stuiver et al, 1998). We used OxCal V 4.2.3 to calibrate ^{14}C ages (Stuiver and Braziunes, 1993; Bronk Ramsey, 2009; Reimer et al., 2013). We applied a marine reservoir correction to account for the marine reservoir for marine radiocarbon samples. In addition to the global marine reservoir, we apply an additional regional correction (ΔR) of 16±11 years using the IntCal13 and Marine13 databases (Reimer et al., 2013). Only two ΔR values are available for the Sumatra area and these (like nearly all ΔR values globally) are based on latest Holocene ages (located north of Sumatra and south of Sumatra). While constraints are few for this correction and do not extend far into the past, we are correlating marine sites to other nearby marine sites, so the local correlations are likely valid (absolute ages will contain additional uncertainty). We used a sedimentation rate based age model which allows estimation of turbidite emplacement ages, accounting for gaps between the sample and turbidite base. We propagated all uncertainties using root mean square (RMS) calculations using estimates of the uncertainties at each step. This calculation included the lab uncertainties, and resulted in the final reported 95.4% error range for each radiocarbon age (see OxCal code **Table S 2-1**). We use a moving average hemipelagic sedimentation rate (see **Appendix S 2-1** for a more detailed description). This calculation includes the lab uncertainties and yields the final reported 95.4% error range for each radiocarbon age. No lab multipliers were

applied to the data because labs now include the uncertainty in their results that was previously accounted for by the lab multiplier (Scott et al., 2003; Goldfinger et al., 2012 a).

We construct a series of OxCal age models to incorporate stratigraphic information into the age calibrations. OxCal uses Bayesian statistics to incorporate prior information (e.g. stratigraphic or age progressive information) into the age calibrations (Bayes and Price, 1763; Bronk Ramsey, 2008). OxCal age models are constructed with two components: the model structure (priors) and the age measurements (likelihood). Because age depositional models often have many independent parameters, OxCal uses Markov Chain Monte Carlo (MCMC) simulations to sample age distributions and generate a final distribution (Bronk Ramsey, 2009). We also build our OxCal age models with nested functions, such as the "Combine" function (discussed below).

For our OxCal age models, we use two depositional models: Sequence and P_Sequence (Bronk Ramsey, 2009). The "Sequence" model considers the stratigraphic order (superposition) of the ages. The "P_Sequence" model considers the stratigraphic order and the relative stratigraphic depth. We use the P_Sequence model for age calibrations within cores because we can make estimates of stratigraphic depth within a core. Because the relative depths are different between cores (due to differences in hemipelagic sedimentation rates and sampling errors), we cannot use P_Sequence, so we use the Sequence model.

For the P_Sequence model, we constrain the depth by using the hemipelagic depth for the samples (Bronk Ramsey, 2009). Because turbidites represent instantaneous changes in sedimentation rate, they do not reflect the long term sedimentation rate between turbidite emplacements. For this reason, we remove the depth associated with the turbidite thicknesses. We also use the OxCal "Date" function to generate synthetic ages for the bases of turbidites that have no direct radiocarbon age sample (Bronk Ramsey, 2001).

For our Sequence age model (Bronk Ramsey, 2009), we use ages from all slope cores in the region of the 2004 SASZ earthquake. There are three ways in which we estimate the age of the correlated turbidites: single ages, combined ages, and synthetic ages. Some correlated turbidites have only a single radiocarbon age determination and this is the age we include in our model. For correlated turbidites that have multiple ages, we use

the OxCal “Combine” function (Bronk Ramsey, 2001). We use our stratigraphic correlations to determine which lab ages to consider for all age Combines. The Combine function takes the lab age Gaussian distributions and combines these distributions prior to calibration. OxCal performs tests to evaluate how well the combined ages fit their combined age distributions. Below we discuss ways in which we discriminate ages that do not pass these tests of best fit. The results of these tests are included in the log file (**Appendix S 2-1**). As with the P_Sequence model, for turbidites that do not have radiocarbon age determinations, we generate synthetic ages with the OxCal “Date” command.

We also provide temporal limits to the posterior age distributions with the OxCal “Boundary” function (Bronk Ramsey, 2008, 2009), a “prior.” We place a Boundary at the “beginning” of the model (oldest) so that the modeled age determination for the earliest age does not significantly extend into the past. We place a boundary and the “end” of the model (youngest) because the sediment cannot be younger than 2007, the year the sediment was collected. We use these boundary functions in the P_Sequence and Sequence age models.

The Combine function calculates a chi-squared test to determine if the sampled ages represent the same age population. For each Combine, a T value is given and a threshold value is given. If the T value rises above the threshold value, the Combine fails the chi-squared test. The Combine function also calculates agreement indices, as described below. While this is simply an analytical test that ignores geologic variability, it remains a useful filter in the absence of other prior information.

The P_Sequence and Sequence analyses, as well as Combine functions, use MCMC simulations to determine the degree to which the prior model agrees with the observations (in terms of likelihoods) with the agreement indices, A, A_{comb}, A_{model}, and $A_{overall}$. “A” identifies which samples do not agree with the model. A_{comb} tests whether the distributions can be combined. Amodel tests to see if the model can be used given the ages used in the model. Aoverall is a product of the other agreement indices. In order to pass, OxCal agreement indices should be over 60% (Bronk Ramsey, 2008) which represents the area of overlap of the PDF’s. We adopt these criteria in our age models.

When age combines fail the chi-squared and agreement index tests, we remove outliers manually as an iterative process. We first include all ages for correlated strata. When tests fail, we examine the geologic context and remove the most probable outlier un-

til all tests pass. We begin with the ages that have the lowest agreement index or are clearly older outliers.

2-2.3 Lithostratigraphic Correlation

We use integrated stratigraphic correlation techniques, including visual lithostratigraphic description (color, texture, and structure, etc.), CT image analysis, and lithostratigraphic log correlation of MSCL geophysical data (Fukuma, 1998; Karlin et al., 2004; Abdeldayem et al., 2004; St-Onge et al., 2004; Hagstrum et al., 2004; Waldmann et al., 2011) to correlate turbidites based on the turbidite "architecture" (Amy and Talling, 2006). Stratigraphic correlation using geophysical signatures representing vertical turbidite structure is a primary tool for testing individual deposits for their areal extent, a significant part of the criteria used to discriminate seismoturbidites from other possible types. Down-core geophysical properties for individual turbidites are reflections of the vertical grain size distribution of the bed (Kneller and McCaffrey, 2003; Amy et al, 2005; Goldfinger et al., 2012 a). Goldfinger et al. (2012 a) call the shape of the down-core geophysical properties for a deposit the "fingerprint" for that deposit. We verified the efficacy of this proxy for the Sumatra lithologies with particle size analysis (cores 96 and 55; **Fig. 2-2**). Others have found that individual turbidite structure, as reflected by grain size proxies, can be uniquely formed for individual turbidites and can be used to trace individual beds between sites (Amy et al., 2005; Amy and Talling, 2006; Goldfinger et al., 2012 a). Turbidites at different locations, that share a common "fingerprint" in this way, may share a similar sequence of sediment stratigraphy. Core geophysical data are plotted versus depth left to right (gamma density, CT density, PMS, MS). Core particle size data are plotted versus depth left to right (Mean, Median, Mode, and d10; d10 is the particle size that 90% of the particles are larger). Also, for this core alone, we plot resistivity (RES, in Ohms) versus depth. Local maxima in particle size data match with local maxima in the geophysical data.

The most sensitive criteria for correlating fine grained turbidites (which may not be visible to the naked eye) is the density profile (Inouchi et al., 1996), which we augment with very high resolution CT density profiles and 3-D CT imagery. Density and magnetic susceptibility tend to co-vary with particle size; larger particles and magnetic minerals are generally denser. An exception to this are tephras, while they have larger MS values, they are not denser than the over- or under-lying hemipelagites. The other MSCL data, p-wave velocity, was less effective because the sensors do not make sufficient contact

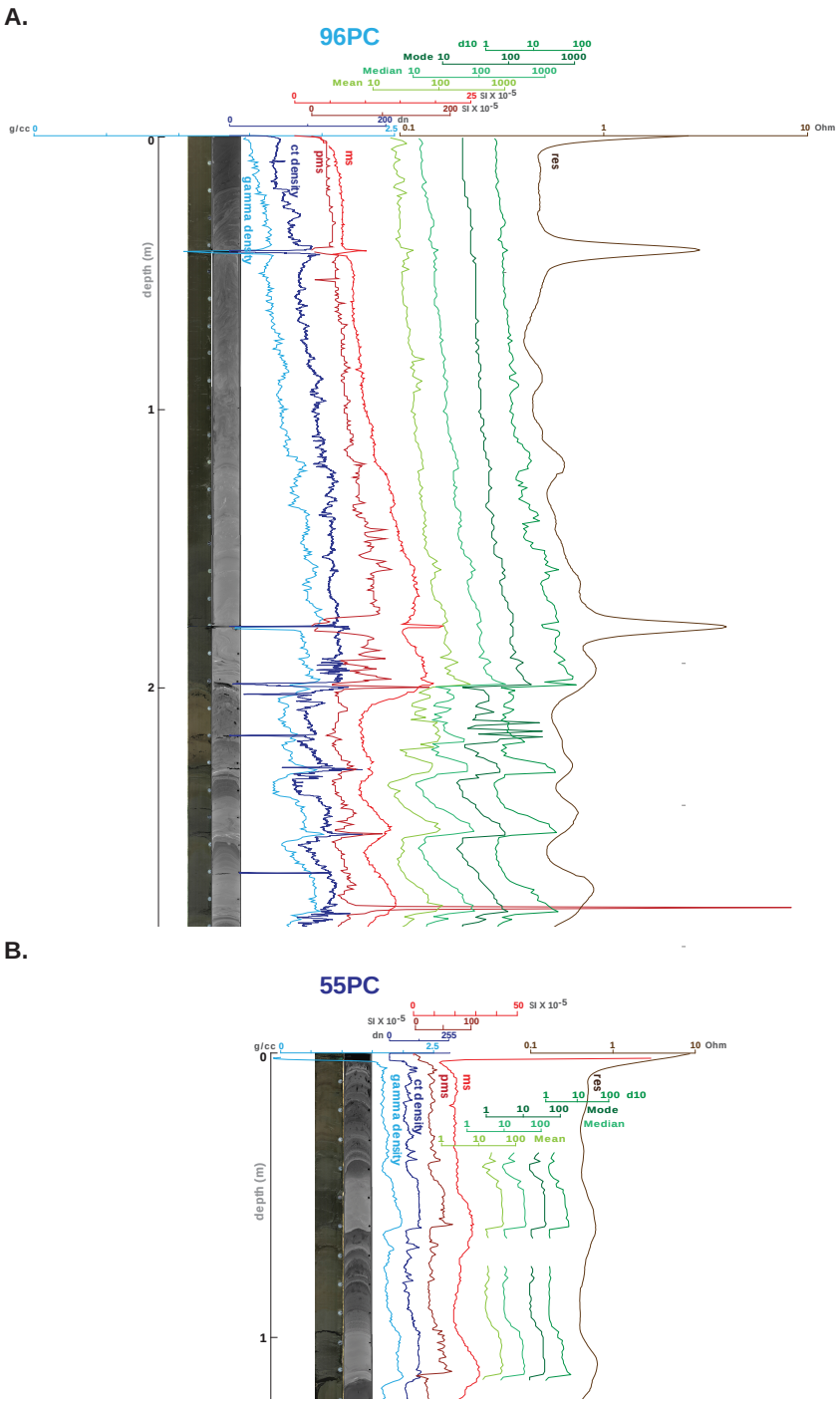

Figure 2-2. Particle Size Proxies. Core geophysical data are compared with particle size data for cores A. 96PC and B. 55PC. Plotted for each core, from left to right, are RGB imagery, CT imagery, gamma density (g/cc , grams per cubic cm in light blue), CT density (dn, image digital number, 0 – 255, dark blue), point magnetic susceptibility (pms, Si X 10^{-5}, dark red), loop point magnetic susceptibility (lms, Si X 10^{-5}, light red), Mean, Median, Mode, and d10 particle size (µm, green) on a logarithmic scale, and resistivity (Ohm, brown). All core geophysical data will be plotted with these same colors and same units.

with the core liner, so there are large gaps and excursions in the data. Resistivity shows a longer wavelength response to the sedimentary structure than the other geophysical data, so we do not use this proxy.

Lithostratigraphic correlation techniques have been used to correlate stratigraphic units since the 1960's (Prell, 1986; Lovlie and Van Veen, 1995). In detail these "fingerprints" represent the time-history of deposition of the turbidite and in several cases linked to plate boundary earthquakes, have been shown to correlate between independent sites separated by large distances and depositional settings (Goldfinger et al., 2008, 2013). The turbidite itself is commonly composed of single or multiple coarse fraction fining upward stacked units termed "pulses". The rarity of a fine tail (Bouma Td and Te; Bouma, 1962) or subsequent hemipelagic sediment between pulses indicates there is commonly little or no temporal separation between units. The lack of temporal separation of the pulses in Cascadia has been inferred to represent deposition over minutes to hours, and thus most likely represent sub-units of a single turbidite (Goldfinger et al., 2012 a). We combine all these correlation tools when possible. The more tools we use successfully for a certain correlation makes that correlation more certain.

2-3.0 Results

The Sumatra slope and trench physiography results in trench segments that are isolated from each other and commonly from isolated slope basins, and therefore offers opportunities to compare the stratigraphic sequences in sites that have unique sediment sources. The basins and trench segments are fed by small canyons that have limited drainage areas on the slope and form small fan/aprons. Slope sites used in this study include cores 109, 108, 104, 103, 102, 97, 96, and 95, which all have isolated sediment sources. In the trench, cores 03, 05, 107, 105, 99, 98, and 94 receive sediment from both upstream ("up trench") in the trench and downslope transport from the continental slope (Patton et al., 2013). **Fig. 2-3** shows the source and possible flow relations for these cores.

We placed core sites in both trench locations and continental slope basin locations. Core locations are given in **Table 2-1** and shown in **Figs. 2-1, 3; S 2-2**. The slope basin sites are necessary because all trench cores are deeper than the CCD, negating the trench sites' usefulness in providing radiocarbon age control. **Fig. 2-3** shows core data for cores 108, 105, 104, 103, and 96 (all regional cores are shown in **Fig. S 2-2**). The light-grey (in CT im-

agery) sand bases of turbidites are easily identified and MSCL maxima in gamma density and magnetic susceptibility correlate well with the CT density maxima.

The lithostratigraphy in the northern Sumatra slope and trench cores is dominated by turbidites interbedded with massive hemipelagic mud and less common tephras. Bioturbation is common and core-induced deformation is observed in some cores. Turbidites are composed of coarse silt to coarse sand bases, with fining upward sand and silt to clay sub-units, additionally slope cores have abundant forams. The coarse fraction is composed of mica and quartz grains with rare mafics, consistent with a Himalayan source of

TABLE 2-1. CORE LOCATION COORDINATES AND CORE INFORMATION

Core Name	Degrees N	Degrees E	Water Depth (m)	Core Length (m)
RR0705-03TC	4.5365°	92.9339°	4,483	1.91
RR0705-03PC	4.5365°	92.9339°	4,483	2.73
RR0705-05TC	4.4804°	92.9267°	4,498	0.91
RR0705-05PC	4.4804°	92.9267°	4,498	3.08
RR0705-16GC	3.2866°	94.0353°	1,911	1.95
RR0705-18GC	3.2761°	94.0198°	1,820	3.14
RR0705-55PC	-4.5197°	100.2131°	6,046	2.61
RR0705-88TC	1.3115°	96.2635°	5,197	0.91
RR0705-88PC	1.3115°	96.2635°	5,197	4.71
RR0705-90MC	1.52°	96.3793°	3,836	0.14
RR0705-93TC	1.7209°	95.8124°	5,040	1.20
RR0705-93PC	1.7209°	95.8124°	5,040	4.92
RR0705-94PC	2.1242°	95.051°	4,918	3.81
RR0705-95PC	2.8745°	94.2061°	3,418	2.23
RR0705-96TC	2.9336°	94.139°	3,410	1.33
RR0705-96PC	2.9336°	94.139°	3,410	4.40
RR0705-97MC	2.9336°	94.139°	3,412	0.68
RR0705-98TC	2.6921°	94.1°	3,410	1.22
RR0705-98PC	2.6921°	94.1°	3,410	4.77
RR0705-102MC	3.6051°	93.6315°	3,073	0.22
RR0705-103TC	3.6051°	93.6315°	3,073	1.63
RR0705-103PC	3.6051°	93.6315°	3,073	4.74
RR0705-104TC	3.8716°	93.4747°	3,476	1.92
RR0705-104PC	3.8716°	93.4747°	3,476	4.58
RR0705-105TC	4.0787°	93.181°	4,486	0.55
RR0705-105PC	4.0787°	93.181°	4,486	2.75
RR0705-107TC	4.327°	92.9177°	4,518	1.79
RR0705-107PC	4.327°	92.9177°	4,518	0.81
RR0705-108TC	4.6598°	93.1428°	2,959	1.28
RR0705-108PC	4.6598°	93.1428°	2,959	3.70
RR0705-109MC	4.6598°	93.1428°	2,959	0.06

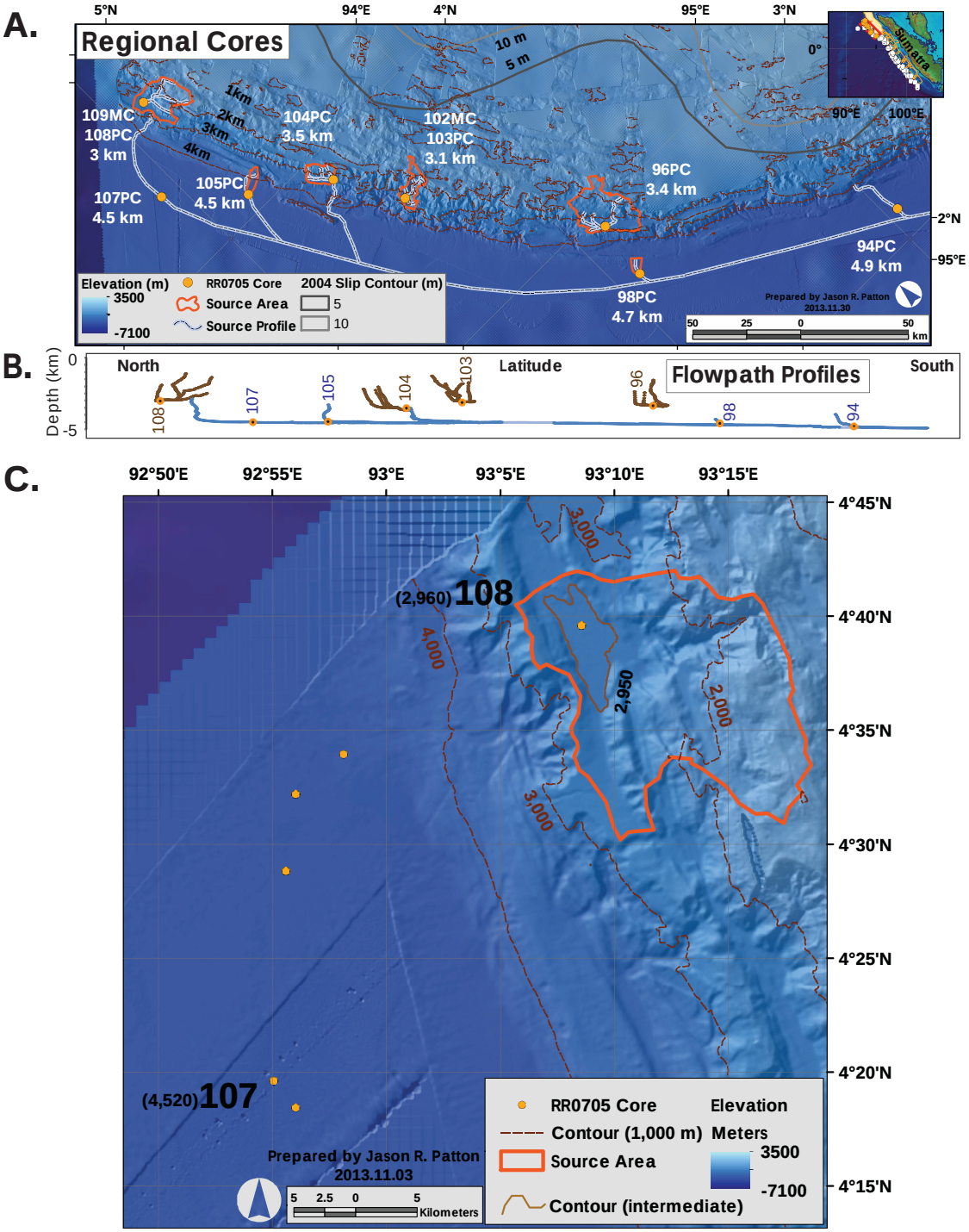

Figure 2-3. Regional Core Sites, Source Areas, and Key Core Stratigraphy. A. Core locations (orange dots) on bathymetric map (Smith and Sandwell, 1997, Graindorge et al., 2008; Ladage et al., 2006) also showing key channel flow paths (light blue) to eight core sites. Slope basin and trench source areas (orange) were determined by outlining drainage divides surrounding all submarine topography contributing potential gravity flows to a given core site. While the region that drains to core 104PC then drains to the

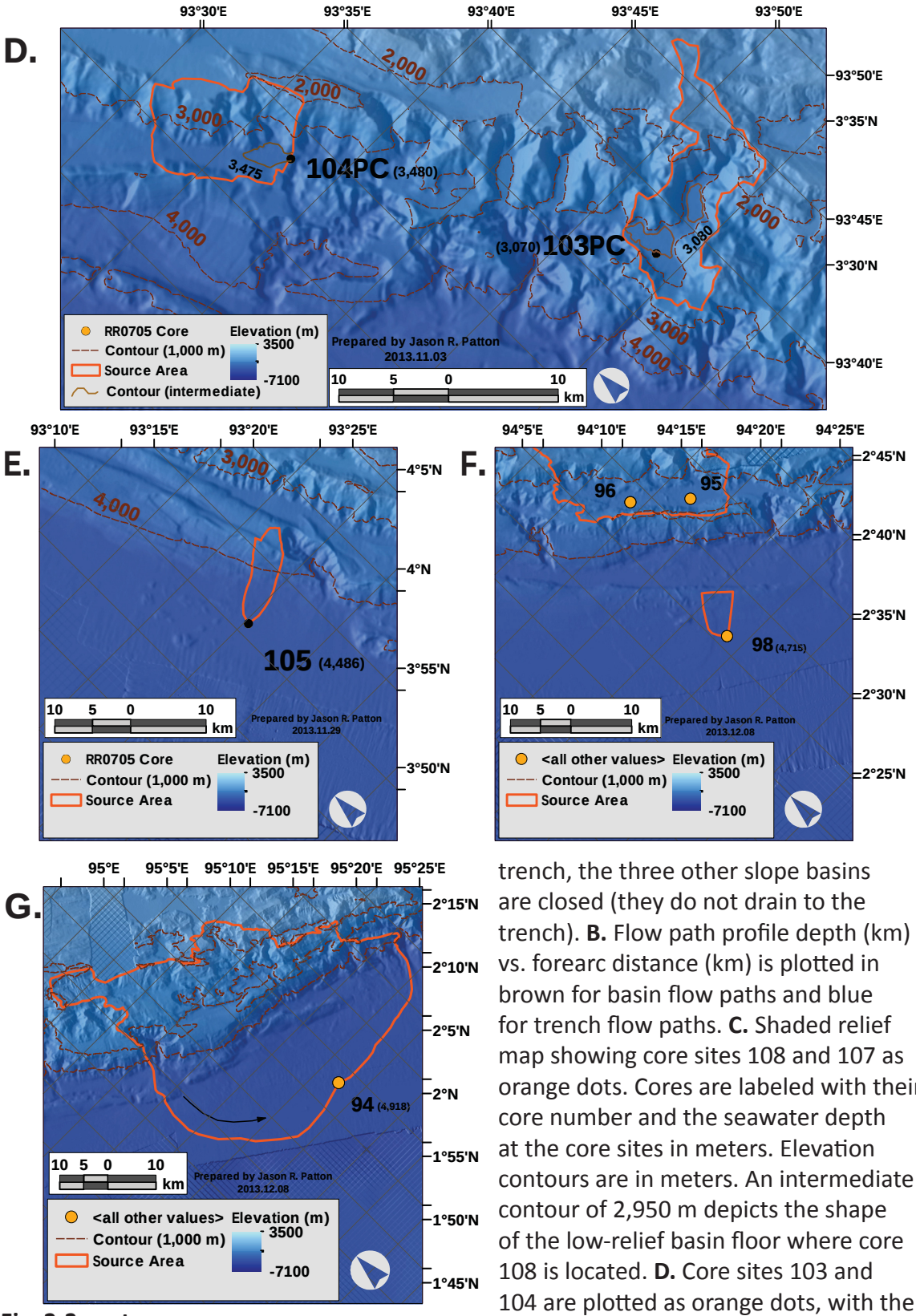

Fig. 2-3 cont.

trench, the three other slope basins are closed (they do not drain to the trench). **B.** Flow path profile depth (km) vs. forearc distance (km) is plotted in brown for basin flow paths and blue for trench flow paths. **C.** Shaded relief map showing core sites 108 and 107 as orange dots. Cores are labeled with their core number and the seawater depth at the core sites in meters. Elevation contours are in meters. An intermediate contour of 2,950 m depicts the shape of the low-relief basin floor where core 108 is located. **D.** Core sites 103 and 104 are plotted as orange dots, with the

H.

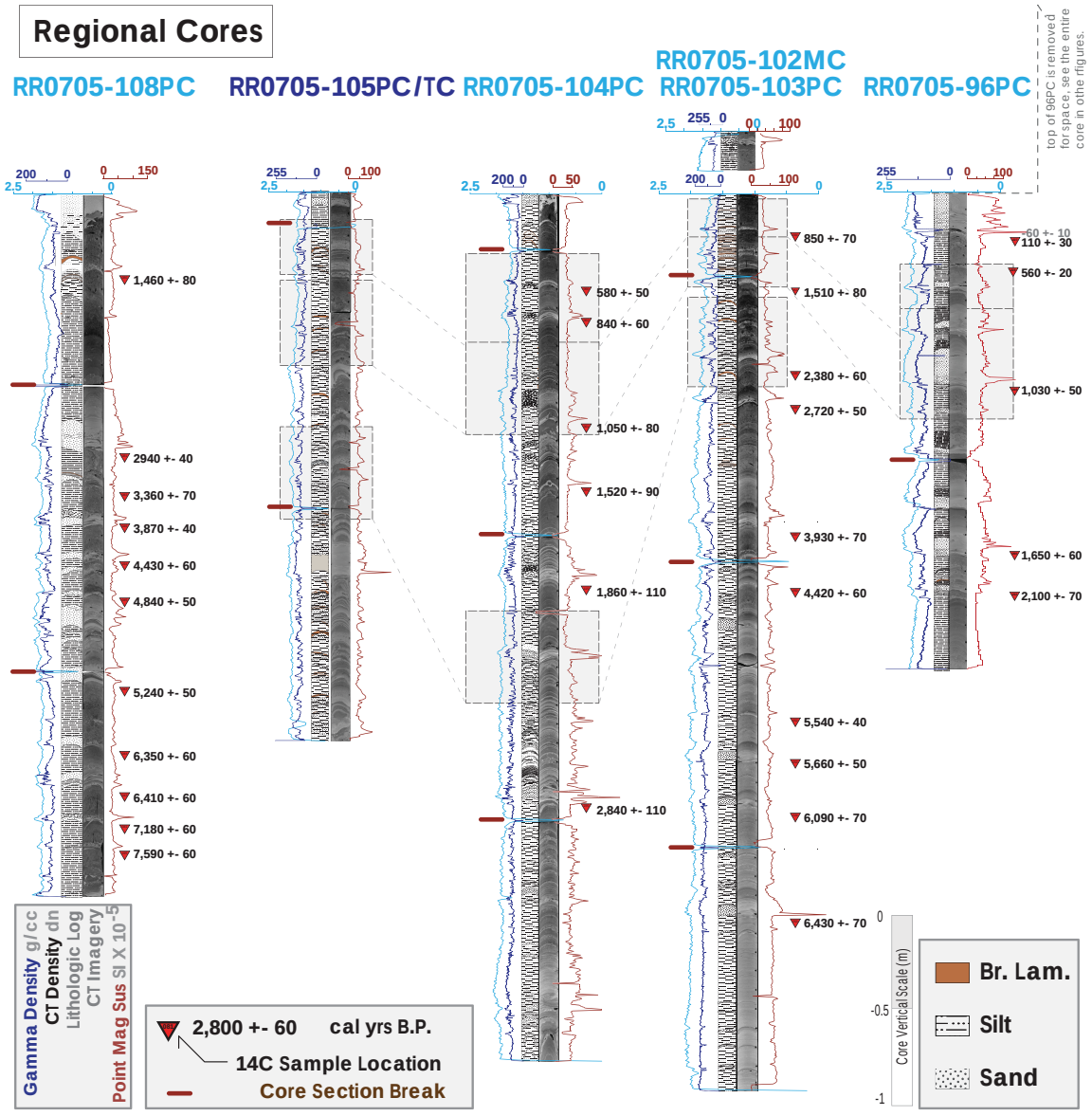

Fig. 2-3 cont.

core depth in meters. Intermediate contours of 3,475 m and 3,080 m depict the shape of the basins. **E.** Core 105 is plotted with the core depth in meters. **F.** Core 98 is plotted with the core depth in meters. **G.** Core 94 is plotted with the core depth in meters. **H.** Five principle cores that we use in our correlations and age models are plotted versus depth in cm. MSCL core geophysical data are plotted (gamma density, CT density, point magnetic susceptibility, from left to right) and CT imagery displays lower density material in darker grey and higher density material in lighter grey. Slope cores are labeled in light blue; trench cores are labeled in dark blue. ^{14}C ages are reported in calendar years before present (cal yr BP; 1950). Grey rectangles refer to **Fig. 2-8**.

the accreting Bengal and Nicobar fans (Stow et al, 1990). Basal turbidite sub-units are composed of primarily foraminiferal hash in some piggyback basin cores. Sand sub-units commonly range in thickness from 0.5 to ~20 cm, are parallel laminated and cross laminated, and commonly underlie massive sand beds. Finer material is composed of silt to clay sized particles (**Fig. 2-4**). 0.5- to 10.5-cm thick primary tephras are rare and can be correlated between sites using electron microprobe and laser ablation ICPMS data (Salisbury et al, 2010, 2012). Similar turbidite stratigraphy is found in all slope basins (cores 108, 104, 103, and 96) and trench sites (cores 107, 105, 98, and 94), spanning 350 km along strike.

We describe the turbidite structure in the RR0705 cores using Bouma (1962), van der Lingen (1969), Stow (1977), and Piper (1978) fine grained classification system divisions and label the sedimentary layers according to these systems (Stow, 1985; **Fig. 2-4A**). A complete Bouma sequence (Bouma, 1962) would comprise superposed divisions Ta, Tb, Tc, Td, Te, and F. Stow and Piper divisions fit within the Bouma division Te, in superposed

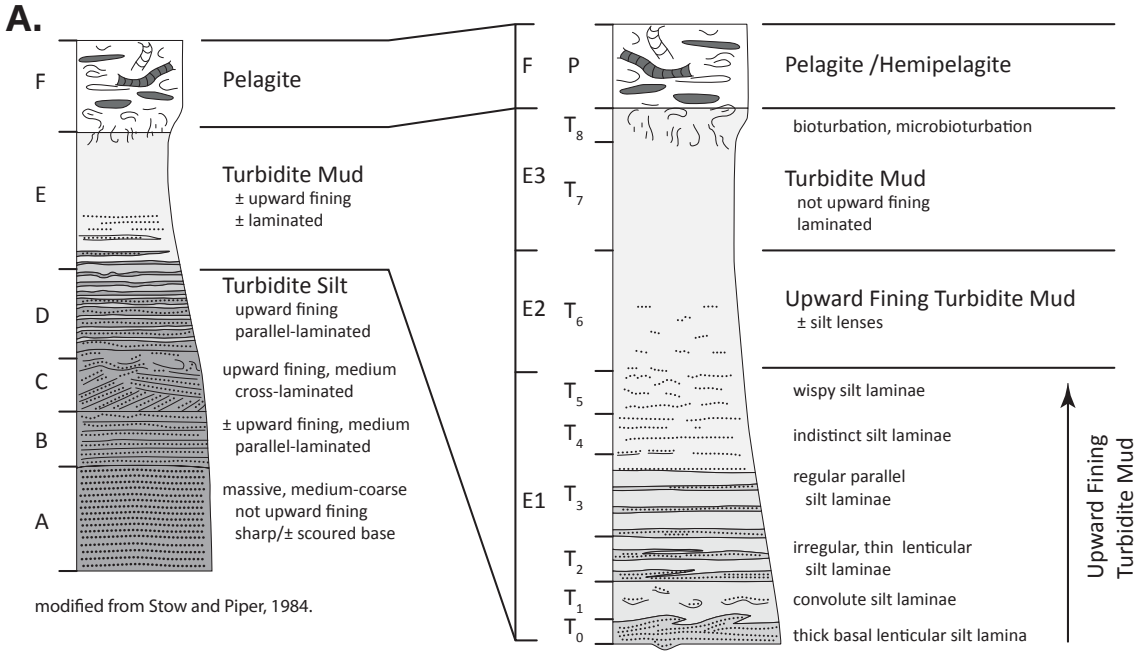

Figure 2-4. Turbidite Division Classification. A. Bouma (1962) and van der Lingen (1969) turbidite structure classification for fine grained turbidites is drafted on the left. Divisions are designated by letters A through F, typically designated with a preceding "T." Stow (1977) and Piper (1978) turbidite structure classification system for fine grained turbidites is drafted on the right. Piper (1978) divisions are designated by E and F letters. Stow (1977) divisions are designated with "T-#." Both Stow and Piper divisions fit within the Bouma Te division. **B.** Turbidites in cores 96PC and 108PC are plotted with turbidite division systems in displayed in **A**. Plotted from left to right are gamma density, CT

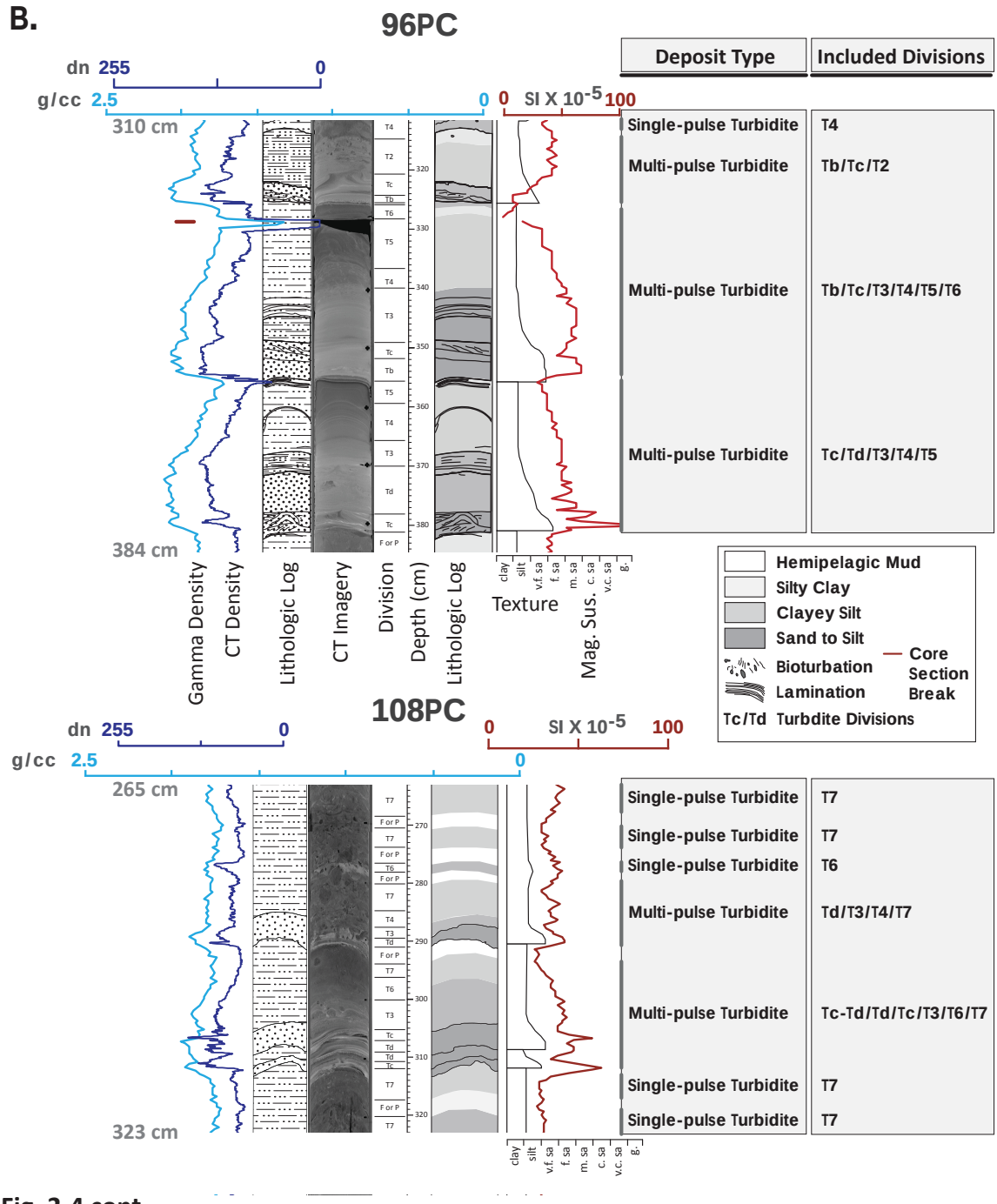

Fig. 2-4 cont.

density, lithologic log (pattern), CT imagery, turbidite division, core depth (cm), lithologic log (grayscale texture), texture (particle size phi scale including, from left to right, clay, silt, very fine sand, fine sand, medium sand, coarse sand, very coarse sand, and gravel), and point magnetic susceptibility. The deposit type (single pulse or multi pulse) and turbidite structure divisions present (included divisions) in each turbidite are listed for each turbidite.

order, E1, E2, E3 or T0, T1, T2, T3, T4, T5, T6, T7, and T8. Not every turbidite has a complete sequence of either system of structural divisions.

We show typical turbidites, some multi-pulse, from cores 96PC and 108PC in **Fig. 2-4B**. Multi-pulse turbidites may have superposed and repeated divisions (e.g. core 108 312-294 cm: Tc-d, Td, Tc, T3, T6, T7) or just superposed divisions (e.g. core 108 291-280 cm: Td, T3, T4, T7). All multi-pulse turbidites have multiple maxima in the geophysical data (commonly reflecting grain size variations) that correspond to the structural divisions.

Forty-five radiocarbon ages and thirty-seven ^{210}Pb samples were analyzed for the cores within the 2004 SASZ earthquake region. **Table 2-2** lists the ^{14}C ages used in our OxCal age models and includes the lab age (in radiocarbon years), calibrated age (in calendar

TABLE 2-2. RADIOCARBON AGE RESULTS FOR AGES ANALYZED IN THE 2004 SASZ EARTHQUAKE REGION

Sample Number	Lab Sample Number *	Sample Name	Core Number	Depth (cm)	Lab Age † (yrs)	Lab Age Error	Cal. Age § (yrs)	Cal. Age Error	Hemi Sed Rate (cm ka^{-1})#	Sed Rate Error
SUM-172	76995	RR0705_108TC_020_022_SUM-172	108TC	21	1930	20	1410	70	16	2
SUM-080	65294	RR0705_108PC_039_041_SUM-080	108PC	40	2020	20	1460	90	16	2
SUM-081	65295	RR0705_108PC_132.5_134.5_SUM-081	108PC	133.5	3040	20	2950	40	12	1
SUM-083	65296	RR0705_108PC_156_158_SUM-083	108PC	157	3500	20	3360	70	12	1
SUM-046	54321	RR0705_108PC_175_177_SUM-046	108PC	176	4070	20	3870	40	7	1
SUM-194	76996	RR0705_108PC_194_196_SUM-194	108PC	195	4340	20	4430	60	15	2
SUM-045	54320	RR0705_108PC_212.5_214.5_SUM-045	108PC	213.5	4630	20	4830	60	18	2
SUM-042	54303	RR0705_108PC_257_259_SUM-042	108PC	256	4840	20	5240	40	15	2
SUM-044	54305	RR0705_108PC_290.5_292.5_SUM-044	108PC	291.5	5950	20	6350	50	11	1
SUM-043	54304	RR0705_108PC_312.5_314.5_SUM-043	108PC	313.5	6120	20	6610	50	7	1
SUM-041	54302	RR0705_108PC_330_332_SUM-041	108PC	331	6690	30	7180	70	4	0
SUM-195	77247	RR0705_108PC_345_347_SUM-195	108PC	346	7180	20	7590	60	4	0
SUM-176	77107	RR0705_104TC_011_013_SUM-176	104TC	12	710	20	310	70	2.7	0
SUM-175	77106	RR0705_104TC_047.5_049.5_SUM-175	104TC	48.5	1220	20	750	80	2.7	0
SUM-060	65529	RR0705_104PC_049.5_051.5_SUM-060	104PC	50.5	1070	20	580	70	10	1
SUM-062	54325	RR0705_104PC_067.5_069.5_SUM-062	104PC	68.25	1270	20	840	50	10	1
SUM-061	65530	RR0705_104PC_122_124_SUM-061	104PC	123	1630	50	1050	70	10	1
SUM-082	65531	RR0705_104PC_158_160_SUM-082	104PC	159	2040	20	1520	60	10	1
SUM-115	65532	RR0705_104PC_207_209_SUM-115	104PC	208	2420	220	1860	100	10	1
SUM-235	107807	RR0705_104PC_326_328_SUM-235	104PC	327	3000	40	2840	110	30	3
SUM-177	76991	RR0705_103TC_012.5_014.5_SUM-177	103TC	13.5	1310	20	820	80	2	0
SUM-178	76992	RR0705_103TC_036_038_SUM-178	103TC	37	1890	20	1380	70	3	0
SUM-179	76993	RR0705_103TC_039_041_SUM-179	103TC	40	2070	20	1650	60	3	0
SUM-180	76994	RR0705_103TC_079_081_SUM-180	103TC	79.5	2990	20	2740	60	3	0
SUM-084	65297	RR0705_103PC_020_022_SUM-084	103PC	21	1230	20	850	50	11	1
SUM-054	54323	RR0705_103PC_049_051_SUM-054	103PC	50	1940	30	1510	80	21	2
SUM-085	65298	RR0705_103PC_092_094_SUM-085	103PC	93	2710	20	2380	70	11	1
SUM-055	54324	RR0705_103PC_111_113_SUM-055	103PC	112	2990	20	2720	40	8	1
SUM-087	65299	RR0705_103PC_174_176_SUM-087	103PC	175	3930	20	3930	70	11	1
SUM-050	54306	RR0705_103PC_209_211_SUM-050	103PC	210	4360	20	4420	50	11	1
SUM-052	54322	RR0705_103PC_277_279_SUM-052	103PC	278	5100	20	5540	30	16	2
SUM-053	65528	RR0705_103PC_300.5_302.5_SUM-053	103PC	301.5	5360	30	5660	50	13	1
SUM-224	107805	RR0705_103PC_324_326_SUM-224	103PC	325	5580	30	6090	70	17	2
SUM-249	117616	RR0705_102MC_065_075_SUM-249	102MC	7	460	20	50	60	NA	NA
SUM-227	107808	RR0705_96PC_206_208_SUM-227	96PC	207	480	20	110	120	6	1
SUM-228	107806	RR0705_96PC_222_224_SUM-228	96PC	223	1150	20	560	20	14	1
SUM-089	65300	RR0705_96PC_287.5_289.5_SUM-089	96PC	288.5	1490	20	1020	50	19	2
SUM-090	65301	RR0705_96PC_374_376_SUM-090	96PC	375	2120	20	1650	70	28	3
SUM-232	107809	RR0705_96PC_399_401_SUM-232	96PC	400	2410	20	2100	160	26	3
SUM-199	80463	RR0705_18GC_000_001_SUM-199	18GC	0.5	3850	20	3780	80	0.9	0
SUM-200	80464	RR0705_18GC_020_021_SUM-200	18GC	20.5	12180	30	13600	150	1.4	0
SUM-201	80465	RR0705_18GC_040_041_SUM-201	18GC	40.5	15380	30	18250	270	1.9	0
SUM-249	107821	RR0705_16GC_005_007 _SUM-249	16GC	6	2800	20	2500	130	3.5	0
SUM-250	107822	RR0705_16GC_021_022_SUM-250	16GC	21.5	8800	30	9430	60	2.4	0
SUM-251	107823	RR0705_16GC_041_042_SUM-251	16GC	41.5	17740	80	20630	420	1.2	0

* Radiocarbon samples were analyzed at the Keck Carbon Cycle Accelerator Mass Spectroscopy Facility at Earth System Science Dept., UC Irvine.

† Lab-reported age errors reported to 2 standard deviations and are reported in radiocarbon years.

§ Calibrated age ranges before A. D. 1950 according to Stuiver and Reimer [2] calculated using marine reserevior correction and regional delta R offset (ΔR = 16); errors are reported to 95.4% error. Ages are eported in calendar years.

Hemipelagic sedimentation rate is calculated from dividing unit thickness by the calibrated age.

- Radiocarbon concentrations are given as fractions of the Modern standard, D ^{14}C, and conventional radiocarbon age, following the conventions of Stuiver and Polach [1].

- Size-dependent sample preparation backgrounds have been subtracted, based on measurements of ^{14}C-free calcite.

- All results have been corrected for isotopic fractionation according to the conventions of Stuiver and Polach [1], with δ^{13}C values measured on prepared graphite using the AMS spectrometer. These can differ from δ^{13}C of the original material, if fractionation ocurred during sample graphitization or the AMS measurement, and are not shown.

years before present, 1950 AD), and the moving average sedimentation rate for that sample. The sample name is a compilation of the cruise name, the core number and type, the sample interval (in cm), and the sample number. We use the sample name in OxCal to track core and stratigraphic information through the age modeling. Synthetic ages generated with P_Sequence age models are designated by gray labels in **Fig. 2-3**. Calibrated ages are plotted in core figures and are used to establish the framework for lithostratigraphic correlation. We found no age inversions (where older ages superpose younger ages) in these age data that span the middle to late Holocene. Three ages from two cores (16GC and 18GC) extend into the latest Pleistocene at depths of approximately 20 cm, resulting in low sedimentation rates. We discuss the results and iterative processes for the age models in the discussion section.

2-3.1 Surficial Turbidite in the 2004 Rupture Zone

The uppermost turbidite in fifteen cores (01GC, 05TC, 26GC, 88TC, 93TC, 94PC, 95PC, 96PC/TC, 97MC, 99MC, 102MC, 104PC/TC, 107PC, 108PC/TC, and 109MC; **Appendix S 2-2, S 2-6**), shares common characteristics of recent deposition based on the lithostratigraphic descriptions, radiometric age estimates, and relative age evaluations. We here present the basis for our correlation of the deposits in these cores. Five cores do not appear to contain a complete deposit and just have the base (01, 26, 104, 107, and 108). It is not possible to evaluate the completeness of the section in six cores due to coring deformation (05, 88, 93, 94, and 109). One core set has a complete deposit when the cores 96PC, 96TC, and 97MC are combined. Sediment in 96PC and 96TC is deformed and compressed in places, so it is difficult to assess the true thickness of the turbidite in these cores. Core 102MC may also have the entire turbidite section, though in a thinner deposit (approximately 6 cm thick; **Appendix S 2-2**).

We use core 96 for our discussion of the sedimentologic characteristics because it is probably complete and has the most expanded section of this deposit, though many of these sedimentologic qualities (e.g. the unconsolidated “soupy” nature of the uppermost turbidite) are shared in all fifteen cores. We scale the TC to the PC based on common stratigraphic contacts, resulting in an estimated thickness of 308 cm (**Fig. 2-5**). We could not determine if 97MC included sediment missing from the top of 96TC, so we did not use this core to add to our estimate of the thickness. Core 96 is located in an enclosed basin (**Fig. 2-5E**) and has an extensive record of the uppermost turbidite as revealed by CHIRP seismic data collected in a cross-basin transect (**Fig. 2-5 E, F**). In this

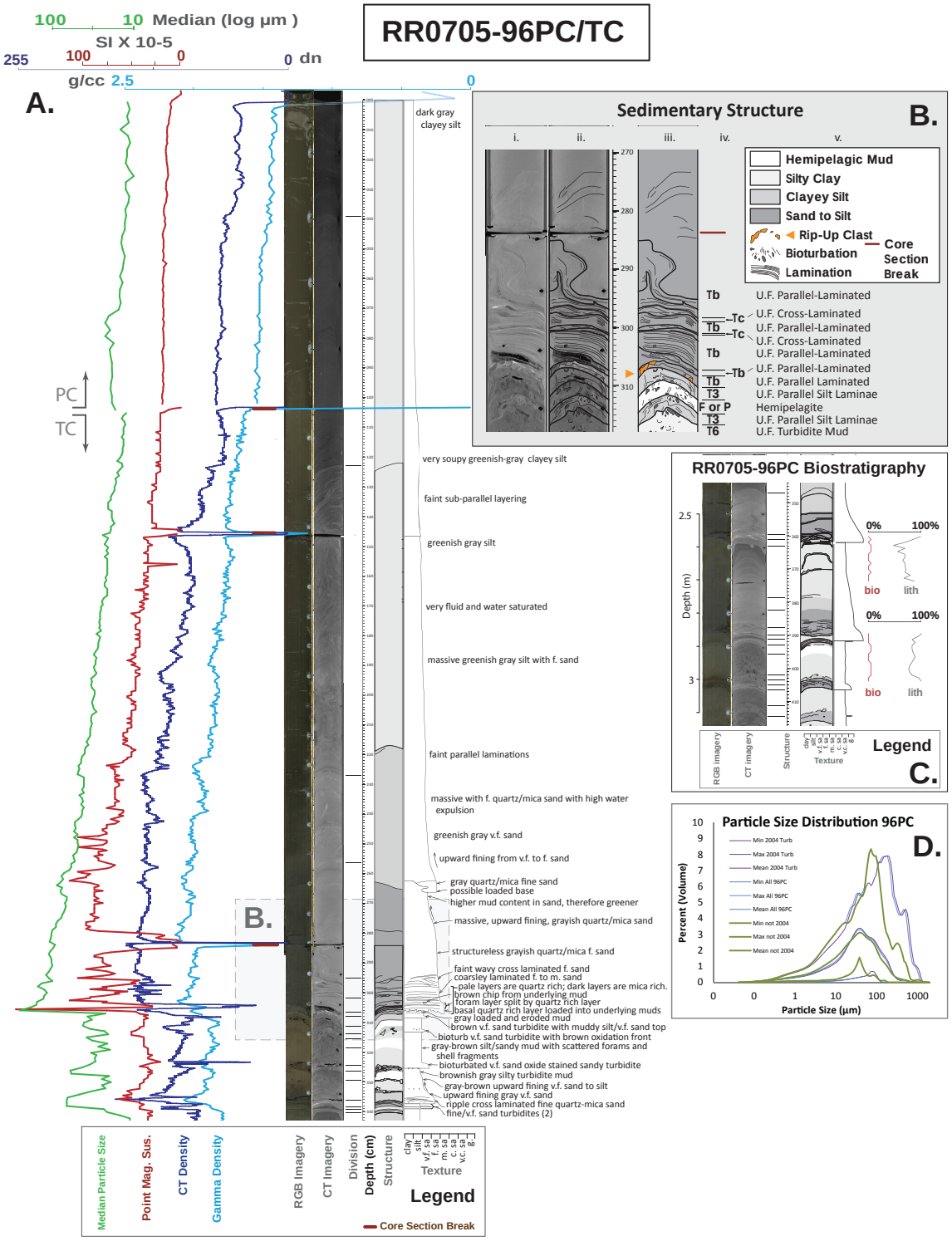

Figure 2-5. RR0705-96PC Core, Site, and Seismologic Record. What is possibly the 2004 turbidite is displayed in this figure from cores 96PC and 96TC, plotted as a composite core. **A.** From left to right, mean grain size (µm, log scale), point magnetic susceptibility (ms, SI X 10^{-5}), gamma density (g/cc), CT density (greyscale digital number), RGB imagery,

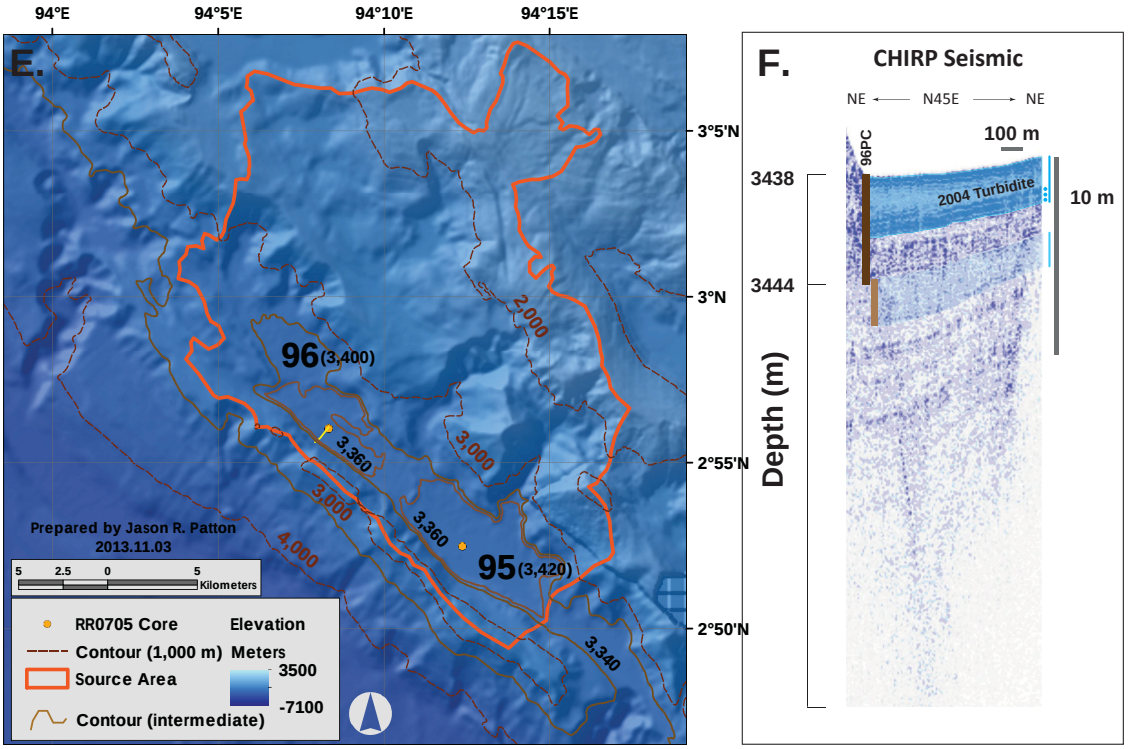

Fig. 2-5 cont.

CT imagery, turbidite structure classification division (e.g. Ta, Bouma, 1962; van der Lingen, 1969; Stow, 1977; Piper, 1978; Stow, 1985), depth (cm), turbidite structure (lithologic log), texture, and the lithologic notes are plotted vs. depth. **B.** Detailed turbidite structure based on CT imagery. From left to right: i. CT imagery uninterpreted, ii. CT imagery interpreted, iii. turbidite structure interpretation, iv. turbidite structure division classification; v. turbidite structure description. **C.** Results from smear slide based vertical biostratigraphic transects for core 96PC. Percent biogenic and percent lithologic are plotted vs. depth in m. **D.** The mean, minimum, and maximum particle size distribution for sediments collected within the uppermost turbidite (in purple) and within hemipelagic sediments underlying the uppermost turbidite (in green) are plotted. These are compared with the combined distributions (in blue). **E.** Core sites 96 and 95 are plotted as orange dots, with the seawater depths (3,400 and 3,420 m respectively). Elevation contours are in meters. Intermediate contours of 3,360 m and 3,340 m depict the shape of the basins. The CHIRP seismic profile is plotted on the map as a yellow line crossing the core 96 core site. **F.** The CHIRP seismic profile crossing the basin at core 96. The core length of 96PC/TC is plotted in brown. Turbidite boundary interpreted in seismic data is overlain in transparent blue. SE-NE profile transect has an orientation of N45E. The lighter brown line and lighter blue polygon designates a possible thick turbidite, the uppermost tail of which is at the base of core 96PC.

core the uppermost turbidite is described as soupy and water laden (lithologic notes, 120 cm, 170 cm; **Fig. 2-5**). The water content was so high that, during shipboard lithologic description, care was required to prevent the sediment from pouring out of the core. The reflectivity of the RGB image is consistent with these observations (the wet sediment is shiny, especially noticeable between 5 and 10 cm). The uppermost sedimentary deposit consists of a multi-pulse, upward fining, quartz-mica, medium sand to silty-clay, turbidite. The turbidite has three main pulses, with additional smaller pulses, as evidenced in the particle size, CT density, gamma density, CT imagery, and sedimentary texture data (**Fig 2-5 A**). The three main pulses are resolvable in these seismic reflection data (blue dots, **Fig. 2-5 F**).We classify the turbidite structures (**Fig 2-5 A, B**) with the same system as in **Fig. 2-4 A**. There is little to no bioturbation, possibly indicating minimal post-depositional time before collection (Fornes et al., 2001). There is no oxidation in the surficial sediment, which may also indicate relative post-depositional time (Sayles et al., 1994; Martin and Sayles, 2003); oxidation of surficial sediments can take months to a few years (Sayles et al., 1994; Martin and Sayles, 2003). Foraminifera are absent in surficial sediment in this and other cores, indicating that a probable lack of hemipelagic sediment at the surface. We see no evidence of hemipelagic material in cores 94, 96, 97, 99, 102, nor 109, while cores 01, 05, 26, 88, 93, 95, 99, 104, 107, and 108 are likely missing their tops and offer no constraint on the presence of hemipelagic sediment at the surface (**Fig. S 2-2**).

The base of the turbidite has some interesting characteristics that may reveal details about the nature of deposition (erosional vs. depositional) and length of time of deposition (rapid or slow). The lowermost laminations include embedded mud clasts, possibly of the underlying sediment. The basal contact of the turbidite shows further evidence of erosion, that the turbidite intruded sediment into the underlying mud. The shape of the basal contact also suggests the turbidite loaded the mud (pushed downwards, deforming the upper contact of the underlying mud).

Remarkably, the CT density of the coarse section of the 102MC uppermost turbidite is quite similar to the geophysical data from core 96PC (**Fig. 2-3**). In the trench, down-trench and south of the 2004 earthquake slip zone, cores 88TC and 93TC contain turbidites that also appear to have similar geophysical fingerprints to that found in core 96PC.

2-3.1.1 Age Constraints

We describe the results of our tests of depositional timing with absolute age (radiometric) and relative age (bioturbation, oxidation, and biostratigraphy). We did not sample cores 108 and 104 because the CT imagery shows evidence of erosion and stratigraphic disturbance (making it difficult to determine what sediment to sample). Core 96PC and core 102MC were better candidates, but there remains a thin turbidite between the age sample and the uppermost turbidite in core 96. Age determinations and calibrations for these two cores are given in **Table 2-3**. We report the lab age, the simple calibrated age (only a gap correction age model), the Sequence age (age model for within the core for 96PC), and the P_Sequence model (a second age model for within the core for 96PC). 102MC is not a candidate for a P_Sequence model because there is only one age sample for this core. Lab ages are reported to 2 sigma error and calibrated ages are reported to 95.4% error. The simple calibrated age is not constrained by any priors, other than the correction for the thickness of the overlying hemipelagic sediment. The Sequence age is only slightly more well constrained with the "priors" of stratigraphic order and the coring date age boundary. The age calibration that includes the most amount of "prior" information is the P_Sequence age, including stratigraphic position as well as stratigraphic order. The stratigraphic thickness "prior" constraint is responsible for the short time span (error range in years).

We do not prefer any age model of any other, but all their error ranges span the year 2004. The BC/AD age ranges for these three models are 1980 ± 60, 1950 ± 60, and 2010 ± 10 years. The simple calibration and sequence age models for core 102MC result in slightly older ages. The 102MC age models include a gap correction, so if the sedimentation rate is slightly underestimated, the age results would be older.

We use the exponential decay of ^{210}Pb activity with depth, and in the presence/absence of ^{137}Cs, indicative of deposition since 1954, to evaluate the timing of deposition for these uppermost sediments. Sediment from cores 94PC and 105PC were analyzed for ^{210}Pb and ^{137}Cs activity using gamma counting (system described in the Methods section). Results are plotted in **Table 2-4 A** and **Fig. 2-6**. Sediment from cores 96PC, 96TC, and 102MC were analyzed for ^{210}Pb activity using the other gamma counting system de-

TABLE 2-3. RADIOCARBON AGES UNDERLYING THE UPPERMOST TURBIDITE IN CORES 96 AND 102.

		Lab		Calibrated		Sequence		P_Sequence	
Core	Sample Name	Age	Error	Age	Error	Age	Error	Age	Error
96PC	RR0705_96PC_206_208_SUM-227	480	20	-30	60	0	60	-60	10
102MC	RR0705_102MC_065_075_SUM-249	460	20	40	40	50	60	na	na

TABLE 2-4 A. ^{210}Pb RESULTS FOR CORES 96PC AND 96TC

Sample Number*	Sample ID †	^{210}Pb (dpm/g)	Error	Depth (cm)
RR0705-96PC				
7169	PR0705-96 PC 22-23	7.93	0.26	222.5
7170	PR0705-96 PC 23-24	7.30	0.24	223.5
7171	PR0705-96 PC 24-25	10.37	0.34	224.5
7172	PR0705-96 PC 25-26	11.22	0.36	225.5
7173	PR0705-96 PC 26-27	8.99	0.30	226.5
7174	PR0705-96 PC 27-28	4.31	0.15	227.5
7175	PR0705-96 PC 28-29	3.97	0.13	228.5
7176	PR0705-96 PC 29-30	6.08	0.21	229.5
7177	PR0705-96 PC 30-31	2.46	0.09	230.5
RR0705-96TC				
7240	PR0705-96 TC 126-127	4.55	0.19	126.5
7241	PR0705-96 TC 127-128	4.62	0.19	127.5
7242	PR0705-96 TC 128-129	4.21	0.18	128.5
7243	PR0705-96 TC 129-130	4.20	0.18	129.5

TABLE 2-4 B. 210Pb RESULTS FOR CORES 96PC, 96TC, and 102MC

Sample Number*	Sample ID †	^{210}Pb (dpm/g)	Error	Depth (cm)
RR0705-96PC				
7169	PR0705-96 PC 22-23	7.93	0.26	222.5
7170	PR0705-96 PC 23-24	7.30	0.24	223.5
7171	PR0705-96 PC 24-25	10.37	0.34	224.5
7172	PR0705-96 PC 25-26	11.22	0.36	225.5
7173	PR0705-96 PC 26-27	8.99	0.30	226.5
7174	PR0705-96 PC 27-28	4.31	0.15	227.5
7175	PR0705-96 PC 28-29	3.97	0.13	228.5
7176	PR0705-96 PC 29-30	6.08	0.21	229.5
7177	PR0705-96 PC 30-31	2.46	0.09	230.5
RR0705-96TC				
7240	PR0705-96 TC 126-127	4.55	0.19	126.5
7241	PR0705-96 TC 127-128	4.62	0.19	127.5
7242	PR0705-96 TC 128-129	4.21	0.18	128.5
7243	PR0705-96 TC 129-130	4.20	0.18	129.5
RR0705-102MC				
7254	PR0705-102 MC 6-7	17.00	0.58	5.5
7253	PR0705-102 MC 7-8	14.01	0.49	6.5
7252	PR0705-102 MC 8-9	6.64	0.24	7.5
7251	PR0705-102 MC 9-10	4.51	0.16	8.5
7250	PR0705-102 MC 10-11	5.53	0.23	9.5
7249	PR0705-102 MC 11-12	5.42	0.22	10.5
7248	PR0705-102 MC 12-13	2.76	0.12	11.5
7247	PR0705-102 MC 13-14	2.47	0.12	12.5
7246	PR0705-102 MC 14-15	2.77	0.13	13.5
7245	PR0705-102 MC 15-16	2.39	0.12	14.5
7244	PR0705-102 MC 16-17	2.53	0.12	15.5

Figure 2-6. ^{210}Pb age data and Possible 2004 Deposit Core Location Map. A. Analytical results are plotted for cores 90MC, 94PC, 96PC, 96TC, and 105TC. ^{210}Pb decay per minute are plotted vs. depth with blue dots, alongside core data. Regressions are plotted for some cores. Core data include core depth (cm), CT imagery, turbidite structure, and sedimentary texture. ^{14}C ages are listed in cal yr BP with 95.4% error. Gray shaded ages are estimates based on our P_Sequence age model, discussed in the text. ^{14}C sample locations are outlined in dashed red lines. **B.** Map showing the cores that contain a deposit that may have resulted following the 2004 SASZ earthquake. Cores with a possible 2004 seismoturbidite are plotted in light orange and labeled with the ocean depth at the core site. Core 90MC, with a possible 2005 seismoturbidite, is plotted in dark orange.

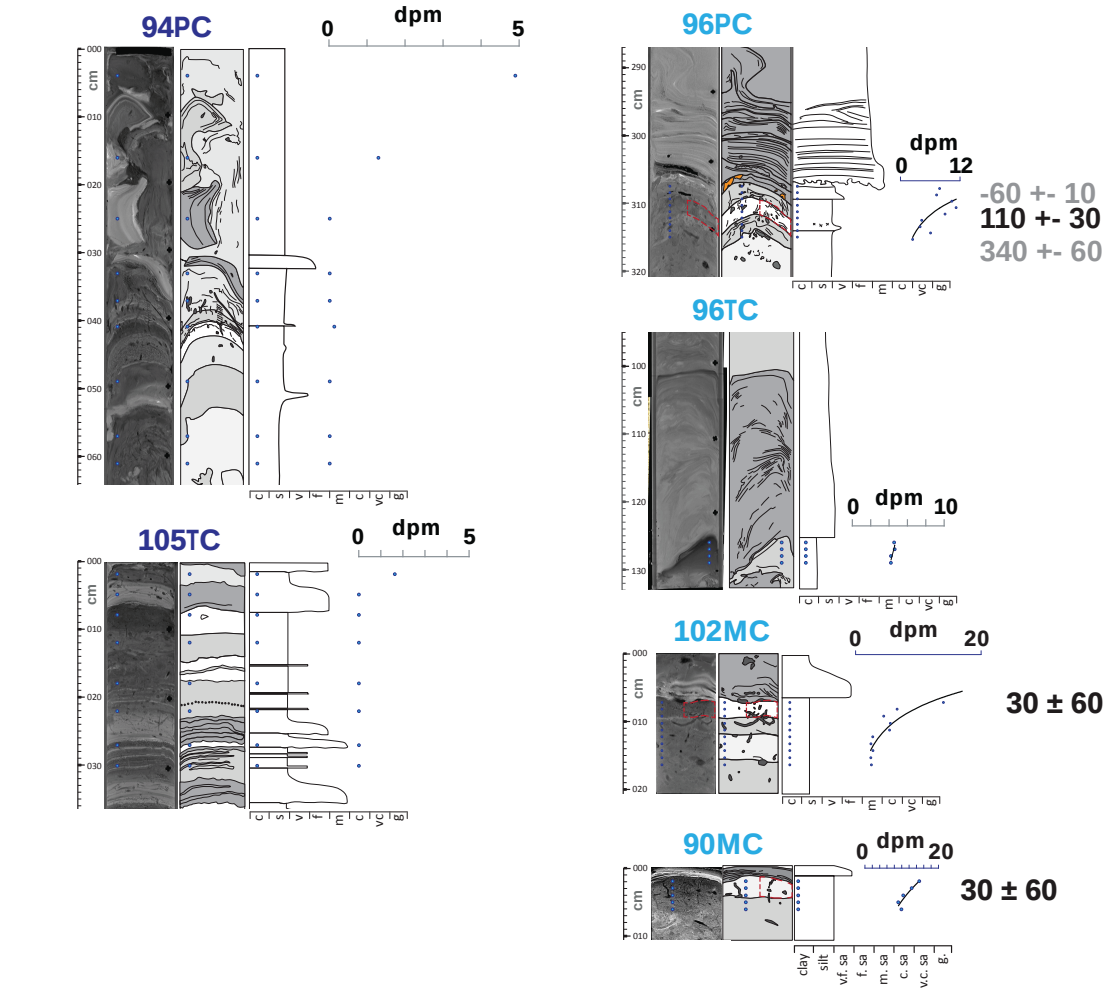
94PC
0
dpm
5
96PC
dpm
0
12
-60 +- 10
110 +- 30
340 +- 60
96TC
0
dpm
10
105TC
0
dpm
5
102MC
0
dpm
20
30 ± 60
90MC
0
dpm
20
30 ± 60
cm
clay
silt
v.f. sa
f. sa
m. sa
c. sa
v.c. sa
g.

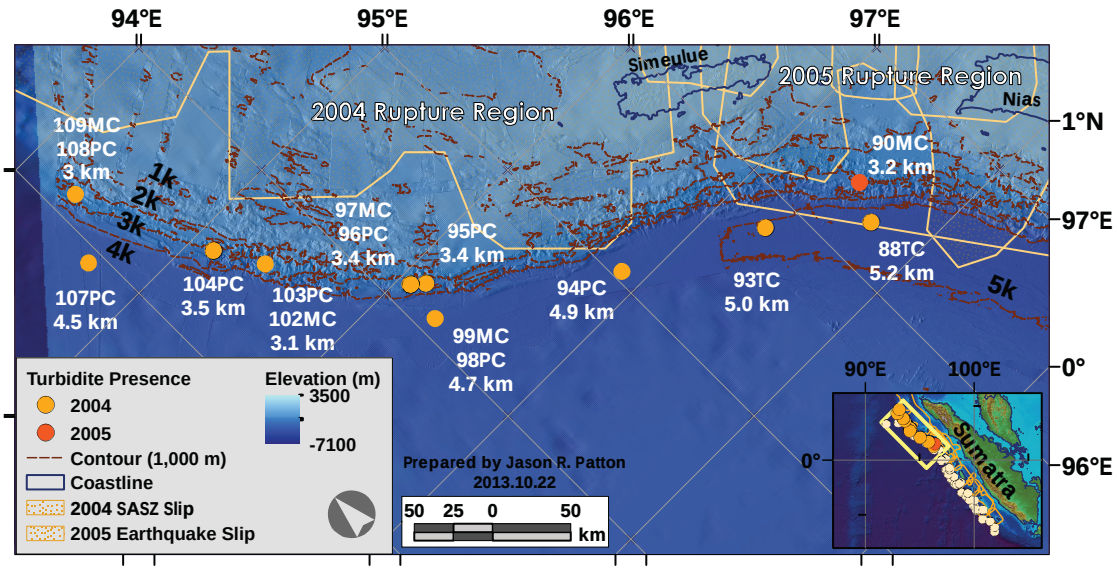
94°E
95°E
96°E
97°E
1°N
97°E
0°
96°E
2004 Rupture Region
2005 Rupture Region
Simeulue
Nias
109MC
108PC
3 km
1k
2k
3k
4k
5k
107PC
4.5 km
104PC
3.5 km
103PC
102MC
3.1 km
97MC
96PC
3.4 km
95PC
3.4 km
99MC
98PC
4.7 km
94PC
4.9 km
93TC
5.0 km
88TC
5.2 km
90MC
3.2 km
Turbidite Presence
2004
2005
Contour (1,000 m)
Coastline
2004 SASZ Slip
2005 Earthquake Slip
Elevation (m)
3500
-7100
Prepared by Jason R. Patton
2013.10.22
50 25 0 50
km
90°E
100°E
0°
Sumatra

scribed in the Methods section. Results are plotted in **Table 2-4 B** and **Fig. 2-6**. No ^{137}Cs activity was measured in core 94PC nor core 105PC.

Each of the five sampling sequences show evidence of excess ^{210}Pb activity underlying the uppermost turbidite in these cores, indicating deposition at least within the past 150 years. The spacing of samples in 94PC and 105TC were located simply to test for presence or absence. Both cores show evidence of recent deposition. We improved our sampling strategy for analyzing the age in 96PC, 96TC, and 102MC by sampling directly beneath the turbidites in depth-adjacent sample locations. 96 and 102 show exponential decay, but 96TC does not, suggesting the sediment in 96TC is very young and probably mixed.

2-3.2 Regional Lithostratigraphy within the 2004 Rupture Zone

Regional correlations of turbidites in our cores are made with integrated stratigraphic correlation techniques. First we present some correlation results that are strongly supported by our methods. These more robust correlations are stronger since they satisfy more criteria including stratigraphic order (superposition), matching sequences of geophysical property signals (fingerprints), etc., and are supported by radiometric age analyses. Then we present the results of our core to core correlations in detail. We mention the correlations that are not as robust, if they satisfy fewer criteria. Reasons for this may be due to a poor stratigraphic record (coring sediment deformation, bioturbation, small dynamic range in particle size/density), lack of radiometric ages (e.g. trench cores), lack of actual correlation, or some other reason. Finally we present the results of our age calibrations and age modeling.

In **Fig. 2-7** we show the compilation of twenty-eight beds we infer to be regionally correlated turbidites, with tie line thickness related to correlation certainty. Of these twenty-eight, 13 to 17 are found in core 108, 22 in core 105, 25 in core 104, 25 in core 103, and 16 to 17 in core 96PC. The three factors that most support our correlations are that these turbidites are in similar stratigraphic sequence, many have shared fingerprints with distinctive details, and they have consistent underlying radiocarbon ages. The more unique the signature, the more able we are able to correlate and more highly we weight that correlation. The superposition and sequence of these deposits with unique signatures provides boundary conditions within cores, between cores (PC and TC pairs), and between core sites. **Fig. 2-7** shows that the strongest correlated beds include regional

turbidites T-1, 4, 5, 6, 7, 8, 9, 10, 13, 16, 19, 21, and 25 (boldest tie lines). We next present several groups of these well-correlated turbidites, T-4 and T-5, T-5 through T-7, and T-15 through T-18 in cores 105, 104, 103, and 96. Examples of these correlations are detailed in **Fig. 2-8** and **Fig. 2-9**.

We here describe the correlations for three turbidite sequences in cores 105, 104, 103 and 96, spanning 170 km and representing a source region of at least 5,000 km^2 (**Fig. 2-3 A**). Cores 104, 103, and 96 are in sedimentologically isolated slope basins and core 105 is in the trench (**Fig. 2-3 A**). Core 104 source areas may be somewhat shared with core 105, but a landward vergent fold in the trench probably isolates 105 from these sources. We first describe the configuration of **Fig. 2-8** and then review these three turbidite sequences. For each sequence, there are three panels; (i) the un-scaled cores, (ii) the un-scaled geophysical properties (MCSL and CT data), and (iii) the "flattened" geophysical properties. The un-scaled core figures are vertically clipped versions of the main core figures, clipped to the stratigraphic section of interest. From left to right, the core figures show gamma density (light blue), CT density (dark blue), the lithologic log, the CT scan, and point magnetic susceptibility (PMS; red). Green tie lines show the correlations for the bases of these turbidites, with certainty designated like in **Fig. 2-7**. We then group each geophysical property data from each core. Each data set has the same range of values for the horizontal axes (gamma density = 0 – 2.5 g/cc; CT density = 0 – 255 dn (gray scale digital number); and PMS = 0 – 100 SI X 10^{-5}). These geophysical data maintain their original vertical scale. The lower panel then shows how geophysical data are flattened to the base of the turbidites using one core at the fixed 100% vertical scale (note the tie-lines are horizontal).

The concept of flattening core data to shared stratigraphic horizons is based on the hypotheses that the stratigraphic sequences in the cores correlate and represent the same sedimentary history. This hypothesis can be tested with unlimited combinations of cores and requires only the assumption that the turbidite deposition consumes zero time. The result is that a flattened core diagram is "hung" on uniform time horizons, represented by the bases and tops of each turbidite. The thicknesses of the turbidites naturally vary between cores at a single site for a variety of reasons. Because turbiditic and hemipelagic sedimentation rates vary for core sites at different sites, the thicknesses of stratigraphic units also vary for those core sites. It is this variability in stratigraphic thickness that is removed when a core sequence is flattened. The technique of flattening simply scales the core data to match these variations in thickness and sedimentation

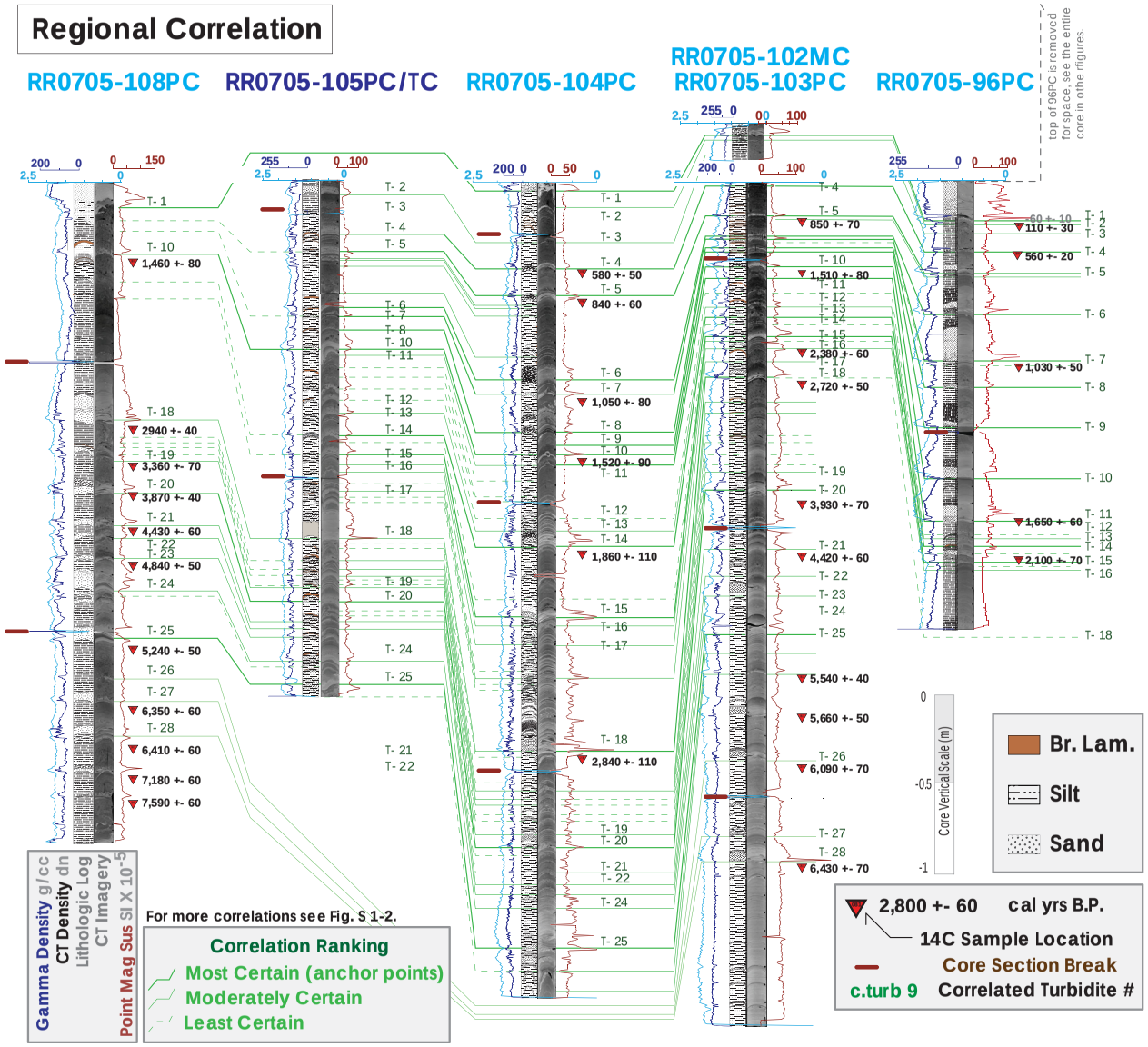

Figure 2-7. Regional Stratigraphic Correlations. Stratigraphic correlations between key cores using lithology, CT, core geophysical properties, and ^{14}C data. MSCL data are plotted and CT imagery displays lower density material in darker grey and higher density material in lighter grey. Slope cores are labeled brown; trench cores are labeled blue. ^{14}C ages are reported in calendar years before present (cal yr BP; 1950). Green correlation tie-lines designate correlation certainty with line thickness and pattern. Correlated turbidites are designated with T-#'s, beginning with the most recent turbidite, T-1.

A) T-4-5

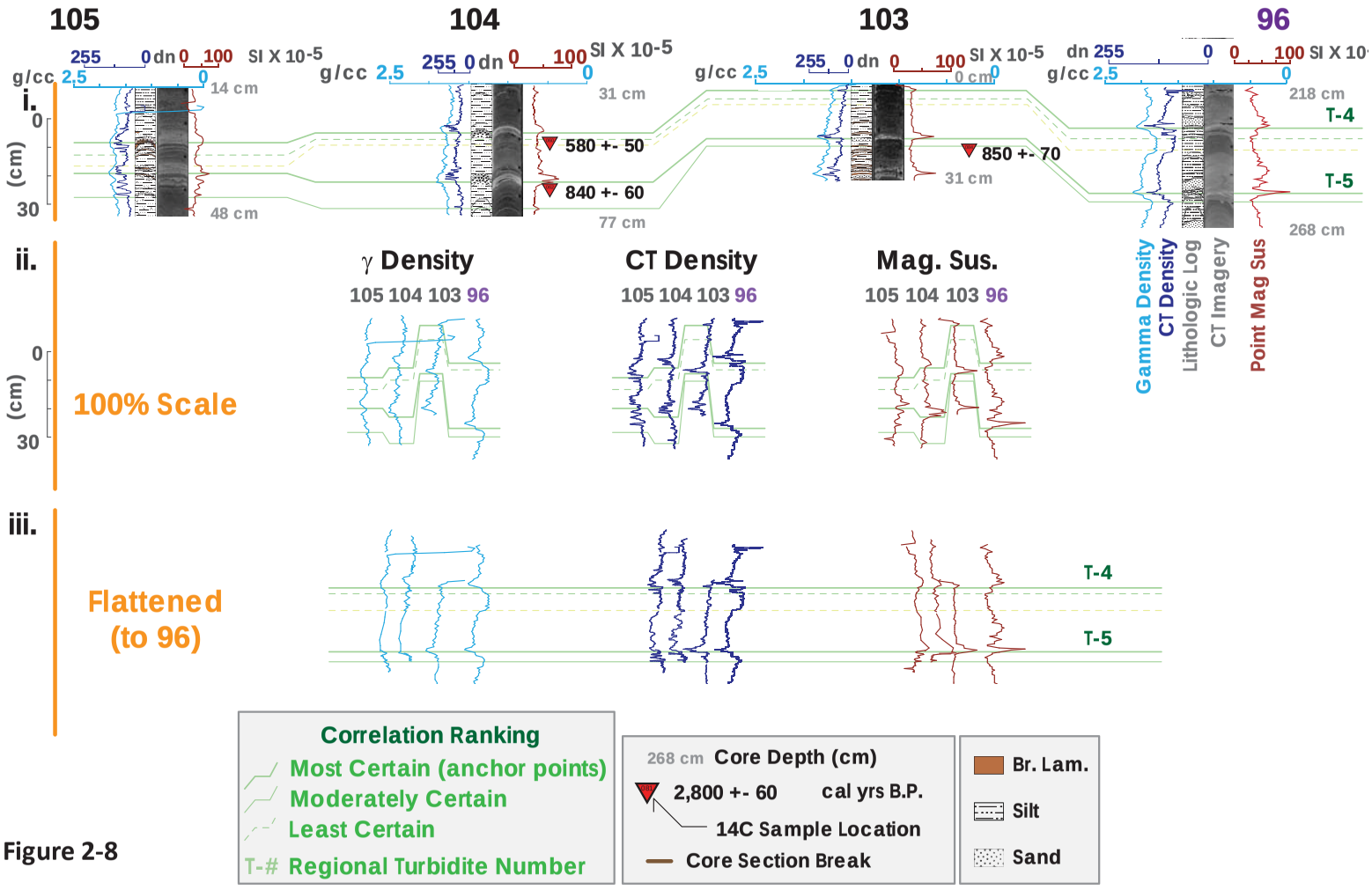

Figure 2-8

B) T-5-7

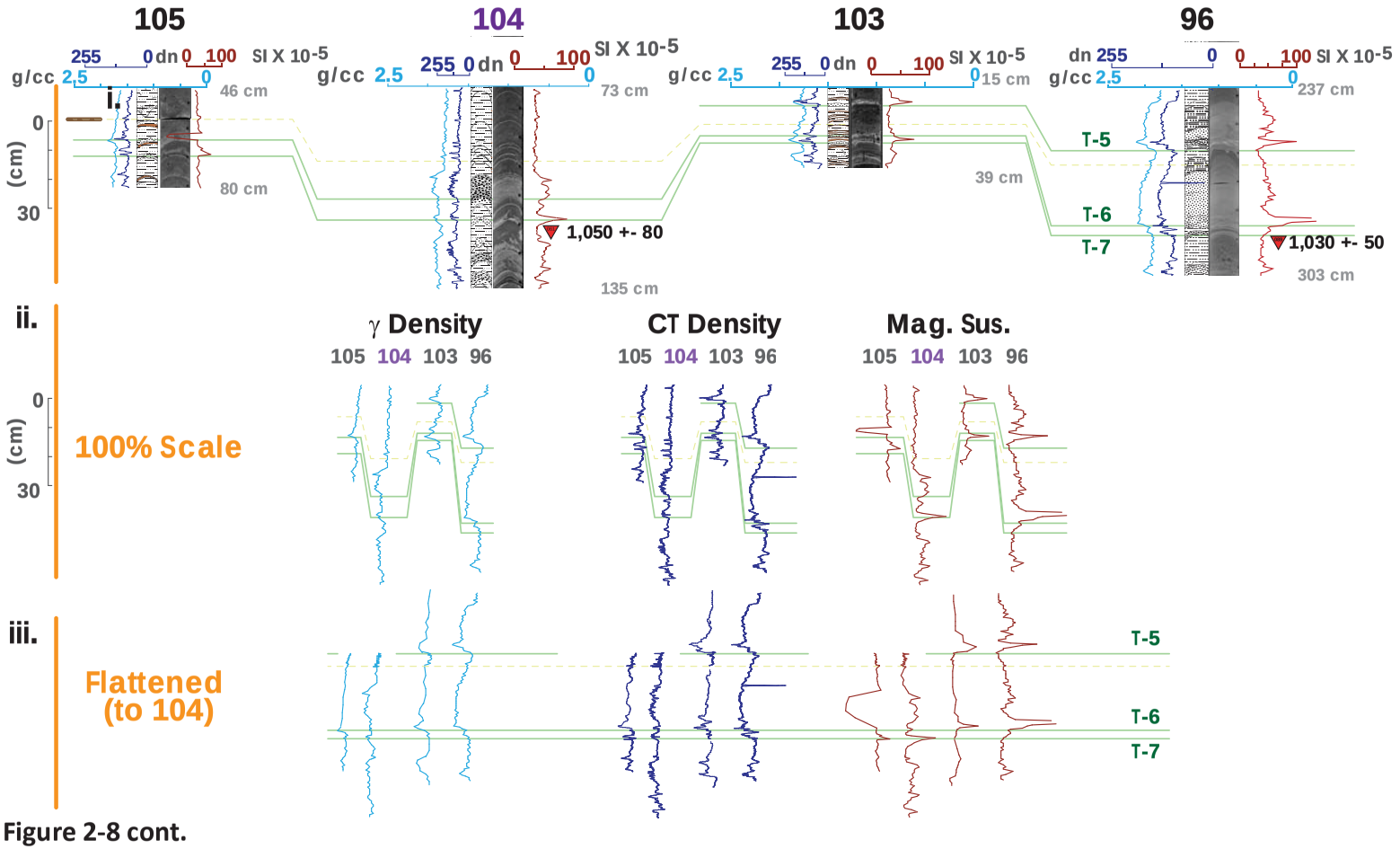

Figure 2-8 cont.

Figure 2-8. Geophysical Flattening. The flattening process is displayed for some correlated turbidites. Geophysical traces are plotted as in **Figure 1- 2-7**. Each turbidite sequence has three panels with different core configurations (left to right: gamma

C) T-15-17

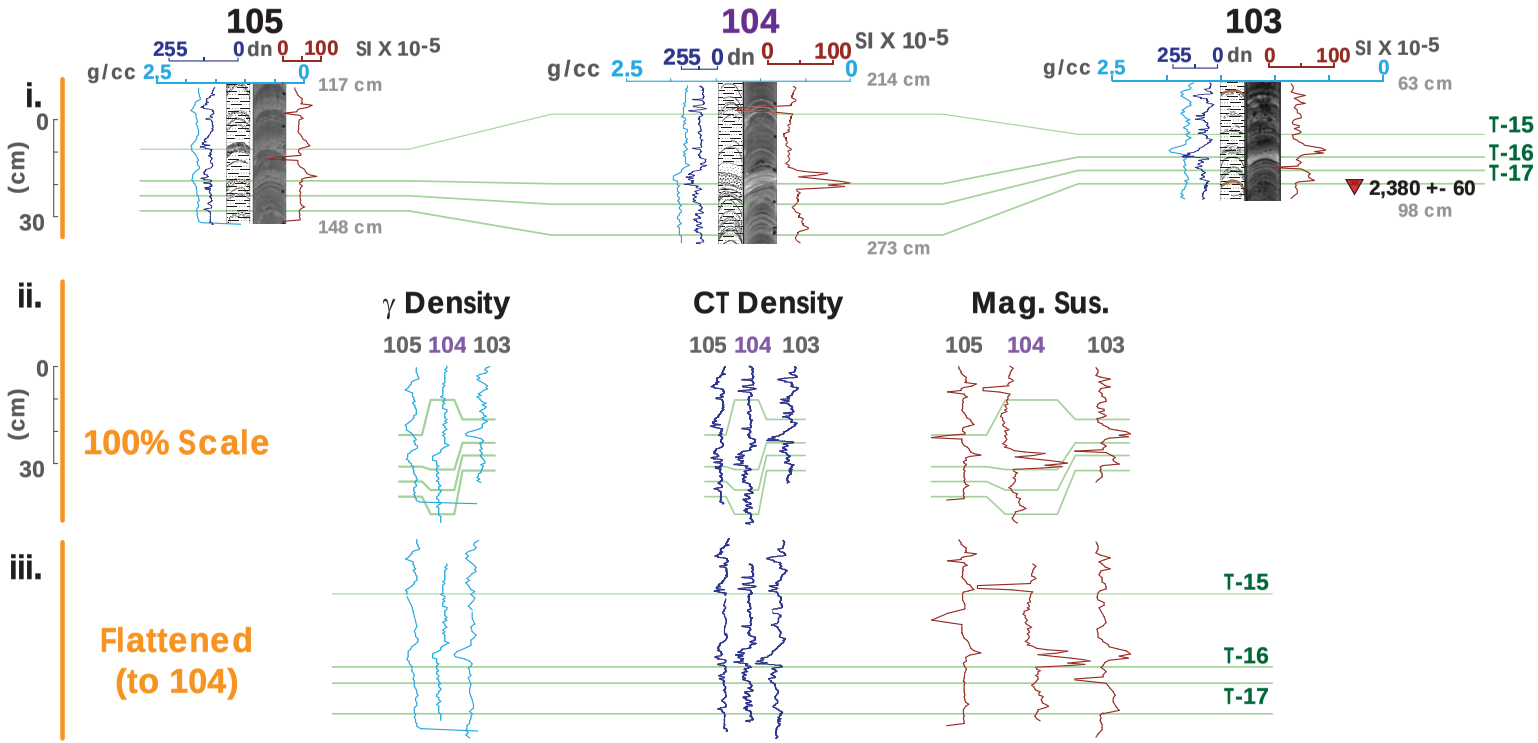

Figure 2-8 cont.

density, CT density, RGB imagery, CT imagery, point magnetic susceptibility, and ^{14}C ages with 95.4% error): i. Vertically true scale of core data, ii. Vertically true scale of geophysical data sets grouped for data type, and iii. Geophysical data are flattened to stratigraphic contacts. Green correlation tie-lines designate correlation certainty with line thickness and pattern. **A.** Turbidites T-4 and T-5 are correlated between cores 105, 104, 103, and 96. **B.** Turbidites T-5 through T-7 are correlated between cores 105, 104, 103, and 96. **C.** Turbidites T-15 through T-18 are correlated between cores 105, 104, and 103.

Figure 2-9. T-18 Correlation. T-18 is correlated between cores 108, 105, 104, 103, and 96 using the same configuration as **Fig. 2-8**. This sedimentary sequence has three panels with different core configurations: i. Vertically true scale of core data (left to right: gamma density, CT density, RGB imagery, CT imagery, point magnetic susceptibility, and ^{14}C ages with 95% error), ii. Vertically true scale of geophysical property data sets grouped for data type, and iii. Geophysical property data are flattened to stratigraphic contacts. Green correlation tie-lines designate the base of T-18 (thick line) and the base of the overlying turbidite (thin line).

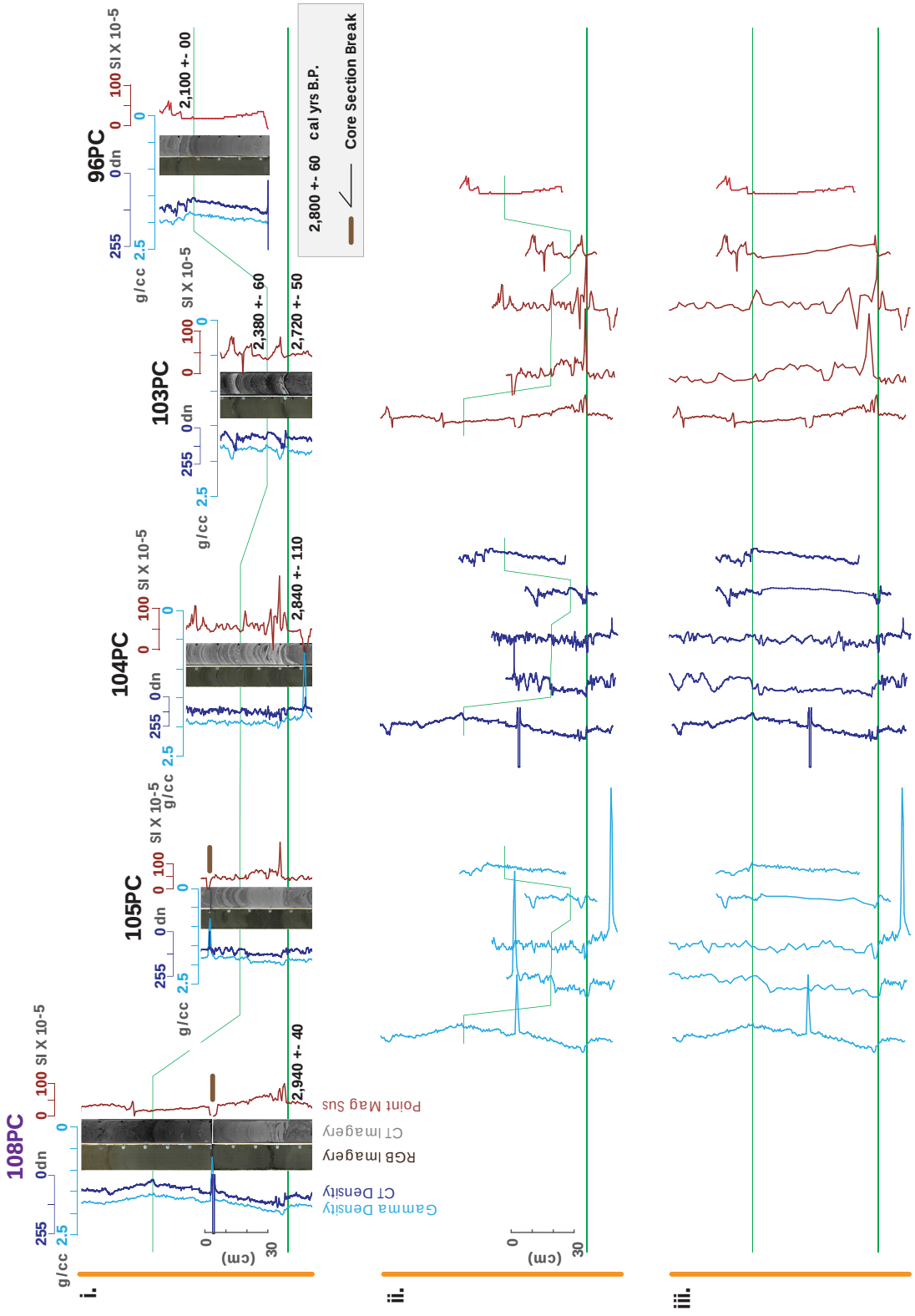
i.
ii.
iii.
108PC
105PC
104PC
103PC
96PC
g/cc
SI X 10-5
Gamma Density
CT Density
RGB Imagery
CT Imagery
Point Mag Sus
(cm)
2,940 +- 40
2,840 +- 110
2,720 +- 50
2,380 +- 60
2,100 +- 00
2,800 +- 60 cal yrs B.P.
Core Section Break

rate. We choose one core (labeled in purple in **Fig. 2-8**) to hold at a fixed vertical scale and then scale ("flatten") the data from other cores to that core. While interpreting our correlations, we flatten all cores to each other; but **Fig. 2-8** shows an example of how we flattened several cores to a single core.

The first turbidite pair T-4 and T-5 are correlated between these four cores, 105, 104, 103, and 96, based on the stratigraphic sequence shared between these cores. T-4 and T-5 are multi-pulse turbidites with fine and very fine sand upward fining to medium to coarse silt. T-4 and T-5 are both preceded by thinner multi-pulse coarse to medium silt turbidites. In core 105, these "precursor" turbidites each have ~3 main pulses and are upward coarsening. While the other cores have lower turbiditic sedimentation rates, the geophysical data show a concomitant upward trend in turbidite mass (coarsening upward), with a multi-pulse geophysical property trend. Cores 104 and 103 have "precursor" turbidites for T-4 that are slightly different (upward fining in core 104; a low mass overall for core 103, resulting in an indistinguishable geophysical fingerprint). The base of the texturally finer part of the tail in T-5 is correlated with a yellow dashed line in **Fig. 2-8 A**. There is a single 14C age for T-4. The two ages for T-5, in cores 104 and 103, have overlap in their error ranges.

With a similarly large regional extent, we correlate T-6 and T-7 between these same cores 105, 104, 103, and 96 (**Fig. 2-8 B**). The overlying sequence of well correlated T-4 and T-5 provide an upper boundary condition for these correlations. T-6 and T-7 in these cores form a sequence of a thin muddy turbidite overlain by a thicker and coarser multi-pulse turbidite. T-7 is a fine sand to silt, multi-pulse turbidite, upwards coarsening in core 96 and upwards fining in cores 105, 104, and 103. T-6 is fine sand to silt, multi-pulse, upwards fining turbidite. In core 104, the base of T-6 is a sequence of ~32 coarse silt to very fine sand, 1-3 mm thick, upwards fining laminations. In core 104, this coarser turbidite head is overlain by the tail that has 1-3 cm coarse silt laminations interbedded with ~6 very fine sand, 1-3 mm thick laminations. One of these coarser laminations is correlated with a yellow dashed line in **Fig. 2-8 B**. T-6 in other cores has a similar depth-density sequence, but 104 has a more expanded section, so the stratigraphic details are less observable in the other cores. The two ^{14}C ages in cores 96 and 104 have overlap in their 95.4% error ranges.

Due to the poor preservation of turbidite structure and the fine texture of turbidites T-15 through T-18 in 96PC, these turbidites are here only correlated between cores 105,

104, and 103 (**Fig. 2-8 C**). These cores span ~70 km and represent a region of at least 2,100 km^2. This turbidite sequence shows how stratigraphic order (superposition) plays a role in addition to the geophysical property trend fingerprints. The dominant turbidite is T-16, a fine sand to silt upward fining multi-pulse turbidite. We compare the sequence T-17, 16, and 15 in regard to the sequential upward change in relative trends of CT density and PMS data. For PMS, T-18 has relative intermediate values, T-17 has lowest values, and T-16 has the largest values. The gamma density sequence begins with the lowest values for T-18, intermediate values for T-17, and the largest values for T-16. These sequential trends match between all three cores. The differences in trends of these geophysical data reflect how these proxies for grain size are imperfect. If they were perfect proxies, the density and PMS trends would match within a core and possibly between cores.

In addition to turbidites T-4 through T-7 and T-15 through T-17 we correlate in **Fig. 2-8**, T-18 has unique sequences that are shared between cores in slope cores (96, 103, 104, and 108) and trench cores (105, 03, 05; Patton et al., 2013).T-18 is a multi-pulse, upward fining, fine sand to silt turbidite (**Fig. 2-9**). PMS data show a large maxima near the base of this deposit, most remarkable in cores 105 and 104, though in 108 and 103 as well. In cores 108 and 105, T-18 is 60 cm and 23 cm thick respectively, with a 20 cm thick sandy base in each core. Core 108 has several upward fining pulses of laminated and massive mud which are only ~3 cm thick in core 105. If the lowermost turbidite in core 96 is T-18, a coarse sandy base of the turbidite, as found in other cores, is missing. Considering the thickness of the tail of this turbidite and turbidites with similar tail thicknesses in other cores, the sandy base may be on the order of tens of centimeters. The three ^{14}C age estimates underlying T-18 in cores 108, 104, and 103 do not have overlap in each of their error ranges. The ages in cores 108 and 104 are slightly older than the age in core 103, though the 95.4% error overlaps for ages in 103 and 104.

In addition to the more well-correlated deposits, which are supported with more correlation criteria; we also describe some more poorly-correlated deposits. Some of these turbidites are well correlated in some cores, but not in other cores. T-12 is poorly correlated between all cores (**Fig. 2-3** and **S 2-2)**. In core 105, 104, and 103, T-12 has a 4 pulse upward fining structure and texture, though is very bioturbated in core 103. Between 108 and 105, T-5, T-7, T-14, and T-15 are not well correlated possibly due to the high bioturbation in core 108. There are fewer apparent turbidites in 108 younger than T-18, making it more challenging to link deposits due simply to the numbers of turbidites and superposition alone.

The first core-to-core comparison is between core 108 in a slope basin and core 107 in the trench. Core 108 is in a small basin that has a 25 meter high sill to the north and a 200 meter sill to the south (**Fig. 2-5**). This basin probably partially drains to the north, given that turbidity current flow depths may be over 100 meters (Muck and Underwood, 1990; Völker et al., 2008). Core 107 is in the trench axis 45 km to the southwest of core 108. Stratigraphy in cores 108PC and 108TC correlate well with no apparent missing sediment from core 108PC. The TC has ~45 cm of repeated stratigraphic section, which happens if the core penetrates the seafloor multiple times (e.g. when the ship is optimally heaving for this to occur). We observe that core 107 has more turbidites between T-1 and T-10. Core 108 is bioturbated in this section, possibly confounding the geophysical property representation of those deposits, making it more difficult to uniquely correlate strata. T-14 in core 108 also has an indistinct geophysical property trend, though is upward fining in both cores. Based solely on the comparison of T-18 between these two cores, this is a poor correlation. The correlation of T-18 between cores 108 and 107 is most supported by the correlation between 107 and 105, presented next.

Moving southward, we compare strata between two trench cores, 107 and 105 (**Fig. S 2-2**). Core 107 is located in the axis of the trench at 4,520 meters water depth. While coring core 107, the core tripped prematurely at ~1,134 meters water depth. This changed the depth configuration of the PC and the TC, leaving the PC as a lower position (the PC cores sediment before the TC). T-1 is present in 107PC, but not 107TC. The TC is typically more likely to sample the uppermost sediment. Sediment in core 107PC is highly disturbed from coring, but is sufficiently preserved to tentatively correlate with 107TC. Core 105 is located on a 20+ km wide terrace that is ~100 meters above the depth of the trench axis at a depth of 4,480 m, 11 km from the trench axis which has a depth of 4,550 meters water depth. Core 105 is west of gently sloping 0.5 km high landward verging anticline (Henstock et al., 2006; Sultan et al., 2009) isolating this core from direct sedimentation from higher relief bathymetry to the east. 105TC sampled ~15 cm more sediment than 105PC, so core 105 is shown as a PC/TC composite core. T-1 is apparently missing in core 105TC. There is some dense sediment at the very top of 105TC, which may be T-1, but that would be difficult to test. The uppermost ^{210}Pb sample has presence of activity beneath this possible T-1 deposit (**Fig. 2-6**). There is no MC at the 105 core site, so we are not certain that the sediment water interface was sampled in 105TC. T-2 in core 107TC is very bioturbated, the gamma density matches nicely between these two cores but the CT density does not. While T-3 in these cores has a low dynamic range in

turbidite texture and geophysical property trends, we correlate the sequence of T-4 and T-5 with high certainty (**Fig. 2-8**), which further supports our correlations of T-2 and T-3. We correlate T-6 through T-10 with high certainty due to shared sequences of geophysical property trends and shared patterns of turbidite structures. In core 107, turbidites underlying T-10, down to T-14, are disturbed due to coring and are therefore more difficult to correlate. In core 107, the turbidites underlying T-14 are muddy and have low dynamic range in density, so do not have characteristic trends in geophysical properties. We correlate the lower turbidites in core 107 with core 105 with less certainty.

Comparing the next set of cores, 105 and 104 distanced 40 km apart, core 104 is located at 3,480 meters water depth near the base of a ~1.5 km tall cliff, within and near the edge of a slope basin that is being dissected by a submarine canyon from the southeast (**Fig. 2-3**). Cores 104PC and 104TC contain the same uppermost stratigraphy, including the coarse sandy base of T-1. Core 104TC includes over 1 m of repeated stratigraphic section. The turbidites in core 104 are more thinly laminated than those in 105, but the geophysical property trends match well for most of these correlated turbidites. Correlations of T-4 through T-7 are presented above. Turbidites underlying T-16 down to T-18 are closely spaced and difficult to interpret. T-18 provides a robust anchor point and boundary condition for the underlying correlations T-19 through T-21. We correlate turbidites T-21 through T-25 with low certainty due to the closely spaced finely laminated turbidites in core 104. These finely laminated turbidites are difficult to distinguish from each other within core 104.

Cores 104 and 103, the next core pair, are distanced 34 km apart. Core 103, at a depth of 3,070 meters, is located near the center of a 2-4 km wide flat-bottomed slope basin that slopes at ~1° to the east, with no resolvable channels (**Fig. 2-3**). The basin is enclosed by a 20 meter sill on the northwestern boundary, which probably permits partial flows of sediment outside of this basin. When combined with 102MC, the same core site as 103PC, we correlate turbidites between cores 103/102 and core 104 with high certainty, ranging from T-1 through T-10, T-16, T-18, T-21, and T-25. Core 103 is missing T-1, but T-1 through T-3 are sampled in core 102, providing stratigraphic overlap of T-2 and T-3 between these cores (**Appendix S 2-2**). The lowest ~50 cm of 103TC contains repeated stratigraphic section. Turbidites in core 103 are much thinner overall, than core 104 (e.g. the base of T-7 is at a depth of 32 cm in core 103 and at a depth of 119 cm in core 104). In cores 103 and 104, the sequence of T-8 and T-9 shows an overall upwards increase in PMS values, helping to uniquely identify these correlated turbidites. The sequence T-10

and T-11 also has matching and superposed geophysical fingerprints in cores 103 and 104. The turbidites between T-11 and T-15 are too bioturbated in core 103, so do not have sufficiently distinguishable geophysical property trends, so those correlations are less certain. The sequence T-15 and T-16 also has matching and superposed geophysical fingerprints in cores 103 and 104. We correlate T-17 less confidently because of the finder texture in core 103 and more numerous laminae in core 104. T-18, T-21, and T-25 have slightly more certain correlations that constrain lesser certain correlations for the interbedded turbidites. T-18 has a higher mass than the over- and underlying turbidites, providing a boundary condition for those other correlations. Cores 103 and 104 have a very distinct PMS trend for T-21, which supports the high certainty of that correlation. There are more turbidites that appear to correlate between 104 and 103 than do to other cores, but these turbidites do not get T numbers because of their limited aerial extent. Due to the closely spaced laminations and lack of hemipelagic sediment in core 104, there are few ^{14}C ages in the lower section. This makes it difficult to test these correlations independently.

We finally present the results of our correlations between cores 103 and 95/96/97 (**Fig. 2-5, 2-7, S 2-2**). Cores 95 and 96/97 are located in two small (~50 square km) enclosed basins, within a larger slope basin that partially drains to the south over a 70 meter high sill at 3,350 meters water depth (**Fig. 2-5 E**). Core 95 contains strata that are correlated one-for-one with strata in core 96, but the sediments in core 95 are quite disturbed, so we leave that core out of the correlation figures and later discussion. The overlap in stratigraphy between 96 PC and TC and 97 MC were presented earlier. Based on the down core trend in ^{210}Pb data, the ~5 cm thick sediment underlying T-1 in core 96TC is likely from the seafloor and is repeated section possibly from the seafloor. Based on this observation, it is possible that the base of T-1 is not in core 96TC. Turbidites in core 96 are generally thicker and less bioturbated than those in core 103. Besides the highly certain correlations presented earlier for **Fig. 2-8**, the turbidites underlying T-11 are more bioturbated, thinner, and finer in texture than most overlying turbidites, owing to the less certain correlations between cores 103 and 96. Finally, since T-18 is not entirely within core 96, this correlation is less certain and untestable.

Trench cores 98 and 94 are the southernmost trench cores in the 2004 earthquake slip region (**Fig. 2-6**). Core 98 is west of gently sloping 0.5 km high landward verging anticline, possibly isolating this core from direct sedimentation from higher relief bathymetry to the east. Core 94 is located off-axis from the trench and downslope of several potential

landslide source areas in the form of submarine canyons, base of slope apron fan channels, and local landslide amphitheater complexes (Patton et al., 2013). In the trench, cores 98PC and 98TC overlap completely and neither sampled the sediment-water interface, evidenced by core 99MC; which has the uppermost turbidite we interpret to be T-1 (**Appendix S 2-2**). Most turbidites in core 98 are muddy with low dynamic range in density/particle size. This, coupled with the lack of ^{14}C ages, leads to generally less certain correlations. At the southern limit of the 2004 earthquake slip region, core 94PC sampled the uppermost turbidite that we interpret as T-1. Core 94 is highly deformed and lacks ^{14}C age control, so these correlations are also less certain (**Appendix S 2-2**). However, ^{210}Pb age data are consistent with our interpretation that this is T-1.

Further south in cores 93 and 88, we make moderately certain correlations with the turbidite underlying the uppermost turbidite in those cores. We correlate these second turbidites in these cores to be T-1 found in our other cores mentioned above (**Appendix S 2-2**). The geophysical property trends are almost identical between these cores and are very similar to the geophysical fingerprint of T-1 in core 96.

2-3.2.1 Radiocarbon Age Results

Raw calibrated ages were presented in **Table 2-2**, but here we present the results of our age model based calibrations for deposits older than T-1. Bayesian modeling of radiocarbon calibrations takes into account varying degrees of stratigraphic information as prior constraints for these calibrations. We utilize P_Sequence age models for within-core age calibrations and present these results in **Fig. 2-7** and **Appendix S2-5 B-E**. We use Sequence age models for the region-wide comparison of ages between cores and summarize these age model results in **Table 2-5**. All ages initially considered in our model are in **Table 2-5 A**. Ages that we consider in our final age model are in **Table 2-5 B**. Below we discuss how we choose which ages to include in our final age models.

Where multiple ^{14}C ages exist for correlated turbidites, and where ages do not suggest erosion or other problems, we test whether they are consistent with our stratigraphic correlation model by using the 'Combine' function in OxCal software (Bronk Ramsey, 2008). "Combined" ages for turbidites 5, 8, 9, 11, and 14, are computed with the combination of either two or three ages (**Appendix S 2-5**). OxCal takes the lab ages and calculates a pooled mean lab age prior to calibration. The result is a probability density function age range, based on the contribution of all combined ages. We evaluate the

Combine results using three criteria: a chi-squared test, the OxCal agreement index "Acomb" (>60), and convergence integral "C" (>95) (Bronk Ramsey, 1995, 2009). The combine function is normally used with the prior information that the samples come from either the same sample, or from the same horizon (Bronk Ramsey, 2008). Our lithostratigraphic correlations constitute the evidence of the same horizon, though with

TABLE 2-5 A. RADIOCARBON AGE OXCAL MODELING RESULTS FOR TURBIDITE AGES IN THE 2004 SASZ EARTHQUAKE REGION

Regional Turbidite Number	Core Number	Sample/Combine Name*	Unmodeled Median Age (yrs BP)†	1 Sigma Error (yrs)	Modeled Median Age (yrs BP) §	1 Sigma Error (yrs)	Acomb #	A **	Excluded
Start	Boundary	T-0 Boundary(2007)	(60)	-	(60)	-	-	100	
1	Synthetic	Sum-T-1	-	-	(30)	40	-	-	
2	96PC	RR0705_96PC_206_208_SUM-227+N(8,1)	50	50	70	50	-	-	
3	104TC	RR0705_104TC_011_013_SUM-176+N(35,3)	300	40	310	40	-	-	
4	Combine	Sum-T-4 Combine	650	10	650	10	70	-	
4	104PC	RR0705_104PC_049.5_051.5_SUM-060+N(9,1)	620	30	650	10	-	80	
4	96PC	RR0705_96PC_222_224_SUM-228+N(8,1)	670	20	650	10	-	70	
5	Combine	Sum-T-5 Combine	730	20	730	20	120	-	
5	104TC	RR0705_104TC_047.5_049.5_SUM-175+N(12,1)	730	30	730	20	-	110	
5	103PC	RR0705_103PC_020_022_SUM-084+N(5)	740	40	730	20	-	120	
6	Synthetic	Sum-T-6	-	-	890	90	-	-	
7	Combine	Sum-T-7 Combine	1,050	40	1,050	40	40	-	
7	104PC	RR0705_104PC_122_124_SUM-061+N(17,2)	1,160	60	1,050	40	-	40	yes
7	96PC	RR0705_96PC_287.5_289.5_SUM-089+N(3)	1,010	40	1,050	40	-	70	
8	Synthetic	Sum-T-8	-	-	1,190	90	-	-	
9	Synthetic	Sum-T-9	-	-	1,350	90	-	-	
10	Combine	Sum-T-10 Combine	1,480	20	1,480	20	10	-	
10	108PC	RR0705_108PC_039_041_SUM-080+N(41,4)	1,520	30	1,480	20	-	70	
10	108TC	RR0705_108TC_020_022_SUM-172+N(44,4)	1,420	40	1,480	20	-	50	yes
10	104PC	RR0705_104PC_158_160_SUM-082+N(5)	1,580	40	1,480	20	-	-	
10	103PC	RR0705_103PC_049_051_SUM-054+N(18,2)	1,450	40	1,480	20	-	120	
10	103TC	RR0705_103TC_036_038_SUM-178+N(23,2)	1,400	40	1,480	20	-	40	yes
11	Combine	Sum-T-11 Combine	1,640	30	1,630	30	110	-	
11	103TC	RR0705_103TC_039_041_SUM-179+N(0)	1,620	40	1,630	30	-	110	
11	96PC	RR0705_96PC_374_376_SUM-090+N(7,1)	1,670	50	1,630	30	-	100	
12	Synthetic	Sum-T-12	-	-	1,730	80	-	-	
13	Synthetic	Sum-T-13	-	-	1,840	90	-	-	
14	104PC	RR0705_104PC_207_209_SUM-115+N(17,2)	2,040	270	1,940	70	-	-	
15	96PC	RR0705_96PC_399_401_SUM-232+N(12,1)	2,010	40	2,030	40	-	-	
16	Synthetic	Sum-T-16	-	-	2,230	150	-	-	
17	Synthetic	Sum-T-17	-	-	2,510	160	-	-	
18	Combine	Sum-T-18 Combine	2,750	20	2,750	20	120	-	
18	108PC	RR0705_108PC_132.5_134.5_SUM-081+N(0)	2,780	30	2,750	20	-	100	
18	104PC	RR0705_104PC_326_328_SUM-235+N(6,1)	2,750	40	2,750	20	-	130	
18	103TC	RR0705_103TC_079_081_SUM-180+N(0)	2,740	30	2,750	20	-	100	
19	108PC	RR0705_108PC_156_158_SUM-083+N(74,7)	3,290	30	3,300	30	-	-	
20	Combine	Sum-T-20 Combine	3,930	30	3,930	30	-	-	
20	108PC	RR0705_108PC_175_177_SUM-046+N(43,4)	4,040	50	3,930	30	-	20	yes
20	103PC	RR0705_103PC_174_176_SUM-087+N(125,13)	3,760	40	3,930	30	-	-	
21	Combine	Sum-T-21 Combine	4,450	30	4,450	30	110	-	
21	108PC	RR0705_108PC_194_196_SUM-194+N(24,2)	4,430	40	4,450	30	-	110	
21	103PC	RR0705_103PC_209_211_SUM-050+N(3)	4,470	40	4,450	30	-	110	
22	Synthetic	Sum-T-22	-	-	4,630	90	-	-	
23	108PC	RR0705_108PC_212.5_214.5_SUM-045+N(46,5)	4,780	30	4,790	30	-	-	
24	Synthetic	Sum-T-24	-	-	4,930	90	-	-	
25	108PC	RR0705_108PC_257_259_SUM-042+N(52,5)	5,070	60	5,110	60	-	-	
26	103PC	RR0705_103PC_324_326_SUM-224+N(17,2)	5,920	40	5,930	40	-	-	
27	108PC	RR0705_108PC_290.5_292.5_SUM-044+N(19,2)	6,320	30	6,320	30	-	-	
28	Combine	Sum-T-28 Combine	6,430	30	6,440	30	90	-	
28	108PC	RR0705_108PC_312.5_314.5_SUM-043+N(53,5)	6,470	40	6,440	30	-	100	
28	103PC	RR0705_103PC_383_385_SUM-253+N(13,1)	6,400	40	6,440	30	-	90	
29	108PC	RR0705_108PC_330_332_SUM-041+N(64,6)	7,140	30	7,140	30	-	-	
30	108PC	RR0705_108PC_345_347_SUM-195+N(174,17)	7,450	30	7,460	30	-	-	
End	Boundary	-8000	-	-	-	-	-	-	

* Sample names that are indented are the ages included in the combine function, named above them.

† Calibrated age and errors reported to 1 standard deviation and are reported in calendar years. Calibrated age ranges before A. D. 1950 according to Stuiver and Reimer calculated using marine reservoir correction and regional delta R offset (ΔR = 16). These ages are the result of simple calibrations, prior to any statistical manipulation during the "Combine" analysis (aka. unmodeled). Synthetic age estimates are designated with sample names "Sum-T-#" and have no unmodeled ages.

§ These are the results of calibration with the "Combine" function. Years are reported as in the unmodeled results.

Agreement Index Acomb.

** Agreement Index A.

some uncertainty. We acknowledge that our combine results may impart a shorter time range than is supported by the a priori age range.

We present here the results of our criteria tests for P_Sequence and Sequence age models and how we used these criteria to remove select ages from our Sequence age models. Of the combines shown in **Figure 2-7** or **Table 2-6**, there were no chi-squared or

TABLE 2-5 B. RADIOCARBON AGE OXCAL MODELING RESULTS FOR TURBIDITE AGES IN THE 2004 SASZ EARTHQUAKE REGION

Regional Turbidite Number	Core Number	Sample/Combine Name*	Unmodeled Median Age (yrs BP)†	1 Sigma Error (yrs)	Modeled Median Age (yrs BP) §	1 Sigma Error (yrs)	Acomb #	A **
Start	Boundary	T-0 Boundary(2007)	(60)	-	(60)	-		
1	Synthetic	Sum-T-1	-	-	(30)	40		
2	96PC	RR0705_96PC_206_208_SUM-227+N(8,1)	50	50	70	50		
3	104TC	RR0705_104TC_011_013_SUM-176+N(35,3)	300	40	300	40		
4	Combine	Sum-T-4 Combine	650	10	650	10		
4	104PC	RR0705_104PC_049.5_051.5_SUM-060+N(9,1)	620	30	650	10	66.4	
4	96PC	RR0705_96PC_222_224_SUM-228+N(8,1)	670	20	650	10		77.6
5	Combine	Sum-T-5 Combine	730	20	730	20		72.3
5	104TC	RR0705_104TC_047.5_049.5_SUM-175+N(12,1)	730	30	730	20	121.4	
5	103PC	RR0705_103PC_020_022_SUM-084+N(5)	740	40	730	20		114.7
6	Synthetic	Sum-T-6	-	-	870	80		116
7	96PC	RR0705_96PC_287.5_289.5_SUM-089+N(3)	1,010	40	1,020	40		
8	Synthetic	Sum-T-8	-	-	1,140	90		
9	Synthetic	Sum-T-9	-	-	1,290	90		
10	Combine	Sum-T-10 Combine	1,420	30	1,430	30		
10	108TC	RR0705_108TC_020_022_SUM-172+N(44,4)	1,420	40	1,430	30	108.3	
10	103PC	RR0705_103PC_049_051_SUM-054+N(18,2)	1,450	40	1,430	30		112.2
10	103TC	RR0705_103TC_036_038_SUM-178+N(23,2)	1,400	40	1,430	30		102.8
11	Combine	Sum-T-11 Combine	1,640	30	1,630	30		99.1
11	103TC	RR0705_103TC_039_041_SUM-179+N(0)	1,620	40	1,630	30	106.2	
11	96PC	RR0705_96PC_374_376_SUM-090+N(7,1)	1,670	50	1,630	30		107.5
12	Synthetic	Sum-T-12	-	-	1,730	80		98.5
13	Synthetic	Sum-T-13	-	-	1,840	90		
14	104PC	RR0705_104PC_207_209_SUM-115+N(17,2)	2,040	270	1,940	70		
15	96PC	RR0705_96PC_399_401_SUM-232+N(12,1)	2,010	40	2,030	40		
16	Synthetic	Sum-T-16	-	-	2,230	150		
17	Synthetic	Sum-T-17	-	-	2,510	160		
18	Combine	Sum-T-18 Combine	2,750	20	2,750	20		
18	108PC	RR0705_108PC_132.5_134.5_SUM-081+N(0)	2,780	30	2,750	20	116.2	
18	104PC	RR0705_104PC_326_328_SUM-235+N(6,1)	2,750	40	2,750	20		100.7
18	103TC	RR0705_103TC_079_081_SUM-180+N(0)	2,740	30	2,750	20		127.1
19	108PC	RR0705_108PC_156_158_SUM-083+N(74,7)	3,290	30	3,300	30		99.2
20	103PC	RR0705_103PC_174_176_SUM-087+N(125,13)	3,760	40	3,760	40		
21	Combine	Sum-T-21 Combine	4,450	30	4,450	30		100.2
21	108PC	RR0705_108PC_194_196_SUM-194+N(24,2)	4,430	40	4,450	30	109.2	
21	103PC	RR0705_103PC_209_211_SUM-050+N(3)	4,470	40	4,450	30		106.6
22	Synthetic	Sum-T-22	-	-	4,630	90		106.5
23	108PC	RR0705_108PC_212.5_214.5_SUM-045+N(46,5)	4,780	30	4,790	30		
24	Synthetic	Sum-T-24	-	-	4,920	80		
25	108PC	RR0705_108PC_257_259_SUM-042+N(52,5)	5,070	60	5,100	60		
26	103PC	RR0705_103PC_324_326_SUM-224+N(17,2)	5,920	40	5,930	40		
27	108PC	RR0705_108PC_290.5_292.5_SUM-044+N(19,2)	6,320	30	6,320	30		
28	Combine	Sum-T-28 Combine	6,430	30	6,440	30		
28	108PC	RR0705_108PC_312.5_314.5_SUM-043+N(53,5)	6,470	40	6,440	30	92.9	
28	103PC	RR0705_103PC_383_385_SUM-253+N(13,1)	6,400	40	6,440	30		99.5
29	108PC	RR0705_108PC_330_332_SUM-041+N(64,6)	7,140	30	7,140	30		90.3
30	108PC	RR0705_108PC_345_347_SUM-195+N(174,17)	7,450	30	7,460	30		
End	Boundary	Start Boundary(-8000)	9,950	-	9,950	-		

* Sample names that are indented are the ages included in the combine function, named above them.

† Calibrated age and errors reported to 1 standard deviation and are reported in calendar years. Calibrated age ranges before A. D. 1950 according to Stuiver and Reimer calculated using marine reservoir correction and regional delta R offset (ΔR = 16). These ages are the result of simple calibrations, prior to any statistical manipulation during the "Combine" analysis (aka. unmodeled). Synthetic age estimates are designated with sample names "Sum-T-#" and have no unmodeled ages.

§ These are the results of calibration with the "Combine" function. Years are reported as in the unmodeled results.

Agreement Index Acomb.

** Agreement Index A.

agreement index failures for the P_Sequence age models. The Sequence age model had several failures for the age combinations (Combine function; **Table 2-5**). Combines for T-7 and T-10 fail the chi-squared test and the agreement index tests. The Combine for T-7 passes the chi-squared test, but initially fails the Acomb index at 39.5% and An of 50.0%. We removed age SUM-061 (core 104PC) from the Combine because the Agreement

TABLE 2-6. RADIOCARBON AGES AND PRESENCE/ABSENCE FOR REGIONAL TURBIDITES IN THE 2004 SASZ EARTHQUAKE REGION

Regional Turbidite Number	Analysis Type *	Source Core(s)	Regional Median Age (yrs BP) †	95% Error (yrs)	Core Presence of Regional Turbidite §									
					108	107	105	104	103	102	98 #	96	95	94 #
1	P_sequence	96PC	-50	10	xx	xx		xx		xx		xx	xx	xx
2	R_date	96PC	100	110			xx	xx			x	xx		x
3	R_date	104TC	310	70			xx	xx			x	xx		x
4	Combine	104PC,96PC	640	30		xx	xx	xx	xx		x	xx	xx	x
5	Combine	C	730	50	xx	xx	xx	xx	xx		x	xx	xx	x
6	Synthetic		870	140	x			xx	xx		x	xx	xx	x
7	R_date	96PC	1,020	70	xx	xx	xx	xx	xx		x	xx	xx	x
8	Synthetic		1,160	170		xx	xx	xx	xx		x	x		x
9	Synthetic		1,270	170		xx	xx	xx	xx		x	xx	xx	x
10	Combine	108TC,103PC,103TC	1,420	50	xx	xx	xx	xx	xx		x	xx	xx	x
11	Combine	103TC,96PC	1,630	60			xx		xx		x	xx	xx	x
12	Synthetic		1,760	150					xx		x	xx		x
13	Synthetic		1,840	160					xx		x	xx		x
14	R_date	104PC	1,930	140	xx		xx	xx	xx		x	xx		x
15	R_date	96PC	2,030	80	x		xx	xx	xx		x	xx		x
16	Synthetic		2,290	280			xx	xx	xx		x	xx		x
17	Synthetic		2,460	280				xx	xx		x	x		x
18	Combine	108PC,104PC,103TC,108PC	2,760	40	xx		xx	xx	xx		x			x
19	R_date	108PC	3,240	70	xx		xx	xx	xx		x			x
20	Combine	108PC,103PC	3,760	70	xx		xx	x	xx		x			
21	Combine	108PC,103PC	4,440	50	xx			x	x		x			
22	Synthetic		4,620	160	xx			x	x		x			
23	R_date	108PC	4,790	60	xx			x	x		x			
24	Synthetic		4,940	160	xx			x	xx		x			
25	R_date	108PC	5,090	110	xx			x	xx					
26	R_date	103PC	5,940	80	xx				x					
27	R_date	108PC	6,320	60	xx				x					
28	Combine	C	6,440	60	xx				x					
29	R_date	108PC	7,140	60	xx									
30	R_date	108PC	7,450	70	xx									

* (1) R_date ages are the result of using the Sequence command in OxCal. (2) Combine are ages based on the "Combine" function in OxCal. (3) Synthetic ages are based on the "Date" command in our OxCal age model. Synthetic ages are not attributed to any "source" core.

† Calibrated age and errors reported to 95% error and are reported in calendar years. Calibrated age ranges before A. D. 1950 according to Stuiver and Reimer calculated using marine reservoir correction and regional delta R offset (ΔR = 16).

§ The more certain that a regional turbidite is present in a given core is designated xx. The less certain that a regional turbidite is present in a given core is designated x.

trench cores with sediments of low dynamic range, or greater coring deformation, are correlated with lesser certainty.

Index “A” was lower at 36.1%, leaving a single age calibration for the T-7 age estimate. The Combine for T-10 initially fails the chi-squared test with 4 degrees of freedom at 5%, Acomb 9%, and An = 31.6%. For the T-10 Combine, we first remove the age SUM-082 because it has the lowest agreement index value for Index “A” at 2.8%. We then applied a Combine with the remaining four ages, but the results still failed with the agreement index “Acomb” at 48.2%. We next removed age SUM-080 (core 108PC) because it had an Index “A” value of 32.5. We include SUM-172, SUM-054, and SUM-178 (from cores 108PC and 103PC respectively) in our final Combine. The final Combine for our T-10 age estimate resulted with a passed chi-squared test and an agreement index Acomb of 109.6%.

2-3.2.2 Regional Stratigraphic Correlation Summary

The more certain correlations temporally span 3.9 ka (T-1 through T-20) in core 108, 2.8 ka in core 104 (T-1 through T-18), ~3.9 ka in cores 102/103 (T-1 through T-20), and 1.6 ka in core 96 (T-1 through T-12; **Fig. 2-3**). These more certain correlations include 9 turbidites in core 108, 9 turbidites in core 107, 18 turbidites in core 105, 19 turbidites in core 104, 19 turbidites in core 103, 11 turbidites in core 96, 7 turbidites in core 98, 7 turbidites in core 94, 5 turbidites in core 93, and possibly 10 turbidites in core 88. When we include lesser certain correlations, there are 13 turbidites in core 107, 23 in core 105 and 18 in core 96. We find that these cores 108, 107, 105, 104, 103, and 96 contain 45%, 87%, 92%, 100%, 100%, and 100% of these correlated turbidites.

We have tested potential correlations between sites within the 2004 rupture zone iteratively using the available age control, patterns of variability in the overall sequence of turbidites, and detailed comparisons for intra- inter-site similarity between individual turbidites. We find that in some cases, individual turbidite characteristics are similar enough, within and between sites, that they may be used to track individual events in the sequence. The stratigraphic sequences with the most unique “fingerprints” (Goldfinger et al, 2013) carry the strongest correlative weight and act as “anchor ties” for our correlations (**Figs. 2-3 and 1-6**). ^{14}C ages provide age control provides a temporal framework for our correlations. We designate turbidites with numbers corresponding to their order down from the seafloor. Turbidites are assigned T-numbers which designate these events as beds which we interpret as regionally correlative (e.g. T-1), counting down from the uppermost turbidite.

2-4. Discussion

2-4.1 The 2004 Turbidite

We use this section to discuss our interpretation that the uppermost turbidite in twelve cores to be the result of strong ground shaking form the 2004 SASZ earthquake. Our interpretation is supported by the lithologic descriptions, sedimentologic properties, and several measures of relative and absolute age. This interpretation is further supported by the similarity of the sediment geophysical properties plotted versus depth and possibly the plots of seismic energy release versus time and latitude.

We found the uppermost turbidites in cores 109, 108, 107, 104, 102, 99, 97, 96, 95, and 94 to be composed of sediment that is grey and has a high water content (i.e. “soupy”), particularly at the seabed. There is no hemipelagic sediment overlying this deposit nor is there oxidation observed of the uppermost sediment in any of these cores. This deposit, if correlated, spans as much as 500 km and is present in cores with unique and isolated sediment source areas (**Fig. 2-3, Appendix S 2-6**)

Oxidation of sediments provides a qualitative assessment of relative age, and oxidation of the uppermost sediment is rapid in most settings. Turbidite tails typically have relatively high organic content compared to hemipelagic and pelagic sediments (e.g. Cowie et al., 1998), reducing the time constant for surface oxidation. In several studies, the response time for oxidation of the upper sediments has been quantified. Hammond et al. (1996) modeled the reactions responsible for O_2 and NO_3 profiles in the central equatorial Pacific. The uppermost sediments were assumed to be mixed at rates described by ^{234}Th and ^{210}Pb profiles. They described a dominant and more labile fraction which oxidized in days to months, and a less labile fraction that oxidized in decades. Sayles et al. (2001) also found response time to be short at 0.3-1.6 years for high flux sites, and 5-80 years for very low flux sites. Smith (1987) found response times of 0.1-0.2 years for high flux sites, and 1-5 years for low flux sites. While detailed data on oxidation rates do not exist for Sumatra, we infer from these studies that oxidation would most likely be apparent if the uppermost event were more that ~ 5 years old at the time of collection, ~ 2.6 years after the 2004 earthquake.

Using the available constraints, our P_Sequence ^{14}C age model for the uppermost turbidite in core 96PC suggests a median age of -60 +- 10 cal yr BP (**Table 2-3**). ^{210}Pb age data in cores 96 and 102 are consistent with an age within the past few decades at most, as

are the radiocarbon ages (**Fig. 2-6, 7**). We therefore interpret this young turbidite as likely the result of the 2004 earthquake, with the evidence spanning a distance of ~350 km along strike, a region of at least 10,500 km^2 (**Fig. 2-3**).

^{137}Cs was undetectable in cores 94PC and 105TC due to at least one of several possible reasons (**Table 2-4**). Either there was insufficient ^{137}Cs in this region of the Indian Ocean to detect given the gamma counting methods of Wheatcroft (Wheatcroft and Summerfield, 2005) or the sediment was deposited prior to 1954. Based on measurements from sea water (Alam et al., 1996), there may have been ^{137}Cs in the sea water. In this case, the ^{137}Cs may not have deposited in sufficient concentration at the sea floor. If sedimentation rates are sufficiently low, and there was sufficient erosion, then we would not expect to find ^{137}Cs activity in these cores.

Site conditions play an important role in proximal sites such as those in this study. Of all cores, core 96PC has the most expanded section of what we interpret to be the 2004 seismoturbidite. The expanded section is possibly due to the core site, found in the center of a 40 km long by 7 km wide slope basin that probably does not drain completely, possibly causing the sediment to pond (**Fig. 2-5 E**). Underlying turbidites are also thicker than interpreted correlatives in other cores, suggesting the reason for thicker deposits is site related. For example, T-6 and T-7 are 23 cm and 30 cm thick in 96, but only 6 and 3 cm thick in 103PC. We use the entire sedimentary section above the oldest ^{14}C age in each core to calculate the overall sedimentation rate (**Table 2-5**). The overall sedimentation rate for the past 2 ka in core 96 is 1.9 ± 0.07 mm/yr, 0.59 ± 0.01 mm/yr in core 103 (minimum since the 2004 deposit is absent in this core), 1.03 ± 0.03 mm/yr in core 104, and 0.45 ± 0.01 mm/yr in core 108 (minimum because, while the base is present the uppermost portion of the possible 2004 deposit is absent). The stratigraphic section in 104PC has a similar overall sedimentation rate as 96PC, though the higher rate at the 104 core site is possibly due to the position at the base of an oversteepened slope (**Fig. 2-3 D**). Since over the past 2 ka the hemipelagic rate varies little along strike (**Table 2-2**), the primary source for variation in overall sedimentation rate is likely due to differences in turbidite deposit thicknesses.

2-4.2 Lithostratigraphic Correlation in the SASZ 2004 Region

The correlated framework shown in **Fig. 2-7** represents a depositional history of turbidites spanning 6,500 years, with a potential for a longer record based on the seismic

reflection results. Our lithostratigraphic correlations are based on correlation criteria, some qualitative (including stratigraphic superposition, geophysical proxy fingerprinting, visual lithostratigraphic descriptions) and some quantitative (relative and absolute ages, and tephrostratigraphy). As listed in the results, when more correlation criteria are satisfied by a particular correlation, the uncertainty in that correlation reduced, and the corresponding tie line is thicker and solid. Radiocarbon age results are plotted for the sediment underlying the correlated turbidites. The map (**Fig. 2-3 A**) shows the core locations and the isolated source areas for the basin cores.

We have presented a few of the key correlations within which the post 6,500 year Holocene turbidite sequences are interpreted as coherent framework. Refer to **Fig. 2-8** for the following discussion of how correlated turbidites may differ between cores. These differences in coarsening or fining upwards (in T-4 / T-5 pair) may be due to either site effects or differences in earthquake ground motion (**Fig. 2-8 A**). The difference (in T-6 / T-8 set) may be due to site conditions or possibly due to variations in the triggering for the source areas of the different cores (**Fig. 2-8 B**).

There are many reasons that might contribute to these differences in structure between turbidites correlated between different cores. Highly bioturbated sediment may alter the geophysical property (changing the shape of the “fingerprint”) or structural interpretation of the turbidite. Highly deformed sediment may not be well correlated if the deposit has a low signal to noise ratio (low dynamic range in density or particle site) because their geophysical property fingerprints are not very unique.

Turbidites T-1 and T-18 have shared characteristics that suggest that T-18 is partially contained in core 96PC. T-1 and T-18 are both much thicker than other turbidites in some cores (**Fig. 2-9**). Core 96 appears to have the muddy tail for the T-18 turbidite, but this is difficult to test since the base of the T-18 deposit is absent. Possibly supporting this hypothesis is the seismic reflection data, which shows an acoustically opaque deposit below the depth of the core that appears to fade upward to a depth overlapped by the core depth (dark brown vertical line in **Fig. 2-5 F**). The spatial limit of the seismic reflection profile is designated by a yellow line in **Fig. 2-5 E**. In core 108, the uppermost turbidite is missing its tail and possibly much of the coarser section as well. This is indicated by the observation that the gamma and CT density of the deposit is high compared to the rest of the core’s turbidites, and decreases little with depth indicating a truncated, dense deposit. Comparing the upward decrease in density of the CT Imagery in T-18 with

T-1 in core 108, T-1 is a much more massive and thick turbidite than all the other turbidites in that core and only slightly more than T-18. If these relations hold true in core 96 alike, then the upward decrease in density in the tail of T-18 is consistent with this difference in turbidite size. Therefore we interpret the lowermost turbidite in core 96PC to correlate with T-18 in core 108.

We note that some turbidites are absent across some intervals in the 2004 rupture region. For example, T-2 to T-6 may not present in core 108 (**Fig. 2-3**). Likewise, T-1 to T-3 appear to be absent in core 103. These omissions may be due to site conditions, erosion, coring ability, or rupture characteristics (slip, directivity, duration of shaking.). If this were due to the result of site physiography and source proximity, cores that are more proximal than ideal in most cases would be expected to generate greater variability, as has been observed in Cascadia (Goldfinger et al., 2008, 2012 a). The missing section in 103 may be the result of over penetration or erosion of the seafloor while coring since core 102 includes an uppermost turbidite that is missing in 103. The uppermost sediment can sometimes be eroded from the sea floor by the piston core during coring due to the high velocity of the corer compared to trigger cores. In this case, the uppermost sediment is missing from both the PC and the TC. The missing section in 108 and 103 may be the result of differences in turbiditic sedimentation rate, leading to increased bioturbation in the more finely grained and thin turbidites (Goldfinger et al., 2013 b), making the turbidites more difficult to distinguish from background sedimentation. These missing sections may also be due to erosion of previous turbidites during the emplacement of any given overlying turbidite. Natural variability of this type is expected even at a predominately seismogenically dominated margin, and observed in Cascadia (Adams, 1990; Goldfinger et al., 2012 a) and elsewhere (Pouderoux et al., 2012). It is also possible, and even likely, that at any single core site, we did not sample in the optimal location. This, given relatively limited time for survey for each site, and the reconnaissance nature of our understanding of local slope processes, may have resulted in potentially missing the best depositional area for a given set of strata.

Another possible explanation for the variation of completeness of the stratigraphic record may be due to features from the earthquake itself. Subduction zone earthquake ruptures generally have non-uniform slip, leading to variations in seismic moment release through space and time (Barrientos and Ward, 1990; Konca et al., 2007; Moreno et al., 2009, 2011). Ground motions at the sea floor likely relate to these variations in slip (Arias, 1970). The ground motions also attenuate in response to a series of factors

including distance to the slip and crustal or site characteristics (e.g. rheology of underlying seascape; Bilek et al., 2004; Bilek, 2007; Mahani and Atkinson, 2013). One core may be a shorter distance to larger slip region (higher energy release) for one earthquake, but at a greater distance than another core for a different earthquake. Ground motions also respond to the direction of slip (Kramer and Lindwall, 2004) so any given submarine slope may be in an orientation that favors or retards slope instability. As the sequences correlate well overall, local variability due to basal erosion, heterogeneous source areas within the region, coring deformation, and site geomorphology would be expected, regardless of the triggering mechanism.

T-1, 4, 5, 6, 7, 8, 9, 10, 13, 16, 18, 21, and 25 are best explained by seismic triggering. T-2, 3, 11, 12, 14, 15, 17, 19, 20, 22, 23, and 24 are less well correlated, but are attributed to a seismogenic trigger due to their spatial extent with isolated sediment source areas. Other thinner and less coarse/dense turbidites are even less well correlated. Some of these turbidites are mentioned as “precursor” turbidites, some are simply in between better correlated turbidites. While these other turbidites may be explained by a seismogenic trigger, we leave them out of our earthquake chronology because of the low certainty of these correlations. In the following section we will further discuss the site controls to deposition at our core sites.

2-4.2.1 Site Effects

We observe some sites within which the individual beds have persistent and similar sedimentary structures. These self-similar repeated sedimentary structures may be due to local geomorphologic conditions or basin effects. For example, cores 104PC and 104TC record what we interpret to be regional turbidites T-1 through T-10, and T-14 through T-25 by correlation to other sites. In these cores though, each bed is replaced by a sequence of many thin coarse pulses as part of their single event structure. The core location for 104 is at the base of a steep slope with ~1.5 km of relief, and the canyon mouth outlet is less than 1 km to the east of the site (**Fig. 2-3 D** and **Fig. S1-3**). We interpret that local retrogressive failure accompanying each seismic event, such as observed by (Piper et al., 1999) may explain the repeated thinly laminated structures in this core.

Another example is core 96, which has finer grained turbidites and higher overall sedimentation rate (turbidites are thicker; **Table 2-7**). Core 96 is located in a closed slope-basin fed by very low relief terrain that does not form large channels (**Fig. 2-5 E)**. The

Table 2-7. OVERALL SEDIMENTATION RATES

Core	Depth*	Error	Age †	Error§	Sed Rate #	Error**
108	344	0	7,590	60	0.45	0.01
104	445	1	4,340	120	1.03	0.03
103	380	1	6,430	70	0.59	0.01
96	400	1	2,100	120	1.90	0.07

* Depth of the deepest age in the core, in cm.

† The deepest calibrated age in the core with uncertainty reported to 95.4% error and reported in calendar years. Calibrated age ranges before A. D. 1950 according to Stuiver and Reimer calculated using marine reservoir correction and regional delta R offset (ΔR = 16).

§ 95.4% Error in calendar years.

Sedimentation Rate in mm per year.

** Root Mean Square error

low relief terrain possibly explains the fine-grained texture. The enclosed basin may be responsible for the relatively over-thickened turbidites. Also, core 103 is in a location that has a low gradient, wide floodplain channel directly upslope, possibly explaining the low dynamic range of turbidite texture in this core (**Fig. 2-5 D**). Core 103 is located at the western edge of a small (~20 km^2) basin with eastward sloping seafloor. This 1° slope may explain the thinner turbidite deposits in this core.

Our interpretation for proximity control on turbidite deposition is supported by looking at some trench cores, 98 and 94; along with some slope cores, 104 and 103. Core 98 is located in the trench in a position protected from higher relief mass wasting processes sourced from the slope by a landward vergent anticline (**Fig. 2-3 F**). The turbidites are thin and less sandy than core 94, likely a result due to this effect (**Fig. S 2-3**). In contrast, core 94 and is located near the mouths of numerous canyon systems, and generally has thicker and sandier turbidites (**Fig. 2-3 G**). One amphitheater shaped landslide source area directly feeds the seafloor surrounding core 94 (arrow designates downslope direction in **Fig. 2-3 G**). Proximal dominance is further supported by stratigraphy in cores 103 and 104. While these cores are closely spaced (34 km; **Fig. 2-3 D**) and correlate well with each other (**Fig. 2-7, 8, 9**), the differences in turbidite style (thickness, structure) may reflect autocyclic forcing. For example, core 104 is located at the base of steep slope faces, so the turbidite beds are thicker overall than in core 103, which is located downstream of several small canyon confluences and has turbidites that are thinner and better organized. The thicker overall deposits in core 104 are possibly due to retrogressive failures of the adjacent high relief source area immediately to the north of this core (**Fig. 2-3 D**). Because they are close in distance, they probably experience a similar magnitude

of ground shaking, reducing the likelihood that ground shaking variation contributes to turbidite structure variation between these cores.

2-4.2.2 Stratigraphic Correlation Summary

The coherence of the turbidite "fingerprints" and radiocarbon ages between isolated basin and trench sites, over 350 km along the strike of the subduction zone, suggests that many or most of the correlated turbidites have a common trigger (**Figs. 2-3, 7, 8, 9, 10**). The good stratigraphic correlation between sites isolated from each other, land sediment sources, and from other triggering mechanisms, coupled with compatible radiocarbon ages suggest that the most likely triggering mechanism is regional earthquakes. Uncorrelated events present at some sites may be random sediment failures or smaller local earthquakes. These uncorrelated turbidites are thin and have low mass with non-unique fingerprints, making it difficult to interpret their origin.

2-4.3 Age relations

Radiocarbon ages provide a test of the temporal coherence of our correlations, but we also use them as a first order control on the age of turbidites and recurrence of earthquakes responsible for those turbidites (detailed radiocarbon methods are described in **Appendix S 2-1**). Trench cores are deeper than the carbonate compensation depth (CCD), so they do not contain calcareous material sufficient for ^{14}C age control. For this reason, correlations between these and other cores do not have an independent test for our stratigraphic correlations. Therefore all of our correlations in the trench cores are tentative (**Fig. 2-7**). One source of aleatory uncertainty is basal erosion. Erosion preceding turbidite deposition would erode the youngest sediments underlying the turbidite, causing ^{14}C ages derived from those sediments to be older than the time of deposition. Erosion may be evaluated by collecting multiple cores at a given site (methods in Goldfinger et al., 2012 a; Pastor et al., 2009). These erosion estimates are minimum estimates because there are no direct observations of the sea floor prior to the deposition of these turbidites, and erosion of all sites may be missed. Due to equipment failures, we were unable to collect multiple cores at each site, limiting our ability to evaluate erosion. Therefore all our age models do not include any assessment of basal erosion. The effect is likely overestimate of event ages, resulting in increased scatter of ages between sites for events if they are synchronous and no effect if they are not.

Figure 2-10. Earthquake Chronology. Space-Time relations for stratigraphy cored in the 2004 rupture region are plotted (vs. forearc distance) as blue circles with 95.4% error bars. Green tie-lines show stratigraphic correlations (thicker = correlation more certain, dashed = less certain). Region-wide events are designated by a horizontal dashed grey line and labeled with peak ages on the left margin, along with the "sequence" age as grey squares with 95.4% error bars. Red x symbols designate correlated turbidites that lack ^{14}C age control. Terrestrial paleoseismic and paleotsunami data are plotted by dots/ diamonds and triangles respectively, as designated in the legend. Data plotted to the left of 108PC are not plotted vs. forearc distance as they are further north than the figure limits. The 2004 earthquake extends beyond the northern latitudinal extent of this figure (Chlieh et al, 2007). See **Figs. S 2-1** and S 2-**5** for more detailed radiocarbon age discussions.

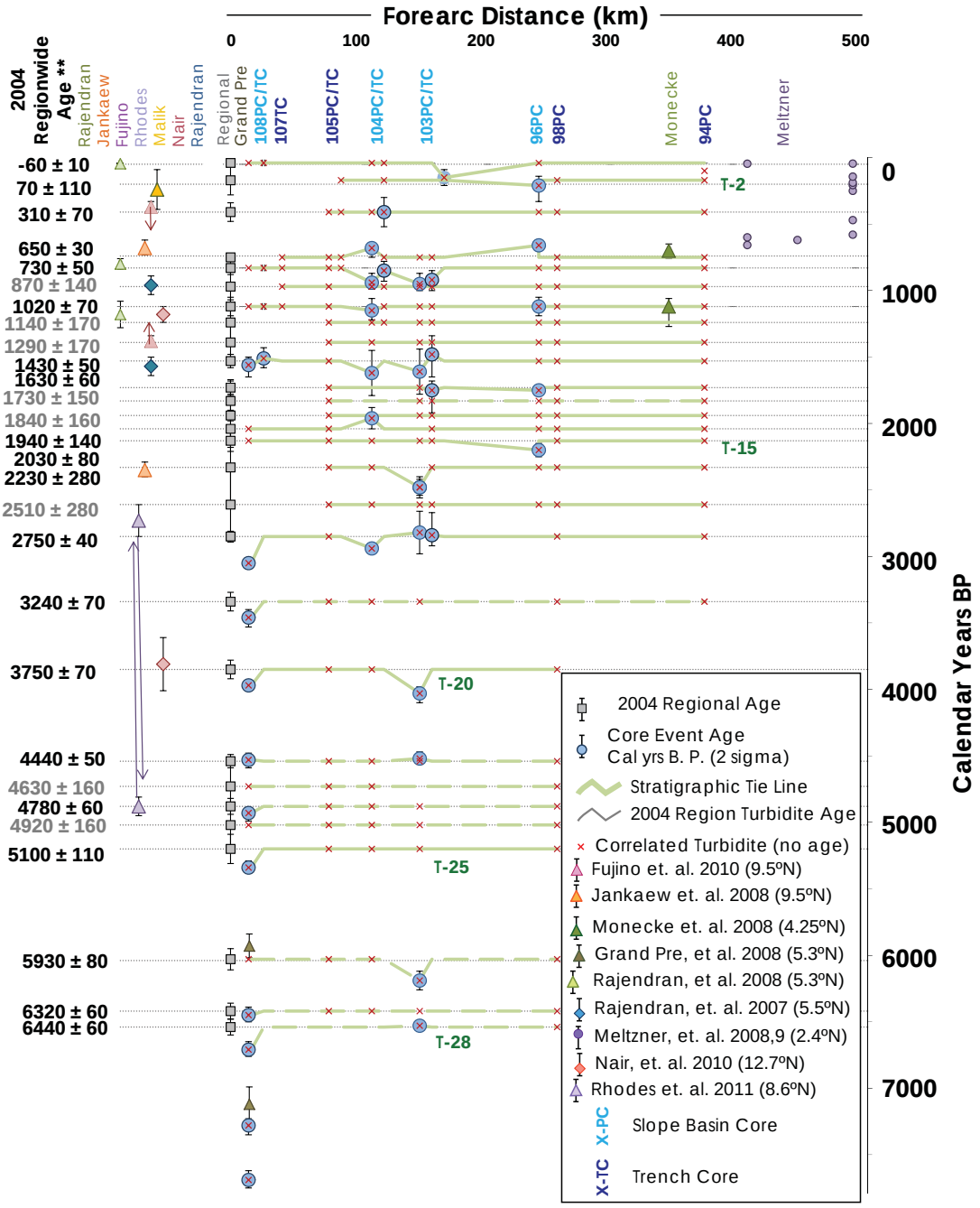

* Single ^{14}C age calibrated and reported according to Stuiver et al., (1998) calculated using marine reservior correction ($\Delta R = 16 \pm 11$). Error reported to 2 standard deviations.
** Peak age selected from peak of PDF for each event. Error is reported to 2 standard deviations.
¥ OxCal v4.1.3 Bronk Ramsey (2009); Marine data from Reimer et al. (2009)

Figure 2-10 cont.

There does not appear to be a systematic control on which ages failed. Some excluded ages are part of a pair of ages from a PC and TC at the same core site (e.g. T-10, cores 104 and 103). In both cases, the TC age is older than the PC age. We pose the TC sample ages may be different because the sediment is more compacted due to the differences between PC and TC coring methods. T-20 has an older age in 108. While there is no evidence for erosion, we find no other sedimentological reason for this older age. None of the excluded ages overlap with ages from overlying nor underlying turbidites, so these age models are not inconsistent with the stratigraphic order of ages in adjacent cores.

After these outlier ages are excluded, the remaining ages satisfy these measures of agreement. The age model is therefore consistent with our stratigraphic correlations within the uncertainties inherent in radiocarbon. The external criteria on which the lithostratigraphic correlations are based support the inference that these horizons, in this context, most likely represent the same event temporally. We therefore have combined them statistically in **Table 2-6** and **Figs. 2-3, 2-7**. The OxCal code and output of our radiocarbon age model with both modeled and un-modeled ages listed in **Table 2-6** are found in **Appendix S 2-5**.

Lithostratigraphy, radiocarbon ages, and geophysical fingerprinting suggest a good correlation of turbidites T-1 through T-28 between cores 108, 105, 104, 103, through T-16 in core 96, and through T-7 in 107; spanning the 2004 rupture zone (**Figs. 2-7 & 2-10**). Less well correlated are turbidites 20 through 24, in cores 108 and 103. Some ages are inconsistent with the preferred stratigraphic interpretations in **Fig. 2-7**, but none of the ages overlap with underlying turbidite ages. These small differences in age may be due to differences in basal erosion (more erosion means an older age) or to minor differences in the marine reservoir (which are not yet resolvable).

2-4.3 Origin of the Sumatra turbidites

2-4.3.1 Rationale

We now review the rationale developed for the attribution of seismogenic triggering of turbidity currents in Cascadia and elsewhere and apply those principles to interpret the sediment stratigraphy in our cores offshore Sumatra. The triggering of submarine landslides offshore Cascadia has been attributed to earthquakes based on multiple lines of evidence. As in Sumatra, one line of evidence is lithostratigraphic correlation based on

the presence of a similar sequences of turbidites based on turbidite mass sequences, age, number of coarse pulses, geophysical fingerprints, and the number of turbidites above external chronostratigraphic data (e.g. the Mazama Ash and a Holocene-Pleistocene faunal boundary; Griggs and Kulm, 1970). Turbidite mass is the integration of density with volume (core cross sectional area times depth), calculated for each turbidite. The number of coarse pulses refers to the number of fining upward subunits with each single bed, as inferred from the geophysical data.

Distinguishing seismoturbidites from those triggered by other mechanisms can be very difficult, and in some cases impossible. Two approaches can be applied, separately or in concert, to make this distinction; (1) sedimentology of the deposits themselves, and (2) correlation of deposits to establish regional synchronous deposition unlikely to be caused by processes other than earthquakes. The principle basis for attributing a seismogenic trigger to the turbidite record is that regional and synchronous deposition is unlikely to have been generated by a trigger other than an earthquake (Goldfinger et al., 2007, 2008, 2012 a; Patton et al., 2013).

One way to correlate turbidites includes the confluence test and Cascadia turbidites pass the confluence test (Adams, 1990, Goldfinger et al., 2003, 2007, 2008, 2012 a). This test assumes that if the channel system has the same number of turbidites above and below a confluence, it can be surmised that the deposits in all locations were laid in the same short period of time lasting minutes to hours (Goldfinger et al., 2012 a). Because of this similarity in stratigraphy between cores in this example, the researchers conclude that the trigger for these turbidity currents affected a broad region (1,000's km^2). These correlations provide the basis and justification for the geophysical fingerprint correlation method. In support of their findings, Goldfinger et al. (2003, 2008, 2012 a) correlate turbidites in cores that sample unique source areas (Cascadia Channel with Juan de Fuca Canyon and Hydrate Ridge Basin West with Rogue Canyon distanced 250 km southwards along strike), a correlation test independent of the confluence test that further supports the areal extent of the trigger for these turbidites. Cascadia margin cores contain deposits that pass multiple tests of synchronous earthquake origin and generally contain multiple coarse fining upward sub-units, consistent with other seismoturbidites (Nakajima and Kanai, 2000; Goldfinger et al., 2008, 2012 a). Goldfinger et al. (2012 a) also correlate the turbidite mass and the number of coarse units to the rupture length of the causative earthquakes. In addition, because seismoturbidites with isolated source areas in Casca-

dia have geophysical property fingerprint based correlations with sufficient similarity to suggest the vertical structure indeed represents allocyclic (seismic) forcing.

Because of the difference in basin and site effects and turbidite channel architecture between Sumatra and Cascadia (Patton et al., 2013), the tests for seismogenic triggering are slightly different. As in Cascadia, we base our correlations largely on three factors (1) sedimentary source isolation (2) deposit geophysical property "fingerprint", and (3) timing or age control. Sumatra cores in slope basins are isolated from each other, so this is used as the primary way to test for regionality of triggers: cores with unique sedimentary sources that have turbidites with shared fingerprints demonstrate that triggers are regional and not local. Most alternate triggers, such as hyperpycnal flow, wave loads, and gas hydrate destabilization, fail this test because these mechanisms do not affect regions of 1,000's km^2.

Finally, the detailed depositional structure of turbidites is likely a combination of several turbidity current forcing factors. Since turbidite deposition is a sedimentary result of the passing turbidity current, the forcing factors probably also control the structure of the turbidite. Factors that promote allocyclic forcing (i.e. sedimentation and erosion controlled by the source or input of sediment flux; Underwood et al., 2005) can include the source of the initial landslide, such as whether the turbidity current is from hyperpycnal flow or a seismogenically triggered landslide (Seilacher, 1969; Shiki et al, 2000; Morey and Goldfinger, 2004; Garret et al., 2011; Goldfinger et al., 2012 A, B). Factors that promote autocyclic forcing (i.e. sedimentation and erosion controlled by local or site processes) include flow dynamics, site geomorphology, and proximity (Middleton, 1967; Nelson et al., 1986; Muck and Underwood, 1990; Kneller and McCaffrey, 1995; Kneller and Buckee, 2000; Mulder et al., 2003; Baas et al., 2004, 2005; Amy et al., 2005, 2006; Dennielou et al., 2006; Felix and Peakall, 2006). These forcing factors may compete depending upon core location, local physiography, and distance to the source region of the turbidity current. If trigger source forcing dominates over a sufficiently large region, turbidites deposited by those turbidity currents that share this common forcing may also share a common turbidite structure. As a result, these turbidites would also share a common "fingerprint."

2-4.3.2 Sumatra Specific Factors

When considering the origin of the turbidite sequences in northern Sumatra, we first review the relevance of different potential triggers in the region of the 2004 SASZ earthquake. Of the potential triggering mechanisms proposed (Adams, 1990; Goldfinger et al., 2003, 2012; Shanmugam, 2008), only a subset of these triggers applies offshore Sumatra. Additionally, several mechanisms do not directly trigger slope failure, but simply precondition slopes for failure (e.g. sediment loading, tectonics oversteepening, and regional gas hydrate destabilization). The remaining mechanisms are: hyperpycnal flows, wave loading, bolide impact, self-failures and earthquakes (intra- and inter-plate). Frequent gas hydrate destabilization events linked to local as opposed to regional temperature changes would likely not occur synchronously, and thus could not be responsible for triggering frequent submarine landslides found in our cores across large areas. Crustal earthquakes and structural over steepening and self-failures would leave behind highly localized deposits because their impact is localized. Bolide impacts may also leave a regional turbidite record, but their recurrence, on the order of 1,000's of years, is far too long to explain the chronostratigraphy in our cores (Rampino and Stothers, 1984; Rampino 1984, 1999, 2002; Ward, 2002; Chesley and Ward, 2006). The remaining process that can be both regional and synchronous include hyperpycnal flows, wave loads (storm and tsunami), and earthquakes, which we discuss below.

1-4.3.2 a *Hyperpycnal Flow*

Very large storms could potentially generate hyperpycnal flows, leaving behind hyperpycnites as the result of fluvial delivery of sediment to the coastal margin or through the resuspension of sediment along the continental shelf. However, the turbidity current source areas of our core sites are isolated from terrigenous input by the broad, unfilled forearc basin in northern Sumatra. In the region of the 2004 SASZ earthquake, core sites are located with landslide source areas that have no direct connection with either continental shelf or fluvial sedimentary systems because the 50 – 70 km wide unfilled Aceh Basin isolates the outer prism from this terrigenous input. The forearc plateau rises an average of 2.2 km above the forearc basin floor, effectively trapping all terrigenous input in the basin. The Sumatra forearc plateau has a number of islands that could provide terrigenous input to sites downslope in the outer forearc. The nearest island, Simeulue, is 130 km to the southeast of our nearest slope core site, and there is no sedimentary pathway linking Simeulue to any of the core sites discussed here. We also note that hy-

perpycnites are reported to initially coarsen upwards and then fine upwards, representing the waxing and then waning of the hyperpycnal flow (Mulder et al., 2003; St-Onge et al., 2004). Turbidites in our cores do not show evidence of this depositional sequence, consistent with the observations of the spatial isolation of landslide source areas that feed our core sites.

1-4.3.2 b *Wave Loading*

Wave loads can potentially trigger submarine landslides in two ways, (1) cyclic changes in pore pressure causing liquefaction induced slope failure and (2) shear failure of sediment on the slope, canyons, or shelf. These wave loads can be induced from storm waves and from tsunami waves.

Significant wave height, Hs (m), and spectral mean and peak wave period, Tm and Tp (s), have been modeled with buoy data and measured using satellite altimetry (Young, 1998; Lemmet et al., 1999; Alves and Young, 2003; Izaguirre et al., 2011) for the northeastern Indian Ocean in the region of our paleoseismic survey. Buoy data models estimate Hs with a 100 year return period to be 3.5 to 9.5 m (Caires and Sterl, 2004). Alves and Young (2003) use GeoSat, ERS-1, and Topex/Poseidon satellite altimetry measurements to estimate Hs with a 100 year return period to be 6 to 10 m. Izaguirre et al. (2011) use TOPEX, Jason-1, Jason-2, EnviSat, GFO and ERS-2 satellite missions from 1992-2010 to estimate Hs with a 20 year return period at 5 to 7 m. Young (1999) calculate Tm and Tp using the Spectral Wave Model WAM (Komen et al., 1984) and find Tm to range from 10-13 s and Tp to range from 6-8 s in the region of our paleoseismic investigation. Measurements collected for these estimates are short lived and may not fully capture the variability, potentially missing extreme events possibly occurring in the past 6,500 years. Given this possible limitation, we adopt these values as characteristic for the northeast Indian Ocean.

Cheng et al (2001) suggest that passing waves, whether storm or tsunami, induce pore pressure loads that increase with each successive wave. If the sediment properties result in undrained conditions, the increased pore pressure may induce liquefaction and induce slope failure. Based on models of cyclic loading and drainage tests, where pore space decreases and shear strength increases, the sediment can result in being more resistant to slope failure (Miyamoto et al., 2004). This cyclic loading, whether from passage of storm or tsunami waves, is likely to retard slope failure. Chang et al. (2004) modeled

this resistance to liquefaction in saturated sandy nearshore settings offshore Taiwan. The maximum depth that liquefaction was induced was 15 m, much shallower than the source areas in this study. Storm wave heights ranged from 1.5 to 7 m and wave periods ranged from 5 to 12 s, both consistent with Hs and Tm and Ts for offshore Sumatra. We therefore conclude that wave loading at depths of 1,500-6,000 m in the source areas for our turbidite cores is unlikely. We note that the lack of cyclones in equatorial waters (Peduzzi et al., 2012) all but rules out massive regional storms as a sediment source via either hyperpycnal flows or wave loading. Were such cyclones present in the past, they would still fail to trigger turbidity currents on the forearc slope with the majority of minimum depths relevant to this study of ~1,500 m.

Weiss (2008) calculated the potential capability of the 2004 SASZ subduction zone tsunami to possibly move find sand in a maximum depth of 985 m in the Bay of Bengal and 335 m in the region of our paleoseismic investigation. Weiss (2008) concluded that tsunamis of similar size or small than the 2004 tsunami would be unlikely to initiate motion on sea floor sediments with low cohesion. Potential source areas for slope cores in this study range from 1.5 to 6 km, all deeper than the Weiss (2008) maximum modeled depth. Core 108 has a small region of potential source area that reaches depths as shallow as ~750m, but since the cores that have correlable deposits have deeper potential source areas, the potential for tsunami wave loading as a trigger for the landslides that resulted in the turbidites in our cores is very limited.

Further evidence contraindicated for tsunami triggering is their frequency. Historic tsunami in the northeast Indian Ocean account for over 100 tsunami between 416 and 2007 A.D. (Dunbar and Stroker, 2008)). Other accounts include ninety tsunami in the Indian Ocean between 326 BC and 2005 AD (Rastogi and Jaiswal, 2006). If these rates were extended through the Holocene, there were possibly 800 tsunami during the time represented by our cores. This frequency is incompatible with the turbidite frequency in our cores so is unlikely to be a common trigger for turbidity currents in the source regions upslope from the RR0705 and SO-002 cores.

2-4.4 Paleoseismic implications

We attribute our correlations a range of certainties based upon how robust our correlation criteria are satisfied (as discussed above). Key correlated turbidites include T-1, T-4, T-5, T-6, T-7, T-15, T-16, T-17, T-18, T-20, and T-25. These correlations are made with

higher certainty and provide boundary conditions for over- and under-lying turbidite correlations. Some turbidite correlations are made with lesser certainty, T-2, T-3, T-8, T-9, T-10, T-11, T-13, T-14, T-19, T-21, T-22, T-23, and T-24. Turbidite correlations with the least certainty include T-12, T-26, T-27, and T-28.

There are some alternative triggers that remain, hyperpycnal flows, wave loading, bolide impact, self-failures and earthquakes (intra- and inter-plate). We have been able to rule out hyperpycnal flows, wave loads, and bolide impacts based on frequency (bolide, tsunami), sedimentary structure (hyperpycnal), and geographic proximity to fluvial sources (hyperpycnal). Self-failures do not explain the regional extent of the deposits found in our cores. The remaining trigger we cannot completely rule out is earthquake triggering due to crustal or slab earthquakes. Whether an earthquake trigger is from the megathrust or from some smaller fault relates directly to the rupture area and shaking intensity.

2-4.4.1 Comparisons to onshore paleoseismology

We compare the timing of turbidite deposition with earthquakes recorded in micro-atoll stratigraphy along the forearc islands of Sumatra (**Fig. 2-10**). We note that the timing of the paleoearthquake record of the Mentawai segment (Sieh et al., 2008) overlap in time (are consistent) with each of the four youngest turbidite ages from this study. However ages from the Mentawai segment are inconsistent (do not overlap) with earthquakes on Simeulue (Meltzner et al, 2010). Thus while long earthquake sequences such as the 2004-2010 sequence along Sumatra may have occurred in the past, they are not necessarily the rule over the 6,500 year record. Further analysis of the turbidites in the 2004-2005 rupture areas may determine whether the 2004-2005 stress triggering relations (McCloskey et al., 2005; Briggs et al., 2006; Hsu et al., 2006; Konca et al., 2007; Chlieh et al., 2007, 2008; Meltzner et al., 2012, 2013; Kopp et al., 2013) are a persistent feature along the Sumatra margin.

We directly compare our results with secondary records of earthquakes in the form of sandy deposits interpreted to be paleotsunami deposits in the terrestrial record. Our turbidite based evidence suggests the ages of the six events prior to 2004 were 70 ± 110, 310 ±70, 650 ± 30, 730 ± 50, 870 ± 140, and 1,020 ± 70 cal yr BP. Based on paleotsunami evidence in Thailand, the penultimate tsunamigenic earthquake recorded onshore in Phra Thong was younger than 270 ± 40 cal yr BP (may correlate with T-3) and the antepenultimate tsunami was younger than 1,280 ±40 cal yr BP (may correlate with T-8 or

T-9; Fujino et al., 2009; Jankaew et al., 2008; **Fig. 2-10**). Based on uplifted marine abrasion platforms, penultimate and ante-penultimate earthquakes occurred 700 ± 40 and 1,080 ± 100 cal yr BP respectively in the Andaman-Nicobar Islands (may correlate with T-5 and T-7 or T-8; Rajendran et al., 2008). Similarly, paleotsunami evidence in Aceh, Sumatra, suggests the penultimate large tsunami timing was 600 ± 60 cal yr BP and the ante-penultimate tsunami timing was 1,020 ± 110 (may correlate with T-4 and T-7 or T-8; Monecke et al., 2008). Based on coral microatoll paleoseismology (Meltzner et al, 2010) the penultimate events comprised a series of earthquakes between 480 ± 10 and 558 ± 2 cal yrs BP (may correlate with T-3 and T-4). Meltzner et al. (2010) speculate about two to three possible missing earthquakes that may have occurred between their penultimate earthquake and the 2004 earthquake. Philibosian et al. (2012) also hypothesize about missing earthquake records in their micro-atoll records along the Mentawai segment of the Sunda megathrust. Thresholds for recording earthquakes with coral micro-atolls are probably different than that for recording earthquakes in sedimentary deposits. The ages for T-2 and T-3 are consistent with their hypothesis if there were two earthquakes, depending upon which coral based earthquake evidence correlates with which turbidite based earthquake evidence (70 ± 110 and 310 ± 70 cal yr BP; **Table 2-6**).

Although these comparisons are somewhat coarse, the offshore evidence is broadly consistent with the early reports of onshore paleoseismic events. Paleotsunami, microatoll, and uplifted abrasion platform evidence also may not record all earthquakes and thus may also represent maximum intervals for recurrence of great earthquakes sensitive to the recording thresholds of the different methods.

1-4.4.2 Temporal Pattern

We calculate mean recurrence intervals (RI) based on turbidite ages within single cores and based on turbidite ages from all cores with three different methods (**Table 2-8**). First we calculate the RI by dividing the age of the oldest turbidite in each core by the regional number of correlated beds for that core. We then calculate the RI by finding the mean RI at each turbidite. Finally we determine the RI by determining the mean interseismic interval in each core. We perform these calculations for each core and then find the mean for all cores (bottom row **Table 2-8**).

Based on ^{14}C ages and the oldest well correlated seismoturbidite (T-18) in core 108PC, the average recurrence interval for earthquakes large enough to generate a correlat-

TABLE 2-8. RECURRENCE INTERVAL ESTIMATES

Oldest Age/T-# *			Mean (T-#/Age) †			Mean (Interseismic Time) §		
Core	R.I. (years)	S.D.	Core	R.I. (years)	S.D.	Core	R.I. (years)	S.D.
108	240	30	108	210	30	108	340	170
104	170	20	104	180	20	104	180	70
103	240	30	103	200	30	103	280	180
96	140	50	96	140	50	96	190	150
all cores #	200	40	all cores #	190	40	all cores #	260	160

* R.I. is calculated by dividing the age of the oldest turbdidite in each core by the regional T number for that core.

† R.I. is calculated by averaging the R.I. calculated at each turbidite that is calculated in the first three columns of this table.

§ R.I. is calculated by averaging the interseismic interval in each core.
# The mean for "all cores" is the mean of the ages in that column (and an rms calculation of the standard deviation).

able geologic record in the region of the 2004 earthquake is 240 ± 30 years (**Table 2-8**). Our estimates for the recurrence of large earthquakes in the region of our cores ranges from 140 ± 50 to 340 ± 170 years. Given a fault normal convergence rate of 34-37 mm a-1 in this region (Subarya et al., 2006) and a coupling ratio of 1, earthquakes like the 2004 earthquake (slip of ~20 m; Chlieh et al., 2007) would yield an average recurrence of 530 - 590 years, somewhat longer than our average recurrence interval. However, we know little of the magnitudes of past earthquakes, nor of the coupling ratio along the SASZ. Our estimate is consistent with the RI estimate from Chlieh et al. (2007) of 140-420 years, which they estimate by dividing the rupture potency (a function of moment magnitude and rigidity; Wesnousky, 2008) by its accumulation rate. Given a RI of ~220 years for events large enough to generate observable turbidites, and that smaller earthquakes may be unrecorded, our interval estimate is a maximum.

We present our down-core RI estimates in **Table 2-9** and plot them versus age and correlated turbidite number in **Fig. 2-11**. Time is in calendar years and listed with 95.4% error. These estimates are calculated by dividing the time between correlated turbidites by the number of correlated turbidites that are represented by that time span. RI estimates have down-core trends that match between cores, supporting our correlations because such similarity would not be expected for other random turbidite generating processes. Goldfinger et al. (2003) found similar between-core matching trends in down-core RI estimates for Cascadia subduction zone earthquakes (their figure 4). Longer RI times are represented by maxima in these plots centered approximately at 600, 4,000, and 6,000 years. The longer RI span maxima centered at 4 ka is a more robust example

TABLE 2-9. DOWN-CORE RECURRENCE INTERVAL

Core	Regional T# *	Age (cal yr BP)	Error	R.I. †	Error	R.I. §	Error
96PC							
	3	110	30	60	30	80	30
	4	560	40	190	50	450	50
	7	1,020	80	170	90	150	90
	11	1,650	100	170	120	160	120
	16	2,100	90	140	130	90	130
103PC							
	5	850	70	210	70	230	70
	10	1,510	80	170	100	130	100
	16	2,380	60	160	100	140	100
	18	2,720	40	160	80	170	80
	20	3,930	70	210	90	600	90
	21	4,420	60	220	100	500	100
	na#	5,540	40				
	na#	5,660	50				
	26	6,090	70	240	90	330	90
	na#	6,430	70				
104PC							
	4	580	50	190	50	210	50
	5	840	60	210	80	260	80
	7	1,050	80	180	100	110	100
	10	1,520	80	170	110	160	110
	14	1,860	110	140	130	90	130
	18	2,840	100	170	150	240	150
108PC							
	10	1,460	70	160	70	170	70
	18	2,950	40	170	80	190	80
	19	3,360	70	190	70	420	70
	20	3,870	40	200	70	500	70
	21	4,430	60	220	70	560	70
	23	4,830	50	220	70	200	70
	25	5,240	40	220	70	200	70
	27	6,350	60	240	70	550	70
	28	6,610	50	240	80	260	80
	na#	7,180	60				
	na#	7,590	60				

* Correlated turbidite number.
† R.I. is calculated by dividing the age of the turbidite by the regional turbidite number minus 1.
§ R.I. is calculated by dividing the preceding interevent time by the number of preceding turbidites
# turbidite age is not regionally correlated with sufficient certainty.

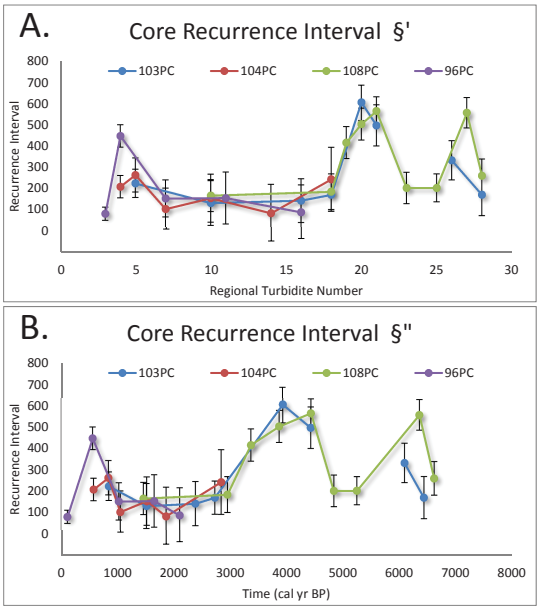

Figure 2-11. Down-Core Recurrence Interval. Recurrence Intervals (RI) are determined by dividing the time between turbidites by the span of turbidites that time represents (**Table 2-8**). The 95.4% error is plotted as vertical error bars. The RI is plotted in a different color for each core. **A.** RI is plotted versus regional turbidite number. **B.** RI is plotted versus age in cal yrs BP.

of time-length varying RI's because it has more direct ages for a more continuous record of correlated turbidites in multiple cores. The RI maxima at 6 ka has fewer correlated turbidites in core 103 than in core 104. The RI trends between cores 96, 103, and 104 for T-3 through T-9 match each other, but the maxima centered at 0.6 ka is much longer for 96 than for the other cores. These down-core variations in RI estimates support our correlation results and may also represent periodicity in subduction zone earthquake supercycles (Sieh et al., 2008; Goldfinger et al., 2013 a).

2-4.4.3 Extent of the 2004 turbidite and the paleoseismic record in segment boundaries

We note that the southernmost evidence for the 2004 turbidite is observed in core 95 in a slope basin and core 88 in the trench (**Fig. 2-12**). Slope cores provide a better constraint to the spatial limitations of ground shaking because their sedimentary sources are spatially restricted. Trench cores are less reliable to base a maximum distance limit for the effect earthquake triggering of turbidity currents because turbidity currents can travel down-trench some unknown distance ("trench mixing"). The nearest slope cores that likely lack a 2004 deposit is 92PC/TC and 91MC. 91MC has sedimentary section not sampled in core 92 and has an uppermost turbidite that is highly bioturbated with presence of forams, supporting our interpretation that this core, at a range of ~100 km from the southern termination of 2004 slip, lacks a 2004 deposit. We do not have radiometric age estimates for this deposit however.

There are few examples of rupture termination as observed in turbidite paleoseismic records with enough core data to constrain them. One such example was recently published for the Sumatra margin. Sumner et al. (2013) collected several cores ~ 50 km south of the rupture zone (Chlieh et al., 2007) of the 2004 Sumatra Mw 9.2 earthquake (cores designated by the prefix SO-002; **Fig. 2-12**). They used SO-002 core data to state that not all large earthquakes generate turbidity currents. The 2004 earthquake did indeed generate a widespread turbidity current (**Figs. 2-3, 2-6, 2-10**), thus the SO-002 and RR0705 cores may be used, instead, as part of a crude sensitivity test for triggering distance along strike. The value of this test is limited by the spatial extent of the SO-002 cores. In addition to the limitations of spatially relevant SO-002 core sites, some were located in flat floored wide basins that have proven to be of limited use for paleoseismology in slope settings, possibly due to insufficient turbidite generating topography or due to the lack of channelized turbidity currents (e.g. cores RR0705-16GC and 18GC with older radiocarbon ages at shallow depths and highly bioturbated sediment with indistinguishable sedimentary structure). Other SO-002 cores were located >30 km from their local canyon, and > 20 km from subdued local slopes. The slope failures leading to these SO-002 core sites are not channelized and thus the turbidity currents rapidly weaken as they spread across the basins (Nelson et al., 1986; Johnson et al., 2005; Patton et al., 2013). Core 2MC (of Sumner et al., 2013) includes a surficial turbidite likely to be the 2004 turbidite based on its thickness and geophysical property fingerprint. Sumner et al. (2013) agree with our interpretation that SO-002-02MC includes a 2004 or 2005 deposit

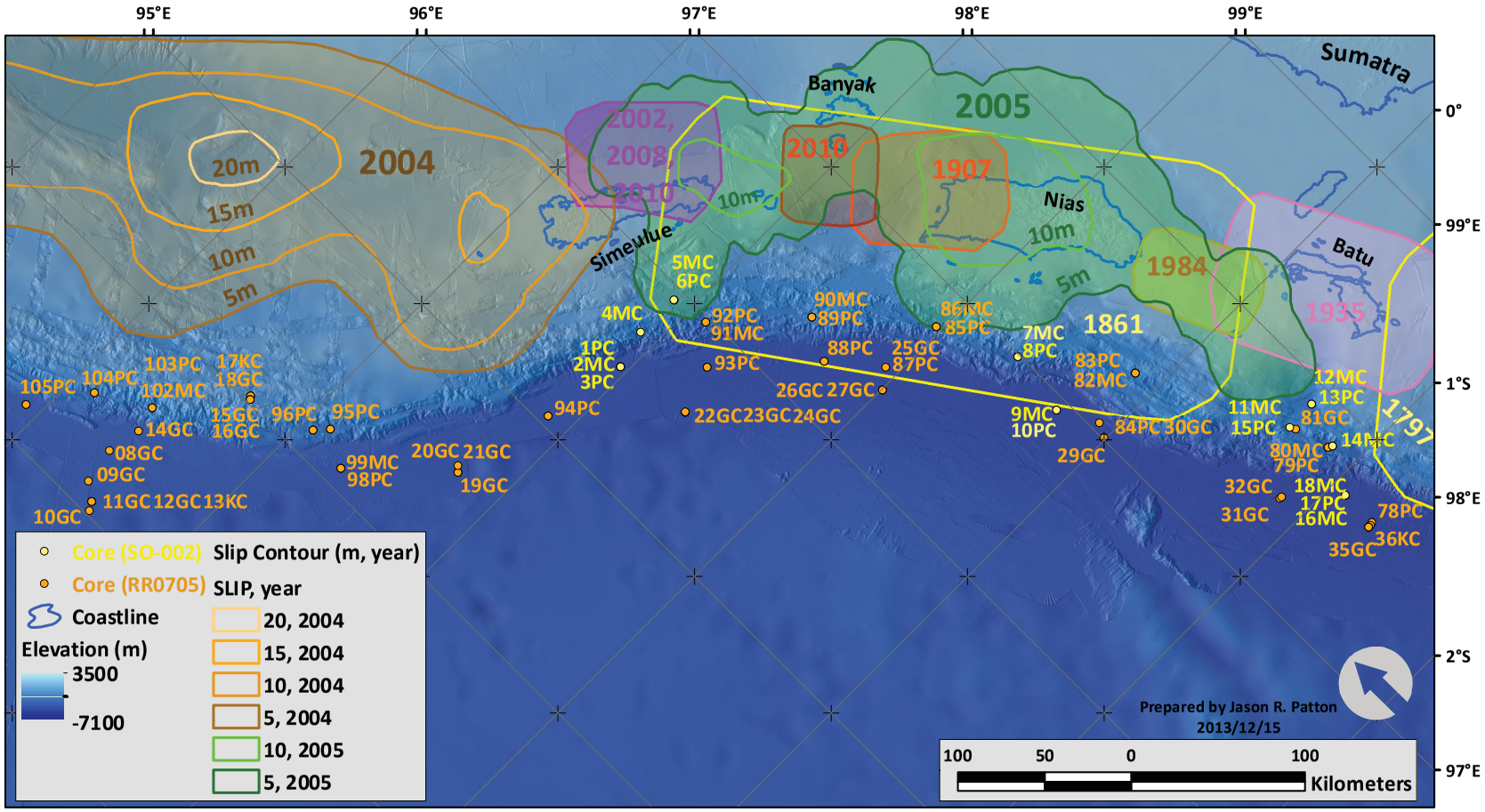

Figure 2-12. RR0705 and SO-002 Core Map. RR0705 and SO-002 cores are plotted in orange and yellow in relation to slip regions for historic earthquakes (Bilham, 2005; Malik et al., 2011) plotted in **Fig. 2-1**.

(their Figure 2 B). This core is located closer to the limit of slip for the 2004 earthquake than are any RR0705 slope cores, including core 96.

Given these limitations, a maximum triggering distance on the order of ~ 50 km for the 2004 event to deposit a record in less than favorable sites is supported by the data. The 2004 earthquake had northward directivity, away from the core sites (Ammon et al., 2005; Ishii et al., 2005; Chlieh et al., 2007). Because of the distance and rupture directivity, the SO-002 slope core sites were not ideal to record a turbidite from the 2004 earthquake. Also, the main slip patch at the southern end of the rupture (i.e. Chlieh et al., 2007) was considerably north of the core sites, thus this value could be very different for other earthquakes. Along strike die-off of ground motions in the Tohoku earthquake at both north and south ends of the rupture was an order of magnitude, from ~ 1 g to ~ 0.1 g in a distance of ~100 km (Goto et al., 2012). Across-strike (along-dip) energy radiation is broader because the energy is largely directed across strike in thrust earthquakes. This is a result of the orientation of maximum stress prior to the earthquake, which is parallel to the across-strike direction. Ground shaking across strike > 0.5 g extended across the forearc and well onshore, over 300 km width, for the Tohoku-Oki earthquake (Goto et al., 2012). Records of ground shaking for the Tohoku-Oki earthquake exceeded 1 g, but these large values are attributed to site conditions that may have amplified the ground shaking (Zhao et al., 2012).

We also observe that the turbidite record becomes less robust in the region of the segment boundary of the 2004-2005 earthquakes, as well as the 2005 region. Segment boundaries typically are characterized by low or no slip during earthquakes and commonly have complex structural and slip transfer mechanisms from one segment to another (Barrientos and Ward, 1990; Bürgmann et al., 2005; Konca et al., 2005; Chlieh et al., 2007, 2008; Schurr et al., 2007; Hok et al., 2011; Kiser et al., 2011; Hayes et al., 2013). They also have many small earthquakes occurring in between large events, leading to a confusing and likely incomplete record (e.g. historic earthquakes offshore Sumatra, **Fig. 2-12**). Briggs et al. (2006) show the 2004 earthquake slip along the 2004-2005 boundary diminishing to zero at the boundary, near the north end of Simeulue Island. We find the turbidite record in the 2004-2005 segment boundary (including our cores and those of Summer et al., 2013), considered in the regional context presented here, consistent with the presence of a persistent segment boundary.

2-4.4.4 Paleoseismograms?

Submarine landslides can be triggered when seismic waves propagate through the landslide source area. If the source-time function (Tanioka and Ruff, 1997; Bilek et al, 2004; Bilek, 2007) of the slope failures drives the sediment flux into the landslide system, and allocyclic forcing dominates (Underwood, 2005; Dennielou et al., 2006), the longitudinal structure of the resultant turbidity current will have maxima associated with the peaks in seismic energy. Therefore, the vertical structure of the turbidity current is expected to have coarse pulses of sediment corresponding to each pulse (maxima) in seismic energy. The general structure would have a coarse grained base and fine upwards, with multiple coarse sub-units for each peak in seismic energy; particle size scaling with seismic energy.

We note that the 2004 turbidite has three major fining upward coarse pulses in our cores and that the 2004 SASZ earthquake has three primary slip sub-events (Lay et al, 2005). There are several minor coarse pulses, for a total of six main pulses in the turbidite base. The relation between the earthquake source-time function and the corresponding deposit originally led previous authors to suggest the deposit structure can be used as a “paleoseismogram” (Seilacher, 1969; Morey and Goldfinger, 2004; Goldfinger et al., 2007, 2012 a). Seilacher suggested that sedimentary structures could develop as the result of seismic loads to existing sedimentary deposits, while Goldfinger et al. suggest that the sediments are deposited following the earthquake record the earthquake source mechanism in the deposit. The source-time functions produced by others (Ishi et al., 2005, Chlieh et al., 2007; Stein and Okal, 2007; Tolstoy and Bohnenstiehl, 2006) are plotted in comparison to the most upper turbidite in core 96PC **Fig. S 2-7**. There is good agreement between these plots of seismic energy release and the vertical sedimentary structure leading us to our comparison (Patton et al., 2013; their figure 6). This interpretation is supported by results from lab experiments that related sediment flux with changes in sequential deposition of sediments with varying density (Garret et al., 2011; Goldfinger et al., 2012 a). We speculate that this uppermost turbidite offshore Sumatra probably satisfies the Goldfinger definition of “paleoseismogram” (Morey and Goldfinger, 2004; Goldfinger et al., 2007, 2012 b).

2-5. Conclusions

Turbidite stratigraphy is ubiquitous in isolated slope basin and trench sites along the northern Sumatra margin. Physiography isolates these sites from terrestrial sediment input, from Himalayan derived sediment, and from large storms, providing good localities to investigate the potential for earthquake paleoseismology. Stratigraphic correlation and radiocarbon ages support serial deposition of synchronous turbidites over the past ~ 6,500 years. Based on the source isolation for these core sites, the correlations designated in **Figs. 2-7, 2-8, 2-9,** and **2-10** represent strong evidence for earthquake triggering of submarine landslides that are responsible for these turbidites.

The fact that these Sumatra cores, in sedimentologically isolated and hydrodynamically unique systems, share turbidites with depositional histories that match in considerable detail, suggests that they also share a common trigger mechanism. For alternative triggers to explain these sequences, these triggers would need to randomly affect the different regions with similar frequency and result in landslides with similar turbidite structures, in the same stratigraphic order. Goldfinger et al. (2003, 2008, 2011, 2012 a, b, 2013 a, b), have proposed that these shared characteristics are, in part, a result of the time history of ground shaking causing a change in sediment flux (submarine landslides) during the earthquake. Correlation of strata is further supported by ^{14}C ages of individual turbidites and hemipelagic intervals between earthquakes.

The youngest turbidite likely correlates with the 26 December 2004 great SASZ Mw 9.2 earthquake. This earthquake triggered turbidity currents in multiple submarine drainage systems that left stratigraphic evidence in the form of multi-pulse turbidites in isolated slope basin and trench depocenters. Previous great earthquakes in the same region have shaken sufficiently to trigger at least 27 (and as many as 30) turbidity currents and deposit corresponding turbidites during the past ~ 6.5 ka, with an average repeat time of 260 ± 160 years. The offshore turbidite record is consistent with both plate motion and land paleoseismic ages for eight prehistoric earthquakes approximately 400, 600, 800, 1,000, 1,500, 2,300, 6,000, and possibly 7,100 years ago. The timing of the four most recent earthquakes is similar to tight clusters of earthquakes recorded by live corals (Sieh et al., 2008) along the Padang/Mentawai segment of the Sumatra subduction zone, 400 km to the south, suggesting along-strike sequences of earthquakes over relatively short time intervals.

We find that selecting core sites is essential when attempting to evaluate the sedimentary record of past earthquakes. Based on the presence of a turbidite we interpret to be the result of the 2004 SASZ earthquake in RR0705 and SO-002 cores, we find a minimum triggering distance for earthquakes of this magnitude to be ~50 km. This is a crude estimate since this measurement is to the edge of the slip models and the maximum shaking intensity responsible for triggering turbidity currents is heterogeneous and anisotropic (e.g. depending upon factors such as slip directivity, slip magnitude, and hanging wall or foot wall position). The best coring sites will conjoin as many positive factors as possible (factors that promote seismogenic triggering of turbidity currents and promote the deposition and preservation of their turbidites). We pose a series of factors that are ideal: core sites nearest maximum shaking intensity (e.g. not at slip patch boundaries), core sites that have high relief sources upslope, core sites that are associated with turbidity current channels and canyons, and core sites that may promote expanded stratigraphic section (such as enclosed basins).

The success of turbidite correlation in Cascadia, the northern San Andreas, and Sumatra suggests that some first order structure of the turbidity current maintains integrity despite the fluid dynamic complexity of turbidity currents. We speculate that the longitudinal heterogeneity of the current, allocyclic forcing imparted by the heterogeneous earthquake rupture itself (the source-time function of the earthquake) may be recorded in the deposits (Morey and Goldfinger, 2004; Goldfinger et al., 2008, 2011, 2012 a; Garret et al., 2011). Our model predicts that these sub-events, minutes apart, may be recorded as discernible coarse pulses within the turbidite that can be correlated over large distances (**Fig. 2-8, 2-9**). A similar conclusion was drawn for Cascadia earthquake turbidites (Goldfinger et al., 2012 a); the mechanism has been tested in flume studies, and is predicted by theory and analog models (Goldfinger et al., 2012 a and references therein, 2012 b; Garret et al., 2011). There may be potential to correlate the seismogenic forcing of these landslides with further work.

Acknowledgements This research was funded by the Ocean Sciences and Earth Sciences Divisions of the National Science Foundation. We thank M. Erhardt, Amy M. Garrett, and Robert H. Porter. for conducting lab analyses; NOC, IFREMER, and BGR for providing key bathymetry and sub-bottom data; UTM, for providing science crew; NOC for providing Russ Wynn; BGR for providing Stefan Ladage; and AIST/GSJ for providing Ken Ikehara. We also thank coring technicians from OSU including Chris Moser, Bob Wilson, Paul Wolscak. Scripps Resident Technicians, the R/V/ Roger Revelle Captain Tom Djardins and crew, and student volunteers and faculty from OSU including Bart DeBaere and Maureen Davies. Further details regarding the cruise and the core locations, please refer to the cruise report here:
http://www.activetectonics.coas.oregonstate.edu/sumatra/report/index.html

Seismoturbidite Record as Preserved at Core Sites along the Cascadia and Sumatra-Andaman Subduction Zone

Jason R. Patton[1], Chris Goldfinger[1], Ann E. Morey[1], Chris Romsos[1], Brandi Black[1], Yusuf Djadjadihardja[2], and Udrekh[2]

1. College of Oceanic and Atmospheric Sciences, Oregon State University, Corvallis, OR 97331 USA. 2. Bandan Penghajian Dan Penerapan Teknologi BPPT 2nd Building, 19th Floor, Jl.MH. Thamrin 8, Jakarta, 10340 Indonesia.

Chapter 3 Abstract

We evaluate turbidite deposition along slope and trench settings for the Cascadia and Sumatra-Andaman subduction zones. Source proximity, basin effects, turbidity current flow path, earthquake rupture patterns, both temporal and spatial, hydrodynamics, and topography all likely play roles in the deposition of the turbidites as evidenced by the vertical structure of the final deposit. Channel systems tend to promote low-frequency components of the content of the current over longer distances, while more proximal slope basins and base-of-slope apron fan settings result in a turbidite structure that is likely influenced by local physiography and other factors. Cascadia's margin is dominated by glacial cycle constructed pathways which promote turbidity current flows for large distances. Sumatra margin pathways do not inherit these sedimentary systems, so turbidity currents appear more localized.

3-1. Introduction

Sedimentation of active margins is commonly dominated by turbidite systems. During sea level high stands, or for regions isolated from terrestrial sedimentation processes, these systems may principally be driven by seismic cycles (Nelson et al., 2011; Goldfinger et al., 2012 a). Accretionary prism architecture provides a first order control on flow paths for mass wasting processes (Bouma 2004, 2006, Bourget et al., 2010; Pouderoux et al., 2012). The prism's morphology in turn is driven by convergence rate, plate coupling, backstop strength, upper plate rheology, and lower plate topography and sedimentation history.

Paleoseismology is a science that can reveal the behavior of a fault system through multiple earthquake cycles (Atwater, 1987; McCalpin, 1996; Atwater and Hemphill-Haley, 1997; Nelson et al., 2006; Goldfinger et al., 2008, 2012 a). Strong ground shaking from rupture of earthquakes has been inferred to trigger turbidity currents that potentially

leave a very long record of past earthquakes in the form of turbidites (Dallimore et al., 2005; Goldfinger et al., 2003, 2008, 2012 a; Inouchi et al., 1996; Karlin et al., 2007; Noda 2004; Okamura, 2004; Shiki 2000; St-Onge et al., 2004). Turbidite paleoseismology uses combined evidence from sedimentology, tests of synchroneity, stratigraphic correlation, and analysis of non-earthquake triggers to develop a reliable earthquake record for submarine fault zones (Adams, 1990; Beatie and Dade, 1996; Goldfinger et al., 2012 a).

Turbidite paleoseismology has been largely successful in regions where an understanding of the flow systems and pathways (including secondary factors) can be developed in order to maximize the potential for success through careful core site selection. While the tectonic interpretation of these deposits is not the principle focus of this paper, it is these interpretations (and correlation of deposits) which allow us to make our observations regarding the forcing factors along these two margins.

In the following sections we describe some site localities and turbidity current pathways along the Sumatra and Cascadia margins. Detailed turbidite correlations and seismogenic trigger rationale in Cascadia are found elsewhere (Goldfinger et. al., 2012 a) and we discuss correlations and seismogenic rationale for Sumatra in this paper. These correlations are used here to provide a framework for discussion of architectural controls on turbidite sedimentation in marginal slope basin and trench settings of the Sumatra and Cascadia margins.

3-1.1 Physical Geography

The sedimentary systems of the continental slope and abyssal plain offshore Sumatra and Cascadia are controlled largely by the tectonics of the accretionary prism and the glacial history of the regional and local sources of terrestrial sediment. There exists a wide range in sedimentary settings along both of the margins off Sumatra and Cascadia (**Fig. 3-1**).

The continental slope is formed by the accretionary prism of the subduction zone and many of these geographical features are controlled by the geometry of the prism (Wang and Davis, 1996; Wang and Hu, 2006). The intersection of the slope with the abyssal plain may be close to the trench axis (Sumatra), or may be the intersection of the frontal fault limb or megathrust with a filled trench (Cascadia). Submarine canyons cross the slope and may headwardly migrate through growing anticlinal folds, into up-slope basins and branch into tributary canyons. Submarine channel systems are meandering

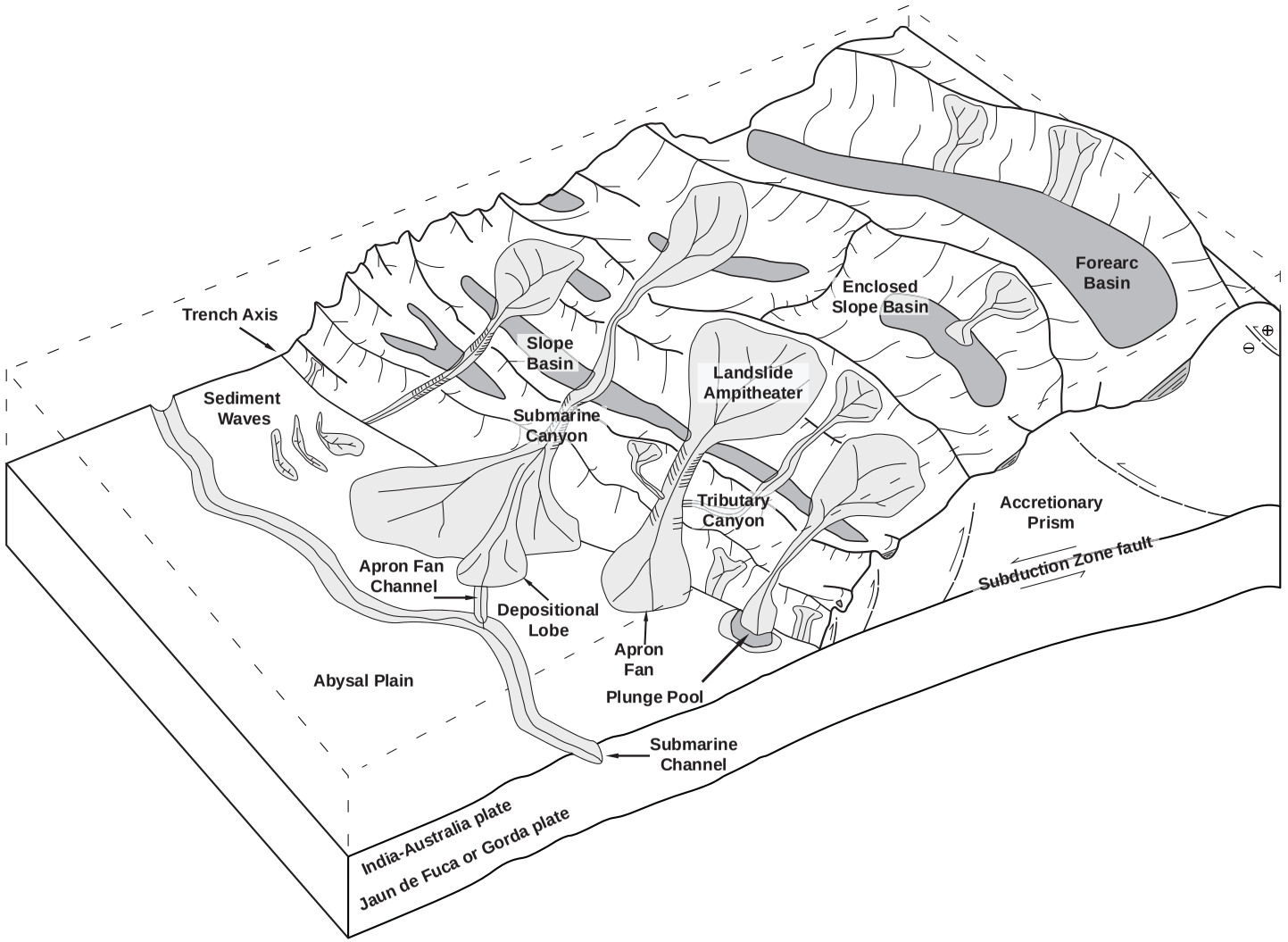

Figure 3-1. Schematic illustration of geomorphic elements of subduction zone trench and slope sedimentary settings. Submarine channels, submarine canyons, dune fields and sediment waves, abyssal plain, trench axis, plunge pool, apron fans, and apron fan channels are labeled here and described in the text.

channels that form in the sediments of the abyssal plain and may follow the trench axis (Carter, 1988). In Sumatra, there is no active channel system in the axis. In Cascadia, the filled trench allows channels to trend away from the slope, following trends defined by Pleistocene fan systems and the age of the subducting Juan de Fuca plate. Channels emanate from submarine canyons and submarine landslide complexes at the base of the slope (Carter, 1988). Dune fields and sediment waves are multibeam-resolvable landforms that have bedforms in the shape of transverse dunes (Nelson et al., 2000). A plunge pool forms in the trench where sediment flows from the slope scour the area at the base of the slope (probably due to the steepness of the slope), forming a recessed pool (Nelson et al., 2000). Apron fans form at the base of the slope and may or may not have apron fan channels incised into their surface (Nelson et al., 2000). In the following sections, we will describe the specific landforms found in Sumatra and Cascadia, their interactions, and the relations to their hosted turbidite stratigraphy.

3-1.2 Sumatra Margin

The India-Australia plate subducts to the northeast at 38 to 57 mm/year beneath the Sunda plate to form the Sumatra-Andaman subduction zone (SASZ) in the northeast Indian Ocean (Subarya et al., 2006; **Fig. 3-2**). Bengal fan channels are ultimately sourced from the Himalayas and formed as a response to climate forcing, particularly during glacial periods (Curray and Moore, 1971; Curray et al., 2003, Weber et al., 2003). Bengal fan deposits thin to the south, as evidenced in ETOPO elevation data (Smith and Sandwell, 1997). Oceanic basement structures are generally buried north of 1° north, and only partially buried south of that latitude (except along the outer rise and trenchward of the outer rise, where these structures are reactivated; the outer rise is a convex-up region west of the trench).

While active Himalayan sedimentation forms a fan in the northwestern Indian Ocean, turbidity current channels in the eastern Bengal fan are inactive since the late Quaternary as they no longer receive active sedimentation from northern sources (Moore et al., 1976; Weber et al., 2003). In the margin offshore northern Sumatra there is but a single relict turbidity current channel (sourced from the north) and it is not located in the trench axis, but is positioned westward of the outer rise, causing it to drain westward towards the Ninetyeast ridge. This relict channel does not reflect the modern gradients in topography as the India-Australia plate flexes here in response to subduction. There are no large channel systems in the trench, other than short (with a

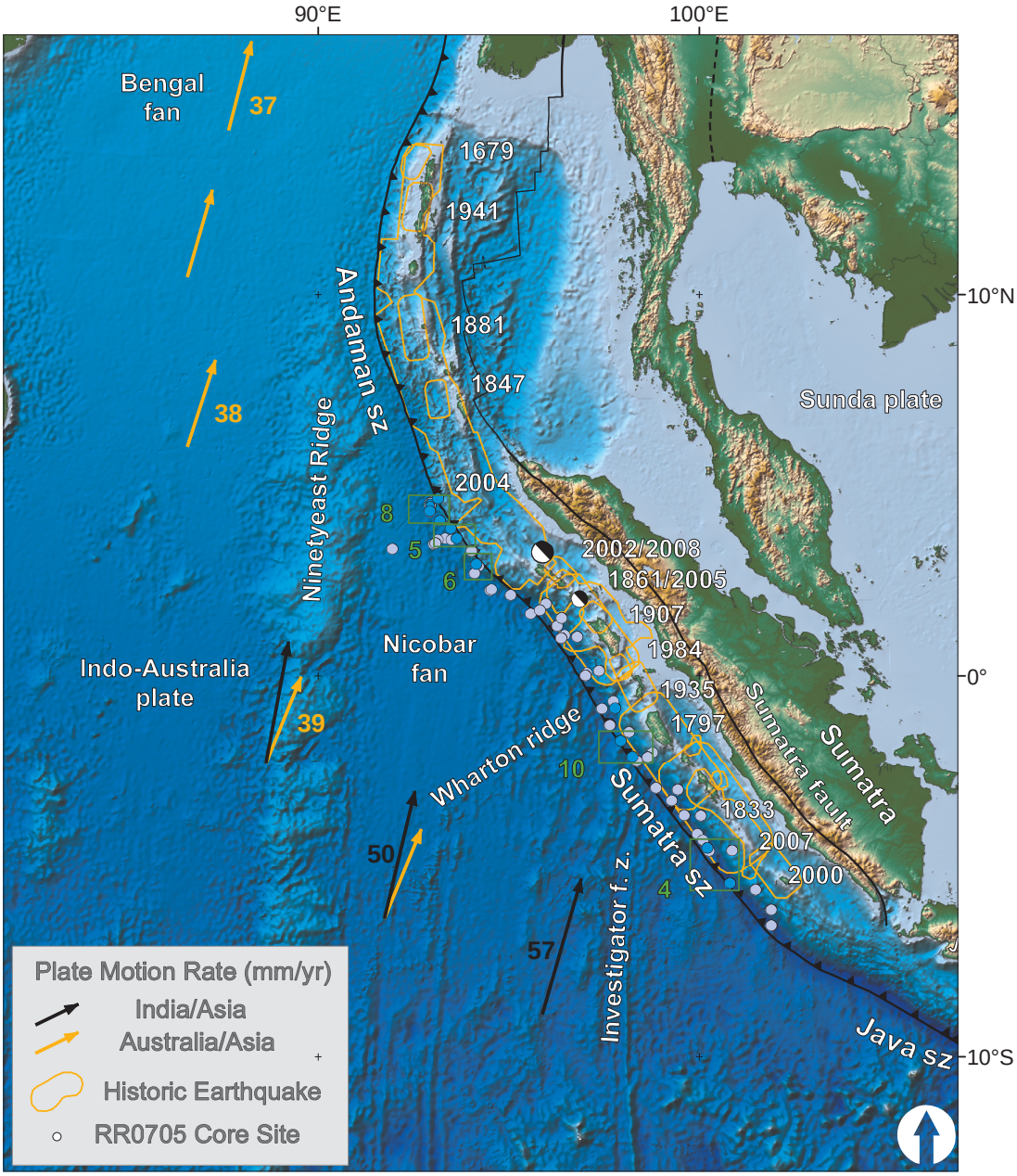

Figure 3-2. Sumatra core location and plate setting map. India-Australia plate subducts northeastwardly beneath the Sunda plate (part of Eurasia) at modern rates (GPS velocities are based on regional modeling of Bock et al, 2003 as plotted in Subarya et al., 2006). Historic earthquake ruptures (Bilham, 2005; Malik et al., 2011) are plotted in orange. Bengal and Nicobar fans cover structures of the India-Australia plate in the northern part of the map. RR0705 cores are plotted as light blue and cores discussed in this paper are darker blue. General location for **Figures 1, 5, 6, 8, and 10** are designated by green rectangles. SRTM bathymetry and topography is in shaded relief and colored vs. depth/elevation (Smith and Sandwell, 1997).

mean length of 7 km) apron fan channels associated with submarine canyons exiting the continental slope and localized submarine landslide amphitheaters. Many of these short channels are offset and deformed by bending moment normal faults, further restricting or altering turbidity current flow in these systems.

Continental margin morphology in western Sumatra is dominated by the upper plate structure of a Tertiary and Quaternary accretionary prism with structural highs and forearc slope basins. Uplifted Tertiary-Quaternary Bengal and Nicobar fan sediments form the core of the duplexed accretionary prism offshore Sumatra, which acts as a local backstop (Fisher et al., 2007; Kopp et al., 2008; Singh et al., 2010; Krabbenhoeft et al., 2010). Topography here is controlled largely by the blocks of sediment up to 4 km thick (Bandopadhyay and Bandopadhyay, 1999; Fisher et al., 2007) uplifted from the India-Australia plate (likely by duplexing of the accretionary complex) to form the upper part of the accretionary prism and marginal plateau (Fisher et al., 2007). Between these blocks and fault anticlines are the piggyback slope basins that archive sediment in which we collected our cores (Fisher et al., 2007; Mosher et al., 2008; Gulick et al., 2011). Slope basins in the Sumatra system are formed atop this fold and thrust belt with submarine canyon systems linking some basins as they cut normal to the trench. Many basins do not drain to the trench and have an expanded Holocene section. Canyon systems tend to be short and drainage catchments relatively small possibly because there are no pathways through the accretionary complex to the forearc basin or continental shelf. The outer forearc is sedimentologically isolated from northern Sumatra by the Aceh, Simeulue, Nias, Pini, Siberut, and Bengkulu Neogene forearc basins (Sieh et al., 2000; Susilohadi et al., 2005) Sediment input from the offshore islands of Simeulue, Nias, and Siberut is possible for some basins in the central and southern Sumatra margin. Similarly the trench provides sedimentologic isolation between sites due to the lack of large channel systems. In addition, core sites in the trench are isolated to sedimentologic sources further north along the SASZ. The trench is likely blocked from sedimentary input from northern sources by the subducting Ninetyeast Ridge and a large landslide at 14º N (Moore et al., 1976).

The trench axis deepens from 4.5 km. to 6.5 km, from north to south, and is filled with sediment four km thick in the north (Gulick et al., 2011), all deeper than the Carbonate Compensation Depth (CCD). Trench fill sediments are sourced from the Bengal and Nicobar fans and partially bury lower plate bending moment normal faults and fracture zones that trend across the trench. Along the central and southern

margin, sediments overlying the oceanic crust thin to less than one km. The trench axis morphology is therefore controlled by transverse structures from 2.25° S southward and the morphology in turn controls turbidite flow within the trench. Where larger lower plate structures like the Investigator fracture zone and the fossil Wharton ridge cross the trench in a northeasterly direction, they block sediment flow southward down the trench axis. The result of these blockages is compartmented sediment basins in the trench axis. A secondary effect is that sediment sources in the trench compartments are restricted to sources of input from adjacent specific slope segments. It is remarkable that these lower plate structures that compartmentalize sediment deposition also align with many historic earthquake rupture limits (Newcomb and McCann, 1987; Ortiz and Bilham, 2003; Sieh et al., 2006; Briggs et al., 2006; Natawidjaja et al, 2004; Chlieh et al., 2007; Meltzner et al, 2010, 2012).

3-1.3 Cascadia Margin

The Juan de Fuca and Gorda plates subduct to the northeast at 36 to 50 mm/year beneath the North America plate (**Fig. 3-3**) to form the Cascadia subduction zone (CSZ) in the northeast Pacific (McCaffrey et al., 2007). Sediment thicknesses on the lower plates decrease from 4km to <1 km, north to south. Sediment thickness may play a role in seismogenic potential and segmentation of the margin due to unmasking of basement structures in southern Cascadia (Goldfinger et al., 2012 a), as it may in Sumatra, where sediment thickness similarly decreases southward. The N-S gradient in incoming sediment thickness results in a smooth plate interface along the northern margin and a relatively rough one in the south, where the subducting Blanco fracture zone and two pseudofaults are exposed (Chaytor et al., 2004; Goldfinger et al., 2012 a). Shorter rupture segments along the southern margin are attributed to this unmasking of basement structure in the south (Goldfinger et al., 2012 a). CSZ fault coupling in submarine settings is evidenced by deformation along accretionary prism faults as motion is transferred from lower plate sinistral faults (Goldfinger et al., 1997). Along with vergence of accretionary prism thrust faults (Goldfinger et al., 1996; Johnson et al., 2005), wedge taper and structural strike in the prism are likely controlled by basal shear stress on the CSZ fault (Goldfinger et al., 1992; 1996; 1997). These all contribute to the variability of plate coupling on the megathrust along both margins.

The accretionary prism here is composed of Tertiary to Quaternary turbidites and hemipelagic mud (Westbrook et al., 1994; Johnson et al., 2005). Basins in the CSZ slope

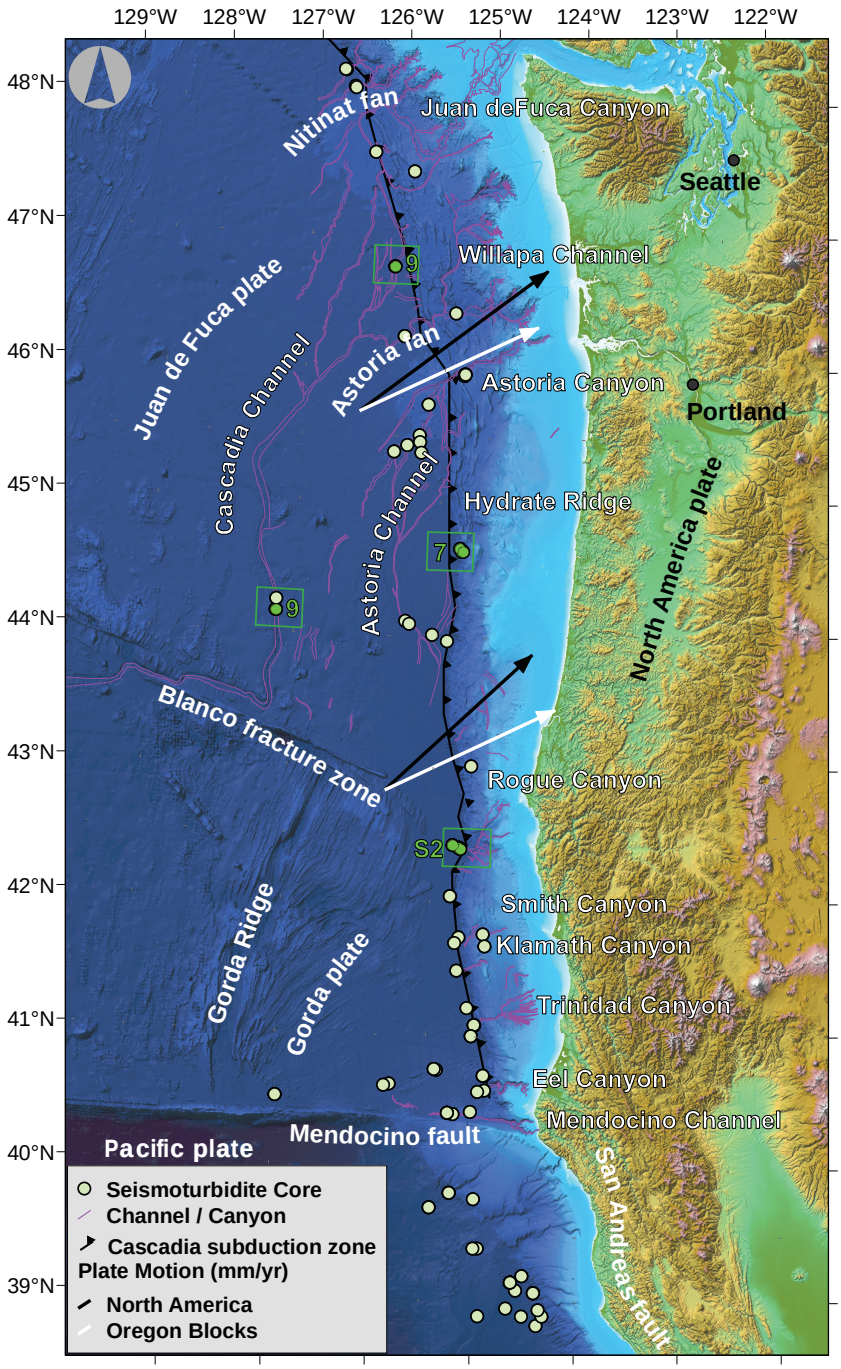

Figure 3-3. Cascadia margin turbidite canyon, channel, and 1999, 2002, and 2009 core location map. Core sites are displayed as green circles and cores discussed in this paper are darker green. Bathymetric grid constructed from multibeam data collected in 1999, 2002, and 2009, Gorda plate swath bathymetry collected in 1997 (Dziak et al., 2001), and archive data available from NGDC. Bathymetry and topography in regions outside these higher resolution data sets are from the SRTM global data set (Smith and Sandwell, 1997). General location for **Figures 7, 9, and Supplemental Figure 3-2** are designated by green rectangles. Multibeam bathymetry data collected recently was compiled by Chris Romsos at Oregon State University (personal communication, 2012).

are piggyback basins formed between the limbs of folds in the accretionary prism. These slope basins are commonly isolated, but are sometimes connected to other basins by relict channel systems, and are occasionally intersected by and connected to slope-perpendicular canyon systems. Several slope basins, notably Hydrate Ridge Basin West (HRBW), are completely isolated from terrestrial or shallow water sediment sources (Goldfinger et al., 2012 a). As in Sumatra, such isolated slope basins collect local sedimentation only from submarine landslides derived from the local slopes that define the basins.

The continental slope of the Cascadia margin is traversed by numerous submarine canyons that deliver an abundant sediment volume to the filled trench from the high-rainfall coastal region and continental interior since (**Fig. 3-3**). The Columbia River, one of the largest rivers in North America, has delivered ~20 million metric tons of sediment per year mostly to the Washington shelf during the late Holocene (Sternberg, 1986; Wolf et al., 1999). During Pleistocene low-stands, when much of the Columbia River drainage basin was glaciated, a greater sediment load was delivered directly to the Cascadia Basin floor turbidite systems (Underwood, 2005). During that time, the broad Astoria and Nitinat Fans were constructed along the northern margin, and filled the subduction-zone trench (Nelson et al., 1968; Nelson et al., 1987; Normark and Reid, 2003; Goldfinger et al., 1997). During the Holocene high stand, sediment from Cascadia rivers was deposited mostly on the shelf and in nearly full shelf basins and upper canyons (Goldfinger et al., 1992; McNeill et al., 2000), with only 5% or less of the load delivered to canyon heads (Sternberg, 1986; Wolf et al., 1999).

A wide variety of modern turbidite systems are found within Cascadia Basin (Nelson et al., 2009, 2001). Base-of-slope sand-rich apron fans, such as Rogue Apron, are defined as small-scale (<10 km), wedge-shaped turbidite systems abutting the base of slope (Nelson et al., 2000, 2009, 2011). They do not have significant channel development detectable in seismic profiles, side-scan mosaics, or swath-bathymetry at the resolution of presently available data (Wolf and Hamer, 1999; this study). Submarine fans, such as Astoria Fan, are turbidite systems with significant channel development that funnel sediment into outer-fan depositional lobes. Another turbidite system type commonly found in active-margin settings is the extensive, tectonically-controlled, deep-sea channel system. Deep-sea channel systems, such as Cascadia Channel, are fed by multiple tributary canyons, extend for hundreds to thousands of kilometers across basin floors and eventually connect with abyssal-plain fans (Carter, 1988; Nelson et al., 2000). Large-scale sediment-

wave or dune fields and plunge pools associated with high gradient canyon mouths and proximal channels, such as those of the Trinidad and Eel systems, also have been observed in swath-bathymetric and sidescan mosaics of basin floors (Nelson et al., 2009, 2000; EEZ-Scan 84 Scientific Staff, 1986; Goldfinger et al., 2012). In a tectonically active setting like the Cascadia margin, folding, faulting, and extensive sediment failures can disrupt canyon and channel pathways of turbidite systems.

3-1.4 Seismoturbidites

Adams (1990), Goldfinger et al. (2003), and Shanmugam (2008) suggest nine plausible triggering mechanisms for turbidity currents: 1) storm wave loads, 2) earthquake ruptures, 3) tsunami wave loads (local or distant), 4) sediment loads, 5) hyperpycnal flows, 6) volcanic explosions, 7) submarine landslides, 8) cyclones, and 9) bolide impacts. Other mechanisms may reduce slope stability (tectonic oversteepening, depositional oversteepening, sea-level lowering, salt movement, glacial loading, biologic erosion), but are likely random and not regional nor synchronous (Inouchi et al., 2996; Goldfinger et al, 2007). Discriminating between these mechanisms is central to using turbidites for paleoseismology. While subduction zones generate sufficient seismicity to seismically strengthen sediments so these settings are more resistant to other triggering mechanisms (Biscontin and Pestana, 2006; Nelson et al., 2011), we will first discuss relevant alternative triggers.

Considering alternative triggers, hyperpycnal storm flow related deposits (hyperpycnites) may have a finer sediment base that initially coarsens upwards (during waxing flow), then fines upwards (as the flow wanes ; Mulder et al., 2003) though this sequence may also not be represented in the deposit. With wave triggers, the landslide source area would be much shallower than the source areas in the region of this study. Tsunami waves and storm waves can cause liquefaction and erosion at upper canyon and shelf depths, but source areas for our cores are not at these shallow depths. Tsunami wash-back sediments have been found in Sumatra (Sugawara et al., 2007) and elsewhere (Bondevik et al., 1997; Fujiwara et al., 2000; van den Bergh et al., 2003; Noda et al., 2007; Abrantes et al., 2008), but these are also at much shallower depths than found in this study. They are relevant in Cascadia, but typically wave related triggering causes upper canyon transport, but not necessarily ignition of a turbidity current that reaches deep water. Gas Hydrate destabilization would leave behind highly localized deposits. Bolide impacts may also lead to turbidites, but their recurrence is far too long to explain

the chronostratigraphy in these cores. These and other mechanisms are discussed in detail for Cascadia in Goldfinger et al. (2012 a). Thus sedimentologic discriminators between these mechanisms are possible, as are frequency comparisons, but these are hardly universal. The primary basis for attributing a seismogenic trigger to the turbidite record is testing for regional and synchronous deposition, combined with comparison to historic and other paleoseismic data (Goldfinger et al., 2007, 2008, 2012 a,).

Earthquakes are well known as subaerial landslide triggers, with a triggering minimum earthquake magnitude of ~Mw=5 (Keeper, 1984), and landslide density found to be greater in areas of stronger ground acceleration (Meunier et al, 2007; Strasser et al., 2006). Earthquakes are also one of the dominant submarine landslide triggers (Hampton et al., 1996; Masson et al., 2006; Goldfinger et al., 2003, 2008, 2012 a), with most historic examples attributed to ground accelerations from earthquakes (Mosher et al., 2010; Shirai et al, 2010; Mosher and Piper, 2007; St. Onge et al., 2004, 2011). Minimum magnitudes for recording seismoturbidites are possibly above Mw=7.1 (Goldfinger et al., 2003) or Mw=7.4 (Nakajima and Kanai, 2000) in subduction zone settings, though smaller magnitudes (Mw = 5.2) have been observed (Lorenzoni et al, 2012 a) and are supported by studies of slope stability and minimum accelerations required for failure (e.g. Goldfinger et al 2012 b).

We test the plausibility of a seismogenic trigger in Sumatra by 1) using tests for synchronous triggering of sedimentologically isolated turbidite systems and 2) using secondary constraints that consider sedimentologic characteristics of the turbidites. When turbidites can be correlated between sites separated by a large distance or between sites isolated from land sources and from each other, synchronous triggering can be inferred and most other triggering mechanisms can be eliminated (Goldfinger et al., 2003, 2008, 2012 a; Shiki, 2000; Gorsline et al., 2000; Nakajima, 2000; Rajendran et al., 2008; Shiki et al., 2000).

Attributing a seismogenic trigger to turbidites generally requires spatial and temporal correlation of individual turbidites (Shiki et al., 2000; Gorsline et al., 2000; Nakajima, 2000; Goldfinger et al., 2003, 2008, 2012 a; Rajendran et al., 2008). Kneller and McCaffrey (2003) and Baas et al. (2005) pose that the vertical structure (Middleton, 1965) is predicted when there are longitudinal (along the flow path) changes in sediment flux within turbidity currents. Source-time functions and rupture geometry of earthquakes may provide this spatial and temporal control on sediment input into

these turbidity current systems. The turbidite structure (stratification) left behind by these flows thus possibly records an approximation of the seismic energy density at the landslide source area (Morey-Ross and Goldfinger, 2004; Goldfinger et al., 2011, 2012 a, b).

Mass wasting along continental margin slope settings has a large range in genetics, from block falls to nepheloid raveling (Nelson et al., 2000; Lorenzoni et al., 2012 b). However little is known about the initial slope failures that lead to turbidity currents along the CSZ and SASZ margins. These turbidity currents may begin as a wide range of mass wasting types, but eventually transform into turbulence driven buoyant sediment rich flows (Nelson et al., 2011). These turbidity currents can travel 100's to 1,000's of kilometers if channels and basins extend that distance (Nelson et al., 1968; Goldfinger et al, 2003; Nelson et al, 2011). When turbidity currents are localized in slope basins, they may only travel much shorter distances or may escape the slope basin margins by flowing uphill, and may be reflected within these slope basins (Kneller and McCaffrey, 1995; Bourget et al, 2011; Pouderoux et al., 2012). When currents travel in restricted settings (slope basins or other settings with no channels), deposits left behind are controlled largely by source proximity (Nelson et al., 1986), but may also be subject to bypassing and hydraulic jumps that complicate the recording at any given site (Goldfinger et al., 2012 a).

Coring for seismoturbidites requires an evaluation of these competing factors so that the coring sites can be optimized to reduce complicating factors while enhancing the likelihood of recording earthquakes. Here we review coring sites from Sumatra and Cascadia as they relate to these competing turbidite structure forcing factors. We also discuss the correlation of these deposits for stratigraphy offshore Sumatra.

3-2. Data and Methods

3-2.1 Site Survey

We mapped the seafloor and shallow subsurface in order to select coring sites in optimal locations for collecting records of turbidity current deposition. For cruises on the R/V Thomas G. Thompson (CSZ: 2009, TN0909 cores), R/V Roger Revelle (CSZ: 2002, RR0702 cores; SASZ: 2007, RR0705 cores), and R/V Melville (CSZ 1999, M9907 cores) where cores were collected for paleoseismic studies, multibeam mapping was essential to evaluate the physiographic setting for the relevant sedimentary systems.

Multibeam sonar mapping of the sea-floor is collected and edited on board so that coring sites can be chosen in real-time (e.g. RR0705 Superquakes07 Cruise Report http://www.activetectonics.coas.oregonstate.edu/sumatra/report/index.html). Prior to the cruises, existing bathymetric data are compiled. Sumatra bathymetry was collected by Japanese (R/V Natsushima: Japan Agency for Marine Earth-Science and Technology, Jamstec), United Kingdom (HMS Scott: UK Royal Navy and Southampton Oceanography Centre, NOCS), French (R/V Marion Dufresne: Ifremer), and German (R/V Sonne: Federal Institute for Geosciences and Natural Resources, BGR) ships and shared utilizing a cooperative agreement with these international institutions and the Indonesian Government (Agency for the Assessment and Application of Technology, BPPT), without which, the coring study would not have been possible (Henstock et al., 2006; Ladage et al., 2006). Prior to the 1999 and 2002 cruises, existing Cascadia bathymetry was compiled by Dziak et al. (2001) and Goldfinger et al. (2003). These Cascadia compilations included older swath bathymetry (including SeaBeam 2000, SeaBeam Classic, and Hydrosweep), as well as multibeam bathymetry. 3.5 kHz Compressed High Intensity Radar Pulse (CHIRP) seismic profiles of the shallow sub-bottom is also an important data set to collect when locating core sites. These data reveal the continuity (or lack thereof) of repeated local turbidite sedimentation, local faulting, and mass wasting deposits, and may be useful in projecting the seismic record beyond the depth limits of coring campaigns.

3-2.2 Coring and Lithostratigraphic Correlation

Piston and gravity coring are the primary methods used to collect strata from the sea floor, supplemented with Kasten-, box-, and multi-cores (the latter two are used to sample the sediment-water interface and the upper-most units with minimal disturbance). Kasten cores are useful as they provide a larger volume of sediment from which volume restricted age samples ($CaCO_3$ foraminiferid tests) are collected. Cores are scanned for geophysical properties (multi sensor core logging (MCSL): gamma density, magnetic susceptibility, p-wave velocity, and resistivity) and then split lengthwise and described on lithostratigraphic data sheets. Following the cruise, cores are then scanned with Computed Tomographic X-ray techniques (CT scans). CT data also provide densostratigraphic information (down-core variation in density) when CT imagery is used for downcore line-scan analysis. Other post-cruise analytical methods that are used include laser diffraction particle size measurements, down-core X-ray Fluorescence (XRF), superconducting rock magnetometer measurements of remnant magnetization,

high-resolution point magnetic susceptibility measurements, ^{210}Pb and ^{137}Cs isotopic analyses, and Accelerator Mass Spectrometry (AMS) radiocarbon age control. Core geophysical methods are further summarized in **Supplementary Document 3-1**.

Cores 55PC and 57PC are used to demonstrate the technique of flattening geophysical data between cores in order to wiggle match the fingerprints (**Fig. 3-4**). All correlations done in this paper are made using this technique, where the vertical scale of one dataset are scaled to match the vertical scale of the other core's dataset, based on the upper and lower stratigraphic contacts of the sedimentary deposits (Thompson et al., 1975). MSCL data for core 57PC is "flattened" to the stratigraphic horizons in core 55PC on the left, and 55PC is flattened to 57PC on the right. The core data being flattened is 50% transparent and plotted on the outside of the core data they are being flattened to. The unflattened core data are scaled at the same vertical scale as in **B**.

For basin cores, we selected cores from a variety of basin and trench settings **(Table 3-1)**. Sumatra cores RR0705-104PC/TC, RR0705-103PC/TC, and RR0705-96PC/TC are each in different basin settings: base of cliff, center of canyon, and center of closed basin respectively (**Figs. 3-2, 3-5, and 3-6**). These cores are located in the region of the 2004 SASZ earthquake (Aceh Segment, Kopp et al., 2008) and span a trench–parallel distance of 350 km. Cascadia cores RR0207-56PC/TC, RR0207-02PC/TC, and RR0207-01KC are all in the same basin: Hydrate Ridge Basin West and are within 4 km of each other (**Fig. 3-7**). The Hydrate Ridge cores are also spaced in relation to the landslide sources from proximal to distal.

For our selected trench cores, also in the Aceh Segment, Sumatra cores RR0705-03PC/TC, RR0705-05PC/TC, and RR0705-107PC/TC are at the northernmost extent of our cores along a 24 km transect (**Fig. 3-8**). Cascadia core M9907-12PC from the Juan de Fuca channel system is then compared with the Cascadia Channel core M9907-23PC, 350 km down-channel (**Fig. 3-9**). We discuss two pairs of Sumatra base of slope apron cores RR0705-38GC, RR0705-37GC, RR0705-41GC, and RR0705-40GC; separated by 60 km in the Siberut Segment (**Fig. 3-10**, Kopp et al., 2008). Then we finally evaluate Cascadia cores TN0909-01JC, M9907-30PC, and M9907-31PC at the base of Rogue Canyon, spanning an 8 km transect (**Fig. S 3-2**). Cruise prefixes for core names will be left out in some cases later in the paper.

Figure 3-4. Correlation of sedimentary units using standard stratigraphic correlation techniques between cores RR0705-55PC and RR0705-57PC. **A.** Bathymetric map with cores plotted as brown dots and depth contours with 500 m spacing. Cores 55PC and 57 PC are located in the trench approximately 120 km from each other. **B.** Stratigraphic correlations between these cores using lithology, CT, and geophysical properties. Multi Sensor Core Log (MSCL) data are plotted beside RGB imagery and CT imagery that displays lower density material in darker grey and higher density material in lighter grey. Gamma density, CT density, point magnetic susceptibility, and loop magnetic susceptibility are plotted left to right as light blue, dark blue, dark red, and light red. The certainty of any individual correlation is ranked and designated by line symbology. **C.** MSCL data for core 57PC is "flattened" to stratigraphic horizons in core 55PC on the left, and 55PC is flattened to 57PC on the right. The core data being flattened is transparent and plotted on the outside of the core data they are being flattened to. The unflattened core data are scaled at the same vertical scale as in B.

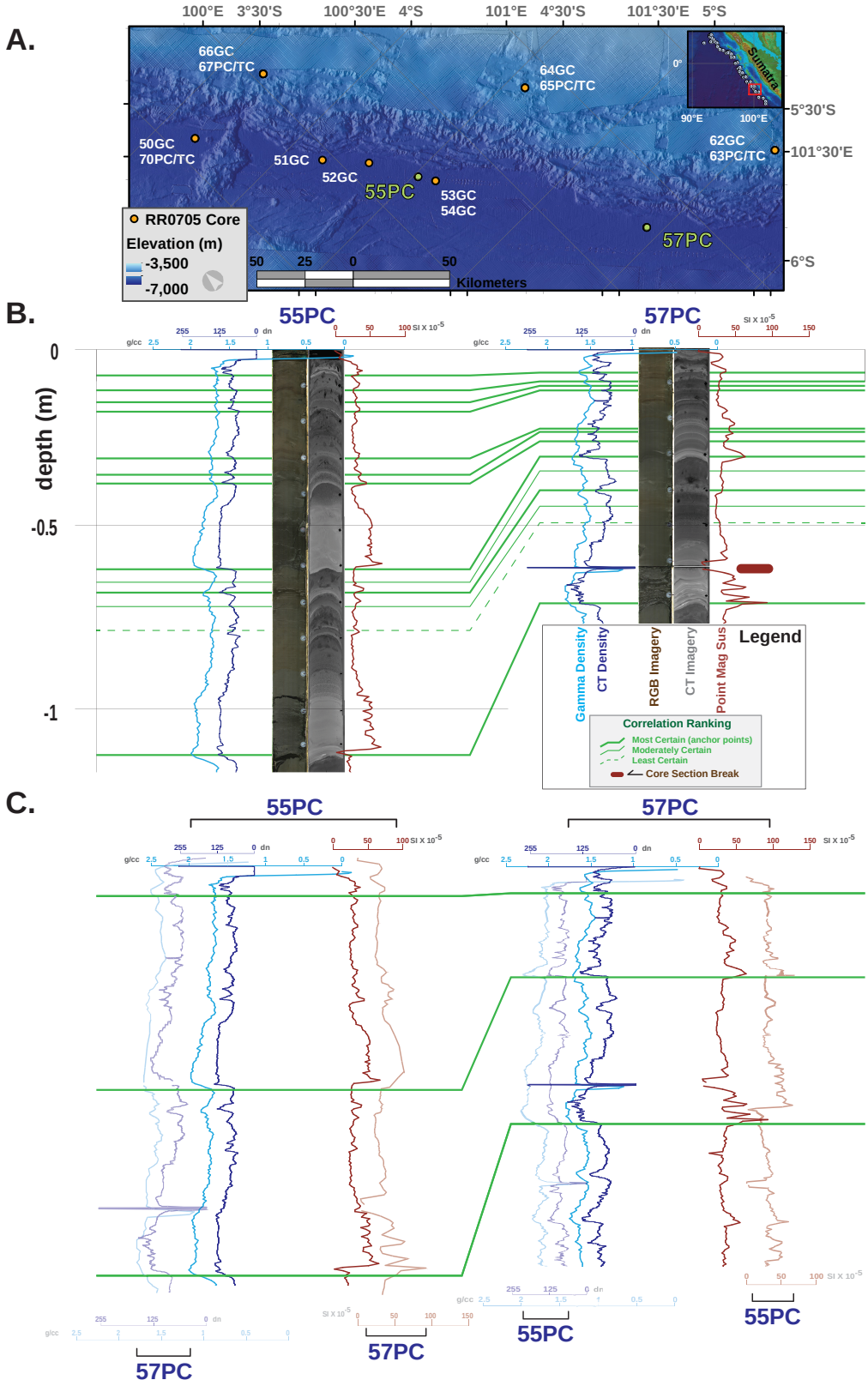

Figure 3-4. Correlation of sedimentary units using standard stratigraphic correlation techniques between cores RR0705-55PC and RR0705-57PC.

Figure 3-5. Sumatra slope basin cores RR0705-104PC and RR0705-103PC. As in all figures and throughout this paper: PC, = Piston core; BC, Box core; KC, Kasten core; GC, Gravity core; MC = Multi core. **A.** Stratigraphic correlations between these cores using lithology, CT, geophysical properties, and ^{14}C data. Multi Sensor Core Log (MSCL) data are plotted beside RGB imagery and CT imagery that displays lower density material in darker grey and higher density material in lighter grey. Gamma density, CT density, point magnetic susceptibility, and loop magnetic susceptibility are plotted left to right as light blue, dark blue, dark red, and light red. Radiocarbon ages are calibrated and reported with 95% error as is true for all ages in this paper (**Supplemental Table 1**). "Repeated section" refers to strata that have been double cored. This happens when the core barrel is accidentally inserted into the sea floor twice or more, thus sampling the same sediments twice or more (104TC has double repeated section). **B.** Core sites are plotted as orange circles on compiled bathymetry data set described in the text (Ladage et al., 2006). Inset map shows location of large map in red (northern margin) and cores in main map are orange dots. **C.** 3.5 kHz CHIRP seismic data collected at core sites are processed in SioSeis and plotted in SeiSee (seismic envelope). Core locations are designated by a red line scaled to core length. The X axis for the seismic plots is not distance, but shot number. These seismic data were collected while the ship was staying on position during coring. **D.** Elevation is plotted versus distance across the basins for cores 104 and 103. Profile locations are plotted as orange lines in **Figure 3-5 B.**

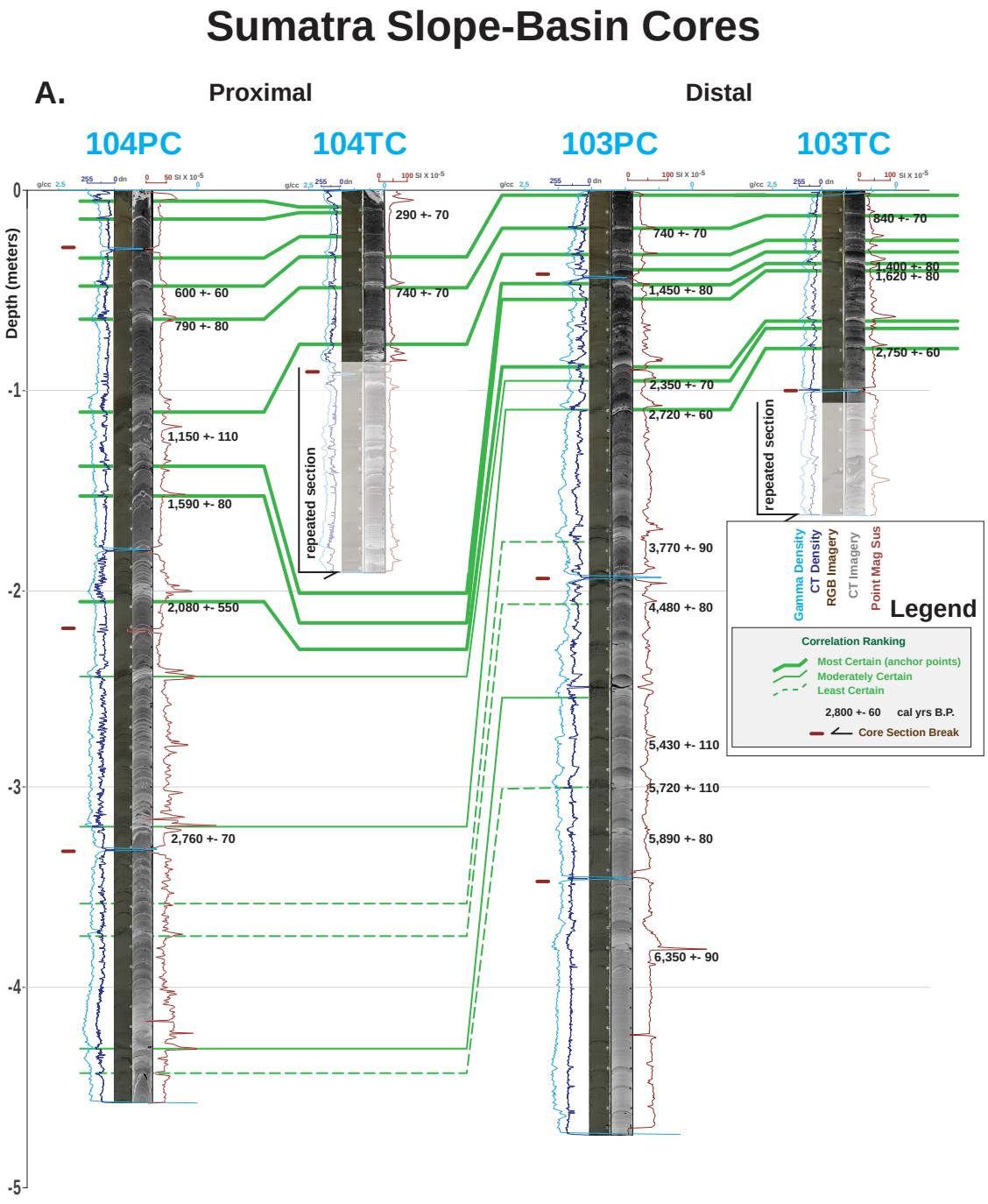

Figure 3-5. Sumatra slope basin cores RR0705-104PC and RR0705-103PC.

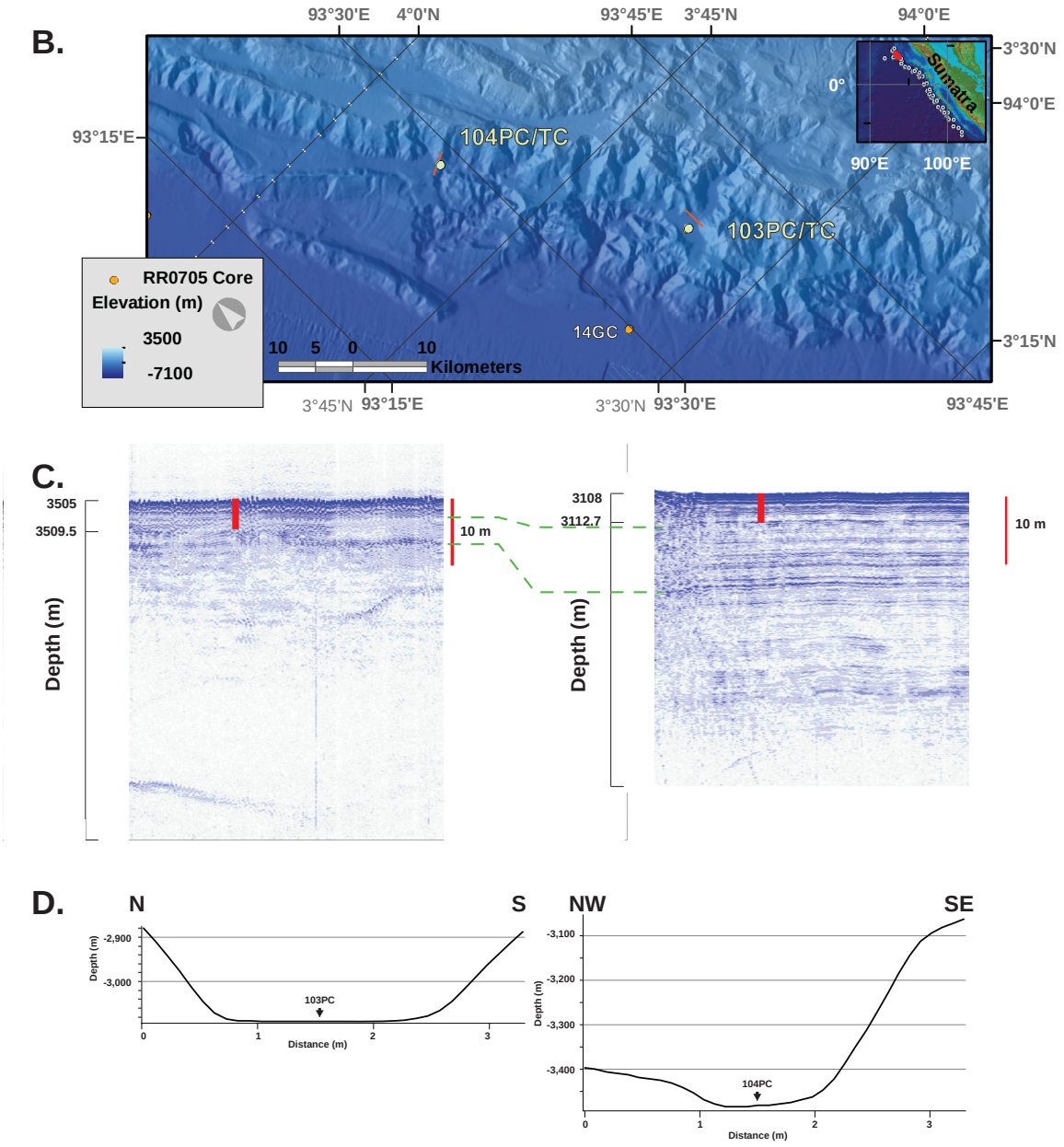

Figure 3-5 (Continued). Sumatra slope basin cores RR0705-104PC and RR0705-103PC.

Figure 3-6. Sumatra slope basin cores with an expanded Holocene section (**Figure 3-3**). **A.** RR0705-96PC is plotted with the same configuration as **Figure 3-2**. Median grain size data are plotted in green with 1 cm spacing. **B.** Particle size distribution data from sample locations at 10 cm spacing found in A are plotted by volume (%) vs. particle size (μm, log scale) with lines generally designating samples' depth where the lighter lines have a larger mean size and are generally lower in section. Differential volume displays the percent volume of each particle size. **C.** Core 96TC is scaled to 96PC and graphically spliced above 96PC to generate this composite core 96PC/TC. Moment release (vs. latitude) in red (Chlieh et al., 2007) and relative amplitude (vs. time) in green (Ishi et al, 2007), brown (Ni et al., 2005), and orange (Tolstoy and Bohnenstiehl, 2006) are scaled to match peaks in the loop ms data from composite core RR0705-96PC/TC. Thick grey tie-lines correlate the beginning of seismic peaks with each other and with base of peaks in the core geophysical data. Thin grey lines show secondary correlations (lower seismic energy and lower amplitude core geophysical data). **D.** Core site locations for cores RR0705-96PC/TC. Inset map shows location of large map in red (northern margin) and cores in main map are orange dots **E.** 3.5 kHz CHIRP seismic data collected at core sites are processed in SioSeis and plotted in SeiSee (seismic envelope). Core location is designated by a red line scaled to core length. **F.** Low angle oblique view of core site, designated by yellow dot. Due to nature of oblique maps, the scale is only relevant nearest the core location.

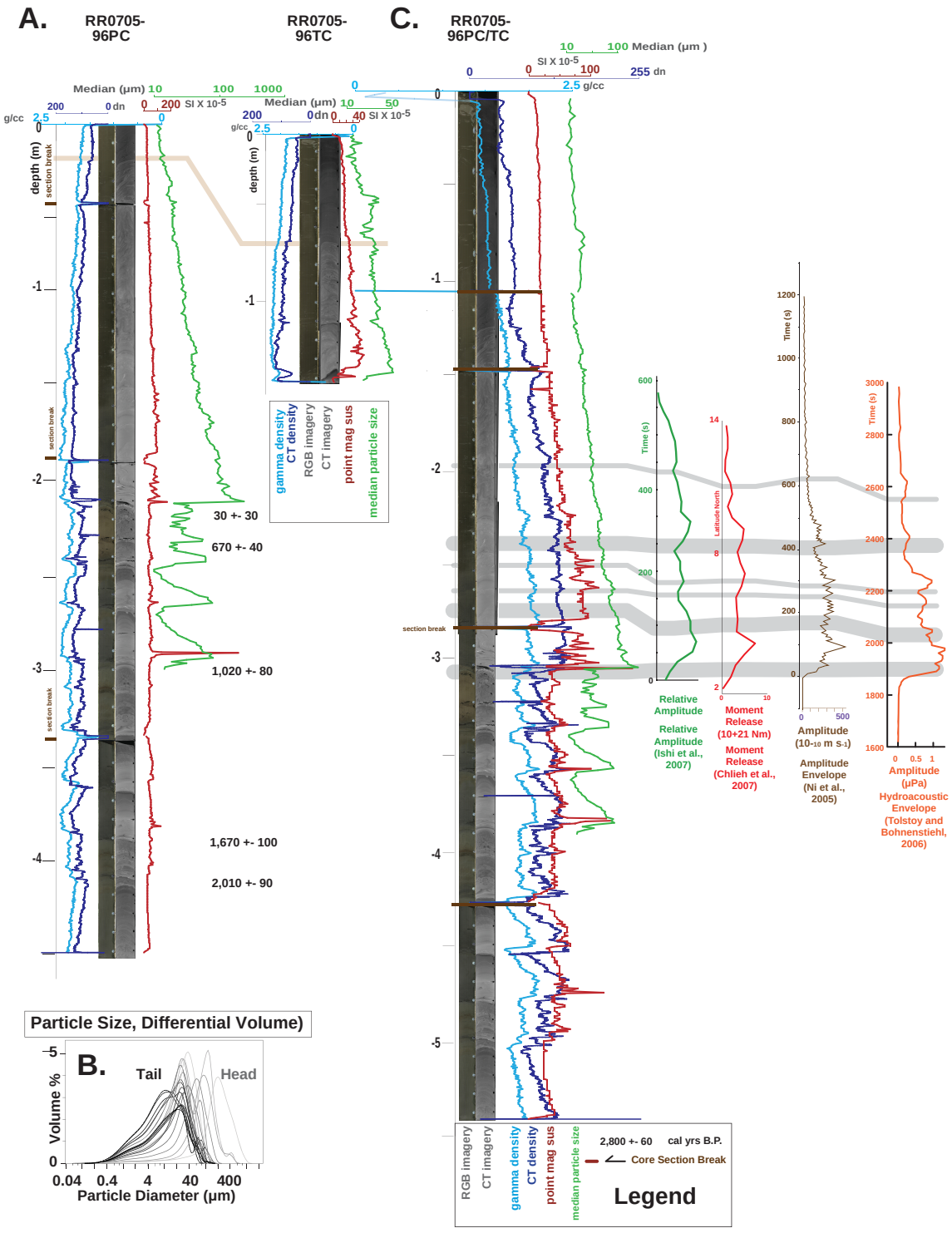

Figure 3-6. Sumatra slope basin cores with an expanded Holocene section (Figure 2-3).

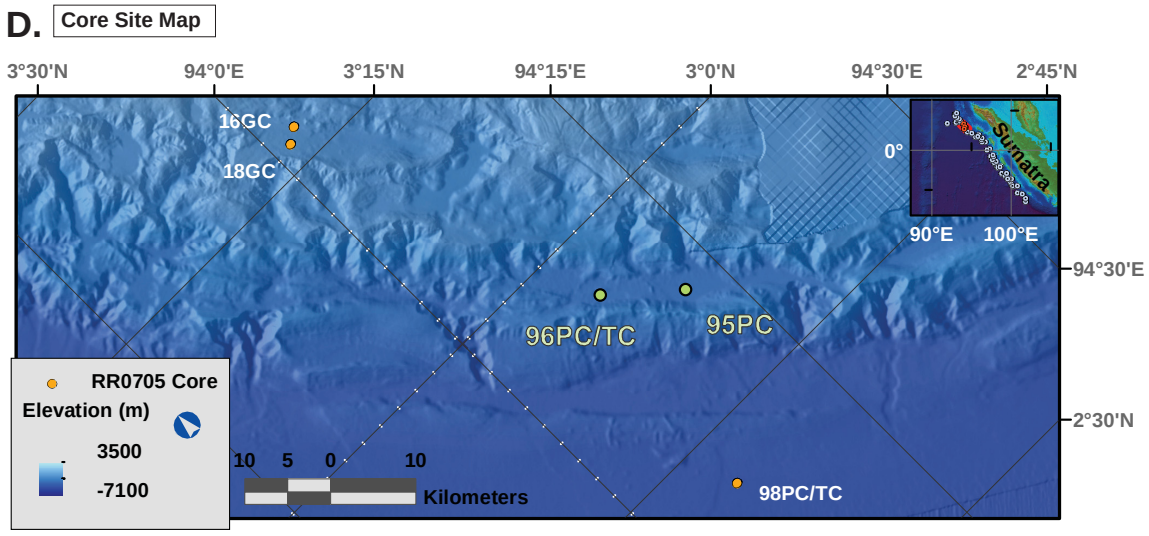

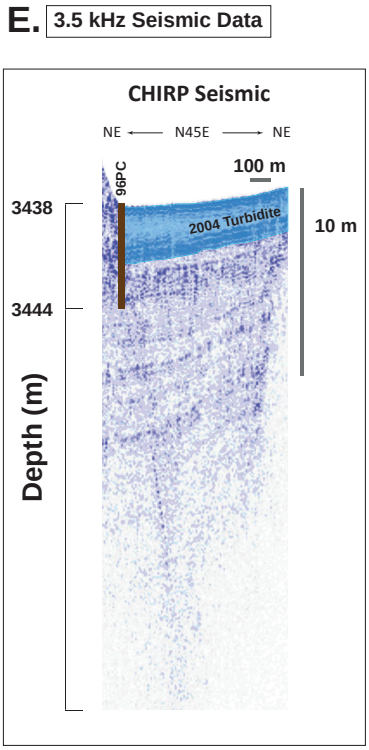

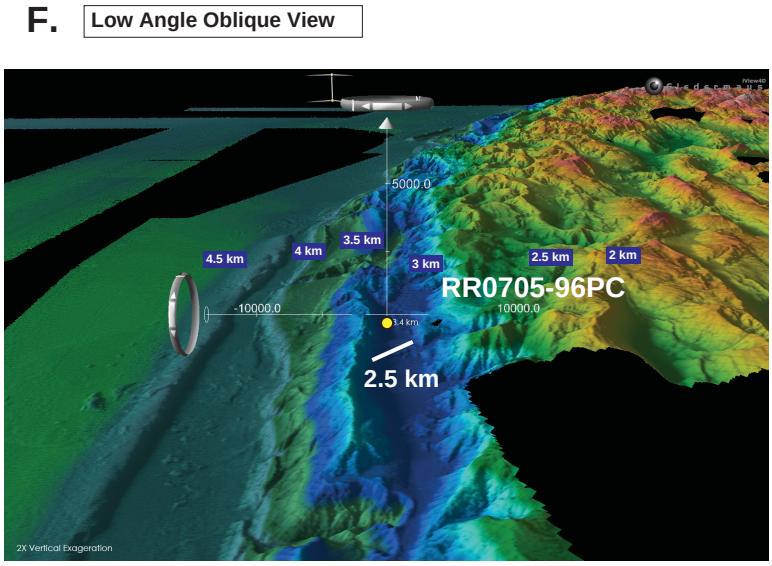

Figure 3-6 (Continued). Sumatra slope basin cores with an expanded Holocene section (Figure 2-3).

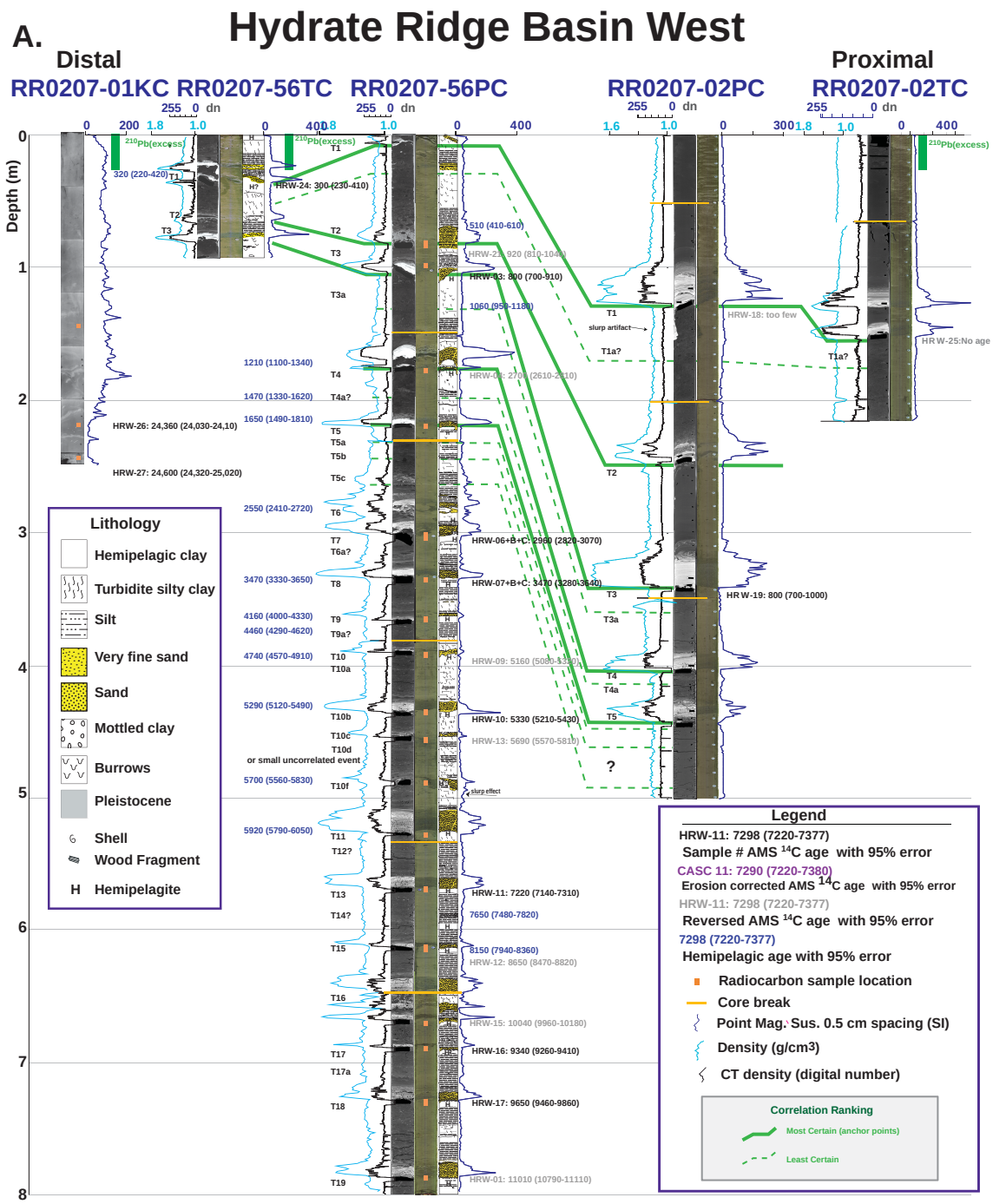

Figure 3-7. Cascadia slope basin cores at Hydrate Ridge West Basin: RR0207-01KC, 56PC/TC, and 02PC/TC. (**Figure 3-3**)**. A.** Site-correlation diagram for Hydrate Ridge Basin West (HRBW) cores. Individual coarse pulses in these turbidites, 02PC/TC in particular, are well-defined, consistent with their proximal setting. MSCL data are plotted along with CT density: gamma density in light blue, CT density in black, and magnetic susceptibility in dark blue. Calibrated radiocarbon ages (Goldfinger et al, 2012) are reported with 95% error. ^{210}Pb activity ("excess"), measured in some cores, shows to what depth recent

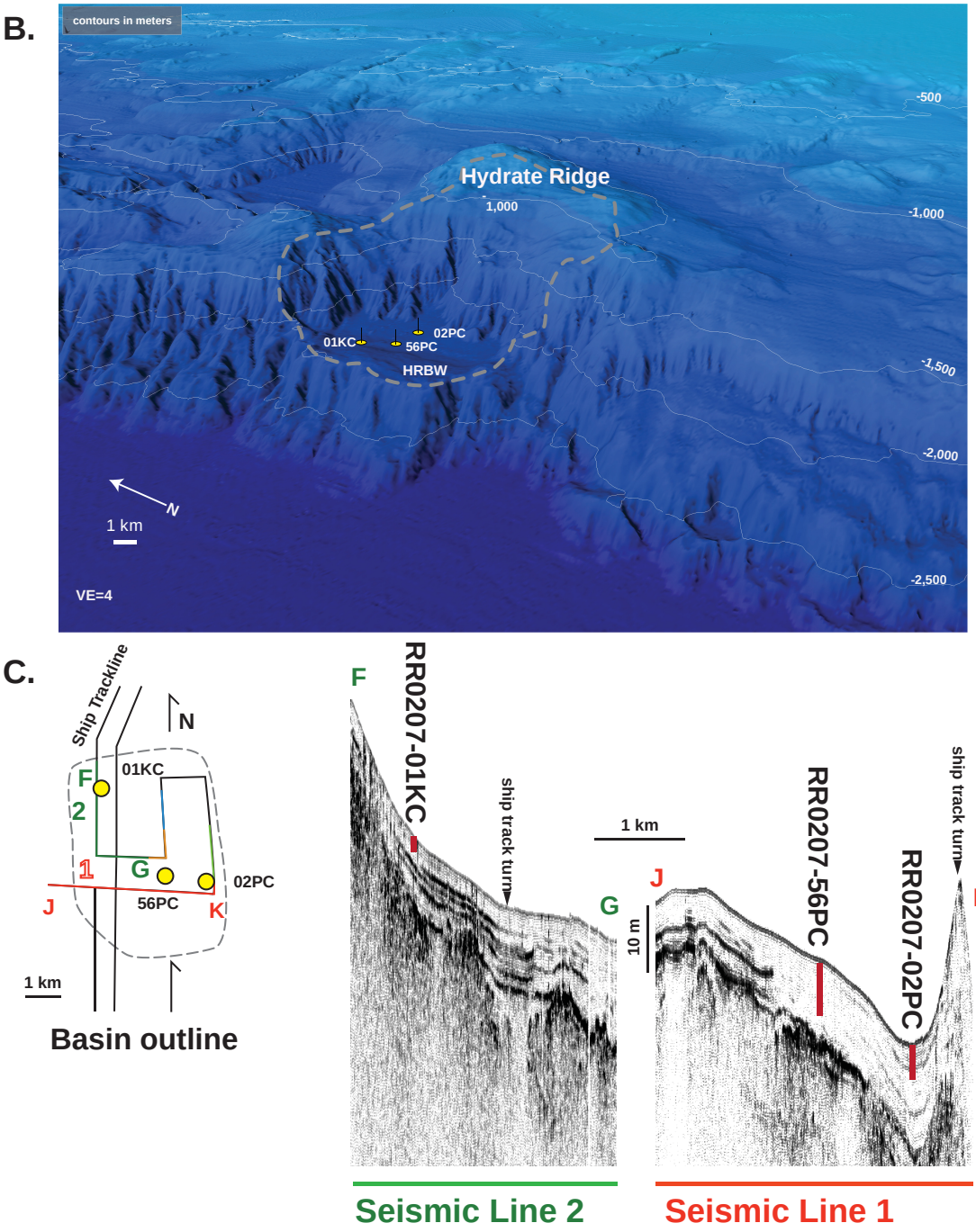

Figure 3-7 (Continued).

sediments were deposited (approx. 150 years; Noller, 2000). **B.** Low angle oblique view of core sites. **C.** 3.5 kHz seismic data collected during transit for our coring cruise TN0909 are processed with Sioseis and the envelope is plotted in Seisee. Inset map: Track lines associated with seismic data are plotted with colors that match the seismic data. Core location is designated by a red line scaled to core length. Cores are plotted in yellow and basin is outlined as dashed grey line.

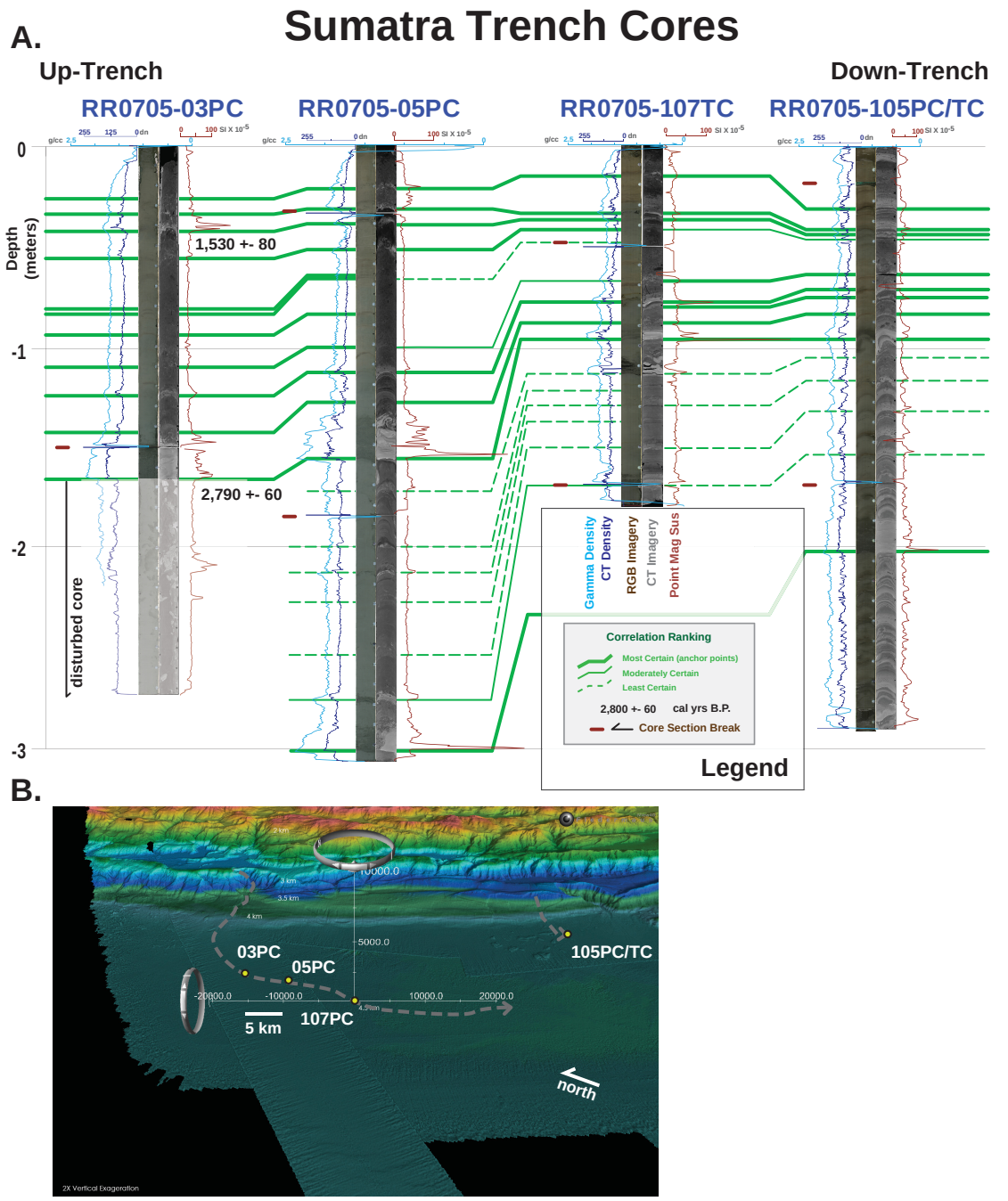

Figure 3-8. Sumatra trench cores RR0705-03PC, RR0705-05PC, RR0705-107TC and RR0705-105PC/TC (**Figure 3-3**). **A.** Cores are plotted in same configuration as **Figure 3-2**. Radiocarbon ages are displayed with 95% error. These ages are from below correlated turbidites in the slope core 108PC/TC (**Supplemental Table 1**). **B.** Low angle oblique view of core sites. Flow pathway from landslide source area to core sites is designated by a grey dashed line. Cores sites are plotted as yellow dots. **C.** Map showing core locations. **D.** Flow pathway profiles as shown in B are plotted with elevation versus distance. Core locations are labeled. **E.** 3.5 kHz CHIRP seismic data collected at core sites are processed

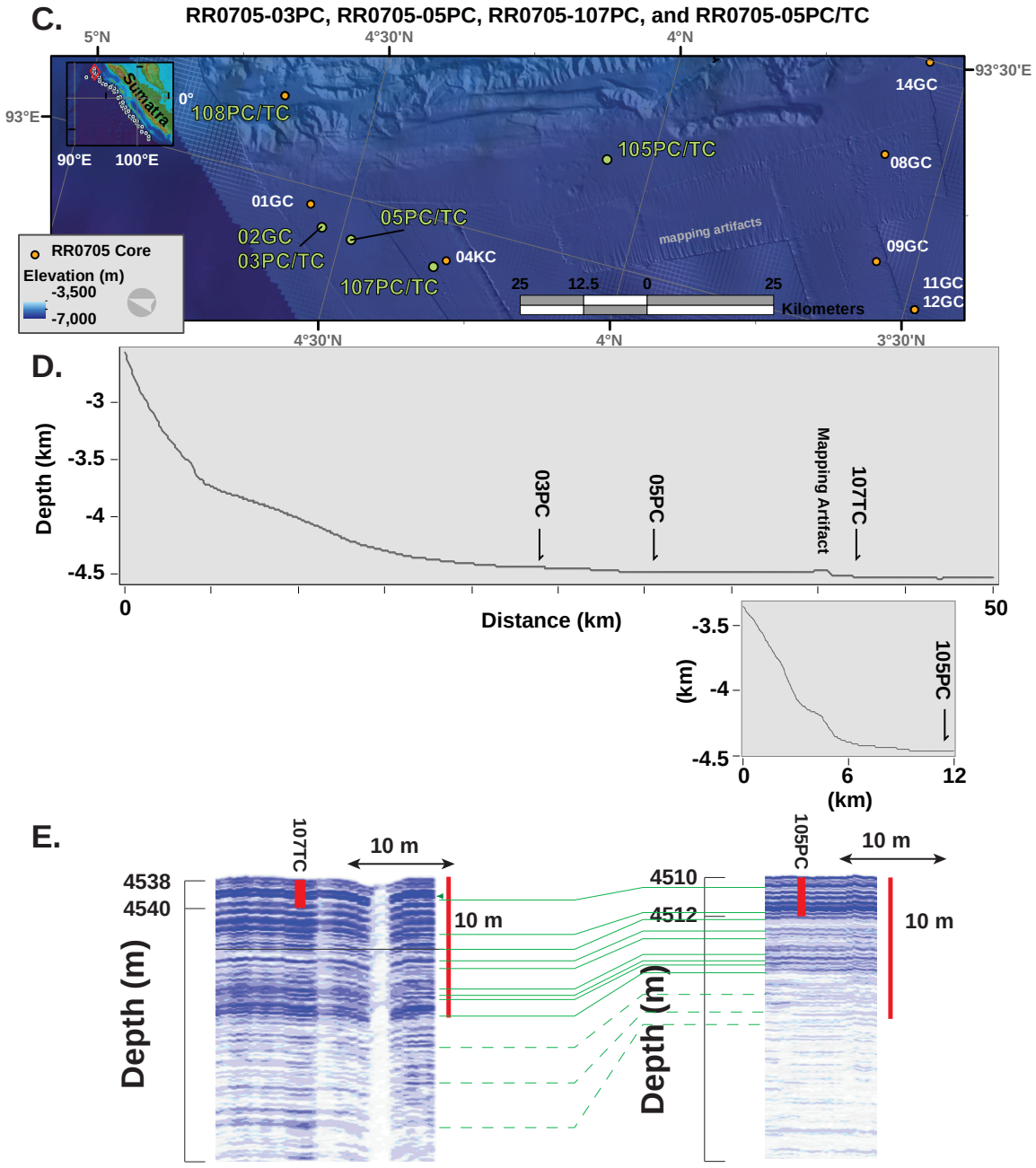

Figure 3-8 (Continued).

in SioSeis and plotted in SeiSee (seismic envelope). Acoustically opaque sediments are marked by a green arrow. Core locations are designated by a red line scaled to core length. The profile is smaller than the dot that designates the core location in **Figure 3-8B**.

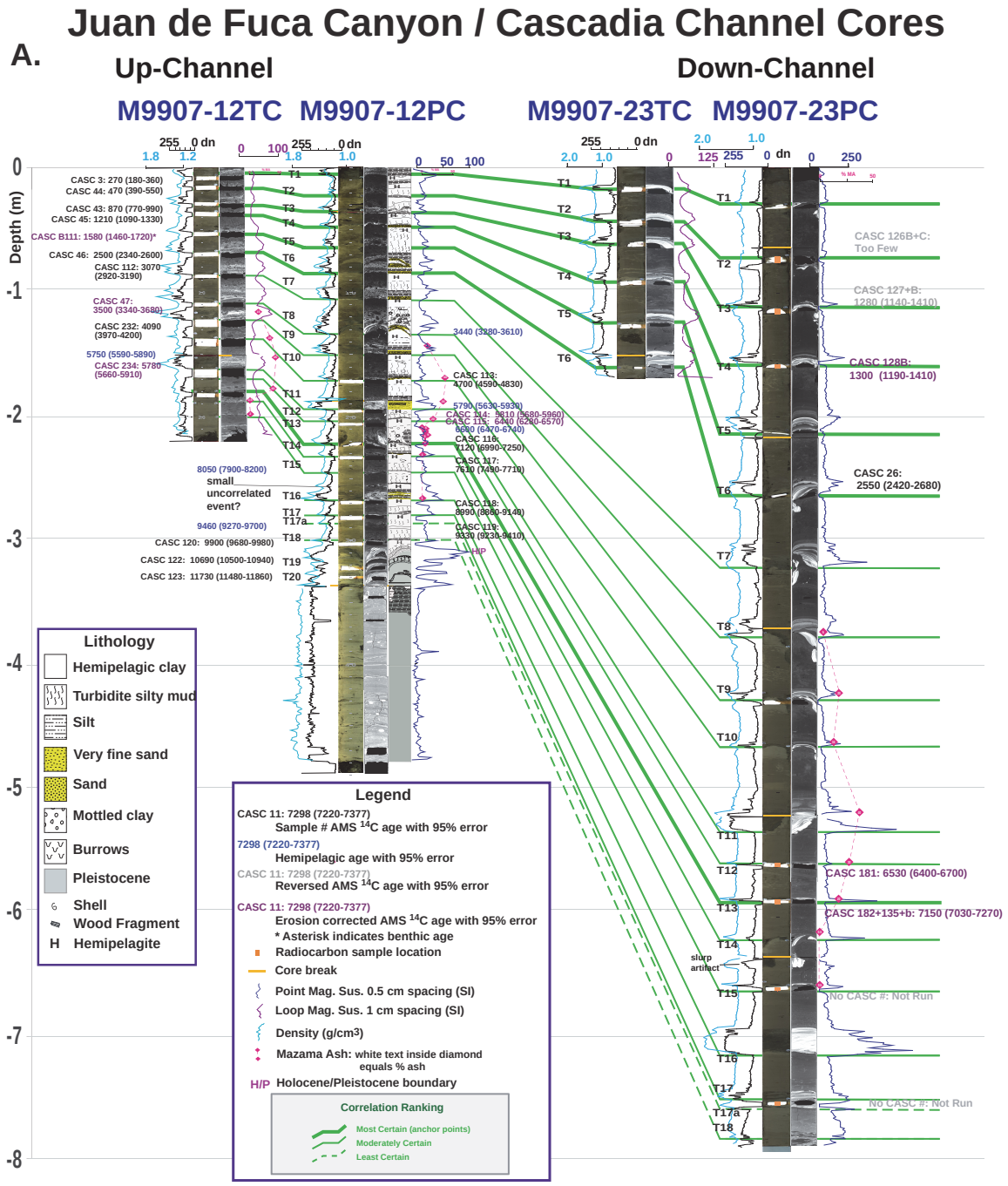

Figure 3-9. Cascadia trench: Juan de Fuca (JDF) channel (a tributary to Cascadia channel) and Cascadia channel cores MM9907-12PC and M9907-23PC/TC (**Figure 3-4**; Goldfinger et al., 2012). **A.** Correlation diagram for cores 12PC and 23PC with core data plotted with same configuration as **Figure 3-7**. **B.** Low angle oblique view of core sites. Because the map is oblique, the scale bar is only relevant nearest the core locations. **C.** CT scan data from cores 23PC (Cascadia channel) and 12PC (Juan de Fuca channel) are compared for three well correlated turbidites T-6, T-7, and T-9. The JDF imagery is

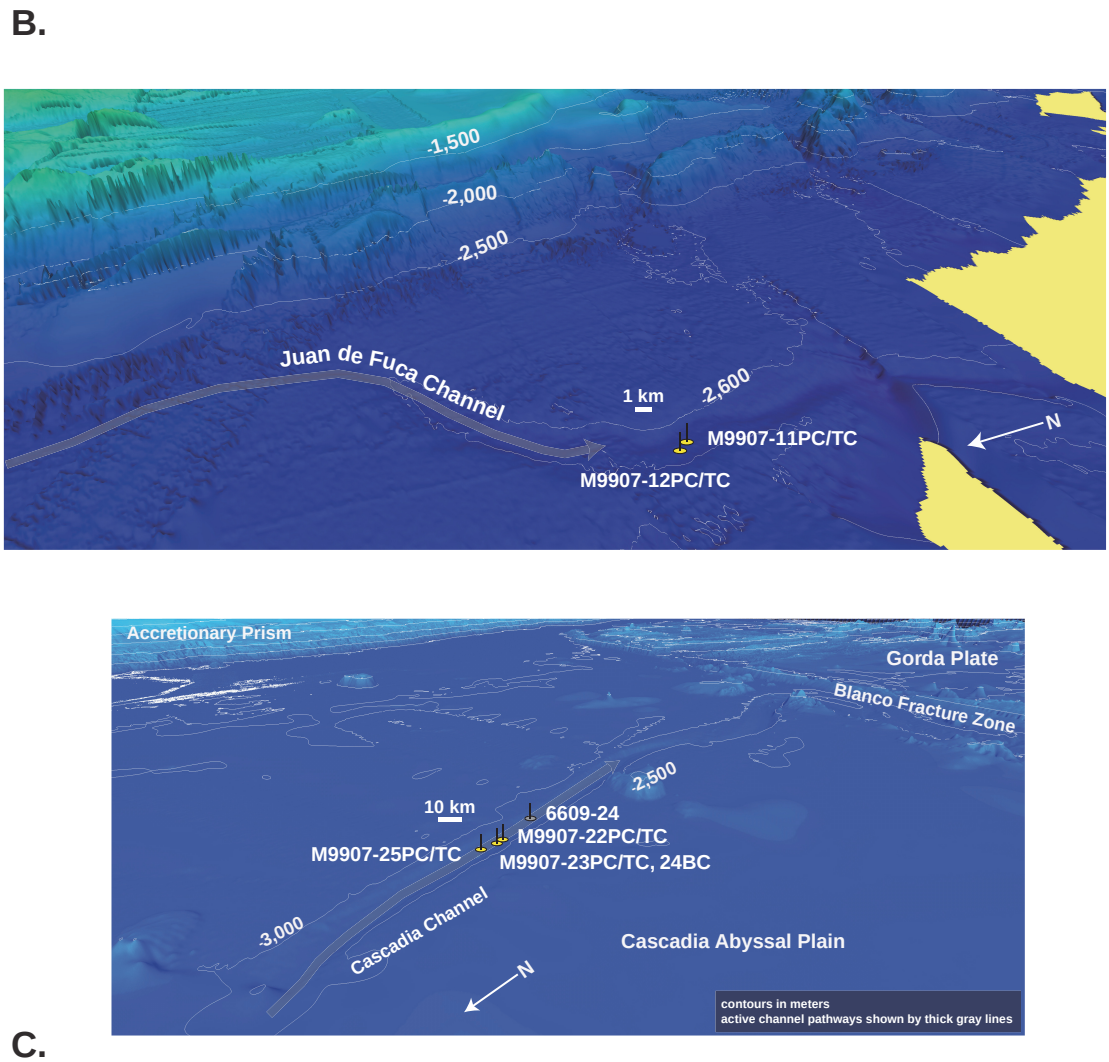

Figure 3-9 (Continued).

"flattened" to the upper and lower sand contacts of the corresponding Cascadia channel units. These examples show the relatively unchanged internal structure of these typical events after passing the confluence at Willapa channel and ~350 km of transport. JDF channel imagery is degraded significantly by numerous small gas evolution voids, but the structural similarity is still evident. The primary structure of two pulses and three pulses for T9 and T6, respectively, is matched by density and magnetic peaks. T7 shows more pulsing (~7) than is resolvable with the geophysical data, but it is apparent in both cores.

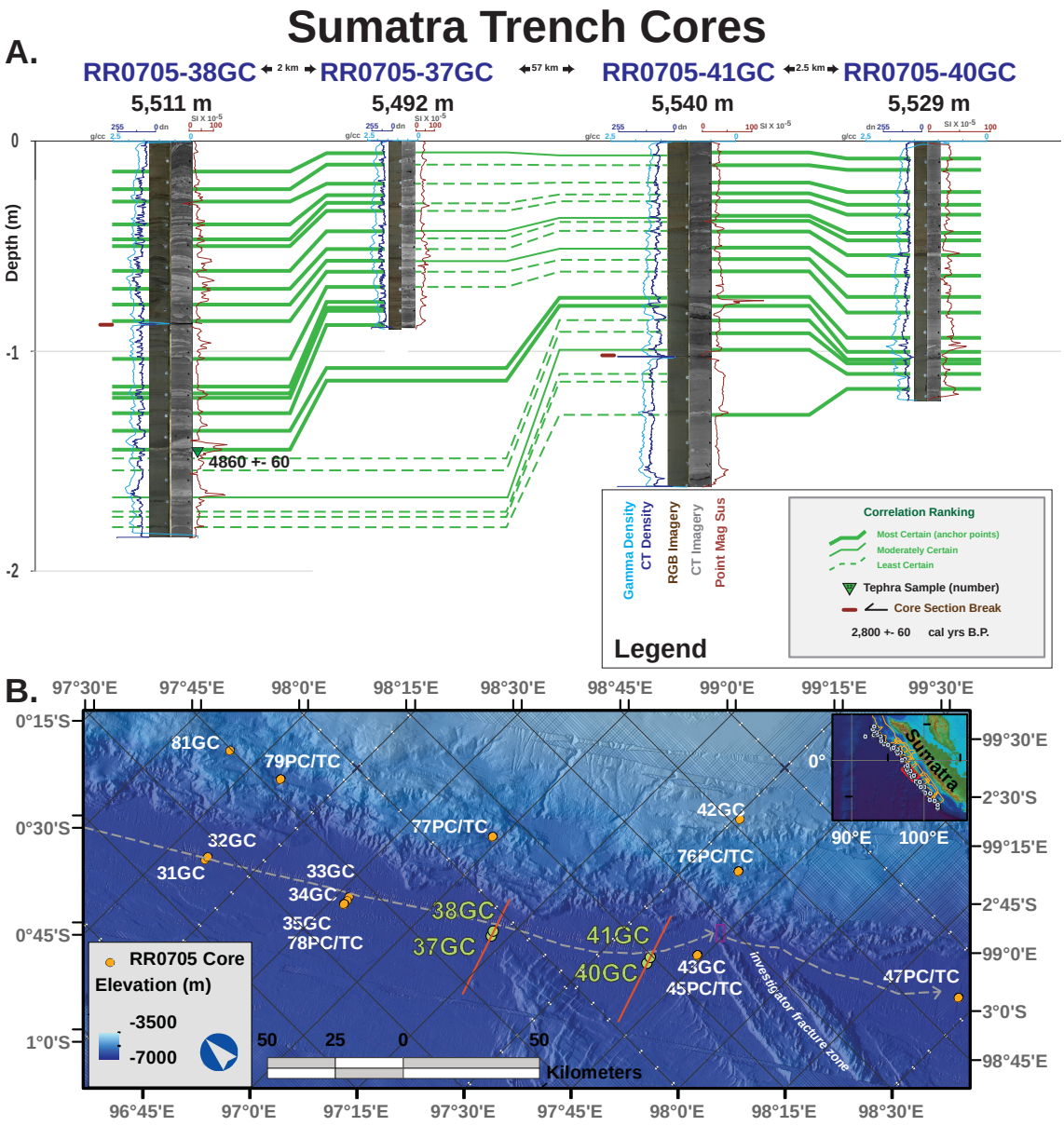

Figure 3-10. Sumatra trench cores RR0705-38GC, RR0705-37GC, RR0705-41GC, and RR0705-40GC (**Figure 3-3**). **A.** Correlation of these cores is shown with green tie lines and core data are plotted with the same configuration as **Figure 3-2.** The radiocarbon age is from hemipelagic sediment underlying the correlated tephra in core 79PC and reported with 95% error (Salisbury et al., 2012; **Supplemental Table 1**). **B.** Core location map with cores plotted as orange circles over multibeam bathymetry, cores 37, 38, 40, and 41 in green (Ladage et al., 2006). Inset map shows location of large map in red (central margin). Dashed grey line shows general trench axis as a potential flow pathway. Purple rectangle shows where the IFZ intersects the trench to isolate these basins (flow pathway barrier). **C.** Elevation is plotted versus distance along a strike line aligned to core pairs. Core locations are labeled in green. Profile locations are plotted as red lines

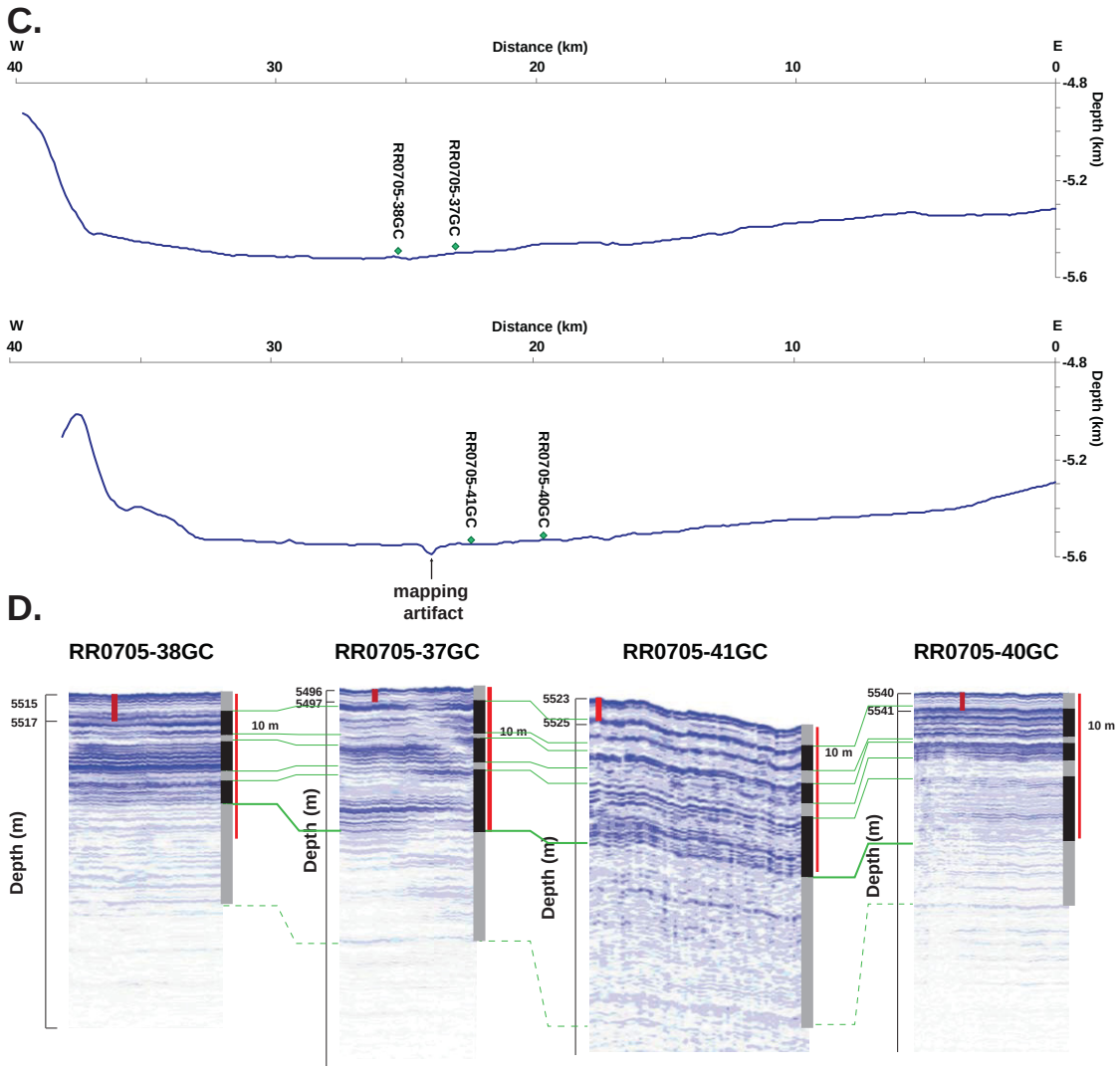

Figure 3-10 (Continued).

in **Figure 3-10 B. D.** 3.5 kHz CHIRP seismic data collected at core sites are processed in SioSeis and plotted in SeiSee (seismic envelope). Core locations are designated by a red line scaled to core length. Horizontal extent of seismic data are unresolvable at the scale in **Figure 3-10 A**. Seismic data for cores 37GC, 38GC, and 40GC were collected while the ship maintained position over the core location. Seismic data for core 41GC were collected while leaving the core site, so the horizontal scale is shown.

Table 3-1. Cores and their depositional settings.

Margin	Core Name	Core Setting	Site Geomorphology	Depth (m)	Latitude	Longitude
Sumatra	RR0705-108PC	Slope Basin	center of wide unconfined valley	2959	4° 39.58' N	93° 08.6'E
Sumatra	RR0705-104PC	Slope Basin	base of slope	3477	3° 52.3' N	93° 28.5'E
Sumatra	RR0705-103PC	Slope Basin	center of wide unconfined valley	3077	3° 36.3'N	93° 37.9'E
Sumatra	RR0705-96PC	Slope Basin	undrained basin	3399	2° 56.0'N	94° 08.4'E
Sumatra	RR0705-79PC	Slope Basin	undrained basin	3833	0° 50.8'S	97° 47.6'E
Sumatra	RR0705-03PC	Trench	trench axis	4443	4° 32.2'N	92° 56.0'E
Sumatra	RR0705-05PC	Trench	trench axis	4480	4° 28.8'n	92° 55.6'E
Sumatra	RR0705-107PC	Trench	above trench floor	4518	4° 19.6'N	92° 55.1'E
Sumatra	RR0705-105PC	Trench	near trench axis	4486	4° 04.7'N	93° 10.9'E
Sumatra	RR0705-38GC	Trench	trench axis	5524	1° 41.9'S	97° 56.3'E
Sumatra	RR0705-37GC	Trench	above trench floor	5497	1° 42.4'S	97° 55.3'E
Sumatra	RR0705-41GC	Trench	trench axis	5620	2° 07.7'S	98° 14.6'E
Sumatra	RR0705-40GC	Trench	above trench floor	5530	2° 08.1'S	98° 13.3'E
Sumatra	RR0705-55PC	Trench	near trench axis	6046	4° 31.2'S	100° 12.8'E
Sumatra	RR0705-57PC	Trench	near trench axis	6069	5° 26.4'S	100° 47.9'E
Cascadia	RR0207-01KC	Slope Basin	undrained basin, Hydrate Ridge West Basin	2110	44° 40.0'N	125° 17.1'W
Cascadia	RR0207-56PC	Slope Basin	undrained basin, Hydrate Ridge West Basin	2250	44° 38.6'N	125° 15.8'W
Cascadia	RR0207-02PC	Slope Basin	undrained basin, Hydrate Ridge West Basin	2311	44° 38.7'N	125° 15.0'W
Cascadia	M9907-12PC	Trench	Cascadia Channel	2658	46° 46.4'N	126° 04.9'W
Cascadia	M9907-23PC	Trench	Cascadia Channel	3211	44° 09.6'N	127° 11.5'W
Cascadia	TN0909-01JC	Trench	Cascadia Channel	3089	42° 26.3'N	125° 16.6'W
Cascadia	M9907-30PC	Trench	base of slope	3112	42° 25.2'N	125° 13.1W
Cascadia	M9907-31PC	Trench	base of slope	3107	42° 24.6'N	125° 12.0'W

3-2.3 Geophysical logging and Lithostratigraphic Correlation

Stratigraphic correlation using geophysical signatures representing vertical turbidite structure is a primary tool for testing individual deposits for their areal extent, a significant part of the criteria used to discriminate seismoturbidites from other possible types. Down-core geophysical properties are used as proxies for particle size, though this is specific to regional lithology and must be tested with detailed grain size measurements. We use laser diffraction particle size measurements (taken with a Beckman-Coulter LS 13 -320 laser counter, Blott and Pye, 2006) to justify this proxy. The form of the geophysical signature of each turbidite is referred to as its “fingerprint” (Goldfinger et al., 2012). Geophysical wiggle matching (fingerprinting: Goldfinger et al., 2007, 2012) of turbidites is based on the correlation of identifiable stratigraphic

characteristics using MSCL data (Fukuma, 1998). This correlation technique has been used to correlate stratigraphic units since the 1960's (Prell, 1986; Lovlie and Van Veen, 1995). In detail these "fingerprints" represent the time-history of deposition of the turbidite and have been shown to correlate between independent sites separated by large distances and depositional settings (Goldfinger et al., 2008, 2012 a). The detailed matching of records has been attributed to generation by the source-time function of the earthquake trigger (Abdeldayem et al., 2004; Karlin et al., 2004; St. Onge et al., 2004; Hagstrum et al., 2004; Goldfinger et al., 2003, 2008, 2012 a and b; Gràcia et al., 2010). The turbidite itself is commonly composed of single or multiple coarse fraction fining upward units termed "pulses". The rarity of a fine tail (Bouma Td and Te) or subsequent hemipelagic sediment between pulses indicates there is commonly little or no temporal separation between units. The lack of temporal separation of the pulses in Cascadia has been inferred to represent deposition over minutes to hours, and thus most likely represent sub-units of a single turbidite (Goldfinger et al., 2012 b).

3-2.4 Age Control

Radiocarbon ages provide an important test to our correlations and there can be some exceptions (detailed methods are in **Document S 3-1**). Sumatra trench cores are deeper than the CCD, so they do not contain calcareous material sufficient for ^{14}C age control. For this reason, correlations between these and other cores do not have an age test for the fingerprint correlation. Radiocarbon discussion for the Cascadia cores is in Goldfinger et al. (2012 a).

The laboratory radiocarbon ages are reported in years before present (BP, measured from 1950) with a two standard deviation lab error (Stuiver et al, 1998). ^{14}C ages are calibrated (Stuiver and Braziunes, 1993) and, for Sumatra ages, a marine reservoir correction of 16±11 years is made using the INTCAL09 database (Reimer et al., 2009). Only two delta R values are available for the Sumatra area, and while constraints are few on this correction, we here are correlating marine sites to other nearby marine sites, thus the local correlations are valid while absolute ages may contain additional uncertainty (see Goldfinger et al., 2012 a for the reservoir correction information for the Cascadia cores). One additional correction we make to the calibrated age is the sediment gap thickness correction (thickness of sediment between the turbidite and the sample). For individual ages, we propagate these uncertainties using RMS (root mean square) calculations using estimates of the uncertainties at each step. This calculation includes

the lab uncertainties and results in the final reported 95% range for each radiocarbon age. No lab multipliers were applied to the data.

In order to evaluate the timing of the possible 2004 turbidite with radiometric techniques, we collected sediment samples below the turbidite at 1 cm spacing. ^{210}Pb and ^{137}Cs isotopic analyses can provide information about the depositional history of the last ~150 years (Noller, 2000). Samples were analyzed using methods developed by Guillaume St. Onge at Institut des sciences de la mer de Rimouski.

3-3. Results

Here we first discuss selected core sites and then compare piggyback basin records of seismoturbidites from Sumatra and Cascadia. We then similarly compare core sites in channels with base of slope apron fans from the trenches of both Sumatra and Cascadia. Slope basin and trench settings provide different forcing factors, so we also used this distinction in the organization of our paper. Slope basins are generally more proximal to their source, but not always, depending upon the setting. Trench cores tend to be more distal (in the trench where there are channels) or proximal (in the trench where there are no channels). Core suffixes are as follows: piston cores (PC), jumbo cores (JC), trigger cores (TC), gravity cores (GC), Kasten cores (KC), box cores (BC), and multi cores (MC). Piston coring includes both the PC or JC (depending on how the cruise scientists label them, technically they are the same, PC is our preference) and the TC, so they generally come in pairs.

3-3.1 Slope Basin Systems

3-3.1.1. Sumatra: Basins

Core 104PC/TC is located in a northwest striking, 2-3 km wide, ~40 km long basin formed on the landward side of a landward vergent fold in the Aceh Segment (Kopp et al, 2008). The basin is filled with locally derived sediment sourced from the surrounding anticlinal folds. Sediment sources on the eastern flank of the basin are steep at a ~10° slope. Core 103PC/TC is located in a similarly formed basin, though the bounding folds are more disrupted by erosional systems with more complex geomorphology. This basin is not linearly shaped like the 104PC/TC basin and the core is located in the center of a 3 km wide basin floor. Core 96PC/TC is located in a ~3km wide, ~35km long, northwest striking basin also formed on the eastern flank of a landward vergent fold.

The lithostratigraphy of the northern Sumatra slope cores is dominated by coarse grained Ta-Te turbidites (Bouma, 1962) and fine grained turbidites (Bouma, 1962; Stow and Piper, 1984) interbedded with massive hemipelagic mud and less common tephras. Bioturbation is common and core-induced deformation is observed in some cores. Turbidites are composed of coarse silt to coarse sand bases, with fining upward sand and silt to clay sub-units, with the addition of abundant forams in slope cores (all of which are above the ~ 4,200 m deep CCD). The coarse fraction is composed of mica and quartz grains with rare mafics, consistent with the well-known and mature Himalayan source of the accreting Bengal and Nicobar fans (Stow et al, 1990). Some slope core basal turbidite sub-units are foraminiferal hash. Sand sub-units commonly range in thickness from 0.5 to ~20 cm and are laminated and cross bedded, commonly underlying massive sand units. Rare thicker sand sub-units range from ~50 to ~100 cm thick. Finer material is composed of silt to clay sized particles. 0.5- to 10.5-cm thick primary tephras are rare and can be correlated between sites using electron microprobe and laser ablation Inductively Coupled Plasma Mass Spectrometer (ICPMS) data (Salisbury et al., 2012) , in the Siberut segment (Kopp et al., 2006).

Figs. 3-5 and 3-6 show core, CHIRP seismic, and bathymetric data for cores 104PC/TC, 103PC/TC, and 96PC/TC. Cores 104, 103, and 96 are in sedimentologically isolated basins within 350 km of each other. The light-grey sand bases of turbidites are easily identified and MSCL magnetic and density maxima correlate well with the CT density maxima and grain size peaks. CT data permit a refined view of the detailed structure of the turbidites and the effects of core disturbance and basal erosion. Gamma and magnetic data reflect signals that average the effects of core disturbance as measurements are made at regular intervals, with measurement volumes perpendicular to the core length. Deformed sediment may no longer have horizontally layered strata (commonly concave downward, when the edges of the core are dragged down by the core liner during coring, Skinner and McCave, 2003). Particle size measurements, plotted in green (**Fig. 3-6 a**) show a good correspondence to the MSCL data, supporting the use of them as proxies for grain size. Overall (total) sedimentation rates for these cores range from 52 cm/ka for 103PC, to 97 cm/ka for core 104PC, to 284 cm/ka for 96PC/TC. We correlate these strata using integrated stratigraphic correlation techniques, including visual lithostratigraphic description (color, texture, and structure, etc.), Computed Tomography (CT) image analysis, and core log “wiggle matching” of MSCL geophysical data. We grade the certainty of our correlations with line-thickness and line-type (solid or dashed) in our figures. The correlations with higher certainty have thicker and solid tie lines.

3-3.1.2. Cascadia: Hydrate Ridge Basin West (HRBW)

Hydrate Ridge is a composite thrust ridge formed from seaward and landward vergent thrust faults (Johnson et al., 2005) within the lower slope of the Cascadia accretionary wedge on the central Oregon continental margin (**Fig. 3-7 C**). The basin flanked on the east and west by slope basins. The isolation of the western slope basin from any canyon or channel system sourced to the east indicates that sedimentation in the slope basin may only be local submarine slope failures of the surrounding bathymetric highs (Hydrate Ridge itself), also supported by the lack of transported Mazama ash in the basin (Goldfinger et al., 2012 a). The most likely sediment-transport pathway into the basin is a small submarine canyon that cuts into the western flank of northern Hydrate Ridge, which is on the eastern side of the basin (**Fig. 3-7 B**); however, several other smaller potential pathways exist from the east and from the north, as well as the broad steep open slopes of the western flank of Hydrate Ridge. These slopes are unconsolidated sandy turbidites uplifted by thrust faulting, and observed directly on Alvin dives 1898-1909 and 2043-2055 (L.D. Kulm, pers. comm.). Hydrate Ridge Basin West is isolated from all terrestrial and shallow water sediment sources, and thus provides an independent environment in which Cascadia turbidites have been recorded (Goldfinger et al., 2012 a).

The textural and mineralogical details of the turbidites in Cascadia Channel (Griggs, 1969), Astoria Fan (Carlson, 1967; Nelson, 1968; Carlson and Nelson, 1969; Nelson, 1976), and regionally (Duncan, 1968; Duncan and Kulm, 1970) are well described. Cascadia turbidites, like those in cores in HRBW, are characterized by upward fining sequences of sand, silt, and clay, with multiple amalgamated pulses, sharp bases, and upward fining of individual sand/silt pulses, when present. These deposits are turbidites (Bouma, 1962) exhibiting Ta-Te divisions, although rarely are all divisions present in a single deposit. Numbers of mud turbidites are observed, primarily along the southern Cascadia margin, and these commonly include further subdivisions of Piper (1978): laminated silt D, laminated mud E1, graded mud E2, and ungraded mud E3 (Goldfinger et al., this volume). The mud turbidites are distinguished from other fine deposits by their sharp bases, organized internal structure, and fining upward sequences. They are well-characterized using the schemes of Bouma (1962) and Piper (1978).

3-3.2. Trench and Abyssal Systems

3-3.2.1. Sumatra: Trench

Turbidity current pathways in the trench offshore Sumatra are sourced mostly from the local continental margin slope. The Sumatra outer slope lacks major canyon systems delivering large sediment loads, thus the numerous smaller canyons deliver much more modest loads to small fan aprons in the trench which have no unifying channel system. The SASZ trench channel systems that are evident are not longer than ~100 km, averaging 7 km.

While there are relict turbidity current channels on the incoming India-Australia plate, they are not found in the axis of the trench and probably do not capture sediment flows sourced from the present accretionary prism. For example, at the latitude of this study, the Box Channel of Moore et al. (1976) is instead located on the outer rise of the flexing India-Australia plate, flowing downslope towards the Ninetyeast Ridge. This is the only potentially active channel in the eastern Bengal Fan, as mapped by Bandopadhyay and Bandopadhyay (1999). Further south, normal faults in the incoming plate disrupt other channels that are older than the Box Channel. In contrast, channels in Cascadia are related to localized high sediment discharge during glacial periods when the shelf was narrow and fluvial systems were directly connected to submarine canyons, so channel systems are mostly relict Pleistocene systems in which modern turbidity currents flow (Nelson et al., 2009; exceptions discussed in Goldfinger et al., 2012).

Cores 03PC, 05PC, 107TC, and 105PC/TC are located near the axis of the trench in the northern margin offshore Sumatra (**Fig. 3-8**). These cores are fed by a channel leading from the base of the slope. The channel is formed as the result of recurrent slope failures from a landslide amphitheater on the western limb of the landward vergent second ridge at 4º 34’ north. This channel initially is ~ 1km wide and rapidly widens and loses definition in the trench. The channel is only resolvable in existing bathymetry near the base of this nearest source canyon. Upper slopes of the canyon are much steeper, approaching 5°. At the core sites, the channel follows the base of a partially buried, east facing, north-striking fault in the downgoing plate. Unlike more longer lived channel systems, like the Box Channel of Moore et al. (1976)or the Cascadia Channel (Nelson et al., 2000), the channel at the core sites does not appear to have a rectangular cross section to confine flow.

Cores 03PC/TC, 05PC/TC, 107TC, and 105PC/TC contain coarse sand and coarse silt turbidites, ranging in thickness from ~5 to ~30 cm. Seismic data show the turbidite (with basal depth of 95 cm in core 107TC) as acoustically opaque, labeled as a green arrow in **Fig. 3-8 E**. Using ages from correlated deposits in the slope core RR0705-108PC (**Document S 3-1**), overall sedimentation rates for these cores range from 53 cm/ka for 03PC and 05PC to 35 cm/ka for core 107TC. Ages plotted alongside 03PC come directly from the ages in core 108PC.

3-3.2.2. Cascadia: Cascadia Channel System

Cascadia has well developed canyons and slope channels that link slope basins with Pleistocene channels formed during sea-level low stands when connected to terrestrial sediment sources (Nelson et al., 2000). These canyons and slope channels in the north have lower channel gradients and form channel systems that traverse the abyssal plain draining towards the south. The southern margin lacks a Pleistocene glacial history so does not have large fans like in the north. Because of the lack of large fans filling the trench and the steeper slope angle of the seaward vergent prism, plunge pools and base of slope aprons dominate the base of slope environment of the southern margin (Nelson et al., 2000).

Juan de Fuca Canyon originates at the Juan de Fuca Strait and, to a lesser extent, likely receives input from coastal rivers in northern Washington. Juan de Fuca canyon has a low gradient and meanders through the growing anticlines of the broad continental slope (Goldfinger et al., 2012 a). Two branches of the Juan de Fuca Canyon exit the continental slope separately and join as a channel at the base of the slope off northern Washington at the head of the Nitinat Fan. Juan de Fuca Channel then bends to the southwest as part of the Nitinat Fan, which apparently has only one primary active Holocene distributary channel in the upper fan system. Core 12 PC/TC was collected in the main channel (**Figs. 3-3 and 3-9**).

Juan de Fuca and Willapa Channels (also comprising the input from Quillayute, Grays, and Quinault Canyons) meet on the southwestern part of Nitinat Fan to form Cascadia Channel. Cascadia deep-sea channel crosses Cascadia Basin, then enters the Blanco fracture zone (**Fig. 3-3**) and continues hundreds of kilometers into Tufts Abyssal Plain. This turbidity-current pathway traverses ~1,000 km of Cascadia Basin and has remained open throughout the late Quaternary up to the present (Nelson et al., 2009; Goldfinger

et al., 2012 a). The active pathway is verified by the occurrence of the youngest turbidite, with an age of 270 (360–180) cal yr B.P. likely corresponding to the A.D. 1700 Cascadia subduction zone earthquake in core 23 PC/TC, collected in Cascadia channel 30 km north of where the channel enters the Blanco fracture zone (**Figs. 3-3 and 3-9**).

Turbidites in core 12PC range in thickness from 5 to 25 cm and are well bioturbated, except for the coarsest and thickest turbidites. Turbidites in core 23PC range in thickness from 20 to 40 cm. These turbidites are generally less bioturbated, except in the units with finest particle size range. Stratal thickness in core 12PC is less than half of that in more distal core 23PC. The overall sedimentation rate for core 12PC is ~32 cm/ka, while the rate at core 23PC is ~84 cm/ka.

3-3.2.3. Sumatra: Trench

The slope offshore Sumatra reflects the lack of a glacial history in this region as there are no locally sourced large fan systems associated with slope sedimentary systems. Most slope canyons deliver sediment to base of slope apron fans in the compartmentalized trench. In some locations the frontal thrust is blocking margin slope sediment delivery directly to the trench (Ladage et al., 2006; Kopp et al., 2008) and fans are smaller with few resolvable fan channels. Once the sediment flows reach the base of the slope, they may be distributed southward within the trench segments based on the regional slope of the trench axis. Current flow in the trench has limited distribution due to blockage of the trench axis by subducting transverse fracture zones and unnamed ridges at -2.23° and -3.74° South.

Cores 38GC, 37GC, 41GC, and 40GC are located in the Siberut Segment (Kopp et al., 2008), in the trench axis, up-slope (up-trench) from the Investigator fracture zone (**Fig. 3-10**). Each pair is ~10 km from the base of the margin slope. While each core pair only spans a ~3 km trench-normal transect, the more proximal cores were collected near the axis of the trench and the other cores located up-slope, more distally on the outer trench wall. **Fig. 3-10** shows these cores with green tie-lines indicating our correlations in the figures. These correlations are made with the same methods described for all correlations in this paper, using lithologic descriptions and flattening stratigraphic horizons using the turbidite fingerprints based on core geophysical data. Trench normal topographic profiles were constructed using a 90 m bathymetric data set (**Fig. 3-10 B**).

All four cores, 38GC, 37GC, 41GC, and 40GC, contain silt and sandy turbidites interbedded with hemipelagic muds. 38GC and 41GC contain a tephra (demarcated with inverted green triangle **Fig. 3-10**) correlated with 7 other cores in the region using major and trace elemental analyses (Salisbury et al., 2012). Ages from RR0705-79PC provide a robust age for this tephra at 4,860 ± 60 calendar years Before Present (cal yrs BP; Stuiver and Polach, 1977), so the age from core 79PC is projected onto these cores (Salisbury et al., 2012; **Fig. 3-10**). Using the stratigraphic series and geophysical correlation, we further correlate this tephra and turbidites spanning over 280 km along the trench (**Fig. S 3-3**), including correlations across the IFZ to core RR0705-45PC and possibly to RR0705-47PC. Sedimentation rates in these cores ranges from 15 to 33 cm/ka.

3-3.2.4. Cascadia: Base of Slope Apron Fan (Rogue)

The southern Cascadia margin lacks the dominant Pleistocene regional fan systems, found in the north, in favor of base of slope apron fans. The steeper gradients of the slope channels in the south, due in part to the lack of fans that fill the trench, are responsible for the presence of base of slope apron fans and plunge pools (Nelson et al., 1986, 2000). We examine the base of slope apron cores at the base of Rogue Canyon, cores 01JC, 30PC, and 31PC.

These three cores were collected at the base of the canyon where there is a small (10 km wide, 50 m thick) base of slope apron fan. The cores are positioned beyond the edge of the fan on the ~flat trench floor. **Fig. S 3-2** shows these core data and the seismic profile compiled and processed in SioSeis. There is very little variation (not more than ~5-10%) in stratal thickness between these cores. Seismic facies thicknesses also do not vary though a slight thickening in the distal direction can be seen. This thickening is possibly due to bypassing of proximal cores due to a hydraulic jump at the base of the slope (Goldfinger et al., 2012 b). Coarse and fine grained turbidites range in thickness from 15 to 50 cm, with an overall sedimentation rate of ~67 cm/ka.

3-4. Discussion

Here we discuss how sedimentation varies between sites, and how physical factors may influence turbidite sedimentation in the Sumatra and Cascadia systems in piggyback slope basins and trench settings. While earthquake triggering is not the principle focus of this paper, we use our correlations as a stratigraphic framework with which to discuss the variations in stratigraphy. Correlations for seismoturbidites, based on

geophysical fingerprinting and lithostratigraphic interpretations, are shown as green lines in the figures. The stratigraphic sequences and individual units with the most unique geophysical "fingerprints" (Goldfinger et al., 2007; 2008; 2012 a) carry the strongest correlative weight and act as "anchor points" for these correlations (**Fig. 3-5**). The correlations between anchor points vary in quality and rely more heavily on the similarity of stratigraphic sequences. These correlations are important as they allow us to make comparisons between coeval deposits in different cores.

3-4.1 Sumatra Systems

In Sumatra, the geologic setting contributes in several ways to localize sedimentation in the slope basins and in the trench. All but two basin core sites (cores 85PC/TC and 92PC/TC; **Fig. S 3-3**) from cruise RR0705 are isolated from sedimentation transported from shallower and terrestrial sources, reducing the susceptibility to processes other than earthquakes (Goldfinger et al., 2012 a). These other settings are more susceptible to other triggering processes because they are either shallower or near terrigenous sources, where those other trigger processes take place (storm and tsunami wave base liquefaction, storm wave resuspension, or hyperpycnal flow from flooding). The uniqueness of each deposit in a core and the similarity of a deposit from one core to the next, combined with the isolation of the sites from terrestrial sources and from one another, argue for a common trigger that leaves a record of each event in every core. However, given the relatively smaller (150 to 1,500 km^2) and more proximal source areas compared to trench sites, site factors could contribute more significantly to the turbidite structure in slope cores. During glacial low stands, only cores in the region of Nias and Siberut islands, which were larger in area, would likely have been influenced by the increase in subaerial exposure in their source drainages. Other core locations remained isolated from terrestrial sources due to the forearc basins and deep water catchments.

Core 104PC/TC is located on a sill at the edge of a partially enclosed basin. At 10 m above the surrounding basin, this low sill probably does not significantly restrict flow from the basin into the adjacent canyon system to the southeast. This core pair is also located at the base of high relief canyons (see profile **Fig. 3-5**) and distanced 250 m horizontally from a steep 1.5 km high cliff, where the upper slopes of the canyons approach 10°. Core 104 is thus proximal to very steep slopes, more so than other core sites. Core 104 has turbidites that characteristically have multiple (10-30) laminated (<1 cm) silt or sand sub-units (e.g. core depth 175-205 cm). We interpret the

numerous small pulses within a single apparently correlative turbidite to be the result of retrogressive failure of the nearby upper canyon slopes. The “stacked” turbidite structure of thin units in this core is unique to this site as compared to interpreted correlative units at other sites. This is analogous to the turbidity currents that responded to retrogressive failures triggered by the 1929 Grand Banks earthquake (Piper and Normark, 2009).

In comparison, core 103PC/TC (**Fig. 3-5**), only 35 km to the southeast of core 104, is located in the center of a 2 km wide, ~0.5° sloped, flat canyon valley. This core records a similar sequence of seismoturbidites as core 104 but also shows that the site conditions exert a secondary control on sedimentation. Upper canyons with slopes of 5-8° feed this wide valley, but no channel system is resolvable given existing bathymetric data (50 m resolution). Core 103 has thin bedded (5-10 cm thick) sandy and silty turbidites. We interpret these to have been the result of turbidity current flows that are unconfined across the wide valley. This core location is more distal with respect to steep source areas than 104 and apparently does not receive the retrogressive failures during each event that apparently occur on the steeper slopes above the site of core 104.

While turbidites in the cores discussed in this section likely have primary structures related to the earthquake source that accounts for primary depositional structure we are correlating (Goldfinger et al., 2008; 2012 a), their structures also have site-related forcing. While the stratigraphic sequences correlate well overall, more local variability is apparent than in the Cascadia cores. This may be because, since the CCD was shallower than the trench in Sumatra causing us to core more along the slope, Sumatra cores were in more proximal positions. Variability due to basal erosion, heterogeneous source areas within the region, and site geomorphology would be expected at such proximal sites, regardless of the triggering mechanism.

We collected core 96PC/TC in a northwest striking, ~2° sloped 3 km wide basin that may drain over a 50 m tall sill to the southeast. The basin has several basin crossing sills with elevations of 10-20 m and, based on our multibeam bathymetric interpretations, are the result of mass transport deposits sourced from the local slope to the east. These sills form small sub-basins within the larger basin. This core pair has the most expanded Holocene section of all slope basin cores collected for this study (**Figs. 3-2 and 3-6**). Three size classes comprise the multi-pulse silt to sandy turbidite sequences at this site. Sand-silt turbidites 20-30 cm thick with 3-4 pulses are interbedded with thinner, 5-10 cm

thick, multi-pulse turbidites. The thinner turbidites are more bioturbated, as in most of our cores offshore Sumatra. The thickest turbidite in core 96 is ~3.5 m thick, compared to less than a meter at all other core sites from the 2007 cruise. This expanded section we here interpret to be the result of ponding in the effectively undrained sub-basin.

We provide a figure that shows our lithologic logs plotted alongside the other core data, including a plot designating hemipelagites from turbidites (**Fig. S 3-4**).We plot particle size for the uppermost turbidite in 96PC using a C/M plot (Passega, 1957, 1964). C/M plots are based on comparison C, the one percentile (d 99), with M, the median grain size and can be used to infer the mode of transport and deposition (Shiki et al, 2000). 96PC C/M data are consistent with turbidites elsewhere (Passega, 1957, 1964; Shiki et al. 2000). ^{210}Pb decay per minute data are also plotted for the sediments underlying the uppermost turbidite and show an exponential decay, supporting the recency of the overlying turbidite.

We interpret that the uppermost turbidite in cores 105, 104, and 96 is most likely the 2004 turbidite. The lack of hemipelagic sediment overlying this turbidite, the lack of consolidation when compared to older strata, its great thickness (over 3 m) at one site, and excess ^{210}Pb the sediments underlying the uppermost turbidite showing an exponential decay are consistent with this interpretation. Also consistent with this interpretation is the radiocarbon age of the underlying sediment of 30 +-30 cal. Yrs. B.P. (**Document S 3-1**). In addition, the MSCL maxima correlate generally with seismologic observation maxima, providing the link to the recently historical earthquake (**Fig. 3-6**). There are mapped many accretionary prism faults (e.g. Graindorge et al, 2008) that are possible earthquake trigger sources. The megathrust remains as the single source that extends between all these core sites, so deposits that are correlated over these large distances are unlikely to be sourced from rupture on these shorter accretionary prism faults. Uncorrelated turbidites may be related to these smaller faults, but we do not have sufficient core spacing to de-confound those relations. The correlations in **Fig. 3-5 A** support the seismologic interpretation for these deposits because the stratigraphic units are correlated between cores at isolated sites across a broad region.

Cores 03PC and 05PC are closely spaced and have almost identical stratal thicknesses, but the more distal core pair 107PC/TC has thinner deposits. This more distal core pair was collected on the upthrown side of a normal fault. The fault controls the channel position, with a scarp ~25 meters above the channel. The thinner section in these cores

may be explained by the upslope position of core 107 where the turbidity currents lose energy flowing up slope, possibly similar to Barkley Canyon and Hydrate Ridge Basin West in Cascadia (Goldfinger et al., 2012 a).

Turbidites in these three cores are well correlated, spanning a distance of 28.5 km (**Fig. 3-8**). Green tie-lines show the correlations and the relative confidence we have in them. We cannot test our correlations with ^{14}C age control due to the lack of datable material at trench depths, although because of our confidence in the stratigraphic correlations to nearby basin sites, we use the ages from correlated units in core 108PC to label the correlated units in core 05PC (**Document S 3-1**). Core 107PC has coring artifacts, therefore we use core 107TC for comparison.

Cores 37GC and 38GC are located on the western side of the trench axis, near the mouth of a slope canyon that dissects several slope basins, collecting sediment discharge sourced from these basins as the flows transport down slope (**Fig. 3-10 B**). In addition, the most trenchward fold has multiple landslide amphitheaters immediately adjacent to the cores, which may further contribute to turbidity currents that reach these cores. In contrast cores 40GC and 41GC, also west of the trench axis, are located adjacent to a slope that has an incipient frontal thrust anticline. This anticline may attenuate turbidity currents sourced to the east as they flow upslope over the fold axis (**Fig. 3-10 B**). Both trench pairs are on transects normal to the margin.

For cores 37GC (distal and uphill) and 38GC, both stratal thickness and seismic facies depth show a thinning of turbidite deposits in the distal and uphill direction (similar to cores 03PC, 05PC, and 107TC). In contrast, cores 40GC (distal and uphill) and 41GC show a ~10° stratal thickening in the distal and upslope direction. Core 40GC is a 6.7 cm diameter “Benthos” gravity core, while core 41GC is a 10.1 cm diameter gravity core. The friction exerted upon layers of sediment (let us call them “soil elements,” Skinner and McCave, 2003) is a combination of the shear strength of the sediment and the skin-friction between the soil element and the core barrel (Skinner and McCave, 2003). For a soil element of unit thickness, the jumbo gravity core has 50% more surface area and a proportional more friction. As more soil is cored, the additional soil elements contribute to the downward force and contribute to a cumulative vertical stress, reducing sediment compaction at the base of the core (Skinner and McCave, 2003). Yet 41GC is compressed and 38GC is expanded. Other factors that affect how sediment is cored include the smearing of sediments along the core-sediment interface and the transfer of pore

pressure transfer of friction directly to the core base. It is possible that there was an hydraulic jump at the base of the slope, causing bypassing at the proximal site and thickening at the distal site (Piper and Normark, 2009; Goldfinger et al., 2012 b)). Any of these factors can explain the difference in stratal thickness between these cores. In addition, the inter-core spacing for each of these two core pairs may be too small to explain the variation in stratal thickness alone, based on source proximity.

3-4.2 Cascadia Systems

In Cascadia isolation from terrestrial sedimentation is also important for studying seismoturbidites. The shelf width, as it relates to glacial cycle sea-level fluctuation, provides a control to this suitability. During low stands, narrow shelf widths allowed connections between river mouths and their respective canyon heads. During high stands, most sites are isolated from direct terrestrial input because the shelf is wider and much of the sediment is captured and swept northward along the shelf by the north flowing winter Davidson Current (Sternberg, 1996). Because of this relation, the turbidite frequency is higher during glacial periods. The modern shelf near the Eel River is amongst the narrowest in Cascadia and turbidite frequency in these Eel Canyon cores is the highest of the entire margin, similar to low-stand times (~70 year recurrence interval, given 54 turbidites in 3,800 years; Goldfinger et al., 2012 a). This may be due to increased seismicity (including tectonic sources in addition to the subduction zone) or to direct terrestrial input. The overall sedimentation rate is also higher in the region of Eel Canyon when compared to cores more northward; Rogue cores span 12,000 years in eight meters and Eel cores span only 3,500 years in 4.5 meters (67 cm/ka vs. 128 cm/ka respectively; Goldfinger et al., 2012 a).

The Holocene stratigraphic record of slope failures preserved as turbidites in the slope basin west of Hydrate Ridge, was studied at three core sites west of the submarine canyon cut into the western flank of Hydrate Ridge (Goldfinger et al., 2008, 2012 a; **Fig. 3-7**). Cascadia cores 56PC/TC, 02PC/TC, and 01KC are all in the same basin and are within 4 km of each other. All Hydrate Ridge cores contain a relatively high silt content that is disseminated throughout even the hemipelagic units, making the distinction of mud-silt turbidites somewhat more difficult. We attribute this to the steep, sandy-silty cliffs exposed immediately to the east where seaward vergent thrust faulting uplifts Hydrate Ridge itself. We suggest these non-cohesive cliffs input a steady rain of sandy-silty

material to the proximal basin floor. A similar relation is observed at proximal Sumatra sites.

Considering a cross-basin transect, the most proximal (furthest east) site to the steep cliff contains a late Holocene (~3,000 years BP to modern) record in piston and trigger core 02PC/TC. The mid-basin site to the west (56PC/TC) contains a complete Holocene record with its base at ~11,000 cal yr B.P. The distal Kasten core site (01KC) may contain a partial Holocene record; however, radiocarbon age control to confirm Holocene stratigraphy was not possible owing to the poor preservation of hemipelagic clay intervals. The only ages obtained from this core are at the base of the section and are late Pleistocene (**Fig. 3-7**). No Mazama ash is present in any of the Hydrate Ridge cores, confirming the isolation of the Hydrate Ridge site from fluvial sources. Core 56PC/TC shows among the best resolution of individual sand units within individual turbidites in existing Cascadia cores, most likely because of its proximal location. With little transport distance and time during transport for distinct inputs to mix following the initiating event, individual fining upward pulses remain more distinct (Goldfinger et al., 2007, 2012 a). Lithostratigraphic descriptions and correlation details are given in Goldfinger et al. (2012 a).

Given the robust correlations between cores 02PC/TC and 56PC/TC (**Fig. 3-7**), source proximity generally controls turbidite thickness (Nelson et al., 1986). The section in proximal core 02PC/TC is about twice the thickness of the equivalent section in core 56PC/TC. The compressed section of 01KC is further evidence of source proximity for control of sedimentation in Hydrate Ridge Basin West, likely exacerbated by the upslope position of the more distal core on the backlimb of the frontal thrust bounding the basin.

In Cascadia, turbidite channel systems help us in several ways. First, they provide the opportunity to sample different regions of the subduction zone. It is also only possible to use the confluence test of Adams (1990) with these linked channel systems. A downside of these channel systems is related to their ability to propagate turbidity currents. In some channel reaches, the channels are so efficient at promoting turbidity current flow that these reaches have evidence of turbidity current bypassing. Some Cascadia Channel cores, particularly just below the confluence with Willapa Channel, show these are areas of non-deposition (Griggs, 1968). Willapa Channel has bare Pleistocene clay at the surface, showing turbidity current bypass of 100%. A second example is lower Astoria Canyon that has gravel deposited in the thalweg and some bypassing of finer

fractions, making levee sites better for turbidite deposition (Goldfinger et al., 2003). This is analogous to the evidence of bypassing found in the sedimentary systems offshore the Grand Banks following the earthquake in 1929 (Piper and Normark, 2009).

The turbidites in cores 12PC/TC and 23PC/TC are well correlated, evidenced by the detailed multi-pulse turbidite structures seen in **Fig. 3-9 C**. 23PC/TC is 330 km downstream from 12PC/TC and the correlations show that channel systems promote the long distance conveyance of turbidity currents, even with a low gradient such as that found in the Cascadia Channel system (**Fig. 3-9**). The channel gradients immediately upstream of 12PC and 23PC are ~1°. This is reasonable given the flow velocity estimates of Griggs (1969) with 5.8 and 3.3 m/s in the upper and middle channels. That these turbidites share such detailed turbidite structure, when separated by 330 km, spanning reaches of non-deposition, strengthens the argument that the turbidity currents maintain the seismogenic signal for large distances.

The Rogue Apron site has a somewhat higher hemipelagic-sedimentation rate (Goldfinger et al., 2012 a, b) compared to the other Cascadia cores and is also a proximal site at the foot of a steep continental slope. Cores 31PC/TC, 30PC/TC, and 01JC/TC form an unequally spaced E-W 7 km transect. In contrast to HRBW cores, the sedimentary section in 01JC/TC, the most distal core, is expanded by ~5%. This small expansion may be due to real variations in deposition or to variations in coring results (e.g. incorrect scope cable length, Skinner and McCave, 2003). One sedimentologic explanation would be that there was a hydraulic jump at the base of the slope, causing proximal cores to be bypassed leaving a thicker deposit at the distal core, similar to the sedimentary response to the morphology offshore the 1929 Grand Banks earthquake (Piper and Normark, 2009). Variations in scope cable length can also change the magnitude of stratigraphic section compaction or extension (caused by over or under pressure from the piston system, Skinner and McCave, 2003).

3-4.3. Cascadia and Sumatra, Similarities and Contrasts

We discussed the factors that contributed to sedimentation of seismoturbidites along the subduction zone settings offshore of Sumatra and Cascadia. Slope basin cores along both margins suggest that turbidity currents are not as well organized in these proximal sites as currents in more distal or channel settings. Channels serve to confine and control flow, as well as serve as filters that allow passage of larger events, filtering out

smaller ones, as well as amalgamating small complexities while apparently preserving significant elements of heterogeneity from the turbidity current. The evidence from more proximal cores is consistent with the preservation of greater inter-core variability in turbidite structure due mostly to the proximal setting. Similar observations have been made at the Hikurangi margin (Pouderoux et al., 2011), where cores MD-3002 and MD-3003 show how local processes strongly control depositional histories, as well as cores collected elsewhere (Summer et al, 2010).

The good stratigraphic correlation between Sumatra core sites isolated from each other, land sediment sources, and from other triggering mechanisms, coupled with compatible radiocarbon ages suggest that the most likely triggering mechanism is regional earthquakes. Uncorrelated events present at some sites may be due to random sediment failures or smaller local earthquakes. These uncorrelated turbidites are thin and have low mass with non-unique fingerprints, making it difficult to interpret their trigger origin.

The youngest turbidite in the northern Sumatra cores most likely triggered by the 26 December 2004 great SASZ Mw 9.1-9.3 earthquake. This event triggered turbidity currents in multiple submarine drainage systems that left stratigraphic evidence in the form of multi-pulse turbidites in isolated slope basin and trench depocenters. Radiocarbon and ^{210}Pb analyses support this conclusion.

The potential of basin sites was initially undervalued in Cascadia, when it was assumed that most turbidity currents of interest would be channelized flows. For this reason, basin sites in Cascadia are few. However during the Sumatra cruise, we were forced to core in slope basins for age control purposes due to the ~ 4,200 meter depth of the CCD; this depth was everywhere exceeded in the trench. Analysis of the Sumatra basin cores and the Hydrate Ridge Basin West cores subsequently revealed the importance of the record of turbidites in these basins, which are commonly quite isolated and thus provide a turbidite record free of terrestrial turbidite sources. In Sumatra all but two basin cores (85PC/TC and 92PC/TC) are completely isolated from terrestrial sources of sedimentation; these two cores are possibly influenced by canyon systems linked to the forearc islands of Siberut and Nias. Cascadia Hydrate Ridge Basin West cores were originally collected in the interest of investigating slope failures related to hydrate destabilization, but were demonstrated to instead record earthquakes (Johnson et al, 2005; Goldfinger et al., 2012 a). Other cores (e.g. M9907-10PC) collected in the slope of

Washington and Oregon did not have the high relief source area required to generate turbidity currents, as evidenced by the lack of turbidites in these cores (Mix, 2012, pers. comm.).

Turbidite sedimentary systems along the margins of Sumatra and Cascadia provide different forcing factors, controlling the spatial likelihood of preserving and later correlating turbidites. Sumatra's margin is compromised by the lack of channel systems in the trench/abyssal plain, making most sites proximal and limiting the spatial extent for any given turbidite deposit. This makes it more difficult to distinguish and correlate the stratigraphic sequences. Cascadia's channel systems and shallow depth (for radiocarbon data) contribute to our ability to correlate seismoturbidites because the channels tend to promote low-frequency components of the content of the current over longer distances and have multiple branches, sampling different regional source areas. These channel sites are excellent locations to develop a stratigraphic framework, where more proximal slope basins and base-of-slope apron fan settings result in a turbidite structure that is likely influenced by local physiography and other factors.

3-5 Conclusion

Based on correlation of similar sequences of individual turbidites between several depositional settings, earthquakes are a principal cause for turbidite deposition along slope and trench settings for the Cascadia and Sumatra-Andaman subduction zones during much or all of the Holocene. Source proximity, basin effects, turbidity current flow path, earthquake rupture patterns (both temporal and spatial), hydrodynamics, and topography all likely play roles in the construction of each turbidite as evidenced by the vertical structure of the final deposits.

Sedimentary systems in both Sumatra and Cascadia have been impacted by processes driven by climate and tectonics. These impacts from the Pleistocene are long lived and continue to have an effect on turbidity current flow paths. Basin records in Sumatra and Cascadia show that local topography has a dominant control on sedimentation, influencing overall section thickness, degree to which small local downslope movement will be recorded, the grain size profiles, and the recording fidelity of transport events. Very proximal sites in both settings appear to record much more detail, in some cases obscuring some components of the turbidite. Relatively more distal cores lose some detail but retain the main elements of seismoturbidites for significant distances down

channel (**Fig. 3-9 B**). “Distal” in this sense may be a matter of only a few km, as both Cascadia and Sumatra cores show strong sorting out of the chaotic proximal deposits into well-organized correlable deposits in distances as short as 1-3 km.

Cascadia’s margin is dominated by Pleistocene formed turbidity current channel pathways which promote turbidity current flows for large distances. Sumatra margin pathways do not inherit these sedimentary systems, so turbidity currents are more localized. The Sumatra margin lacks a locally sourced supply of sediment, thus there are no large fan systems affecting turbidity current transport in the trench. Bengal/ Nicobar fan sediments extend from the shelf in the northern Bay of Bengal to at least the southern tip of Sumatra, but have not been active since the late Pleistocene (Moore et al., 1976; Weber et al., 2003). Holocene hemipelagic sedimentation rates are lower in this equatorial location (des Combes et al., 1999; Kahru et al, 2010), further contributing to the lack of large fans and sediment sources for sheet flow turbidites sourced on the slope. In Cascadia the regional draping of abyssal plain sedimentation on the incoming plate is sourced locally. In Sumatra, this sedimentation was originally sourced in the Himalayas to the North and is now sourced locally through recycling of accreted material in the accretionary prism. Because Bengal Fan sedimentation processes are no longer active in the Sumatra trench (Weber et al., 2003), the channel systems on the incoming plate are relict systems and disrupted by reactivated normal faults in the downgoing plate. The lack of trench axial channels (channels in the axis of the trench) retards the propagation of turbidity currents down trench, indicated by the strong relation between particle size and point sediment sources of the turbidity currents in the Sumatra trench.

The presence or absence of turbidite channel systems exerts a first order control on sedimentation in the trench in these two sedimentary systems. The absence of long trench-parallel channel systems in Sumatra is due to interruption by subducting features and a low sedimentation rate since at least the Pleistocene. These two factors appear to limit turbidity current transport in the trench. Cascadia basin has some channel systems, but also does not have a trench parallel transport system for a different reason; the trench is filled with the large Astoria and Nitinat fans and instead has channels that trend away from the major fan systems, out into Cascadia basin for long distances. Sites in the southern CSZ where there are no large fans tend to be small aprons or plunge pools, more like the Sumatra trench. In Sumatra the proximity to localized source areas generally controls the thickness and coarseness of turbidite deposits. In Cascadia,

the cores and the 3.5 kHz seismic data suggest that sheet flow mass wasting is more common, accounting for greater consistency of the deposits.

Channel configuration controls the distance that turbidity currents can travel in Sumatra and Cascadia. Formed during low stands with high sediment discharge, Juan de Fuca and Cascadia Channel systems have rectangular cross sections which may tend to promote high flow velocities that maintain flows throughout this study area. In contrast, channel systems in Sumatra are limited in length or not detectable, so the down-trench flow propagation of coarse grained turbidity currents appears to be quite short. Turbidites in Cascadia show that both point source and sheet sources contribute to the sedimentary record in the trench (see also Goldfinger et al., 2012 b). Somewhat in contrast, turbidites in Sumatra suggest that point sources are more important with respect to the aerial distribution of turbidity currents.

Consistent reproduction of similar structure across depositional settings in both margins reinforces the need for a common source mechanism to explain the observed correlations. The best explanation of the observed consistency is an earthquake source. Both Cascadia and Sumatra turbidites show evidence of strong local influences on turbidite structure that are consistent with proximity to and type of locally sourced sediment failures. Variability is higher in proximal settings, but so also is the fidelity of recording details of the turbidity current. We interpret the effects to be superimposed on the initial longitudinal flow structure of the turbidity current, allowing observation of the influences of both the initial structure and the local modifications to each resulting turbidite. Long channel systems, more prevalent in Cascadia, tend to promote low-frequency components of the content of the current over longer distances with some loss of detail with distance.

Acknowledgements This research was funded by the Ocean Sciences and Earth Sciences Divisions of the National Science Foundation. We thank M. Erhardt, Amy M. Garrett, and Robert H. Porter. for conducting lab analyses; NOC, IFREMER, and BGR for providing key bathymetry and sub-bottom data; UTM, for providing science crew; NOC for providing Russ Wynn; BGR for providing Stefan Ladage; and AIST/GSJ for providing Ken Ikehara. We also thank coring technicians from OSU including Chris Moser, Bob Wilson, Paul Wolscak. Scripps Resident Technicians, the R/V/ Roger Revelle Captain Tom Djardins and crew, and student volunteers and faculty from OSU including Bart DeBaere and Maureen Davies. Further details regarding the cruise and the core locations, please refer to the cruise report here:
http://www.activetectonics.coas.oregonstate.edu/sumatra/report/index.html

Slope Stability: Factor of Safety along the Seismically Active Continental Slope Offshore Sumatra

Jason R. Patton[1], Chris Goldfinger[1], Yusuf Djadjadihardja[2], and Udrekh[2]

1. College of Oceanic and Atmospheric Sciences, Oregon State University, Corvallis, OR 97331 USA. 2. Bandan Penghajian Dan Penerapan Teknologi BPPT 2nd Building, 19th Floor, Jl.MH. Thamrin 8, Jakarta, 10340 Indonesia.

Chapter 4 Abstract

Recent papers have documented the probability that turbidites deposited along and downslope of subduction zone accretionary prisms are likely the result of strong ground shaking from earthquakes. Given the damaging nature of these earthquakes, along with the casualties from the associated tsunamis, the spatial and temporal patterns of these earthquakes can inform us about how subduction zone faults be evaluated with paleo-seismic coring and seismic reflection methods. We evaluate slope stability for seafloor topography along the Sunda subduction offshore Sumatra, Indonesia. We use sediment material properties, from local (Sumatra) and analogous sites, to constrain our estimates of static slope stability Factor of Safety (FOS) analyses. We then use ground motion prediction equations to estimate ground motion intensity (Arias Intensity, AI) and acceleration (Peak Ground Acceleration, PGA), to constrain seismic loads for pseudostatic slope stability FOS analyses. The ground motions taper rapidly with distance from the fault plane, consistent with ground motion – fault distance relations measured during the 2011 Tohoku-Oki subduction zone earthquake. We determine the shaking threshold, at some locations upslope of our cores, using the Morgenstern method of slices probabilistic analysis for 2-D profiles. We also conduct Critical Acceleration (Ac) and Newmark Displacement (Dn) FOS analyses of multibeam bathymetry of the seafloor. In addition, we use estimates of ground motion modeled with a 2004 Sumatra-Andaman subduction zone (SASZ) earthquake fault slip model, to also compare with our static FOS analyses of seafloor topography. For slopes that contribute to core sites in the 2004 SASZ earthquake slip region, we compare the contribution of 2004 shaking intensities with shaking intensities from generic earthquakes of magnitude 6 through 9.

All slope and trench sites are statically stable (FOS < 1) and sensitive to ground motions generated by earthquakes of magnitude greater than 7. We conclude that for earth-

quakes of magnitude 6 to 9, PGA of 0.4-0.6 to 1.4-2.5 g would be expected, respectively, from existing GMPE's. However, saturation of accelerations in the accretionary wedge may limit actual accelerations to less than 1 g (Skarlatoudis and C. B. Papazacho, 2012; Stewart et al., 2013). Arias intensities of 0.4-1.7 to 7.9-33 m/s are estimated for the M = 6 and M = 9 events, respectively, are expected in the source regions of piggyback basins for local slope failures. Typical sites have mean Dn displacements of 0.1, 1.6, 7.7, and 16 cm for earthquakes of M = 6, 7, 8, and 9; suggested thresholds for displacement range between 5 and 10 cm. Thus the observed turbidite stratigraphy in the Sumatra piggyback basins can be explained by local ground motions during earthquakes with magnitude greater than ~7, given the static stability. Seismoturbidite paleoseismic data suggest a repeat time of 260 ± 160 years, possibly insufficient to destabilize slopes through sediment accumulation alone. Ground shaking along the continental slope offshore Sumatra is a function of distance to the fault ("Rdist") for generic earthquakes and for the 2004 SASZ earthquake. Landslide dimensions may relate to Mw and Rdist, but possibly dominated by site conditions. Estimates of ground motion depend upon the rate of attenuation with distance (i.e. the shape of the attenuation curve; PGA vs. AI).

4-1 Introduction

The Sumatra-Andaman subduction zone (SASZ) generates earthquakes of magnitudes up to ~9.2 historically in segmented ruptures, possibly controlled by variations in sediment thickness and crustal structures (Chhibber, H. 1934; Newcomb and McCann, 1987; Rivera et al., 2002; Abercrombie et al., 2003; Bilham, 2005; Natawidjaja et al., 2006; Konca et al., 2008; Sieh et al., 2008; Bothara, 2010; Kanamori et al., 2010; Meltzner et al., 2010, 2012; Malik et al., 2011; Philibosian et al., 2012). Paleoseismology can reveal the behavior of a fault through multiple earthquake cycles by using longer time spans than possible with historical and instrumental records (McCalpin, 1996; Goldfinger et al., 2012). Submarine (and sublacustrine) paleoseismology is benefitted because the sedimentary record, while it comprises secondary evidence for earthquakes (McCalpin, 2009), can commonly be well preserved for long time scales.

Strong ground shaking from earthquake rupture has been inferred to trigger turbidity currents that potentially leave a very long record of past earthquakes in the form of turbidites (Dallimore et al., 2005; Enkin et al., 2013; Goldfinger et al., 2003, 2008, 2012; Inouchi et al., 1996; Karlin et al., 2007; Noda 2008; Rajendran et al., 2008; Shiki 2000; Nakajima and Kanai, 2000; St-Onge et al., 2004, 2012). Initial assessment of the turbidite

stratigraphy and the paleoseismology of the Sunda subduction zone and an initial examination of styles of sediment transport have been presented in Patton et al., (2013 a b).

In this paper we evaluate slope stability along the submarine slopes on the accretionary prism offshore Sumatra, upslope of core sites selected for R/V Roger Revelle cruise RR0705/KNOX05RR in 2007 and used in the initial paleoseismic studies (Patton et al., 2013 a). We choose ground motion prediction equations (GMPE's) and apply our estimates of ground motion as seismic loads to our Factor of Safety (FOS) slope stability analyses and compare those results with static FOS analyses.

4-1.1 Physical Geography

The India-Australia plate subducts to the northeast at 38 to 57 mm/year relative to the Sunda plate, forming the SASZ in the northeast Indian Ocean (Subarya et al., 2006; **Fig. 4-1 A**). The historic earthquakes (Newcomb and McCann, 1977; Ortiz and Bilham, 2003; Sieh et al., 2006; Briggs et al., 2006; Natawidjaja et al, 2004; Chlieh et al., 2007, 2008; Konca et al., 2007, 2008; Meltzner et al, 2010, 2012; Philibosian et al., 2012) plotted in **Fig. 4-1 A** ruptured along this subduction zone fault, including the 2004 and 2005 SASZ earthquakes (Chlieh et al., 2007, 2008). Bengal and Nicobar fan deposits thin to the south, as evidenced in ETOPO elevation data (Smith and Sandwell, 1997). Bengal fan channels are ultimately sourced from the Himalayas (Moore et al., 1982) and formed as a response to climate forcing, particularly during glacial periods (Curray and Moore, 1971; Curray et al., 2003, Weber et al., 1997, 2003). Oceanic basement structures are generally buried north of 1° north and only partially buried south of that latitude. An exception is along the outer rise and trenchward of the outer rise, where these structures are reactivated. The outer rise, a convex-up region west of the trench, is the region of great earthquakes on 2012 April 11, magnitude 8.6 and 8.2 (McGuire and Beroza, 2012, Duputel et al., 2012; Wiseman and Bürgmann, 2012).

The continental slope along the accretionary prism offshore Sumatra has structural highs and piggyback basins that generally control sediment flow. Offshore Sumatra, the SASZ trench deepens from 4.5 km in the north to 6.5 km in the south (Moore et al., 1982; Patton et al., 2013 a), consistent with the deepening of the oceanic crust (Franke et al., 2008). Submarine landslides along the prism slopes are ubiquitous. Submarine seafloor slope angles range from ~0° to ~55°.

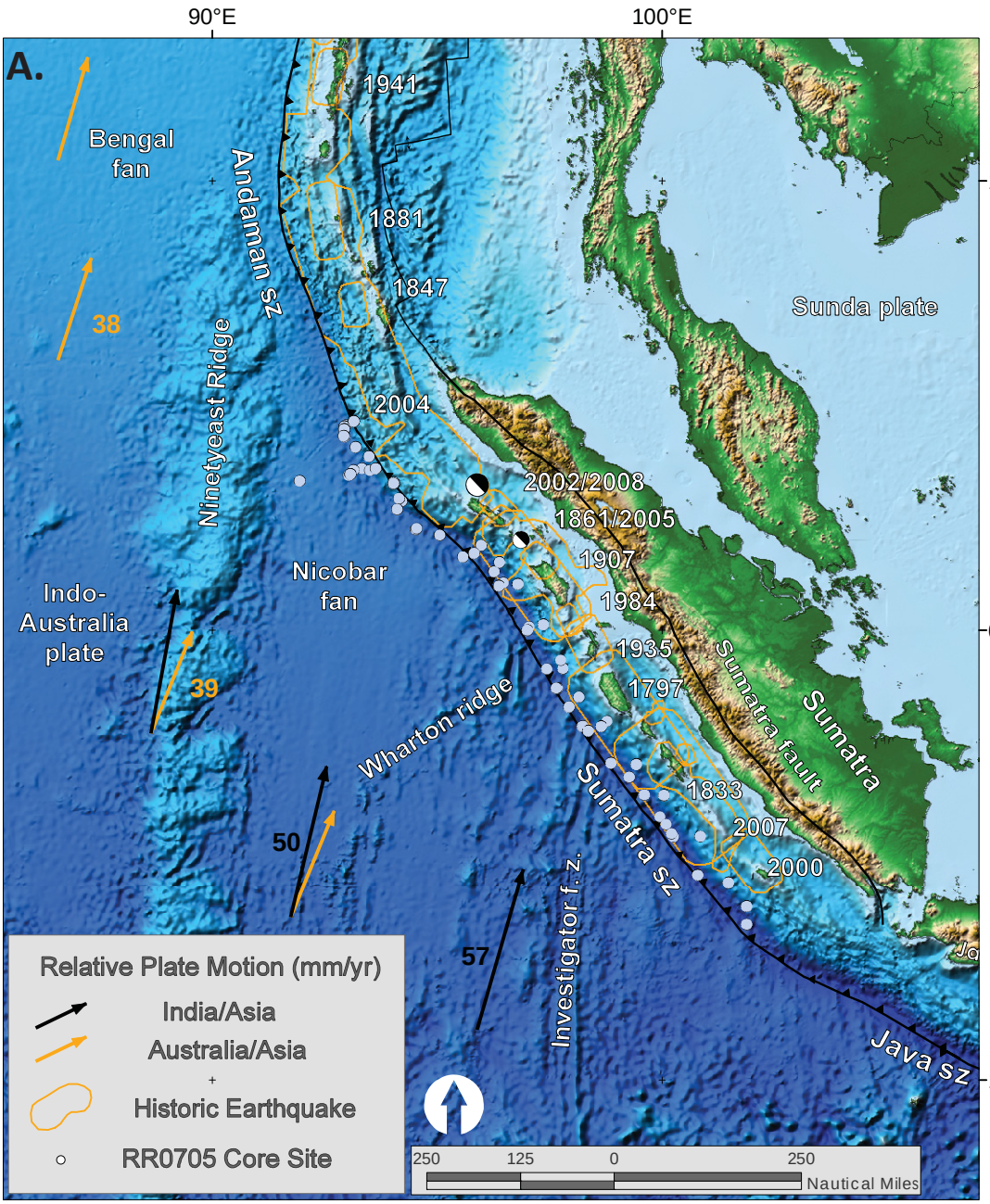

Figure 4-1. Sumatra core location and plate setting map with sedimentary and erosive systems figure. A. India-Australia plate subducts northeastwardly beneath the Sunda plate (part of Eurasia) at modern rates (GPS velocities are based on regional modeling of Bock et al, 2003 as plotted in Subarya et al., 2006). Historic earthquake ruptures (Bilham, 2005; Malik et al., 2011) are plotted in orange. Bengal and Nicobar fans cover structures of the India-Australia plate in the northern part of the map. RR0705 cores are plotted as light blue. SRTM bathymetry and topography is in shaded relief and colored vs. depth/ elevation (Smith and Sandwell, 1997). B. Schematic illustration of geomorphic elements of subduction zone trench and slope sedimentary settings. Submarine channels, submarine canyons, dune fields and sediment waves, abyssal plain, trench axis, plunge pool, apron fans, and apron fan channels are labeled here.

B.

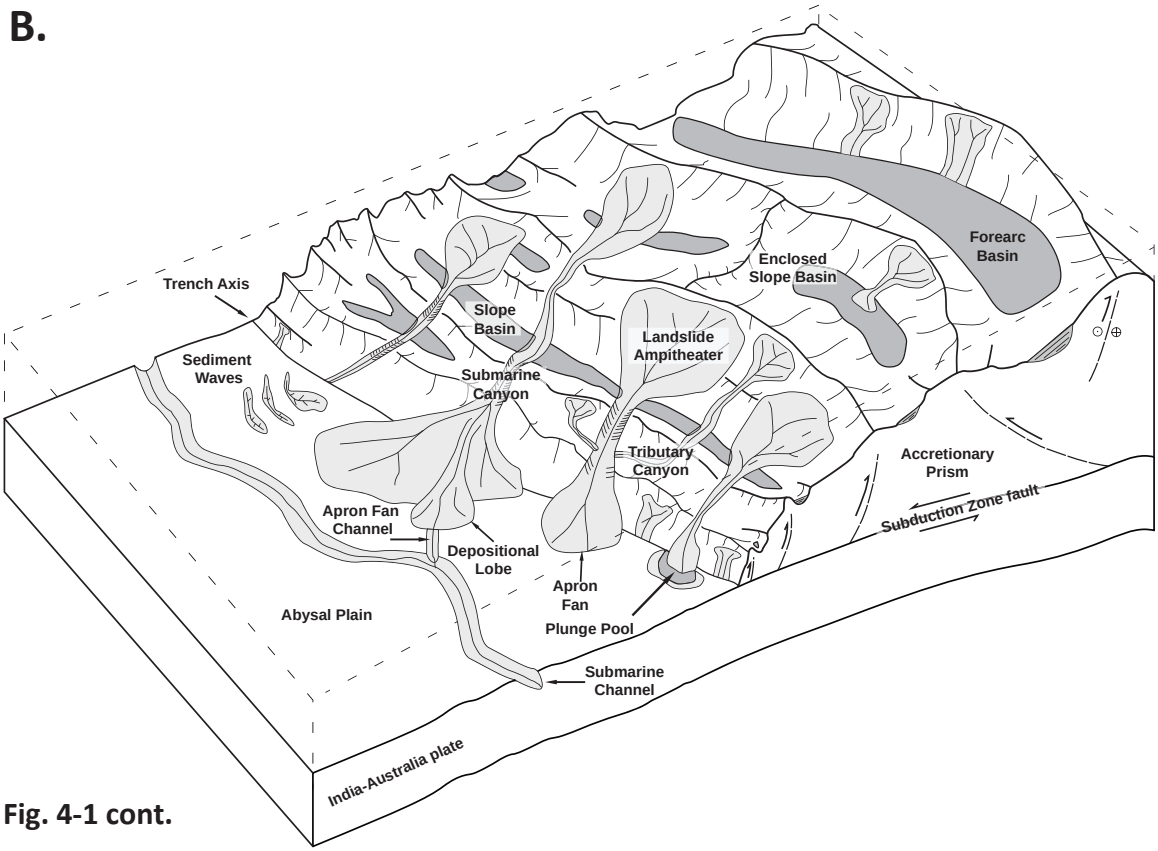

Fig. 4-1 cont.

There exist a wide range of erosive and sedimentary settings offshore Sumatra, where many of these geographical features are controlled by the geometry of the accretionary prism (Patton et al., 2013 a; **Fig. 4-1 B**). Submarine canyons cross the slope and may headwardly migrate through growing anticlinal folds, into up-slope basins, and branch intro tributary canyons. Many of these canyons are short and drainage catchments relatively small (few to tens of square kilometers), possibly because there are few pathways through the accretionary complex (Patton et al., 2013 a). Many slope basins do not drain to the trench and have an expanded Holocene sedimentary section. Submarine channels that form in the abyssal plain and may follow the trench axis (Carter, 1988) emanate from the mouths of submarine canyons and submarine landslide complexes at the base of the slope. These landslide complexes sometimes form amphitheater scallop shaped landforms, suggesting rotational failure. Some landslide scarps are also tabular shaped, suggesting translational failures. There are large (100's to 1,000's square meters) block failures that leave intact blocks deposited in the trench, though these are rare and ancient. Many head-scarps of these block failure landslides are east and downslope of the crests of anticlinal folds, suggesting they are older than the uplift age of those folds be-

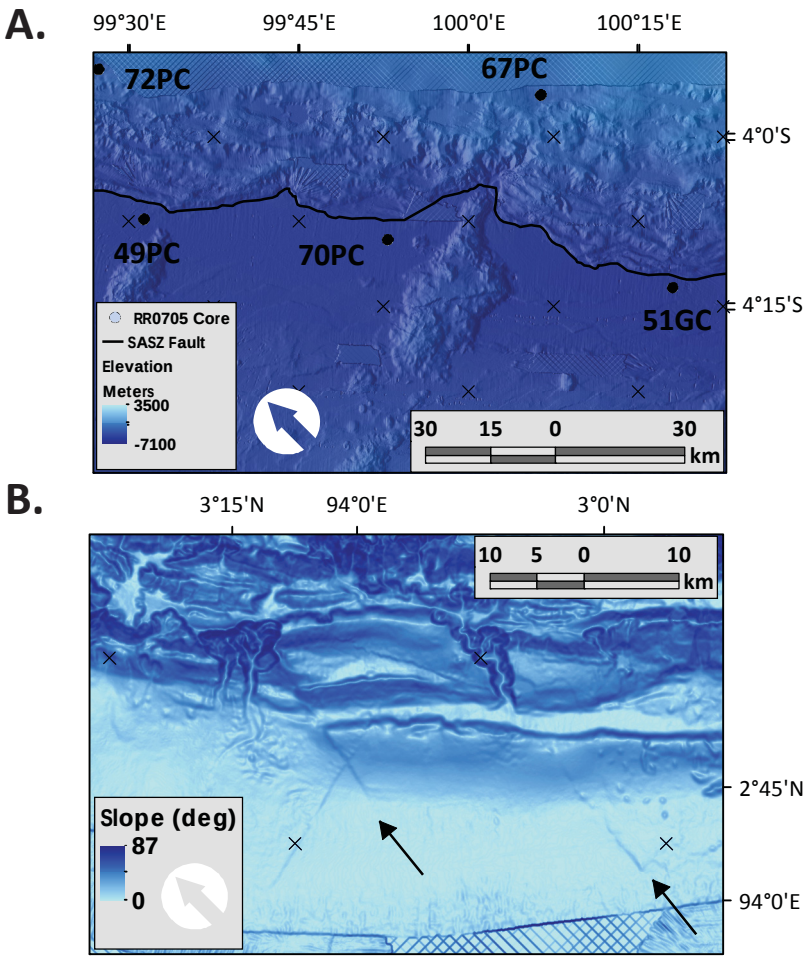

Figure 4-2. Active deformation at subduction zone trench map. The fault reflects the heterogeneous coupling ratio, here imparted due to variations in crustal topography. A. Bathymetry is plotted with color overlain upon a shaded relief map. Salient formed in the deformation front of the Sunda subduction zone. B. Bathymetry is plotted as slope in degrees. Fracture zones in India-Australia plate are reactivated and exert strain on accretionary prism materials through fault locking on the megathrust. Faults are labeled with black arrows. Ancient block failures can be seen in the southeast and even older failures are present in the northwest.

cause the landslides would need to fail upslope in their current positions. In some cases, these blocks are also on the crests and upper slopes of anticlinal folds, further supporting our interpretation of their old age (e.g. the southeastern end of **Fig. 4-2 B**, there are some blocks on the crest of a landward vergent fold). Because these block failures are rare, slope failures along the slope offshore Sumatra are possibly debris flows that transform into turbidity currents. Unlike settings with a high Pleistocene local sedimentation rate, like Cascadia (Patton et al., 2013 a), channels offshore Sumatra tend to be short (five to a few tens of km, mean length = 7 km) and do not form along the trench axis.

Lower plate structure dominates topography in the downgoing plate, including the fossil Wharton ridge and numerous north-northeast striking fracture zones, including the Investigator fracture zone (**Fig. 4-1 A**). The oceanic crust of the India-Australia plate has a large range in thickness; 22-km in the region of the Ninetyeast ridge (Krishna et al., 2001), 5-km west of the 2004 SASZ earthquake (Franke et al, 2008; Sing et al., 2008; and Klingelhoefer et al., 2010), to 3.5- to 4.5-km along the fossil Wharton ridge (Sing et al., 2010). Sediments overlying the crust range in thickness from 4 km near the latitude of the 2004 SASZ earthquake (Franze et al., 2008; Klingelhoefer et al., 2010; Gulick et al., 2011) to ~0.5 km in the region of the 2000 SASZ earthquake (Dean et al., 2010). Steps in the depth to crust and in the thickness of overlying sediment coincides with some of these fracture zones (Franke et al., 2008). These changes in crustal and sediment thickness may contribute to the segmentation of the subduction zone (DeShon et al., 2005; Dean et al., 2010). Salients in the base of the accretionary prism form where fracture zones and crustal topography related to spreading center volcanism are evidence for differential plate coupling (Ruff and Kanamori, 1980, 1983; Franke et al., 2008; Kopp et al., 2008; **Fig. 4-2 A**). Plate locking (Wang and Dixon, 2008) along the subduction zone is also evident where displacements on fracture zone faults in the downgoing plate are transferred to the accretionary prism along the lower slope (Graindorge et al., 2008; Kopp et al., 2008; **Fig. 4-2 B**). These fracture zones may be persistent boundaries to slip, especially if the faults offset plates of disparate age and temperature. Due to the lack of active sedimentation from the north, trench axis morphology is controlled by transverse structures from 2.25° S southward.

4-1.2 Landslides

One of the most common landscape responses and most damaging hazards related to earthquakes is landslides (Keefer, 1984; Jibson, 1993; Brink et al., 2009; Jibson and Harp, 2011; Schulz et al., 2012). Over 11,000 landslides were documented associated with the 1994 Northridge Mw 6.7 blind thrust earthquake (Jibson, 2000) and 60,000 landslides triggered during the 2008 Wenchuan earthquake (Gorum et al., 2011). Earthquakes can change the pore pressure and shear strength in geologic materials, leading to slope failure (Jibson, 1993; Wright and Rathje, 2003) and may be triggered with a minimum earthquake magnitude ~Mw = 5 (Keefer, 1984; Jibson and Harp, 2012). Landslide concentration (landslides per km^2; Keefer, 2000; Gorum et al., 2011) is generally higher in areas of stronger ground motion (Meunier et al, 2007; Strasser et al., 2006; Jibson and Harp,

2012). In submarine settings, these landslides can transform into turbidity currents, leaving a sedimentary record of the ground shaking (Goldfinger et al., 2003, 2012, 2013) and they can displace sea water sufficiently to generate tsunami waves (Wright and Rathje, 2003). Earthquake magnitude thresholds for submarine landslides at active margins are poorly constrained (Mw = 7.1 in Cascadia, Goldfinger et al., 2003, 2012, 2013; Mw = 7.2 and 7.4 on the Kushiro fan, Noda et al., 2008; Mw = 7.4 in Japan, Nakajima and Kanai, 2000; Mw = 7.9 along the San Andreas fault, Goldfinger et al., 2007, 2008; Mw = 7.3 in northern California/Cascadia, Wilson and Keefer, 1985; Rollins and Stein, 2010; Mw = 5.2 in Venezuela, Lorenzoni et al, 2012), probably because the evidences are difficult to observe. The wide range in minimum threshold magnitudes may also be due to how different tectonic settings may affect ground shaking. Settings with faster attenuation with distance (i.e. “low Q” sites) may have larger minimum thresholds, where settings with lower attenuation with distance (i.e. “high Q” sites) may have smaller minimum thresholds

Initial seismic analysis of dams used the seismic coefficient method, by applying a static horizontal inertial force using a static limit analysis (Hynes-Griffin and Franklin, 1984). Later, analyses dealt with the cyclic liquefaction of granular sediment, comparing the applied dynamic shear stresses to the cyclic strength of materials tested in the laboratory (Seed et al., 1975; Seed, 1979; Seed and Idriss, 1983). We use the Newmark Displacement method in this paper because it can estimate the permanent deformation that might occur where liquefaction does not take place (Newmark, 1965). Newmark’s method models a landslide as a rigid block on an inclined plane. When the base of the block experiences a critical acceleration, it will slide. Newmark Displacement is the cumulative motion of the block as it is subjected to these seismic accelerations. The displacement estimates will only be certain if the material properties are well known (Wilson and Keefer, 2003; Jibson, 2009).

We conduct two forms of slope stability analysis, Newmark infinite slope displacement analysis and Morgenstern-Price method of slices “factor of safety” analysis (Morgenstern and Price, 1965; Spencer, 1967). Newmark displacement analysis (Newmark, 1965; Morgenstern, 1967) is typically used for a regional scale assessment (Lee et al., 1999; Jibson, 2007; Strasser et al, 2011), because often there is a lack of detailed data about the subsurface materials nor a resolved velocity model at the site scale. We use the method of slices technique at the site scale. We conduct slope stability for two purposes; test-

ing for general seismic response of slopes (Infinite Slope and Slices) and testing for 2004 SASZ rupture specific response of slopes (Infinite Slope).

4-1.3 Ground Motions

Keefer (1984) studied historical earthquakes and earthquake intensity data to investigate the relations between landslide distributions and the seismic parameters Keefer considered are, earthquake magnitude, shaking intensity (Modified Mercalli), and the distance to the epicenter or fault rupture to find that the aerial response of landslides to earthquakes range from 0 km^2 at M = 4 to 500,000 km^2 at M = 9.2. Factors that control the aerial extent of these landslides include earthquake magnitude, local geologic conditions, earthquake focal depth, and the specific ground motions from a particular event (Keefer, 1985). Petersen et al. (2004) conducted a probabilistic seismic hazard analyses for parts of Sumatra, which included the application of regional earthquake source models. Their models were based on assumptions that historic seismicity supported the use of a characteristic earthquake model, but that was before the 2004 and 2005 SASZ earthquakes (which falsified their assumption). We estimate Arias Intensity (AI; Arias, 1970) and Peak Ground Acceleration (PGA) ground motions for the SASZ fault and apply those estimates as inputs to the slope stability calculations. PGA is a measure of the maximum ground acceleration from an earthquake, measured in units of gravity (g, where g is defined as 9.81 m/s^2). AI measures ground shaking intensity as the integral of the square of the acceleration-time history and correlates with structural performance of buildings, liquefaction, and seismic slope stability (Arias, 1970; Kayen et al., 1997; Travasarou et al., 2003). Prior measurements of seismic intensity were developed using descriptive and qualitative observations, but information contained in instrumental records is used to assign the AI scale for any given earthquake and site. The Kayen et al. (1997) and Travasarou et al. (2003) models are based on strong motion data from varyingly extensive earthquake catalogs. Limitations to any certain model are governed by the limit of data used by any individual study and are assessed for reliability by considering the residuals between predicted and observed ground motions.

Ground motion prediction models for earthquake faults, and the earthquakes they generate, were developed that relate earthquake magnitude and distance to the fault with ground motions at or near the ground surface (Keefer, 1985; Youngs et al., 1997). Records of strong motion from seismometers are classified by earthquake type, site type

(geomechanical properties of the crust and sediment at any given location), fault geometry (related to any given location), and plate tectonic setting. The authors then calculated regressions for each set of classified seismological data. The Ground Motion Prediction Equations (GMPEs) are published with terms for each classification term. The application of these GMPEs is limited to scenarios with conditions similar to those that contributed to the GMPE models. The processes that most authors include as terms of their regressions comprise distance and material attenuation, magnitude and distance scaling, and "soil" response (we use the engineering definition of soil, not the pedogenic definition).

Developed primarily to provide an input to seismic hazard analyses worldwide (Atkinson and Boore, 2003, Petersen et al., 2004), these models initially had a small inventory of seismologic data (Arias, 1970; Joyner and Boore, 1982, 1988; Crouse, 1991; Wilson, 1993; Campbell, 1997; Kayen, 1997; Gregor, 2002). Improvements have been made in recent years as more strong motion seismologic records, at closer fault distances, have been considered in their model regressions (Boore, 2003; Atkinson and Boore, 2003; Travasarou et al., 2003, Boore and Atkinson, 2008; Atkinson and Boore, 2011; Zhao et al, 2012). Specific earthquakes are modeled to develop the attenuation relations in a specific region (these attenuation relations vary regionally, Atkinson and Boore, 2003), that can later be applied elsewhere if some assumptions are made about the differences between the sites used to form the attenuation relations and the sites the to which the model is being applied. Sorensen et al. (2007) used a 2-D fault slip model to estimate PGA and Peak Ground Velocity (PGV) for the 2004 SASZ earthquake. We compare the Sorensen et al. (2007) model results with our ground motion model results and, later, our core data.

We use these ground motion prediction relations (Zhao et al., 2007; Travasarou et al., 2003) and ground motion modeling results (Sorensen et al., 2007) to provide constraint to the seismic load for the pseudostatic FOS analyses in this paper. We adopt the Zhao et al. (2007) spectral acceleration attenuation model for PGA that uses terms for site class,, earthquake fault type, tectonic regime, and distance and magnitude attenuation with distance, allowing the regressions to consider these effects separately (Zhao et al., 2007). The Zhao et al. (2007) model adopts the basic relations established by Abrahamson and Youngs (1992). We adopt the Travasarou et al. (2003) attenuation relations for AI. Their point-source model and coefficients are determined with non-linear regression analyses using random effects (Travasarou et al., 2003). While PGA can be a poor indicator of damage to structures because it is related only to the amplitude of ground motion,

AI is a more reliable predictor of damage because it incorporates frequency content and the duration of ground motion (Travasarou et al., 2003). However, AI has larger aleatory variability, so is better for settings that are dominated by short period characteristics of ground motion (Travasarou et al, 2003). We compare models of slope stability that include only AI with those that include both AI and PGA (Jibson et al., 2007).

4-2 Data and Methods

We use 90-meter resolution bathymetric data as our base data to conduct infinite slope FOS analysis with raster algebra and method of slices FOS analysis on 2-D seafloor profiles. The infinite slope method is conducted in a GIS system where raster data are modified with raster algebra to produce new raster products with solutions that represent the equations discussed in this section. The method of slices analyses are performed with a computer program that considers a geometrical relation that balances material forces with seismic forces.

Newmark infinite slope technique balances driving forces with resisting forces to estimate the stability of a rigid block on an inclined slope (Newmark, 1965). When the driving force exceeds the resisting force, the Factor of Safety (FOS) is <1 and is unstable and may fail or slide (**Fig. 4-3**). Parameters labeled in **Fig. 4-3** include: τ = the shear stress on the failure plane, u = pore pressure, σ = normal stress on the failure plane, w = the unit weight of the block material, z = the depth of the assumed failure plane, α = the slope angle, m = proportion of slide that is saturated, and Ah = seismic acceleration in g's. This "block" also has an associated critical acceleration (seismic load) that is a force threshold over which the block fails/slides. The block may not fail at this threshold and requires more force. Therefore, to account for this additional threshold, a minimum displacement model is used in these analyses (aka the Newmark Displacement). We conduct dynamic slope stability based upon force balance relations developed by Newmark (1965) and most recently refined by Jibson (1993, 2007, and 2009) and Jibson et al., (2000). Jibson et al. (2007) double integrates the earthquake acceleration-time history that exceeds the threshold acceleration required to overcome basal resistance and initiate sliding. We

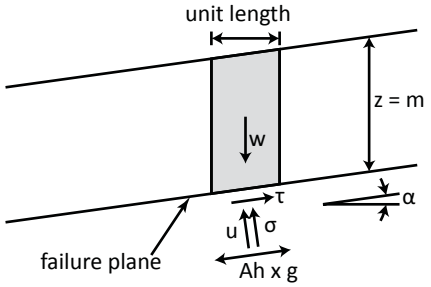

Figure 4-3. Force and Mass balance diagram. This is an illustration of the infinite slope factor of safety configuration, modified from Hadj-Hamou and Kavazanjian (1985). Units are defined in the text.

use these empirical relations to estimate sliding block displacements given ground shaking based on the plate geometry for the megathrust offshore Sumatra and earthquake magnitudes 6, 7, 8, and 9. We first estimate the static FOS for submarine slopes, find the critical acceleration for these slopes based on the FOS analysis, and finally determine the Newmark Displacement for a given range of earthquake magnitude.

Newmark Displacement includes the characterization of two key relations (1) dynamic slope stability and (2) earthquake induced ground motion. Bathymetry provided by the Sumatra bathymetric cooperative is used as the basis for determining slopes. Sumatra bathymetry was collected by Japanese (R/V Natsushima: Japan Agency for Marine Earth-Science and Technology, Jamstec), United Kingdom (HMS Scott: UK Royal Navy and Southampton Oceanography Centre, NOCS), French (R/V Marion Dufresne: Ifremer), and German (R/V Sonne: Federal Institute for Geosciences and Natural Resources, BGR) ships and shared utilizing a cooperative agreement with these international institutions and the Indonesian Government (Agency for the Assessment and Application of Technology, BPPT; Henstock et al., 2006; Ladage et al., 2006). We create a slab model of the subduction zone fault and apply ground motions driven from the fault, to the seafloor topography. We then use these ground motions as the source of seismic load in the Newmark Displacement analyses.

In order to consider more deep-seated forms of slope failure, that might violate assumptions associated with Newmark Displacement, we conduct site specific FOS analyses based on slope profiles adjacent to our core sites. We utilize computer based 2-D slope stability factor of safety (deterministic) and probability of failure (probabilistic) on circular surfaces in “soil” using vertical slice limit equilibrium methods (Morgenstern and Price, 1965; Spencer, 1967). This method of analysis was initially developed by Fellenius (1927, 1936) and Taylor (1937, 1948). For the slices procedure, the potential slide mass is divided into a number of elements or “slices,” then a force and momentum balance procedure is performed on each slice, summing the forces across all slices to determine the factor of safety for that slide surface (**Fig. 4-4**). This technique can be used to model stability before or after failure (Strasser et al., 2011).

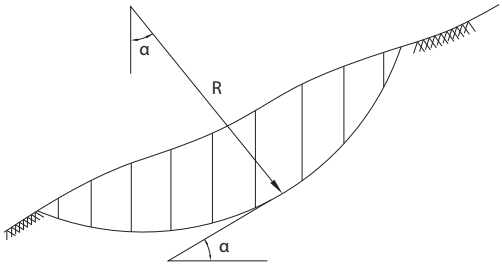

Figure 4-4. Method of Slices schematic diagram. Schematic illustration depicting a generic slope divided into slices as used in the method of slices factor of safety analyses, modified from Chowdhury (2010).

We query ground motion information restricted by potential sedimentary source areas for a series of cores in the region of the 2004 SASZ earthquake. We do this to make some estimates of the energy content of ground shaking that is likely to contribute to slope stability in source areas that potentially contribute to sedimentation at our core sites. We consider our modeled estimates of AI, PGA, and finally, PGA modeled by Sorensen et al. (2007). We then compare these results with sediment core data to determine the potential impact of ground motions on sedimentation offshore Sumatra at our core sites.

4-2.1 Assumptions

Infinite slope analysis is considered when a few assumptions about material rheology, mass, saturation, pore pressure, etc. are satisfied. Slope failures are translational where the ratio between failure depth (slide thickness) and the lateral extent of slope failures is sufficiently small to ignore edge effects (Strasser et al., 2011). Infinite slopes assume fluid steady seepage is parallel to the slope, forces on the sides of any given "block" are equal and opposite at all points in the block, and that the stress conditions are also homogeneous and isotropic (Hadj-Hamou and Kavazanjian, 1985). Furthermore, Newmark's method treats the slide material as a "rigid-plastic body" that does not deform internally, that the block does not experience displacements at accelerations less than Ac, and that the failure surface is concentrated along a narrow discrete shear zone (Jibson, 2007). One large source of aleatory uncertainty is the selection of material properties. We use sediment material and strength properties from cores in the region and from sediments in similar settings and assume that these sediment properties represent the sediment we model in our calculations.

The geometry we use for ground motion estimates is limited because the seafloor bathymetry has a 90-meter resolution, so the real slopes have a higher variation than modeled in our calculations. We assume the multibeam bathymetry represents the real seafloor shape. The resolution and nature of the multibeam systems smooth bathymetric data locally, making the slope values used in our calculation likely to represent minimum values.

One of the largest sources of uncertainty is the shape and spatial position of the fault slab that we use to model the ground motions. Given the short distances from the fault to the landslide source regions, the uncertainties in ground motion relations based on global observations, and the likely saturation of ground motions at short ranges (Skarla-

toudis and Papazachose, 2012) this source of uncertainty likely contributes little to the variation in ground motions at the seafloor. Based on these assumptions, the results are only approximations of slope stability for the seafloor that we model.

4-2.2 Infinite Slope Factor of Safety

We use FOS relations derived by Jibson (2000; their equation 2):

$$FOS = (c'/\gamma * t * \sin\alpha) + (\tan\phi'/\tan\alpha) - (m*\gamma_w*\tan\phi'/\gamma*\tan\alpha) \quad (\mathbf{1})$$

Variables in the numerator tend to correlate positively with slope stability (favor no slope failure) and variables in the denominator tend to correlate positively with slope instability (favor slope failure). Parameters are as follows: c' is effective cohesion (kPa), γ is unit sediment weight (kN/m^3), t is slide thickness (meters), α is slope angle (degrees), ϕ› is effective angle of internal friction (degrees), m is percent of slide thickness below water table (100% in our submarine setting), and γ_w is the unit weight of water (kN/m^3). Parameter values for FOS analysis are given in **Table 4-1**. Material properties are discussed in **Suppl. 4-1**. We calculate the slope from the bathymetry surface and then calculate the trigonometric functions based on this slope data. All raster algebra used in our analyses that use a trigonometric function is based on these data sets (e.g. tanα).

Material property data from a variety of sources are considered. Sultan et al. (2009) provide geotechnical data for cores collected in the region of the 2004 SASZ earthquake. Johnson et al. (2012) evaluated mechanical properties for in situ surficial cohesive marine sediments. Hempel (1995) provide shear strength data for sediment in Kasten cores collected along the Cascadia margin. We consider cohesion (shear strength) from sediment in the uppermost 60 cm of sediment because those are the sediments we consider to most likely fail consistently during earthquake induced ground motions. We use effec-

Table 4-1. Parameters used in infinite slope Factor of Safety analysis (Jibson et al., 2000).

Cohesion[1]	Unit Weight Sediment[2]	Unit Weight Water	Effective Angle of Internal Friction[3]	Slide Thickness	Proportion Saturated
kPa	Kn/m^3	Kn/m^3	degrees	feet	%
c'	γ	γ_w	Φ'	t	m
5.6	15.9	9.81	27.2	1	100%

1. Cohesion values from Hempel (1985), Sultan et al. (2009), and Johnson et al. (2012)
2. Unit Weight Sediment parameter from Sultan et al. (2009)
3. Angle of Friction comes from uppermost sediments in cores from Tan et al. (2006)

tive angle of internal friction data collected by Tan et al. (2006) for sediments at ODP site 1244, Hydrate Ridge, Cascadia margin.

4-2.3 Ground Motion Predictions

We use two types of ground motion predictions to conduct our infinite slope models. First we use a stochastic model of ground motion based on earthquake magnitude and the fault geometry related to seismicity and distance to seafloor bathymetry. We use this model to impart ground motions for generic subduction zone earthquakes. Then we use ground motion data modeled for the 2004 SASZ earthquake (Sorensen et al., 2007), apply those specific ground motions to the seafloor, and compare those results with the cores and shallow seismic data in that region.

4-2.3.1 Synthetic Earthquake Ground Motion

We evaluate and consider multiple ground motion prediction equations developed for subduction zones and other settings for earthquakes of magnitude 6, 7, 8, and 9. Early models considered different fault-distance geometries and were limited by the earthquake data sourced to generate these empirical relations (Wilson, 1993; Kayen et al., 1997; Campbell, 1997). As the earthquake catalog increased in size, the new regressions were better fits to these new data (Gregor et al., 2002; Atkinson and Boore, 2003; Campbell, 2003; Travasarou et al, 2003; Zhao et al., 2006, 2010, 2012; Boore and Atkinson, 2008; Atkinson and Boore, 2011). Data from near fault and large magnitude earthquakes remain a sparse contributor to the catalog and the largest source of epistemic uncertainty (Atkinson and Boore, 2011).

Peak Ground Velocity (PGV), Peak Ground Acceleration (PGA), and Arias Intensity (AI) are different ways to quantify the ground motion due to initial earthquake motion, along with forms of attenuation through the crust and geological materials. People consider the maxima of ground motion from PGV and PGA data, as well as the frequency content of these measures. These maxima may be reached multiple times, so AI is considered to capture this possibility in that it is an integration of all ground motions during the earthquake motion (in the case that critical acceleration/velocity is reached more than once; Arias, 1970). AI is a ground motion relation that measures ground motion as the integral of the square of the acceleration-time history (Travasarou et al., 2003). AI actually con-

tains information about the energy content of the recorded earthquake (Hsieh and Lee, 2011). That we use AI in our analyses is justified by the correlation of landslide density with Arias Intensity (Lee et al., 2008).

We select the model of Zhao et al. (2006, 2007) to model PGA ground motions for submarine slopes. While the Boore and Atkinson (2008) model includes a larger earthquake catalog, they consider the Joyner-Boore fault distance, which is the distance to the surface trace of the fault (which does not reflect the ground motions expected at subduction zones when using a stochastic model). The Zhao et al. (2006) model considers in their regression the significant effects of source distance, source type, and faulting mechanism. Zhao et al. (2006) consider their simple model to predict accelerations that are unbiased over magnitude and distance. They also consider fewer terms for site classes than other models, so their results are more applicable to a range of tectonic settings, especially settings and earthquake magnitudes and hypocentral distances not sourced in their regressions (Zhao et al., 2004, 2006). We list parameter values used in our ground motion predictions in **Table 4-2**.

We select the model of Travasarou et al. (2003) to model AI ground motions for submarine slopes in our analyses. Earlier models (Wilson, 1993; Kayen et al., 1997) generated unreasonably large values of intensity, especially at distances nearest the fault. The major controls for PGA and AI are the distance to the fault and earthquake magnitude. Secondary factors include site class terms (soil or bedrock type), source and path terms, sense of motion (reverse or normal type earthquake), and subduction (interface) or slab

Table 4-2. Parameters used in ground motion predictions for PGA (Zhao et al., 2006).

Coefficients for Source and Path Terms of the Models in the Present Study

a	b	c	d	e	FR	SL	SS	SSL
1.101	-0.00564	0.0055	1.08	0.01412	0.251	0	2.607	-0.528

Coefficients for Site Class Terms and Prediction Error

CH	C1	C2	C3	C4	r	s	rT
0.293	1.111	1.344	1.355	1.42	0.604	0.398	0.723

Table 4-2 cont.

Coefficients for Magnitude Terms (interevent residuals)

QC	WC	τC	QI	WI	τI	PS	QS	WS	τS
0	0	0.303	0	0	0.308	0.1392	0.1584	-0.0529	0.321

Terms for Earthquake Mechanism

Fr	SI	SS	SSL	Ck	hc
1	1	0	0	1.355	15

type event. These attenuation regression models use the National Earthquake Hazard Reduction Program (NEHRP) Site Class Definitions (Dobry et al., 2000; Atkinson and Boore, 2003). Site classes range from A to E are defined by the shear wave seismic velocity in the upper 30 meters. Thirty meters was chosen because there is a lack of velocity data deeper than 30 m and because it does not contribute considerable variability in regression models (Joyner and Fumal, 1984; Boore et al., 1997). Based on seismic velocity (Vs) ranges for NEHRP site classes, we select coefficients for NHERP class D for our AI estimates (Travasarou et al., 2003). We list parameter values used in our ground motion predictions in **Table 4-3**. Travasarou et al. (2003) do not include saturation of AI at short distances with increasing magnitude because their intra-event residuals (how they measure their regression versus the observed ground motions) at distances less than 10 km show no bias (i.e. their model represents the data at small distances; their figure 11). This supports our justification to use AI calculations at distances less than 10 km. One downside of their model is that it does not include magnitudes greater than Mw 7.6, so while their relations probably do work at larger magnitudes, they could not test this assertion.

We assume that the earthquake may occur anywhere on the fault. While some earthquakes appear to rupture specific regions of any given fault (Briggs et al., 2006; Bilek, 2007; Sieh, et al., 2008; Meltzner et al., 2010, 2012; Wang, 2010), we cannot assume that the fault will not rupture elsewhere (Tillman et al., 2010; Shulgin et al., 2013). Recent earthquakes may have ruptured into the mantle (Singh et al., 2008; Dessa et al., 2009; Zhan et al., 2012) and up-dip towards the trench (Fujiwara et al., 2011; Ide et al., 2011; Kodaira et al., 2012; Kozdon and Dunham, 2013). In this sense, the focal depth

Table 4-3. Parameters used in ground motion prediction (Travasarou et al., 2003.)

Coefficients											
				M<7.6	M>7.6	M<7.6	M>7.6	M<7.6	M>7.6	M<7.6	M>7.6
c1	c2	c3	c4	s11	s11	s12	s12	s21	s21	s22	s22
2.8	-1.981	20.72	-1.703	0.454	0.616	0.101	0	0.479	1.013	0.334	0

Table 4-3 cont.

Coefficients		soil type	soil type	normal	reverse
f1	f2	Sc	Sd	Fn	Fr
-0.166	0.512	0	1	0	1

is the same as the distance to the fault for the Zhao et al. (2006) and Travasarou et al. (2003) models.

The form of the equation for PGA (Zhao et al., 2006; equation 1) is:

$$Log_e(Y) = a * M_w + b * Rdist - log_e(Rdist + (c * exp(d * M_w)) + e(h - h_c) * \delta h + F_R + S_I + S_S + C_k \quad (\mathbf{2})$$

Where Y is PGA (cm/s^2), M_w is moment magnitude, x is source distance (distance to fault), h is focal depth (same as x), h_c is a depth constant, δh is a dummy variable that activates the e(h-h_c) term when h < h_c, F_R designates a reverse fault, S_I designates an interface event, S_S designates a subduction event, Ck is a site class term, and a, b, c, d, and e are coefficients defined by regression performed by Zhao et al. (2006). Because we are modeling a reverse mechanism on the megathrust, S_I and S_S terms are zero and F_R is 1 (**Fig. 4-5**).

The form of equation for AI (Travasarou et al., 2003; equation 12) is:

$$\ln AI = c1 + c2 * (M_w - 6) + c3 * \ln(M_w/6) + c4 * \ln(Rdist) + (S11 + S12 * (M_w-6)) * Sc + (S21 + s22 * (M_w-6)) * S_d + f1 * F_n + f2 * F_r \quad (\mathbf{3})$$

AI is Arias Intensity in m/sec, M_w is earthquake moment magnitude, Rdist is the closest distance to the fault, and for a reverse earthquake, Fn is 0 and Fr is 1. Other coefficients were determined by Travasarou et al. (2003) by regression (their Table III). We plot AI as a function of distance for three fault thicknesses, using the material properties in **Table 4-1** (**Fig. 4-6**).

4-2.3.2 Fault Slab Model

In order to model generic earthquake ground motions, we construct a fault slab model to constrain the parameter distance to the fault (Rdist, also known as Rseis; Campbell, 1997). We use slab contours derived from seismicity and published by the USGS (Hayes et al., 2012). We construct our own up-dip limit to the slab because the published models do not consider the thickness of sediment on the downgoing slab. Based on seismic profiles (Bunting et al., 2008, Singh et al., 2008, 2010; Shulgin et al., 2013) sediment thickness ranges from 4 km in the northern margin to <500 m in the southern margin. The decrease in sediment thickness is due to the decreased proximity to the source of sediment in the north (Bengal and Nicobar fans). While there is evidence that there are

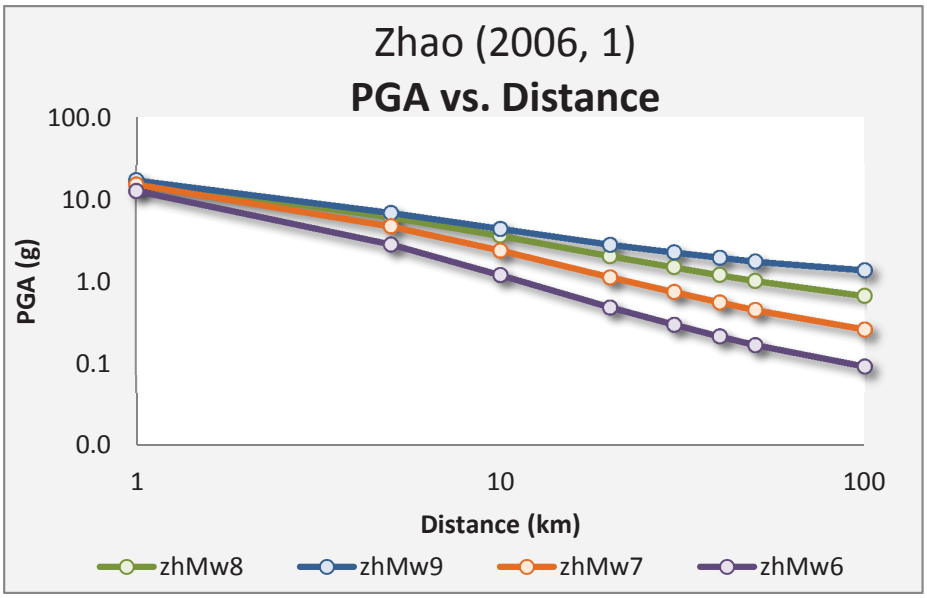

Figure 4-5. Ground Motion predictions for Peak Ground Acceleration (PGA), in g. These data represent the form of ground motion predictions regressed by Zhao et al. (2006, equation 1), equation (2) for earthquakes of four magnitudes (M = 6, 7, 8, and 9 are purple, green, orange, and blue). "Distance" is the shortest distance between the ground surface and the fault plane (Rdist).

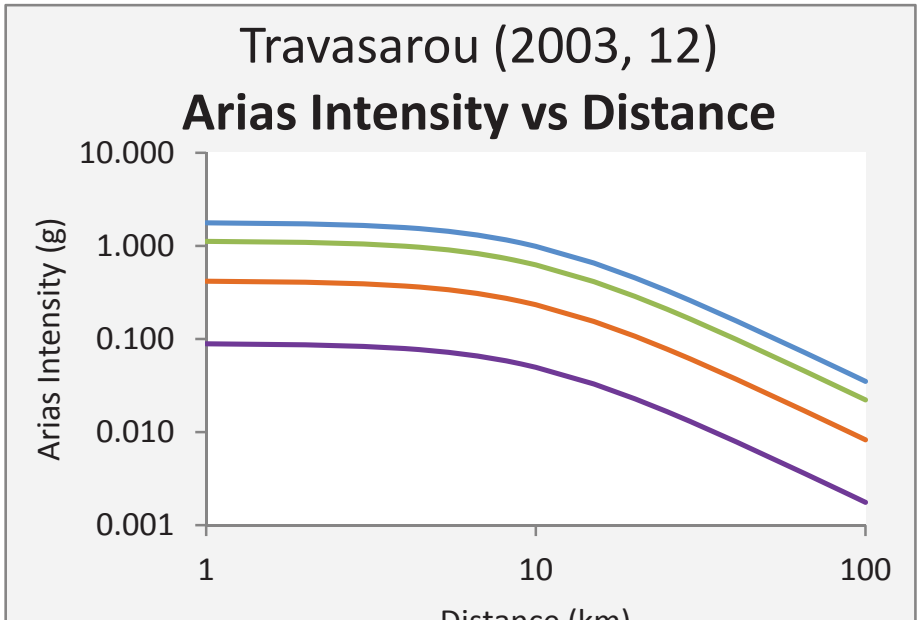

Figure 4-6. Ground Motion predictions for Arias Intensity (AI), in m/sec. These data represent the form of ground motion predictions regressed by Travasarou et al. (2003, equation 12), equation (3) for earthquakes of four magnitudes (M = 6, 7, 8, and 9 are purple, green, orange, and blue). "Distance" is the shortest distance between the round surface and the fault plane (Rdist).

steps in thickness (Dean et al., 2010; Shulgin et al., 2013), we consider a linear change in thickness, north to south, because we do not have the data resolution to estimate these step changes in thickness with substantial certainty. We create a raster slab model using the ArcGIS tool "Topo to Raster" using the USGS slab contours and our 3-D polyline for the up-dip limit of the slab. We call this raster Rdepth. For locations ocean ward of the up-dip limit of our slab model (in the abyssal plain), we estimate Rdist based on the distance from the uppermost location of our slab model (the 3-D polyline used in the slab raster construction). We combine the Rdepth and Rdist data into a composite raster Rdist, plotted vs horizontal distance in **Fig. 4-7**. For calculations that use the shortest distance to the fault, we use the Rdist raster.

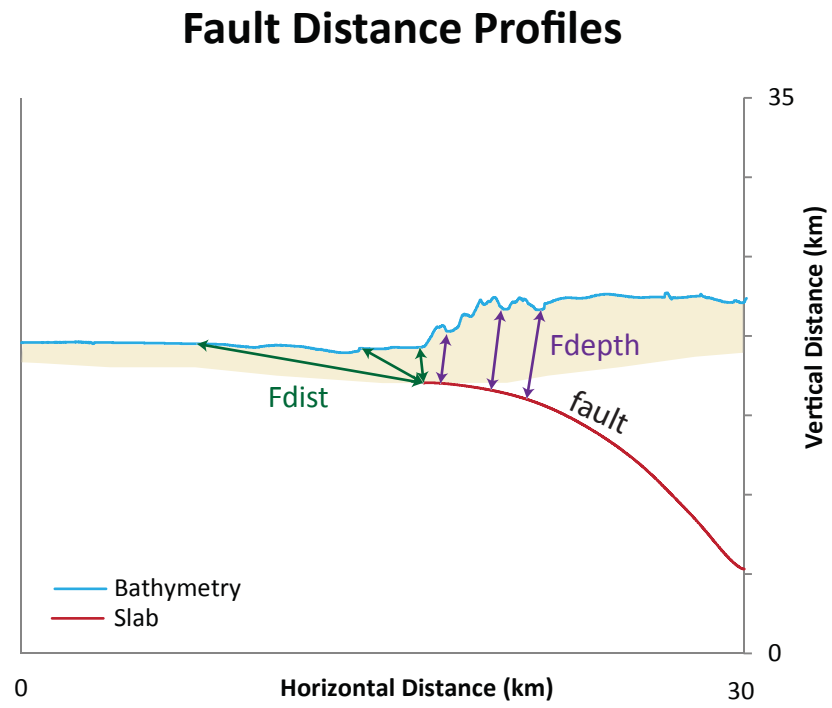

Figure 4-7. Distances plotted for the fault and bathymetric geometry for the subduction zone offshore Sumatra. Seafloor bathymetry profile is plotted as a light blue line, the fault plane (slab) is plotted in red. The cream shaded region under the bathymetry and above the fault represents the general position of sediments overlying the oceanic crust of the Indo-Australia plate. Rdist is calculated by the length of Fdepth distances east of the trench (purple arrows) and Fdist distances west of the trench (green arrows).

4-2.3.3 2004 Earthquake

For the earthquake specific case, we choose the only existing ground motion model for the 2004 SASZ earthquake (Sorensen et al., 2007). We use the PGA simulations from Sorensen et al. (2007) as input for a pseudostatic infinite slope FOS analysis that does not use Arias Intensity (Hadj-Hamou and Kavazanjian, 1985).

Sorensen et al. (2007) use a multi asperity fault model (Yagi, 2004), with the USGS epicenter, to model ground motions in the region surrounding the 2004 SASZ earthquake (**Fig. 4-8**). The fault is broken into sub-faults that represent the asperities (regions of high slip). They combine a deterministic model for low frequencies (0.1-1 Hz) and a semi-stochastic model for high frequencies (1-10 Hz). A regional seismic anelastic attenuation relation of $Q = 100f^{0.8}$ is used and the simulations were performed on a 144 point grid with 1.5° latitude-longitude spacing. Q is a measure of the rate of attenuation of seismic waves, called the seismic quality factor (Stein and Wysession, 2003), which is inversely proportional to attenuation (attenuation = 1/Q). Q is poorly constrained in this region (Sorensen et al., 2007). Their model output is then converted to a smoothed surface, which is the form we adopt for our modeling. There are other earthquake slip models for the 2004 SASZ earthquake (Ammon et al., 2005; Ishii et al., 2005, 2007; Vigny et al.,

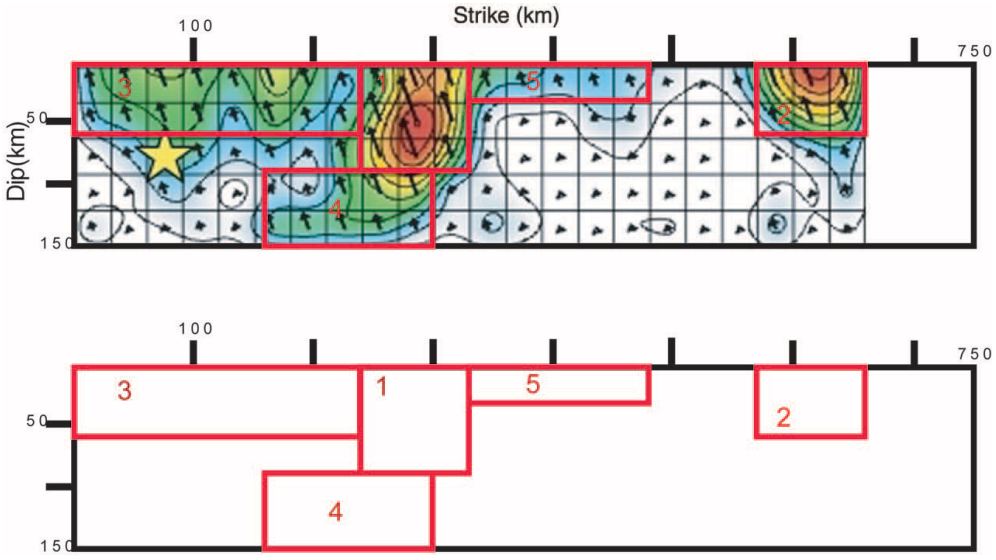

Figure 4-8. The 2004 SASZ earthquake 2-D fault model. This model (Yagi et al., 2004) is used by Sorensen et al. (2007) to estimate ground motions for the 2004 SASZ earthquake. The red rectangles show the sub-faults designated to have the largest slip.

2005; Bosci et al., 2006; Subarya et a;., 2006; Banjeree et al., 2007; Chlieh et al., 2007, 2008; Hu and Wang, 2012), but the Yagi (2004) model is the only one used to simulate ground motions. Another limitation of the Sorensen et al. (2007) model is that it is compared with a single record of strong motion located approximately 650 km from the earthquake hypocenter. Sorensen et al. (2007) also tested their model by simulating ground motions in Banda Aceh and comparing those results with estimates of observed Modified Mercalli intensities. Their simulations reached accelerations reaching 140 cm/sec2, consistent with MM intensity of VII and JMA seismic intensity of 5+ to 6- (Tobita et al., 2006).

Sorensen et al. (2007) compared their results with seismic records of the 2004 SASZ earthquake. Their results generally agreed with the seismic data recorded during the 2004 SASZ earthquake at the PPI site (part of the JSINET seismic network, Ishida et al., 1999), at 600 km distance from the epicenter. Shaking intensity observations in Banda Aceh, converted to ground motions, corresponded to PGA of 300 cm/sec^2 and PGV of 80 cm/sec. Simulations presented by Sorensen et al. (2007) estimated ground motions at Banda Aceh as 140 cm/sec^2 (PGA) and 60 cm/sec (PGV).

The form of the equation for pseudostatic slope stability from Hadj-Hamou and Kavazanjian (1985; their equation 7) is:

$$FOS = (c + (1 – m * (y/y')) * ((1 - R))/(Ah + \sin\alpha) * (\cos\alpha * \tan\phi) \quad (\mathbf{4})$$

The parameters are as follows: c = cohesion (kPa), m = slide thickness (m), R = distance to the fault (m), Ah = horizontal seismic acceleration (g, Sorensen et al., 2007), α is the slope of the submarine ground surface (degrees), ϕ is angle of internal friction (degrees). The values we use in our analyses are included in **Table 4-4**.

4-2.4 Newmark Displacement

We estimate a Newmark Displacement as a function of landslide critical acceleration and earthquake ground motion intensity (Ambraseys and Menu, 1988; Jibson, 1993; Jibson et al., 1998, 2000). **Fig. 4-9** shows how the acceleration and velocity are integrated to determine cumulative offset of infinite slopes. Recently a larger catalog of earthquakes has been evaluated for new empirical regressions (Jibson, 2007; Hsieh and Lee, 2011). Jibson (2007) consider 2,270 strong motion records from 30 global earthquakes; Hsieh and Lee

Table 4-4. Parameters used in pseudostatic analysis considering ground motions calculated by Sorensen et al. (2007).

Slide Thickness	Unit Weight Water	Total Weight Sediment[1]	Cohesion[1]	Angle of Internal Friction[3]
h	γw	γt	c	ϕ
m	pcf	pcf	kPa	degrees
1	125	62.45	5.551	27.1

1. Total Weight Sediment parameter from Sultan et al. (2009)

2. Cohesion values from Hempel (1985), Sultan et al. (2009), and Johnson et al. (2012)

3. Angle of Friction comes from uppermost sediments in cores from Tan et al. (2006)

(2011) use 1,343 records from six earthquakes, ranging in magnitude from 5.3 to 7.6 and 6.7 to 7.6 respectively.

For Newmark Displacement, we consider Jibson (2007) relations that consider Arias Intensity and critical acceleration (Jibson, 2007; equation 9; **Fig. 4-10**) and that consider Arias Intensity, critical acceleration, and Amax (peak acceleration, or PGA) (Jibson, 2007; equation 10; **Fig. 4-11**).

$$\log Dn = 2.401 * \log AI - 3.481 * \log Ac - 3.230 \pm 0.656 \quad (5)$$

$$\log Dn = 0.561 * \log AI - 3.833 * \log(Ac/Amax) - 1.474 \pm 0.616 \quad (6)$$

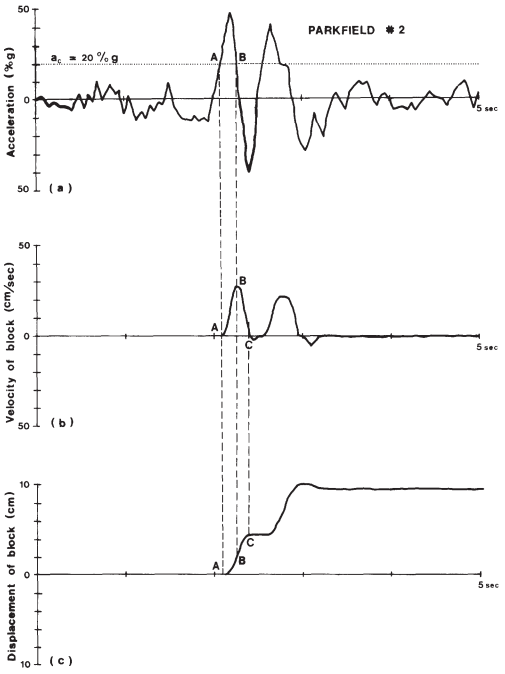

Figure 4-9. Illustration of the derivation for cumulative Newmark displacement. These plots are based on earthquake energy-time plot for the 6 August 1979 Coyote Lake earthquake, California (modified from Wilson and Keefer, 1983). A. strong-motion record with critical acceleration {dotted line) superimposed, B. velocity of block versus time, and C. displacement of block versus time.

Dn is the Newmark Displacement in cm, AI is Arias Intensity (m/sec), Ac is critical acceleration (g), and Amax is peak ground acceleration (g). Jibson (2007) equation 9 (our equation 5) fits their earthquake source data with an R^2 value of 0.71. Jibson (2007) equation 10 (our equation 6) fits their earthquake source data

with an R^2 value of 0.75, with a standard deviation of approximately ± 0.5 log units. Their regressions result results in modeled displacements that span about an order of magnitude, therefore this type of analysis should only be conducted on a regional scale. Varia-

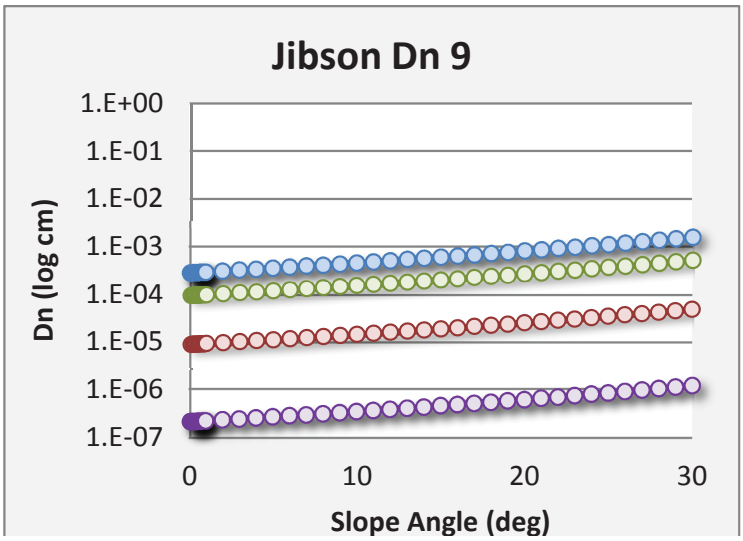

Figure 4-10. Newmark Displacement (Dn) plots, in cm, using equation 5. This plot is for generic slopes given four earthquake magnitudes (M = 6, 7, 8, and 9 are purple, green, orange, and blue). These relations are for Jibson et al. (2007, equation 9), using Arias Intensity using equation 5.

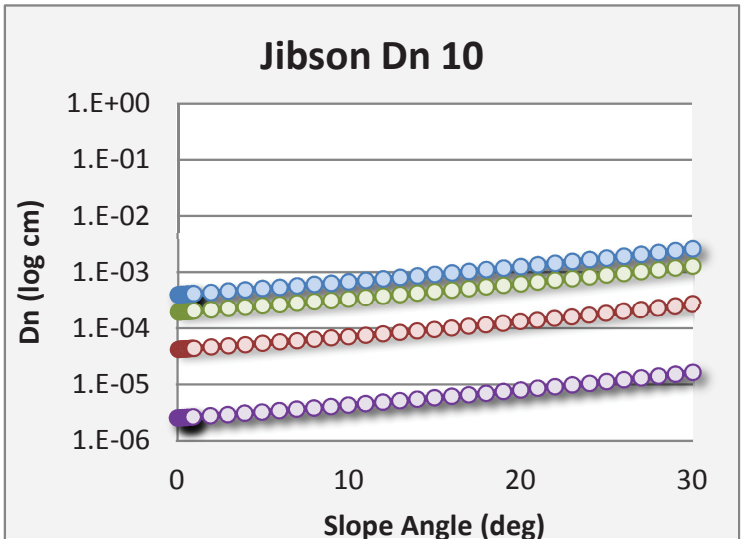

Figure 4-11. Newmark Displacement (Dn) plots, in cm, using equation 6. This plot is for generic slopes given four earthquake magnitudes (M = 6, 7, 8, and 9 are purple, green, orange, and blue). These relations are for Jibson et al. (2007, equation 10), using Arias Intensity and PGA using equation 6.

tions in site conditions are the source of variation in their ground motion attenuation models. Critical acceleration (Ac) is a measure of dynamic stability and takes the form of Jibson et al., (2000; equation 1):

$$Ac = (FOS - 1) * g * \sin\alpha \quad (\mathbf{7})$$

where g is acceleration due to gravity (g = 9.81 m/s^2), FOS is the static factor of safety, and α is the slope angle of the seafloor surface. We plot Ac as a function of slide thickness (**Fig. 4-12**) and as a function of earthquake magnitude (**Fig. 4-13**). Thicker deposits have a higher threshold for instability. The critical acceleration ratio (CAR) relates Ac with Amax and shows that steeper slopes drive the relations with lower CAR ratios for steeper slopes. We use the CAR in equation 6.

For comparison with Jibson (2007), we select the Newmark Displacement regression from Hsieh and Lee (2011). Their model was created to evaluate the Jibson (1993) and Jibson et al. (1998) models, also evaluated and improved upon by Jibson (2007). Hsieh and Lee (2011) found that for Jibson (1993) and Jibson et al. (1998), logDn is proportional to logAc when Ac is large, however logDn and Ac are linearly proportional for all values of Ac. They added a term to account for this discrepancy in the Jibson forms, developing new relations for IA, Ac, and Dn. They conclude with two forms of these regressed formulae, a global form and a local form. Hsieh and Lee (2011) also provide coefficients for site conditions (soil vs. rock). They recommend that the local form be used in Taiwan and other active orogens because their attenuation relations are more similar to those of Taiwan. Hsieh and Lee (2011) suggest the global form of their regression be used away from active orogens, but the difference in fit for these regressions is small, so may not matter for regional analyses. Their local form for soil sites (Hsieh and Lee, 2011; equation 15) is shown here:

$$\log Dn = 0.802 * \log Ia - 19.246 * Ac + 12.757 * Ac * \log Ia + 2.153 \pm 0.445 \quad (\mathbf{8})$$

4-2.5 Method of Slices Factor of Safety

We select forty-nine sites to conduct FOS analysis using the Bishop method of slices technique. Improved variants of this technique have been developed and are all available in most modern slope stability analysis software. We chose to consider the models of Morgenstern-Price (Morgenstern and Price, 1965) and Spencer (Spencer, 1967). The same general principles of force balance apply here as they did for infinite slope analysis.

We first conduct these analyses with a static seismic load (g = 0), then apply a seismic load of g = 1, and finally we iterate increasingly lower seismic loads until the results is a stable slope. This resultant seismic load we attribute to be the critical acceleration for each site.

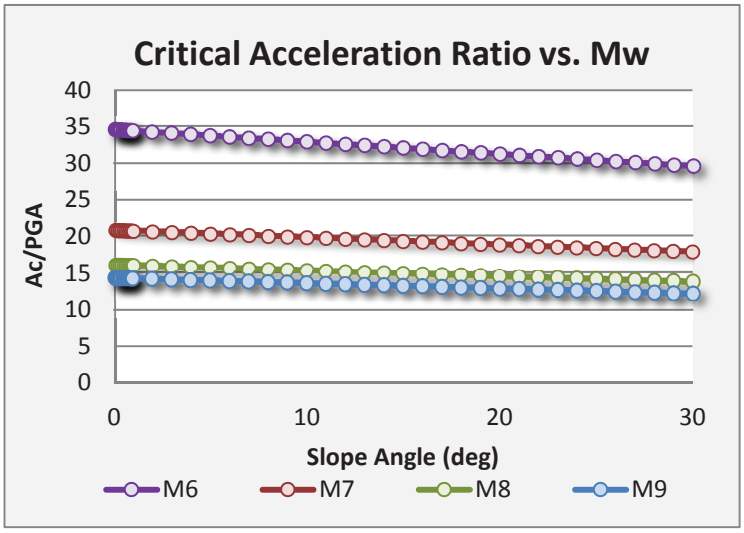

Figure 4-12. Critical Acceleration (Ac) is plotted vs. slope angle. This plot is for generic slopes given three landslide thicknesses (t = 0.1, 0.3, and 1 m are red, green, and blue). These relations are for Jibson et al. (2000) equation 1, using the static FOS determined.

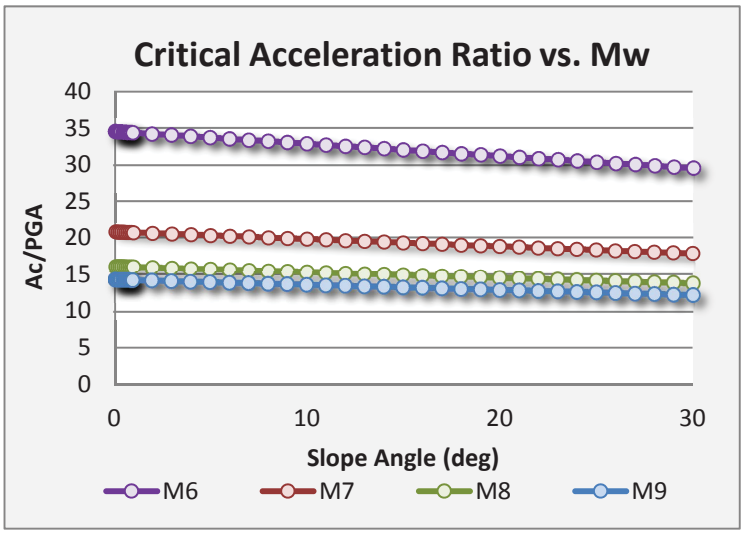

Figure 4-13. Critical Acceleration Ratio (CAR; Jibson et al., 2007) is plotted versus slope angle. This plot is for four earthquake magnitudes (M = 6, 7, 8, and 9 are purple, green, orange, and blue). The CAR is based on results for Ac (Figure 12) and PGA (Figure 5).

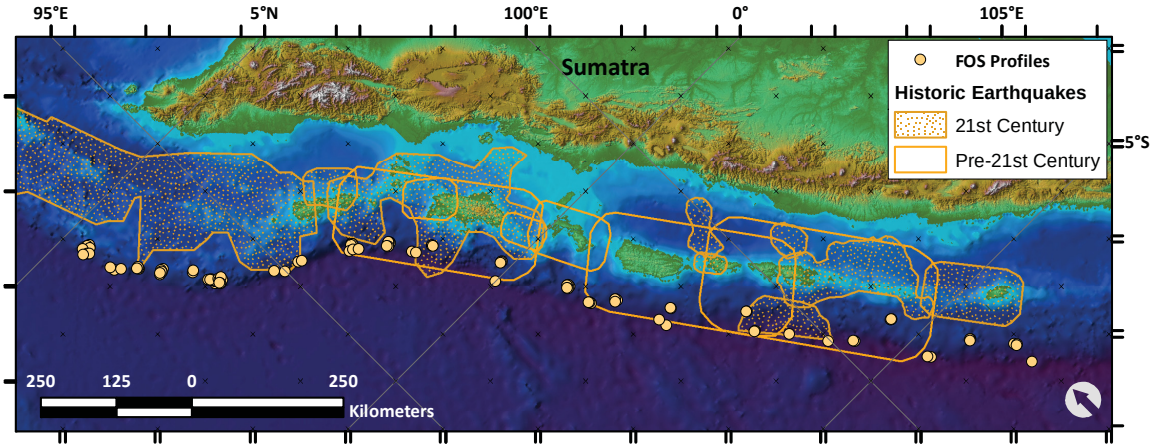

Figure 4-14. Site-scale FOS location map. Core locations are plotted as orange circles on this map that also shows some historic earthquake ruptures (Bilham, 2005; Malik et al., 2011), plotted in orange (twenty-first century earthquakes are designated by the hachured pattern; Briggs et al., 2006; Chlieh et al., 2007, 2008; Philobosian et al., 2012).

We use SLIDE 6.0 (Rocscience, 2013) software for our analyses and we choose a probabilistic approach for material properties and for seismic loading. We choose circular surfaces with composite solutions. We model the surficial materials and use material properties appropriate for surficial materials. Boundaries for the 2-D profiles are taken from ArcGIS profile measuring tools sampling the bathymetry data provided by the Sumatra multibeam surface. Profiles were measured along the seafloor directly upslope of our core sites (**Fig. 4-14**).

Material properties used here are taken from sediment core data discussed in the infinite slope section. Material properties considered include Unsaturated and Saturated Sediment Weight (kN/m^3), Cohesion (kPa), Angle of Internal Friction or "Phi" (degrees), water table based pore pressure (HU = 1, or 100% saturated), and excess pore pressure coefficient B-bar (Bishop, 1954; Skempton, 1954). Material properties are further discussed in **Suppl. 4-1**. We choose the Mohr-Coulomb strength relations for our analyses. Cohesion, Phi, and Unsaturated Unit Weight are provided with a standard deviation for the probabilistic analyses so they could be considered random variables. The variation of these properties is used directly to establish the variation for the random variables. Parameter values are listed in **Table 4-5**.

We use an auto refine search method to find the critical slip surfaces for given slopes measured from 90 meter resolution multi-beam bathymetry (Malwaki, et al., 2001). For sampling during the probabilistic search, we use latin-hypercube sampling, with the

"Global Minimum" strategy (Saucier, 2000). Random numbers are generated using the Park and Miller v.3 method (using a random number seed based on the time the analysis is run). Sensitivity Analysis is used to test the convergence of the latin-hypercube sampling to determine the minimum sample size. The latin-hypercube method gives similar results to a Monte Carlo sampling technique, but with fewer samples (Saucier, 2000).

Table 4-5.1 Material Weight

Grain Sediment Density[1]	Dry (Unsaturated) Unit Weight[2]	Void Ratio	Saturated Unit Weight[3]				
Gs	γ_{dry}	e	γ_{sat}	γ_{sat} std dev	min	max	distr.
g/cc	kN/m3		kN/m3				
2.575	7.35	2.61	15.90	1.11	3.33	3.33	normal

1. Sediment Grain Density as measured in sediment cores from the Indian Ocean (Anderson, 1971).
2. Dry Unit Weight as calculated from Gs, γ_{dry}, and e.
3. Saturated Unit Weight as measured in sediment cores located near the base of the slope offshore Sumatra (Sultan et al., 2009).

Table 4-5.2. Material Strength

Strength Type[1]	Cohesion[2]					Angle of Internal Friction[3]				
	c' mean	c' std. dev.	min	max	distr.	ϕ mean	ϕ std. dev.	min	max	distr.
	kPa					degrees				
Mohr-Coulomb	5.55	2.6	5	5	normal	27.1	4.10	12.3	12.3	normal

1. Strength Type, where shear stress $\tau = c' + (\sigma'_n \times \tan\phi')$
2. Cohesion, as a function of shear strength, measured from uppermost sections of sediment cores (Hempel, 1985; Sultan et al., 2009; Johnson et al., 2012)

Table 4-5.3. Pore Pressure

Specific Weight Sea-Water	Excess Pore Pressure[1]	Initial Pore Pressure$_2$
γ_w	B-bar	Hu
kN/m3		
10.3	1	1

1. Excess pore pressure is determined from seismic load, where B-bar is defined by the relation $\Delta u = B\Delta\sigma_v$. B-bar is the overall pore pressure coefficeint for a meterial (Skempton, 1954)
2. Pore pressure coefficient Hu is based on the inclination of the water surface above any given point. Hu = 1 indicates hydrostatic conditions.

Table 4-5.4. Seismic Load

Horizontal EQ Acceleration					Vertical EQ Acceleration					Correlation Coefficient
Ah	Ah std dev	min	max	distr.	Av	Av std dev	min	max	distr.	
g					g					
1	0.5	1	1	normal	1	0.5	1	1	normal	0.5

Typical sample size tends to be around 10,000, but may be as high as 100,000 and low as 5,000. We use a sensitivity analysis to determine the sample size sufficient to converge the FOS results. We constrain the slices to 100 and use a Half Sine interslice force function. Excess pore pressure generated by seismic forces contributes to the balance of forces with a pore fluid weight of 10.3 kN/m^3 (for sea water; Rocscience, 2013).

We calculate the static FOS for all forty-nine sites to test the stability of sites without a seismic load, then we apply a seismic load of 1 g, both vertical and horizontal. GMPE models use higher order terms in their attenuation relations that produce saturation of ground motion with magnitude. This allows their relations to reflect the strong motion records from large magnitude earthquakes in Peru (Rodriguez-Marek et al, 2010), 2010 Chile (Boroschek et al., 2012) and 2011 Japan (Zhao et al., 2012; Abrahamson et al., 2014). These earthquake records provide magnitude saturation limits for our assumption of 1 g maximum acceleration (Stewart et al, 2013). The seismic loads are considered as random variable with a standard deviation for probabilistic analyses. Seismic forces are defined as a product of the seismic coefficient and the slice weight and are applied to the centroid of the slice. We choose a correlation coefficient for horizontal and vertical loads with a value of + 0.5, making the assumption that the sense of loading (positive or negative) is the same for both loads (horizontal and vertical).

We choose 1 g as a conservative seismic load based on the scaling of ground motion predictions regressed by Zhao et al. (2012) which include strong motion records from the 2011 March 11 Mw 9.0 Tohoku-Oki earthquake. Considering some of the sites may have excessive accelerations (up to 2.73 g; Furumura et al., 2011), we choose a conservative estimate of maximum acceleration based on their model shown in their figure 1. We take their figure and visually extend their regressed trend to shorter fault distances (**Fig. 4-15**). Zhao et al. (2012) plot their best fit regression with a concave up shape, with an increasing PGA at a fault distance of 45 km. Their 2006 paper (Zhao et al., 2006) data are plotted in red to a fault distance of 20 km. We extend these trends in red with lines in orange. While their data suggest larger accelerations (we extend their 2012 best fit line as an orange dashed line), we take this best fit line and assume the acceleration will saturate near 1 g (Skarlatoudis et al., 2012; Stewart et al., 2013). Our extension of their best fit line is plotted in solid purple in **Fig. 4-15**. Earlier models may have under-predicted PGA at short fault distances due to the smaller earthquake catalogs used in their regressions.

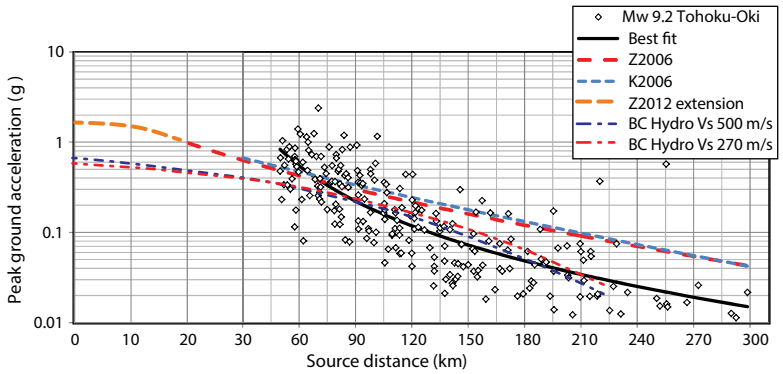

Figure 4-15. Peak ground acceleration vs. distance. Strong motion data from the 11 March 2011 Tohoku-Oki earthquake are plotted as diamonds (Zhao et al., 2012) and ground motion predictions are plotted (Zhao et al., 2006 and 2012; Kanno et al., 2006; Abrahamson et al., 2014), modified from Zhao et al., 2012. Hypothetical extension of the mean regression line (Zhao et al. 2012) is plotted as an orange dashed line.

Method of Slices solutions that consider both force and moment equilibrium are considered "rigorous" and the Morgenstern and Price method (Morgenstern and Price, 1965) is implemented in our analyses (Loukidis et al., 2003). Forces included in this method are displayed in **Fig. 4-16** (Chowdhury, 2010, their figure 5.8). Pw refers to pore water pressure, E designates interslice normal forces, T designates interslice shear force, weight of the slice = dW, dS is the mobilized shear stress, while x and y terms define the slice geometry (y – yt designates the vertical position of the interslice forces). The slip surface in this figure is given an "arbitrary" shape because the slip surface may not be approximated by a circular shape (Chowdhury, 2010).

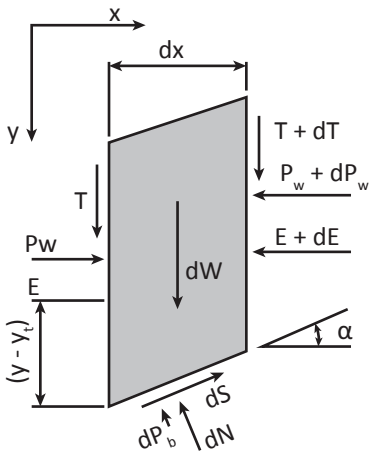

Figure 4-16. Force and Mass balance diagram. This illustrates a unit slice, modified from Chowdhury (2010). Key components include the balance between adjacent blocks and the underlying slope material. Units are defined in the text.

We finally perform a series of calculations for these 2-D profiles in order to estimate the critical seismic load required to make the slopes unstable. We do this iteratively, beginning at larger accelerations, lowering the seismic load incrementally, until the FOS is less than one. We determine the critical acceleration with a 0.01 g resolution.

4-3 Results

Regional static FOS analyses show that resisting forces are greater than downslope driving forces along the majority of slopes for both infinite slope and method of slices methods. Ground motion estimates range from 0.4 to 1.6 g (PGA) and 0.4 to 150 m/s (AI). When these seismic loads are applied to these regional infinite slope analyses, an increasing proportion of slopes are pseudostatically unstable with increasing seismic load. This is also true for site scale FOS analyses (**Fig. 4-17)**. Critical acceleration derived for these site scale 2-D FOS analyses were between 0.01 and 0.12 g.

4-3.1 Ground Motions and Infinite Slope FOS for Generic Earthquakes

We summarize the PGA, AI, Ac, and Dn for sites considered for the site scale analyses (**Table 4-6**). These data are from locations collocated with the site-scale FOS analyses locations (the location is chosen as the centroid for the 2-D profiles used in the method of slices analyses). We choose these locations because they represent the slopes that possibly contribute to sediments deposited at our core locations, rather than data associated with the core locations themselves. Mean PGA for the four seismic loads increase from 0.6 to 1.5 g. Mean AI range from 2 to 40 m/s. The mean Ac for all sites is 3.0 g. We plot modeled ground motions PGA and AI for four earthquake magnitudes vs. forearc distance and Rdist (**Fig. 4-17**). Decay in ground motion with distance (distance attenuation) matches that plotted in **Figs. 4-5 and 4-6**.

We plot PGA and AI for four earthquake magnitudes 6, 7, 8, and 9 (**Fig. 4-18**). Increasing ground motion is represented by darker green and is divided into five intensity magnitude bins. Increases in PGA and AI are consistent with the fault geometry we created for these analyses. Locations nearest the trench reveal that in the southern margin, Rdist is closer to the seafloor due to the southerly decrease in sediment thickness overlying the oceanic crust. This is particularly evident for plots of M 6, where the width of the largest size class (darkest green) is wider in the southern margin (on the right) and non-existent in the northern margin (on the left). This observation can be made for both PGA and AI.

Table 4-6. Regional slope stability statistics for Newmark Displacement, Critical Acceleration, PGA, and AI.

	Critical Acceleration [1]	PGA [2]				AI [3]			
	g	g				m/s			
	Ac	Mw6	Mw7	Mw8	Mw9	Mw6	Mw7	Mw8	Mw9
min	0.6	0.4	0.7	1.1	1.4	0.4	2	5	8
max	9.5	1.0	1.3	1.5	1.6	8	35	95	150
mean	3.0	0.6	1.1	1.4	1.5	2	9	25	40
std dev	1.5	0.1	0.1	0.1	0.0	1	6	17	28

	Static FOS [4]	Jibson Newmark Displacement [5]							
		Equation 9				Equation 10			
		cm							
	FOS	Mw6	Mw7	Mw8	Mw9	Mw6	Mw7	Mw8	Mw9
min	1.0	0.1	0.1	0.1	0.1	0.1	0.1	0.1	0.1
max	1.0	1	21	38	40	2	24	38	38
mean	1.0	0.1	1	1	2	0.1	1	1	1
std dev	0.0	0.1	3	6	6	0.3	3	5	6

1. Critical Acceleration (Wilson and Keefer, 1983, 1985; Jibson et al., 2000)
2. Peak Ground Acceleration (Zhao et al., 2006)
3. Arias Intensity (Travasarou et al., 2003)
4. Static FOS (Jibson et al., 2000)
5. Newmark Displacement (Jibson, 2007)

For earthquake magnitude 7, many collocated slope core sites exceed 1 g PGA, but there are a few collocated trench core sites that exceed 1 g. However, for earthquake magnitude 8, most all slope core sites exceed 1 g PGA, along with many trench sites. Most all slope and trench core sites exceed 1 g PGA for earthquakes of M = 9. AI relations show a similar relation to earthquake magnitude.

We query the ground motion results limited to areas upslope of some core sites in order to evaluate the shaking intensity (energy) content for the slopes above these core sites. We delineate these potential sedimentary source areas with orange polygons in **Fig. 4-19**. Sedimentary source areas (orange) were determined by outlining drainage divides surrounding all submarine topography contributing potential gravity flows to a given core site. We limit these results to slope cores because their sources are more certainly estimated, while trench core source areas may extend up slope from within the trench. We also limit these results to cores in the 2004 region so that we may compare the ground motions from generic earthquakes with the ground motions from the 2004 SASZ

earthquake and the sediments found in cores from this region. We plot slope versus Rdist for these four source areas to show the range in slope angles and distances to the megathrust fault (**Fig. 4-19**).

We plot our calculations of PGA and AI versus slope angle for core sites in **Fig. 4-19** for earthquakes of magnitude M = 6, 7, 8, and 9 in **Fig. 4-20**. For generic subduction zone interface earthquakes, PGA values are in magnitude limited groups with narrow ranges of intensity for each earthquake magnitude. For these generic earthquakes, AI values are generally also in distinct groups, but the ranges for M = 8 and M = 9 earthquakes have some overlap. While the PGA range decreases with earthquake magnitude, the AI range increases with earthquake magnitude.

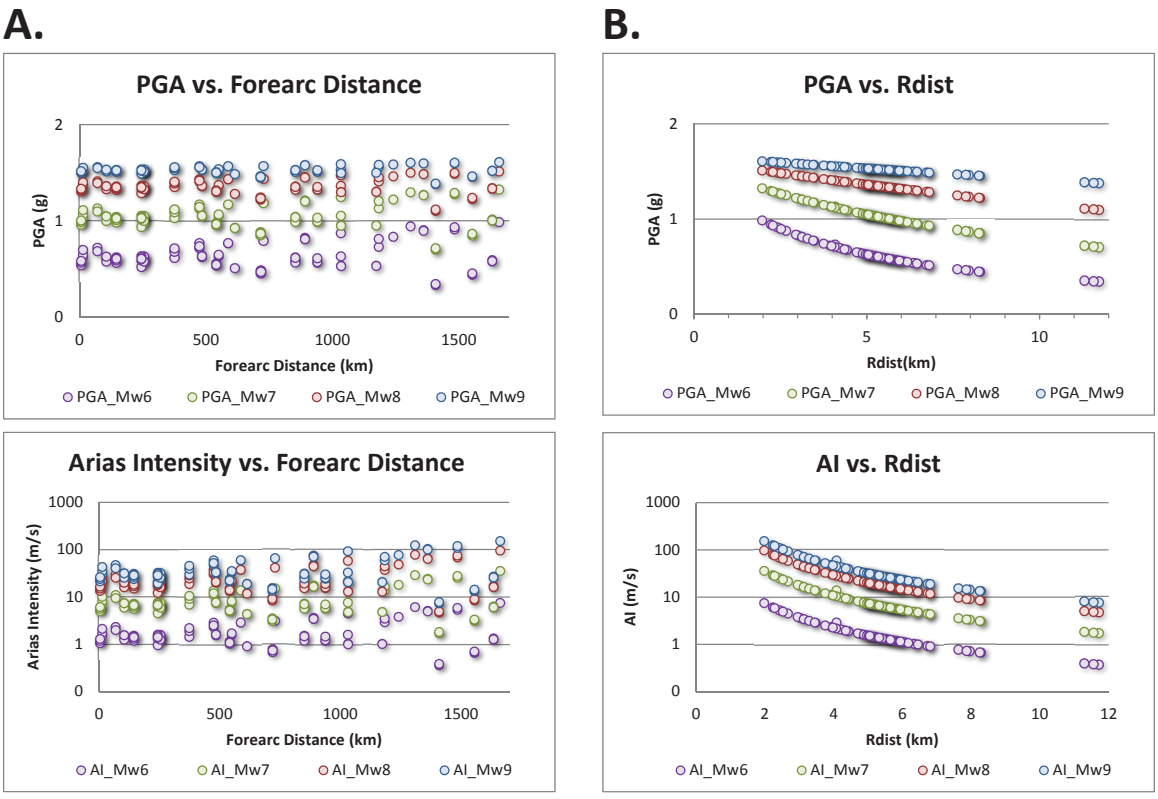

Figure 4-17. Modeled ground motions measured at sites plotted in Figure 4-14. These sites are plotted, magnitudes are displayed in color (M = 6, 6, 7, and 9 are purple, green, orange, and blue). A. PGA and AI are plotted vs. forearc distance, the distance along the subduction zone trench measured from the northernmost extent of multibeam bathymetry used in this paper. B. PGA and AI are plotted vs. Rdist, the distance from the sites to the fault.

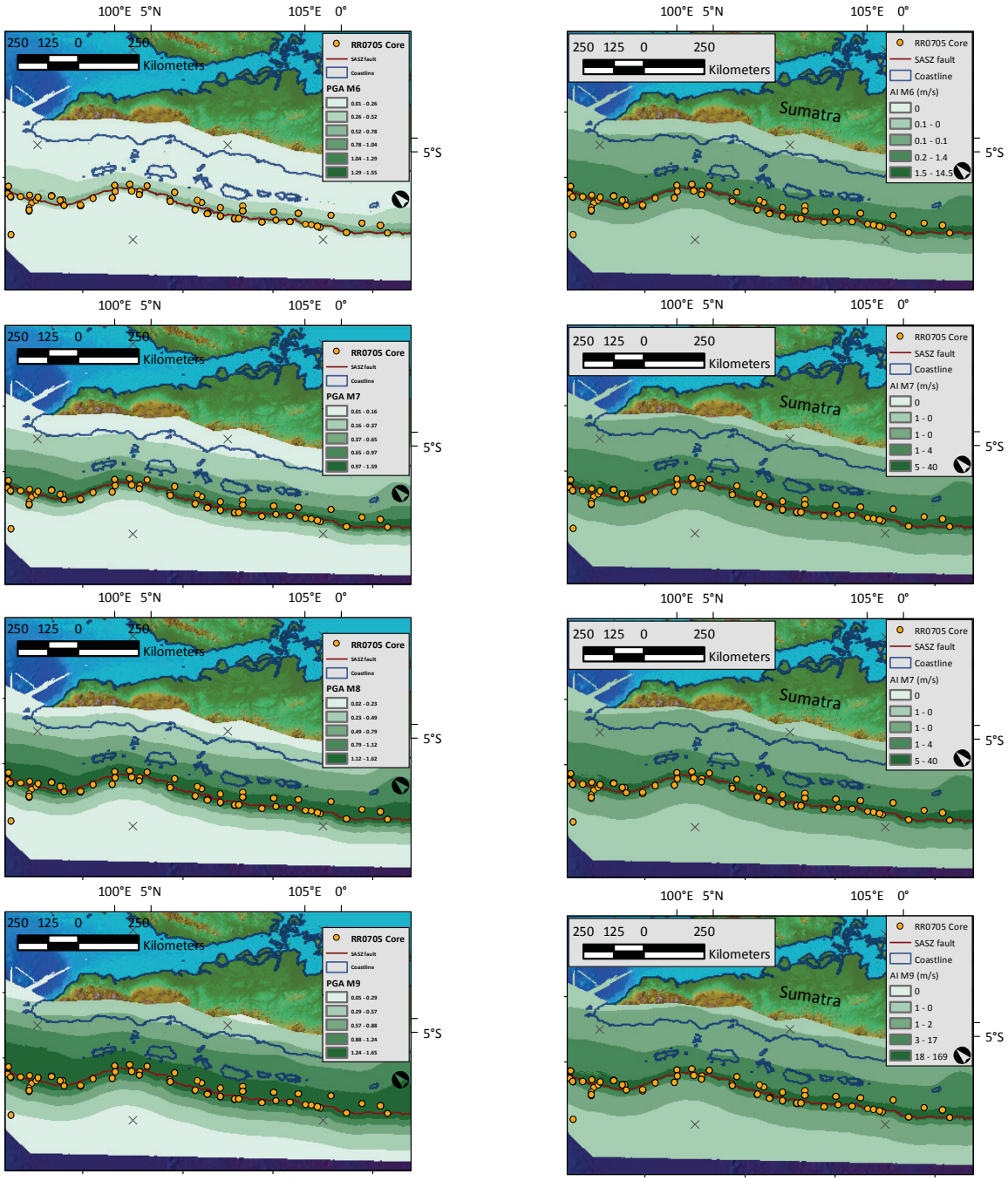

Figure 4-18. PGA and AI are plotted for four earthquake magnitudes 6, 7, 8, and 9. (Travasarou et al., 2003; Zhao et al., 2006). A. PGA results are placed in five linearly spaced equal bins of increasing magnitude as darker green. B. AI results are placed in five $\log_{10}$ spaced bins of increasing magnitude as darker green.

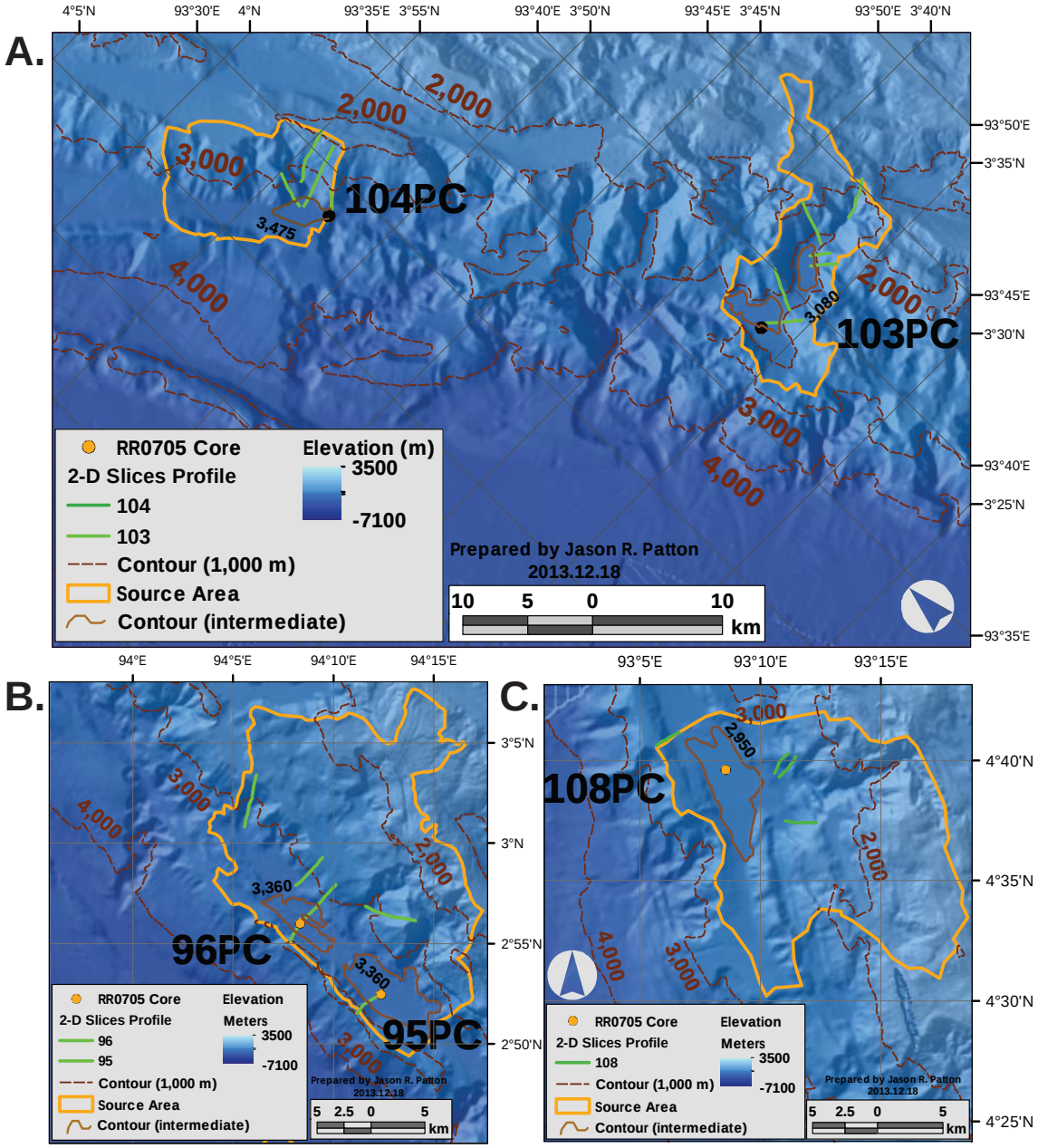

Figure 4-19. Source area site maps. Source areas for sediment that may deliver submarine landslides to some core sites. Slope basin and trench source areas (orange) were determined by outlining drainage divides surrounding all submarine topography contributing potential gravity flows to a given core site. Green and blue lines show the location of profiles we use for our 2-D FOS analyses. A. Shaded relief map showing sore sites 103 and 104 plotted as orange dots. Intermediate contours of 3,475 m and 3,080 m depict the shape of the basins. B. Core sites 96 and 95 are plotted as orange dots, with the seawater depths (3,400 and 3,420 m respectively). Elevation contours are in meters. Intermediate contours of 3,360 m and 3,340 m depict the shape of the basins. C. Core site 108 is plotted with an intermediate contour (2,950 m) in brown. D. For these core sites, we plot Slope (degrees) versus Rdist (m), with colors and outline patterns associated with each site.

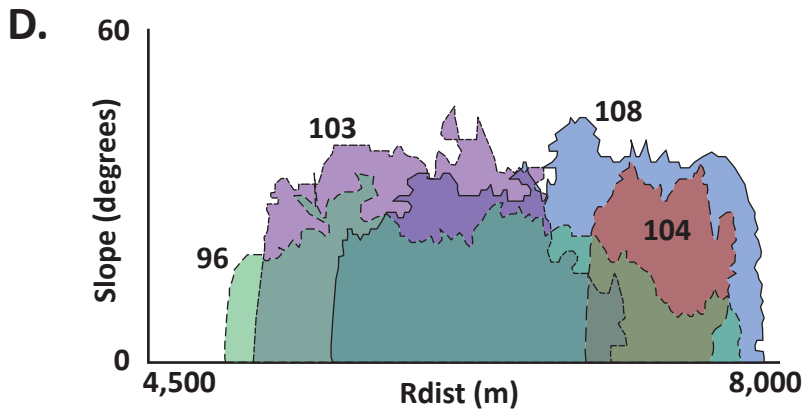

Fig. 4-19 cont.

Summary statistics for FOS analyses are listed in **Table 4-6.** Static FOS results show that almost all core sites and site-scale sites are stable (FOS ≥ 1). Newmark Displacement for earthquakes M = 6 are negligible, larger magnitudes have sufficient energy to destabilize slopes above most core sites. The maximum Newmark Displacement for these sites ranges from 1 to 40 cm.

Two core pairs are used for locations to evaluate the variation in ground motion with earthquake magnitude; cores 104 and 103 (including 102, collocated with 103) and cores 96 and 95. We select these cores sites 103 and 104 since they have slopes with similar distances to the megathrust and similar shaking intensity from the 2004 SASZ earthquake. We compare the 103 and 104 site source areas with the core 96 site source area because these sites represent regions that are have different 2004 SASZ earthquake shaking intensities and the 2004 seismoturbidite thicknesses are also different. The 2004 seismoturbidite is ~350 cm thick in core 96 and ~6 cm thick in 102. We will later discuss the consequences of these differences. **Fig. 4-21** shows the static FOS for slopes adjacent to adjacent to these core sites. **Figs. 4-22 and 4-23** show the pseudostatic FOS based on four earthquake magnitudes 6, 7, 8, and 9 using three models at the two core site regions displayed in **Fig. 4-21**: Jibson (2007) equation 9, Jibson (2007) equation 10, and Hsieh and Lee (2011).

4-3.2 Ground Motions and Infinite Slope FOS for the 2004 SASZ Earthquake

We model pseudostatic slope stability by applying the Sorensen et al. (2007) seismic loads and find an increase in pseudostatic slope stability, concomitant to the decrease in

PGA and PGV with distance from the epicenter of the 2004 SASZ earthquake. With short epicentral distance, all slopes are unstable. With greater epicentral distance, only steeper slopes are unstable (**Fig. 4-24**).

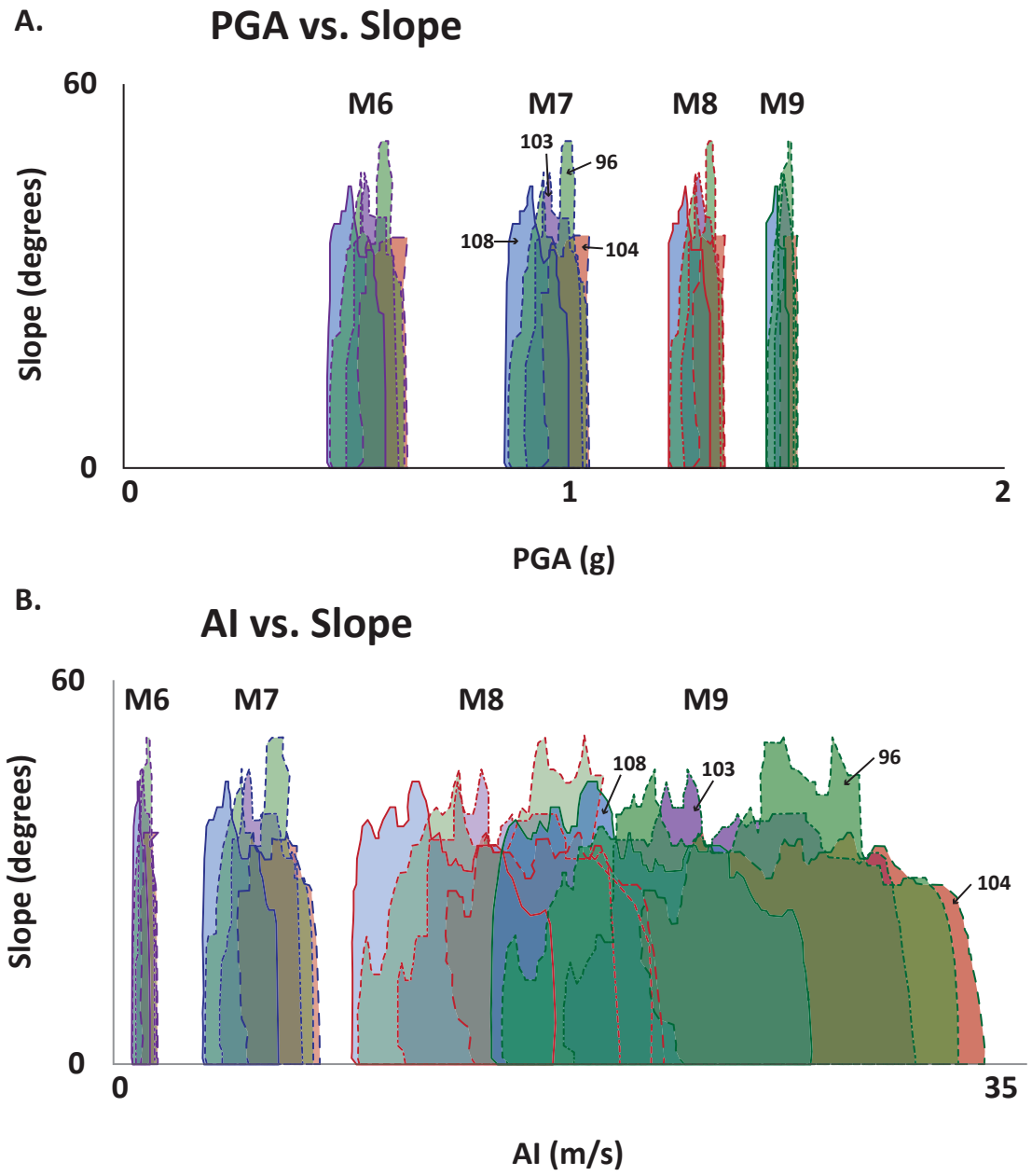

Figure 4-20. Ground motion contributions to core site source areas. We plot envelopes of A. PGA (g) and B. AI (m/s) versus slope (degrees) for four earthquake magnitudes M = 6, 7, 8, and 9 with purple, blue, red, and green outlines respectively. We use different line symbols for four slope cores 96, 103, 104, and 108 with fill colors green, purple, red, and blue respectively.

In **Fig. 4-25** we plot the 2004 SASZ earthquake PGA modeled by Sorensen et al. (2007) versus slope angle for core sites in **Fig. 4-19**. Slopes contributing to sediments in core 96 has the lowest range of PGA and core 108 has an intermediate PGA content. Slopes upslope of cores 103 and 104 have PGA content that overlaps and have the largest PGA ranges of these cores. Of the 15 cores that we hypothesize to contain the 2004 seismoturbidite, only two cores appear to have the entire deposit. The thickness of this

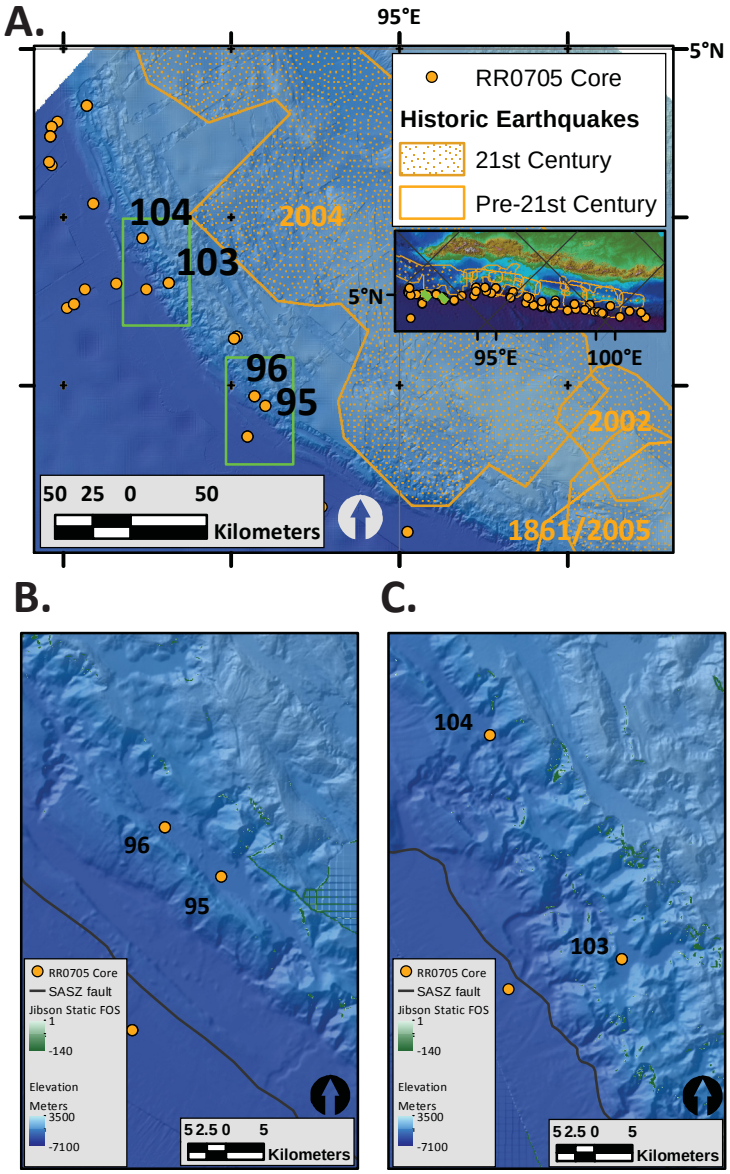

Figure 4-21. Static FOS slope stability maps. Results for two regions near fault slip during the 2004 SASZ earthquake. A. Cores as they relate to the 2004 SASZ earthquake (Chlieh et al., 2007). B. Cores 95 and 96. C. Cores 104 and 103.

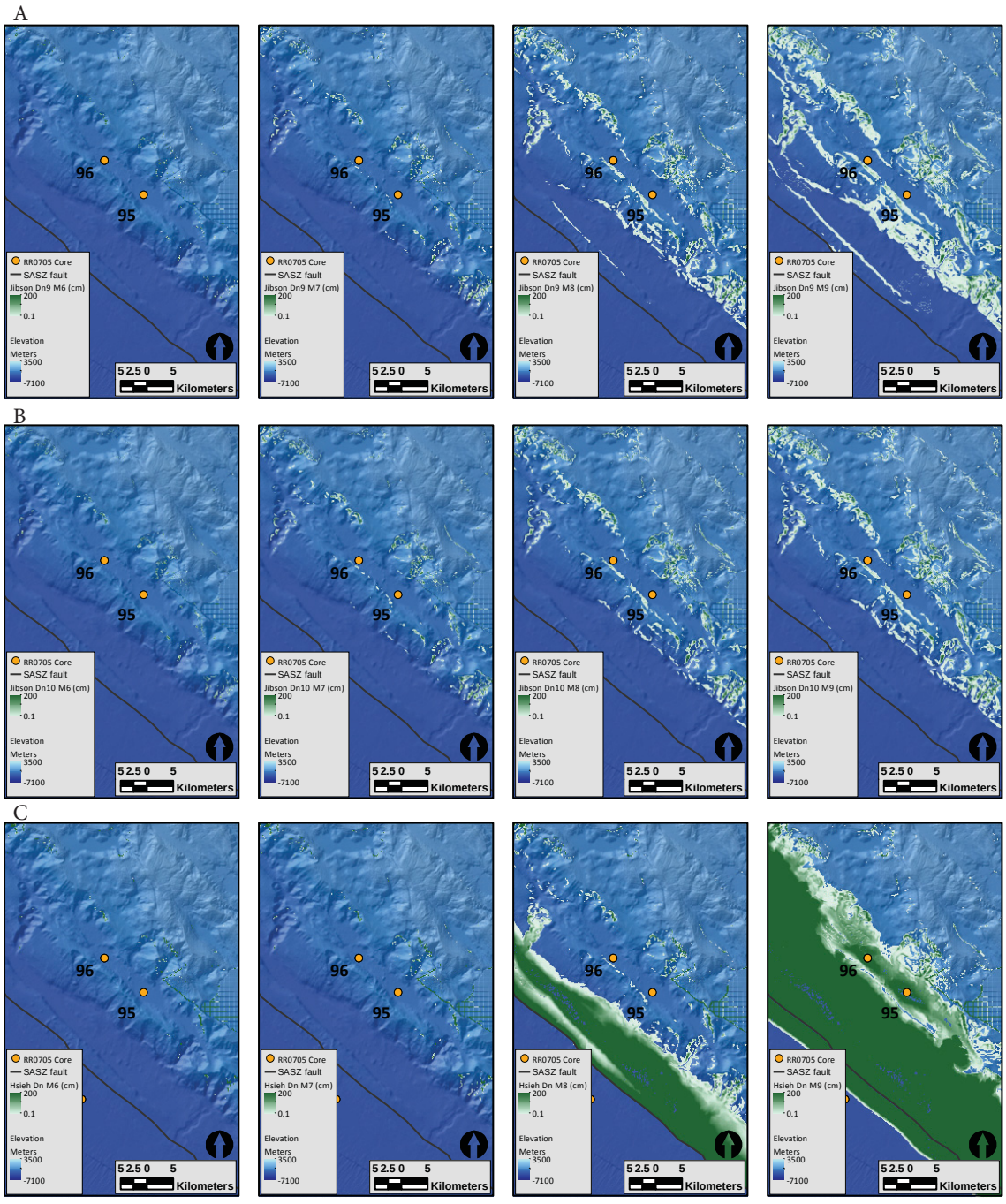

Figure 4-22. Slope stability for regions surrounding cores 96 and 95. Results are plotted in relation to a series of slope stability analysis results, each series is plotted with the same relations: (A) pseudostatic FOS equation 5, (B) pseudostatic FOS equation 6, (C) pseudostatic FOS equation 8 for earthquakes of magnitude M = 6, 7, 8, and 9 (left to right). Cores are plotted as orange dots. FOS is displayed with increasing instability with darker green. Stable FOS > 1 is transparent.

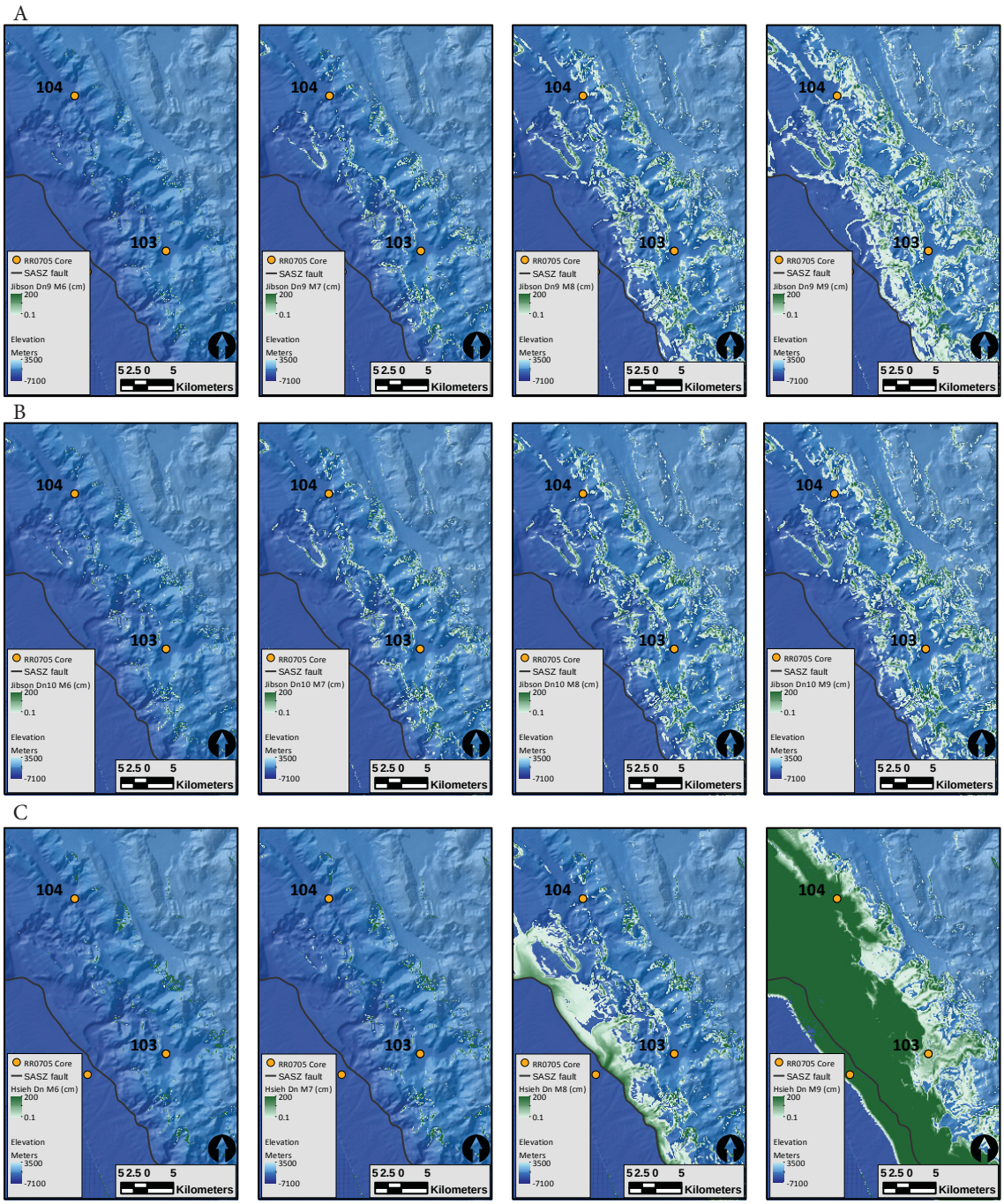

Figure 4-23. Slope stability for regions surrounding cores 104 and 103. Results are plotted in relation to a series of slope stability analysis results, each series is plotted with the same relations: (A) pseudostatic FOS equation 5, (B) pseudostatic FOS equation 6, (C) pseudostatic FOS equation 8 for earthquakes of magnitude M = 6, 7, 8, and 9 (left to right). Cores are plotted as orange dots. FOS is displayed with increasing instability with darker green. Stable FOS > 1 is transparent.

uppermost turbidite in the composite core 96 PC/TC is in excess of 3 meters, though only 6 cm thick in core 102MC, which was collected at the same site as 103. We cannot consider the thickness of the deposit at other core sites since the tail of the turbidite is missing in these other cores.

4-3.3 2-D Profile FOS: Method of Slices

All profiles (but one) show a static FOS above one and all profiles show a FOS less than one for seismic load of 1 g. Probability of failure with a seismic load of 1 g was above 99.65% for all forty-nine sites. The mean static FOS is 1.32 ± .29 and the mean 1 g FOS is 0.01 ± 0.01 (1 sigma).

We evaluated parameter space for variables of cohesion, sediment unit weight, and angle of internal friction along with Rdist and Mw. Distance to the fault plane (Rdist), slope, and Mw were much larger contributors to FOS values than the material properties (**Fig. 4-26 and 4-27**). We present the results from all of our analyses in **Appendix 4-2**.

We list a statistical summary of results for our critical acceleration estimates in **Table 4-7**. From left to right we list the critical acceleration (FSac, g), FSac (deterministic), FSac (mean), PFac, and some ratios that compare residuals between the static and critical seismic acceleration FOS with the static and critical seismic acceleration FOS. Critical acceleration is the magnitude load required to make a 2-D slope profile unstable (FOS < 1). FS refers to the factor of safety. Deterministic refers to the factor of safety for one slip surface, the global minimum slip surface (the least stable of all calculated slip surfaces). The mean factor of safety is the mean of the factor of safety for all slip surfaces. PF refers to the probability of failure, where the number of failed slip surfaces are divided by the number of total slip surfaces.

We will later evaluate the relations between static and seismic factor of safety, as they relate to the critical seismic acceleration with the next series of results. FSac/FSstatic is the ratio between the critical seismic acceleration and static factor of safety for each site. FSstatic-FSac/FS static is the ratio between the difference of static and critical seismic acceleration factor of safety divided by the static factor of safety. FSstatic-FSac/FSac is the ratio of the same difference divided by the critical seismic acceleration factor of safety. These critical acceleration data are plotted versus profile number and core number in **Fig. 4-28**. Sites that have a higher critical seismic acceleration threshold also have

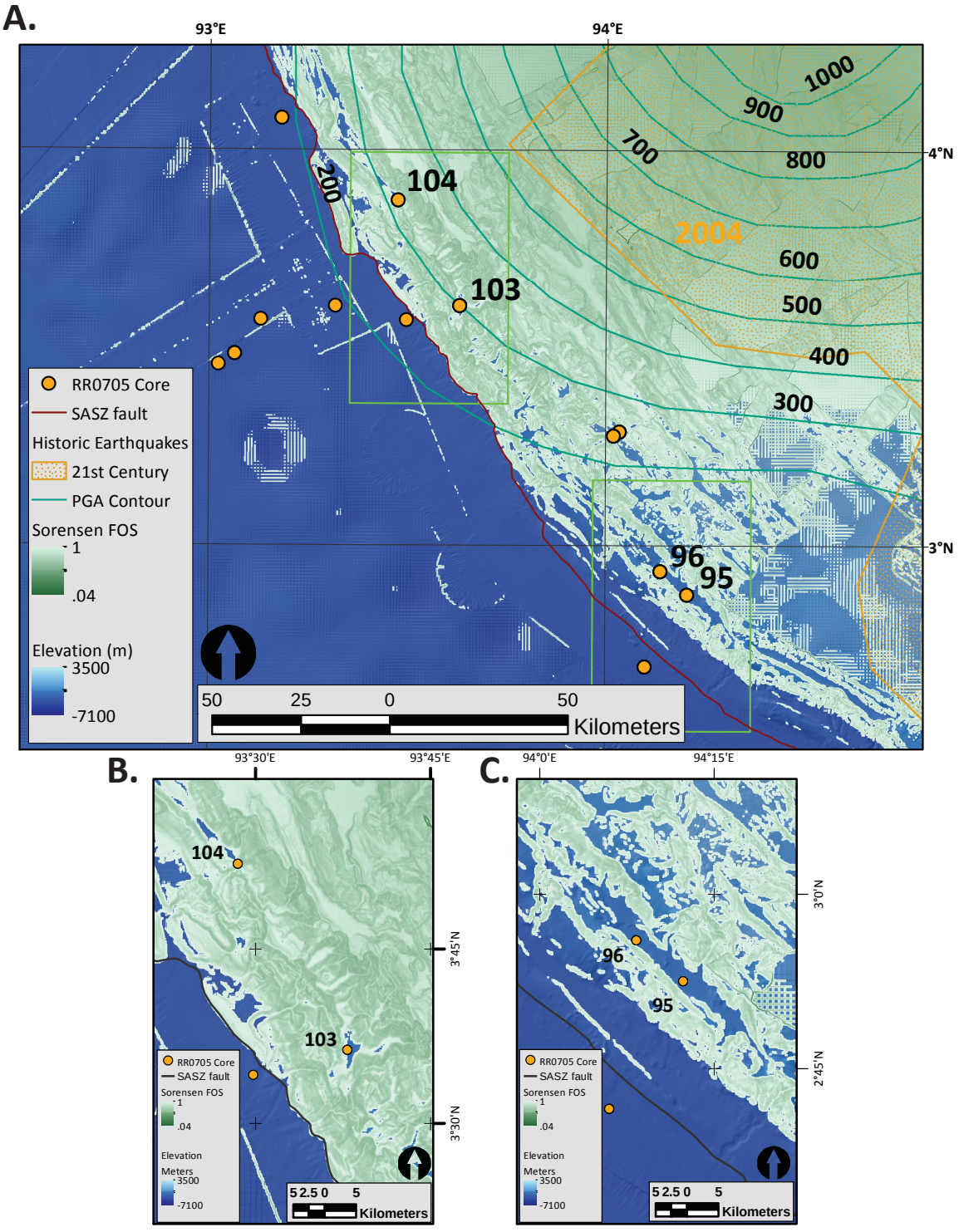

Figure 4-24. Pseudostatic FOS results for the 2004 SASZ earthquake. Results are plotted using Sorensen et al. (2007) PGA as input for seismic loads using methods of Hadj-Hamou and Kavazanjian (1985). Increasing slope instability is displayed as darker green. A. PGA (cm/s^2) is plotted as green contours (Sorensen et al., 2007). Cores 104, 103, 96, and 95 are labeled (Figure 14). The 2004 SASZ earthquake slip region is shown in orange. B. FOS for core sites 104/103. C. FOS for core sites 96/95.

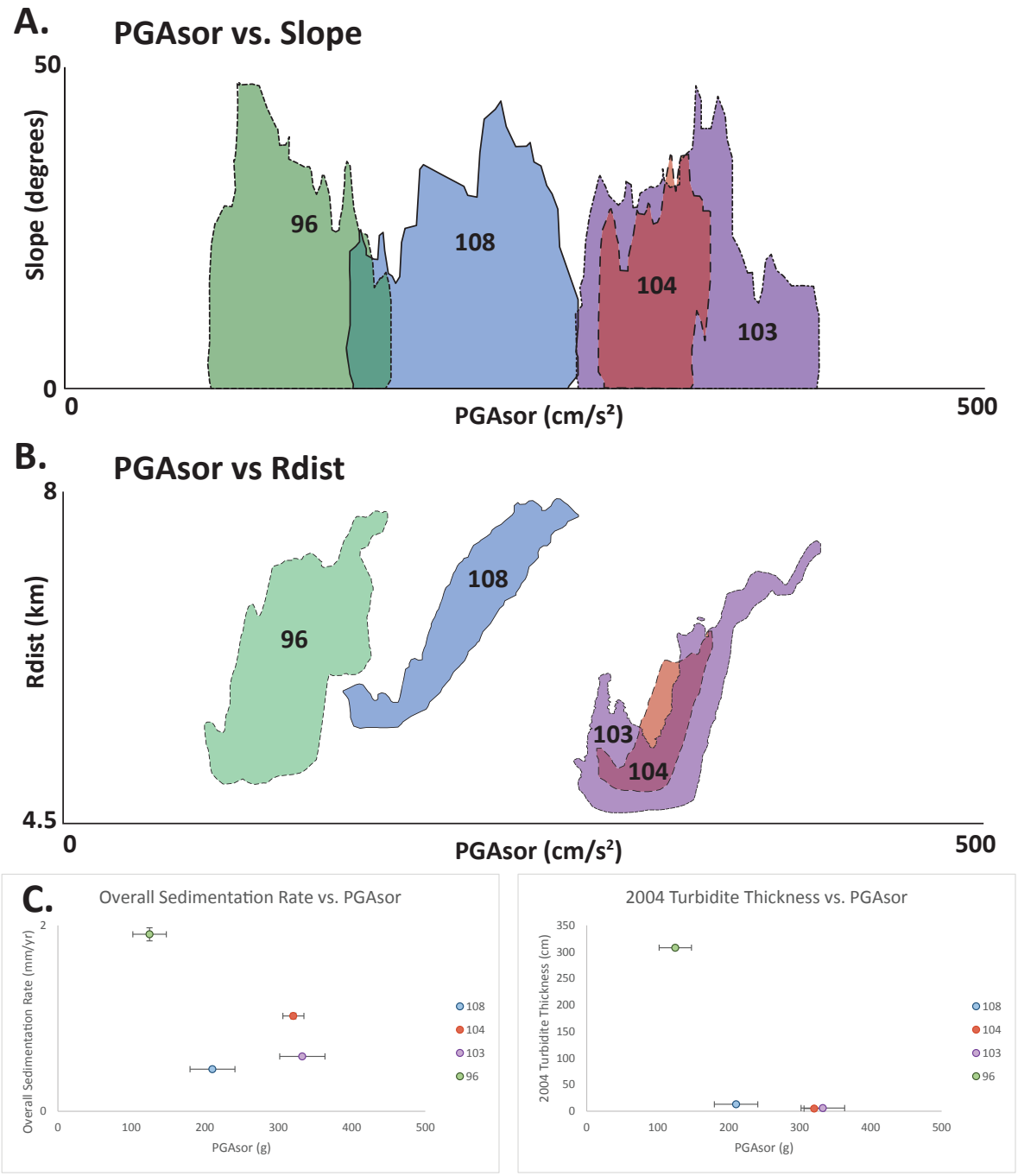

Figure 4-25. Sorensen PGA (g) vs. slope and Rdist. A. We plot envelopes of the PGA content from the Sorensen et al. (2007) model, versus slope (degrees), for cores 96, 103, 104, and 108 in green, purple, red, and blue respectively. B. We plot PGA content from Sorensen et al. (2007) versus Rdist (m). C. Overall sedimentation rate (mm per year) and 2004turbidite thickness (cm) versus PGA modeled by Sorensen et al. (2007).

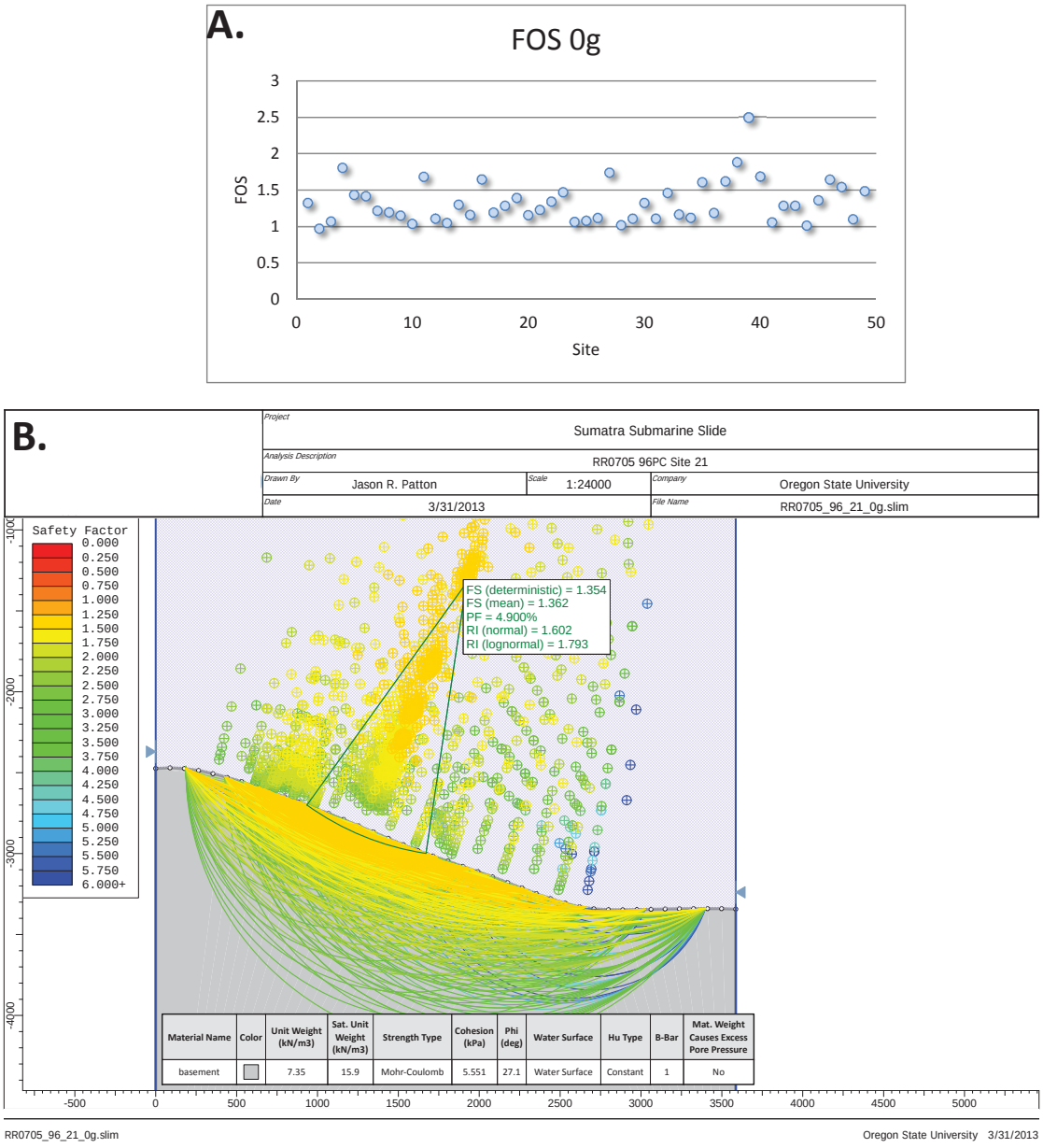

Figure 4-26. Method of Slices Static FOS results. A. The static FOS global minimum results for all sites are plotted as blue dots. B. The 2-D slope profile for site 21 above core 96 is plotted with all slide failure surfaces colored according to FOS legend on left. The global minimum surface is plotted in green and results are placed in a box oriented to the axis of rotation for the global minimum surface. Material properties are summarized in a table.

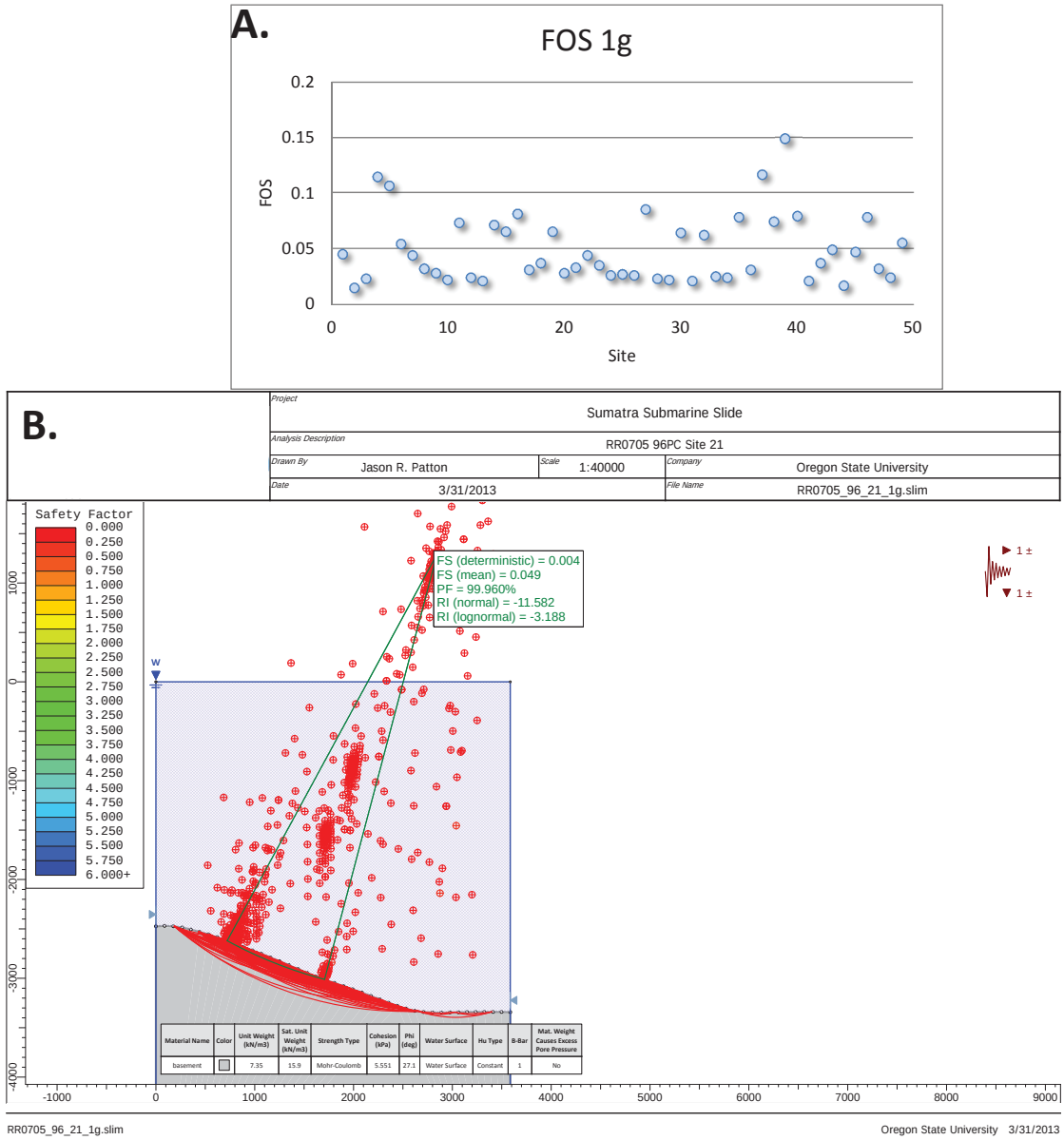

Figure 4-27. Method of Slices Seismic Load FOS results. A. The pseudostatic FOS global minimum results for all sites are plotted as blue dots. B. The 2-D slope profile for site 21 above core 96 is plotted with all slide failure surfaces colored according to FOS legend on left. The global minimum surface is plotted in green and results are placed in a box oriented to the axis of rotation for the global minimum surface. Material properties are summarized in a table.

TABLE 4-7. Critical Acceleration at Slice Profile Sites

	FSac (g)	FSac (Deterministic)	FSac (Mean)	PFac	FSac/FSstatic	FSstatic-FSac/FSstatic	FSstatic-FSac/FSac
mean	0.04	0.93	0.95	64%	0.73	0.27	0.42
std dev	0.02	0.03	0.03	5%	0.13	0.13	0.32
min	0.01	0.82	0.87	55%	0.36	0.05	0.05
max	0.12	0.98	0.99	76%	0.95	0.64	1.76

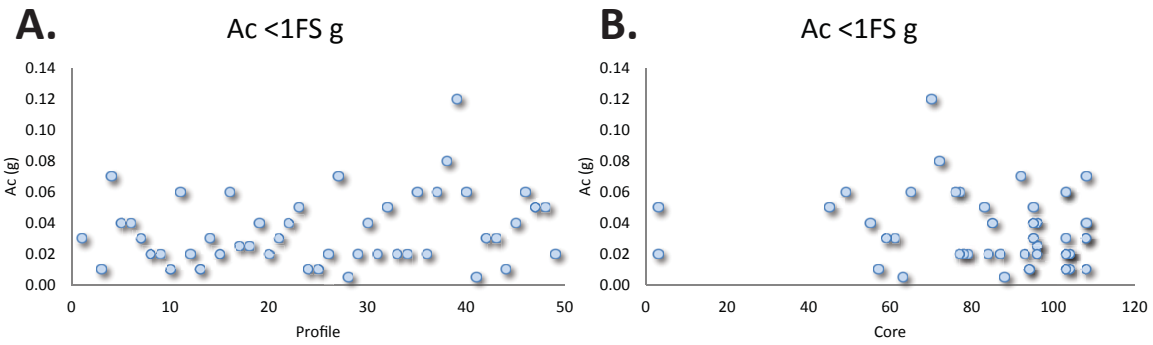

Figure 4-28. Critical acceleration for 2-D profiles. We plot the critical acceleration (g) for instability along our 2-D surface profiles vs. A. profile number and B. core number.

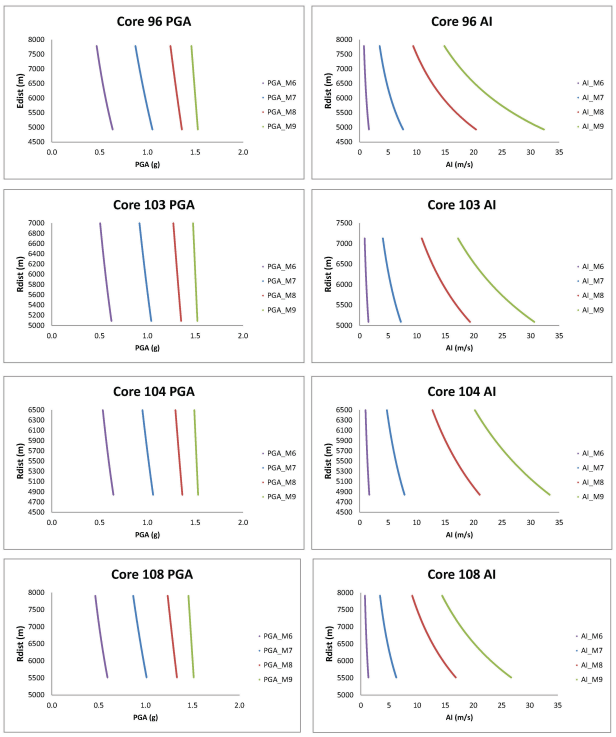

Figure 4-29. Ground motions at core site source areas. We plot A. PGA (g) and B. AI (m/s) versus Rdist for earthquakes of magnitudes M = 6, 7, 8, and 9.

a larger difference between the static and seismic factor of safety. Also, as the difference between the static and seismic factor of safety diverge, the critical seismic acceleration threshold increases. Finally, the sites that are seismically safer (lower FSac), also have a larger difference between the static and seismic factor of safety.

4-4 Discussion and Conclusion

At the bathymetric settings we evaluated offshore Sumatra, slopes that feed our core sites are stable under static conditions, yet unstable when loaded with seismic forces using reasonable Ground Motion Prediction Equation models applied to the fault model we constructed. These findings are consistent with both infinite slope and method of slices FOS analyses. Ground motions modeled for the 2004 Sumatra-Andaman subduction zone earthquake (Sorensen et al., 2007) also provide sufficient energy to drive some slopes in the region to fail, especially those sufficiently close to the earthquake slip patch. We find that during the 2004 Sumatra-Andaman subduction zone earthquake, shaking intensity for sedimentary source areas was not the primary factor controlling turbidite thickness.

4-4.1 Ground Motions

The ground motion predictions we use are limited by the source earthquakes, in their databases, that they are based upon (Petersen et al., 2004; Atkinson and Boore, 2011; Abrahamson et al., 2013). There remains a paucity of strong ground motions at near fault locations (<10 km; Atkinson and Boore, 2003), large magnitude earthquakes (> M = 8.3, Atkinson and Boore, 2003; > M = 8, Zhao et al., 2006) and site amplification factors are likely regionally variable (Stewart et al., 2013). Recently collected strong motion data from the 2011 Tohoku-Oki earthquake have yet to be fully implemented into ground motion relations (Zhao et al., 2012). Our results for Dn for earthquakes with M = 9 should consider these limitations, but we cannot due to the lack of details in the literature (Zhao et al., 2012 leave out definitions for constants “f” and “ra” in their paper).

One source of epistemic uncertainty for GMPE’s is the ability to find functions that describe the magnitude scaling (Stewart et al., 2013). Some models handle this with linear scaling terms, but when higher order regressions are used, the relations saturate with increasing magnitude (Skarlatoudis and Papazachose, 2012; Stewart et al., 2013). Accelerations measured during the Maule and Tohoku-Oki earthquakes support saturation of ground motions at large magnitudes (**Fig. 4-15**; Zhao et al., 2012; Stewart et al., 2013). The error associated with most GMPE’s ranges over an order of magnitude, which contributes to the large uncertainties for these regional analyses (Zhao et al., 2012). Considering the limitations of GMPE’s we consider, slopes are susceptible to smaller earthquakes, where the GMPE’s have a larger source of data (so are less uncertain). Given the

lack of more site specific data with regard to site effects like sedimentary basins, using GMPEs to model ground motions is still considered the best tool to make regional assessments of landslide susceptibility (Allstadt et al., 2013).

4-4.2 Slope Stability

Newmark Displacement formulations of Jibson (2007) and Hsieh and Lee (2011) show remarkable differences, especially with earthquake magnitude M = 9. Hsieh and Lee (2011) relations show a more sensitive response to earthquake magnitude than do the Jibson (2007) relations. Jibson considers logAI and logAc in equation 5 and logAc and logCAR (log(Ac/PGA)) in equation 6. Hsieh and Lee (2011) consider log IA and Ac in their relations. Critical acceleration (Ac) includes the FOS calculation, which is dependent upon material properties and slope angle. Given Jibson (2007) considers the log of Critical Acceleration, the Hsieh and Lee (2011) relations impart a greater effect due to the material properties of sediment than do Jibson (2007). This may explain the differences in our results.

Displacement along an infinite slope may not necessarily lead to slope failures. The more ductile the materials, the larger the displacement could be prior to failure (Jibson, 1993). What a sufficient displacement for any given site must be determined for each site based on assumptions about the material properties at that site. Submarine settings are more difficult to directly evaluate the geotechnical properties. Terrestrial earthquake triggered landslides provide a more direct measure of the displacement sufficient to generate failure. Wieczorek et al. (1985) found that 5 cm displacement led to slope failures in northern California. Keefer and Wilson (1989) concluded that 10 cm was sufficient for coherent landslides in arid southern California. Jibson and Keefer (1993) used a range of 5-10 cm for landslides in the Mississippi River valley. We use 5 cm as a threshold because the sediment material properties in the submarine environment may be more susceptible to failure. 5 cm is still within the range used in some subaerial settings.

Sorensen et al. (2007) do not provide a contour for 0 PGA, so it is difficult to constrain the lateral limit of slope instability. We do not have confidence with the results beyond the 200 m/sec^2 contour. We suspect that the distance between the 200 and 400 contours is a good estimate of the distance that our results can be extrapolated (~25 km), but possibly twice that distance is reasonable (~50 km). Confounding this is found in core 96PC, in which has the thickest deposit attributed to the 2004 SASZ earthquake. Given

the proximity of this core's source area, we propose that this core site may contribute to the expanded section. Core 96 is situated in the center of a basin lying between two anticlinal folds. Given that this basin does not drain to the trench, sedimentary thicknesses may be increased here.

Material properties remain a large source of aleatory uncertainty in our analyses. While there are geotechnical data from sediments in the region where our cores are located, little is known about the variation of these geotechnical properties at distances from the source cores (Sultan et al., 2009). The two key factors, cohesion (shear strength) and angle of internal friction, are important factors, but Rdist and earthquake magnitude have a much more strong control on Newmark Displacement (the Ac coefficient is negative in the Jibson, 2007 relations, but has terms of both sign in Hsieh and Lee, 2011). Materials that behave visco-elastically may attenuate ground shaking more rapidly, so our results may be slight overestimates (Jibson, 1993; Jibson et al., 1994).

Sites that have a higher critical seismic acceleration threshold also have a larger difference between the static and seismic factor of safety (**Fig. 4-30**). Also, as the difference between the static and seismic factor of safety diverge, the critical seismic acceleration threshold increases. Finally, the sites that are seismically safer (lower FSac), also have a larger difference between the static and seismic factor of safety. These results make sense because slopes that are steeper would require lower levels of seismic acceleration to generate displacement.

4-4.3 Ground Motion and Sediment Cores

We compare shaking intensity upslope from selected core sites for generic earthquakes and for the 2004 SASZ earthquake (Sorensen et al., 2007). **Fig. 4-19 D** shows how the slope distribution and Rdist ranges vary for the four slope basin sites. Source areas for cores 103 and 104 are spatially close, and have a similar range in slope angles, but do not have an overlapping range in Rdist. Core 104 has a higher overall sedimentation rate than core 103, which is anti-correlated with Rdist. Something other than Rdist must be responsible for the difference in sedimentation rates.

For a PGA and AI applied during a generic earthquake, each site has a similar capacity to shake with intensity related to Mw (**Fig. 4-20**). Therefore, if there is a difference in site response at these regions, it is not due to Rdist, but the spatial relation to slip distribu-

tion and site effects (geomorphology, **Fig. 4-25**). For the 2004 SASZ earthquake, the PGA content for four slope basin core sites reflects directly the distance to regions of larger slip (**Fig. 4-24**). However, for the 2004 SASZ earthquake, shaking in source areas has an inverse relation to turbidite thickness (**Fig. 4-25 C**). Even though each source area may have a range of shaking intensities related to heterogeneous slip on during megathrust earthquakes, the site effects may be more significant factors controlling the thickness of turbidites.

Ranges in PGA and AI shaking intensity for generic earthquakes are different, AI range increases with increasing earthquake magnitude and PGA range decreases with increasing earthquake magnitude. For four core sites (**Fig. 4-19**), we plot PGA and AI versus Rdist for earthquakes of magnitude M = 6, 7, 8, and 9 (**Fig. 4-29**). The shape of the attenuation curves drives the distribution (range) of ground motion intensity for each of these four core sites potential source areas (**Fig. 4-30**).

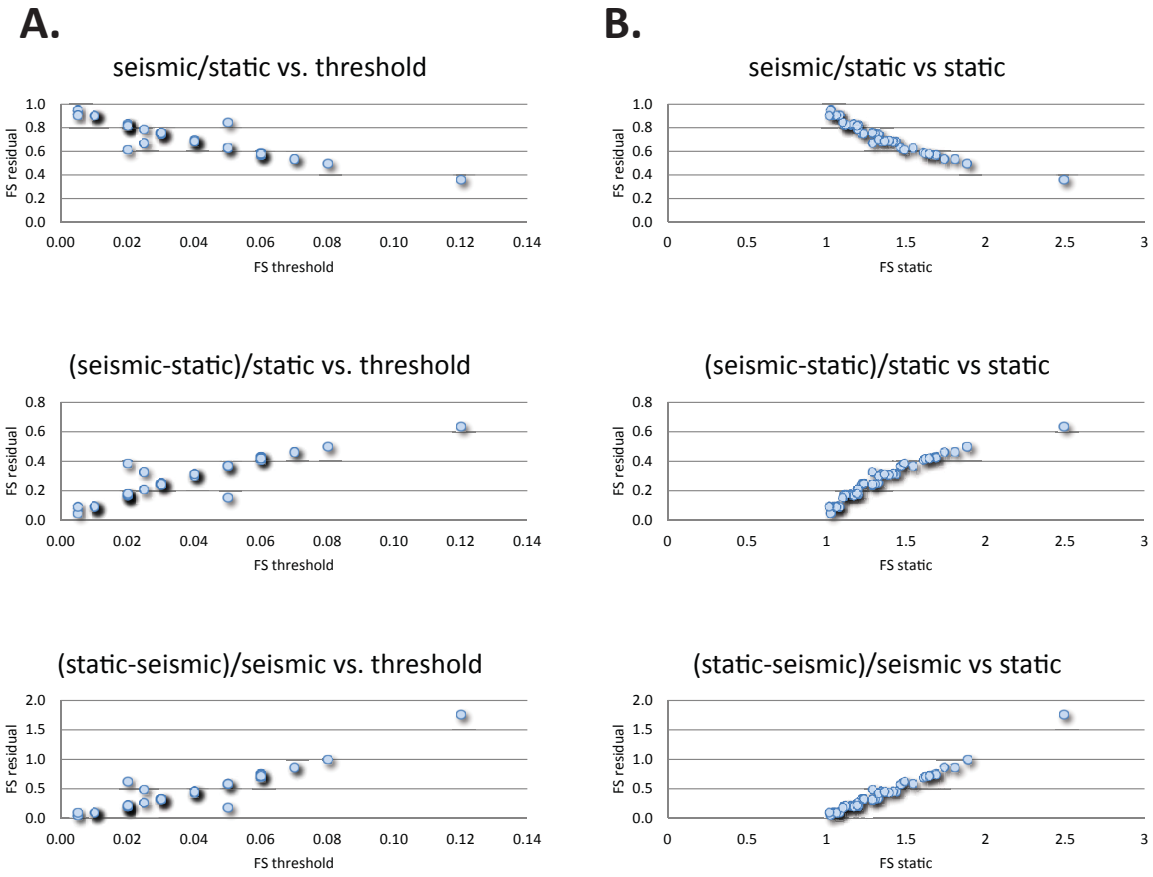

Figure 4-30. 2-D slices FOS seismic-static ratios. We plot various residuals for differences between static, seismic, and thresholds for FOS. A. FS residual vs FS threshold. B. FS residual vs. FS static.

Ground shaking along the continental slope offshore Sumatra is a function of distance to the fault (Rdist) for generic earthquakes and for the 2004 SASZ earthquake. Landslide dimensions may relate to Mw and Rdist, but are probably dominated by site conditions for some earthquakes. Estimates of ground motion depend upon the shape of the attenuation curve (PGA vs. AI) versus Rdist, the smaller the distance to the earthquake slip, the wider range in AI and shorter range in PGA.

4-4.4 Future Directions

There remain some improvements that could be made to decrease epistemic and aleatoric uncertainty in these analyses. Some of these improvements are unattainable. The assumption of a stochastic fault source can be modified based on the geodetic analyses that have been used to invert GPS data into plate locking or coupling ratio (Chlieh et al., 2008; Prawirodirdjo et al., 2010). Assuming earthquake slip is heterogeneous and collocated with patches of higher coupling ratio, these zones of “locking” may provide better insight towards potential seismic slope stability. The application of heterogeneous slip to new GMPEs, that consider recent great earthquakes, would improve the results of seismic slope stability calculations in the region offshore Sumatra. This is especially true for turbidites that could be attributed to a given historic earthquake (which has a slip model) or generic segmented fault rupture.

Sediment material properties are probably the most elusive parameter to constrain. To better characterize sediments at the seafloor, we could acquire the backscatter data that is associated with the multibeam bathymetry we use for this study (Lee et al., 2000). These backscatter data could be minimally calibrated with the sediment material properties collected at the locations of the cores collected by Sultan et al. (2009); their cores and backscatter data were collected on the same cruise, which makes their correlation more valid.

Recent seismic slope stability modeling for the Seattle region used site scale modeling to improve their estimates of slope instability based on a series of data sets and models we were unable to implement for our regional analyses. Allstadt et al. (2013) used synthetic broadband seismograms in order to capture a fuller range of slope displacements (Frankel, 2009). Landslide triggering is frequency dependent (Jibson et al., 2004), so models like the ones we used that do not take this into account tend to underestimate landslide hazard. Allstadt et al. (2013) were also able to model 3-D basin amplification for Seattle,

which we were unable to do because we do not have the data for such a regional analysis. Allstadt et al. (2013) compared their site specific analyses with generic models constructed using GMPEs models (Travasarou et al, 2003). Allstadt et al. (2013) found these AI based models produced results with large uncertainty. Allstadt et al. (2013) recognize that, while site scale analyses like they did for Seattle are better, regional analyses based on GMPEs are a good approximation for failures because they are simpler and less time consuming, especially if the uncertainty in ground motions (like for AI) is included and not just the mean values. We do have some seismic reflection data for our slope basins that may be used for a site specific analysis, but we are not confident that the time investment would be justifiable.

Acknowledgements This research was funded by the Ocean Sciences and Earth Sciences Divisions of the National Science Foundation. We thank M. Erhardt, Amy M. Garrett, and Robert H. Porter. for conducting lab analyses; NOC, IFREMER, and BGR for providing key bathymetry and sub-bottom data; UTM, for providing science crew; NOC for providing Russ Wynn; BGR for providing Stefan Ladage; and AIST/GSJ for providing Ken Ikehara. We also thank coring technicians from OSU including Chris Moser, Bob Wilson, Paul Wolscak. Scripps Resident Technicians, the R/V/ Roger Revelle Captain Tom Djardins and crew, and student volunteers and faculty from OSU including Bart DeBaere and Maureen Davies. Further details regarding the cruise and the core locations, please refer to the cruise report here:
http://www.activetectonics.coas.oregonstate.edu/sumatra/report/index.html

Introduction References

Briggs, R.W., Sieh, K., Meltzner, A.J., Natawidjaja, D.H., Galetzka, J., Suwargadi, B., Hsu, Y.-j., Simons, M., Hananto, N.D., Suprihanto, I., Prayudi, D., Avouac, J., Prawirodirdjo, L., Bock, Y., 2006. Deformation and Slip Along the Sunda Megathrust in the Great 2005 Nias-Simeulue Earthquake. Science 311, 1897-1901.

Chlieh, M., Avouac, J.P., Sieh, K., Natawidjaja, D.H., Galetzka, J., 2008. Heterogeneous coupling of the Sumatran megathrust constrained by geodetic and paleogeodetic measurements. Journal of Geophysical Research 113, 31.

Dura, T., Rubin, C.M., Kelsey, H.M., Horton, B.P., Hawkes, A., Vane, C.H., Daryono, M., Grand Pre, C., Ladinsky, T., Bradley, S., 2011. Stratigraphic record of Holocene coseismic subsidence, Padang, West Sumatra. Journal of Geophysical Research 116, 2156-2202.

Goldfinger, C., Nelson, C.H., Morey, A., Johnson, J.E., Gutierrez-Pastor, J., Eriksson, A.T., Karabanov, E., Patton, J., Gracia, E., Enkin, R., Dallimore, A., Dunhill, G., Vallier, T., 2012. Turbidite Event History: Methods and Implications for Holocene Paleoseismicity of the Cascadia Subduction Zone, USGS Professional Paper # 178. U.S. Geological Survey, Reston, VA.

Goldfinger, C., Morey, A., Black, B., Patton, J.R., 2013. Spatially Limited Mud Turbidites on the Cascadia Margin: Segmented Earthquake Ruptures. Natural Hazards and Earth System Sciences 13, 2109-2146.

Meltzner, A.J., Sieh, K., Chiang, H., Shen, C., Suwargadi, B.W., Natawidjaja, D.H., Philbosian, B., Briggs, R.W., Galetzka, J., 2010. Coral evidence for earthquake recurrence and an A.D. 1390–1455 cluster at the south end of the 2004 Aceh–Andaman rupture. Journal of Geophysical Research 115, 1-46.

Meltzner, A.J., Sieh, K., Chiang, H.-W., Shen, C.-C., Suwargadi, B.W., Natawidjaja, D.H., Philibosian, B., Briggs, R.W., 2012. Persistent termini of 2004- and 2005-like ruptures of the Sunda megathrust. Journal of Geophysical Research 117, 15.

Morgenstern, N.R., 1967. Submarine Slumping and the Initiation of Turbidity Currents, in: R., R.A. (Ed.), Marine Géotechnique. University of Illinois Press, Chicago, Ill, pp. 189-220.

Morgenstern, N.R., Price, W.E., 1965. The Analysis of the Stability of General Slip Surfaces. Géotechnique 15, 79-93.

Natawidjaja, D.H., Sieh, K., Ward, S.N., Cheng, H., Edwards, R.L., Galetzka, J., Suwargadi, B.W., 2004. Paleogeodetic Records of Seismic and Aseismic Subduction from Central Sumatran Microatolls, Indonesia. Journal of Geophysical Research 109, 37.

Natawidjaja, D.H., Sieh, K., Chlieh, M., Galetzka, J., Suwargadi, B., Cheng, H., Edwards, R.L., Avouac, J., Ward, S.N., 2006. Source parameters of the great Sumatran megathrust earthquakes of 1797 and 1833 inferred from coral microatolls. Journal of Geophysical Research 111, 37.

Newmark, N.M., 1965. Effects of Earthquakes on Dams and Embankments. Géotechnique 15, 139-159.

Patton, J.R., Goldfinger, C., Morey, A., Romsos, C., Black, B., Djadjadihardja, Y., Udrek., 2013. Seismoturbidite record as preserved at core sites at the Cascadia and Sumatra–Andaman subduction zones. Natural Hazards and Earth Systems Science 13, 833-867.

Philibosian, B., Sieh, K., Natawidjaja, D.H., Chiang, H., Shen, C., Suwargadi, B., Hill, E.M., Edwards, R.L., 2012. An ancient shallow slip event on the Mentawai segment of the Sunda megathrust, Sumatra. Journal of Geophysical Research 117, 12.

Prawirodirdjo, L., McCaffrey, R., Chadwell, C.D., Bock, Y., Subarya, C., 2010. Geodetic observations of an earthquake cycle at the Sumatra subduction zone: Role of interseismic strain segmentation. Journal of Geophysical Research 115, 15.

Sieh, K., Natawidjaja, D.H., Meltzner, A.J., Shen, C., Cheng, H., Li, K., Suwargadi, B.W., Galetzka, J., Philbosian, B., Edwards, R.L., 2008. Earthquake Supercycles Inferred from Sea-Level Changes Recorded in the Corals of West Sumatra. Science 322, 1674-1678.

Skarlatoudis, A.A., Papazachose, C.B., 2012. Preliminary Study of the Strong Ground Motions of the Tohoku, Japan, Earthquake of 11 March 2011: Assessing the Influence of Anelastic Attenuation and Rupture Directivity. Seismological Research Letters 83, 119-129.

Sorensen, M.B., Atakan, K., Pulido, N., 2007. Simulated Strong Ground Motions for the Great M 9.3 Sumatra–Andaman Earthquake of 26 December 2004. BSSA 97, S139-S151.

Stewart, J.P., Midorikawa, S., Graves, R.W., Khodaverdi, K., Kishida, T., Miura, H., Bozorgnia, Y., Campbell, K.W., 2013. Implications of the Mw9.0 Tohoku-Oki Earthquake for Ground Motion Scaling with Source, Path, and Site Parameters. Earthquake Spectra 29, S1 - S21.

Stow, D.A.V., 1990. Sediment facies and processes on the distal Bengal Fan, Leg 116. ODP Texas & M University College Station; UK distributors IPOD Committee NERC Swindon.

Underwood, M.B., Hoke, K.D., Fisher, A.T., Davis, E.E., Giambalvo, E., Hlsdorff, L.Z., Spinelli, G.A., 2005. Provenance, Stratigraphic Architecture, and Hydrogeologic Influence of Turbidites on The Mid-Ocean Ridge Flank of Northwestern Cascadia Basin, Pacific Ocean. Journal of Sedimentary Research 75, 149-164.

Chapter 1 References

Abdeldayem, A.L., Ikehara, K., Yamazaki, T., 2004. Flow path of the 1993 Hokkaido-Nansei-oki earthquake seismoturbidite, southern margin of the Japan sea north basin, inferred from anisotropy of magnetic susceptibility. Geophysical Journal International 157, 15-24.

Abercrombie, R.E., Antolik, M., Ekstrom, G., 2003. The June 2000 Mw 7.9 earthquakes south of Sumatra: Deformation in the India–Australia Plate. Journal of Geophysical Research 108, 16.

Adams, J., 1984. Active deformation of the Pacific Northwest continental margin. Tectonics v.5, p. 449-472.

Adams, J., 1990. Paleoseismicity of the Cascadia subduction zone: Evidence from turbidites off the Oregon-Washington Margin. Tectonics v. 9, p. 569-584.

Alam, M.N., Chowdhury, M.I., Kamal, M.G., S., Mahmood, N.M., A. K. M., Saikat, S.Q., 1996. Radioactivity of 134Cs, 137Cs and 4°K in Sea-water of the Bay of Bengal. Applied Radiation Isotopes 47, 33-35.

Almagor, G., Wiseman, G., 1991. Analysis of Submarine Slumping in the Continental Slope off the Southern Coast of Israel. Marine Geotechnology 10, 303-342.

Alves, J.H.G.H., Young, I.R., 2003. On estimating extreme wave heights using combined Geosat, Topex/Poseidon and ERS-1 altimeter data. Applied Ocean Research 25, 167-186.

Amy, L.A., Talling, P.J., Peakall, J., Wynn, R.B., Arzola Thynne, R.G., 2005. Bed geometry used to test recognition criteria of turbidites and (sandy) debrites. Sedimentary Geology 179, 163-174.

Amy, L.A., Talling, P.J., 2006. Anatomy of turbidites and linked debrites based on long distance (120 · 30 km) bed correlation, Marnoso Arenacea Formation, Northern Apennines, Italy. Sedimentology 53, 161-212.

Arias, A., 1970. A measure of Earthquake Intensity. Massachusetts Institute of Technology Press, Cambridge, Mass.

Atkinson, G.M., Boore, D.M., 2003. Empirical Ground-Motion Relations for Subduction-Zone Earthquakes and Their Application to Cascadia and Other Regions. BSSA 93, 1703-1729.

Atkinson, G.M., Boore, D.M., 2011. Modifications to Existing Ground-Motion Prediction Equations in Light of New Data. BSSA 101, 1121-1135.

Atwater, B.F., 1987. Evidence for great Holocene earthquakes along the outer coast of Washington State. Science v. 236, p. 942-944.

Atwater, B.F., Hemphill-Haley, E., 1997. Recurrence intervals for great earthquakes of the past 3500 years at northeastern Willapa Bay, Washington. U.S. Geological Survey Professional Paper 1576, 108 p.

Baas, J.H., Van Kesteren, W., Postma, G., 2004. Deposits of depletive high-density turbidity currents: a flume analogue of bed geometry, structure and texture. Sedimentology 51, 1053-1088.

Baas, J.H., McCaffrey, W.D., Haughton, P.D.W., Choux, C., 2005. Coupling between suspended sediment distribution and turbulence structure in a laboratory turbidity current. Journal of Geophysical Research 110, 20.

Bacon, C.R., 1983. Eruptive history of Mount Mazama and Crater Lake Caldera, Cascade Range, U.S.A. J. Volcanol. Geotherm. Res. v. 18, p. 57-115.

Bacon, C.R., Lanphere, M.A., 2006. Eruptive history and geochronology of Mount Mazama and the Crater Lake region, Oregon. GSA Bulletin 118, 1331-1359.

Bandopadhyay, A., Bandopadhyay, R.R., 1999. Thermogenic Hydrocarbons in the Mid-proximal Bengal Fan, West of the Andaman -Nicobar Islands. Marine Georesources and Geotechnology 17, 1-16.

Barrientos, D.E., Ward, S.N., 1990. The 1960 Chile earthquake; inversion for slip distribution from surface deformation. Geophysical Journal International 103, 589-598.

Bayes, M., Price, M., 1763. An Essay towards Solving a Problem in the Doctrine of Chances. By the Late Rev. Mr. Bayes, F. R. S. Communicated by Mr. Price, in a Letter to John Canton, A. M. F. R. S. Philosophical Transactions of the Royal Society 53, 370-418.

Bejar-Pizarro, M., Socquet, A., Armijo, R., Carrizo, D., Genrich, J., Simons, M., 2013. Andean structural control on interseismic coupling in the North Chile subduction zone. Nature Geoscience 6, 462-467.

Bilek, S.L., Lay, T., Ruff, L.J., 2004. Radiated seismic energy and earthquake source duration variations from teleseismic source time functions for shallow subduction zone thrust earthquakes. Journal of Geophysical Research 109, 14.

Bilek, S.L., 2007. Using Earthquake Source Durations along the Sumatra–Andaman Subduction System to Examine Fault-Zone Variations. BSSA 97, 9.

Bilham, R., 2005. Partial and Complete Rupture of the Indo-Andaman Plate Boundary 1847 - 2004. Seismological Research Letters 76, 299-311.

Biscontin, G., Pestana, J.M., Nadim, F., 2004. Seismic triggering of submarine slides in soft cohesive soil deposits. Marine Geology 203, 341-354.

Blott, S.J., Pye, K., 2006. Particle size distribution analysis of sand-sized particles by laser diffraction: an experimental investigation of instrument sensitivity and the effects of particle shape. Sedimentology 53, 671-685.

Bock, Y., Prawirodirdjo, L., Genrich, J.F., Stevens, C.W., McCaffrey, R., Subarya, C., Puntodewo, S.S.O., Calais, E., 2003. Crustal motion in Indonesia from Global Positioning System measurements. Journal of Geophysical Research 108, doi:10.1029/2001JB000324.

Boore, D.M., Atkinson, G.M., 2008. Ground-Motion Prediction Equations for the Average Horizontal Component of PGA, PGV, and 5%-Damped PSA at Spectral Periods between 0.01 s and 10.0 s. Earthquake Spectra 24, 99-138.

Bothara, J., Beetham, R.D., Brunston, D., Stannard, M., Brown, R., Hyland, C., Lewis, W., Miller, S., Sanders, R., Sulistio, Y., 2010. General observations of effects of the 30th September 2009 Padang earthquake, Indonesia. Bulletin of the New Zealand Society for Earthquake Engineering 43, 143-173.

Bouma, A.H., 1962. Sedimentology of Some Flysch Deposits. Elsevier Publishing, 168 pp.

Bouma, A.H., 2004. Key controls on the characteristics of turbidite systems. Geological Society, London.

Briggs, R.W., Sieh, K., Meltzner, A.J., Natawidjaja, D., Galetzka, J., Suwargadi, B., Hsu, Y.-j., Simons, M., Hananto, N., Suprihanto, I., Prayudi, D., Avouac, J.-P., Prawirodirdjo, L., Bock, Y., 2006. Deformation and Slip Along the Sunda Megathrust in the Great 2005 Nias-Simeulue Earthquake. Science 311, 1897-1901.

Bronk Ramsey, C., 1995. Radiocarbon calibration and analysis of stratigraphy: The OxCal program. Radiocarbon 37, 425-430.

Bronk Ramsey, C., 2001. Development of the Radiocarbon Program OxCal. Radiocarbon 43, 355-363.

Bronk Ramsey, C., 2008. Deposition models for chronological records. Quaternary Science Reviews 27, 42-60.

Bronk Ramsey, C., 2009. Bayesian Analysis of Radiocarbon Dates. Radiocarbon 51, 337-360.

Bürgmann, R., Kogan, M.G., Steblov, G.S., Hilley, G., Levin, V.E., Apel, E., 2005. Interseismic coupling and asperity distribution along the Kamchatka subduction zone. Journal of Geophysical Research 110, doi:10.1029/2005JB003648.

Caires, S., Sterl, A., 2005. 100-year return value estimates for ocean wind speed and significant wave height from the ERA-40 data. J. Climate 18, 1032-1048.

Campbell, K.W., 1997. Empirical Near-Source Attenuation Relationships for Horizontal and Vertical Components of Peak Ground Acceleration, Peak Ground Velocity, and Pseudo-Absolute Acceleration Response Spectra. Seismological Research Letters 68, 154-179.

Carpenter, R., Petersen, M.L., Bennet, J.T., 1982. 210Pb-derived sediment accumulation and mixing rates for the Washington continental slope. Marine Geology 48, 135-164.

Carter, R.M., 1988. The nature and evolution of deep-sea channel systems. Basin Research 1, 41-54.

Chang, C.-H., Chien, L.-K., Chang, Y.-H., 2004. 3-D Liquefaction potential analysis of seabed at nearshore area. Journal of Marine Science and Technology 12, 141-151.

Cheng, L.B., Sumer, M., Freds, J., 2001. Solutions of pore pressure build up due to progressive waves. Int. J. Numer. Anal. Meth. Geomech. 25, 887-907.

Chesley, S.R., Ward, S.N., 2006. A Quantitative Assessment of the Human and Economic Hazard from Impact-generated Tsunami. Natural Hazards 38, 355-374.

Chhibber, H., 1934. Geology of Burma. McMillan, London, England.

Chlieh, M., Avouac, J.-P., Hjorleifsdottir, V., Song, T.-R.A., Ji, C., Sieh, K., Sladen, A., Hebert, H., Prawirodirdjo, L., Bock, Y., Galetzka, J., 2007. Coseismic Slip and Afterslip of the Great (Mw 9.15) Sumatra-Andaman Earthquake of 2004. Bulletin of the Seismological Society of America 97, S152-S173.

Chlieh, M., Avouac, J.P., Sieh, K., Natawidjaja, D.H., Galetzka, J., 2008. Heterogeneous coupling of the Sumatran megathrust constrained by geodetic and paleogeodetic measurements. Journal of Geophysical Research 113.

Chmelik, F.B., Bouma, A.H., Rezak, R., 1969. Comparison of Electrical Logs and Physical Parameters of Marine Sediment Cores, Gulf Coast Association of Geological Societies. Gulf Coast Association of Geological Societies, pp. 63-70.

Colella, H., Dieterich, J.H., Richards-Dinger, K., Rubin, A., 2012. Complex characteristics of slow slip events in subduction zones reproduced in multi-cycle simulations. Geophysical Research Letters 39, 5.

Cowie, G., Calvert, S., De Lange, G., Keil, R.H., J., 1998. Extents and implications of organic matter alteration at oxidation fronts in turbidites from the Madeira abyssal plain, in: Weaver, P.P.E., Schmincke, H.U., Firth, J.V., Duffield, W. (Eds.), Proceedings of the Ocean Drilling Program, Scientific Results, pp. 581-589.

Dallimore, A., Thomson, R.E., Bertram, M.A., 2005. Modern to late Holocene deposition in an anoxic fjord on the west coast of Canada: Implications for regional oceanography, climate and paleoseismic history. Marine Geology 219, 47-60.

Davis, E., Kinoshita, M., Becker, K., Wang, K., Asano, A., Ito, Y., 2013. Episodic deformation and inferred slow slip at the Nankai subduction zone during the first decade of CORK borehole pressure and VLFE monitoring. Earth and Planetary Science Letters 368, 110-118.

Dean, S., McNeil, L.C., Henstock, T., Bull, J.M., Gulick, S.P.S., Austin Jr., J.A., Bangs, N.L.B., Djadjadihardja, Y., Permana, H., 2010. Contrasting Décollement and Prism Properties over the Sumatra 2004□2005 Earthquake Rupture Boundary. Science 329, 207-210.

Dennielou, B., Huchon, A., Beaudouin, C., Berné, S., 2006. Vertical grain-size variability within a turbidite levee: Autocyclicity or allocyclicity? A case study from the Rhône neofan, Gulf of Lions, Western Mediterranean. Marine Geology 234, 191-213.

Drab, L., Ferrari, A.H., Schmidt, S., Martinez, P., 2012. The earthquake sedimentary record in the western part of the Sea of Marmara, Turkey. Natural Hazards and Earth System Sciences 12, 1235-1254.

Dunbar, R.B., Stroker, K.J., 2008. National Geophysical Data Center Historical Natural Hazard Event Databases. Eos Trans. AGU, Abs. 89.

Dura, T., Rubin, C.M., Kelsey, H.M., Horton, B.P., Hawkes, A., Vane, C.H., Daryono, M., Grand Pre, C., Ladinsky, T., Bradley, S., 2011. Stratigraphic record of Holocene coseismic subsidence, Padang, West Sumatra. Journal of Geophysical Research 116, 2156-2202.

Ericson, D.B., Ewing, M., Heezen, B.C., 1952. Turbdity Currents and Sediments in the North Atlantic. AAPG Bull. 36, 489-511.

Fairbanks, R.G., Mortlock, R.A., Chiu, T.-C., Cao, L., Kaplan, A., Guilderson, T.P., Fairbanks, T.W., Bloom, A.L., Gootes, P.M., Nadeau, M.-J., 2005. Radiocarbon calibration curve spanning 0 to 50,000 years BP based on paired 230Th/ 234U/ 238U and 14C dates on pristine corals. Quaternary Science Reviews 24, 1781-1796.

Faure, G., Mensing, T.M., 2005. Isotopes Principles and Applications, 3rd ed. John Wiley and Sons, New York.

Felix, M., Peakall, J., 2006. Transformation of debris flows into turbidity currents: mechanisms inferred from laboratory experiments. Sedimentology 53, 107-123.

Fisher, D., Mosher, D., Austin, J.A., Gulick, S.P., Masterlark, T., Moran, K., 2007. Active deformation across the Sumatran forearc over the December 2004 Mw 9.2 rupture. Geology 35, 99-102.

Flynn, W.W., 1968. The determination of low levels of polonium-210 in environmental materials. Analytica Chimica Acta 43, 221-227.

Fornes, W.L., DeMaster, D.J., Smith, C.R., 2001. A particle introduction experiment in Santa Catalina Basin: Testing the age-dependent mixing hypothesis. Journal of Marine Research 59, 97–112.

Fujino, S., Naruse, H., Matsumoto, D., Jarupongsakul, T., Sphawajruksakul, A., Sakakura, N., 2009. Stratigraphic evidence for pre-2004 tsunamis in southwestern Thailand. Marine Geology 262, 25-28.

Fujiwara, T., Kodaira, S., No, T., Kaiho, Y., Takahashi, N., Kaneda, Y., 2011. The 2011 Tohoku-Oki Earthquake: Displacement Reaching the Trench Axis. Science 334, 1240.

Fukuma, K., 1998. Origin and applications of whole-core magnetic susceptibility of sediments and volcanic rocks from Leg 152. Proceedings of the Ocean Drilling Program: Scientific Results 152, 271-280.

Garrett, A.M., Goldfinger, C., Patton, J.R., Morey, A.M., 2011. "Paleoseismograms": Testing a Hypothesis of Source-Time Function Recording of Paleoearthquakes. EOS Trans. AGU.

Gilmore, G., Hemingway, J.D., 1995. Practical Gamma-Ray Spectrometry. Wiley, New York.

Goldfinger, C., 2009. Sub-Aqueous Paleoseismology, in: McCalpin, J.P. (Ed.), Paleoseismology, 95 ed. Academic Press, pp. 119-170.

Goldfinger, C., 2010. Submarine Paleoseismology Based on Turbidite Records. Annual Review of Marine Science 3, 35-66.

Goldfinger, C., 2011. Possible turbidite record of earthquake source characteristics: a small scale test. U.S.G.S. Final Technical Report, N.H.R.P. Award 07HQGR0064.

Goldfinger, C., Nelson, C.H., Johnson, J.E., 2003. Holocene Earthquake Records From the Cascadia Subduction Zone and Northern San Andreas Fault Based on Precise Dating of Offshore Turbidites. Annual Reviews of Earth and Planetary Sciences 31, 555-577.

Goldfinger, C., Morey, A.E., Nelson, C.H., Gutierrez-Pastor, J., Johnson, J.E., Karabanov, E., Chaytor, J., Ericsson, A., 2007. Rupture Lengths and Temporal History of Significant Earthquakes on the Offshore and North Coast Segments of the Northern San Andreas Fault Based on Turbidite Stratigraphy. Earth and Planetary Science Letters 254, 9-27.

Goldfinger, C., Grijalva, K., Burgmann, R., Morey, A.E., Johnson, J.E., Nelson, C.H., Gutierrez-Pastor, J., Ericsson, A., Karabanov, E., Chaytor, J.D., Patton, J., Gracia, E., 2008. Late Holocene Rupture of the Northern San Andreas Fault and Possible Stress Linkage to the Cascadia Subduction Zone Bulletin of the Seismological Society of America 98, 861-889.

Goldfinger, C., Nelson, C.H., Morey, A., Johnson, J.E., Gutierrez-Pastor, J., Eriksson, A.T., Karabanov, E., Patton, J., Gracia, E., Enkin, R., Dallimore, A., Dunhill, G., and Vallier, T., 2012 a. Turbidite Event History: Methods and Implications for Holocene Paleoseismicity of the Cascadia Subduction Zone, USGS Professional Paper # 178. U.S. Geological Survey, Reston, VA.

Goldfinger, C., Garrett, A.M., Patton, J.R., Morey, A.E., 2012 b. Paleoseismograms: Can Turbidite Deposits Record Flow Unsteadiness Imparted by Earthquakes? EOS Trans. AGU.

Goldfinger, C., Ikeda, Y., Yeats, R.S., Ren, J., 2013 a. Superquakes and Supercycles. Seismological Research Letters 84, 24-32.

Goldfinger, C., Morey, A., Black, B., Patton, J.R., 2013 b. Spatially Limited Mud Turbidites on the Cascadia Margin: Segmented Earthquake Ruptures. Natural Hazards and Earth System Sciences 13, 2109-2146.

Gonzalez-Yajimovich, O.E., Gorsline, D.S., Douglas, R.G., 2007. Frequency and sources of basin floor turbidites in Alfonso Basin, Gulf of California, Mexico: Products of slope failures. Sedimentary Geology 199, 91-105.

Gorsline, D.S., De Diego, T., Nava-Sanchez, E.H., 2000. Seismically triggered turbidites in small margin basins: Alfonso Basin, Western Gulf of California and Santa Monica Basin, California Borderland. Sedimentary Geology 135, 21-35.

Goto, H., Morikawa, H., Inatani, M., Ogura, Y., Tokue, S., Zhang, X.-X., Iwasaki, M., Araki, M., Sawada, S., Zerva, A., 2012. Very Dense Seismic Array Observations in Furukawa District, Japan. Seismological Research Letters 83, 765-774.

Gràcia, E., Vizcaino, A., Escutia, C., Asioli, A., Rodés, Á., Pallàs, R., Garcia-Orellana, J., Lebreiro, S., Goldfinger, C., 2010. Holocene earthquake record offshore Portugal (SW Iberia): Testing turbidite paleoseismology in a slow-convergence margin. Quaternary Science Reviews 29, 1156-1172.

Graindorge , D., Klingelhoefer, F., Sibuet, J.-C., McNeill , L., Henstock, T.J., Dean, S., Gutscher, M.-A., Dessa, J.X., Permana, H., Singh, S.C., Leau, H., White, N., Carton, H., Malod, J.A., Rangin, C., Aryawan, K.G., Chaubey, A.K., Chauhan, A., Galih, D.R., Greenroyd, C.J., Laesanpura, A., Prihantono, J., Royle, G., Shankar, U., 2008. Impact of lower plate structure on upper plate deformation at the NW Sumatran convergent margin from seafloor morphology Earth and Planetary Science Letters 275, 201-210.

Grand Pre, C., Horton, B., Kelsey, H., Rubin, C., Hawkes, A., Natawidjaja, D.H., Daryono, M., Yulianto, E., 2008. Application of Microfossils to Reconstruct a Paleoseismic Record of the Sunda Subduction Megathrust, Northern Sumatra, Eos Trans. AGU.

Grantz, A., Phillips, R.L., Mullen, M.W., Starratt, S.W., Jones, G.A., Naidu, A.S., 1996. Character, paleoenvironment, rate of accumulation, and evidence for seismic triggering of Holocene turbidites, Canada Abyssal Plain, Arctic Ocean. Marine Geology 133, 51-73.

Griggs, G.B., 2011. The First Ocean Floor Evidence of Great Cascadia Earthquakes. EOS Trans. AGU 92, 325-336.

Griggs, G.B., Kulm, L.D., 1970. Sedimentation in Cascadia Deep-Sea Channel. Geological Society of America Bulletin 81, 1361-1384.

Grumet, N.S., Abram, N.J., Beck, J.W., Dunbar, R.B., Gagan, M.K., Guilderson, T.P., Hantoro, W.S., Suwargadi, B.W., 2004. Coral radiocarbon records of Indian Ocean water mass mixing and wind-induced upwelling along the coast of Sumatra, Indonesia. Journal of Geophysical Research 109.

Hagstrum, J.T., Atwater, B.F., Sherrod, B.L., 2004. Paleomagnetic correlation of late Holocene earthquakes among estuaries in Washington and Oregon. G3 5, doi:10.1029/2004GC000736.

Hammond, D.E., McManus, J., Berelson, W.M., Kilgore, T.E., Pope, R.H., 1996. Early diagenesis of organic material in equatorial Pacific sediments: stoichiometry and kinetics. Deep-Sea Research II 43, 1365-1412.

Hampton, M.A., Bouma, A.H., Carlson, P.R., Molnia, B.F., Clukey, E.C., Survey, U.S.G., Sangrey, D.A., University, C., 1978. Quantitative Study of Slope Instability in the Gulf of Alaska, Offshore Technology Conference, Houston, TX, pp. 2307-2318.

Hampton, M.A., Lee, H.J., Locat, J., 1996. Submarine landslides. Reviews of Geophysics 34, 33-59.

Hayes, G.P., Bergman, E., Johnson, K.L., Benz, H.M., Brown, L., Meltzer, A.S., 2013. Seismotectonic framework of the 2010 February 27Mw 8.8 Maule, Chile earthquake sequence. Geophysical Journal International 195, 1034-1051.

Heki, K., Mitsui, Y., 2013. Accelerated pacific plate subduction following interplate thrust earthquakes at theJapan trench. Earth and Planetary Science Letters 363, 44-49.

Hemphill-Haley, E., 1995. Diatom evidence for earthquake-induced subsidence and tsunami 300 yr ago in southern coastal Washington. Gelogical Society of America Bulletin vol. 107, pp. 367-378.

Henkart, P., 2011. SIOSEIS—The introduction: software package sponsored by the National Science Foundation and the Scripps Industrial Associates, http://sioseis.ucsd.edu/sioseis.html.

Henstock, T.J., McNeill, L.C., Tappin, J.R., 2006. Seafloor morphology of the Sumatran subduction zone: Surface rupture during megathrust earthquakes? Geology 34, 485-488.

Hindle, D., Mackey, K., 2011. Earthquake recurrence and magnitude and seismic deformation of the northwestern Okhotsk plate, northeast Russia. Journal of Geophysical Research 116, 12.

Hok, S., Fukuyama, E., Hashimoto, C., 2011. Dynamic rupture scenarios of anticipated Nankai-Tonankai earthquakes, southwest Japan. Journal of Geophysical Research 116, 22 p.

Holbourn, A., Kuhnt, W., Xu, J., 2011. Indonesian Throughflow variability during the last 140 ka: the Timor Sea outflow, Special Publications ed. The Geological Society of London, London.

Hsu, Y.-j., Simons, M., Avouac, J., Galetzka, J., Sieh, K., Chlieh, M., Natawidjaja, D.H., Prawirodirdjo, L., Bock, Y., 2006. Frictional Afterslip Following the 2005 Nias-Simeulue Earthquake, Sumatra. Science 312, 1921-1926.

Hughen, K., Lehman, S., Southon, J., Overpeck, J., Marchal, O., Herring, C., Turnbull, J., 2004. 14C Activity and Global Carbon Cycle Changes Over the Past 50,000 Years, Science, pp. 202-207.

Huh, C.A., Su, C.C., Liang, W.T., Ling, C.Y., 2004. Linkages between turbidites in the southern Okinawa Trough and submarine earthquakes. Geophysical Research Letters 31.

Huh, C.-A., Su, C.-C., Wang, C.-H., Lee, S.-Y., Lin, I.-T., 2006. Sedimentation in the Southern Okinawa Trough -- Rates, turbidites and a sediment budget. Marine Geology 231, 129-139.

Ide, S., 2013. The proportionality between relative plate velocity and seismicity in subduction zones. Nature Geoscience, 5.

Inouchi, Y., Kinugasa, Y., Kumon, F., Nakano, S., Yasumatsu, S., Shiki, T., 1996. Turbidites as records of intense palaeoearthquakes in Lake Biwa, Japan. Sed. Geol. v. 104, p. 117-125.

Ishii, M., Shearer, P.M., Houston, H., Vidale, J.E., 2005. Extent, duration and speed of the 2004 Sumatra-Andaman earthquake imaged by the Hi-Net array. Nature 435, 933.

Izaguirre, C., Mendez, F.J., Mendez, M., Losada, I.J., 2011. Global extreme wave height variability based on satellite data. Geophysical Research Letters 38, 6.

Jankaew, K., Atwater, B.F., Sawai, Y., Charoentitirat, T., Martin, M.E., Prendergast, A., 2008. Medieval forewarning of the 2004 Indian Ocean tsunami in Thailand. Nature 455, 1228-1231.

Jibson, R.W., Harp, E.L., 2012. Extraordinary Distance Limits of Landslides Triggered by the 2011 Mineral, Virginia, Earthquake. BSSA 102, 2368-2377.

Johnson, J.E., Goldfinger, C., Trehu, A.M., Bangs, N.L.B., Torres, M.E., Chevallier, J., 2005. North-South Variability in The History Of Deformation and Fluid Venting Across Hydrate Ridge, Cascadia Margin, Proceedings of the Ocean Drilling Program; scientific results; drilling gas hydrates on Hydrate Ridge, Cascadia continental margin; covering Leg 204 of the cruises of the drilling vessel JOIDES Resolution; Victoria, British Columbia, Canada, p. 16.

Kagan, Y.Y., Jackson, D.D., Geller, R.J., 2012. Characteristic Earthquake Model, 1884–2011, R.I.P. Seismological Research Letters 83, 951-953.

Kanamori, H., Rivera, L., Lee, W.H.K., 2010. Historical seismograms for unravelling a mysterious earthquake: The 1907 Sumatra Earthquake. Geophysical Journal International 183, 358-374.

Karig, D.E., Lawrence, M.B., Moore, G.F., Curray, J.R., 1980. Structural framework of the forearc basin, NW Sumatra. Geological Society of London Journal v. 137, p. 77-91.

Karlin, R.C., Abella, S.E.B., 1992. Paleoearthquakes in the Puget Sound region recorded in sediments from Lake Washington, U.S.A. Science 258, 1617-1620.

Karlin, R.E., Abella, S.E.B., 1996. A history of Pacific Northwest earthquakes recorded in Holocene sediments from Lake Washington. Journal of Geophysical Research, B, Solid Earth and Planets 101, 6137-6150.

Karlin, R.E., Holmes, M., Abella, S.E.B., Sylwester, R., 2004. Holocene landslides and a 3500-year record of Pacific Northwest earthquakes from sediments in Lake Washington. Geological Society of America Bulletin 116, 94-108.

Karlin, R., Seitz, G., 2007. A Basin Wide Record of Earthquakes at Lake Tahoe: Validation of the Earthquake Induced Turbidite Model with Sediment Core Analysis: Collaborative Research with UNR and SDSU, Final Technical Report for 07HQGR0014 and 07HQGR0008. USGS NEHRP.

Kayen, R.E., Mitchell, J.K., 1997. Assessment of Liquefaction Potential During Earthquakes by Arias Intensity. Journal of Geotechnical and Geoenvironmental Engineering 123, 1162-1174.

Keefer, D.K., 1984. Landslides caused by earthquakes. GSA Bulletin 95, 406-421.

Kelsey, H.M., Witter, R.C., Hemphill-Haley, E., 2002. Plate-boundary earthquakes and tsunamis of the past 5500 yr, Sixes River estuary, southern Oregon. Geological Society of America Bulletin 114, 298-314.

Kelsey, H.M., Nelson, A.R., Hemphill-Haley, E., Witter, R.C., 2005. Tsunami history of an Oregon coastal lake reveals a 4600 yr record of great earthquakes on the Cascadia subduction zone. GSA Bulletin 117, 1009-1032.

Kiser, E., Ishii, M., 2011. The 2010 Mw 8.8 Chile earthquake: Triggering on multiple segments and frequency dependent rupture behavior. Geophysical Research Letters 38, 6 p.

Klug, C., Cashman, K.V., Bacon, C.R., 2002. Structure and physical characteristics of pumice from the climactic eruption of Mount Mazama (Crater Lake), Oregon. Bulletin of Volcanology 34, 486-501.

Kneller, B., Buckee, C., 2000. The structure and fluid mechanics of turbidity currents: a review of some recent studies and their geological implications. Sedimentology 47, 62-94.

Kneller, B., McCaffrey, B., 1995. Modeling the Effects of Salt-Induced Topography on Deposition from Turbidity Currents, in: Travis, C., Vendeville, B., Harrison, H.L., Peel, F.J., Hudec, M.R., Perkins, B.f. (Eds.), Gulf Coast Section Society of Economic Paleontologists and Mineralogists Foundation Sixteenth annual research conference. Society of Economic Paleontologists, Gulf Coast Section (GCSSEPM) Foundation, Houston, TX, pp. 137-145.

Komen, G.J., Cavaleri, L., Donelan, M., Hasselmann, K., Hasselmann, S., Janssen, P.A.E.M., 1994. Dynamics and Modeling of Ocean Waves. Cambridge University Press.

Konca, A.O., Hjorleifsdottir, V., Song, T.A., Avouac, J., Helmberger, D., Ji, C., Briggs, R.W., Meltzner, A.J., 2007. Rupture Kinematics of the 2005 Mw 8.6 Nias–Simeulue Earthquake from the Joint Inversion of Seismic and Geodetic Data. BSSA 97, S307-S322.

Konca, A.O., Avouac, J., Sladen, A., Meltzner, A.J., Sieh, K., Fang, P., Li, Z., Galetzka, J., Genrich, J., Chlieh, M., Natawidjaja, D.H., Bock, Y., Fielding, E.J., Ji, C., Helmberger, D., 2008. Partial Rupture of a Locked Patch of the Sumatra Megathrust During the 2007 Earthquake Sequence. Nature 456, 631-635.

Kopp, H., 2013. Invited review paper: The control of subduction zone structural complexity and geometry on margin segmentation and seismicity. Tectonophysics 589, 1-16.

Kramer, S.L., Lindwall, N.W., 2004. Dimensionality and Directionality Effects in Newmark Sliding Block Analyses. Journal of Geotechnical and Geoenvironmental Engineering 130, 303-315.

Ladage, S., Weinrebe, W., Gaedicke, C., Barckhausen, U., Flueh, E.R., Heyde, I., Krabbenhoeft, A., H. Kopp, S.F., Djadjadihardja, Y., 2006. Bathymetric Survey Images Structure off Sumatra. EOS Trans. AGU 87.

Lamb, M.P., Tonolio, H., Parker, G., 2006. Trapping of sustained turbidity currents by intraslope minibasins. Sedimentology 53, 147-160.

Lay, T., Kanamori, H., Ammon, C.J., Nettles, M., Ward, S.N., Aster, R.C., Beck, S.L., Bilek, S.L., Brudzinski, M.R., Butler, R., DeShon, H.R., Ekstrom, G., Satake, K., Sipkin, S., 2005. The Great Sumatra-Andaman Earthquake of 26 December 2004. Science 308, 1127-1133.

Lees, J.A., Flower, R.J., Ryves, D., Vologina, E., Sturm, M., 1998 a. Identifying sedimentation patterns in Lake Baikal using whole core and surface scanning magnetic susceptibility. Journal of Paleolimnology 20, 187-202.

Lees, J.A., Fowler, R.J., Appleby, P.G., 1998 b. Mineral magnetic and physical properties of surficial sediments and onshore samples from the southern basin of Lake Baikal, Siberia. Journal of Paleolimnology 20, 175-186.

Lees, W.H., Bennet, R.E., Meagher, K.L., 1972. A method of estimating magnitude of local earthquakes from signal duration, in: Report, O.F. (Ed.). USGS.

Leonard, L.J., Hyndman, R.D., Mazzotti, S., 2004. Coseismic subsidence in the 1700 great Cascadia earthquake: Coastal estimates versus elastic dislocation models. GSA Bulletin 116, 655.

Levesque, C.L., Locat, J., Leroueil, S., 2006. Dating submarine mass movements triggered by earthquakes in the Upper Saguenay Fjord, Quebec, Canada. Norweigan Journal of Geology 86, 231-242.

Lorenzoni, L., Thunell, R.C., Benitez-Nelson, C.R., Hollander, D., Martinez, N., Tappa, E., Varela, R.n., Astor, Y., Muller-Karger, F.E., 2012. The Importance of Subsurface Nepheloid Layers in Transport and Delivery of Sediments to the Eastern Cariaco Basin, Venezuela. Deep-Sea Research I 56, 2249-2262.

Lovlie, R., Van Veen, P., 1995. Magnetic susceptibility of a 180 m sediment core: reliability of incremental sampling and evidence for a relationship between susceptibility and gamma activity, in: Turner, P., Turner, A. (Eds.), Palaeomagnetic applications in hydrocarbon exploration and production. Geological Society, London, Special Publication, 98, pp. 259-266.

Lowe, D.R., 1982. Sediment Gravity Flows: II. Depositional Models with Special Reference to the Deposits of High-Density Turbidity Currents. Journal of Sedimentary Petrology 52, 0279-0297.

Luternauer, J.L., Liam Finn, W.D., 1983. Stability of the Fraser River Delta Front. Canadian Geotechnical Journal 20, 603-616.

Madsen, O.S., 1994. Spectral wave-current bottom boundary layer flows, 24th International Conference, Coastal Engineering Research Council. ASCE, pp. 384-398.

Mahani, A.B., Atkinson, G.M., 2013. Regional Differences in Ground-Motion Amplitudes of Small-to-Moderate Earthquakes across North America. BSSA 103, 17.

Malik, J.N., Shishikura, M., Echigo, T., Ikeda, Y., Satake, K., Kayanne, H., Sawai, Y., Murty, C.V.R., Dikshit, D., 2011. Geologic evidence for two pre-2004 earthquakes during recent centuries near Port Blair, South Andaman Island, India. Geology 39, 559-562.

Martin, W.R., Sayles, F.L., 2003. The Recycling of Biogenic Material at the Seafloor. Treatise on Geochemistry 7, 37-65.

Masson, D.G., Harbitz, C.B., Wynn, R.B., Pedersen, G., Løvholt, F., 2006. Submarine landslides: processes, triggers and hazard prediction. Philosophical Transactions of the Royal Society 364, 2009-2039.

Masson, D.G., Wynn, R.B., Talling, P.J., 2010. Large Landslides on Passive Continental Margins: Processes, Hypotheses and Outstanding Questions, in: Mosher, D.C., Shipp, R.C., Moscardelli, L., Chaytor, J.D., Baxter, C.D.P., Lee, H.J., Urgeles, R. (Eds.), Submarine Mass Movements and Their Consequences. Springer, New York, pp. 153-165.

Matson, R.G., Moore, G., 1992. Structural Influence on Neogene Subsidence in the Central Sumatra Fore-Arc Basin. American Association of Petroleum Geologists, Tulsa, OK.

McCalpin, J.P., 2009. Field Techniques in Paleoseismology - Terrestrial Environments, in: McCalpin, J.P. (Ed.), Paleoseismology, 95 ed. Academic Press, pp. 29-118.

McCalpin, J.P., Nelson, A.R., 1996. Introduction to Paleoseismology, in: McCalpin, J.P. (Ed.), Paleoseismology, 1 ed. Academic Press, San Diego, pp. 1-32.

Meltzner, A.J., K. Sieh, Abrams, M., Agnew, D.C., Hudnut, K.W., Avouac, J.-P., Natawidjaja, D.H., 2006. Uplift and subsidence associated with the great Aceh-Andaman earthquake of 2004. J. Geophys. Res. 111, B02407.

Meltzner, A.J., Sieh, K., Chiang, H., Shen, C., Suwargadi, B.W., Natawidjaja, D.H., Philobosian, B., Briggs, R.W., Galetzka, J., 2010. Coral evidence for earthquake recurrence and an A.D. 1390–1455 cluster at the south end of the 2004 Aceh–Andaman rupture. Journal of Geophysical Research 115, 1-46.

Meltzner, A.J., Sieh, K., Chiang, H.-W., Shen, C.-C., Suwargadi, B.W., Natawidjaja, D.H., Philibosian, B., Briggs, R.W., 2012. Persistent termini of 2004- and 2005-like ruptures of the Sunda megathrust. Journal of Geophysical Research 117, 15.

Meunier, P., Hovius, N., Haines, A.J., 2007. Regional patterns of earthquake-triggered landslides and their relation to ground motion. Geophysical Research Letters 34.

Michels, K.H., Suckow, A., Breitzke, M., Kudrass, H.R., Kottke, B., 2003. Sediment transport in the shelf canyon ‘‘Swatch of No Ground’’ (Bay of Bengal). Deep-Sea Research II 50, 1003-1022.

Middleton, G.V., 1967. Experiments on Density and Turbidity Currents 111. Deposition of Sediment. Canadian Journal fo Earth Sciences 4, 475-505.

Miyamoto, J., Sassa, S., Sekiguchi, H., 2004. Progressive solidification of a liquefied sand layer during continued wave loading. Geotechnique 54, 617-629.

Moernaut, J., Batist, M.D., Charlet, F., Heirman, K., Chapron, E., Pino, M., Brümmer, R., Urrutia, R., 2007. Giant earthquakes in South-Central Chile revealed by Holocene mass-wasting events in Lake Puyehue. Sedimentary Geology 195, 239-256.

Monecke, K., Finger, W., Klarer, D., Kongo, W., McAdoo, B., Moore, A., Sudrajat, S., 2008. A 1,000-year sediment record of tsunami recurrence in northern Sumatra. Nature 455, 1232-1234.

Monecke, K., S.Anselmetti, F., Becker, A., Schnellmann, M., Sturm, M., Giardini, D., 2006. Earthquake-induced deformation structures in lake deposits: A Late Pleistocene to Holocene paleoseismic record for Central Switzerland. Eclogae geol. Helv. 99, 343-362.

Moore, D.G., Curray, J.R., Emmell, F.J., 1976. Large submarine slide (olistostrome) associated with Sunda arc subduction zone, northeast Indian Ocean. Marine Geology 21, 211-226.

Moore, G.F., Karig, D.E., 1980. Structural Geology of Nias Island, Indonesia: Implications for Subduction Zone Tectonics. Science 280, 193-223.

Moreno, M.S., Bolte, J., Klotz, J., Melnick, D., 2009. Impact of megathrust geometry on inversion of coseismic slip from geodetic data: Application to the 1960 Chile earthquake. geophysical Research Letters 36, 5.

Moreno, M.S., Melnick, D., Rosenau, M., Bolte, J., Klotz, J., Echtler, H., Baez, J., Bataille, K., Chen, J., Bevis, M., Hase, H., Oncken, O., 2011. Heterogeneous plate locking in the South–Central Chile subduction zone: Building up the next great earthquake. Earth and Planetary Science Letters 305, 413-424.

Morey, A., Goldfinger, C., 2004. Physical Property Correlations from Cascadia Great Earthquakes: What Are They Telling Us About The Triggering Events? EOS Trans. AGU 85.

Morgenstern, N.R., 1967. Submarine Slumping and the Initiation of Turbidity Currents, in: R., R.A. (Ed.), Marine Géotechnique. University of Illinois Press, Chicago, Ill, pp. 189-220.

Mosher, D.C., Moscardelli, L., Shipp, R.C., Chaytor, J.D., Baxter, C.D.P., Lee, H.J., Urgeles, R., 2010. Submarine Mass Movements and Their Consequences, in: Mosher, D.C., Shipp, R.C., Moscardelli, L., Chaytor, J.D., Baxter, C.D.P., Lee, H.J., Urgeles, R. (Eds.), Submarine Mass Movements and Their Consequences. Springer, New York, pp. 1-8.

Muck, M.T., Underwood, M.B., 1990. Upslope flow of turbidity currents: A comparison among field observations, theory, and laboratory models. Geology 18, 54-57.

Mulder, T., Syvitski, J.P.M., Migeon, S., Faugeres, J.-C., Savoye, B., 2003. Marine hyperpycnal flows; initiation, behavior and related deposits; a review. Marine and Petroleum Geology 20, 861-882.

Murray, J., Segall, P., 2002. Testing time-predictable earthquake recurrence by direct measurement of strain accumulation and release. Nature 419, 287-288.

Nair, R.R., Buynevich, I., Goble, R.J., Srinivasan, P., Murthy, S.G.N., Kandipal, S.C., Lakshmi, C.S.V., Trivedi, I.D., 2010. Subsurface Images Shed Light on Past Tsunamis in India. EOS 91, 489-490.

Nakajima, T., 2000 a. Initiation processes of turbidity currents; implications for assessments of recurrence intervals of offshore earthquakes using turbidites. Bulletin of the Geological Survey of Japan 51, 79-87.

Nakajima, T., Kanai, Y., 2000 b. Sedimentary features of seismoturbidites triggered by the 1983 and older historical earthquakes in the eastern margin of the Japan Sea. Sedimentary Geology 135, 1-19.

Natawidjaja, D.H., Sieh, K., Ward, S.N., Cheng, H., Edwards, R.L., Galetzka, J., Suwargadi, B.W., 2004. Paleogeodetic Records of Seismic and Aseismic Subduction from Central Sumatran Microatolls, Indonesia. Journal of Geophysical Research 109, 37.

Natawidjaja, D.H., Sieh, K., Chlieh, M., Galetzka, J., Suwargadi, B., Cheng, H., Edwards, R.L., Avouac, J., Ward, S.N., 2006. Source parameters of the great Sumatran megathrust earthquakes of 1797 and 1833 inferred from coral microatolls. Journal of Geophysical Research 111, 37.

Nelson, A.R., Kelsey, H.M., Witter, R.C., 2006. Great earthquakes of variable magnitude at the Cascadia subduction zone. Quaternary Research 65, 354-365.

Nelson, C.H., Kulm, L.D., Carlson, P.R., Duncan, J.R., 1968. Mazama ash in the northeastern Pacific. Science v. 161, p. 47-49.

Nelson, C.H., Meyer, A.W., Thor, D., Larsen, M., 1986. Crate Lake, Oregon: A restricted basin with base-of-slope aprons of nonchanellized turbidites. Geology 14, 238-241.

Newcomb, K.R., McCann, W.R., 1987. Seismic History and Seismotectonics of the Sunda Arc. Journal of Geophysical Research 92, 421-439.

Ninis, D., Little, T.A., Van Dissen, R.J., Litchfield, N.J., Smith, E.G.C., Wang, N.R., U., Henderson, C.M., 2013. Slip Rate on the Wellington Fault, New Zealand, during the Late Quaternary: Evidence for Variable Slip during the Holocene. BSSA 103, 559-579.

Noda, A., 2004. Turbidites along Kushiro Canyon, in: Satake, K., Goldfinger, C. (Ed.), Workshop on Turbidites as Earthquake Recorders. AIST, Geological Survey of Japan, Tsukuba, Japan.

Noda, A., TuZino, T., Kanai, Y., Furukawa, R., Uchida, J.-i., 2008. Paleoseismicity along the southern Kuril Trench deduced from submarine-fan turbidites. Marine Geology 254, 73-90.

Noller, J.S., 2000. Lead-210 Geochronology. AGU Reference Shelf 4, 115-120.

Obermeier, S.F., Dickenson, S.E., 2000. Liquefaction evidence for the strength of ground motions resulting from Late Holocene Cascadia subduction earthquakes, with emphasis on the event of 1700 A.D. Bulletin of the Seismological Society of America 90, 876-896.

Okamura, Y., 2004. Paleoseismology of deep-sea faults based on marine surveys in Japan Sea, in: Satake, K., Goldfinger, C. (Ed.), Workshop on Turbidites as Earthquake Recorders. AIST, Geological Survey of Japan, Tsukuba, Japan.

Parsons, T., 2012 a. Paleoseismic interevent times interpreted for an unsegmented earthquake rupture forecast. Geophysical Research Letters 39, 6.

Parsons, T., Console, R., Falcone, G., Murru, M., Yamashima, K., 2012 b. Comparison of characteristic and Gutenberg–Richter models for time-dependentM ≥ 7.9 earthquake probability in the Nankai-Tokai subduction zone, Japan. Geophysical Journal International 190, 1673-1688.

Patton, J.R., Goldfinger, C., Morey, A., Romsos, C., Black, B., Djadjadihardja, Y., Udrek., 2013. Seismoturbidite record as preserved at core sites at the Cascadia and Sumatra–Andaman subduction zones. Natural Hazards and Earth Systems Science 13, 833-867.

Peduzzi, P., Chatenoux, B., Dao, H., De Bono, A., Herold, C., Kossin, J., Mouton, F., Nordbeck, O., 2012. Global trends in tropical cyclone risk. Nature Climate Change 2, 289-294.

Peterson, C.D., Madin, I.P., 1997. Coseismic paleoliquefaction evidence in the central Cascadia margin, USA Oregon Geology 59, 51-74.

Philibosian, B., Sieh, K., Natawidjaja, D.H., Chiang, H., Shen, C., Suwargadi, B., Hill, E.M., Edwards, R.L., 2012. An ancient shallow slip event on the Mentawai segment of the Sunda megathrust, Sumatra. Journal of Geophysical Research 117, 12.

Piper, D.J.W., 1978. Turbidite Muds and Silts on Deep-sea Fans and Abyssal Plains, in: Stanley, D.J., and Kelling, G. (Ed.), Sedimentation in Submarine Canyons, Fans and Trenches. Dowden, Hutchinson & Ross, Stroudsburg, Pennsylvania, pp. p. 163-176.

Piper, D.J.W., Cochonat, P., Morrison, M.L., 1999. The sequence of events around the epicentre of the 1929 Grand Banks earthquake: Initiation of debris flows and turbidity current inferred from sidescan sonar. Sedimentology vol. 46, pp. 79-97.

Pouderoux, H., Proust, J.-N., Lamarche, G., Orpin, A., Neil, H., 2012. Postglacial (After 18 Ka) Deep-Sea Sedimentation Along the Hikurangi Subduction Margin (New Zealand): Characterisation, Timing and Origin of Turbidites. Marine Geology 295-298, 51-76.

Prell, W.L., Imbrie, J., Martinson, D.G., Morley, J.J., Pisias, N.G., Shackleton, N.J., Streeter, H.F., 1986. Graphic Correlation Of Oxygen Isotope Stratigraphy Application To The Late Quaternary. Paleoceanography 1, 137-162.

Rajendran, C.P., Rajendran, K., Anu, R., Earnest, A., Machado, T., Mohan, P.M., Freymueller, J., 2007. Crustal Deformation and Seismic History Associated with the 2004 Indian Ocean Earthquake: A Perspective from the Andaman–Nicobar Islands. BSSA 97, S174-S191.

Rajendran, K., Rajendran, C.P., Earnest, A., Ravi Prasad, G.V., Dutta, K., Ray, D.K., Anu, R., 2008. Age estimates of coastal terraces in the Andaman and Nicobar Islands and their tectonic implications. Tectonophysics 455, 52-60.

Rampino, M.R., 1984. Terrestrial Mass Extinctions, Cometary Impacts and the Sun's Motion Perpendicular to the Galactic Plane. Nature 308, 709-712.

Rampino, M.R., 1999. Impact Crises, Mass Extinctions, and Galactic Dynamics: The Case for a Unified Theory. Geological Society of America, Special Paper 339 339, 241-248.

Rampino, M.R., 2002. Role of the Galaxy in Periodic Impacts and Mass Extinctions on the Earth. Geological Society of America, Special Paper 356 356, 667-678.

Rampino, M.R., Stothers, R.B., 1984. Geological Rhythms and Cometary Impacts. Science 226, 1427.

Rastogi, B.K., Jaiswal, R.K., 2006. A Catalog of Tsunamis in the Indian Ocean. Science of Tsunami Hazards 25, 128-143.

Ratzov, G., Collot, J.-Y., Sosson, M., Migeon, S., 2010. Mass-transport deposits in the northern Ecuador subduction trench: Result of frontal erosion over multiple seismic cycles. Earth and Planetary Science Letters 296, 89-102.

Reimer, P.J., Baillie, M.G.L., Bard, E., Bayliss, A., Beck, J.W., Bertrand, C.J.H., Blackwell, P.G., Ramsey, C.B., Buck, C.E., Burr, G.S., Edwards, R.L., Friedrich, M., Grootes, P.M., Guilderson, T.P., Hajas, I., Heaton, T.J., Hogg, A.G., Hughen, K.A., Kaiser, K.F., Kromer, B., McCormac, F.G., Manning, S.W., Reimer, R.W., Richards, D.A., Southon, J.R., Talamo, S., van der Plicht, J., Weyhenmeyer, C.E., 2009. INTCAL09 and MARINE09 Radiocarbon Age Calibration Curves, 0–50,000 Years cal BP. Radiocarbon 51, 1111-1150.

Reimer, P.J., Bard, E., Bayliss, A., Beck, J.W., Blackwell, P.G., Ramsey, C.B., Grootes, P.M., Guilderson, T.P., Haflidason, H., Hajdas, I., Hatté, D., Heaton, T.J., Hoffman, D.L., Hogg, A.G., Hughen, K.A., Kaiser, K.F., Kromer, B., Manning, S.W., Niu, M., Reimer, R.W., Richards, D.A., Scott, E.M., Southon, J.R., Staff, R.A., Turney, C.S.M., Van der Plicht, J., 2013. IntCal13 and Marine13 Radiocarbon Age Calibration Curves 0□50,000 Years cal BP.

Rhodes, B.P., Kirby, M.E., Jankaew, K., Choowong, M., 2011. Evidence for a mid-Holocene tsunami deposit along the Andaman coast of Thailand preserved in a mangrove environment. Marine Geology 282, 255-267.

Rivera, L., Sieh, K., Helmberger, D., Natawidjaja, D.H., 2002. A Comparative Study of the Sumatran Subduction-Zone Earthquakes of 1935 and 1984. BSSA 92, 1721-1736.

Robbins, J.A., Edgington, D.N., Kemp, A.L.W., 1978. Comparative 210Pb, 137Cs, and Pollen Geochronologies of Sediments from Lakes Ontario and Erie. Quaternary Research 10, 256-278.

Robinson, W.L., Conrado, C.L., Bogen, K.T., Stoker, A.C., 2003. The effective and environmental half-life of 137Cs at Coral Islands at the former US nuclear test site. Journal of Environmental Radioactivity 69, 207-223.

Rollins, J.C., Stein, R.S., 2010. Coulomb Stress Interactions Among M ≥ 5.9 Earthquakes in the Gorda Deformation Zone and on the Mendocino Fault Zone, Cascadia Subduction Zone, and Northern San Andreas Fault. Journal of Geophysical Research 115, 19 pp.

Ross, D.A., 1971. Mass Physical Properties and Slope Stability of Sediments of the Northern Middle America Trench. journal of Geophysical Research 76, 704-712.

Ruff, L., Kanamori, H., 1980. Seismicity and the subduction process. Physics of the Earth and Planetary Interiors v. 23, p. 240-252.

Salisbury, M., Kent, A., Patton, J., Goldfinger, C., Djadjadihardja, Y., Udrekh, U., 2010. Deep-sea ash layers reveal evidence of large Pleistocene and Holocene volcanic eruptions from Sumatra, Indonesia, 2010 Fall Meeting, AGU. EOS transactions.

Salisbury, M., Patton, J., Kent, A., Goldfinger, C., Djadjadihardja, Y., Udrekh, U., 2012. Newly discovered deep-sea ash layers reveal evidence of large Holocene volcanic eruptions from Sumatra, Indonesia. Journal of Volcanology and Geothermal Research 231-232, 61-71.

Sarı, E., Çağatay, M., 2006. Turbidites and their association with past earthquakes in the deep Çınarcık Basin of the Marmara Sea. Geo-Marine Letters 26, 69-76.

Satake, K., Atwater, B., 2007. Long-Term Perspectives on Giant Earthquakes and Tsunamis at Subduction Zones. Annual Review of Earth and Planet Sciences 35, 349-374.

Sayles, F.L., Martin, W.R., Deuser, W.G., 1994. Response of benthic oxygen demand to particulate organic carbon supply in the deep sea near Bermuda. Nature 371, 686-689.

Sayles, F.L., Martin, W.R., Chase, Z., Anderson, R.F., 2001. Benthic remineralization and burtial of biogenic SiO2, CaCO3, organic carbon, and detrital material in the Southern Ocean along a transect at 170° west. Deep-Sea Research II 48, 43223-44383.

Schimmelmann, A., Hendy, I.L., Dunn, L., Pak, D.K., Lange, C.B., 2013. Revised ~2000-year chronostratigraphy of partially varved marine sediment in Santa Barbara Basin, California. GFF, 1-7.

Schlagenhauf, A., Manighetti, I., Benedetti, L., Gaudemer, Y., Finkel, R., Malavieille, J., Pou, K., 2011. Earthquake supercycles in Central Italy, inferred from 36Cl exposure dating. Earth and Planetary Science Letters 307, 487-500.

Scholz, C.H., 2010. Large Earthquake Triggering, Clustering, and the Synchronization of Faults. BSSA 100, 901-909.

Schulz, W.H., Galloway, S.L., Higgins, J.D., 2012. Evidence for earthquake triggering of large landslides in coastal Oregon, USA. Geomorphology 141-142, 88-98.

Schurr, B., Asch, G., Rosenau, M., Wang, R., Oncken, O., Barrientos, D.E., Salazar, P., Vilotte, J.P., 2007. The 2007 M7.7 Tocopilla northern Chile earthquake sequence: Implications for along-strike and downdip rupture segmentation and megathrust frictional behavior. Journal of Geophysical Research 117, 19 p.

Scott, E.M., 2003. The Fourth International Radiocarbon Intercomparison (FIRI). Radiocarbon 45, 135-285.

Seilacher, A., 1969. Fault-Graded Beds Interpreted as Seismites. Sedimentology 13, 155-159.

Shanmugam, G., 2008. The constructive functions of tropical cyclones and tsunamis on deep-water sand deposition during sea level highstand: Implications for petroleum exploration. AAPG Bulletin 92, 443-471.

Shiki, T., 1996. Reading of the trigger records of sedimentary events--a problem for future studies. Sed. Geol. v. 104, p. 249-255.

Shiki, T., Kumon, F., Inouchi, Y., Kontani, Y., Sakamoto, T., Tateishi, M., Matsubara, H., Fukuyama, K., 2000. Sedimentary features of the seismo-turbidites, Lake Biwa, Japan. Sedimentary Geology vol. 135, pp. 37-50.

Shimazaki, K., Nakata, T., 1980. Time-predictable recurrence model for large earthquakes. Geophys. Res. Lett. v. 7, p. 279-281.

Shirai, M., Omura, A., Wakabayashi, T., Uchida, J.-i., Ogami, T., 2010. Depositional age and triggering event of turbidites in the western Kumano Trough, central Japan during the last ca. 100 years. Marine Geology 271, 225-235.

Sieh, K., Natawidjaja, D., 2000. Neotectonics of the Sumatran fault. J. Geophys. Res. 105, 28295.

Sieh, K., Natawidjaja, D.H., Meltzner, A.J., Shen, C., Cheng, H., Li, K., Suwargadi, B.W., Galetzka, J., Philobosian, B., Edwards, R.L., 2008. Earthquake Supercycles Inferred from Sea-Level Changes Recorded in the Corals of West Sumatra. Science 322, 1674-1678.

Smith, K.L., 1987. Food energy supply and demand: a discrepancy between particulate organic carbon flux and sediment community oxygen consumption in the deep ocean. Limnology and Oceanography 32, 201-220.

Smith, S., Karlin, R.E., Kent, G.M., Seitz, G.G., Driscoll, N.W., 2013. Holocene subaqueous paleoseismology of Lake Tahoe. GSA Bulletin 125, 691-708.

Smith, W.H.F., Sandwell, D.T., 1997. Global seafloor topography from satellite altimetry and ship depth soundings. Science 277, 1957-1962.

Song, T.-R.A., Simons, M., 2003. Large Trench-Parallel Gravity Variations Predict Seismogenic Behavior in Subduction Zones. Science 301, 630-633.

Song, S.G., Beroza, G.C., Segall, P., 2008. A Unified Source Model for the 1906 San Francisco Earthquake. Bulletin of the Seismological Society of America 98.

Sorensen, M.B., Atakan, K., Pulido, N., 2007. Simulated Strong Ground Motions for the Great M 9.3 Sumatra–Andaman Earthquake of 26 December 2004. BSSA 97, S139-S151.

Stein, S., Okal, E., 2007. Ultralong Period Seismic Study of the December 2004 Indian Ocean Earthquake and Implications for Regional Tectonics and the Subduction Process. BSSA 97, S279-S295.

St-Onge, G., Mulder, T., Piper, D.J.W., Hillaire-Marcel, C., Stoner, J.S., 2004. Earthquake and flood-induced turbidites in the Saguenay Fjord (Québec): a Holocene paleoseismicity record. Quaternary Science Reviews 23, 283-294.

Stow, D.A.V., 1977. Late Quaternary Stratigraphy and Sedimentation on the Nova Scotian Outer Continental Margin. Dalhousie University.

Stow, D.A.V., 1985. Deep-sea clastics: where are we and where are we going? Geological Society of London, Special Publications 18, 67-93.

Stow, D.A.V., 1990. Sediment facies and processes on the distal Bengal Fan, Leg 116. ODP Texas & M University College Station; UK distributors IPOD Committee NERC Swindon.

Stow, D.A.V., Bowen, A.J., 1980. A Physical Model for the transport and sorting of fine-grained sediment by turbidity currents. Sedimentology 27, 31-46.

Stow, D.A.V., Shanmugam, G., 1980. Sequence of Structures in Fine-Grained Turbdites: Comparison of Recent Deep-Sea and Ancient Flysch Sediments. Sedimentary Geology 25, 23-42.

Stow, D.A.V., Piper, D.J.W., 1984. Deep water fine grained sediments: facies models, in: Stow, D.A.V., Piper, D.J.W. (Eds.), Fine Grained Sediments, Deep-Water Processes and Facies. 15, pp. 611–646.

Stuiver, M., Polach, H.A., 1977. Discussion: Reporting of 14C data. Radiocarbon vol. 19, pp. 355-363.

Stuiver, M., Braziunas, T.F., 1993. Modeling Atmospheric 14C Influences and 14C Ages of Marine Samples to 10,000 BC. Radiocarbon 35, 137-189.

Stuiver, M., Reimer, P.J., Braziunas, T.F., 1998. High precision radiocarbon age calibration for terrestrial and marine samples. Radiocarbon 40, 1127-1151.

Subarya, C., Chlieh, M., Prawirodirdjo, L., Avouac, J., Bock, Y., Sieh, K., Meltzner, A.J., Natawidjaja, D.H., McCaffrey, R., 2006. Plate-boundary deformation associated with the great Sumatra–Andaman earthquake. Nature 440, 46-51.

Sultan, N., Cattaneo, A., Sibuet, J.-C., Schneider, J.-L., 2009. Deep sea in situ excess pore pressure and sediment deformation off NW Sumatra and its relation with the December 26, 2004 Great Sumatra-Andaman Earthquake. Intl. J. Earth Sci. 98, 823-837.

Sultan, N., Cochonot, P., canals, M., Cattaneo, A., Dennielou, B., Haflidason, H., Laberg, J.S., Mienert, J., Trincardi, F., Urgeles, R., Vorren, T.O., Wilson, C., 2004. Triggering mechanisms of slope instability processes and sediment failures on continental margins: a geotechnical approach. Marine Geology 213, 219-231.

Sumner, E., Talling, P.J., Amy, L.A., 2009. Deposits of flows transitional between turbidity current and debris flow. Geology 37, 991-994.

Sumner, E., Siti, M., McNeil, L.C., Talling, P.J., Henstock, T., Wynn, R., Djadjadihardja, Y., Permana, H., 2013. Can turbidites be used to reconstruct a paleoearthquake record for the central Sumatran margin? Geology 41, 763-766.

Susilohadi, S., Gaedickea, C., Ehrhardt, A., 2005. Neogene structures and sedimentation history along the Sunda forearc basins off southwest Sumatra and southwest Java. Marine Geology 219, 133-154.

Syvitski, J.P.M., Schafer, C.T., 1996. Evidence for an earthquake-triggered basin collapse in Saguenay Fjord, Canada. Sed. Geol. v. 104, p. 127-153.

Tanioka, Y., Ruff, L.J., 1997. Source Time Functions. Seismological Research Letters 68, 386-400.

Thomson, R.E., Davis, E.E., Heesemann, M., Villinger, H., 2010. Observations of long-duration episodic bottom currents in the Middle America Trench: Evidence for tidally initiated turbidity flows. Journal of Geophysical Research 115, 23.

Tilmann, F.J., Craig, T.J., Grevemeyer, I., Suwargadi, B., Kopp, H., Flueh, E., 2010. The updip seismic/aseismic transition of the Sumatra megathrust illuminated by aftershocks of the 2004 Aceh-Andaman and 2005 Nias events Geophysical Journal International 181, 1261-1274.

Tiwari, R.K., Rao, K.N.N., 1998. Correlated variations and periodicity of global CO2, biological mass extinctions and extra-terrestrial bolide impacts over the past 250 million years and possible geodynamical implications. Geofizika 15.

Tolstoy, M., Bohnenstiehl, D.R., 2006. Hydroacoustic contributions to understanding the December 26th 2004 great Sumatra–Andaman Earthquake. Survey of Geophysics 27, 633-646.

Travasarou, T., Bray, J.D., Abrahamson, N.A., 2003. Empirical attenuation relationship for Arias Intensity. Earthquake Engineering and Structural Dynamics 32, 1133-1155.

Underwood, M.B., Hoke, K.D., Fisher, A.T., Davis, E.E., Giambalvo, E., Hlsdorff, L.Z., Spinelli, G.A., 2005. Provenance, Stratigraphic Architecture, and Hydrogeologic Influence of Turbidites on The Mid-Ocean Ridge Flank of Northwestern Cascadia Basin, Pacific Ocean. Journal of Sedimentary Research 75, 149-164.

Van Daele, M., Gnudde, V., Duyck, P., Pino, M., Urrutia, R., De Batist, M., 2013. Multidirectional, synchronously-triggered seismo-turbidites and debrites revealed by X-ray computed tomography (CT). Sedimentology, 20.

Van Der Lingen, G.J., 1969. The Turbidite Problem. New Zealand Journal of Geology and Geophysics 12, 7-50.

Völker, D., Reichel, T., Wiedicke, M., Heubeck, C., 2008. Turbidites deposited on Southern Central Chilean seamounts: Evidence for energetic turbidity currents. Marine Geology 251, 15-31.

Waldmann, N., Anselmetti, F.S., Ariztegui, D., Austin Jr., J.A., Pirouz, M., Moy, C.M., Dunbar, R.B., 2011. Holocene mass-wasting events in Lago Fagnano, Tierra del Fuego (54˚S): implications for paleoseismicity of the Magallanes-Fagnano transform fault. Basin Research 23, 171-190.

Ward, S.N., 2002. Planetary cratering: A probabilistic approach. Journal of Geophysical Research 107, 11.

Wells, R.E., Blakely, R.J., Sugiyama, Y., Scholl, D.W., Dinterman, P.A., 2003. Basin-centered asperities in great subduction zone earthquakes: A link between slip, subsidence, and subduction erosion. Journal of Geophysical Research 108, doi:10.1029/2002JB002072.

Wesnousky, S.G., 1994. The Gutenberg-Richter or characteristic earthquake distribution, which is it?

Wesnousky, S.G., 2008. Displacement and Geometrical Characteristics of Earthquake Surface Ruptures: Issues and Implications for Seismic-Hazard Analysis and the Process of Earthquake Rupture. BSSA 98, 1609-1632.

Wheatcroft, R.A., Sommerfield, C.K., 2005. River sediment flux and shelf accumulation rates on the Pacific Northwest margin. Continental Shelf Research 25, 311-332.

Wilson, C., Keefer, D.K., 1985. U.S.G.S. Professional Paper 1360: Predicting Areal Limits of Earthquake-Induced Landsliding, in: Ziony, J.I. (Ed.), U.S.G.S. Professional Paper. U.S Geological Survey, Washington, D. C., pp. 317-345.

Wilson, R.C., 1993. Relation of Arias Intensity to Magnitude and Distance in California. USGS.

Wiseman, K., Bürgmann, R., 2011. Stress and Seismicity Changes on the Sunda Megathrust Preceding the 2007 Mw 8.4 Earthquake. BSSA 101, 313-326.

Witter, R.C., Zhang, Y., Wang, K., Priest, G.R., Goldfinger, C., Stimely, L.L., English, J.T., Ferro, P.A., 2011. Simulating Tsunami Inundation at Bandon, Coos County, Oregon, Using Hypothetical Cascadia and Alaska Earthquake Scenarios, in: DOGAMI (Ed.). State of Oregon, pp. 1-63.

Witter, R.C., Zhang, Y.J., Wang, K., Priest, G., Goldfinger, C., Stimely, L., English, J., Ferro, P., 2013. Simulated tsunami inundation for a range of Cascadia megathrust earthquake scenarios at Bandon, Oregon, USA. Geosphere 9, 22.

Wright, S.G., Rathje, E.M., 2003. Triggering Mechanisms of Slope Instability and their Relationship to Earthquakes and Tsunamis. Pure and Applied Geophysics 160, 1865.

Yeats, R.S., 2007. Paleoseismology: Why can't earthquakes keep on schedule? Geology 35, 863-864.

Young, I.R., 1999. Seasonal Variability of the Global Ocean Wind and Wave Climate. International Journal of Climatology 19, 931-950.

Youngs, R.R., Chiou, S.J., Silva, W.J., Humphrey, J.R., 1997. Strong Ground Motion Attenuation Relationships for Subduction Zone Earthquakes. Seismological Research Letters 68, 58-78.

Zdanowicz, C.M., Zielinski, G.A., Germani, M.S., 1999. Mount Mazama eruption: Calendrical age verified and atmospheric impact assessed. Geology v. 27, p. 621-624.

Zhao, J.X., Xu, H., 2012. Magnitude-Scaling Rate in Ground-Motion Prediction Equations for Response Spectra from Large Subduction Interface Earthquakes in Japan. BSSA 102, 222-235.

Chapter 2 References

Abdeldayem, A.L., Ikehara, K. and Yamazaki, T., Flow Path of the 1993 Hokkaido-Nansei-Oki Earthquake Seismoturbidite, Southern Margin of the Japan Sea North Basin, Inferred from Anisotropy of Magnetic Susceptibility, Geophysical Journal International, 157, 15-24, 2004.

Abrantes, F., Alt-Epping, U., Lebreiro, S., Voelker, A., and Schneider, R., Sedimentological Record of Tsunamis on Shallow-Shelf Areas: The Case of the 1969 Ad and 1755 AD Tsunamis on the Portuguese Shelf Off Lisbon, Marine Geology, 249, 283-293, 2008.

Adams, J., Paleoseismicity of the Cascadia Subduction Zone: Evidence from Turbidites off the Oregon-Washington Margin, Tectonics, v. 9, p. 569-584, 1990.

Atwater, B.F., Evidence for Great Holocene Earthquakes Along the Outer Coast of Washington State, Science, v. 236, p. 942-944, 1987.

Atwater, B.F. and Hemphill-Haley, E., Recurrence Intervals for Great Earthquakes of the Past 3500 Years at Northeastern Willapa Bay, Washington, U.S. Geological Survey Professional Paper, 1576, 108 p., 1997.

Baas, J.H., McCaffrey, W.D., Haughton, P.D.W. and Choux, C., Coupling between Suspended Sediment Distribution and Turbulence Structure in a Laboratory Turbidity Current, Journal of Geophysical Research, 110, 20 p., 2005.

Bandopadhyay, A. and Bandopadhyay, R. R., Thermogenic Hydrocarbons in the Mid-Proximal Bengal Fan, West of the Andaman -Nicobar Islands, Marine Georesources and Geotechnology, 17, 1-16, 1999.

Beattie, P. D. and Dade, W. B., Is Scaling in Turbidite Deposition Consistent with Forcing by Earthquakes, Journal of Sedimentary Research, 66, 909-915, 1996.

Bilham, R., Partial and Complete Rupture of the Indo-Andaman Plate Boundary 1847 - 2004., Seismological Research Letters, 76, 299-311, 2005.

Biscontin, G. and Pestana, J. M., Factors Affecting Seismic Response of Submarine Slopes, Natural Hazards and Earth System Sciences, 6, 97-107, 2006.

Blott, S.J. and Pye, K., Particle Size Distribution Analysis of Sand-Sized Particles by Laser Diffraction: An Experimental Investigation of Instrument Sensitivity and the Effects of Particle Shape, Sedimentology, 53, 671-685, 2006.

Bondevik, S., Svendsen, J. I., and Mangerud, J., Tsunami Sedimentary Facies Deposited by the Storegga Tsunami in Shallow Marine Basins and Coastal Lakes, Western Norway, Sedimentology, 44, 1115-1131, 1997.

Bouma, A. H., Key Controls on the Characteristics of Turbidite Systems, Confined Turbidite System, 9-22, 2004.

Bouma, A.H., Sedimentology of Some Flysch Deposits, Elsevier Publishing, 168 pp, 1962.

Bouma, A. H., Delery, A. M. and Benavides-lglesias, A., Basin Characteristics, Tectonic History, and Grain Size Are Main Influences in the Transport and Deposition of Turbidity Currents, Gulf Coast Association of Geological Societies Transactions, 56, 103-118, 2006.

Bourget, J., Zaragosi, S., Ellouz-Zimmermann, S., Ducassou, E., Prins, M.A., Garlan, T., Lanfumey, V., Schneider, J.-L., Rouillard, P. and Giraudeau, J., Highstand Vs. Lowstand Turbidite System Growth in the Makran Active Margin: Imprints of High-Frequency External Controls on Sediment Delivery Mechanisms to Deep Water Systems, Marine Geology, 274, 187-208, 2010.

Bourget, J., Zargosi, S., Ellouz-Zimmermann, N., Mouchot, N., Garlans, T., Schneider, J., Lanfumey, V. and Lallemant, S., Turbidite System Architecture and Sedimentary Processes Along Topographically Complex Slopes: The Makran Convergent Margin, Sedimentology, 58, 376-406, 2011.

Briggs, R. W., Sieh, K., Meltzner, A. J., Natawidjaja, D., Galetzka, J., Suwargadi, B., Hsu, Y., Simons, M., Hananto, N., Suprihanto, I., Prayudi, D., Avouac, J., Prawirodirdjo, L. and Bock, Y., Deformation and Slip Along the Sunda Megathrust in the Great 2005 Nias-Simeulue Earthquake, Science, 311, 1897-1901, 2006.

Carlson, P.R., Marine Geology of Astoria Submarine Canyon, Marine Geology, PhD Thesis, Oregon State University, 259 pp., 1967.

Carlson, P., R. and Nelson, C. H., Sediments and Sedimentary Structures of the Astoria Submarine Canyon-Fan System, Northeast Pacific, Sedimentary Petrology, 39, 1269-1282, 1969.

Carter, R. M., The Nature and Evolution of Deep-Sea Channel Systems, Basin Research, 1, 41-54, 1988.

Chaytor, J. D., Goldfinger, C., Dziak, R. P. and Fox, C. G., Active Deformation of the Gorda Plate: Constraining Deformation Models with New Geophysical Data, Geology, 32, 353-356, 2004.

Chlieh, M., Avouac, J-P., Hjorleifsdottir, V., Song, T-R A., Ji, Chen , Sieh, K., Sladen, A., Hebert, H., Prawirodirdjo, L., Bock, Y. and Galetzka, J., Coseismic Slip and Afterslip of the Great (Mw 9.15) Sumatra-Andaman Earthquake of 2004, Bulletin of the Seismological Society of America, 97, S152-S173, 2007.

Chlieh, M., Avouac, J. P., Sieh, K., Natiwidjaja, D. H. and Galetzka, J., Heterogeneous Coupling of the Sumatran Megathrust Constrained by Geodetic and Paleogeodetic Measurements, Journal of Geophysical Research, 113, 31 pp. 2008.

Combes, H. J. D., Caulet, J. and Tribovillard, N. P., Pelagic Productivity Changes in the Equatorial Area of the Northwest Indian Ocean During the Last 400,000 Years, Marine Geology, 158, 27-55, 1999.

Curray, J. R. and Moore, D. G., Growth of the Bengal Deep-Sea Fan and Denudation in the Himalayas, GSA Bulletin, 82, 563-572, 1971.

Curray, J. R., Emmel, F. J. and Moore, D. G., The Bengal Fan: Morphology, Geometry, Stratigraphy, History and Processes, Marine and Petroleum Geology, 19, 1191-1223, 2003.

Dallimore, A., Thomson, R.E. and Bertram, M.A., Modern to Late Holocene Deposition in an Anoxic Fjord on the West Coast of Canada: Implications for Regional Oceanography, Climate and Paleoseismic History, Marine Geology, 219, 47-60, 2005.

Drexler, T. M., Nittrouer, C. A. and Mullenbach, B. L., Impact of Local Morphology on Sedimentation in a Submarine Canyon, ROV Studies in Eel Canyon, Northern California, U.S.A, Journal of Sedimentary Research, 76, 839-853, 2006.

Duncan, J.R. and Kulm, L.D., Mineralogy, Provenance and Dispersal History of Late Quaternary Deep-Sea Sands in Cascadia Basin and Blanco Fracture Zone, JSP, 40, 874-887, 1970.

Duncan, R.A., Late Pleistocene and Postglacial Sedimentation and Stratigraphy of Deep-Sea Environments off Oregon, Ph.D. thesis, 222 pp., 1968.

Dziak, R. P., Fox, C. G., Bobbitt, A. and Goldfinger, C., Bathymetric Map of the Gorda Plate: Structural and Geomorphological Processes Inferred from Mulitbeam Surveys, Marine Geophysical Researches, 22, 235-250, 2001.

EEZ-SCAN-84-Scientific-Staff, Atlas of the Exclusive Economic Zone, Western Conterminous United States., 1986.

Fisher, D., Mosher, D., Austin, J.A., Gulick, S.P., Masterlark, T. and Moran, K., Active Deformation across the Sumatran Forearc over the December 2004 Mw 9.2 Rupture, Geology, 35, 99-102, 2007.

Fukuma, K., Origin and Applications of Whole-Core Magnetic Susceptibility of Sediments and Volcanic Rocks from Leg 152, Proceedings fo the Ocean Drilling Program: Scientific Results, 152, 271-280, 1998.

Goldfinger, C., Possible Turbidite Record of Earthquake Source Characteristics: A Small Scale Test., U.S.G.S. Final Technical Report, N.E.H.R.P. Award 07HQGR0064, 2011.

Goldfinger, C., Kulm, L.D., Yeats, R.S., Appelgate, B., MacKay, M. and Moore, G.F., Transverse Structural Trends Along the Oregon Convergent Margin: Implications for Cascadia Earthquake Potential, Geology, v. 20, 141-144, 1992.

Goldfinger, C., Kulm, L.D., Yeats, R.S., Appelgate, B., MacKay, M. and Cochrane, G.R., Active Strike-Slip Faulting and Folding of the Cascadia Plate Boundary and Forearc in Central and Northern Oregon, Assessing and Reducing Earthquake Hazards in the Pacific Northwest, Professional Paper 1560, p. 223-256, 1996.

Goldfinger, C., Kulm, L.D., Yeats, R.S., McNeill, L.C. and Hummon, C., Oblique Strike-Slip Faulting of the Central Cascadia Submarine Forearc, Journal of Geophysical Research, 102, 8217-8243, 1997.

Goldfinger, C., Nelson, C.H. and Johnson, J. E., Deep-Water Turbidites as Holocene Earthquake Proxies: The Cascadia Subduction Zone and Northern San Andreas Fault Systems, Annali Geofisica, 46, 1169-1194, 2003.

Goldfinger, C., Morey, A. E., Nelson, C.H., Gutierrez-Pastor, J, Johnson, J. E., Karabanov, E., Chaytor, J. and Ericsson, A., Rupture Lengths and Temporal History of Significant Earthquakes on the Offshore and North Coast Segments of the Northern San Andreas Fault Based on Turbidite Stratigraphy, Earth and Planetary Science Letters, 254, 9-27, 2007.

Goldfinger, C., Grijalva, K., Burgmann, R., Morey, A. E., Johnson, J. E., Nelson, C.H., Gutierrez-Pastor, J, Ericsson, A., Karabanov, E., Chaytor, J.D., Patton, J. and Gracia, E., Late Holocene Rupture of the Northern San Andreas Fault and Possible Stress Linkage to the Cascadia Subduction Zone Bulletin of the Seismological Society of America, 98, 861-889, 2008.

Goldfinger, C., Nelson, C.H., Morey, A., Johnson, J.E., Gutierrez-Pastor, J., Eriksson, A.T., Karabanov, E., Patton, J., Gracia, E., Enkin, R., Dallimore, A., Dunhill, G. and Vallier, T., Turbidite Event History: Methods and Implications for Holocene Paleoseismicity of the Cascadia Subduction Zone, USGS Professional Paper # 178, 2012 a.

Goldfinger, C., Morey, A., Black, B., and Patton, J., Spatially Limited Mud Turbidites on the Cascadia Margin: Segmented Earthquake Ruptures?, in Pantosti, D., Gracia, E., Lamarche, G., Nelson, C.H., and Tinti, S., eds., Research Conference Submarine Paleoseismology: The Offshore Search of Large Holocene Earthquakes: Obergurgl, Austria, Natural Hazards and Earth System Sciences. 2012 b.

Gorsline, D.S., De Diego, T. and Nava-Sanchez, E.H., Seismically Triggered Turbidites in Small Margin Basins: Alfonso Basin, Western Gulf of California and Santa Monica Basin, California Borderland, Sedimentary Geology, 135, 21-35, 2000.

Gràcia, E., Vizcaino, A., Escutia, C., Asioli, A., Rodés, Á., Pallàs, R., Garcia-Orellana, J., Lebreiro, S. and Goldfinger, C., Holocene Earthquake Record Offshore Portugal (Sw Iberia): Testing Turbidite Paleoseismology in a Slow-Convergence Margin, Quaternary Science Reviews, 29, 1156-1172, 2010.

Graindorge , D. , Klingelhoefer, F. , Sibuet, J., McNeill , L., Henstock, T. J., Dean, S., Gutscher, M., Dessa, J. X., Permana, H., Singh, S. C., Leau, H., White, N., Carton, H., Malod, J. A., Rangin, C., Aryawan, K. G., Chaubey, A. K., Chauhan, A., Galih, D. R., Greenroyd, C. J., Laesanpura, A., Prihantono, J., Royle, G., and Shankar, U., Impact of Lower Plate Structure on Upper Plate Deformation at the Nw Sumatran Convergent Margin from Seafloor Morphology Earth and Planetary Science Letters, 275, 201-210, 2008.

Griggs, G.B., Carey, JR. A.G. and Kulm, L.D., Deep-Sea Sedimentation and Sediment-Fauna Interaction in Cascadia Channel and N Cascadia Abyssal Plain, Deep-Sea Research, 16, 157-170, 1969.

Gulick, S. P. S., Austin, J. A. Jr, McNeill, L.C., Bangs, N. L. B., Martin, K. M., Henstock, T. J., Bull, J. M., Dean, S., Djadjadihardja, Y. S. and Permana, H., Updip Rupture of the 2004 Sumatra Earthquake Extended by Thick Indurated Sediments, Nature Geoscience, 4, 453-456, 2011.

Hagstrum, J.T., Atwater, B. F. and Sherrod, B.L., Paleomagnetic Correlation of Late Holocene Earthquakes among Estuaries in Washington and Oregon, G3, 5, doi:10.1029/2004GC000736, 2004.

Hampton, M.A., Lee, H.J. and Locat, J., Submarine Landslides, Rev. Geophys., 34, 33-59, 1996.

Henstock, T.J., McNeill, L.C. and Tappin, J.R., Seafloor Morphology of the Sumatran Subduction Zone: Surface Rupture During Megathrust Earthquakes?, Geology, 34, 485-488, 2006.

Inouchi, Y., Kinugasa, Y., Kumon, F., Nakano, S., Yasumatsu, S. and Shiki, T., Turbidites as Records of Intense Palaeoearthquakes in Lake Biwa, Japan, Sed. Geol., v. 104, p. 117-125, 1996.

Ishii, Miaki, Shearer, Peter M., Houston, Heidi and Vidale, John E., Extent, Duration and Speed of the 2004 Sumatra-Andaman Earthquake Imaged by the Hi-Net Array, Nature, 435, 933, 2005.

Johnson, J. E., Goldfinger, C., Trehu, A. M., Bangs, N. L.B., Torres, M. E. and Chevallier, J., North-South Variability in the History of Deformation and Fluid Venting across Hydrate Ridge, Cascadia Margin, Proceedings of the Ocean Drilling Program; scientific results; drilling gas hydrates on Hydrate Ridge, Cascadia continental margin; covering Leg 204 of the cruises of the drilling vessel JOIDES Resolution; Victoria, British Columbia, Canada, 16 pp., 2005.

Kahru, M., Gille, S. T., Murtugudde, R., Strutton, P. G., Manzano, M., Sarabia, Wang, H. and Mitchell, B. G., Global Correlations between Winds and Ocean Chlorophyll, Journal of Geophysical Research, 115, 11 pp., 2010.

Karlin, R. E., Holmes, M., Abella, S. E. B. and Sylwester, R., Holocene Landslides and a 3500-Year Record of Pacific Northwest Earthquakes from Sediments in Lake Washington, Geological Society of America Bulletin, 116, 94-108, 2004.

Karlin, R. and Seitz, G., A Basin Wide Record of Earthquakes at Lake Tahoe: Validation of the Earthquake Induced Turbidite Model with Sediment Core Analysis: Collaborative Research with UNR and SDSU, Final Technical Report for 07HQGR0014 and 07HQGR0008, 18 pp. 2007.

Keefer, D. K., Landslides Caused by Earthquakes, GSA Bulletin, 95, 406-421, 1984.

Kneller, B. and McCaffrey, B., Modeling the Effects of Salt-Induced Topography on Deposition from Turbidity Currents, Gulf Coast Section Society of Economic Paleontologists and Mineralogists Foundation Sixteenth annual research conference, 16, 137-145, 1995.

Kopp, H., Weinrebe, W., Ladage, S., Barckhausen, U., Klaeschen, D., Flueh, E. R., Gaedicke, C., Djajadihardja, Y., Grevemeyer, I., Krabbenhoeft, A., Papenbergn, C. and Zillmern, M., Lower Slope Morphology of the Sumatra Trench System, Basin Research, 20, 519-529, 2008.

Krabbenhoeft, A., Weinrebe, R. W., Kopp, H., Flueh, E. R., Ladage, S., Papenberg, C., Planert, L. and Djajadihardja, Y., Bathymetry of the Indonesian Sunda Margin-Relating Morphological Features of the Upper Plate Slopes to the Location and Extent of the Seismogenic Zone, Natural Hazards and Earth System Sciences, 10, 1899-1911, 2010.

Ladage, S., Weinrebe, W., Gaedicke, C., Barckhausen, U., Flueh, E.R., Heyde, I., Krabbenhoeft, A., H. Kopp, S. Fajar and Djardjardihardja, Y., Bathymetric Survey Images Structure Off Sumatra, EOS Trans. AGU, 87, 2006.

Lorenzoni, L., Thunell, R. C, Benitez-Nelson, C. R., Hollander, D., Martinez, N., Tappa, E., Varela, R., Astor, Y. and Muller-Karger, F. E., The Importance of Subsurface Nepheloid Layers in Transport and Delivery of Sediments to the Eastern cariaco basin, Venezuela, Deep-Sea Research I, 56, 2249-2262, 2012 a.

Lorenzoni, L., Benitez-Nelson, C. R., Thunell, R. C., Hollander, D., Varela, R., Astor, Y., Audemard, F. A. and Muller-Karger, F. E., Potential Role of Event-Driven Sediment Transport on Sediment Accumulation in the Cariaco Basin, Venezuela, Marine Geology, 307-310, 105-110, 2012 b.

Lovlie, R. and Van Veen, P., Magnetic Susceptibility of a 180 M Sediment Core: Reliability of Incremental Sampling and Evidence for a Relationship between Susceptibility and Gamma Activity, Palaeomagnetic Applications in Hydrocarbon Exploration and Production, 259-266, 1995.

Malik, J. N., Shishikura, M., Echigo, T., Ikeda, Y., Satake, K., Kayanne, H., Sawai, Y., Murty, C. V. R. and Dikshit, D., Geologic Evidence for Two Pre-2004 Earthquakes During Recent Centuries near Port Blair, South Andaman Island, India, Geology, 39, 559-562, 2011.

Masson, D. G., Harbitz, C. B., Wynn, R. B., Pedersen, G. and Løvholt, F., Submarine Landslides: Processes, Triggers and Hazard Prediction, Philosophical Transactions of the Royal Society, 364, 2009-2039, 2006.

Maurin, T. and Rangin, C., Impact of the 90°E Ridge at the Indo-Burmese Subduction Zone Imaged from Deep Seismic Reflection Data, Marine Geology, 266, 143-455, 2009.

McCaffrey, R., Qamar, A., King, R.W., Wells, R.W., Khazaradze, G., Williams, C., Stevens, C., Vollick, J.J. and Zwick, P.C., Fault Locking, Block Rotation and Crustal Deformation in the Pacific Northwest, Geophysical Journal International, 2007.

McCaffrey, W. D., Choux, C. M., Baas, J. H. and Haughton, P. D. W., Spatio-Temporal Evolution of Velocity Structure, Concentration and Grain-Size Stratification within Experimental Particulate Gravity Currents, Marine and Petroleum Geology, 20, 851-860, 2003.

McCalpin, J. P. and Nelson, A. R., Introduction to Paleoseismology, Paleoseismology, 62, 1-32, 1996.

McNeill, L. C., Goldfinger, C., Kulm, L. V. D. and Yeats, R. S., Tectonics of the Neogene Cascadia Forearc Basin: Investigations of a Deformed Late Miocene Unconformity, Bulletin of the Geological Society of America, 112, 1209-1224, 2000.

Meltzner, A. J., Sieh, K., Chiang, H., Shen, C., Suwargadi, B. W., Natawidjaja, D. H., Philbosian, B., Briggs, R. W. and Galetzka, J., Coral Evidence for Earthquake Recurrence and an A.D. 1390–1455 Cluster at the South End of the 2004 Aceh–Andaman Rupture, Journal of Geophysical Research, 115, 1-46, 2010.

Meltzner, A. J., Sieh, K., Chiang, H., Shen, C., Suwargadi, B. W., Natawidjaja, D. H., Philibosian, B. and Briggs, R. W., Persistent Termini of 2004- and 2005-Like Ruptures of the Sunda Megathrust, Journal of Geophysical Research, 117, 15 pp., 2012.

Meunier, P., Hovius, N. and Haines, A. J., Regional Patterns of Earthquake-Triggered Landslides and Their Relation to Ground Motion, Geophysical Research Letters, 34, 5 pp., 2007.

Moore, D.G., Curray, J.R. and Emmell, F.J., Large Submarine Slide (Olistostrome) Associated with Sunda Arc Subduction Zone, Northeast Indian Ocean, Marine Geology, 21, 211-226, 1976.

Mosher, D.C., Jr., J.A. Austin, Fisher, D. and Gulick, S.P.S., Deformation of the Northern Sumatra Accretionary Prism from High-Resolution Seismic Reflection Profiles and ROV Observations, Marine Geology, 252, 89-99, 2008.

Mosher, D. C. and Piper, D., Analysis of Multibeam Seafloor Imagery of the Laurentian Fan and the 1929 Grand Banks Landslide Area, Submarine mass movements and their consequences; 3rd international symposium. , 27, 77-88, 2007.

Mosher, D. C., Moscardelli, L., Shipp, R. C., Chaytor, J. D., Baxter, C. D. P., Lee, H. J. and Urgeles, R., Submarine Mass Movements and Their Consequences, Submarine Mass Movements and Their Consequences, 28, 1-8, 2010.

Mulder, T., Syvitski, J. P. M., Migeon, S., Faugeres, J., and Savoye, B., Marine Hyperpycnal Flows; Initiation, Behavior and Related Deposits; a Review, Marine and Petroleum Geology, 20, 861-882, 2003.

Nakajima, T., Initiation Processes of Turbidity Currents; Implications for Assessments of Recurrence Intervals of Offshore Earthquakes Using Turbidites, Bulletin of the Geological Survey of Japan, v. 51, p. 79-87, 2000.

Nakajima, T. and Kanai, Y., Sedimentary Features of Seismoturbidites Triggered by the 1983 and Older Historical Earthquakes in the Eastern Margin of the Japan Sea, Sedimentary Geology, 135, 1-19, 2000.

Natawidjaja, D.H., Sieh, K., Ward, S.N., Cheng, H., Edwards, R. L., Galetzka, J. and Suwargadi, B.W., Paleogeodetic Records of Seismic and Aseismic Subduction from Central Sumatran Microatolls, Indonesia, Journal of Geophysical Research, 109, 37, 2004.

Nelson, A. R., Kelsey, H. M. and Witter, R. C., Great Earthquakes of Variable Magnitude at the Cascadia Subduction Zone, Quaternary Research, 65, 354-365, 2006.

Nelson, C.H., Late Pleistocene and Holocene Depositional Trends, Processes and History of Astoria Deep-Sea Fan, Mar. Geol., 20, 129-173, 1976.

Nelson, C.H., Kulm, L.D., Carlson, P.R. and Duncan, J.R., Mazama Ash in the Northeastern Pacific, Science, v. 161, p. 47-49, 1968.

Nelson, C. H., Meyer, A. W., Thor, D. and Larsen, M., Crater Lake, Oregon: A Restricted Basin with Base-of-Slope Aprons of Nonchanellized Turbidites, Geology, 14, 238-241, 1986.

Nelson, C.H., Hampton, M.A., Karl, H.A. and Barber, J.H. Jr., Astoria Fan, a Trench-Filling Elongate Deep-Sea Fan, Tectonics, sedimentation and evolution of the Eel River and associated coastal basins of Northern California, Misc. Publication 37, 113-120, 1987.

Nelson, C.H., Carlson, P.R. and Bacon, C.R., The Mount Mazama Climactic Eruption (~6900 Yr B.P.) and Resulting Convulsive Sedimentation on the Crater Lake Caldera Floor, Continent, and Ocean Basin, Geological Society of America, Special Paper 229, 37-57, 1988.

Nelson, C.H., Goldfinger, C., Johnson, J.E. and Dunhill, G., Variation of Modern Turbidite Systems Along the Subduction Zone Margin of Cascadia Basin and Implications for Turbidite Reservoir Beds, Deep-water Reservoirs of the World, 31 pp., 2000.

Nelson, C. H., Escutia, C., Goldfinger, C., Karabanov, E., Gutierrez-Pastor, J. and DeBatist, M., External Controls on Modern Clastic Turbidite Systems: Three Case Studies, Society for Sedimentary Geology, 92, 57-76, 2009.

Nelson, C. H., Escutia, C., Damuth, J. E. and Twichell, D. C., Interplay of Mass-Transport and Turbidite-System Deposits in Different Active Tectonic and Passive Continental Margin Settings: External and Local Controlling Factors, Society for Sedimentary Geology, 96, 39-66, 2011.

Newcomb, K. R. and McCann, W. R., Seismic History and Seismotectonics of the Sunda Arc, Journal of Geophysical Research, 92, 421-439, 1987.

Ni, S., Kanamori, H. and Helmberger, D., Energy Radiation from the Sumatra Earthquake, Nature, 434, 582, 2005.

Noda, A., Turbidites Along Kushiro Canyon, Workshop on Turbidites as Earthquake Recorders, 2004.

Noda, A., Katayama, H., Sagayama, T., Suga, K., Uchida, Y., Satake, K., Abe, K., and Okamura, Y., Evaluation of Tsunami Impacts on Shallow Marine Sediments: An Example from the Tsunami Caused by the 2003 Tokachi-Oki Earthquake, Northern Japan, Sedimentary Geology, 200, 314-327, 2007.

Noller, J. S., Sowers, J. M. and Lettis, W. R., Quaternary Geochronology, AGU Reference Shelf 4, 2000.

Normark, William R. and Reid, Jane A., Extensive Deposits on the Pacific Plate from Late Pleistocene North American Glacial Lake Outbursts, The Journal of Geology, 222, 617-637, 2003.

Okamura, Y., Paleoseismology of Deep-Sea Faults Based on Marine Surveys in Japan Sea, Workshop on Turbidites as Earthquake Recorders, 2004.

Ortiz, M. and Bilham, R., Source Area and Rupture Parameters of the 31 December Mw = 7.9 Car Nicobar Earthquake Estimated from Tsunamis Recorded in the Bay of Bengal, J. Geophys. Res., 108, 2003.

Passega, R., Texture as Characteristic of Clastic Deposition, AAPG Bull., 41, 1952-1984, 1957.

Passega, R., Grain Size Representation by CM Patterns as a Geological Tool, Journal of Sedimentary Petrology, 34, 830-847, 1964.

Piper, D.J.W. Turbidite muds and silts on deepsea fans and abyssal plains. In Stanley, D.J., and Kelling, G. (Eds.), Sedimentation in Submarine Canyons, Fans and Trenches: Stroudsburg, PA (Dowden, Hutchinson and Ross), 163-175, 1978.

Piper, D. J. W. and Normark, W. R., Processes That Initiate Turbidity Currents and Their Influence on Turbidites: A Marine Geology Perspective, journal of Sedimentary Research, 79, 347-362, 2009.

Prell, W. L., Imbrie, J., Martinson, D. G., Morley, J. J., Pisias, N. G., Shackleton, N. J., and Streeter, H. F., Graphic Correlation of Oxygen Isotope Stratigraphy Application to the Late Quaternary, Paleoceanography, 1, 137-162, 1986.

Pouderoux, H., Proust, J., Lamarche, G., Orpin, A. and Neil, H., Postglacial (after 18 Ka) Deep-Sea Sedimentation Along the Hikurangi Subduction Margin (New Zealand): Characterisation, Timing and Origin of Turbidites, Marine Geology, 295-298, 51-76, 2012.

Rajendran, K., Rajendran, C. P, Earnest, A., Ravi Prasad, G. V., Dutta, K., Ray, D. K. and Anu, R., Age Estimates of Coastal Terraces in the Andaman and Nicobar Islands and Their Tectonic Implications, Tectonophysics, 455, 52-60, 2008.

Reid, J. A. and Normark, W. R., Tufts Submarine Fan: Turbidity-Current Gateway to Escanaba Trough, USGS Bulletin 2216, 26 pp., 2003.

Reimer, P. J., Baillie, M. G. L., Bard, E., Bayliss, A., Beck, J. W., Bertrand, C. J. H., Blackwell, P. G., Ramsey, C. B., Buck, C. E., Burr, G. S., Edwards, R. L., Friedrich, M., Grootes, P. M., Guilderson, T. P., Hajas, I., Heaton, T. J., Hogg, A. G., Hughen, K. A., Kaiser, K. F., Kromer, B., McCormac, F. G., Manning, S. W., Reimer, R. W., Richards, D. A., Southon, J. R., Talamo, S., van der Plicht, J. and Weyhenmeyer, C. E., Intcal09 and Marine09 Radiocarbon Age Calibration Curves, 0–50,000 Years Cal Bp, Radiocarbon, 51, 1111-1150, 2009.

Ruff, L. and Kanamori, H., Seismicity and the Subduction Process, Physics of the Earth and Planetary Interiors, v. 23, 240-252, 1980.

Salisbury, M., Patton, J., Kent, A., Goldfinger, C., Djadjadihardja, Y. and Udrekh, U., Newly Discovered Deep-Sea Ash Layers Reveal Evidence of Large Holocene Volcanic Eruptions from Sumatra, Indonesia, Journal of Volcanology and Geothermal Research, 231-232, 61-71, 2012.

Shanmugam, G., The Constructive Functions of Tropical Cyclones and Tsunamis on Deep-Water Sand Deposition During Sea Level Highstand: Implications for Petroleum Exploration, AAPG Bulletin, 92, 443-471, 2008.

Shiki, T., Kumon, F., Inouchi, Y., Kontani, Y., Sakamoto, T., Tateishi, M., Matsubara, H. and Fukuyama, K., Sedimentary Features of the Seismo-Turbidites, Lake Biwa, Japan, Sedimentary Geology, vol. 135, 37-50, 2000.

Shirai, M., Omura, A., Wakabayashi, T., Uchida, J. and Ogami, T., Depositional Age and Triggering Event of Turbidites in the Western Kumano Trough, Central Japan During the Last Ca. 100 Years, Marine Geology, 271, 225-235, 2010.

Sieh, K., Sumatran Megathrust Earthquakes: From Science to Saving Lives, Philosophical Transactions of the Royal Society, 364, 1947-1963, 2006.

Sieh, K. and Natawidjaja, D., Neotectonics of the Sumatran Fault, J. Geophys. Res., 105, 28295, 2000.

Singh, S. C., Hananto, N. D., Chauhan, A. P. S., Permana, H., Denolle, M., Hendriyana, A. and Natawidjaja, D., Evidence of Active Backthrusting at the Ne Margin Ofmentawai Islands, Swsumatra, Geophysical Journal International, 180, 703-714, 2010.

Skinner, L.C. and McCave, I.N., Analysis and Modeling of Gravity- and Piston Coring Based on Soil Mechanics, Marine Geology, 199, 181-204, 2003.

Smith, W. H.F. and Sandwell, D. T., Global Seafloor Topography from Satellite Altimetry and Ship Depth Soundings, Science, 277, 1957-1962, 1997.

Stein, S. and Okal, E., Ultralong Period Seismic Study of the December 2004 Indian Ocean Earthquake and Implications for Regional Tectonics and the Subduction Process, BSSA, 97, S279-S295, 2007.

Sternberg, R.W., Transport and Accumulation of River-Derived Sediment on the Washington Continental Shelf, J. Geol. Soc. London, 143, 945-956, 1986.

St-Onge, G., Mulder, T., Piper, D. J.W., Hillaire-Marcel, C. and Stoner, J. S., Earthquake and Flood-Induced Turbidites in the Saguenay Fjord (Québec): A Holocene Paleoseismicity Record, Quaternary Science Reviews, 23, 283-294, 2004.

St-Onge, G., Chapron, E., Mulsow, S., Salas, M., Viel, M., Debret, M., Foucher, A., Mulder, T., Winiarski, T., Desmet, M., Costa, P. J.M., Ghaleb, B., Jaouen, A. and Locat, J., Comparison of Earthquake-Triggered Turbidites from the Saguenay (Eastern Canada) and Reloncavi (Chilean Margin) Fjords: Implications for Paleoseismicity and Sedimentology, Sedimentary Geology, 243-244, 89-107, 2012.

Stow D.A.V, Sediment Facies and Processes on the Distal Bengal Fan, Leg 116, 377-396; In: Proc., scientific results, ODP, Leg 116, distal Bengal Fan (1990), Editor Cochran J. R. and et al., p. 377-396, 1990.

Stow, D.A.V. and Piper, D.J.W., Deep-Water Fine-Grained Sediments: Facies Models, Fine-Grained Sediments: Deep-Water Processes and Facies, 611-646, 1984.

Strasser, M., Anselmetti, F. S., Fäh, D., Giardini, D. and Schnellmann, M., Magnitudes and Source Areas of Large Prehistoric Northern Alpine Earthquakes Revealed by Slope Failures in Lakes, Geology, 34, 1005-1008, 2006.

Stuiver, M. and Polach, H.A., Discussion: Reporting of ^{14}C Data, Radiocarbon, vol. 19, pp. 355-363, 1977.

Stuiver, M. and Braziunas, T. F., Modeling Atmospheric ^{14}C Influences and ^{14}C Ages of Marine Samples to 10,000 Bc, Radiocarbon, 35, 137-189, 1993.

Stuiver, M., Reimer, P.J. and Braziunas, T. F., High Precision Radiocarbon Age Calibration for Terrestrial and Marine Samples, Radiocarbon, 40, 1127-1151, 1998.

Subarya, C., Chlieh, M., Prawirodirdjo, L., Avouac, J., Bock, Y., Sieh, K., Meltzner, A. J., Natawidjaja, D. H. and McCaffrey, R., Plate-Boundary Deformation Associated with the Great Sumatra–Andaman Earthquake, Nature, 440, 46-51, 2006.

Sugawara, D., Minoura, K., Nemoto, N., Tsukawaki, S., Goto, K., and Imamura, F., Foraminiferal Evidence of Submarine Sediment Transport and Deposition by Backwash During the 2004 Indian Ocean Tsunami, Island Arc, 2009, 13 pp.

Summer, E., Siti, M., McNeill, L. C., Talling, P. J., Wynn, R., Henstock, T., Djardihardja, Y. and Permana, H., Testing the Validity of Using Turbidites as an Earthquake Proxy on the Sumatran Margin, Abstract T11d-2129, Fall Meeting, AGU, San Francisco, Calif., 13-17 Dec., 2010.

Susilohadi, S., Gaedickea, C. and Ehrhardt, A., Neogene Structures and Sedimentation History Along the Sunda Forearc Basins Off Southwest Sumatra and Southwest Java, Marine Geology, 219, 133-154, 2005.

Thompson, R., Battarbee, R. W., O'Sulliuan, P. E. and Oldfield, F., Magnetic Susceptibility of Lake Sediments, Limnology and Oceanography, 20, 687-698, 1975.

Tolstoy, M. and Bohnenstiehl, D. R., Hydroacoustic Contributions to Understanding the December 26th 2004 Great Sumatra–Andaman Earthquake, Survey of Geophysics, 27, 633-646, 2006.

Underwood, M.B., Hoke, K. D., Fisher, A. T., Davis, E. E., Giambalvo, E., Hlsdorff, L. Z. and Spinelli, G. A., Provenance, Stratigraphic Architecture, and Hydrogeologic Influence of Turbidites on the Mid-Ocean Ridge Flank of Northwestern Cascadia Basin, Pacific Ocean, Journal of Sedimentary Research, 75, 149-164, 2005.

van den Bergh, G.D., Boer, W., de Haas, H., van Weering, Tj.C.E., and van Wijhe, R., Shallow Marine Tsunami Deposits in Teluk Banten (Nw Java, Indonesia), Generated by the 1883 Krakatau Eruption, Marine Geology, 197, 13-34, 2003.

Wang, K. and Hu, Y., Accretionary Prisms in Subduction Earthquake Cycles: The Theory of Dynamic Coulomb Wedge, Journal of Geophysical Research, 111, 16, 2006.

Wang, W. and Davis, D. M., Sandbox Model Simulation of Forearc Evolution and Noncritical Wedges, Journal of Geophysical Research, 101, 11,329-11,339, 1996.

Weber, M.E., Erlenkeuser, H., Wiedicke-Hombach, M. and Kudrass, H.R., Bengal Fan Sediment Transport Activity and Response to Climate Forcing Inferred from Sediment Physical Properties, Sedimentary Geology, 155, 361-381, 2003.

Westbrook, G.K., Carson, B. and Party, Shipboard Scientific, Summary of Cascadia Drilling Results, Proceedings of the Ocean Drilling Program, Initial Reports, v. 146 (Part 1), p. 389-396, 1994.

Wiseman, K. and Bürgmann, R., Stress and Seismicity Changes on the Sunda Megathrust Preceding the 2007 Mw 8.4 Earthquake, BSSA, 101, 313-326, 2011.

Wolf, S.C., Nelson, C.H., Hamer, M.R., Dunhill, G. and Phillips, R.L., The Washington and Oregon Mid-Shelf Silt Deposit and Its Relation to the Late Holocene Columbia River Sediment Budget, USGS Open File Report 99-173, 1999.

Chapter 3 References

Abrahamson, N.A., Youngs, R.R., 1992. A Stable Algorithm for Regression Analyses Using the Random Effects Model. BSSA 82, 505-510.

Abrahamson, N.A., Silva, W.J., Kamal, R., 2013. Update of the AS08 Ground-Motion Prediction Equations Based on the NGA-West2 Data Set, PEER Report No. 2013/04. Pacific Earthquake Engineering Research Center, University of California, Berkeley, CA, pp. 174.

Allstadt, K., Vidale, J.E., Frankel, A.D., 2013. A Scenario Study of Seismically Induced Landsliding in Seattle Using Broadband Synthetic Seismograms. BSSA 103, 22.

Ambraseys, N.N., Menu, J.M., 1988. Earthquake Induced Ground Displacements. Earthquake Engineering and Structural Dynamics 16, 985-1006.

Ammon, C.J., Ji, C., Thio, H.-K., Robinson, D., Ni, S., Hjorleifsdottir, V., Kanamori, H., Lay, T., Das, S., Helmberger, D., Ichinose, G., Polet, J., Wald, D., 2005. Rupture Process of the 2004 Sumatra-Andaman Earthquake. Science 308, 1133-1139.

Arias, A., 1970. A measure of Earthquake Intensity. Massechusetts Institute of Technology Press, Cambridge, Mass.

Atkinson, G.M., Boore, D.M., 2003. Empirical Ground-Motion Relations for Subduction-Zone Earthquakes and Their Application to Cascadia and Other Regions. BSSA 93, 1703-1729.

Atkinson, G.M., Boore, D.M., 2011. Modifications to Existing Ground-Motion Prediction Equations in Light of New Data. BSSA 101, 1121-1135.

Banerjee, P., Pollitz, P., Nagarajan, B., B¨urgmann, R., 2007. Coseismic slip distributions of the 26 December 2004 Sumatra-Andaman and 28 March 2005 Nias earthquakes from GPS static offsets. Bulletin of the Seismological Society of America.

Bilek, S.L., 2007. Influence of Subducting Topography on Earthquake Rupture, in: Dixon, T.H., Moore, J.C. (Eds.), The Seismogenic Zone of Subduction Zone Faults. Columbia University Press, New York, pp. 123-146.

Bilham, R., 2005. Partial and Complete Rupture of the Indo-Andaman Plate Boundary 1847 - 2004. Seismological Research Letters 76, 299-311.

Bishop, A.W., 1954. The Use of Pore-Pressure Coefficients in Practice. Géotechnique 4, 148-152.

Bock, Y., Prawirodirdjo, L., Genrich, J.F., Stevens, C.W., McCaffrey, R., Subarya, C., Puntodewo, S.S.O., Calais, E., 2003. Crustal motion in Indonesia from Global Positioning System measurements. Journal of Geophysical Research 108, doi:10.1029/2001JB000324.

Boore, D.M., 2003. Simulation of Ground Motion Using the Stochastic Method. Pure and Applied Geophysics 160, 635-676.

Boore, D.M., Joyner, W.B., Fumal, T.E., 1997. Equations for Estimating Horizontal Response Spectra and Peak Acceleration from Western North American Earthquakes: A Summary of Recent Work. Seismological Research Letters 68, 128-153.

Boore, D.M., Atkinson, G.M., 2008. Ground-Motion Prediction Equations for the Average Horizontal Component of PGA, PGV, and 5%-Damped PSA at Spectral Periods between 0.01 s and 10.0 s. Earthquake Spectra 24, 99-138.

Boroschek, R.L., Contreras, V., Kwak, D.Y., Stewart, J.P., 2012. Strong Ground Motion Attributes of the 2010 Mw 8.8 Maule, Chile, Earthquake. Earthquake Spectra 28, S19-S38.

Boschi, E., Casarotti, E., Devoti, R., Melini, D., Piersanti, A., Pietrantonio, G., Riguzzi, F., 2006. Coseismic deformation induced by the Sumatra earthquake. Journal of Geodynamics 42, 52-62.

Bothara, J., Beetham, R.D., Brunston, D., Stannard, M., Brown, R., Hyland, C., Lewis, W., Miller, S., Sanders, R., Sulistio, Y., 2010. General observations of effects of the 30th September 2009 Padang earthquake, Indonesia. Bulletin of the New Zealand Society for Earthquake Engineering 43, 143-173.

Briggs, R.W., Sieh, K., Meltzner, A.J., Natawidjaja, D.H., Galetzka, J., Suwargadi, B., Hsu, Y.-j., Simons, M., Hananto, N.D., Suprihanto, I., Prayudi, D., Avouac, J., Prawirodirdjo, L., Bock, Y., 2006. Deformation and Slip Along the Sunda Megathrust in the Great 2005 Nias-Simeulue Earthquake. Science 311, 1897-1901.

Bunting, T., Singh, S.C., Bayly, M., Christie, P., 2008. Seismic Imaging of the fault that caused the great Indian Ocean earthquake of 26 December 2004, and the resulting catastrophic tsunami. Leading Edge 27, 1272-1281.

Campbell, K.W., 1997. Empirical Near-Source Attenuation Relationships for Horizontal and Vertical Components of Peak Ground Acceleration, Peak Ground Velocity, and Pseudo-Absolute Acceleration Response Spectra. Seismological Research Letters 68, 154-179.

Campbell, K.W., 2003. Prediction of Strong Ground Motion Using the Hybrid Empirical Method and Its Use in the Development of Ground-Motion (Attenuation) Relations in Eastern North America. BSSA 93, 1012-1033.

Carter, R.M., 1988. The nature and evolution of deep-sea channel systems. Basin Research 1, 41-54.

Chhibber, H., 1934. Geology of Burma. McMillan, London, England.

Chlieh, M., Avouac, J.-P., Hjorleifsdottir, V., Song, T.-R.A., Ji, C., Sieh, K., Sladen, A., Hebert, H., Prawirodirdjo, L., Bock, Y., Galetzka, J., 2007. Coseismic Slip and Afterslip of the Great (Mw 9.15) Sumatra-Andaman Earthquake of 2004. Bulletin of the Seismological Society of America 97, S152-S173.

Chlieh, M., Avouac, J.P., Sieh, K., Natawidjaja, D.H., Galetzka, J., 2008. Heterogeneous coupling of the Sumatran megathrust constrained by geodetic and paleogeodetic measurements. Journal of Geophysical Research 113, 31.

Chowdhury, R., 2010. Geotechnical Slope Analysis. Taylor and Francis, The Netherlands.

Crouse, C.B., 1991. Ground-motion attenuation equations for earthquakes on the Cascadia subduction zone Earthquake Spectra 7, 201-236.

Curray, J.R., Moore, D.G., 1971. Growth of the Bengal Deep-Sea Fan and Denudation in the Himalayas. GSA Bulletin 82, 563-572.

Curray, J.R., Emmel, F.J., Moore, D.G., 2003. The Bengal Fan: Morphology, geometry, stratigraphy, history and processes. Marine and Petroleum Geology 19, 1191-1223.

Dean, S., McNeil, L.C., Henstock, T., Bull, J.M., Gulick, S.P.S., Austin Jr., J.A., Bangs, N.L.B., Djadjadihardja, Y., Permana, H., 2010. Contrasting Décollement and Prism Properties over the Sumatra 2004–2005 Earthquake Rupture Boundary. Science 329, 207-210.

DeShon, H.R., Engdahl, E.R., Thurber, C.H., Brudzinski, M., 2005. Constraining the boundary between the Sunda and Andaman subduction systems: Evidence from the 2002 Mw 7.3 Northern Sumatra earthquake and aftershock relocations of the 2004 and 2005 great earthquakes. Geophysical Research Letters 32, 5.

Dobry, R., Borcherdt, R.D., Crouse, C.B., Power, M.S., Rinne, E.E., Seed, H.B., 2000. New SIte Coefficients and Site Classification System Used in Recent Building Seismic Code Provisions. Earthquake Spectra 16, 41-67.

Duputel, Z., Kanamori, H., Tsai, V.C., Rivera, L., Meng, L., Ampuero, J., Stock, J., 2012. The 2012 Sumatra Great Earthquake Sequence. Earth and Planetary Science Letters 351-352, 247-257.

Fellenius, W., 1936. Calculation of Stability of Earth Dams, 2nd Congress Large Dams, p. 445.

Franke, D., Schnabel, M., Ladage, S., Tappin, D.R., Neben, S., Djadjadihardja, Y., Mu¨ller, R.D., Kopp, H., Gaedicke, C., 2008. The great Sumatra–Andaman earthquakes —Imaging the boundary between the ruptures of the great 2004 and 2005 earthquakes. Earth and Planetary Science Letters 269, 118-130.

Frankel, A.D., 2009. A Constant Stress-Drop Model for Producing Broadband Synthetic Seismograms: Comparison with the Next Generation Attenuation Relations. BSSA 99, 664-680.

Fujiwara, T., Kodaira, S., No, T., Kaiho, Y., Takahashi, N., Kaneda, Y., 2011. The 2011 Tohoku-Oki Earthquake: Displacement Reaching the Trench Axis. Science 334, 1240.

Furumura, T., Takemura, S., Noguchi, S., Takemoto, T., Maeda, T., Iwai, K., Padhy, S., 2011. Strong ground motions from the 2011 off-the Pacific-Coast-of-Tohoku, Japan (Mw=9.0) earthquake obtained from a dense nationwide seismic network. Landslides 8, 333-338.

Goldfinger, C., Nelson, C.H., Johnson, J.E., 2003. Holocene Earthquake Records From the Cascadia Subduction Zone and Northern San Andreas Fault Based on Precise Dating of Offshore Turbidites. Annual Reviews of Earth and Planetary Sciences 31, 555-577.

Goldfinger, C., Morey, A.E., Nelson, C.H., Gutierrez-Pastor, J., Johnson, J.E., Karabanov, E., Chaytor, J., Ericsson, A., 2007. Rupture Lengths and Temporal History of Significant Earthquakes on the Offshore and North Coast Segments of the Northern San Andreas Fault Based on Turbidite Stratigraphy. Earth and Planetary Science Letters 254, 9-27.

Goldfinger, C., Grijalva, K., Burgmann, R., Morey, A.E., Johnson, J.E., Nelson, C.H., Gutierrez-Pastor, J., Ericsson, A., Karabanov, E., Chaytor, J.D., Patton, J., Gràcia, E., 2008. Late Holocene Rupture of the Northern San Andreas Fault and Possible Stress Linkage to the Cascadia Subduction Zone Bulletin of the Seismological Society of America 98, 861-889.

Goldfinger, C., Nelson, C.H., Morey, A., Johnson, J.E., Gutierrez-Pastor, J., Eriksson, A.T., Karabanov, E., Patton, J., Gràcia, E., Enkin, R., Dallimore, A., Dunhill, G., Vallier, T., 2012. Turbidite Event History: Methods and Implications for Holocene Paleoseismicity of the Cascadia Subduction Zone, USGS Professional Paper # 178. U.S. Geological Survey, Reston, VA.

Goldfinger, C., Morey, A., Black, B., Patton, J.R., 2013. Spatially Limited Mud Turbidites on the Cascadia Margin: Segmented Earthquake Ruptures. Natural Hazards and Earth System Sciences 13, 2109-2146.

Gorum, T., Fan, X., van Westen, C.J., Huang, R.Q., Xu, Q., Tang, C., Wang, G., 2011. Distribution pattern of earthquake-induced landslides triggered by the 12 May 2008 Wenchuan earthquake. Geomorphology 133, 152-167.

Gregor, N.J., Silva, W.J., Wong, I.G., Youngs, R.R., 2002. Ground-Motion Attenuation Relationships for Cascadia Subduction Zone Megathrust Earthquakes Based on a Stochastic Finite-Fault Model. BSSA 92, 1923-1932.

Hadj-Hamou, T., Kavazanjian Jr., E., 1985. Seismic Stability of Gentle Infinite Slopes. J. Geotechnical Eng. 111, 681-697.

Hayes, G.P., Wald, D.J., Johnson, R.L., 2012. Slab 1.0: A Three Dimensional Model of Global Subduction Zone Geometries. Journal of Geophysical Research 117, 1-15.

Hempel, P., 1995. Dewatering of sediments along the Cascadia Margin: Evidence from geotechnical properties, in: Carson, B., Westbrook, G.K., Musgrave, R.J., Suess, E. (Eds.), Proceedings of the Ocean Drilling Program, Scientific Results. Ocean Drilling Program, College Station TX, pp. pp. 257-274.

Hsieh, S., Lee, C., 2011. Empirical estimation of the Newmark displacement from the Arias intensity and critical acceleration. Engineering Geology 122, 34-42.

Hynes-Griffin, M.E., Franklin, A.G., 1985. Rationalizing the Seismic Coefficient Method. Department of the Army, US Army Corps of Engineers, p. 37.

Ide, S., Baltay, A., Beroza, G.C., 2011. Shallow Dynamic Overshoot and Energetic Deep Rupture in the 2011 Mw 9.0 Tohoku-Oki Earthquake. Science 332, 1426-1429.

Ishii, M., Shearer, P.M., Houston, H., Vidale, J.E., 2005. Extent, duration and speed of the 2004 Sumatra-Andaman earthquake imaged by the Hi-Net array. Nature 435, 933.

Ishii, M., Shearer, P.M., Houston, H., Vidale, J.E., 2007. Teleseismic P wave imaging of the 26 December 2004 Sumatra-Andaman and 28 March 2005 Sumatra earthquake ruptures using the Hi-net array. Journal of Geophysical Research 112.

Jibson, R.W., 1993. Predicting Earthquake-Induced Landslide Displacements Using Newmark's Sliding Block Analysis. Transportation Research Record 1411, 9-17.

Jibson, R.W., 2007. Regression models for estimating coseismic landslide displacement. Engineering Geology 91, 209-218.

Jibson, R.W., 2009. Using Landslides for Paleoseismic Analysis, in: McCalpin, J.P. (Ed.), Paleoseismology, 2 ed. Academic Press, USA, pp. 565-601.

Jibson, R.W., Keefer, D.K., 1993. Analysis of the seismic origin of landslides: Examples from the New Madrid seismic zone. GSA Bulletin 105, 521-536.

Jibson, R.W., Prentice, C.S., Borissoff, B.A., Rogozhin, E.A., Langer, C.J., 1994. Some Observations of Landslides Triggered by the 29 April 1991 Racha Earthquake, Republic of Georgia. BSSA 84, 963-973.

Jibson, R.W., Harp, E.L., Michael, J.A., 1998. A Method for Producing Digital Probabilistic Seismic Landslide Hazard Maps: An Example from the Los Angeles, California, Area, USGS Open-File Report 98-113. U.S. Geological Survey, Reston, VA.

Jibson, R.W., L., H.E., Michael, J.A., 2000. A method for producing digital probabilistic seismic landslide hazard maps. Engineering Geology 58, 271-289.

Jibson, R.W., Harp, E.L., 2012. Extraordinary Distance Limits of Landslides Triggered by the 2011 Mineral, Virginia, Earthquake. BSSA 102, 2368-2377.

Johnson, B.D., Barry, M.A., Boudreau, B., P., Jumars, P.A., Dorgan, K.M., 2012. In situ tensile fracture toughness of surficial cohesive marine sediments. Geo-Mar. Lett. 32, 39-48.

Joyner, W.B., Boore, D.M., 1982. Prediction of Earthquake Response Spectra, U.S.G.S. Professional Paper 82-977. U.S. Geological Survey, Washington D.C., p. 17.

Joyner, W.B., Fumal, T.E., 1984. Use of measured shear-wave velocity for predicting geologic site effects on strong ground motion, Proceedings Eighth World Conference on Earthquake Engineering, San Francisco, pp. 777-783.

Joyner, W.B., Boore, D.M., 1988. Measurement, Characterisation, and Prediction of Strong Ground Motion, Proceedings of Earthquake Engineering and Soil Dynamics. ASCE, Park City, Utah, p. 60.

Kanamori, H., Rivera, L., Lee, W.H.K., 2010. Historical seismograms for unravelling a mysterious earthquake: The 1907 Sumatra Earthquake. Geophysical Journal International 183, 358-374.

Kanno, T., Narita, A., Morikawa, N., Fujiwara, H., Fukushima, Y., 2006. A New Attenuation Relation for Strong Ground Motion in Japan Based on Recorded Data. BSSA 96, 879-897.

Kayen, R.E., Mitchell, J.K., 1997. Assessment of Liquefaction Potential During Earthquakes by Arias Intensity. Journal of Geotechnical and Geoenvironmental Engineering 123, 1162-1174.

Keefer, D.K., 1984. Landslides caused by earthquakes. GSA Bulletin 95, 406-421.

Keefer, D.K., 2000. Statistical analysis of an earthquake-induced landslide distribution — the 1989 Loma Prieta, California event. Engineering Geology 58, 231-249.

Keefer, D.K., 2002. Investigating Landslides Caused by Earthquakes – A Historical Review. Surveys in Geophysics 23, 473-510.

Keefer, D.K., Wilson, R.C., 1989. Predicting Earthquake-Induced Landslides, With Emphasis on Arid and Semi-Arid Environments. Inland Geological Society, Riverside, CA.

Klingelhoefer, F., Gutscher, M., Ladage, S., Dessa, J., Graindorge, D., Franke, D., André, C., Permana, H., Yudistira, T., Chauhan, A.P.S., 2010. Limits of the seismogenic zone in the epicentral region of the 26 December 2004 great Sumatra-Andaman earthquake: Results from seismic refraction and wide-angle reflection surveys and thermal modeling. Journal of Geophysical Research 115, 23.

Kodaira, S., No, T., Nakamura, Y., Fujiwara, H., Kaiho, Y., Miura, H., Takahashi, N., Kaneda, Y., Taira, A., 2012. Coseismic fault rupture at the trench axis during the 2011 Tohoku-oki earthquake. Nature Geoscience 5, 646-650.

Konca, A.O., Hjorleifsdottir, V., Song, T.A., Avouac, J., Helmberger, D., Ji, C., Briggs, R.W., Meltzner, A.J., 2007. Rupture Kinematics of the 2005 Mw 8.6 Nias–Simeulue Earthquake from the Joint Inversion of Seismic and Geodetic Data. BSSA 97, S307-S322.

Konca, A.O., Avouac, J., Sladen, A., Meltzner, A.J., Sieh, K., Fang, P., Li, Z., Galetzka, J., Genrich, J., Chlieh, M., Natawidjaja, D.H., Bock, Y., Fielding, E.J., Ji, C., Helmberger, D., 2008. Partial Rupture of a Locked Patch of the Sumatra Megathrust During the 2007 Earthquake Sequence. Nature 456, 631-635.

Kopp, H., Weinrebe, W., Ladage, S., Barckhausen, U., Klaeschen, D., Flueh, E.R., Gaedicke, C., Djajadihardja, Y., Grevemeyer, I., Krabbenhoeft, A., Papenbergn, C., Zillmern, M., 2008. Lower slope morphology of the Sumatra trench system. Basin Research 20, 519-529.

Kozdon, J.E., Dunham, E.M., 2013. Rupture to the Trench: Dynamic Rupture Simulations of the 11 March 2011 Tohoku Earthquake. BSSA 103, 1,275-271,289.

Lee, C., Huang, C., J., L., Pan, K., Lin, M., Dong, J., 2008. Statistical Approach to Earthquake Induced Landslide Susceptibility. Engineering Geology 100, 43-58.

Lee, H.J., Dartnell, P., Minasian, D., Wong, F., 2000. A GIS-based regional analysis of the potential for shallow-seated submarine slope failure, in: Bromhead, E., Dixon, N., Ibsen, M.-L. (Eds.), 8th International Symposium on Landslides. Telford, Thomas Limited, Cardiff, p. 1684.

Lee, H.J., Greene, H.G., Edwards, B.D., 2009. Submarine landslides of the Southern California Borderland, in: Lee, H.J., Piper, D.J.W. (Eds.), Earth Science in the Urban Ocean: The Southern California Continental Borderland: GSA Special Paper 454, 454 ed.

Lorenzoni, L., Benitez-Nelson, C.R., Thunell, R.C., Hollander, D., Varela, R., Astor, Y., Audemard, F.A., Muller-Karger, F.E., 2012. Potential role of event-driven sediment transport on sediment accumulation in the Cariaco Basin, Venezuela. Marine Geology 307-310, 105-110.

Loukidis, D., Bandini, P., Salgado, R., 2003. Stability of seismically loaded slopes using limit analysis. Geotechnique 53, 463-479.

Malik, J.N., Shishikura, M., Echigo, T., Ikeda, Y., Satake, K., Kayanne, H., Sawai, Y., Murty, C.V.R., Dikshit, D., 2011. Geologic evidence for two pre-2004 earthquakes during recent centuries near Port Blair, South Andaman Island, India. Geology 39, 559-562.

Malwaki, A.I.H., Hassan, W.F., Sarma, S.K., 2001. Global Search Method For Locating General Slip Surface Using Monte Carlo Techniques. Journal of Geotechnical and Geoenvironmental Engineering 127, 12.

McGuire, J.J., Beroza, G.C., 2012. A Rogue Earthquake Off Sumatra. Science 336, 1,118-111,119.

Meltzner, A.J., Sieh, K., Chiang, H., Shen, C., Suwargadi, B.W., Natawidjaja, D.H., Philbosian, B., Briggs, R.W., Galetzka, J., 2010. Coral evidence for earthquake recurrence and an A.D. 1390–1455 cluster at the south end of the 2004 Aceh–Andaman rupture. Journal of Geophysical Research 115, 1-46.

Meltzner, A.J., Sieh, K., Chiang, H.-W., Shen, C.-C., Suwargadi, B.W., Natawidjaja, D.H., Philibosian, B., Briggs, R.W., 2012. Persistent termini of 2004- and 2005-like ruptures of the Sunda megathrust. Journal of Geophysical Research 117, 15.

Meunier, P., Hovius, N., Haines, A.J., 2007. Regional patterns of earthquake-triggered landslides and their relation to ground motion. Geophysical Research Letters 34.

Moore, G.F., Curray, J.R., Emmel, F.J., 1982. Sedimentation in the Sunda Trench and forearc region. Geological Society, London, Special Publications 10, 245-258.

Morgenstern, N.R., 1967. Submarine Slumping and the Initiation of Turbidity Currents, in: R., R.A. (Ed.), Marine Géotechnique. University of Illinois Press, Chicago, Ill, pp. 189-220.

Morgenstern, N.R., Price, W.E., 1965. The Analysis of the Stability of General Slip Surfaces. Géotechnique 15, 79-93.

Murphy, J.R., O'Brien, L.J., 1977. The correlation of Peak Ground Acceleration Amplitude with Seismic Intensity and other Physical Parameters. BSSA 37, 877-915.

Nakajima, T., Kanai, Y., 2000. Sedimentary features of seismoturbidites triggered by the 1983 and older historical earthquakes in the eastern margin of the Japan Sea. Sedimentary Geology 135, 1-19.

Natawidjaja, D.H., Sieh, K., Ward, S.N., Cheng, H., Edwards, R.L., Galetzka, J., Suwargadi, B.W., 2004. Paleogeodetic Records of Seismic and Aseismic Subduction from Central Sumatran Microatolls, Indonesia. Journal of Geophysical Research 109, 37.

Natawidjaja, D.H., Sieh, K., Chlieh, M., Galetzka, J., Suwargadi, B., Cheng, H., Edwards, R.L., Avouac, J., Ward, S.N., 2006. Source parameters of the great Sumatran megathrust earthquakes of 1797 and 1833 inferred from coral microatolls. Journal of Geophysical Research 111, 37.

Newcomb, K.R., McCann, W.R., 1987. Seismic History and Seismotectonics of the Sunda Arc. Journal of Geophysical Research 92, 421-439.

Newmark, N.M., 1965. Effects of Earthquakes on Dams and Embankments. Géotechnique 15, 139-159.

Noda, A., TuZino, T., Kanai, Y., Furukawa, R., Uchida, J.-i., 2008. Paleoseismicity along the southern Kuril Trench deduced from submarine-fan turbidites. Marine Geology 254, 73-90.

Ortiz, M., Bilham, R., 2003. Source area and rupture parameters of the 31 December Mw = 7.9 Car Nicobar earthquake estimated from tsunamis recorded in the Bay of Bengal. J. Geophys. Res. 108.

Patton, J.R., Goldfinger, C., Morey, A., Romsos, C., Black, B., Djadjadihardja, Y., Udrek., 2013 a. Seismoturbidite record as preserved at core sites at the Cascadia and Sumatra–Andaman subduction zones. Natural Hazards and Earth Systems Science 13, 833-867.

Patton, J.R., Goldfinger, C., Djadjadihardja, Y., Udrek, 2013 b. Slope Stability: Factor of Safety along the Seismically Active Continental Slope Offshore Sumatra. EOS Trans. AGU 94.

Petersen, M.D., Dewey, J., Hartzell, S., Mueller, C., Harmsen, S., Frankel, A.D., Rukstales, K., 2004. Probabilistic seismic hazard analysis for Sumatra, Indonesia and across the Southern Malaysian Peninsula. Tectonophysics 390, 141-158.

Philibosian, B., Sieh, K., Natawidjaja, D.H., Chiang, H., Shen, C., Suwargadi, B., Hill, E.M., Edwards, R.L., 2012. An ancient shallow slip event on the Mentawai segment of the Sunda megathrust, Sumatra. Journal of Geophysical Research 117, 12.

Rivera, L., Sieh, K., Helmberger, D., Natawidjaja, D.H., 2002. A Comparative Study of the Sumatran Subduction-Zone Earthquakes of 1935 and 1984. BSSA 92, 1721-1736.

Rocscience, 2013. SLIDE v6.0 2-D limit equilibrium slope stability analysis, 6.0 ed, Toronto, CA.

Rodriguez-Marek, A., Bay, J.A., Park, K., Montalva, G.A., Cortez-Flores, A., Wartman, J., Boroschek, R.L., 2010. Engineering Analysis of Ground Motion Records from the 2001 Mw 8.4 Southern Peru Earthquake. Earthquake Spectra 26, 499-524.

Rollins, J.C., Stein, R.S., 2010. Coulomb Stress Interactions Among M ≥ 5.9 Earthquakes in the Gorda Deformation Zone and on the Mendocino Fault Zone, Cascadia Subduction Zone, and Northern San Andreas Fault. Journal of Geophysical Research 115, 19 pp.

Ruff, L., Kanamori, H., 1980. Seismicity and the subduction process. Physics of the Earth and Planetary Interiors v. 23, p. 240-252.

Ruff, L., Kanamori, H., 1983. Seismic coupling and uncoupling at subduction zones. Tectonophysics v. 99, p. 99-117.

Sarma, S.K., 1975. Seismic Stability of Earth Dams and Embankments. Géotechnique 25, 743-761.

Saucier, R., 2000. Computer Generation of Statistical Distributions, paper ARL-TR-2168, . Army Research Laboratory.

Schulz, W.H., Galloway, S.L., Higgins, J.D., 2012. Evidence for earthquake triggering of large landslides in coastal Oregon, USA. Geomorphology 141-142, 88-98.

Seed, H.B., Iddriss, I.M., 1971. Simplified Procedure for Evaluating Soil Liquefaction Potential. Journal of the Soil Mechanics and Foundations Division, Proceedings of the American Society of Civil Engineers 97, 1249-1273.

Seed, H.B., Muraka, R., Lysmer, J., Iddriss, I.M., 1976. Relationships of Maximum Acceleration, Maximum Velocity, Distance From Source, and Local Site Conditions for Moderately Strong Earthquakes. BSSA 66, 1323-1342.

Shulgin, A., Kopp, H., Klaeschen, D., Papenberg, C., Tilmann, F.J., Flueh, E., Franke, D., Barckhausen, U., Krabbenhoeft, A., Djadjadihardja, Y., 2013. Subduction system variability across the segment boundary of the 2004/2005 Sumatra megathrust earthquakes. Earth and Planetary Science Letters 365, 108-119.

Sieh, K., 2006. Sumatran megathrust earthquakes: from science to saving lives. Philosophical Transactions of the Royal Society 364, 1947-1963.

Sieh, K., Natawidjaja, D.H., Meltzner, A.J., Shen, C., Cheng, H., Li, K., Suwargadi, B.W., Galetzka, J., Philbosian, B., Edwards, R.L., 2008. Earthquake Supercycles Inferred from Sea-Level Changes Recorded in the Corals of West Sumatra. Science 322, 1674-1678.

Singh, S.C., Carton, H., Tapponnier, P., Hananto, N.D., Chauhan, A.P.S., Hartoyo, D., Bayly, M., Moreljopranoto, S., Bunting, T., Christie, P., Lubis, H., Martin, J., 2008. Seismic evidence for broken oceanic crust in the 2004 Sumatra earthquake epicentral region. Nature Geoscience 1, 777-781.

Singh, S.C., Hananto, N.D., Chauhan, A.P.S., Permana, H., Denolle, M., Hendriyana, A., Natawidjaja, D., 2010. Evidence of Active Backthrusting at the NE Margin of Mentawai Islands, SW Sumatra. Geophysical Journal International 180, 703-714.

Skarlatoudis, A.A., Papazachose, C.B., 2012. Preliminary Study of the Strong Ground Motions of the Tohoku, Japan, Earthquake of 11 March 2011: Assessing the Influence of Anelastic Attenuation and Rupture Directivity. Seismological Research Letters 83, 119-129.

Skempton, A.W., 1954. The Pore-Pressure Coefficients A and B. Géotechnique 4, 143-147.

Smith, W.H.F., Sandwell, D.T., 1997. Global seafloor topography from satellite altimetry and ship depth soundings. Science 277, 1957-1962.

Sorensen, M.B., Atakan, K., Pulido, N., 2007. Simulated Strong Ground Motions for the Great M 9.3 Sumatra–Andaman Earthquake of 26 December 2004. BSSA 97, S139-S151.

Spencer, E., 1967. A Method of Analysis of the Stability of Embankments Assuming Parallel Inter-Slice Forces. Géotechnique 17, 11-26.

Stein, S., Wysession, M., 2003. Introduction to Seismology, Earthquakes, and Earth Structure. Blackwell Publishing, Boston.

Stewart, J.P., Midorikawa, S., Graves, R.W., Khodaverdi, K., Kishida, T., Miura, H., Bozorgnia, Y., Campbell, K.W., 2013. Implications of the Mw9.0 Tohoku-Oki Earthquake for Ground Motion Scaling with Source, Path, and Site Parameters. Earthquake Spectra 29, S1 - S21.

Stow, D.A.V., 1990. Sediment facies and processes on the distal Bengal Fan, Leg 116. ODP Texas & M University College Station; UK distributors IPOD Committee NERC Swindon.

Strasser, M., Anselmetti, F.S., Fäh, D., Giardini, D., Schnellmann, M., 2006. Magnitudes and Source Areas of Large Prehistoric Northern Alpine Earthquakes Revealed by Slope Failures in Lakes. Geology 34, 1005-1008.

Strasser, M., Hilbe, M., Anselmetti, F.S., 2011. Mapping basin-wide subaquatic slope failure susceptibility as a tool to assess regional seismic and tsunami hazards. Marine Geophysical Researches 32, 331-347.

Subarya, C., Chlieh, M., Prawirodirdjo, L., Avouac, J., Bock, Y., Sieh, K., Meltzner, A.J., Natawidjaja, D.H., McCaffrey, R., 2006. Plate-boundary deformation associated with the great Sumatra–Andaman earthquake. Nature 440, 46-51.

Sultan, N., Cattaneo, A., Sibuet, J.-C., Schneider, J.-L., 2009. Deep sea in situ excess pore pressure and sediment deformation off NW Sumatra and its relation with the December 26, 2004 Great Sumatra-Andaman Earthquake. Intl. J. Earth Sci. 98, 823-837.

Tan, B., Germaine, J.T., Flemmings, P.B., 2006. Data Report: Consolidation And Strength Characteristics Of Sediments From ODP Site 1244, Hydrate Ridge, Cascadia Continental Margin, in: Trehu, A.M., Bohrmann, G., Torres, M.E., Colwell, F.S. (Eds.), Proceedings of the Ocean Drilling Program, Scientific Results. Ocean Drilling Program.

Taylor, D.W., 1948. Fundamentals of Soil Mechanics. Wiley, New York City, New York.

Taylor, G.H., 1937. Ground-water in Utah. Transactions, American Geophysical Union 2, 536-541.

ten Brink, U.S., Lee, H.J., Geist, E.L., Twichell, D.C., 2009. Assessment of tsunami hazard to the U.S. East Coast using relationships between submarine landslides and earthquakes. Marine Geology 264, 65-73.

Tilmann, F.J., Craig, T.J., Grevemeyer, I., Suwargadi, B., Kopp, H., Flueh, E., 2010. The Updip Seismic/Aseismic Transition of the Sumatra Megathrust Illuminated by Aftershocks of the 2004 Aceh-Andaman and 2005 Nias Events Geophysical Journal International 181, 1261-1274.

Tobita, T., Iai, S., Chairullah, B., Asper, W., 2006. Reconnaissance report of the 2004 Great Sumatra-Andaman, Indonesia, Earthquake – Damage to geotechnical works in Banda Aceh and Meulaboh –. Journal of Natural Disaster Science 28, 35-41.

Travasarou, T., Bray, J.D., Abrahamson, N.A., 2003. Empirical attenuation relationship for Arias Intensity. Earthquake Engineering and Structural Dynamics 32, 1133-1155.

Vigny, C., Simons, W.J.F., Abu, S., Bamphenyu, R., Satirapod, C., Choosakul, N., Subarya, C., A., S., K. Omar, K., H.Z., A., Ambrosius, B.A.C., 2005. Insight into the 2004 Sumatra–Andaman earthquake from GPS measurements in southeast Asia. Nature 436, 201-206.

Wang, K., 2010. Finding Fault in Fault Zones. Science 329, 152-153.

Wang, K., Dixon, T.H., 2004. “Coupling” Semantics and Science in Earthquake Research. EOS 85, 177-178.

Weber, M.E., Erlenkeuser, H., Wiedicke, M.H., Kudrass, H.R., Hubscher, C., 1997. Active growth of the Bengal Fan during sea-level rise and highstand. Geology 25, 315-318.

Weber, M.E., Wiedicke-Hombach, M., Kudrass, H.R., Erlenkeuser, H., 2003. Bengal Fan sediment transport activity and response to climate forcing inferred from sediment physical properties. Sedimentary Geology 155, 361-381.

Wilson, C., Keefer, D.K., 1985. U.S.G.S. Professional Paper 1360: Predicting Areal Limits of Earthquake-Induced Landsliding, in: Ziony, J.I. (Ed.), U.S.G.S. Professional Paper. U.S Geological Survey, Washington, D. C., pp. 317-345.

Wilson, R.C., 1993. Relation of Arias Intensity to Magnitude and Distance in California. USGS.

Wright, S.G., Rathje, E.M., 2003. Triggering Mechanisms of Slope Instability and their Relationship to Earthquakes and Tsunamis. Pure and Applied Geophysics 160, 1865.

Yagi, Y., 2004. Preliminary results of rupture process for 2004 off coast of Northern Sumatra giant earthquake, International Institute of Seismology and Earthquake Engineering.

Yerkes, R.F., Greene, H.G., Tinsley, J.C., Lajoie, K.R., 1981. Maps showing seismotectonic setting of the Santa Barbara channel area, California, 1169 ed.

Youngs, R.R., Chiou, S.J., Silva, W.J., Humphrey, J.R., 1997. Strong Ground Motion Attenuation Relationships for Subduction Zone Earthquakes. Seismological Research Letters 68, 58-78.

Zhan, Z., Helmberger, D., Simons, M., Kanamori, H., Wu, W., Cubas, N., Dupatel, Z., Chu, R., Tsai, V.C., Avouac, J., Hudnut, K.W., Ni, S., Hetland, E., Culaciati, F.H.O., 2012. Anomalously Steep Dips of Earthquakes in the 2011 Tohoku-Oki Source Region and Possible Explanations. Earth and Planetary Science Letters 353-354, 121-133.

Zhao, J.X., 2010. Geometric Spreading Functions and Modeling of Volcanic Zones for Strong-Motion Attenuation Models Derived from Records in Japan. BSSA 100, 712-732.

Zhao, J.X., Zhang, J., Asano, A., Ohno, Y., Oouchi, T., Takahashi, T., Ogawa, H., Irikura, K., Thio, H.K., Somerville, P.G., Fukushima, Y., Fukushima, Y., 2006. Attenuation Relations of Strong Ground Motion in Japan Using Site Classification Based on Predominant Period. BSSA 96, 898-913.

Zhao, J.X., Irikura, K., Zhang, J., Fukushima, Y., Somerville, P.G., Saiki, T., Okada, h., Takahashi, T., 2004. Site classification for strong motion stations in Japan using h/v response spectral ratio 13th World Conference of Earthquake Engineering, Vancouver, B. C., Canada.

Zhao, J.X., Xu, H., 2012. Magnitude-Scaling Rate in Ground-Motion Prediction Equations for Response Spectra from Large Subduction Interface Earthquakes in Japan. BSSA 102, 222-235.

APPENDICES

Appendix S 2-1 Core Geophysics and Age Control Methods

Core Geophysics

The 144 cores collected offshore Sumatra (**Appendix. S2-6**) were scanned at sea with a GEOTEK Multi Sensor Core Logger (MSCL), obtaining P-wave velocity, gamma ray density, resistivity, and loop magnetic susceptibility (MS) at 0.5 cm spaced intervals in 1.5-m length sections. Split cores were imaged with a high resolution line-scan digital camera and the lithostratigraphy was described. High resolution point MS data were collected using a Bartington MS2E point sensor at 0.5 cm spacing. The cores were imaged with the Oregon State University Aquilion 64 slice X-ray Computed Tomography (CT) system with a nominal voxel size of 0.5 mm.

Age Control Methods

Age control for stratigraphy is provided by Accelerator Mass Spectrometer (AMS) ^{14}C and ^{210}Pb radiometric techniques. ^{14}C data is based on decay with a half-life of 5,730 years and is useful for strata between ~300 - ~35,000 years old (Stuiver and Braziunes, 1993). ^{210}Pb data, based on a shorter half-life of 22 years (Noller, 2000), provides information about sedimentary deposition for the past ~150 years. We use ^{210}Pb age data to constrain the timing of deposition for the most recently deposited sediments.

To estimate ages of the turbidites using radiocarbon, we extract the calcium carbonate shells of planktic foraminifers preserved in the hemipelagic sediment below each turbidite to provide a maximum limiting age. We utilized planktic foraminiferid species as they most closely represent the age of the youngest sea water, the surface water that is most closely in ^{14}C equilibrium with the atmosphere. We sample below each turbidite because this is the sediment closest in age to the turbidite. We do not use the age of the sediment above the turbidite because the boundary between the top of the turbidite tail and the hemipelagic sediment is difficult to identify reliably and bioturbation is concentrated at this boundary. These methods are outlined in Goldfinger et al. (2011a).

Trench core sites were deeper than the Carbonate Compensation Depth (CCD), the depth below which foraminiferid $CaCO_3$ tests dissolve faster than they are deposited. Therefore foraminiferid abundance was nil in trench core sediments, so ^{14}C age control applies only to the slope cores.

Sediment samples were removed from the cores while avoiding the 0.5 cm of material nearest the core walls to avoid visible or undetected deformation and friction drag along the core walls. In some cases, highly irregular turbidite bases resulted in sampling an interval below the basal irregularities, and applying a correction to the hemipelagic thickness called the gap correction. Hemipelagic sediment samples were freeze dried to separate clay particles to improve rinsing through a sieve, washed in a dilute Calgon (sodium hexametaphosphate) solution to keep the fine particles in suspension, sieved through a 125 µm stainless steel sieve, then dried in a warm oven. Typically 25-50 individual planktic foraminifers (depending on size/weight) were identified then removed from this dried >

125 μm size fraction using a fine sable brush moistened with distilled water. Foraminiferal sample ages were determined using Accelerator Mass Spectrometry (AMS) methods at the Keck AMS facility at University of California, Irvine in collaboration with John Southon.

The primary sources of radiocarbon error include variation of the age in surface and near surface sea water, the sedimentation rate, the level of atmospheric radiocarbon in the atmosphere, and the basal erosion during turbidite emplacement. There does not yet exist sufficient prehistoric benthic-planktic age pairs with which to construct an age model in this region, so the reservoir correction is probably the largest source of error in this study and we have no way to evaluate this source of epistemic error. While we can evaluate basal visually to some extent, and differential erosion can be inferred between nearby cores from differences in hemipelagic thickness and the ^{14}C ages (Goldfinger et al., 2011a), there will likely be undetected erosion in these data. Sedimentation rates are calculated using ^{14}C age estimates and thickness of hemipelagic sediment. Sedimentation rates are used to calculate ages for turbidites that have no direct age.

The radiocarbon ages are reported in years before present (BP, measured from 1950) with a 2 standard deviation lab error (Stuiver et al., 1998). ^{14}C ages are calibrated (Stuiver and Polach, 1977) and a marine reservoir correction of 16±11 years is made using the Marine09 database (Reimer et al., 2009). Only two delta R values are available for the Sumatra area, and while constraints are few on this correction, we here are correlating marine sites to other nearby marine sites, thus the local correlations are valid while absolute ages may contain additional uncertainty. One additional correction we make to the calibrated age is the sediment gap thickness correction (thickness of sediment between the turbidite and the sample; see OxCal code below). For individual ages, we propagate these uncertainties using RMS (root mean square) calculations using estimates of the uncertainties at each step. This calculation includes the lab uncertainties and results in the final reported 95% error range for each radiocarbon age. In later sections of the paper, we calculate region wide mean event ages. For these, we average the ages (using the combine function in OxCal), and again apply RMS calculations to the averaged error ranges to produce the 95% error ranges for each averaged age. No lab multipliers were applied to the data.

OxCal Code

Code for Table 2-5 A

```
Options()
{
 Plot()
 BCAD=FALSE;
 Curve("Marine13","Marine13.14c");
 Delta_R("LocalMarine",16,11);
 Sequence("2004 Region Gap")
 {
  Boundary("Start", -8000);
  R_Date("RR0705_108PC_345_347_SUM-195", 7175, 20)+N(174,17);
  Boundary("T-29")
  {
  };
  R_Date("RR0705_108PC_330_332_SUM-041", 6685, 25)+N(64,6);
  Boundary("T-28")
  {
  };
  {
   Combine("Sum-T-28")
   {
    R_Date("RR0705_108PC_312.5_314.5_SUM-043", 6115, 20)+N(53,5);
    R_Date("RR0705_103PC_383_385_SUM-253", 6020, 25)+N(13,1);
   };
  };
  Boundary("T-27")
  {
  };
  R_Date("RR0705_108PC_290.5_292.5_SUM-044", 5950, 20)+N(19,2);
  Boundary("T-26")
  {
  };
  R_Date("RR0705_103PC_324_326_SUM-224", 5575, 25)+N(17,2);
  Boundary("T-25")
  {
  };
  R_Date("RR0705_108PC_257_259_SUM-042", 4840, 20)+N(52,5);
  Boundary("T-24")
  {
  };
  Date("Sum-T-24");
```

```
Boundary("T-23")
{
};
R_Date("RR0705_108PC_212.5_214.5_SUM-045", 4625, 20)+N(46,5);
Boundary("T-22")
{
};
Date("Sum-T-22");
Boundary("T-21")
{
};
{
 Combine("Sum-T-21")
 {
  R_Date("RR0705_108PC_194_196_SUM-194", 4340, 20)+N(24,2);
  R_Date("RR0705_103PC_209_211_SUM-050", 4360, 20)+N(3,0);
 };
};
Boundary("T-20")
{
};
{
 Combine("Sum-T-20")
 {
  R_Date("RR0705_108PC_175_177_SUM-046", 4070, 15)+N(43,4);
  R_Date("RR0705_103PC_174_176_SUM-087", 3925, 20)+N(125,13);
 };
};
Boundary("T-19")
{
};
R_Date("RR0705_108PC_156_158_SUM-083", 3500, 15)+N(74,7);
Boundary("T-18")
{
};
{
 Combine("Sum-T-18")
 {
  R_Date("RR0705_108PC_132.5_134.5_SUM-081", 3035, 15)+N(0,0);
  R_Date("RR0705_104PC_326_328_SUM-235", 3000, 35)+N(6,1);
  R_Date("RR0705_103TC_079_081_SUM-180", 2985, 20)+N(0,0);
 };
};
```

```
Boundary("T-17")
{
};
Date("Sum-T-17");
Boundary("T-16")
{
};
Date("Sum-T-16");
Boundary("T-15")
{
};
R_Date("RR0705_96PC_399_401_SUM-232", 2410, 20)+N(12,1);
Boundary("T-14")
{
};
R_Date("RR0705_104PC_207_209_SUM-115", 2420, 220)+N(17,2);
Boundary("T-13")
{
};
Date("Sum-T-13");
Boundary("T-12")
{
};
Date("Sum-T-12");
Boundary("T-11")
{
};
{
 Combine("Sum-T-11")
 {
  R_Date("RR0705_103TC_039_041_SUM-179", 2065, 20)+N(0,0);
  R_Date("RR0705_96PC_374_376_SUM-090", 2115, 20)+N(7,1);
 };
};
Boundary("T-10")
{
};
{
 Combine("Sum-T-10")
 {
  R_Date("RR0705_108PC_039_041_SUM-080", 2015, 15)+N(41,4);
  R_Date("RR0705_108TC_020_022_SUM-172", 1930, 20)+N(44,4);
  R_Date("RR0705_104PC_158_160_SUM-082", 2040, 20)+N(5,0);
```

```
 R_Date("RR0705_103PC_049_051_SUM-054", 1940, 25)+N(18,2);
 R_Date("RR0705_103TC_036_038_SUM-178", 1890, 20)+N(23,2);
};
};
Boundary("T-9")
{
};
Date("Sum-T-9");
Boundary("T-8")
{
};
Date("Sum-T-8");
Boundary("T-7")
{
};
{
Combine("Sum-T-7")
{
 R_Date("RR0705_104PC_122_124_SUM-061", 1630, 45)+N(17,2);
 R_Date("RR0705_96PC_287.5_289.5_SUM-089", 1490, 15)+N(3,0);
};
};
Boundary("T-6")
{
};
Date("Sum-T-6");
Boundary("T-5")
{
};
{
Combine("Sum-T-5")
{
 R_Date("RR0705_104TC_047.5_049.5_SUM-175", 1220, 20)+N(12,1);
 R_Date("RR0705_103PC_020_022_SUM-084", 1225, 20)+N(5,0);
};
};
Boundary("T-4")
{
};
{
Combine("Sum-T-4")
{
 R_Date("RR0705_104PC_049.5_051.5_SUM-060", 1065, 20)+N(9,1);
```

```
  R_Date("RR0705_96PC_222_224_SUM-228", 1145, 15)+N(8,1);
 };
};
Boundary("T-3")
{
};
R_Date("RR0705_104TC_011_013_SUM-176", 705, 20)+N(35,3);
Boundary("T-2")
{
};
R_Date("RR0705_96PC_206_208_SUM-227", 480, 15)+N(8,1);
Boundary("T-1")
{
};
Date("Sum-T-1");
Boundary("T-0", 2007)
{
};
};
```

OxCal Code

Code for Table 2-5 B

```
Options()
{
 Plot()
 BCAD=FALSE;
 Curve("Marine13","Marine13.14c");
 Delta_R("LocalMarine",16,11);
 Sequence("2004 Region Gap")
 {
  Boundary("Start", -8000);
  R_Date("RR0705_108PC_345_347_SUM-195", 7175, 20)+N(174,17);
  Boundary("T-29")
  {
  };
  R_Date("RR0705_108PC_330_332_SUM-041", 6685, 25)+N(64,6);
  Boundary("T-28")
  {
  };
```

```
{
 Combine("Sum-T-28")
 {
  R_Date("RR0705_108PC_312.5_314.5_SUM-043", 6115, 20)+N(53,5);
  R_Date("RR0705_103PC_383_385_SUM-253", 6020, 25)+N(13,1);
 };
};
Boundary("T-27")
{
};
R_Date("RR0705_108PC_290.5_292.5_SUM-044", 5950, 20)+N(19,2);
Boundary("T-26")
{
};
R_Date("RR0705_103PC_324_326_SUM-224", 5575, 25)+N(17,2);
Boundary("T-25")
{
};
R_Date("RR0705_108PC_257_259_SUM-042", 4840, 20)+N(52,5);
Boundary("T-24")
{
};
Date("Sum-T-24");
Boundary("T-23")
{
};
R_Date("RR0705_108PC_212.5_214.5_SUM-045", 4625, 20)+N(46,5);
Boundary("T-22")
{
};
Date("Sum-T-22");
Boundary("T-21")
{
};



{
 Combine("Sum-T-21")
 {
  R_Date("RR0705_108PC_194_196_SUM-194", 4340, 20)+N(24,2);
  R_Date("RR0705_103PC_209_211_SUM-050", 4360, 20)+N(3,0);
 };
```

```
};
Boundary("T-20")
{
};



{
 Combine("Sum-T-20")
 {
  R_Date("RR0705_103PC_174_176_SUM-087", 3925, 20)+N(125,13);
 };
};
Boundary("T-19")
{
};
R_Date("RR0705_108PC_156_158_SUM-083", 3500, 15)+N(74,7);
Boundary("T-18")
{
};



{
 Combine("Sum-T-18")
 {
  R_Date("RR0705_108PC_132.5_134.5_SUM-081", 3035, 15)+N(0,0);
  R_Date("RR0705_104PC_326_328_SUM-235", 3000, 35)+N(6,1);
  R_Date("RR0705_103TC_079_081_SUM-180", 2985, 20)+N(0,0);
 };
};
Boundary("T-17")
{
};
Date("Sum-T-17");
Boundary("T-16")
{
};
Date("Sum-T-16");
Boundary("T-15")
{
};
R_Date("RR0705_96PC_399_401_SUM-232", 2410, 20)+N(12,1);
```

```
Boundary("T-14")
{
};
R_Date("RR0705_104PC_207_209_SUM-115", 2420, 220)+N(17,2);
Boundary("T-13")
{
};
Date("Sum-T-13");
Boundary("T-12")
{
};
Date("Sum-T-12");
Boundary("T-11")
{
};



{
 Combine("Sum-T-11")
 {
  R_Date("RR0705_103TC_039_041_SUM-179", 2065, 20)+N(0,0);
  R_Date("RR0705_96PC_374_376_SUM-090", 2115, 20)+N(7,1);
 };
};
Boundary("T-10")
{
};



{
 Combine("Sum-T-10")
 {
  R_Date("RR0705_108TC_020_022_SUM-172", 1930, 20)+N(44,4);
  R_Date("RR0705_103PC_049_051_SUM-054", 1940, 25)+N(18,2);
  R_Date("RR0705_103TC_036_038_SUM-178", 1890, 20)+N(23,2);
 };
};
Boundary("T-9")
{
};
Date("Sum-T-9");
```

```
Boundary("T-8")
{
};
Date("Sum-T-8");
Boundary("T-7")
{
};
R_Date("RR0705_96PC_287.5_289.5_SUM-089", 1490, 15)+N(3,0);
Boundary("T-6")
{
};
Date("Sum-T-6");
Boundary("T-5")
{
};



{
 Combine("Sum-T-5")
 {
  R_Date("RR0705_104TC_047.5_049.5_SUM-175", 1220, 20)+N(12,1);
  R_Date("RR0705_103PC_020_022_SUM-084", 1225, 20)+N(5,0);
 };
};
Boundary("T-4")
{
};



{
 Combine("Sum-T-4")
 {
  R_Date("RR0705_104PC_049.5_051.5_SUM-060", 1065, 20)+N(9,1);
  R_Date("RR0705_96PC_222_224_SUM-228", 1145, 15)+N(8,1);
 };
};
Boundary("T-3")
{
};
R_Date("RR0705_104TC_011_013_SUM-176", 705, 20)+N(35,3);
```

```
  Boundary("T-2")
  {
  };
  R_Date("RR0705_96PC_206_208_SUM-227", 480, 15)+N(8,1);
  Boundary("T-1")
  {
  };
  Date("Sum-T-1");
  Boundary("T-0", 2007)
  {
  };
 };
};
```

Radiocarbon Age Model Logs

These log files include the input and output for each of the OxCal Age Models in these papers.

Age Model Name	Short Description
2004 All Ages	This is the age model that includes all the ages (**Table 2-2, 2-5 A**)
2004 Passes	This is the age model that only includes ages that meet our criteria (**Table 2-5 B**).
96PC 2004	The Sequence age model for core 96PC (**Table 2-3**)
102MC 2004	The Sequence age model for core 102MC (**Table 2-3**)
96PC P_Sequence	The P_Sequence age model for core 96PC (**Table 2-7**)
103PC P_Sequence	The P_Sequence age model for core 103PC (**Table 2-7**)
103TC P_Sequence	The P_Sequence age model for core 103TC (**Table 2-7**)
104PC P_Sequence	The P_Sequence age model for core 104PC (**Table 2-7**)
104TC P_Sequence	The P_Sequence age model for core 104TC (**Table 2-7**)
108PC P_Sequence	The P_Sequence age model for core 108PC (**Table 2-7**)

2004 All Ages

OxCal v4.2.3 Bronk Ramsey (2013); r:5
IntCal13 atmospheric curve (Reimer et al 2013)
FALSE
OxCal v4.2.3 Bronk Ramsey (2013); r:5
Marine13 Curve(Marine13.14c)
Marine13 marine curve (Reimer et al 2013)
LocalMarine Delta_R(16,11)
68.2% probability
3 (68.2%) 29
95.4% probability
-7 (95.4%) 39
-8000
: -8000
(Boundary Start
Start Boundary(-8000)
68.2% probability
8002BC (68.2%) 8001BC
95.4% probability
8002BC (95.4%) 8001BC
) Boundary Start
RR0705_108PC_345_347_SUM-195 R_Date(7175,20)
68.2% probability
5702BC (68.2%) 5645BC
95.4% probability
5727BC (95.4%) 5619BC
N(174,17)
68.2% probability
157 (68.2%) 191
95.4% probability
140 (95.4%) 208
(Calculate
RR0705_108PC_345_347_SUM-195+N(174,17)
68.2% probability
5532BC (68.2%) 5465BC
95.4% probability
5566BC (95.4%) 5433BC
) Calculate
T-29 Boundary()
RR0705_108PC_330_332_SUM-041 R_Date(6685,25)
68.2% probability
5287BC (68.2%) 5220BC
95.4% probability
5318BC (95.4%) 5192BC
N(64,6)
68.2% probability
58 (68.2%) 70
95.4% probability
52 (95.4%) 76
(Calculate
RR0705_108PC_330_332_SUM-041+N(64,6)
68.2% probability
5224BC (68.2%) 5155BC
95.4% probability
5256BC (95.4%) 5126BC
) Calculate
T-28 Boundary()
RR0705_108PC_312.5_314.5_SUM-043 R_Date(6115,20)
68.2% probability
4621BC (68.2%) 4527BC
95.4% probability
4666BC (95.4%) 4493BC
N(53,5)
68.2% probability
48 (68.2%) 58
95.4% probability
43 (95.4%) 63
(Calculate
RR0705_108PC_312.5_314.5_SUM-043+N(53,5)
68.2% probability
4566BC (68.2%) 4474BC
95.4% probability
4614BC (95.4%) 4440BC
) Calculate
RR0705_103PC_383_385_SUM-253 R_Date(6020,25)

68.2% probability
4511BC (68.2%) 4431BC
95.4% probability
4546BC (95.4%) 4370BC
N(13,1)
68.2% probability
12 (68.2%) 14
95.4% probability
11 (95.4%) 15
(Calculate
RR0705_103PC_383_385_SUM-253+N(13,1)
68.2% probability
4499BC (68.2%) 4418BC
95.4% probability
4533BC (95.4%) 4356BC
) Calculate
(Combine Sum-T-28
Posterior
68.2% probability
4514BC (68.2%) 4455BC
95.4% probability
4546BC (95.4%) 4427BC
Agreement 94.4%
Posterior
68.2% probability
4514BC (68.2%) 4455BC
95.4% probability
4546BC (95.4%) 4427BC
Agreement 95.4%
Sum-T-28 Combine()
X2-Test: df=1 T=1.326(5% 3.841)
68.2% probability
4514BC (68.2%) 4455BC
95.4% probability
4546BC (95.4%) 4427BC
Agreement n=2 Acomb= 92.9%(An= 50.0%)
) Combine Sum-T-28
T-27 Boundary()
RR0705_108PC_290.5_292.5_SUM-044 R_Date(5950,20)
68.2% probability
4428BC (68.2%) 4357BC
95.4% probability
4455BC (95.4%) 4331BC
N(19,2)
68.2% probability
17 (68.2%) 21
95.4% probability
15 (95.4%) 23
(Calculate
RR0705_108PC_290.5_292.5_SUM-044+N(19,2)
68.2% probability
4408BC (68.2%) 4338BC
95.4% probability
4436BC (95.4%) 4312BC
) Calculate
T-26 Boundary()
RR0705_103PC_324_326_SUM-224 R_Date(5575,25)
68.2% probability
4023BC (68.2%) 3956BC
95.4% probability
4071BC (95.4%) 3926BC
N(17,2)
68.2% probability
15 (68.2%) 19
95.4% probability
13 (95.4%) 21
(Calculate
RR0705_103PC_324_326_SUM-224+N(17,2)
68.2% probability
4005BC (68.2%) 3940BC
95.4% probability
4055BC (95.4%) 3908BC
) Calculate
T-25 Boundary()
RR0705_108PC_257_259_SUM-042 R_Date(4840,20)
68.2% probability
3247BC (68.2%) 3106BC
95.4% probability
3302BC (95.4%) 3067BC

N(52,5)
68.2% probability
47 (68.2%) 57
95.4% probability
42 (95.4%) 62
(Calculate
RR0705_108PC_257_259_SUM-042+N(52,5)
68.2% probability
3194BC (68.2%) 3055BC
95.4% probability
3249BC (95.4%) 3013BC
) Calculate
T-24 Boundary()
Sum-T-24
T-23 Boundary()
RR0705_108PC_212.5_214.5_SUM-045 R_Date(4625,20)
68.2% probability
2899BC (68.2%) 2856BC
95.4% probability
2952BC (95.4%) 2830BC
N(46,5)
68.2% probability
41 (68.2%) 51
95.4% probability
36 (95.4%) 56
(Calculate
RR0705_108PC_212.5_214.5_SUM-045+N(46,5)
68.2% probability
2854BC (68.2%) 2809BC
95.4% probability
2905BC (95.4%) 2782BC
) Calculate
T-22 Boundary()
Sum-T-22
T-21 Boundary()
RR0705_108PC_194_196_SUM-194 R_Date(4340,20)
68.2% probability
2542BC (68.2%) 2466BC
95.4% probability
2580BC (95.4%) 2434BC
N(24,2)
68.2% probability
22 (68.2%) 26
95.4% probability
20 (95.4%) 28
(Calculate
RR0705_108PC_194_196_SUM-194+N(24,2)
68.2% probability
2517BC (68.2%) 2442BC
95.4% probability
2557BC (95.4%) 2409BC
) Calculate
RR0705_103PC_209_211_SUM-050 R_Date(4360,20)
68.2% probability
2560BC (68.2%) 2480BC
95.4% probability
2606BC (95.4%) 2455BC
N(3)
68.2% probability
3 (68.2%) 4
95.4% probability
3 (95.4%) 4
(Calculate
RR0705_103PC_209_211_SUM-050+N(3)
68.2% probability
2557BC (68.2%) 2478BC
95.4% probability
2603BC (95.4%) 2451BC
) Calculate
(Combine Sum-T-21
Posterior
68.2% probability
2527BC (68.2%) 2472BC
95.4% probability
2550BC (95.4%) 2450BC
Agreement 104.4%
Posterior
68.2% probability
2527BC (68.2%) 2472BC
95.4% probability

2550BC (95.4%) 2450BC
Agreement 108.4%
Sum-T-21 Combine()
X2-Test: df=1 T=0.196(5% 3.841)
68.2% probability
2527BC (68.2%) 2472BC
95.4% probability
2550BC (95.4%) 2450BC
Agreement n=2 Acomb=109.2%(An= 50.0%)
) Combine Sum-T-21
T-20 Boundary()
RR0705_108PC_175_177_SUM-046 R_Date(4070,15)
68.2% probability
2189BC (68.2%) 2097BC
95.4% probability
2213BC (95.4%) 2029BC
N(43,4)
68.2% probability
39 (68.2%) 47
95.4% probability
35 (95.4%) 51
(Calculate
RR0705_108PC_175_177_SUM-046+N(43,4)
68.2% probability
2145BC (68.2%) 2053BC
95.4% probability
2171BC (95.4%) 1985BC
) Calculate
RR0705_103PC_174_176_SUM-087 R_Date(3925,20)
68.2% probability
1975BC (68.2%) 1889BC
95.4% probability
2022BC (95.4%) 1862BC
N(125,13)
68.2% probability
112 (68.2%) 138
95.4% probability
99 (95.4%) 151
(Calculate
RR0705_103PC_174_176_SUM-087+N(125,13)
68.2% probability
1854BC (68.2%) 1765BC
95.4% probability
1903BC (95.4%) 1729BC
) Calculate
(Combine Sum-T-20
Posterior
68.2% probability
2006BC (68.2%) 1967BC
95.4% probability
2024BC (95.4%) 1913BC
Warning! Poor agreement - A= 20.0%(A'c= 60.0%)
Poor agreement 20.0%
Posterior
68.2% probability
2006BC (68.2%) 1967BC
95.4% probability
2024BC (95.4%) 1913BC
Warning! Poor agreement - A= 1.6%(A'c= 60.0%)
Poor agreement 1.6%
Sum-T-20 Combine()
X2-Test: df=1 T=15.216(5% 3.841)
Warning! X-Test fails at 5% - Sum-T-20 X2-Test: df=1 T=15.216(5% 3.8)
68.2% probability
2006BC (68.2%) 1967BC
95.4% probability
2024BC (95.4%) 1913BC
Warning! Poor agreement - n=2 Acomb= 1.7%(An= 50.0%)
Poor agreement n=2 Acomb= 1.7%(An= 50.0%)
) Combine Sum-T-20
T-19 Boundary()
RR0705_108PC_156_158_SUM-083 R_Date(3500,15)
68.2% probability
1449BC (68.2%) 1386BC
95.4% probability

1488BC (95.4%) 1362BC
N(74,7)
68.2% probability
67 (68.2%) 81
95.4% probability
60 (95.4%) 88
(Calculate
RR0705_108PC_156_158_SUM-083+N(74,7)
68.2% probability
1376BC (68.2%) 1311BC
95.4% probability
1416BC (95.4%) 1284BC
) Calculate
T-18 Boundary()
RR0705_108PC_132.5_134.5_SUM-081 R_Date(3035,15)
68.2% probability
859BC (68.2%) 798BC
95.4% probability
895BC (95.4%) 786BC
N(0)
68.2% probability
-0 (68.2%) 1
95.4% probability
-0 (95.4%) 1
(Calculate
RR0705_108PC_132.5_134.5_SUM-081+N(0)
68.2% probability
858BC (68.2%) 798BC
95.4% probability
896BC (95.4%) 785BC
) Calculate
RR0705_104PC_326_328_SUM-235 R_Date(3000,35)
68.2% probability
840BC (68.2%) 768BC
95.4% probability
894BC (95.4%) 747BC
N(6,1)
68.2% probability
5 (68.2%) 7
95.4% probability
4 (95.4%) 8
(Calculate
RR0705_104PC_326_328_SUM-235+N(6,1)
68.2% probability
835BC (68.2%) 761BC
95.4% probability
888BC (95.4%) 741BC
) Calculate
RR0705_103TC_079_081_SUM-180 R_Date(2985,20)
68.2% probability
813BC (68.2%) 768BC
95.4% probability
856BC (95.4%) 747BC
N(0)
68.2% probability
-0 (68.2%) 1
95.4% probability
-0 (95.4%) 1
(Calculate
RR0705_103TC_079_081_SUM-180+N(0)
68.2% probability
812BC (68.2%) 768BC
95.4% probability
854BC (95.4%) 746BC
) Calculate
(Combine Sum-T-18
Posterior
68.2% probability
816BC (68.2%) 789BC
95.4% probability
839BC (95.4%) 777BC
Agreement 98.7%
Posterior
68.2% probability
816BC (68.2%) 789BC
95.4% probability
839BC (95.4%) 777BC
Agreement 128.7%
Posterior
68.2% probability

816BC (68.2%) 789BC
95.4% probability
839BC (95.4%) 777BC
Agreement 102.1%
Sum-T-18 Combine()
X2-Test: df=2 T=1.421(5% 5.991)
68.2% probability
816BC (68.2%) 789BC
95.4% probability
839BC (95.4%) 777BC
Agreement n=3 Acomb=116.2%(An=40.8%)
) Combine Sum-T-18
T-17 Boundary()
Sum-T-17
T-16 Boundary()
Sum-T-16
T-15 Boundary()
RR0705_96PC_399_401_SUM-232 R_Date(2410,20)
68.2% probability
124BC (68.2%) 32BC
95.4% probability
162BC (95.4%) 9AD
N(12,1)
68.2% probability
11 (68.2%) 13
95.4% probability
10 (95.4%) 14
(Calculate RR0705_96PC_399_401_SUM-232+N(12,1)
68.2% probability
110BC (68.2%) 20BC
95.4% probability
150BC (95.4%) 21AD
) Calculate
T-14 Boundary()
RR0705_104PC_207_209_SUM-115 R_Date(2420,220)
68.2% probability
372BC (68.2%) 164AD
95.4% probability
696BC (95.4%) 398AD
N(17,2)
68.2% probability
15 (68.2%) 19
95.4% probability
13 (95.4%) 21
(Calculate RR0705_104PC_207_209_SUM-115+N(17,2)
68.2% probability
355BC (68.2%) 181AD
95.4% probability
679BC (95.4%) 415AD
) Calculate
T-13 Boundary()
Sum-T-13
T-12 Boundary()
Sum-T-12
T-11 Boundary()
RR0705_103TC_039_041_SUM-179 R_Date(2065,20)
68.2% probability
287AD (68.2%) 379AD
95.4% probability
257AD (95.4%) 411AD
N(0)
68.2% probability
-0 (68.2%) 1
95.4% probability
-0 (95.4%) 1
(Calculate RR0705_103TC_039_041_SUM-179+N(0)
68.2% probability
288AD (68.2%) 378AD
95.4% probability
256AD (95.4%) 411AD
) Calculate
RR0705_96PC_374_376_SUM-090 R_Date(2115,20)
68.2% probability
237AD (68.2%) 329AD
95.4% probability
178AD (95.4%) 362AD

N(7,1)
68.2% probability
6 (68.2%) 8
95.4% probability
5 (95.4%) 9
(Calculate
RR0705_96PC_374_376_SUM-090+N(7,1)
68.2% probability
244AD (68.2%) 335AD
95.4% probability
184AD (95.4%) 369AD
) Calculate
(Combine Sum-T-11
Posterior
68.2% probability
273AD (68.2%) 338AD
95.4% probability
251AD (95.4%) 369AD
Agreement 101.9%
Posterior
68.2% probability
273AD (68.2%) 338AD
95.4% probability
251AD (95.4%) 369AD
Agreement 106.9%
Sum-T-11 Combine()
X2-Test: df=1 T=0.942(5% 3.841)
68.2% probability
273AD (68.2%) 338AD
95.4% probability
251AD (95.4%) 369AD
Agreement n=2 Acomb=106.2%(An=
50.0%)
) Combine Sum-T-11
T-10 Boundary()
RR0705_108PC_039_041_SUM-080 R_
Date(2015,15)
68.2% probability
360AD (68.2%) 425AD
95.4% probability
311AD (95.4%) 455AD
N(41,4)
68.2% probability
37 (68.2%) 45
95.4% probability
33 (95.4%) 49
(Calculate
RR0705_108PC_039_041_SUM-
080+N(41,4)
68.2% probability
401AD (68.2%) 466AD
95.4% probability
353AD (95.4%) 497AD
) Calculate
RR0705_108TC_020_022_SUM-172 R_
Date(1930,20)
68.2% probability
446AD (68.2%) 531AD
95.4% probability
418AD (95.4%) 567AD
N(44,4)
68.2% probability
40 (68.2%) 48
95.4% probability
36 (95.4%) 52
(Calculate
RR0705_108TC_020_022_SUM-
172+N(44,4)
68.2% probability
489AD (68.2%) 575AD
95.4% probability
462AD (95.4%) 612AD
) Calculate
RR0705_104PC_158_160_SUM-082 R_
Date(2040,20)
68.2% probability
331AD (68.2%) 411AD
95.4% probability
274AD (95.4%) 429AD
N(5)
68.2% probability
4 (68.2%) 5
95.4% probability
4 (95.4%) 5
(Calculate
RR0705_104PC_158_160_SUM-082+N(5)

68.2% probability
335AD (68.2%) 416AD
95.4% probability
280AD (95.4%) 434AD
) Calculate
RR0705_103PC_049_051_SUM-054 R_
Date(1940,25)
68.2% probability
434AD (68.2%) 524AD
95.4% probability
402AD (95.4%) 567AD
N(18,2)
68.2% probability
16 (68.2%) 20
95.4% probability
14 (95.4%) 22
(Calculate
RR0705_103PC_049_051_SUM-
054+N(18,2)
68.2% probability
452AD (68.2%) 541AD
95.4% probability
421AD (95.4%) 584AD
) Calculate
RR0705_103TC_036_038_SUM-178 R_
Date(1890,20)
68.2% probability
484AD (68.2%) 575AD
95.4% probability
445AD (95.4%) 606AD
N(23,2)
68.2% probability
21 (68.2%) 25
95.4% probability
19 (95.4%) 27
(Calculate
RR0705_103TC_036_038_SUM-
178+N(23,2)
68.2% probability
507AD (68.2%) 597AD
95.4% probability
467AD (95.4%) 630AD
) Calculate
(Combine Sum-T-10
Posterior
68.2% probability
457AD (68.2%) 485AD
95.4% probability
444AD (95.4%) 511AD
Agreement 64.9%
Posterior
68.2% probability
457AD (68.2%) 485AD
95.4% probability
444AD (95.4%) 511AD
Warning! Poor agreement - A= 54.8%(A'c=
60.0%)
Poor agreement 54.8%
Posterior
68.2% probability
457AD (68.2%) 485AD
95.4% probability
444AD (95.4%) 511AD
Warning! Poor agreement - A= 1.8%(A'c=
60.0%)
Poor agreement 1.8%
Posterior
68.2% probability
457AD (68.2%) 485AD
95.4% probability
444AD (95.4%) 511AD
Agreement 124.7%
Posterior
68.2% probability
457AD (68.2%) 485AD
95.4% probability
444AD (95.4%) 511AD
Warning! Poor agreement - A= 38.7%(A'c=
60.0%)
Poor agreement 38.7%
Sum-T-10 Combine()
X2-Test: df=4 T=15.726(5% 9.488)
Warning! X-Test fails at 5% - Sum-T-10 X2-
Test: df=4 T=15.726(5% 9.5)
68.2% probability
457AD (68.2%) 485AD

95.4% probability
444AD (95.4%) 511AD
Warning! Poor agreement - n=5 Acomb= 7.6%(An= 31.6%)
Poor agreement n=5 Acomb= 7.6%(An= 31.6%)
) Combine Sum-T-10
T-9 Boundary()
Sum-T-9
T-8 Boundary()
Sum-T-8
T-7 Boundary()
RR0705_104PC_122_124_SUM-061 R_Date(1630,45)
68.2% probability
705AD (68.2%) 820AD
95.4% probability
680AD (95.4%) 889AD
N(17,2)
68.2% probability
15 (68.2%) 19
95.4% probability
13 (95.4%) 21
(Calculate RR0705_104PC_122_124_SUM-061+N(17,2)
68.2% probability
723AD (68.2%) 836AD
95.4% probability
696AD (95.4%) 907AD
) Calculate RR0705_96PC_287.5_289.5_SUM-089 R_Date(1490,15)
68.2% probability
900AD (68.2%) 975AD
95.4% probability
857AD (95.4%) 1006AD
N(3)
68.2% probability
3 (68.2%) 4
95.4% probability
3 (95.4%) 4
(Calculate RR0705_96PC_287.5_289.5_SUM-089+N(3)
68.2% probability
905AD (68.2%) 975AD
95.4% probability
859AD (95.4%) 1010AD
) Calculate
(Combine Sum-T-7
Posterior
68.2% probability
859AD (68.2%) 928AD
95.4% probability
817AD (95.4%) 966AD
Warning! Poor agreement - A= 38.1%(A'c= 60.0%)
Poor agreement 38.1%
Posterior
68.2% probability
859AD (68.2%) 928AD
95.4% probability
817AD (95.4%) 966AD
Agreement 69.4%
Sum-T-7 Combine()
X2-Test: df=1 T=3.842(5% 3.841)
Warning! X-Test fails at 5% - Sum-T-7 X2-Test: df=1 T=3.842(5% 3.8)
68.2% probability
859AD (68.2%) 928AD
95.4% probability
817AD (95.4%) 966AD
Warning! Poor agreement - n=2 Acomb= 39.0%(An= 50.0%)
Poor agreement n=2 Acomb= 39.0%(An= 50.0%)
) Combine Sum-T-7
T-6 Boundary()
Sum-T-6
T-5 Boundary()
RR0705_104TC_047.5_049.5_SUM-175 R_Date(1220,20)
68.2% probability
1179AD (68.2%) 1245AD
95.4% probability

1140AD (95.4%) 1277AD
N(12,1)
68.2% probability
11 (68.2%) 13
95.4% probability
10 (95.4%) 14
(Calculate
RR0705_104TC_047.5_049.5_SUM-175+N(12,1)
68.2% probability
1191AD (68.2%) 1256AD
95.4% probability
1153AD (95.4%) 1289AD
) Calculate
RR0705_103PC_020_022_SUM-084 R_Date(1225,20)
68.2% probability
1173AD (68.2%) 1241AD
95.4% probability
1131AD (95.4%) 1274AD
N(5)
68.2% probability
4 (68.2%) 5
95.4% probability
4 (95.4%) 5
(Calculate
RR0705_103PC_020_022_SUM-084+N(5)
68.2% probability
1178AD (68.2%) 1247AD
95.4% probability
1138AD (95.4%) 1279AD
) Calculate
(Combine Sum-T-5
Posterior
68.2% probability
1193AD (68.2%) 1242AD
95.4% probability
1175AD (95.4%) 1267AD
Agreement 114.0%
Posterior
68.2% probability
1193AD (68.2%) 1242AD
95.4% probability
1175AD (95.4%) 1267AD
Agreement 115.4%
Sum-T-5 Combine()
X2-Test: df=1 T=0.069(5% 3.841)
68.2% probability
1193AD (68.2%) 1242AD
95.4% probability
1175AD (95.4%) 1267AD
Agreement n=2 Acomb=121.4%(An=50.0%)
) Combine Sum-T-5
T-4 Boundary()
RR0705_104PC_049.5_051.5_SUM-060 R_Date(1065,20)
68.2% probability
1294AD (68.2%) 1351AD
95.4% probability
1286AD (95.4%) 1396AD
N(9,1)
68.2% probability
8 (68.2%) 10
95.4% probability
7 (95.4%) 11
(Calculate
RR0705_104PC_049.5_051.5_SUM-060+N(9,1)
68.2% probability
1303AD (68.2%) 1359AD
95.4% probability
1294AD (95.4%) 1405AD
) Calculate
RR0705_96PC_222_224_SUM-228 R_Date(1145,15)
68.2% probability
1255AD (68.2%) 1295AD
95.4% probability
1225AD (95.4%) 1310AD
N(8,1)
68.2% probability
7 (68.2%) 9
95.4% probability
6 (95.4%) 10
(Calculate

RR0705_96PC_222_224_SUM-228+N(8,1)
68.2% probability
1262AD (68.2%) 1303AD
95.4% probability
1233AD (95.4%) 1318AD
) Calculate
(Combine Sum-T-4
Posterior
68.2% probability
1292AD (68.2%) 1317AD
95.4% probability
1280AD (95.4%) 1329AD
Agreement 74.9%
Posterior
68.2% probability
1292AD (68.2%) 1317AD
95.4% probability
1280AD (95.4%) 1329AD
Agreement 74.8%
Sum-T-4 Combine()
X2-Test: df=1 T=3.163(5% 3.841)
68.2% probability
1292AD (68.2%) 1317AD
95.4% probability
1280AD (95.4%) 1329AD
Agreement n=2 Acomb= 66.4%(An= 50.0%)
) Combine Sum-T-4
T-3 Boundary()
RR0705_104TC_011_013_SUM-176 R_Date(705,20)
68.2% probability
1583AD (68.2%) 1660AD
95.4% probability
1540AD (95.4%) 1673AD
N(35,3)
68.2% probability
32 (68.2%) 38
95.4% probability
29 (95.4%) 41
(Calculate
RR0705_104TC_011_013_SUM-176+N(35,3)
68.2% probability
1616AD (68.2%) 1695AD
95.4% probability
1574AD (95.4%) 1709AD
) Calculate
T-2 Boundary()
RR0705_96PC_206_208_SUM-227 R_Date(480,15)
Warning! Date may extend out of range - 480+/-15BP
Warning! Date probably out of range - 480+/-15BP
68.2% probability
1865AD (68.2%) ...
95.4% probability
1818AD (95.4%) ...
N(8,1)
68.2% probability
7 (68.2%) 9
95.4% probability
6 (95.4%) 10
(Calculate
RR0705_96PC_206_208_SUM-227+N(8,1)
68.2% probability
1872AD (32.6%) 1920AD
1926AD (35.6%) ...
95.4% probability
1828AD (95.4%) ...
) Calculate
T-1 Boundary()
Sum-T-1
2007
: 2007
(Boundary T-0
T-0 Boundary(2007)
68.2% probability
2006AD (68.2%) 2007AD
95.4% probability
2006AD (95.4%) 2007AD
) Boundary T-0
(Sequence 2004 Region Gap
2004 Region Gap Sequence()
) Sequence 2004 Region Gap

Posterior
(MCMC(30000)
Warning! Poor agreement - A= 15.6%(A'c= 60.0%)
Warning! Poor agreement - A= 9.2%(A'c= 60.0%)
LocalMarine Posterior
68.2% probability
0 (68.2%) 20
95.4% probability
-10 (95.4%) 30
Agreement 96.5%
Start Posterior
68.2% probability
8002BC (68.2%) 8001BC
95.4% probability
8002BC (95.4%) 8001BC
Agreement 100.0%
Posterior
68.2% probability
5540BC (68.2%) 5472BC
95.4% probability
5572BC (95.4%) 5439BC
RR0705_108PC_345_347_SUM-195 Posterior
68.2% probability
5710BC (68.2%) 5650BC
95.4% probability
5736BC (95.4%) 5621BC
Agreement 98.5%
Posterior
68.2% probability
156 (68.2%) 190
95.4% probability
139 (95.4%) 207
Agreement 100.0%
T-29 Posterior
68.2% probability
5417BC (68.2%) 5201BC
95.4% probability
5508BC (95.4%) 5164BC
Posterior
68.2% probability
5225BC (68.2%) 5155BC
95.4% probability
5256BC (95.4%) 5129BC
RR0705_108PC_330_332_SUM-041 Posterior
68.2% probability
5288BC (68.2%) 5220BC
95.4% probability
5318BC (95.4%) 5195BC
Agreement 99.8%
Posterior
68.2% probability
58 (68.2%) 70
95.4% probability
52 (95.4%) 76
Agreement 99.9%
T-28 Posterior
68.2% probability
5198BC (25.4%) 5008BC
4737BC (1.1%) 4726BC
4719BC (41.7%) 4466BC
95.4% probability
5200BC (95.4%) 4461BC
Sum-T-28 Posterior
68.2% probability
4517BC (68.2%) 4461BC
95.4% probability
4549BC (95.4%) 4431BC
Posterior
68.2% probability
4517BC (68.2%) 4461BC
95.4% probability
4549BC (95.4%) 4431BC
Agreement 99.9%
Posterior
68.2% probability
4517BC (68.2%) 4461BC
95.4% probability
4549BC (95.4%) 4431BC
Agreement 89.8%
T-27 Posterior
68.2% probability
4477BC (68.2%) 4385BC

95.4% probability
4511BC (95.4%) 4340BC
Posterior
68.2% probability
4407BC (68.2%) 4338BC
95.4% probability
4434BC (95.4%) 4314BC
RR0705_108PC_290.5_292.5_SUM-044 Posterior
68.2% probability
4426BC (68.2%) 4356BC
95.4% probability
4452BC (95.4%) 4333BC
Agreement 102.0%
Posterior
68.2% probability
17 (68.2%) 21
95.4% probability
15 (95.4%) 23
Agreement 99.8%
T-26 Posterior
68.2% probability
4398BC (66.4%) 4148BC
4141BC (1.8%) 4131BC
95.4% probability
4413BC (95.4%) 3983BC
Posterior
68.2% probability
4010BC (68.2%) 3941BC
95.4% probability
4064BC (95.4%) 3913BC
RR0705_103PC_324_326_SUM-224 Posterior
68.2% probability
4026BC (68.2%) 3960BC
95.4% probability
4081BC (95.4%) 3931BC
Agreement 98.9%
Posterior
68.2% probability
15 (68.2%) 19
95.4% probability
13 (95.4%) 21
Agreement 100.0%
T-25 Posterior
68.2% probability
3970BC (21.5%) 3764BC
3748BC (0.8%) 3739BC
3571BC (0.4%) 3567BC
3478BC (45.2%) 3126BC
3113BC (0.3%) 3110BC
95.4% probability
3985BC (95.0%) 3099BC
3093BC (0.4%) 3087BC
Posterior
68.2% probability
3227BC (68.2%) 3096BC
95.4% probability
3254BC (95.4%) 3037BC
RR0705_108PC_257_259_SUM-042 Posterior
68.2% probability
3278BC (68.2%) 3146BC
95.4% probability
3306BC (95.4%) 3090BC
Agreement 98.7%
Posterior
68.2% probability
47 (68.2%) 57
95.4% probability
42 (95.4%) 62
Agreement 100.1%
T-24 Posterior
68.2% probability
3160BC (68.2%) 2967BC
95.4% probability
3215BC (95.4%) 2874BC
Sum-T-24 Posterior
68.2% probability
3049BC (68.2%) 2873BC
95.4% probability
3145BC (95.4%) 2832BC
T-23 Posterior
68.2% probability
2948BC (68.2%) 2822BC
95.4% probability

3084BC (95.4%) 2804BC
Posterior
68.2% probability
2856BC (68.2%) 2813BC
95.4% probability
2907BC (95.4%) 2788BC
RR0705_108PC_212.5_214.5_SUM-045
Posterior
68.2% probability
2901BC (68.2%) 2859BC
95.4% probability
2952BC (95.4%) 2836BC
Agreement 99.3%
Posterior
68.2% probability
41 (68.2%) 51
95.4% probability
36 (95.4%) 56
Agreement 100.1%
T-22 Posterior
68.2% probability
2851BC (68.2%) 2711BC
95.4% probability
2879BC (95.4%) 2567BC
Sum-T-22 Posterior
68.2% probability
2786BC (68.2%) 2593BC
95.4% probability
2833BC (95.4%) 2514BC
T-21 Posterior
68.2% probability
2656BC (68.2%) 2486BC
95.4% probability
2784BC (95.4%) 2466BC
Sum-T-21 Posterior
68.2% probability
2523BC (68.2%) 2468BC
95.4% probability
2548BC (95.4%) 2448BC
Posterior
68.2% probability
2523BC (68.2%) 2468BC
95.4% probability
2548BC (95.4%) 2448BC
Agreement 106.6%
Posterior
68.2% probability
2523BC (68.2%) 2468BC
95.4% probability
2548BC (95.4%) 2448BC
Agreement 106.5%
T-20 Posterior
68.2% probability
2511BC (50.6%) 2278BC
2265BC (0.6%) 2261BC
2088BC (16.9%) 1988BC
95.4% probability
2518BC (95.4%) 1984BC
Sum-T-20 Posterior
68.2% probability
2007BC (68.2%) 1967BC
95.4% probability
2023BC (95.4%) 1914BC
Posterior
68.2% probability
2007BC (68.2%) 1967BC
95.4% probability
2023BC (95.4%) 1914BC
Warning! Poor agreement - A= 19.9%(A'c= 60.0%)
Poor agreement 19.9%
Posterior
68.2% probability
2007BC (68.2%) 1967BC
95.4% probability
2023BC (95.4%) 1914BC
Warning! Poor agreement - A= 1.6%(A'c= 60.0%)
Poor agreement 1.6%
T-19 Posterior
68.2% probability
1985BC (35.4%) 1759BC
1749BC (0.4%) 1746BC
1722BC (0.5%) 1718BC
1600BC (0.5%) 1597BC
1580BC (1.4%) 1566BC

1561BC (1.0%) 1554BC
1543BC (29.0%) 1360BC
95.4% probability
1988BC (95.4%) 1351BC
Posterior
68.2% probability
1380BC (68.2%) 1316BC
95.4% probability
1417BC (95.4%) 1292BC
RR0705_108PC_156_158_SUM-083 Posterior
68.2% probability
1453BC (68.2%) 1392BC
95.4% probability
1489BC (95.4%) 1369BC
Agreement 99.7%
Posterior
68.2% probability
67 (68.2%) 81
95.4% probability
60 (95.4%) 88
Agreement 100.2%
T-18 Posterior
68.2% probability
1336BC (15.4%) 1241BC
1235BC (2.3%) 1215BC
1062BC (1.0%) 1055BC
1041BC (49.6%) 797BC
95.4% probability
1341BC (95.4%) 796BC
Sum-T-18 Posterior
68.2% probability
818BC (68.2%) 789BC
95.4% probability
842BC (95.4%) 777BC
Posterior
68.2% probability
818BC (68.2%) 789BC
95.4% probability
842BC (95.4%) 777BC
Agreement 100.3%
Posterior
68.2% probability
818BC (68.2%) 789BC
95.4% probability
842BC (95.4%) 777BC
Agreement 127.3%
Posterior
68.2% probability
818BC (68.2%) 789BC
95.4% probability
842BC (95.4%) 777BC
Agreement 99.5%
T-17 Posterior
68.2% probability
816BC (68.2%) 607BC
95.4% probability
834BC (95.4%) 343BC
Sum-T-17 Posterior
68.2% probability
763BC (68.2%) 440BC
95.4% probability
800BC (95.2%) 236BC
228BC (0.2%) 223BC
T-16 Posterior
68.2% probability
606BC (68.2%) 206BC
95.4% probability
754BC (95.4%) 118BC
Sum-T-16 Posterior
68.2% probability
404BC (68.2%) 106BC
95.4% probability
621BC (95.4%) 56BC
T-15 Posterior
68.2% probability
232BC (68.2%) 46BC
95.4% probability
476BC (95.4%) 8BC
Posterior
68.2% probability
128BC (68.2%) 40BC
95.4% probability
163BC (95.4%) 3BC
RR0705_96PC_399_401_SUM-232 Posterior

68.2% probability
141BC (68.2%) 53BC
95.4% probability
175BC (95.4%) 14BC
Agreement 97.8%
Posterior
68.2% probability
11 (68.2%) 13
95.4% probability
10 (95.4%) 14
Agreement 100.2%
T-14 Posterior
68.2% probability
105BC (68.2%) 17AD
95.4% probability
148BC (95.4%) 109AD
Posterior
68.2% probability
70BC (68.2%) 77AD
95.4% probability
123BC (95.4%) 165AD
RR0705_104PC_207_209_SUM-115 Posterior
68.2% probability
87BC (68.2%) 59AD
95.4% probability
140BC (95.4%) 148AD
Agreement 130.1%
Posterior
68.2% probability
15 (68.2%) 19
95.4% probability
13 (95.4%) 21
Agreement 99.9%
T-13 Posterior
68.2% probability
39BC (68.2%) 142AD
95.4% probability
97BC (95.4%) 236AD
Sum-T-13 Posterior
68.2% probability
21AD (68.2%) 201AD
95.4% probability
50BC (95.4%) 276AD
T-12 Posterior
68.2% probability
87AD (68.2%) 267AD
95.4% probability
13BC (95.4%) 320AD
Sum-T-12 Posterior
68.2% probability
157AD (68.2%) 303AD
95.4% probability
49AD (95.4%) 341AD
T-11 Posterior
68.2% probability
224AD (68.2%) 336AD
95.4% probability
115AD (95.4%) 368AD
Sum-T-11 Posterior
68.2% probability
284AD (68.2%) 348AD
95.4% probability
257AD (95.4%) 377AD
Posterior
68.2% probability
284AD (68.2%) 348AD
95.4% probability
257AD (95.4%) 377AD
Agreement 107.2%
Posterior
68.2% probability
284AD (68.2%) 348AD
95.4% probability
257AD (95.4%) 377AD
Agreement 98.9%
T-10 Posterior
68.2% probability
341AD (68.2%) 468AD
95.4% probability
288AD (95.4%) 482AD
Sum-T-10 Posterior
68.2% probability
457AD (68.2%) 484AD
95.4% probability
442AD (95.4%) 509AD

Posterior
68.2% probability
457AD (68.2%) 484AD
95.4% probability
442AD (95.4%) 509AD
Agreement 68.1%
Posterior
68.2% probability
457AD (68.2%) 484AD
95.4% probability
442AD (95.4%) 509AD
Warning! Poor agreement - A= 52.1%(A'c= 60.0%)
Poor agreement 52.1%
Posterior
68.2% probability
457AD (68.2%) 484AD
95.4% probability
442AD (95.4%) 509AD
Warning! Poor agreement - A= 2.0%(A'c= 60.0%)
Poor agreement 2.0%
Posterior
68.2% probability
457AD (68.2%) 484AD
95.4% probability
442AD (95.4%) 509AD
Agreement 124.1%
Posterior
68.2% probability
457AD (68.2%) 484AD
95.4% probability
442AD (95.4%) 509AD
Warning! Poor agreement - A= 36.7%(A'c= 60.0%)
Poor agreement 36.7%
T-9 Posterior
68.2% probability
462AD (68.2%) 578AD
95.4% probability
449AD (95.4%) 722AD
Sum-T-9 Posterior
68.2% probability
492AD (68.2%) 675AD
95.4% probability
470AD (95.4%) 798AD
T-8 Posterior
68.2% probability
565AD (68.2%) 796AD
95.4% probability
496AD (95.4%) 871AD
Sum-T-8 Posterior
68.2% probability
684AD (68.2%) 873AD
95.4% probability
566AD (95.4%) 912AD
T-7 Posterior
68.2% probability
776AD (68.2%) 916AD
95.4% probability
641AD (95.4%) 956AD
Sum-T-7 Posterior
68.2% probability
862AD (68.2%) 930AD
95.4% probability
822AD (95.4%) 967AD
Posterior
68.2% probability
862AD (68.2%) 930AD
95.4% probability
822AD (95.4%) 967AD
Warning! Poor agreement - A= 35.7%(A'c= 60.0%)
Poor agreement 35.7%
Posterior
68.2% probability
862AD (68.2%) 930AD
95.4% probability
822AD (95.4%) 967AD
Agreement 73.1%
T-6 Posterior
68.2% probability
881AD (68.2%) 1036AD
95.4% probability
844AD (95.4%) 1163AD
Sum-T-6 Posterior

68.2% probability
970AD (0.9%) 973AD
979AD (67.3%) 1161AD
95.4% probability
905AD (95.4%) 1215AD
T-5 Posterior
68.2% probability
1106AD (68.2%) 1237AD
95.4% probability
969AD (95.4%) 1257AD
Sum-T-5 Posterior
68.2% probability
1193AD (68.2%) 1241AD
95.4% probability
1175AD (95.4%) 1265AD
Posterior
68.2% probability
1193AD (68.2%) 1241AD
95.4% probability
1175AD (95.4%) 1265AD
Agreement 114.8%
Posterior
68.2% probability
1193AD (68.2%) 1241AD
95.4% probability
1175AD (95.4%) 1265AD
Agreement 116.3%
T-4 Posterior
68.2% probability
1231AD (68.2%) 1298AD
95.4% probability
1197AD (95.4%) 1315AD
Sum-T-4 Posterior
68.2% probability
1293AD (68.2%) 1317AD
95.4% probability
1281AD (95.4%) 1331AD
Posterior
68.2% probability
1293AD (68.2%) 1317AD
95.4% probability
1281AD (95.4%) 1331AD
Agreement 77.7%
Posterior
68.2% probability
1293AD (68.2%) 1317AD
95.4% probability
1281AD (95.4%) 1331AD
Agreement 72.1%
T-3 Posterior
68.2% probability
1296AD (56.7%) 1465AD
1526AD (0.7%) 1529AD
1545AD (10.8%) 1590AD
95.4% probability
1293AD (95.4%) 1653AD
Posterior
68.2% probability
1611AD (68.2%) 1689AD
95.4% probability
1572AD (95.4%) 1705AD
RR0705_104TC_011_013_SUM-176 Posterior
68.2% probability
1575AD (68.2%) 1655AD
95.4% probability
1536AD (95.4%) 1670AD
Agreement 99.0%
Posterior
68.2% probability
32 (68.2%) 38
95.4% probability
29 (95.4%) 41
Agreement 100.0%
T-2 Posterior
68.2% probability
1689AD (68.2%) 1875AD
95.4% probability
1625AD (95.4%) 1940AD
Posterior
68.2% probability
1832AD (68.2%) 1919AD
95.4% probability
1772AD (1.8%) 1793AD
1812AD (93.6%) 1962AD
RR0705_96PC_206_208_SUM-227 Poste-

rior
  68.2% probability
    1825AD (68.2%) 1911AD
  95.4% probability
    1763AD (1.9%) 1785AD
    1804AD (93.5%) 1953AD
 Agreement 92.3%
Posterior
  68.2% probability
    7 (68.2%) 9
  95.4% probability
    6 (95.4%) 10
 Agreement 100.0%
T-1 Posterior
  68.2% probability
    1903AD (68.2%) 2002AD
  95.4% probability
    1839AD (95.4%) 2010AD
Sum-T-1 Posterior
  68.2% probability
    1957AD (68.2%) 2010AD
  95.4% probability
    1889AD (95.4%) 2010AD
T-0 Posterior
  68.2% probability
    2006AD (68.2%) 2007AD
  95.4% probability
    2006AD (95.4%) 2007AD
 Agreement 100.0%
) MCMC(240000)

2004 Passes

OxCal v4.2.3 Bronk Ramsey (2013); r:5
IntCal13 atmospheric curve (Reimer et al 2013)
FALSE
OxCal v4.2.3 Bronk Ramsey (2013); r:5
Marine13 Curve(Marine13.14c)
Marine13 marine curve (Reimer et al 2013)
LocalMarine Delta_R(16,11)
68.2% probability
3 (68.2%) 29
95.4% probability
-7 (95.4%) 39
-8000
: -8000
(Boundary Start
Start Boundary(-8000)
68.2% probability
8002BC (68.2%) 8001BC
95.4% probability
8002BC (95.4%) 8001BC
) Boundary Start
RR0705_108PC_345_347_SUM-195 R_Date(7175,20)
68.2% probability
5702BC (68.2%) 5645BC
95.4% probability
5727BC (95.4%) 5619BC
N(174,17)
68.2% probability
157 (68.2%) 191
95.4% probability
140 (95.4%) 208
(Calculate
RR0705_108PC_345_347_SUM-195+N(174,17)
68.2% probability
5532BC (68.2%) 5465BC
95.4% probability
5566BC (95.4%) 5433BC
) Calculate
T-29 Boundary()
RR0705_108PC_330_332_SUM-041 R_Date(6685,25)
68.2% probability
5287BC (68.2%) 5220BC
95.4% probability
5318BC (95.4%) 5192BC
N(64,6)
68.2% probability
58 (68.2%) 70
95.4% probability
52 (95.4%) 76
(Calculate
RR0705_108PC_330_332_SUM-041+N(64,6)
68.2% probability
5224BC (68.2%) 5155BC
95.4% probability
5256BC (95.4%) 5126BC
) Calculate
T-28 Boundary()
RR0705_108PC_312.5_314.5_SUM-043 R_Date(6115,20)
68.2% probability
4621BC (68.2%) 4527BC
95.4% probability
4666BC (95.4%) 4493BC
N(53,5)
68.2% probability
48 (68.2%) 58
95.4% probability
43 (95.4%) 63
(Calculate
RR0705_108PC_312.5_314.5_SUM-043+N(53,5)
68.2% probability
4566BC (68.2%) 4474BC
95.4% probability
4614BC (95.4%) 4440BC
) Calculate
RR0705_103PC_383_385_SUM-253 R_Date(6020,25)

68.2% probability
4511BC (68.2%) 4431BC
95.4% probability
4546BC (95.4%) 4370BC
N(13,1)
68.2% probability
12 (68.2%) 14
95.4% probability
11 (95.4%) 15
(Calculate
RR0705_103PC_383_385_SUM-253+N(13,1)
68.2% probability
4499BC (68.2%) 4418BC
95.4% probability
4533BC (95.4%) 4356BC
) Calculate
(Combine Sum-T-28
Posterior
68.2% probability
4514BC (68.2%) 4455BC
95.4% probability
4546BC (95.4%) 4427BC
Agreement 94.4%
Posterior
68.2% probability
4514BC (68.2%) 4455BC
95.4% probability
4546BC (95.4%) 4427BC
Agreement 95.4%
Sum-T-28 Combine()
X2-Test: df=1 T=1.326(5% 3.841)
68.2% probability
4514BC (68.2%) 4455BC
95.4% probability
4546BC (95.4%) 4427BC
Agreement n=2 Acomb= 92.9%(An= 50.0%)
) Combine Sum-T-28
T-27 Boundary()
RR0705_108PC_290.5_292.5_SUM-044 R_Date(5950,20)
68.2% probability
4428BC (68.2%) 4357BC
95.4% probability
4455BC (95.4%) 4331BC
N(19,2)
68.2% probability
17 (68.2%) 21
95.4% probability
15 (95.4%) 23
(Calculate
RR0705_108PC_290.5_292.5_SUM-044+N(19,2)
68.2% probability
4408BC (68.2%) 4338BC
95.4% probability
4436BC (95.4%) 4312BC
) Calculate
T-26 Boundary()
RR0705_103PC_324_326_SUM-224 R_Date(5575,25)
68.2% probability
4023BC (68.2%) 3956BC
95.4% probability
4071BC (95.4%) 3926BC
N(17,2)
68.2% probability
15 (68.2%) 19
95.4% probability
13 (95.4%) 21
(Calculate
RR0705_103PC_324_326_SUM-224+N(17,2)
68.2% probability
4005BC (68.2%) 3940BC
95.4% probability
4055BC (95.4%) 3908BC
) Calculate
T-25 Boundary()
RR0705_108PC_257_259_SUM-042 R_Date(4840,20)
68.2% probability
3247BC (68.2%) 3106BC
95.4% probability
3302BC (95.4%) 3067BC

N(52,5)
68.2% probability
47 (68.2%) 57
95.4% probability
42 (95.4%) 62
(Calculate
RR0705_108PC_257_259_SUM-042+N(52,5)
68.2% probability
3194BC (68.2%) 3055BC
95.4% probability
3249BC (95.4%) 3013BC
) Calculate
T-24 Boundary()
Sum-T-24
T-23 Boundary()
RR0705_108PC_212.5_214.5_SUM-045 R_Date(4625,20)
68.2% probability
2899BC (68.2%) 2856BC
95.4% probability
2952BC (95.4%) 2830BC
N(46,5)
68.2% probability
41 (68.2%) 51
95.4% probability
36 (95.4%) 56
(Calculate
RR0705_108PC_212.5_214.5_SUM-045+N(46,5)
68.2% probability
2854BC (68.2%) 2809BC
95.4% probability
2905BC (95.4%) 2782BC
) Calculate
T-22 Boundary()
Sum-T-22
T-21 Boundary()
RR0705_108PC_194_196_SUM-194 R_Date(4340,20)
68.2% probability
2542BC (68.2%) 2466BC
95.4% probability
2580BC (95.4%) 2434BC
N(24,2)
68.2% probability
22 (68.2%) 26
95.4% probability
20 (95.4%) 28
(Calculate
RR0705_108PC_194_196_SUM-194+N(24,2)
68.2% probability
2517BC (68.2%) 2442BC
95.4% probability
2557BC (95.4%) 2409BC
) Calculate
RR0705_103PC_209_211_SUM-050 R_Date(4360,20)
68.2% probability
2560BC (68.2%) 2480BC
95.4% probability
2606BC (95.4%) 2455BC
N(3)
68.2% probability
3 (68.2%) 4
95.4% probability
3 (95.4%) 4
(Calculate
RR0705_103PC_209_211_SUM-050+N(3)
68.2% probability
2557BC (68.2%) 2478BC
95.4% probability
2603BC (95.4%) 2451BC
) Calculate
(Combine Sum-T-21
Posterior
68.2% probability
2527BC (68.2%) 2472BC
95.4% probability
2550BC (95.4%) 2450BC
Agreement 104.4%
Posterior
68.2% probability
2527BC (68.2%) 2472BC
95.4% probability

2550BC (95.4%) 2450BC
Agreement 108.4%
Sum-T-21 Combine()
X2-Test: df=1 T=0.196(5% 3.841)
68.2% probability
2527BC (68.2%) 2472BC
95.4% probability
2550BC (95.4%) 2450BC
Agreement n=2 Acomb=109.2%(An=50.0%)
) Combine Sum-T-21
T-20 Boundary()
RR0705_103PC_174_176_SUM-087 R_Date(3925,20)
68.2% probability
1975BC (68.2%) 1889BC
95.4% probability
2022BC (95.4%) 1862BC
N(125,13)
68.2% probability
112 (68.2%) 138
95.4% probability
99 (95.4%) 151
(Calculate
RR0705_103PC_174_176_SUM-087+N(125,13)
68.2% probability
1854BC (68.2%) 1765BC
95.4% probability
1903BC (95.4%) 1729BC
) Calculate
(Combine Sum-T-20
Posterior
68.2% probability
1854BC (68.2%) 1765BC
95.4% probability
1903BC (95.4%) 1729BC
Agreement 100.0%
Sum-T-20 Combine()
X2-Test: df=0 T=1.000(5% 0.000)
68.2% probability
1854BC (68.2%) 1765BC
95.4% probability
1903BC (95.4%) 1729BC
Agreement n=1 Acomb=100.0%(An=70.7%)
) Combine Sum-T-20
T-19 Boundary()
RR0705_108PC_156_158_SUM-083 R_Date(3500,15)
68.2% probability
1449BC (68.2%) 1386BC
95.4% probability
1488BC (95.4%) 1362BC
N(74,7)
68.2% probability
67 (68.2%) 81
95.4% probability
60 (95.4%) 88
(Calculate
RR0705_108PC_156_158_SUM-083+N(74,7)
68.2% probability
1376BC (68.2%) 1311BC
95.4% probability
1416BC (95.4%) 1284BC
) Calculate
T-18 Boundary()
RR0705_108PC_132.5_134.5_SUM-081 R_Date(3035,15)
68.2% probability
859BC (68.2%) 798BC
95.4% probability
895BC (95.4%) 786BC
N(0)
68.2% probability
-0 (68.2%) 1
95.4% probability
-0 (95.4%) 1
(Calculate
RR0705_108PC_132.5_134.5_SUM-081+N(0)
68.2% probability
858BC (68.2%) 798BC
95.4% probability
896BC (95.4%) 785BC

) Calculate
RR0705_104PC_326_328_SUM-235 R_
Date(3000,35)
68.2% probability
840BC (68.2%) 768BC
95.4% probability
894BC (95.4%) 747BC
N(6,1)
68.2% probability
5 (68.2%) 7
95.4% probability
4 (95.4%) 8
(Calculate
RR0705_104PC_326_328_SUM-
235+N(6,1)
68.2% probability
835BC (68.2%) 761BC
95.4% probability
888BC (95.4%) 741BC
) Calculate
RR0705_103TC_079_081_SUM-180 R_
Date(2985,20)
68.2% probability
813BC (68.2%) 768BC
95.4% probability
856BC (95.4%) 747BC
N(0)
68.2% probability
-0 (68.2%) 1
95.4% probability
-0 (95.4%) 1
(Calculate
RR0705_103TC_079_081_SUM-180+N(0)
68.2% probability
812BC (68.2%) 768BC
95.4% probability
854BC (95.4%) 746BC
) Calculate
(Combine Sum-T-18
Posterior
68.2% probability
816BC (68.2%) 789BC
95.4% probability
839BC (95.4%) 777BC
Agreement 98.7%
Posterior
68.2% probability
816BC (68.2%) 789BC
95.4% probability
839BC (95.4%) 777BC
Agreement 128.7%
Posterior
68.2% probability
816BC (68.2%) 789BC
95.4% probability
839BC (95.4%) 777BC
Agreement 102.1%
Sum-T-18 Combine()
X2-Test: df=2 T=1.421(5% 5.991)
68.2% probability
816BC (68.2%) 789BC
95.4% probability
839BC (95.4%) 777BC
Agreement n=3 Acomb=116.2%(An=
40.8%)
) Combine Sum-T-18
T-17 Boundary()
Sum-T-17
T-16 Boundary()
Sum-T-16
T-15 Boundary()
RR0705_96PC_399_401_SUM-232 R_
Date(2410,20)
68.2% probability
124BC (68.2%) 32BC
95.4% probability
162BC (95.4%) 9AD
N(12,1)
68.2% probability
11 (68.2%) 13
95.4% probability
10 (95.4%) 14
(Calculate
RR0705_96PC_399_401_SUM-
232+N(12,1)
68.2% probability

110BC (68.2%) 20BC
95.4% probability
150BC (95.4%) 21AD
) Calculate
T-14 Boundary()
RR0705_104PC_207_209_SUM-115 R_Date(2420,220)
68.2% probability
372BC (68.2%) 164AD
95.4% probability
696BC (95.4%) 398AD
N(17,2)
68.2% probability
15 (68.2%) 19
95.4% probability
13 (95.4%) 21
(Calculate
RR0705_104PC_207_209_SUM-115+N(17,2)
68.2% probability
355BC (68.2%) 181AD
95.4% probability
679BC (95.4%) 415AD
) Calculate
T-13 Boundary()
Sum-T-13
T-12 Boundary()
Sum-T-12
T-11 Boundary()
RR0705_103TC_039_041_SUM-179 R_Date(2065,20)
68.2% probability
287AD (68.2%) 379AD
95.4% probability
257AD (95.4%) 411AD
N(0)
68.2% probability
-0 (68.2%) 1
95.4% probability
-0 (95.4%) 1
(Calculate
RR0705_103TC_039_041_SUM-179+N(0)
68.2% probability
288AD (68.2%) 378AD
95.4% probability
256AD (95.4%) 411AD
) Calculate
RR0705_96PC_374_376_SUM-090 R_Date(2115,20)
68.2% probability
237AD (68.2%) 329AD
95.4% probability
178AD (95.4%) 362AD
N(7,1)
68.2% probability
6 (68.2%) 8
95.4% probability
5 (95.4%) 9
(Calculate
RR0705_96PC_374_376_SUM-090+N(7,1)
68.2% probability
244AD (68.2%) 335AD
95.4% probability
184AD (95.4%) 369AD
) Calculate
(Combine Sum-T-11
Posterior
68.2% probability
273AD (68.2%) 338AD
95.4% probability
251AD (95.4%) 369AD
Agreement 101.9%
Posterior
68.2% probability
273AD (68.2%) 338AD
95.4% probability
251AD (95.4%) 369AD
Agreement 106.9%
Sum-T-11 Combine()
X2-Test: df=1 T=0.942(5% 3.841)
68.2% probability
273AD (68.2%) 338AD
95.4% probability
251AD (95.4%) 369AD
Agreement n=2 Acomb=106.2%(An=50.0%)

) Combine Sum-T-11
T-10 Boundary()
RR0705_108TC_020_022_SUM-172 R_
Date(1930,20)
68.2% probability
446AD (68.2%) 531AD
95.4% probability
418AD (95.4%) 567AD
N(44,4)
68.2% probability
40 (68.2%) 48
95.4% probability
36 (95.4%) 52
(Calculate
RR0705_108TC_020_022_SUM-
172+N(44,4)
68.2% probability
489AD (68.2%) 575AD
95.4% probability
462AD (95.4%) 612AD
) Calculate
RR0705_103PC_049_051_SUM-054 R_
Date(1940,25)
68.2% probability
434AD (68.2%) 524AD
95.4% probability
402AD (95.4%) 567AD
N(18,2)
68.2% probability
16 (68.2%) 20
95.4% probability
14 (95.4%) 22
(Calculate
RR0705_103PC_049_051_SUM-
054+N(18,2)
68.2% probability
452AD (68.2%) 541AD
95.4% probability
421AD (95.4%) 584AD
) Calculate
RR0705_103TC_036_038_SUM-178 R_
Date(1890,20)
68.2% probability
484AD (68.2%) 575AD
95.4% probability
445AD (95.4%) 606AD
N(23,2)
68.2% probability
21 (68.2%) 25
95.4% probability
19 (95.4%) 27
(Calculate
RR0705_103TC_036_038_SUM-
178+N(23,2)
68.2% probability
507AD (68.2%) 597AD
95.4% probability
467AD (95.4%) 630AD
) Calculate
(Combine Sum-T-10
Posterior
68.2% probability
498AD (68.2%) 558AD
95.4% probability
475AD (95.4%) 580AD
Agreement 112.7%
Posterior
68.2% probability
498AD (68.2%) 558AD
95.4% probability
475AD (95.4%) 580AD
Agreement 98.7%
Posterior
68.2% probability
498AD (68.2%) 558AD
95.4% probability
475AD (95.4%) 580AD
Agreement 103.1%
Sum-T-10 Combine()
X2-Test: df=2 T=0.985(5% 5.991)
68.2% probability
498AD (68.2%) 558AD
95.4% probability
475AD (95.4%) 580AD
Agreement n=3 Acomb=108.3%(An=
40.8%)

) Combine Sum-T-10
T-9 Boundary()
Sum-T-9
T-8 Boundary()
Sum-T-8
T-7 Boundary()
RR0705_96PC_287.5_289.5_SUM-089
R_Date(1490,15)
68.2% probability
900AD (68.2%) 975AD
95.4% probability
857AD (95.4%) 1006AD
N(3)
68.2% probability
3 (68.2%) 4
95.4% probability
3 (95.4%) 4
(Calculate
RR0705_96PC_287.5_289.5_SUM-
089+N(3)
68.2% probability
905AD (68.2%) 975AD
95.4% probability
859AD (95.4%) 1010AD
) Calculate
T-6 Boundary()
Sum-T-6
T-5 Boundary()
RR0705_104TC_047.5_049.5_SUM-175
R_Date(1220,20)
68.2% probability
1179AD (68.2%) 1245AD
95.4% probability
1140AD (95.4%) 1277AD
N(12,1)
68.2% probability
11 (68.2%) 13
95.4% probability
10 (95.4%) 14
(Calculate
RR0705_104TC_047.5_049.5_SUM-
175+N(12,1)
68.2% probability
1191AD (68.2%) 1256AD
95.4% probability
1153AD (95.4%) 1289AD
) Calculate
RR0705_103PC_020_022_SUM-084 R_
Date(1225,20)
68.2% probability
1173AD (68.2%) 1241AD
95.4% probability
1131AD (95.4%) 1274AD
N(5)
68.2% probability
4 (68.2%) 5
95.4% probability
4 (95.4%) 5
(Calculate
RR0705_103PC_020_022_SUM-084+N(5)
68.2% probability
1178AD (68.2%) 1247AD
95.4% probability
1138AD (95.4%) 1279AD
) Calculate
(Combine Sum-T-5
Posterior
68.2% probability
1193AD (68.2%) 1242AD
95.4% probability
1175AD (95.4%) 1267AD
Agreement 114.0%
Posterior
68.2% probability
1193AD (68.2%) 1242AD
95.4% probability
1175AD (95.4%) 1267AD
Agreement 115.4%
Sum-T-5 Combine()
X2-Test: df=1 T=0.069(5% 3.841)
68.2% probability
1193AD (68.2%) 1242AD
95.4% probability
1175AD (95.4%) 1267AD
Agreement n=2 Acomb=121.4%(An=
50.0%)

) Combine Sum-T-5
T-4 Boundary()
RR0705_104PC_049.5_051.5_SUM-060
R_Date(1065,20)
68.2% probability
1294AD (68.2%) 1351AD
95.4% probability
1286AD (95.4%) 1396AD
N(9,1)
68.2% probability
8 (68.2%) 10
95.4% probability
7 (95.4%) 11
(Calculate
RR0705_104PC_049.5_051.5_SUM-
060+N(9,1)
68.2% probability
1303AD (68.2%) 1359AD
95.4% probability
1294AD (95.4%) 1405AD
) Calculate
RR0705_96PC_222_224_SUM-228 R_
Date(1145,15)
68.2% probability
1255AD (68.2%) 1295AD
95.4% probability
1225AD (95.4%) 1310AD
N(8,1)
68.2% probability
7 (68.2%) 9
95.4% probability
6 (95.4%) 10
(Calculate
RR0705_96PC_222_224_SUM-228+N(8,1)
68.2% probability
1262AD (68.2%) 1303AD
95.4% probability
1233AD (95.4%) 1318AD
) Calculate
(Combine Sum-T-4
Posterior
68.2% probability
1292AD (68.2%) 1317AD
95.4% probability
1280AD (95.4%) 1329AD
Agreement 74.9%
Posterior
68.2% probability
1292AD (68.2%) 1317AD
95.4% probability
1280AD (95.4%) 1329AD
Agreement 74.8%
Sum-T-4 Combine()
X2-Test: df=1 T=3.163(5% 3.841)
68.2% probability
1292AD (68.2%) 1317AD
95.4% probability
1280AD (95.4%) 1329AD
Agreement n=2 Acomb= 66.4%(An=
50.0%)
) Combine Sum-T-4
T-3 Boundary()
RR0705_104TC_011_013_SUM-176 R_
Date(705,20)
68.2% probability
1583AD (68.2%) 1660AD
95.4% probability
1540AD (95.4%) 1673AD
N(35,3)
68.2% probability
32 (68.2%) 38
95.4% probability
29 (95.4%) 41
(Calculate
RR0705_104TC_011_013_SUM-
176+N(35,3)
68.2% probability
1616AD (68.2%) 1695AD
95.4% probability
1574AD (95.4%) 1709AD
) Calculate
T-2 Boundary()
RR0705_96PC_206_208_SUM-227 R_
Date(480,15)
Warning! Date may extend out of range -
480+/-15BP

Warning! Date probably out of range -480+/-15BP
68.2% probability
1865AD (68.2%) ...
95.4% probability
1818AD (95.4%) ...
N(8,1)
68.2% probability
7 (68.2%) 9
95.4% probability
6 (95.4%) 10
(Calculate RR0705_96PC_206_208_SUM-227+N(8,1)
68.2% probability
1872AD (32.6%) 1920AD
1926AD (35.6%) ...
95.4% probability
1828AD (95.4%) ...
) Calculate T-1 Boundary()
Sum-T-1
2007
: 2007
(Boundary T-0
T-0 Boundary(2007)
68.2% probability
2006AD (68.2%) 2007AD
95.4% probability
2006AD (95.4%) 2007AD
) Boundary T-0
(Sequence 2004 Region Gap
2004 Region Gap Sequence()
) Sequence 2004 Region Gap
Posterior
(MCMC(30000)
Overall agreement 104.4%
Dynamic agreement 96.9%
LocalMarine Posterior
68.2% probability
1 (68.2%) 21
95.4% probability
-10 (95.4%) 31
Agreement 98.1%
Start Posterior
68.2% probability
8002BC (68.2%) 8001BC
95.4% probability
8002BC (95.4%) 8001BC
Agreement 100.0%
Posterior
68.2% probability
5539BC (68.2%) 5472BC
95.4% probability
5571BC (95.4%) 5439BC
RR0705_108PC_345_347_SUM-195 Posterior
68.2% probability
5709BC (68.2%) 5650BC
95.4% probability
5733BC (95.4%) 5622BC
Agreement 98.8%
Posterior
68.2% probability
156 (68.2%) 190
95.4% probability
139 (95.4%) 207
Agreement 100.2%
T-29 Posterior
68.2% probability
5420BC (1.6%) 5414BC
5407BC (66.6%) 5200BC
95.4% probability
5508BC (95.4%) 5164BC
Posterior
68.2% probability
5224BC (68.2%) 5155BC
95.4% probability
5255BC (95.4%) 5128BC
RR0705_108PC_330_332_SUM-041 Posterior
68.2% probability
5287BC (68.2%) 5221BC
95.4% probability
5318BC (95.4%) 5195BC
Agreement 100.1%
Posterior

68.2% probability
58 (68.2%) 70
95.4% probability
52 (95.4%) 76
Agreement 99.8%
T-28 Posterior
68.2% probability
5196BC (25.5%) 5004BC
4997BC (0.4%) 4993BC
4738BC (0.4%) 4734BC
4725BC (41.9%) 4468BC
95.4% probability
5207BC (95.4%) 4466BC
Sum-T-28 Posterior
68.2% probability
4517BC (68.2%) 4461BC
95.4% probability
4549BC (95.4%) 4431BC
Posterior
68.2% probability
4517BC (68.2%) 4461BC
95.4% probability
4549BC (95.4%) 4431BC
Agreement 99.9%
Posterior
68.2% probability
4517BC (68.2%) 4461BC
95.4% probability
4549BC (95.4%) 4431BC
Agreement 90.1%
T-27 Posterior
68.2% probability
4476BC (68.2%) 4384BC
95.4% probability
4511BC (95.4%) 4341BC
Posterior
68.2% probability
4404BC (68.2%) 4338BC
95.4% probability
4433BC (95.4%) 4313BC
RR0705_108PC_290.5_292.5_SUM-044
Posterior
68.2% probability
4426BC (68.2%) 4356BC
95.4% probability
4452BC (95.4%) 4333BC
Agreement 102.1%
Posterior
68.2% probability
17 (68.2%) 21
95.4% probability
15 (95.4%) 23
Agreement 100.2%
T-26 Posterior
68.2% probability
4396BC (68.2%) 4131BC
95.4% probability
4413BC (95.4%) 3982BC
Posterior
68.2% probability
4010BC (68.2%) 3941BC
95.4% probability
4063BC (95.4%) 3911BC
RR0705_103PC_324_326_SUM-224 Posterior
68.2% probability
4026BC (68.2%) 3960BC
95.4% probability
4078BC (95.4%) 3929BC
Agreement 99.2%
Posterior
68.2% probability
15 (68.2%) 19
95.4% probability
13 (95.4%) 21
Agreement 100.1%
T-25 Posterior
68.2% probability
3969BC (19.7%) 3784BC
3779BC (1.2%) 3761BC
3728BC (0.4%) 3724BC
3519BC (1.6%) 3502BC
3484BC (45.3%) 3121BC
95.4% probability
3981BC (95.4%) 3090BC
Posterior

68.2% probability
3225BC (68.2%) 3096BC
95.4% probability
3255BC (95.4%) 3037BC
RR0705_108PC_257_259_SUM-042 Posterior
68.2% probability
3277BC (68.2%) 3149BC
95.4% probability
3306BC (95.4%) 3091BC
Agreement 98.6%
Posterior
68.2% probability
47 (68.2%) 57
95.4% probability
42 (95.4%) 62
Agreement 99.9%
T-24 Posterior
68.2% probability
3158BC (68.2%) 2964BC
95.4% probability
3215BC (95.4%) 2872BC
Sum-T-24 Posterior
68.2% probability
3047BC (68.2%) 2869BC
95.4% probability
3148BC (95.4%) 2834BC
T-23 Posterior
68.2% probability
2949BC (68.2%) 2822BC
95.4% probability
3077BC (95.4%) 2804BC
Posterior
68.2% probability
2856BC (68.2%) 2813BC
95.4% probability
2906BC (95.4%) 2789BC
RR0705_108PC_212.5_214.5_SUM-045
Posterior
68.2% probability
2901BC (68.2%) 2860BC
95.4% probability
2950BC (95.4%) 2836BC
Agreement 99.8%
Posterior
68.2% probability
41 (68.2%) 51
95.4% probability
36 (95.4%) 56
Agreement 100.1%
T-22 Posterior
68.2% probability
2852BC (68.2%) 2713BC
95.4% probability
2880BC (95.4%) 2570BC
Sum-T-22 Posterior
68.2% probability
2791BC (68.2%) 2595BC
95.4% probability
2833BC (95.4%) 2517BC
T-21 Posterior
68.2% probability
2661BC (68.2%) 2488BC
95.4% probability
2786BC (95.4%) 2467BC
Sum-T-21 Posterior
68.2% probability
2523BC (68.2%) 2468BC
95.4% probability
2548BC (95.4%) 2448BC
Posterior
68.2% probability
2523BC (68.2%) 2468BC
95.4% probability
2548BC (95.4%) 2448BC
Agreement 106.7%
Posterior
68.2% probability
2523BC (68.2%) 2468BC
95.4% probability
2548BC (95.4%) 2448BC
Agreement 106.3%
T-20 Posterior
68.2% probability
2514BC (46.3%) 2243BC
2235BC (1.6%) 2221BC

2015BC (1.5%) 2002BC
1986BC (0.8%) 1979BC
1968BC (18.0%) 1831BC
95.4% probability
2519BC (95.4%) 1813BC
Sum-T-20 Posterior
68.2% probability
1856BC (68.2%) 1767BC
95.4% probability
1904BC (95.4%) 1733BC
Posterior
68.2% probability
1856BC (68.2%) 1767BC
95.4% probability
1904BC (95.4%) 1733BC
Agreement 99.6%
T-19 Posterior
68.2% probability
1772BC (22.6%) 1660BC
1655BC (0.5%) 1652BC
1642BC (1.2%) 1636BC
1631BC (0.8%) 1627BC
1601BC (0.9%) 1596BC
1585BC (1.9%) 1575BC
1565BC (1.8%) 1555BC
1536BC (38.6%) 1357BC
95.4% probability
1829BC (95.4%) 1332BC
Posterior
68.2% probability
1379BC (68.2%) 1316BC
95.4% probability
1417BC (95.4%) 1292BC
RR0705_108PC_156_158_SUM-083 Posterior
68.2% probability
1452BC (68.2%) 1391BC
95.4% probability
1489BC (95.4%) 1368BC
Agreement 99.8%
Posterior
68.2% probability
67 (68.2%) 81
95.4% probability
60 (95.4%) 88
Agreement 99.8%
T-18 Posterior
68.2% probability
1340BC (22.6%) 1206BC
1194BC (0.7%) 1189BC
1044BC (0.4%) 1041BC
1022BC (44.5%) 798BC
95.4% probability
1347BC (95.4%) 796BC
Sum-T-18 Posterior
68.2% probability
817BC (68.2%) 789BC
95.4% probability
842BC (95.4%) 777BC
Posterior
68.2% probability
817BC (68.2%) 789BC
95.4% probability
842BC (95.4%) 777BC
Agreement 100.7%
Posterior
68.2% probability
817BC (68.2%) 789BC
95.4% probability
842BC (95.4%) 777BC
Agreement 127.3%
Posterior
68.2% probability
817BC (68.2%) 789BC
95.4% probability
842BC (95.4%) 777BC
Agreement 99.4%
T-17 Posterior
68.2% probability
816BC (68.2%) 601BC
95.4% probability
834BC (95.4%) 347BC
Sum-T-17 Posterior
68.2% probability
759BC (68.2%) 433BC
95.4% probability

799BC (95.4%) 232BC
T-16 Posterior
68.2% probability
593BC (68.2%) 204BC
95.4% probability
750BC (95.4%) 115BC
Sum-T-16 Posterior
68.2% probability
404BC (68.2%) 105BC
95.4% probability
617BC (95.4%) 52BC
T-15 Posterior
68.2% probability
227BC (68.2%) 43BC
95.4% probability
465BC (95.4%) 4BC
Posterior
68.2% probability
125BC (68.2%) 38BC
95.4% probability
160BC (95.4%) 3BC
RR0705_96PC_399_401_SUM-232 Posterior
68.2% probability
136BC (68.2%) 50BC
95.4% probability
172BC (95.4%) 15BC
Agreement 98.1%
Posterior
68.2% probability
11 (68.2%) 13
95.4% probability
10 (95.4%) 14
Agreement 99.9%
T-14 Posterior
68.2% probability
105BC (68.2%) 16AD
95.4% probability
148BC (95.4%) 103AD
Posterior
68.2% probability
70BC (68.2%) 73AD
95.4% probability
123BC (95.4%) 159AD
RR0705_104PC_207_209_SUM-115 Posterior
68.2% probability
88BC (68.2%) 55AD
95.4% probability
140BC (95.4%) 143AD
Agreement 130.5%
Posterior
68.2% probability
15 (68.2%) 19
95.4% probability
13 (95.4%) 21
Agreement 100.0%
T-13 Posterior
68.2% probability
41BC (68.2%) 134AD
95.4% probability
96BC (95.4%) 233AD
Sum-T-13 Posterior
68.2% probability
16AD (68.2%) 195AD
95.4% probability
50BC (95.4%) 275AD
T-12 Posterior
68.2% probability
80AD (68.2%) 261AD
95.4% probability
14BC (95.4%) 316AD
Sum-T-12 Posterior
68.2% probability
151AD (68.2%) 301AD
95.4% probability
49AD (95.4%) 340AD
T-11 Posterior
68.2% probability
219AD (68.2%) 334AD
95.4% probability
106AD (95.4%) 366AD
Sum-T-11 Posterior
68.2% probability
284AD (68.2%) 348AD
95.4% probability

257AD (95.4%) 377AD
Posterior
68.2% probability
284AD (68.2%) 348AD
95.4% probability
257AD (95.4%) 377AD
Agreement 107.3%
Posterior
68.2% probability
284AD (68.2%) 348AD
95.4% probability
257AD (95.4%) 377AD
Agreement 99.0%
T-10 Posterior
68.2% probability
325AD (36.5%) 414AD
426AD (3.0%) 434AD
439AD (28.7%) 508AD
95.4% probability
288AD (95.4%) 548AD
Sum-T-10 Posterior
68.2% probability
492AD (68.2%) 552AD
95.4% probability
472AD (95.4%) 577AD
Posterior
68.2% probability
492AD (68.2%) 552AD
95.4% probability
472AD (95.4%) 577AD
Agreement 112.2%
Posterior
68.2% probability
492AD (68.2%) 552AD
95.4% probability
472AD (95.4%) 577AD
Agreement 102.6%
Posterior
68.2% probability
492AD (68.2%) 552AD
95.4% probability
472AD (95.4%) 577AD
Agreement 99.3%
T-9 Posterior
68.2% probability
504AD (68.2%) 642AD
95.4% probability
481AD (95.4%) 774AD
Sum-T-9 Posterior
68.2% probability
552AD (68.2%) 736AD
95.4% probability
511AD (95.4%) 846AD
T-8 Posterior
68.2% probability
621AD (68.2%) 845AD
95.4% probability
546AD (95.4%) 916AD
Sum-T-8 Posterior
68.2% probability
729AD (68.2%) 912AD
95.4% probability
613AD (95.4%) 954AD
T-7 Posterior
68.2% probability
820AD (68.2%) 958AD
95.4% probability
687AD (95.4%) 990AD
Posterior
68.2% probability
902AD (68.2%) 972AD
95.4% probability
856AD (95.4%) 1002AD
RR0705_96PC_287.5_289.5_SUM-089
Posterior
68.2% probability
898AD (68.2%) 970AD
95.4% probability
851AD (95.4%) 1000AD
Agreement 99.9%
Posterior
68.2% probability
3 (68.2%) 4
95.4% probability
3 (95.4%) 4
Agreement 100.0%

T-6 Posterior
68.2% probability
914AD (68.2%) 1059AD
95.4% probability
882AD (95.4%) 1175AD
Sum-T-6 Posterior
68.2% probability
1007AD (68.2%) 1172AD
95.4% probability
937AD (95.4%) 1217AD
T-5 Posterior
68.2% probability
1115AD (68.2%) 1237AD
95.4% probability
997AD (95.4%) 1257AD
Sum-T-5 Posterior
68.2% probability
1194AD (68.2%) 1242AD
95.4% probability
1175AD (95.4%) 1265AD
Posterior
68.2% probability
1194AD (68.2%) 1242AD
95.4% probability
1175AD (95.4%) 1265AD
Agreement 114.9%
Posterior
68.2% probability
1194AD (68.2%) 1242AD
95.4% probability
1175AD (95.4%) 1265AD
Agreement 116.2%
T-4 Posterior
68.2% probability
1232AD (68.2%) 1298AD
95.4% probability
1198AD (95.4%) 1316AD
Sum-T-4 Posterior
68.2% probability
1293AD (68.2%) 1318AD
95.4% probability
1281AD (95.4%) 1331AD
Posterior
68.2% probability
1293AD (68.2%) 1318AD
95.4% probability
1281AD (95.4%) 1331AD
Agreement 77.9%
Posterior
68.2% probability
1293AD (68.2%) 1318AD
95.4% probability
1281AD (95.4%) 1331AD
Agreement 72.0%
T-3 Posterior
68.2% probability
1297AD (54.4%) 1462AD
1474AD (1.9%) 1482AD
1547AD (11.9%) 1599AD
95.4% probability
1293AD (95.4%) 1655AD
Posterior
68.2% probability
1610AD (68.2%) 1691AD
95.4% probability
1572AD (95.4%) 1705AD
RR0705_104TC_011_013_SUM-176 Posterior
68.2% probability
1576AD (68.2%) 1656AD
95.4% probability
1537AD (95.4%) 1670AD
Agreement 98.8%
Posterior
68.2% probability
32 (68.2%) 38
95.4% probability
29 (95.4%) 41
Agreement 100.0%
T-2 Posterior
68.2% probability
1693AD (68.2%) 1880AD
95.4% probability
1623AD (95.4%) 1938AD
Posterior
68.2% probability

1832AD (68.2%) 1922AD
95.4% probability
1772AD (1.7%) 1792AD
1813AD (93.7%) 1962AD
RR0705_96PC_206_208_SUM-227 Posterior
68.2% probability
1825AD (68.2%) 1913AD
95.4% probability
1764AD (1.4%) 1784AD
1805AD (94.0%) 1953AD
Agreement 93.0%
Posterior
68.2% probability
7 (68.2%) 9
95.4% probability
6 (95.4%) 10
Agreement 99.7%
T-1 Posterior
68.2% probability
1902AD (68.2%) 2003AD
95.4% probability
1842AD (95.4%) 2010AD
Sum-T-1 Posterior
68.2% probability
1957AD (68.2%) 2010AD
95.4% probability
1892AD (95.4%) 2010AD
T-0 Posterior
68.2% probability
2006AD (68.2%) 2007AD
95.4% probability
2006AD (95.4%) 2007AD
Agreement 100.0%
) MCMC(240000)

96PC 2004

OxCal v4.1.2 Bronk Ramsey (2009); r:5
IntCal04 atmospheric curve (Reimer et al 2004)
FALSE
OxCal v4.1.2 Bronk Ramsey (2009); r:5
Marine Curve(Marine09.14c)
Marine data from Reimer et al (2009);
LocalMarine Delta_R(16,11)
 68.2% probability
  5 (68.2%) 28
 95.4% probability
  -7 (95.4%) 39
Start Boundary()
RR0705_96PC_206_208_SUM-227 R_Date(480,15)
Warning! Date may extend out of range - 480+/-15BP
Warning! Date probably out of range - 480+/-15BP
 68.2% probability
  1865AD (68.2%) ...
 95.4% probability
  1818AD (95.4%) ...
N(67,7)
 68.2% probability
  60 (68.2%) 74
 95.4% probability
  53 (95.4%) 81
(Calculate
RR0705_96PC_206_208_SUM-227+N(67,7)
 68.2% probability
  1937AD (21.6%) 1974AD
  1988AD (46.6%) ...
 95.4% probability
  1889AD (95.4%) ...
) Calculate
2007
 : 2007
(Boundary Revelle
Revelle Boundary(2007)
 68.2% probability
  2006AD (68.2%) 2007AD
 95.4% probability
  2006AD (95.4%) 2007AD
) Boundary Revelle
(Sequence 96PC 2004 Turbidite
96PC 2004 Turbidite Sequence()
) Sequence 96PC 2004 Turbidite
Posterior
(MCMC(30000)
Overall agreement 102.0%
Dynamic agreement 102.4%
LocalMarine Posterior
 68.2% probability
  5 (68.2%) 27
 95.4% probability
  -7 (95.4%) 38
 Agreement 100.5%
Start Posterior
 68.2% probability
  1756AD (68.2%) 2007AD
 95.4% probability
  1477AD (0.2%) 1480AD
  1488AD (1.1%) 1502AD
  1516AD (0.4%) 1521AD
  1526AD (93.6%) 2008AD
Posterior
 68.2% probability
  1941AD (68.2%) 2007AD
 95.4% probability
  1893AD (95.4%) 2011AD
 Agreement 99.3%
RR0705_96PC_206_208_SUM-227 Posterior
 68.2% probability
  1872AD (68.2%) 1942AD
 95.4% probability
  1825AD (95.4%) 1949AD
 Agreement 103.5%
Posterior
 68.2% probability

60 (68.2%) 74
95.4% probability
53 (95.4%) 81
Agreement 100.1%
Revelle Posterior
68.2% probability
2006AD (68.2%) 2007AD
95.4% probability
2006AD (95.4%) 2007AD
Agreement 100.0%
) MCMC(120000)

102MC 2004

OxCal v4.1.2 Bronk Ramsey (2009); r:5
IntCal04 atmospheric curve (Reimer et al 2004)
FALSE
OxCal v4.1.2 Bronk Ramsey (2009); r:5
Marine Curve(Marine09.14c)
Marine data from Reimer et al (2009);
LocalMarine Delta_R(16,11)
 68.2% probability
  5 (68.2%) 28
 95.4% probability
  -7 (95.4%) 39
Start Boundary()
RR0705_102MC_065_075_SUM-249 R_Date(455,20)
Warning! Date may extend out of range - 455+/-20BP
Warning! Date probably out of range - 455+/-20BP
 68.2% probability
  1885AD (68.2%) ...
 95.4% probability
  1834AD (95.4%) ...
N(5)
 68.2% probability
  4 (68.2%) 5
 95.4% probability
  4 (95.4%) 5
(Calculate
RR0705_102MC_065_075_SUM-249+N(5)
 68.2% probability
  1890AD (68.2%) ...
 95.4% probability
  1840AD (95.4%) ...
) Calculate
(Sequence 96PC 2004 Turbidite
96PC 2004 Turbidite Sequence()
) Sequence 96PC 2004 Turbidite
2007
 : 2007
(Boundary Revelle
Revelle Boundary(2007)
 68.2% probability
  2006AD (68.2%) 2007AD
 95.4% probability
  2006AD (95.4%) 2007AD
) Boundary Revelle
(Sequence
Sequence()
) Sequence
Posterior
(MCMC(30000)
Overall agreement 101.6%
Dynamic agreement 102.1%
LocalMarine Posterior
 68.2% probability
  2 (68.2%) 25
 95.4% probability
  -10 (95.4%) 36
 Agreement 99.2%
Start Posterior
 68.2% probability
  1619AD (68.2%) 1939AD
 95.4% probability
  1374AD (1.1%) 1387AD
  1409AD (94.3%) 1948AD
Posterior
 68.2% probability
  1897AD (68.2%) 1956AD
 95.4% probability
  1841AD (95.4%) 1959AD
 Agreement 104.7%
RR0705_102MC_065_075_SUM-249 Posterior
 68.2% probability
  1894AD (68.2%) 1953AD
 95.4% probability
  1840AD (95.4%) 1953AD
 Agreement 104.1%
Posterior
 68.2% probability
  5 (68.2%) 5

95.4% probability
5 (95.4%) 5
Agreement 100.0%
Revelle Posterior
68.2% probability
2006AD (68.2%) 2007AD
95.4% probability
2006AD (95.4%) 2007AD
Agreement 100.0%
) MCMC(120000)

96PC P_Sequence

OxCal v4.1.2 Bronk Ramsey (2009); r:5
IntCal04 atmospheric curve (Reimer et al 2004)
FALSE
0.371
0.356
0.339
0.267
0.237
0.227
0.185
0.128
0.12
0.11
0.05
0.04
0.02
0.015
0.01
0
0
OxCal v4.1.2 Bronk Ramsey (2009); r:5
Marine Curve(Marine09.14c)
Marine data from Reimer et al (2009);
LocalMarine Delta_R(16,11)
68.2% probability
5 (68.2%) 28
95.4% probability
-7 (95.4%) 39
Start Boundary()
RR0705_96PC_399_401_SUM-232 R_Date(2410,20)
68.2% probability
123BC (68.2%) 32BC
95.4% probability
162BC (95.4%) 9AD
96PC-35.6
96PC-33.9
RR0705_96PC_374_376_SUM-090 R_Date(2115,20)
68.2% probability
235AD (68.2%) 325AD
95.4% probability
175AD (95.4%) 364AD
96PC-23.7
96PC-22.7
96PC-18.5
RR0705_96PC_287.5_289.5_SUM-089 R_Date(1490,15)
68.2% probability
901AD (68.2%) 974AD
95.4% probability
861AD (95.4%) 1006AD
96PC-12
96PC-11
96PC-5
96PC-4
RR0705_96PC_222_224_SUM-228 R_Date(1145,15)
68.2% probability
1254AD (68.2%) 1296AD
95.4% probability
1225AD (95.4%) 1310AD
96PC-1.5
RR0705_96PC_206_208_SUM-227 R_Date(480,15)
Warning! Date may extend out of range - 480+/-15BP
Warning! Date probably out of range - 480+/-15BP
68.2% probability
1865AD (68.2%) ...
95.4% probability
1818AD (95.4%) ...
96PC-0
2007
: 2007
(Boundary Revelle
Revelle Boundary(2007)
68.2% probability
2006AD (68.2%) 2007AD
95.4% probability

2006AD (95.4%) 2007AD
) Boundary Revelle
(P_Sequence RR0705-96PC
RR0705-96PC P_Sequence(1000,50)
) P_Sequence RR0705-96PC
Page
Depth_Model
Posterior
(MCMC(30000)
Warning! Poor agreement - A= 2.3%(A'c= 60.0%)
Warning! Poor agreement - A= 2.1%(A'c= 60.0%)
LocalMarine Posterior
68.2% probability
12 (68.2%) 34
95.4% probability
1 (95.4%) 44
Agreement 93.1%
Start Posterior
68.2% probability
183BC (68.2%) 125BC
95.4% probability
312BC (2.8%) 277BC
253BC (0.2%) 250BC
225BC (92.4%) 76BC
RR0705_96PC_399_401_SUM-232 Posterior
68.2% probability
183BC (68.2%) 125BC
95.4% probability
312BC (2.8%) 277BC
253BC (0.2%) 250BC
225BC (92.4%) 76BC
Warning! Poor agreement - A= 44.0%(A'c= 60.0%)
Poor agreement 44.0%
96PC-35.6 Posterior
68.2% probability
120BC (68.2%) 53BC
95.4% probability
211BC (1.9%) 186BC
174BC (93.5%) 10BC
96PC-33.9 Posterior
68.2% probability
48BC (68.2%) 24AD
95.4% probability
128BC (0.3%) 125BC
111BC (95.1%) 65AD
RR0705_96PC_374_376_SUM-090 Posterior
68.2% probability
265AD (68.2%) 335AD
95.4% probability
230AD (95.4%) 365AD
Agreement 103.4%
96PC-23.7 Posterior
68.2% probability
400AD (68.2%) 472AD
95.4% probability
362AD (95.4%) 509AD
96PC-22.7 Posterior
68.2% probability
444AD (68.2%) 518AD
95.4% probability
405AD (95.4%) 555AD
96PC-18.5 Posterior
68.2% probability
635AD (68.2%) 707AD
95.4% probability
600AD (95.4%) 743AD
RR0705_96PC_287.5_289.5_SUM-089 Posterior
68.2% probability
901AD (68.2%) 956AD
95.4% probability
879AD (95.4%) 985AD
Agreement 112.2%
96PC-12 Posterior
68.2% probability
935AD (68.2%) 990AD
95.4% probability
911AD (95.4%) 1020AD
96PC-11 Posterior
68.2% probability
978AD (68.2%) 1034AD

95.4% probability
952AD (95.4%) 1062AD
96PC-5 Posterior
68.2% probability
1242AD (68.2%) 1288AD
95.4% probability
1218AD (95.4%) 1307AD
96PC-4 Posterior
68.2% probability
1288AD (68.2%) 1327AD
95.4% probability
1265AD (95.4%) 1345AD
RR0705_96PC_222_224_SUM-228 Posterior
68.2% probability
1383AD (68.2%) 1400AD
95.4% probability
1375AD (95.4%) 1410AD
Warning! Poor agreement - A= 0.0%(A'c= 60.0%)
Poor agreement 0.0%
96PC-1.5 Posterior
68.2% probability
1531AD (68.2%) 1679AD
95.4% probability
1475AD (95.4%) 1749AD
RR0705_96PC_206_208_SUM-227 Posterior
68.2% probability
1814AD (68.2%) 1882AD
95.4% probability
1719AD (18.2%) 1788AD
1805AD (77.2%) 1903AD
Agreement 66.0%
96PC-0 Posterior
68.2% probability
2003AD (68.2%) 2008AD
95.4% probability
1994AD (95.4%) 2008AD
Revelle Posterior
68.2% probability
2006AD (68.2%) 2007AD
95.4% probability
2006AD (95.4%) 2007AD
Agreement 100.0%
depthModel Posterior
68.2% probability
99BC (68.2%) 30BC
95.4% probability
183BC (1.5%) 164BC
158BC (93.9%) 13AD
depthModel Posterior
68.2% probability
14BC (68.2%) 58AD
95.4% probability
78BC (95.4%) 102AD
depthModel Posterior
68.2% probability
74AD (68.2%) 148AD
95.4% probability
20AD (95.4%) 186AD
depthModel Posterior
68.2% probability
162AD (68.2%) 233AD
95.4% probability
114AD (95.4%) 268AD
depthModel Posterior
68.2% probability
249AD (68.2%) 318AD
95.4% probability
212AD (95.4%) 349AD
depthModel Posterior
68.2% probability
336AD (68.2%) 409AD
95.4% probability
300AD (95.4%) 441AD
depthModel Posterior
68.2% probability
426AD (68.2%) 501AD
95.4% probability
390AD (95.4%) 535AD
depthModel Posterior
68.2% probability
517AD (68.2%) 591AD
95.4% probability
480AD (95.4%) 627AD

depthModel Posterior
68.2% probability
609AD (68.2%) 681AD
95.4% probability
572AD (95.4%) 716AD
depthModel Posterior
68.2% probability
700AD (68.2%) 770AD
95.4% probability
665AD (95.4%) 805AD
depthModel Posterior
68.2% probability
794AD (68.2%) 856AD
95.4% probability
762AD (95.4%) 889AD
depthModel Posterior
68.2% probability
888AD (68.2%) 943AD
95.4% probability
864AD (95.4%) 970AD
depthModel Posterior
68.2% probability
974AD (68.2%) 1029AD
95.4% probability
948AD (95.4%) 1058AD
depthModel Posterior
68.2% probability
1061AD (68.2%) 1116AD
95.4% probability
1032AD (95.4%) 1144AD
depthModel Posterior
68.2% probability
1149AD (68.2%) 1201AD
95.4% probability
1121AD (95.4%) 1226AD
depthModel Posterior
68.2% probability
1238AD (68.2%) 1284AD
95.4% probability
1213AD (95.4%) 1304AD
depthModel Posterior
68.2% probability
1331AD (68.2%) 1362AD
95.4% probability
1312AD (95.4%) 1376AD
depthModel Posterior
68.2% probability
1740AD (68.2%) 1853AD
95.4% probability
1667AD (95.4%) 1884AD
) MCMC(240000)

103PC P_Sequence

OxCal v4.1.2 Bronk Ramsey (2009); r:5
IntCal04 atmospheric curve (Reimer et al 2004)
FALSE
0.874
0.829
0.827
0.752
0.734
0.632
0.62
0.523
0.458
0.39
0.282
0.254
0.232
0.186
0.169
0.122
0
OxCal v4.1.2 Bronk Ramsey (2009); r:5
Marine Curve(Marine09.14c)
Marine data from Reimer et al (2009);
LocalMarine Delta_R(16,11)
 68.2% probability
  5 (68.2%) 28
 95.4% probability
  -7 (95.4%) 39
Start Boundary()
RR0705_103PC_383_385_SUM-253 R_Date(6020,25)
 68.2% probability
  4512BC (68.2%) 4431BC
 95.4% probability
  4546BC (95.4%) 4370BC
103PC-82.9
RR0705_103PC_324_326_SUM-224 R_Date(5575,25)
 68.2% probability
  4025BC (68.2%) 3956BC
 95.4% probability
  4075BC (95.4%) 3925BC
RR0705_103PC_300.5_302.5_SUM-053 R_Date(5360,25)
 68.2% probability
  3786BC (68.2%) 3701BC
 95.4% probability
  3861BC (95.4%) 3660BC
RR0705_103PC_277_279_SUM-052 R_Date(5095,20)
 68.2% probability
  3537BC (63.6%) 3438BC
  3419BC (4.6%) 3405BC
 95.4% probability
  3585BC (95.4%) 3374BC
103PC-63
103PC-62
RR0705_103PC_209_211_SUM-050 R_Date(4360,20)
 68.2% probability
  2560BC (68.2%) 2480BC
 95.4% probability
  2607BC (95.4%) 2455BC
RR0705_103PC_174_176_SUM-087 R_Date(3925,20)
 68.2% probability
  1975BC (68.2%) 1889BC
 95.4% probability
  2023BC (95.4%) 1862BC
103PC-39
RR0705_103PC_111_113_SUM-055 R_Date(2985,20)
 68.2% probability
  813BC (68.2%) 766BC
 95.4% probability
  854BC (95.4%) 745BC
RR0705_103PC_092_094_SUM-085 R_Date(2705,15)
 68.2% probability
  461BC (68.2%) 382BC
 95.4% probability

509BC (95.4%) 367BC
103PC-23.2
RR0705_103PC_049_051_SUM-054 R_
Date(1940,25)
68.2% probability
438AD (68.2%) 528AD
95.4% probability
402AD (95.4%) 570AD
103PC-16.9
RR0705_103PC_020_022_SUM-084 R_
Date(1225,20)
68.2% probability
1174AD (68.2%) 1241AD
95.4% probability
1130AD (95.4%) 1275AD
2007
: 2007
(Boundary Revelle
Revelle Boundary(2007)
68.2% probability
2006AD (68.2%) 2007AD
95.4% probability
2006AD (95.4%) 2007AD
) Boundary Revelle
(P_Sequence RR0705-103PC
RR0705-103PC P_Sequence(1000,50)
) P_Sequence RR0705-103PC
Page
Depth_Model
Posterior
(MCMC(30000)
Warning! Poor agreement - A= 12.1%(A'c=
60.0%)
Warning! Poor agreement - A= 12.4%(A'c=
60.0%)
LocalMarine Posterior
68.2% probability
-10 (68.2%) 13
95.4% probability
-20 (95.4%) 25
Agreement 66.8%
Start Posterior
68.2% probability
4515BC (68.2%) 4447BC
95.4% probability
4555BC (95.4%) 4412BC
RR0705_103PC_383_385_SUM-253 Poste-
rior
68.2% probability
4515BC (68.2%) 4447BC
95.4% probability
4555BC (95.4%) 4412BC
Agreement 106.5%
103PC-82.9 Posterior
68.2% probability
4182BC (68.2%) 4121BC
95.4% probability
4222BC (95.4%) 4089BC
RR0705_103PC_324_326_SUM-224 Poste-
rior
68.2% probability
4166BC (68.2%) 4106BC
95.4% probability
4209BC (95.4%) 4077BC
Warning! Poor agreement - A= 3.7%(A'c=
60.0%)
Poor agreement 3.7%
RR0705_103PC_300.5_302.5_SUM-053
Posterior
68.2% probability
3736BC (68.2%) 3687BC
95.4% probability
3761BC (95.4%) 3659BC
Agreement 98.0%
RR0705_103PC_277_279_SUM-052 Poste-
rior
68.2% probability
3612BC (68.2%) 3574BC
95.4% probability
3624BC (95.4%) 3542BC
Warning! Poor agreement - A= 28.2%(A'c=
60.0%)
Poor agreement 28.2%
103PC-63 Posterior
68.2% probability
3093BC (68.2%) 3006BC

95.4% probability
3135BC (95.4%) 2961BC
103PC-62 Posterior
68.2% probability
3028BC (68.2%) 2942BC
95.4% probability
3071BC (95.4%) 2897BC
RR0705_103PC_209_211_SUM-050 Posterior
68.2% probability
2499BC (68.2%) 2455BC
95.4% probability
2527BC (95.4%) 2401BC
Agreement 75.3%
RR0705_103PC_174_176_SUM-087 Posterior
68.2% probability
2015BC (68.2%) 1945BC
95.4% probability
2046BC (95.4%) 1901BC
Agreement 80.5%
103PC-39 Posterior
68.2% probability
1565BC (68.2%) 1461BC
95.4% probability
1616BC (95.4%) 1411BC
RR0705_103PC_111_113_SUM-055 Posterior
68.2% probability
796BC (68.2%) 756BC
95.4% probability
819BC (95.4%) 730BC
Agreement 93.4%
RR0705_103PC_092_094_SUM-085 Posterior
68.2% probability
461BC (68.2%) 392BC
95.4% probability
502BC (95.4%) 377BC
Agreement 103.0%
103PC-23.2 Posterior
68.2% probability
211BC (68.2%) 96BC
95.4% probability
264BC (95.4%) 38BC
RR0705_103PC_049_051_SUM-054 Posterior
68.2% probability
400AD (68.2%) 475AD
95.4% probability
356AD (95.4%) 516AD
Agreement 80.1%
103PC-16.9 Posterior
68.2% probability
566AD (68.2%) 665AD
95.4% probability
521AD (95.4%) 716AD
RR0705_103PC_020_022_SUM-084 Posterior
68.2% probability
1066AD (68.2%) 1139AD
95.4% probability
1055AD (95.4%) 1188AD
Warning! Poor agreement - A= 19.2%(A'c= 60.0%)
Poor agreement 19.2%
Revelle Posterior
68.2% probability
2006AD (68.2%) 2007AD
95.4% probability
2006AD (95.4%) 2007AD
Agreement 100.0%
depthModel Posterior
68.2% probability
4372BC (68.2%) 4298BC
95.4% probability
4411BC (95.4%) 4261BC
depthModel Posterior
68.2% probability
4221BC (68.2%) 4154BC
95.4% probability
4259BC (95.4%) 4120BC
depthModel Posterior
68.2% probability
4097BC (68.2%) 4032BC
95.4% probability

4131BC (95.4%) 3995BC
depthModel Posterior
68.2% probability
3984BC (68.2%) 3916BC
95.4% probability
4019BC (95.4%) 3882BC
depthModel Posterior
68.2% probability
3867BC (68.2%) 3805BC
95.4% probability
3901BC (95.4%) 3772BC
depthModel Posterior
68.2% probability
3748BC (68.2%) 3698BC
95.4% probability
3774BC (95.4%) 3668BC
depthModel Posterior
68.2% probability
3612BC (68.2%) 3572BC
95.4% probability
3624BC (95.4%) 3542BC
depthModel Posterior
68.2% probability
3516BC (68.2%) 3456BC
95.4% probability
3538BC (95.4%) 3419BC
depthModel Posterior
68.2% probability
3415BC (68.2%) 3342BC
95.4% probability
3446BC (95.4%) 3302BC
depthModel Posterior
68.2% probability
3311BC (68.2%) 3232BC
95.4% probability
3346BC (95.4%) 3191BC
depthModel Posterior
68.2% probability
3208BC (68.2%) 3123BC
95.4% probability
3246BC (95.4%) 3081BC
depthModel Posterior
68.2% probability
3104BC (68.2%) 3016BC
95.4% probability
3146BC (95.4%) 2971BC
depthModel Posterior
68.2% probability
2996BC (68.2%) 2911BC
95.4% probability
3040BC (95.4%) 2865BC
depthModel Posterior
68.2% probability
2892BC (68.2%) 2807BC
95.4% probability
2931BC (95.4%) 2760BC
depthModel Posterior
68.2% probability
2783BC (68.2%) 2703BC
95.4% probability
2825BC (95.4%) 2660BC
depthModel Posterior
68.2% probability
2675BC (68.2%) 2602BC
95.4% probability
2714BC (95.4%) 2559BC
depthModel Posterior
68.2% probability
2561BC (68.2%) 2505BC
95.4% probability
2598BC (95.4%) 2460BC
depthModel Posterior
68.2% probability
2441BC (68.2%) 2377BC
95.4% probability
2471BC (95.4%) 2331BC
depthModel Posterior
68.2% probability
2293BC (68.2%) 2215BC
95.4% probability
2331BC (95.4%) 2170BC
depthModel Posterior
68.2% probability
2141BC (68.2%) 2061BC
95.4% probability
2180BC (95.4%) 2019BC

depthModel Posterior
68.2% probability
1991BC (68.2%) 1917BC
95.4% probability
2023BC (95.4%) 1872BC
depthModel Posterior
68.2% probability
1860BC (68.2%) 1771BC
95.4% probability
1902BC (95.4%) 1724BC
depthModel Posterior
68.2% probability
1726BC (68.2%) 1631BC
95.4% probability
1774BC (95.4%) 1580BC
depthModel Posterior
68.2% probability
1591BC (68.2%) 1491BC
95.4% probability
1642BC (95.4%) 1440BC
depthModel Posterior
68.2% probability
1456BC (68.2%) 1351BC
95.4% probability
1506BC (95.4%) 1301BC
depthModel Posterior
68.2% probability
1314BC (68.2%) 1216BC
95.4% probability
1368BC (95.4%) 1169BC
depthModel Posterior
68.2% probability
1176BC (68.2%) 1082BC
95.4% probability
1223BC (95.4%) 1037BC
depthModel Posterior
68.2% probability
1033BC (68.2%) 952BC
95.4% probability
1076BC (95.4%) 911BC
depthModel Posterior
68.2% probability
886BC (68.2%) 825BC
95.4% probability
921BC (95.4%) 795BC
depthModel Posterior
68.2% probability
716BC (68.2%) 646BC
95.4% probability
746BC (95.4%) 602BC
depthModel Posterior
68.2% probability
457BC (68.2%) 390BC
95.4% probability
499BC (95.4%) 375BC
depthModel Posterior
68.2% probability
236BC (68.2%) 125BC
95.4% probability
288BC (95.4%) 67BC
depthModel Posterior
68.2% probability
21AD (68.2%) 140AD
95.4% probability
40BC (95.4%) 196AD
depthModel Posterior
68.2% probability
290AD (68.2%) 385AD
95.4% probability
235AD (95.4%) 433AD
depthModel Posterior
68.2% probability
515AD (68.2%) 609AD
95.4% probability
472AD (95.4%) 660AD
depthModel Posterior
68.2% probability
723AD (68.2%) 825AD
95.4% probability
673AD (95.4%) 877AD
depthModel Posterior
68.2% probability
936AD (68.2%) 1027AD
95.4% probability
897AD (95.4%) 1081AD
depthModel Posterior

68.2% probability
1122AD (68.2%) 1202AD
95.4% probability
1101AD (95.4%) 1251AD
depthModel Posterior
68.2% probability
1270AD (68.2%) 1358AD
95.4% probability
1233AD (95.4%) 1406AD
depthModel Posterior
68.2% probability
1418AD (68.2%) 1510AD
95.4% probability
1374AD (95.4%) 1553AD
depthModel Posterior
68.2% probability
1570AD (68.2%) 1655AD
95.4% probability
1525AD (95.4%) 1696AD
depthModel Posterior
68.2% probability
1722AD (68.2%) 1798AD
95.4% probability
1683AD (95.4%) 1831AD
depthModel Posterior
68.2% probability
1880AD (68.2%) 1935AD
95.4% probability
1850AD (95.4%) 1954AD
) MCMC(240000)

103TC P_Sequence

OxCal v4.1.2 Bronk Ramsey (2009); r:5
IntCal04 atmospheric curve (Reimer et al 2004)
FALSE
0.091
0.091
0.053
0.038
0.038
0.018
0
OxCal v4.1.2 Bronk Ramsey (2009); r:5
Marine Curve(Marine09.14c)
Marine data from Reimer et al (2009);
LocalMarine Delta_R(16,11)
68.2% probability
5 (68.2%) 28
95.4% probability
-7 (95.4%) 39
Start Boundary()
RR0705_103TC_079_081_SUM-180 R_Date(2985,20)
68.2% probability
813BC (68.2%) 766BC
95.4% probability
854BC (95.4%) 745BC
103TC-9.1
RR0705_103TC_039_041_SUM-179 R_Date(2065,20)
68.2% probability
281AD (68.2%) 375AD
95.4% probability
256AD (95.4%) 416AD
RR0705_103TC_036_038_SUM-178 R_Date(1890,20)
68.2% probability
487AD (68.2%) 577AD
95.4% probability
448AD (95.4%) 609AD
103TC-3.8
RR0705_103TC_012.5_014.5_SUM-177 R_Date(1310,20)
68.2% probability
1065AD (68.2%) 1149AD
95.4% probability
1041AD (95.4%) 1186AD
2007
: 2007
(Boundary Revelle
Revelle Boundary(2007)
68.2% probability
2006AD (68.2%) 2007AD
95.4% probability
2006AD (95.4%) 2007AD
) Boundary Revelle
(P_Sequence RR0705-103TC
RR0705-103TC P_Sequence(1000,50)
) P_Sequence RR0705-103TC
Page
Depth_Model
Posterior
(MCMC(30000)
Overall agreement 91.2%
Dynamic agreement 92.4%
LocalMarine Posterior
68.2% probability
5 (68.2%) 29
95.4% probability
-6 (95.4%) 40
Agreement 99.0%
Start Posterior
68.2% probability
813BC (68.2%) 766BC
95.4% probability
855BC (95.4%) 745BC
RR0705_103TC_079_081_SUM-180 Posterior
68.2% probability
813BC (68.2%) 766BC
95.4% probability
855BC (95.4%) 745BC
Agreement 99.3%

103TC-9.1 Posterior
68.2% probability
812BC (68.2%) 764BC
95.4% probability
856BC (95.4%) 741BC
RR0705_103TC_039_041_SUM-179 Posterior
68.2% probability
262AD (68.2%) 331AD
95.4% probability
235AD (95.4%) 380AD
Agreement 94.4%
RR0705_103TC_036_038_SUM-178 Posterior
68.2% probability
537AD (68.2%) 605AD
95.4% probability
495AD (95.4%) 632AD
Agreement 93.3%
103TC-3.8 Posterior
68.2% probability
539AD (68.2%) 607AD
95.4% probability
496AD (95.4%) 639AD
RR0705_103TC_012.5_014.5_SUM-177 Posterior
68.2% probability
1095AD (68.2%) 1173AD
95.4% probability
1056AD (95.4%) 1205AD
Agreement 92.2%
Revelle Posterior
68.2% probability
2006AD (68.2%) 2007AD
95.4% probability
2006AD (95.4%) 2007AD
Agreement 100.0%
depthModel Posterior
68.2% probability
310BC (68.2%) 126BC
95.4% probability
398BC (95.4%) 38BC
depthModel Posterior
68.2% probability
291AD (68.2%) 371AD
95.4% probability
261AD (95.4%) 421AD
depthModel Posterior
68.2% probability
696AD (68.2%) 828AD
95.4% probability
640AD (95.4%) 898AD
depthModel Posterior
68.2% probability
1365AD (68.2%) 1570AD
95.4% probability
1277AD (95.4%) 1675AD
) MCMC(1920000)

104PC P_Sequence

OxCal v4.1.2 Bronk Ramsey (2009); r:5
IntCal04 atmospheric curve (Reimer et al 2004)
FALSE
0.416
0.401
0.386
0.341
0.308
0.234
0.17
0.148
0.11
0.09
0.058
0.029
0.01
0
OxCal v4.1.2 Bronk Ramsey (2009); r:5
Marine Curve(Marine09.14c)
Marine data from Reimer et al (2009);
LocalMarine Delta_R(16,11)
 68.2% probability
  5 (68.2%) 28
 95.4% probability
  -7 (95.4%) 39
Start Boundary()
RR0705_104PC_326_328_SUM-235 R_Date(3000,35)
 68.2% probability
  841BC (68.2%) 766BC
 95.4% probability
  894BC (95.4%) 746BC
104PC-40.1
104PC-38.6
104PC-34.1
104PC-30.8
RR0705_104PC_207_209_SUM-115 R_Date(2420,220)
 68.2% probability
  371BC (68.2%) 161AD
 95.4% probability
  701BC (0.7%) 675BC
  666BC (94.7%) 404AD
RR0705_104PC_158_160_SUM-082 R_Date(2040,20)
 68.2% probability
  326AD (68.2%) 415AD
 95.4% probability
  273AD (95.4%) 432AD
104PC-14.8
RR0705_104PC_122_124_SUM-061 R_Date(1630,45)
 68.2% probability
  708AD (68.2%) 821AD
 95.4% probability
  680AD (95.4%) 890AD
RR0705_104PC_067.5_069.5_SUM-062 R_Date(1265,15)
 68.2% probability
  1125AD (68.2%) 1210AD
 95.4% probability
  1075AD (95.4%) 1227AD
RR0705_104PC_049.5_051.5_SUM-060 R_Date(1065,20)
 68.2% probability
  1294AD (68.2%) 1351AD
 95.4% probability
  1286AD (95.4%) 1397AD
104PC-2.9
104PC-1
2007
: 2007
(Boundary Revelle
Revelle Boundary(2007)
 68.2% probability
  2006AD (68.2%) 2007AD
 95.4% probability
  2006AD (95.4%) 2007AD
) Boundary Revelle
(P_Sequence RR0705-104PC
RR0705-104PC P_Sequence(1000,50)

) P_Sequence RR0705-104PC
Page
Depth_Model
Posterior
(MCMC(30000)
Warning! Poor agreement - A= 23.4%(A'c= 60.0%)
Warning! Poor agreement - A= 21.9%(A'c= 60.0%)
LocalMarine Posterior
68.2% probability
9 (68.2%) 33
95.4% probability
-2 (95.4%) 45
Agreement 93.0%
Start Posterior
68.2% probability
965BC (5.4%) 952BC
935BC (62.8%) 836BC
95.4% probability
996BC (95.4%) 789BC
RR0705_104PC_326_328_SUM-235 Posterior
68.2% probability
965BC (5.4%) 952BC
935BC (62.8%) 836BC
95.4% probability
996BC (95.4%) 789BC
Warning! Poor agreement - A= 36.9%(A'c= 60.0%)
Poor agreement 36.9%
104PC-40.1 Posterior
68.2% probability
867BC (68.2%) 754BC
95.4% probability
921BC (95.4%) 705BC
104PC-38.6 Posterior
68.2% probability
784BC (68.2%) 671BC
95.4% probability
843BC (95.4%) 621BC
104PC-34.1 Posterior
68.2% probability
547BC (68.2%) 429BC
95.4% probability
606BC (95.4%) 374BC
104PC-30.8 Posterior
68.2% probability
370BC (68.2%) 252BC
95.4% probability
427BC (95.4%) 194BC
RR0705_104PC_207_209_SUM-115 Posterior
68.2% probability
33AD (68.2%) 140AD
95.4% probability
13BC (95.4%) 204AD
Agreement 110.0%
RR0705_104PC_158_160_SUM-082 Posterior
68.2% probability
390AD (68.2%) 470AD
95.4% probability
378AD (95.4%) 540AD
Warning! Poor agreement - A= 44.2%(A'c= 60.0%)
Poor agreement 44.2%
104PC-14.8 Posterior
68.2% probability
559AD (68.2%) 653AD
95.4% probability
526AD (95.4%) 710AD
RR0705_104PC_122_124_SUM-061 Posterior
68.2% probability
860AD (48.3%) 915AD
922AD (19.9%) 952AD
95.4% probability
832AD (95.4%) 986AD
Warning! Poor agreement - A= 22.8%(A'c= 60.0%)
Poor agreement 22.8%
RR0705_104PC_067.5_069.5_SUM-062 Posterior
68.2% probability
1075AD (68.2%) 1143AD

95.4% probability
1060AD (95.4%) 1180AD
Agreement 72.7%
RR0705_104PC_049.5_051.5_SUM-060 Posterior
68.2% probability
1350AD (68.2%) 1405AD
95.4% probability
1310AD (95.4%) 1414AD
Warning! Poor agreement - A= 59.9%(A'c= 60.0%)
Poor agreement 59.9%
104PC-2.9 Posterior
68.2% probability
1645AD (68.2%) 1735AD
95.4% probability
1600AD (95.4%) 1774AD
104PC-1 Posterior
68.2% probability
1870AD (68.2%) 1935AD
95.4% probability
1833AD (95.4%) 1956AD
Revelle Posterior
68.2% probability
2006AD (68.2%) 2007AD
95.4% probability
2006AD (95.4%) 2007AD
Agreement 100.0%
depthModel Posterior
68.2% probability
837BC (68.2%) 724BC
95.4% probability
895BC (95.4%) 676BC
depthModel Posterior
68.2% probability
732BC (68.2%) 617BC
95.4% probability
790BC (95.4%) 564BC
depthModel Posterior
68.2% probability
625BC (68.2%) 509BC
95.4% probability
684BC (95.4%) 454BC
depthModel Posterior
68.2% probability
518BC (68.2%) 401BC
95.4% probability
578BC (95.4%) 344BC
depthModel Posterior
68.2% probability
411BC (68.2%) 294BC
95.4% probability
469BC (95.4%) 236BC
depthModel Posterior
68.2% probability
305BC (68.2%) 189BC
95.4% probability
358BC (95.4%) 128BC
depthModel Posterior
68.2% probability
196BC (68.2%) 82BC
95.4% probability
251BC (95.4%) 23BC
depthModel Posterior
68.2% probability
87BC (68.2%) 25AD
95.4% probability
139BC (95.4%) 86AD
depthModel Posterior
68.2% probability
25AD (68.2%) 132AD
95.4% probability
26BC (95.4%) 192AD
depthModel Posterior
68.2% probability
133AD (68.2%) 235AD
95.4% probability
93AD (95.4%) 299AD
depthModel Posterior
68.2% probability
244AD (68.2%) 339AD
95.4% probability
212AD (95.4%) 405AD
depthModel Posterior
68.2% probability
354AD (68.2%) 439AD

95.4% probability
337AD (95.4%) 509AD
depthModel Posterior
68.2% probability
496AD (68.2%) 591AD
95.4% probability
468AD (95.4%) 646AD
depthModel Posterior
68.2% probability
655AD (68.2%) 750AD
95.4% probability
615AD (95.4%) 800AD
depthModel Posterior
68.2% probability
814AD (68.2%) 901AD
95.4% probability
779AD (95.4%) 944AD
depthModel Posterior
68.2% probability
1011AD (68.2%) 1089AD
95.4% probability
980AD (95.4%) 1129AD
depthModel Posterior
68.2% probability
1192AD (68.2%) 1262AD
95.4% probability
1161AD (95.4%) 1293AD
depthModel Posterior
68.2% probability
1367AD (68.2%) 1427AD
95.4% probability
1326AD (95.4%) 1447AD
depthModel Posterior
68.2% probability
1568AD (68.2%) 1657AD
95.4% probability
1523AD (95.4%) 1699AD
depthModel Posterior
68.2% probability
1796AD (68.2%) 1872AD
95.4% probability
1754AD (95.4%) 1904AD
) MCMC(240000)

104TC P_Sequence

OxCal v4.1.2 Bronk Ramsey (2009); r:5
IntCal04 atmospheric curve (Reimer et al 2004)
FALSE
0.022
0.021
0.012
0.007
0
OxCal v4.1.2 Bronk Ramsey (2009); r:5
Marine Curve(Marine09.14c)
Marine data from Reimer et al (2009);
LocalMarine Delta_R(16,11)
68.2% probability
5 (68.2%) 28
95.4% probability
-7 (95.4%) 39
Start Boundary()
RR0705_104TC_047.5_049.5_SUM-175
R_Date(1220,20)
68.2% probability
1179AD (68.2%) 1246AD
95.4% probability
1140AD (95.4%) 1277AD
104TC-2.1
104TC-1.2
RR0705_104TC_011_013_SUM-176 R_
Date(705,20)
68.2% probability
1584AD (68.2%) 1661AD
95.4% probability
1540AD (95.4%) 1673AD
2007
: 2007
(Boundary Revelle
Revelle Boundary(2007)
68.2% probability
2006AD (68.2%) 2007AD
95.4% probability
2006AD (95.4%) 2007AD
) Boundary Revelle
(P_Sequence RR0705-104TC
RR0705-104TC P_Sequence(1000,50)
) P_Sequence RR0705-104TC
Page
Depth_Model
Posterior
(MCMC(30000)
Overall agreement 101.1%
Dynamic agreement 102.5%
LocalMarine Posterior
68.2% probability
3 (68.2%) 27
95.4% probability
-9 (95.4%) 39
Agreement 98.1%
Start Posterior
68.2% probability
1171AD (68.2%) 1241AD
95.4% probability
1127AD (95.4%) 1275AD
RR0705_104TC_047.5_049.5_SUM-175
Posterior
68.2% probability
1171AD (68.2%) 1241AD
95.4% probability
1127AD (95.4%) 1275AD
Agreement 97.6%
104TC-2.1 Posterior
68.2% probability
1190AD (68.2%) 1270AD
95.4% probability
1139AD (95.4%) 1325AD
104TC-1.2 Posterior
68.2% probability
1440AD (68.2%) 1556AD
95.4% probability
1375AD (95.4%) 1598AD
RR0705_104TC_011_013_SUM-176 Poste-
rior
68.2% probability
1612AD (68.2%) 1670AD

95.4% probability
1565AD (95.4%) 1683AD
Agreement 106.7%
Revelle Posterior
68.2% probability
2006AD (68.2%) 2007AD
95.4% probability
2006AD (95.4%) 2007AD
Agreement 100.0%
depthModel Posterior
68.2% probability
1859AD (68.2%) 1980AD
95.4% probability
1781AD (95.4%) 2001AD
) MCMC(120000)

108PC P_Sequence

OxCal v4.1.2 Bronk Ramsey (2009); r:5
IntCal04 atmospheric curve (Reimer et al 2004)
FALSE
1.153
1.117
1.077
1.043
1.034
0.892
0.842
0.819
0.812
0.721
0.605
0.523
0.523
0.221
0
OxCal v4.1.2 Bronk Ramsey (2009); r:5
Marine Curve(Marine09.14c)
Marine data from Reimer et al (2009);
LocalMarine Delta_R(16,11)
68.2% probability
5 (68.2%) 28
95.4% probability
-7 (95.4%) 39
Start Boundary()
RR0705_108PC_345_347_SUM-195 R_Date(7175,20)
68.2% probability
5704BC (68.2%) 5644BC
95.4% probability
5729BC (95.4%) 5619BC
RR0705_108PC_330_332_SUM-041 R_Date(6685,25)
68.2% probability
5287BC (68.2%) 5220BC
95.4% probability
5320BC (95.4%) 5191BC
RR0705_108PC_312.5_314.5_SUM-043 R_Date(6115,20)
68.2% probability
4621BC (68.2%) 4526BC
95.4% probability
4667BC (95.4%) 4495BC
RR0705_108PC_290.5_292.5_SUM-044 R_Date(5950,20)
68.2% probability
4429BC (68.2%) 4357BC
95.4% probability
4456BC (95.4%) 4331BC
108PC-103.4
RR0705_108PC_257_259_SUM-042 R_Date(4840,20)
68.2% probability
3247BC (68.2%) 3106BC
95.4% probability
3302BC (95.4%) 3067BC
108PC-84.2
108PC-81.9
RR0705_108PC_212.5_214.5_SUM-045 R_Date(4625,20)
68.2% probability
2899BC (68.2%) 2856BC
95.4% probability
2953BC (95.4%) 2829BC
RR0705_108PC_194_196_SUM-194 R_Date(4340,20)
68.2% probability
2542BC (68.2%) 2466BC
95.4% probability
2581BC (95.4%) 2433BC
RR0705_108PC_175_177_SUM-046 R_Date(4070,15)
68.2% probability
2190BC (68.2%) 2096BC
95.4% probability
2214BC (95.4%) 2029BC
RR0705_108PC_156_158_SUM-083 R_Date(3500,15)
68.2% probability

1447BC (68.2%) 1387BC
95.4% probability
1487BC (95.4%) 1362BC
RR0705_108PC_132.5_134.5_SUM-081
R_Date(3035,15)
68.2% probability
861BC (68.2%) 797BC
95.4% probability
896BC (95.4%) 784BC
RR0705_108PC_039_041_SUM-080 R_
Date(2015,15)
68.2% probability
358AD (68.2%) 429AD
95.4% probability
301AD (95.4%) 458AD
2007
: 2007
(Boundary Revelle
Revelle Boundary(2007)
68.2% probability
2006AD (68.2%) 2007AD
95.4% probability
2006AD (95.4%) 2007AD
) Boundary Revelle
(P_Sequence RR0705-108PC
RR0705-108PC P_Sequence(1000,50)
) P_Sequence RR0705-108PC
Page
Depth_Model
Posterior
(MCMC(30000)
Warning! Poor agreement - A= 0.3%(A'c=
60.0%)
Warning! Poor agreement - A= 0.2%(A'c=
60.0%)
LocalMarine Posterior
68.2% probability
0 (68.2%) 33
95.4% probability
-6 (95.4%) 40
Agreement 87.2%
Start Posterior
68.2% probability
5659BC (68.2%) 5612BC
95.4% probability
5686BC (95.4%) 5563BC
RR0705_108PC_345_347_SUM-195 Poste-
rior
68.2% probability
5659BC (68.2%) 5612BC
95.4% probability
5686BC (95.4%) 5563BC
Agreement 62.5%
RR0705_108PC_330_332_SUM-041 Poste-
rior
68.2% probability
5260BC (68.2%) 5203BC
95.4% probability
5300BC (95.4%) 5177BC
Agreement 96.2%
RR0705_108PC_312.5_314.5_SUM-043
Posterior
68.2% probability
4686BC (68.2%) 4637BC
95.4% probability
4716BC (95.4%) 4602BC
Warning! Poor agreement - A= 34.5%(A'c=
60.0%)
Poor agreement 34.5%
RR0705_108PC_290.5_292.5_SUM-044
Posterior
68.2% probability
4436BC (68.2%) 4373BC
95.4% probability
4456BC (95.4%) 4342BC
Agreement 103.7%
108PC-103.4 Posterior
68.2% probability
4374BC (68.2%) 4302BC
95.4% probability
4404BC (95.4%) 4266BC
RR0705_108PC_257_259_SUM-042 Poste-
rior
68.2% probability
3319BC (68.2%) 3275BC
95.4% probability

3333BC (95.4%) 3246BC
Warning! Poor agreement - A= 37.3%(A'c= 60.0%)
Poor agreement 37.3%
108PC-84.2 Posterior
68.2% probability
3071BC (68.2%) 3011BC
95.4% probability
3104BC (95.4%) 2985BC
108PC-81.9 Posterior
68.2% probability
2950BC (68.2%) 2897BC
95.4% probability
2988BC (95.4%) 2878BC
RR0705_108PC_212.5_214.5_SUM-045 Posterior
68.2% probability
2909BC (68.2%) 2864BC
95.4% probability
2952BC (95.4%) 2849BC
Agreement 91.7%
RR0705_108PC_194_196_SUM-194 Posterior
68.2% probability
2517BC (68.2%) 2461BC
95.4% probability
2554BC (95.4%) 2441BC
Agreement 107.5%
RR0705_108PC_175_177_SUM-046 Posterior
68.2% probability
1993BC (64.5%) 1938BC
1924BC (3.7%) 1918BC
95.4% probability
2036BC (95.4%) 1901BC
Warning! Poor agreement - A= 2.2%(A'c= 60.0%)
Poor agreement 2.2%
RR0705_108PC_156_158_SUM-083 Posterior
68.2% probability
1310BC (68.2%) 1252BC
95.4% probability
1330BC (95.4%) 1220BC
Warning! Poor agreement - A= 0.8%(A'c= 60.0%)
Poor agreement 0.8%
RR0705_108PC_132.5_134.5_SUM-081 Posterior
68.2% probability
1037BC (29.4%) 1021BC
1004BC (38.8%) 987BC
95.4% probability
1045BC (95.4%) 972BC
Warning! Poor agreement - A= 0.0%(A'c= 60.0%)
Poor agreement 0.0%
RR0705_108PC_039_041_SUM-080 Posterior
68.2% probability
415AD (29.2%) 459AD
496AD (39.0%) 542AD
95.4% probability
398AD (95.4%) 550AD
Warning! Poor agreement - A= 32.4%(A'c= 60.0%)
Poor agreement 32.4%
Revelle Posterior
68.2% probability
2006AD (68.2%) 2007AD
95.4% probability
2006AD (95.4%) 2007AD
Agreement 100.0%
depthModel Posterior
68.2% probability
5451BC (68.2%) 5371BC
95.4% probability
5491BC (95.4%) 5332BC
depthModel Posterior
68.2% probability
5216BC (68.2%) 5141BC
95.4% probability
5254BC (95.4%) 5096BC
depthModel Posterior
68.2% probability
4938BC (68.2%) 4841BC

95.4% probability
4987BC (95.4%) 4795BC
depthModel Posterior
68.2% probability
4661BC (68.2%) 4606BC
95.4% probability
4690BC (95.4%) 4570BC
depthModel Posterior
68.2% probability
4512BC (68.2%) 4447BC
95.4% probability
4542BC (95.4%) 4414BC
depthModel Posterior
68.2% probability
4367BC (68.2%) 4295BC
95.4% probability
4399BC (95.4%) 4258BC
depthModel Posterior
68.2% probability
4227BC (68.2%) 4140BC
95.4% probability
4269BC (95.4%) 4095BC
depthModel Posterior
68.2% probability
4084BC (68.2%) 3987BC
95.4% probability
4130BC (95.4%) 3939BC
depthModel Posterior
68.2% probability
3938BC (68.2%) 3838BC
95.4% probability
3986BC (95.4%) 3789BC
depthModel Posterior
68.2% probability
3787BC (68.2%) 3692BC
95.4% probability
3836BC (95.4%) 3644BC
depthModel Posterior
68.2% probability
3638BC (68.2%) 3549BC
95.4% probability
3685BC (95.4%) 3506BC
depthModel Posterior
68.2% probability
3484BC (68.2%) 3409BC
95.4% probability
3522BC (95.4%) 3374BC
depthModel Posterior
68.2% probability
3326BC (68.2%) 3281BC
95.4% probability
3344BC (95.4%) 3251BC
depthModel Posterior
68.2% probability
3228BC (68.2%) 3172BC
95.4% probability
3252BC (95.4%) 3142BC
depthModel Posterior
68.2% probability
3128BC (68.2%) 3067BC
95.4% probability
3157BC (95.4%) 3040BC
depthModel Posterior
68.2% probability
3024BC (68.2%) 2966BC
95.4% probability
3060BC (95.4%) 2941BC
depthModel Posterior
68.2% probability
2915BC (68.2%) 2869BC
95.4% probability
2958BC (95.4%) 2852BC
depthModel Posterior
68.2% probability
2835BC (68.2%) 2778BC
95.4% probability
2872BC (95.4%) 2753BC
depthModel Posterior
68.2% probability
2751BC (68.2%) 2689BC
95.4% probability
2786BC (95.4%) 2661BC
depthModel Posterior
68.2% probability
2664BC (68.2%) 2601BC
95.4% probability

2698BC (95.4%) 2572BC
depthModel Posterior
68.2% probability
2576BC (68.2%) 2512BC
95.4% probability
2608BC (95.4%) 2489BC
depthModel Posterior
68.2% probability
2486BC (68.2%) 2423BC
95.4% probability
2521BC (95.4%) 2398BC
depthModel Posterior
68.2% probability
2398BC (68.2%) 2330BC
95.4% probability
2435BC (95.4%) 2299BC
depthModel Posterior
68.2% probability
2311BC (68.2%) 2237BC
95.4% probability
2347BC (95.4%) 2204BC
depthModel Posterior
68.2% probability
2218BC (68.2%) 2146BC
95.4% probability
2257BC (95.4%) 2112BC
depthModel Posterior
68.2% probability
2126BC (68.2%) 2056BC
95.4% probability
2166BC (95.4%) 2021BC
depthModel Posterior
68.2% probability
2031BC (68.2%) 1965BC
95.4% probability
2072BC (95.4%) 1935BC
depthModel Posterior
68.2% probability
1903BC (68.2%) 1823BC
95.4% probability
1946BC (95.4%) 1784BC
depthModel Posterior
68.2% probability
1742BC (68.2%) 1652BC
95.4% probability
1786BC (95.4%) 1606BC
depthModel Posterior
68.2% probability
1573BC (68.2%) 1485BC
95.4% probability
1618BC (95.4%) 1443BC
depthModel Posterior
68.2% probability
1396BC (68.2%) 1322BC
95.4% probability
1436BC (95.4%) 1291BC
depthModel Posterior
68.2% probability
989BC (68.2%) 934BC
95.4% probability
1010BC (95.4%) 909BC
depthModel Posterior
68.2% probability
896BC (68.2%) 828BC
95.4% probability
926BC (95.4%) 795BC
depthModel Posterior
68.2% probability
805BC (68.2%) 724BC
95.4% probability
837BC (95.4%) 684BC
depthModel Posterior
68.2% probability
708BC (68.2%) 623BC
95.4% probability
747BC (95.4%) 578BC
depthModel Posterior
68.2% probability
614BC (68.2%) 521BC
95.4% probability
658BC (95.4%) 475BC
depthModel Posterior
68.2% probability
517BC (68.2%) 419BC
95.4% probability
562BC (95.4%) 368BC

depthModel Posterior
68.2% probability
421BC (68.2%) 317BC
95.4% probability
468BC (95.4%) 268BC
depthModel Posterior
68.2% probability
323BC (68.2%) 217BC
95.4% probability
374BC (95.4%) 170BC
depthModel Posterior
68.2% probability
226BC (68.2%) 117BC
95.4% probability
275BC (95.4%) 70BC
depthModel Posterior
68.2% probability
128BC (68.2%) 21BC
95.4% probability
179BC (95.4%) 31AD
depthModel Posterior
68.2% probability
32BC (68.2%) 79AD
95.4% probability
80BC (95.4%) 129AD
depthModel Posterior
68.2% probability
72AD (68.2%) 180AD
95.4% probability
23AD (95.4%) 224AD
depthModel Posterior
68.2% probability
170AD (68.2%) 280AD
95.4% probability
123AD (95.4%) 319AD
depthModel Posterior
68.2% probability
272AD (68.2%) 376AD
95.4% probability
227AD (95.4%) 413AD
depthModel Posterior
68.2% probability
365AD (27.8%) 409AD
423AD (40.4%) 480AD
95.4% probability
333AD (95.4%) 500AD
depthModel Posterior
68.2% probability
478AD (23.4%) 518AD
524AD (44.8%) 590AD
95.4% probability
445AD (95.4%) 616AD
depthModel Posterior
68.2% probability
621AD (68.2%) 731AD
95.4% probability
568AD (95.4%) 770AD
depthModel Posterior
68.2% probability
754AD (68.2%) 867AD
95.4% probability
700AD (95.4%) 919AD
depthModel Posterior
68.2% probability
889AD (68.2%) 1008AD
95.4% probability
836AD (95.4%) 1061AD
depthModel Posterior
68.2% probability
1031AD (68.2%) 1146AD
95.4% probability
973AD (95.4%) 1199AD
depthModel Posterior
68.2% probability
1168AD (68.2%) 1283AD
95.4% probability
1112AD (95.4%) 1336AD
depthModel Posterior
68.2% probability
1311AD (68.2%) 1422AD
95.4% probability
1254AD (95.4%) 1471AD
depthModel Posterior
68.2% probability
1452AD (68.2%) 1555AD
95.4% probability

1399AD (95.4%) 1600AD
depthModel Posterior
68.2% probability
1596AD (68.2%) 1689AD
95.4% probability
1547AD (95.4%) 1730AD
depthModel Posterior
68.2% probability
1745AD (68.2%) 1819AD
95.4% probability
1704AD (95.4%) 1850AD
depthModel Posterior
68.2% probability
1895AD (68.2%) 1945AD
95.4% probability
1868AD (95.4%) 1962AD
) MCMC(240000)

Appendix S 2-3 Low Angle Oblique Site Maps

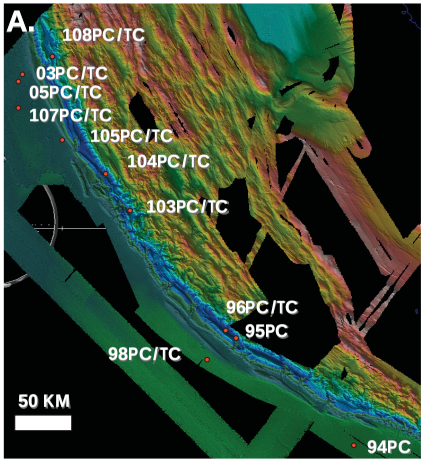

Figure S 2-3. Low-Angle Oblique Site Maps. RR0705 Core locations are plotted so that the geomorphology of the core sites can be evaluated with respect to preserved stratigraphy. Depth contours are also plotted. Bathymetry was collected while at sea and also provided by our collaborators from the UK, Japan, France, and Germany (Ladage et al., 2006). A. map showing relative locations of cores as orange dots (**Fig. S 2-2**). White scale bar is 50 km. B. through H. Larger scale, low angle oblique views of core sites (orange dots). Orientation arrows (in white) point in the direction of North and Up (vertical). Vertical and horizontal units are in meters.

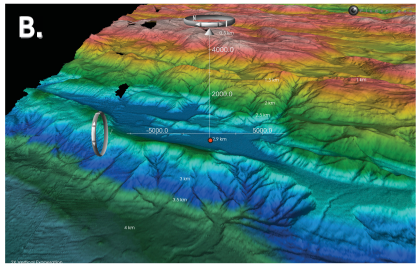

RR0705 108PC/TC

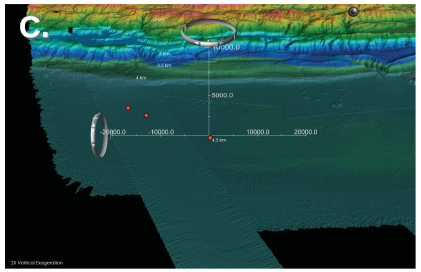

RR0705 05PC/TC, 03PC/TC and 107PC/TC

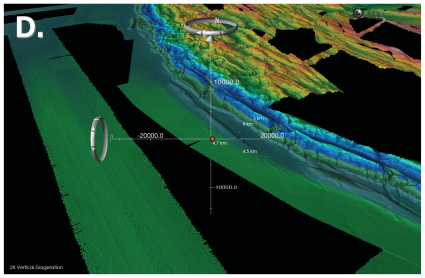

RR0705 98PC/TC

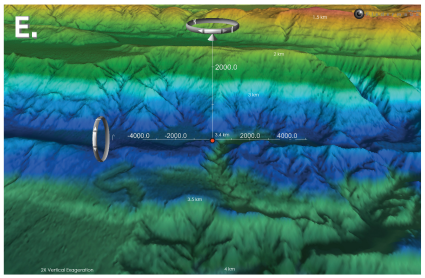

RR0705 104PC/TC

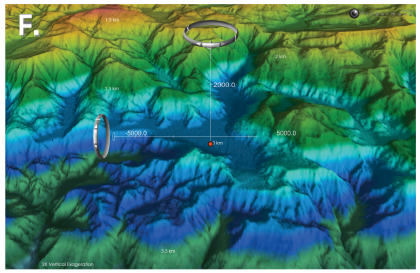

RR0705 103PC/TC

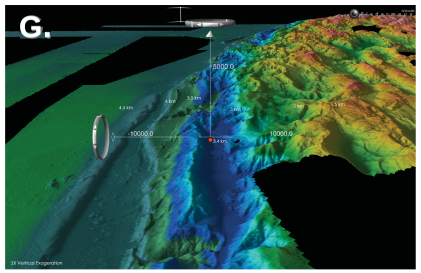

RR0705 96PC/TC and 95PC/TC

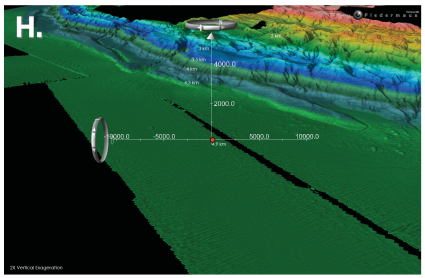

RR0705 94PC

RR0705 108PC/TC

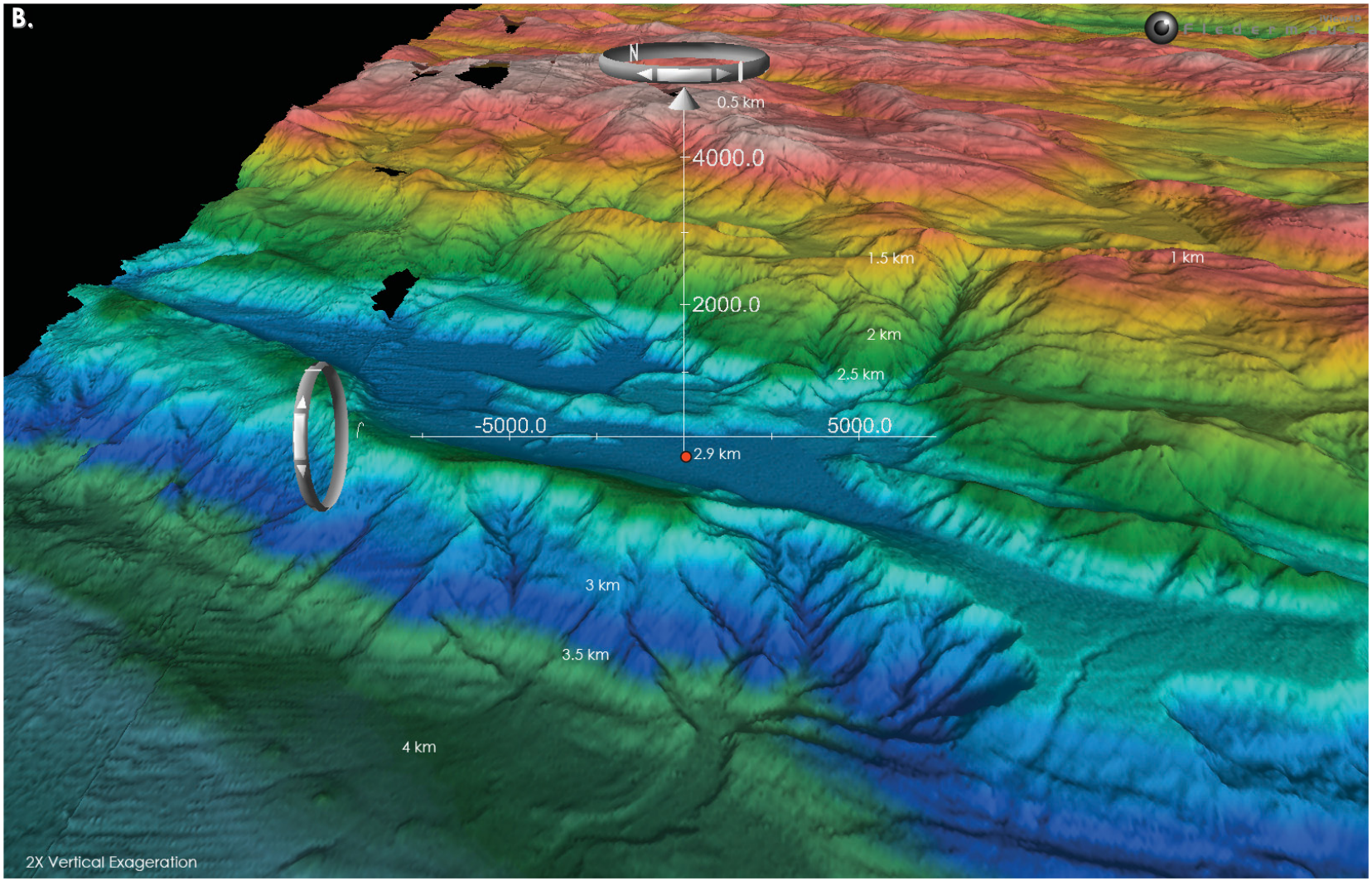

RR0705 107PC/TC

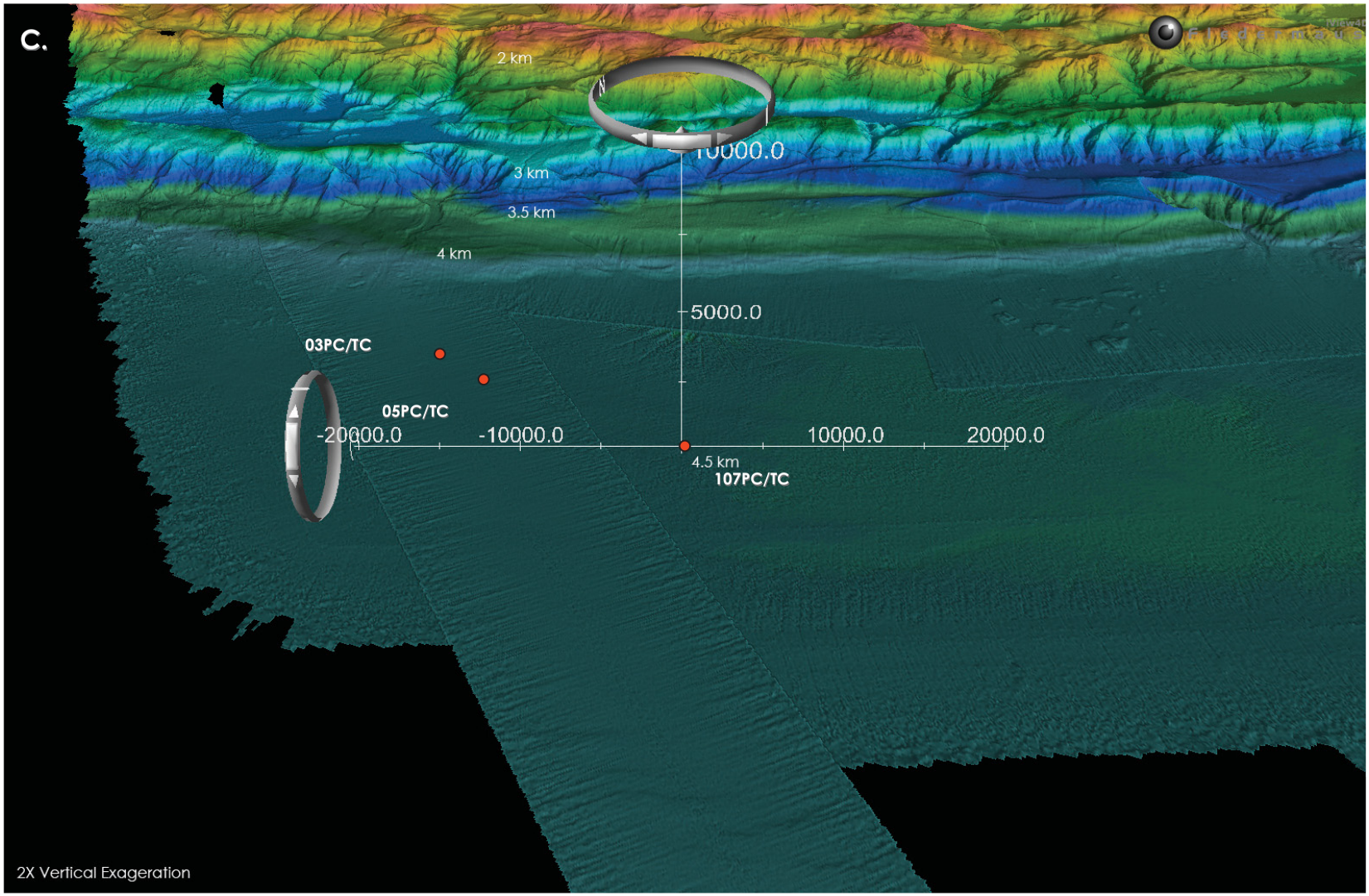

RR0705 98PC/TC

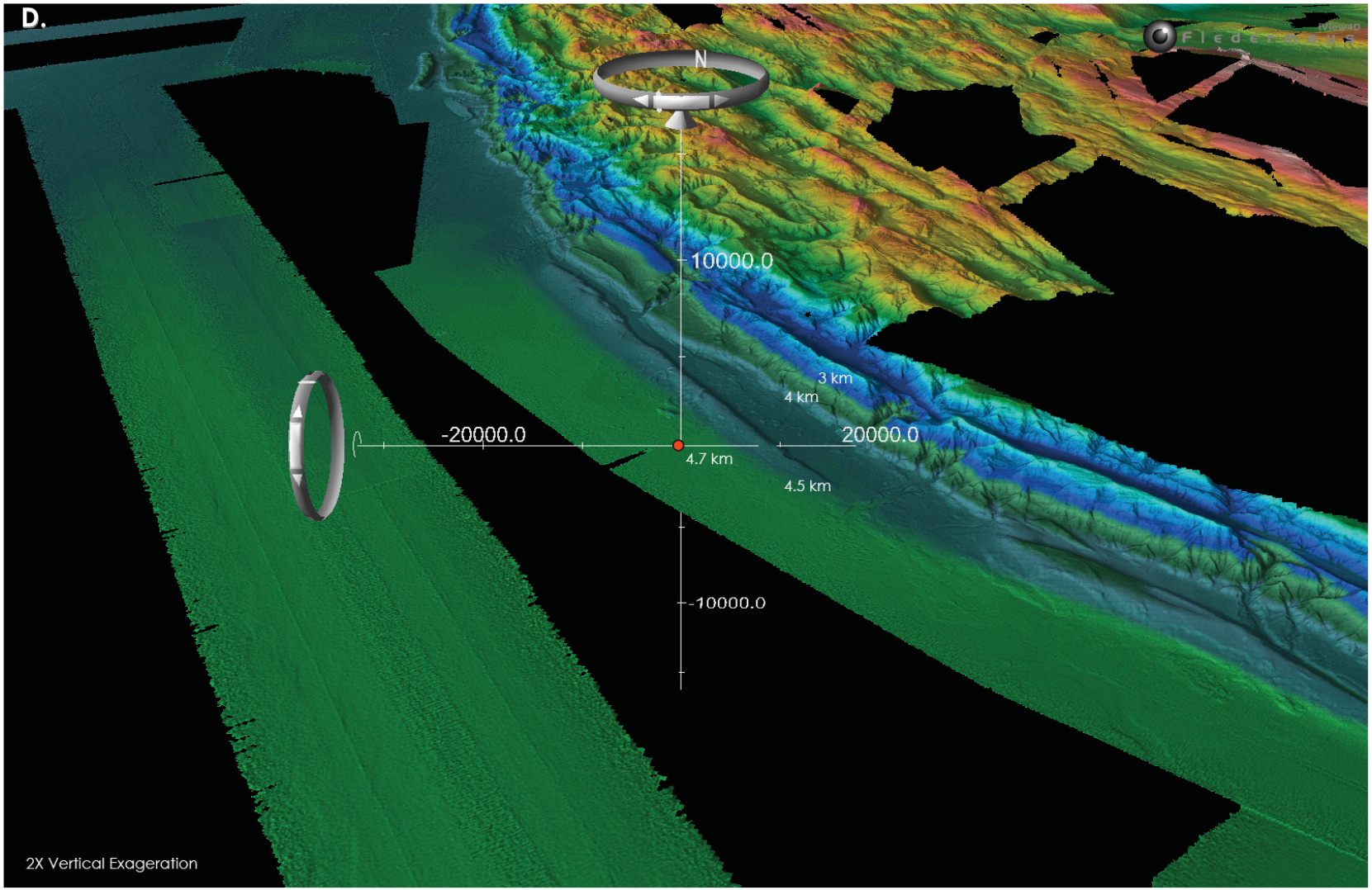

RR0705 104PC/TC

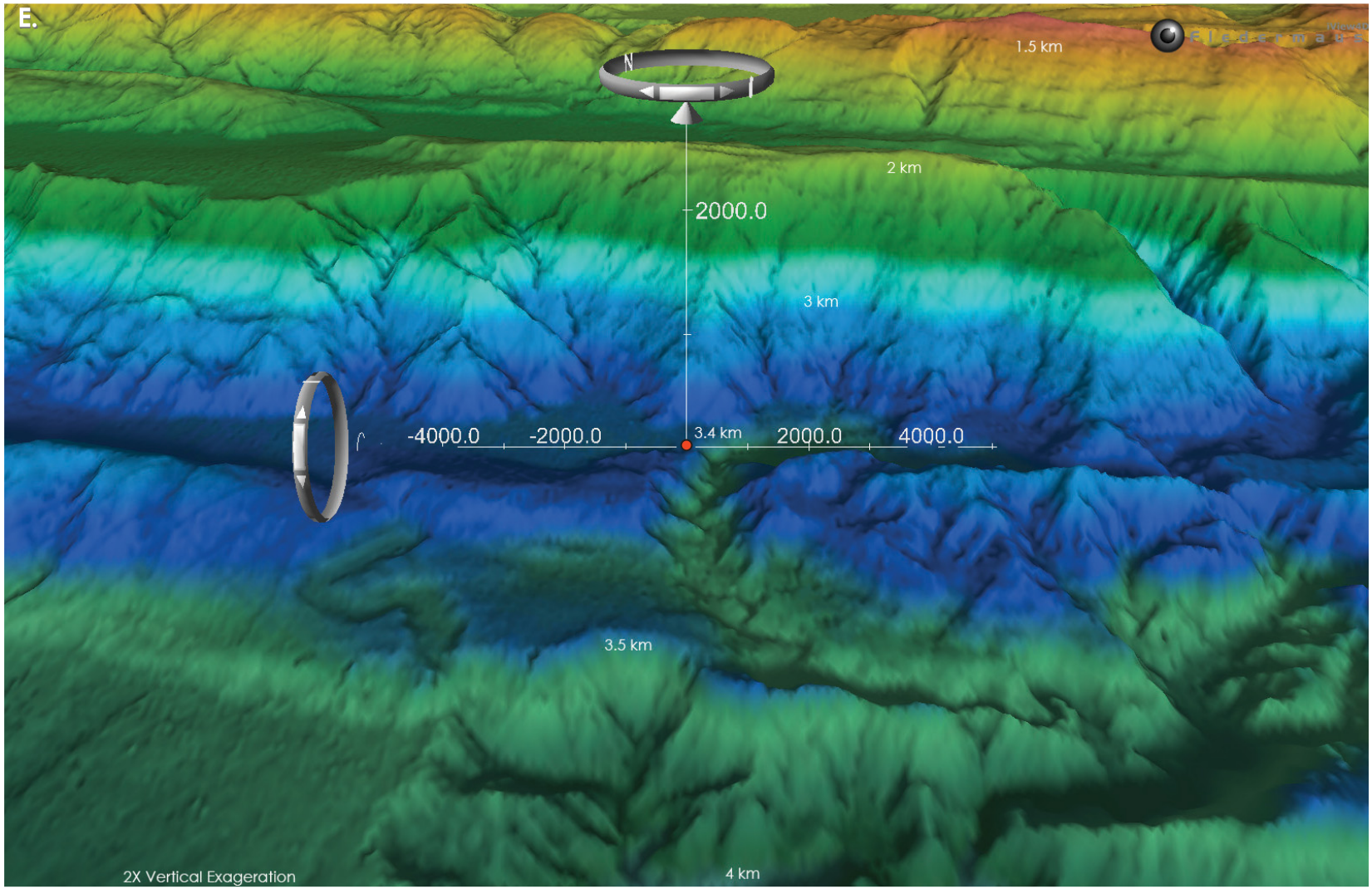

RR0705 103PC/TC

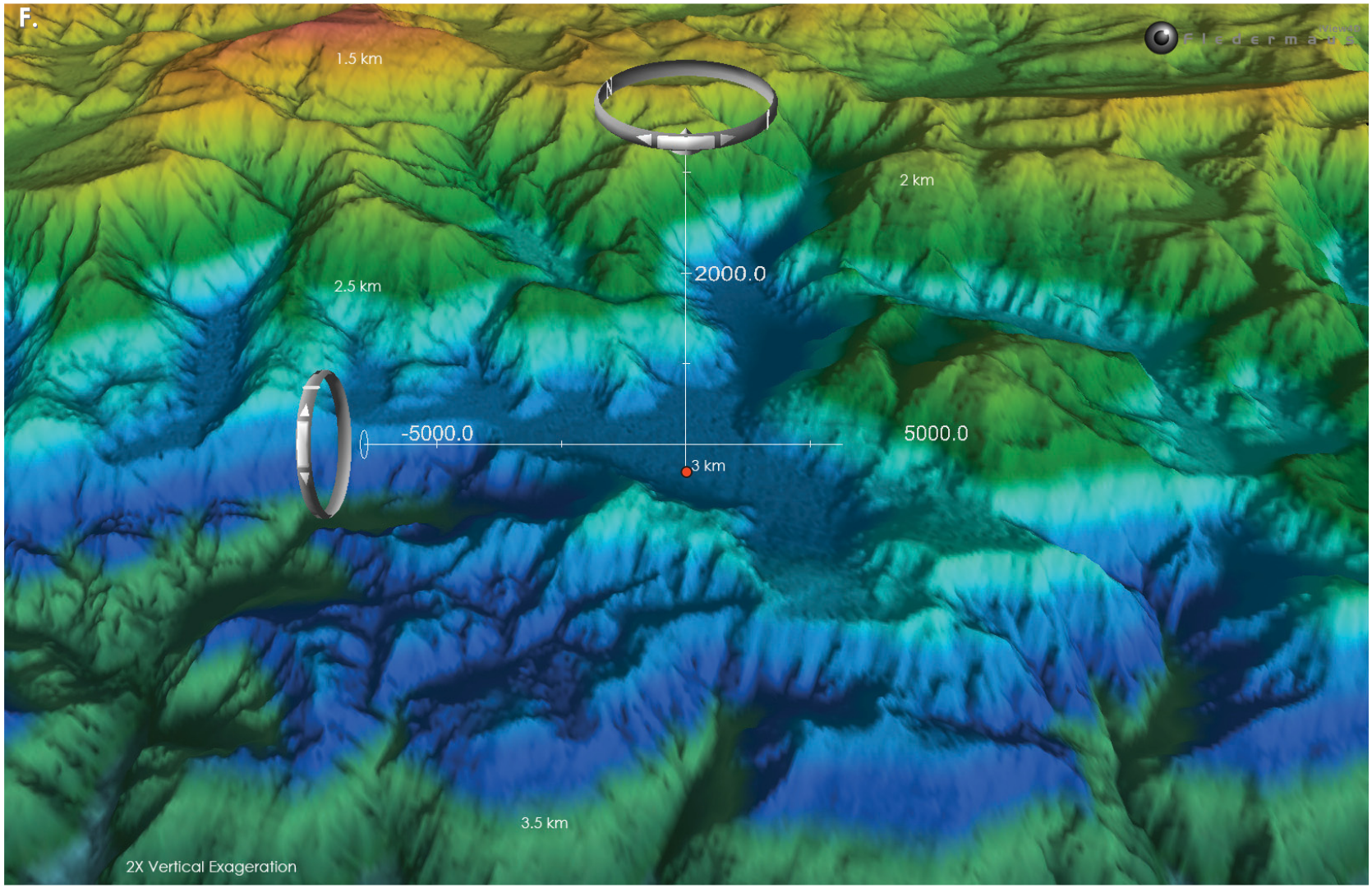

RR0705 96PC/TC and 95PC/TC

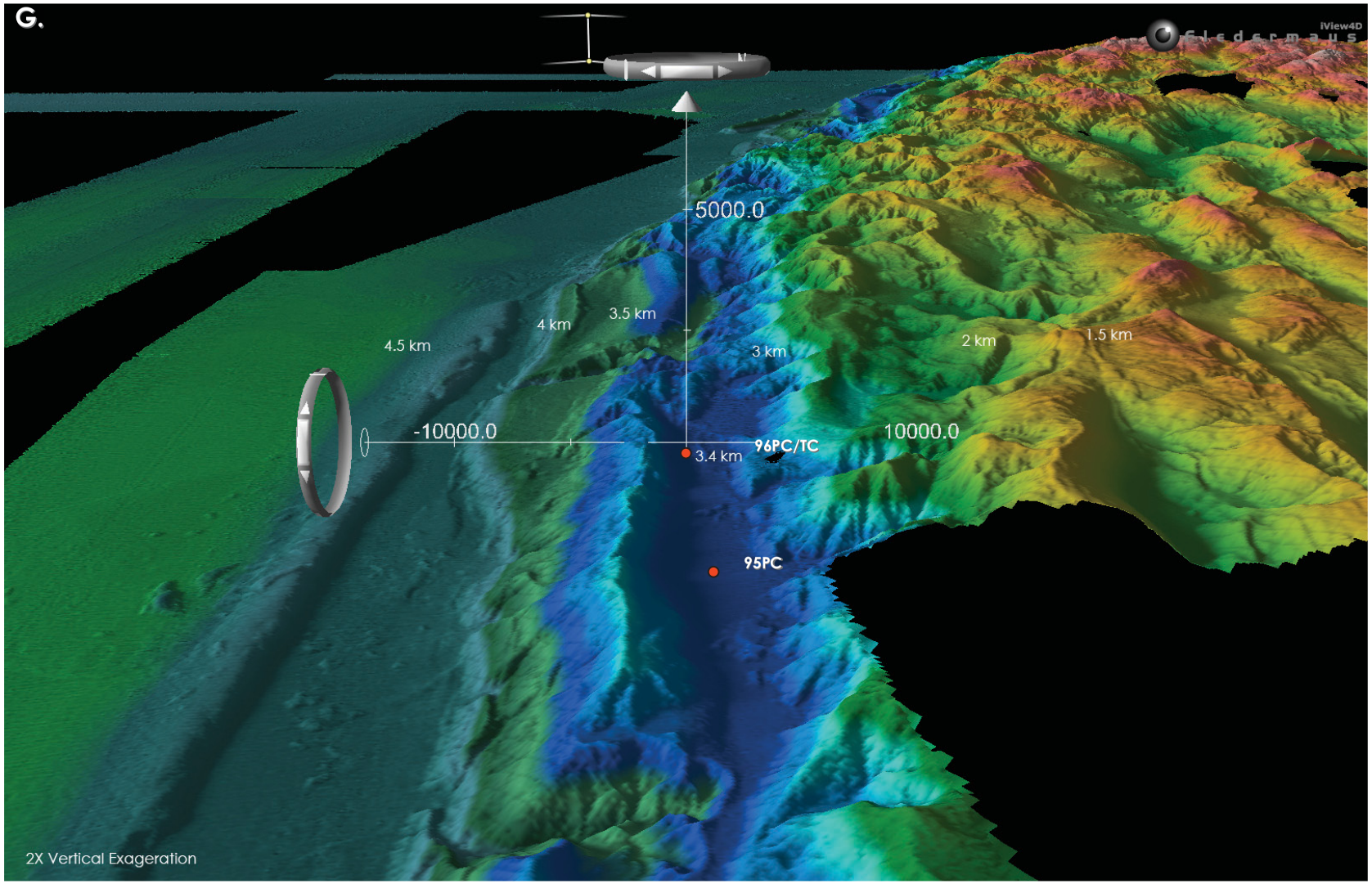

RR0705 94PC

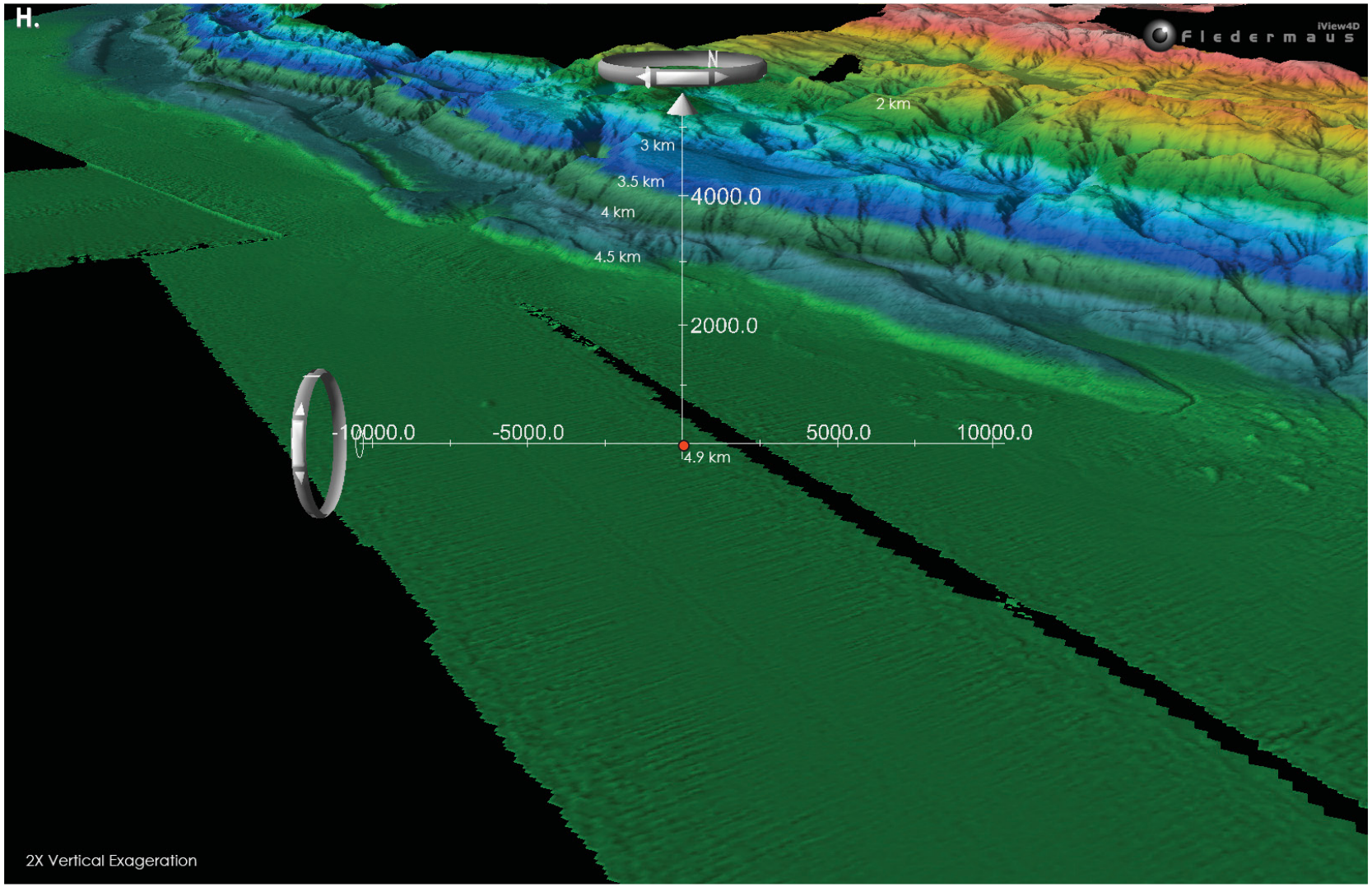
H.
iView4D
Fledermaus
N
2 km
3 km
3.5 km
4 km
4.5 km
4000.0
2000.0
-10000.0
-5000.0
5000.0
10000.0
4.9 km
2X Vertical Exageration

Appendix S 2-7 96PC/TC and 26 December 2004 Sumatra-Andaman Subduction Zone Earthquake Seismologic Observations

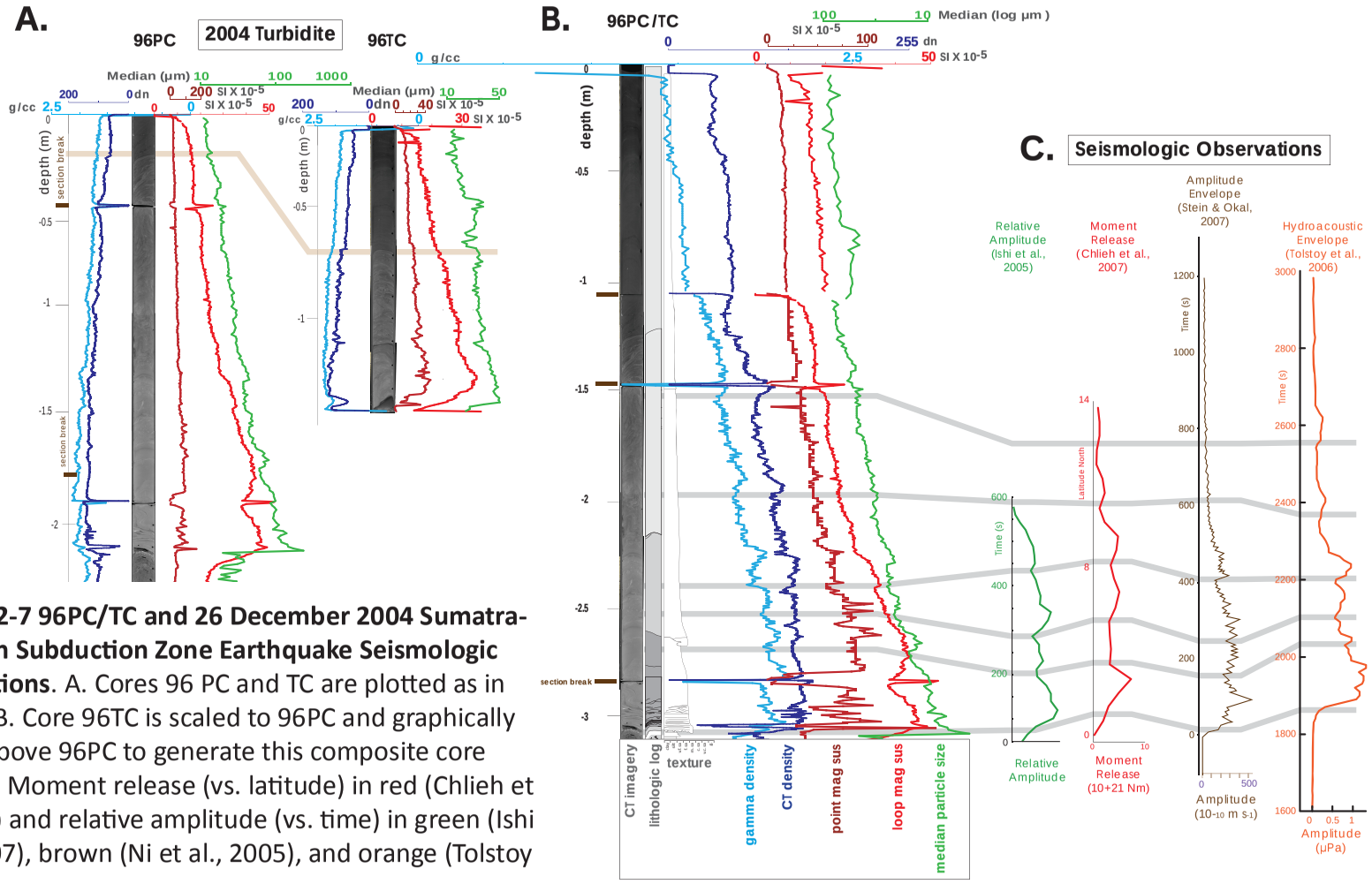

Figure S 2-7 96PC/TC and 26 December 2004 Sumatra-Andaman Subduction Zone Earthquake Seismologic Observations. A. Cores 96 PC and TC are plotted as in Fig. 2-5. B. Core 96TC is scaled to 96PC and graphically spliced above 96PC to generate this composite core 96PC/TC. Moment release (vs. latitude) in red (Chlieh et al., 2007) and relative amplitude (vs. time) in green (Ishi et al, 2007), brown (Ni et al., 2005), and orange (Tolstoy and Bohnenstiehl, 2006) are scaled to match peaks in the loop ms data from composite core RR0705-96PC/TC. Thick grey tie-lines correlate the beginning of seismic peaks with each other and with base of peaks in the core geophysical data.

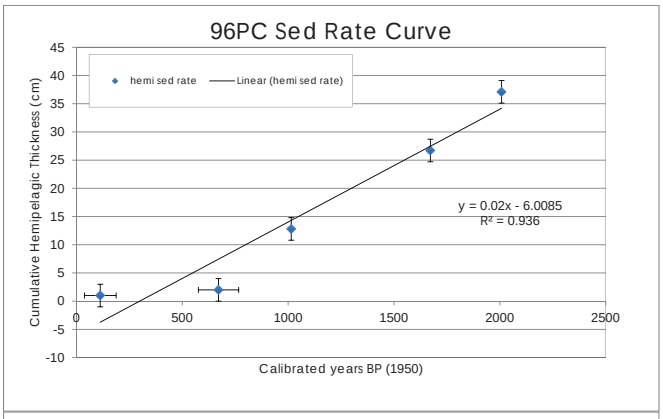

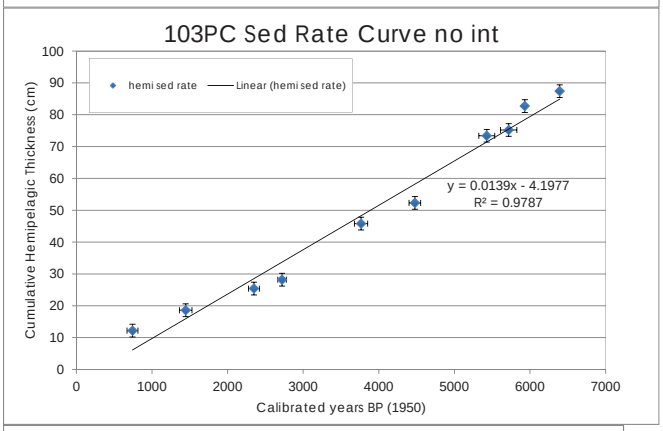

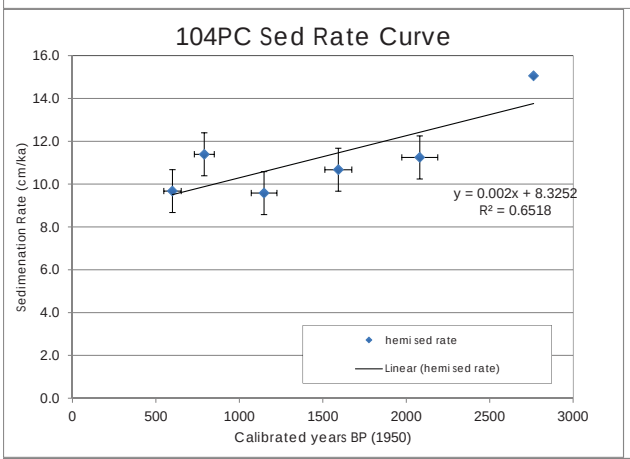

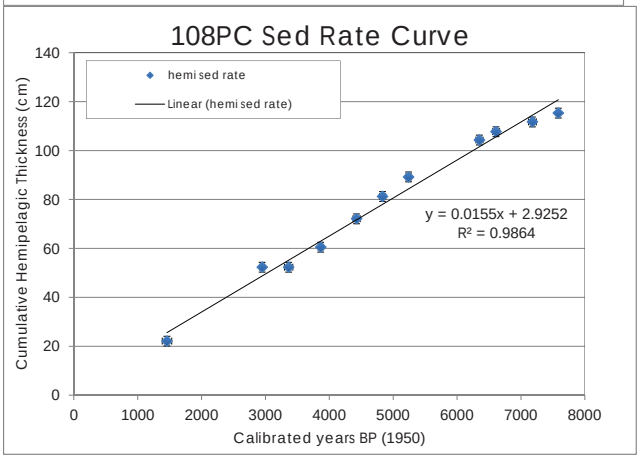

Appendix S 2-8. Sedimentation Rates for cores 96, 103, 104, and 108.

These sedimentation rates are based on calibrated radiocarbon ages and an estimate of the thickness of hemipelagic sediment overlying them. Cumulative hemipelagic thickness, with 1 standard deviation error bar, is plotted on the vertical axis. Calibrated age, in calendar years before present (1950 AD) are plotted with 95.4% error on the horizontal axis. The sedimentation rates are based on the linear regression.

Supplemental Document S 2-9: Turbidite Classification

We adopt turbidite classifications to describe the stratigraphy in our sediment cores (Stow and Shanmugam, 1980; Stow and Piper, 1984). We choose to combine the Bouma sequence with the Stow sequence. Bouma uses turbidite structure to break out five main parts of a typical turbidite sequence (Bouma, 1962). This model further refined by van der Lingen (1969). Piper (1978) and Stow (1977) further subdivide Te into several more divisions, also based on turbidite structure. Below are the major criteria that define these divisions. We adopt Bouma (1962) and Stow (1977) for our research.

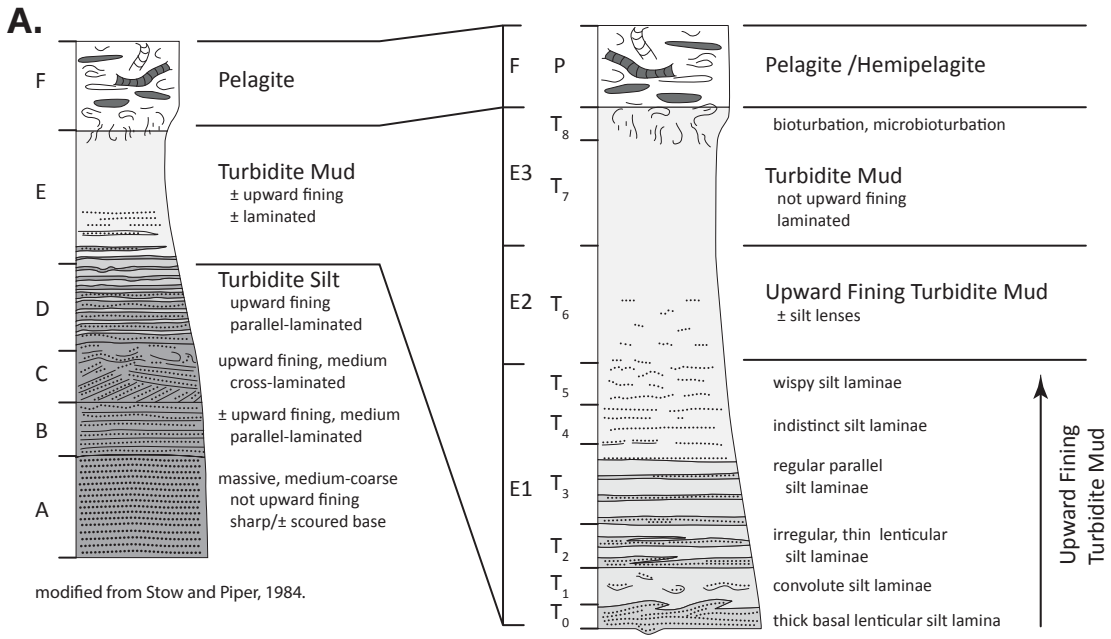

Turbidite Division Classification. A. Bouma (1962) and van der Lingen (1969) turbidite structure classification for fine grained turbidites is drafted on the left. Divisions are designated by letters A through F, typically designated with a preceding "T." Stow (1977) and Piper (1978) turbidite structure classification system for fine grained turbidites is drafted on the right. Piper (1978) divisions are designated by E and F letters. Stow (1977) divisions are designated with "T-#." Both Stow and Piper divisions fit within the Bouma Te division.

Bouma Sequence(Bouma, 1962)

- Te: Massive, ungraded mudstone, sometimes with evidence of trace fossils (i.e., bioturbation). The Bouma E layer is often missing, or difficult to differentiate from the Bouma D layer below.
- Td: Parallel-laminated siltstone.
- Tc: Ripple-laminated fine-grained sandstone. Often the ripple laminations are deformed into convolute laminations and flame structures.
- Tb: Planar-laminated fine- to medium-grained sandstone. The base of Bouma B often has features known as sole markings, such as flute casts, groove casts and parting lineation.
- Ta: Massive to normally graded, fine- to coarse-grained sandstone, often with pebbles and/or rip-up clasts of shale near the base. Dish structures may be present. The base of the sandstone, below A, is sometimes eroded into underlying strata.

Piper Sequence (Piper, 1978)

- Tf hemipelagic or pelagic sediment
- Te3 ungraded mud
- Te2 graded mud
- Te1 laminated mud
- Td laminated sand and silt

Stow Sequence (Stow, 1977)

- P pelagite or hemipelagite, bioturbated
- T8 turbidite (+ part pelagite), microbioturbated
- T7 ungraded mud, occasionally with silt pseudonodules
- T6 graded mud, often with dispersed silt lenses
- T5 wispy convolute silt laminae in mud
- T4 indistinct, discontinuous silt laminae in mud
- T3 thin, regular, continuous parallel silt laminae in mud
- T2 thin, irregular, slightly lenticular silt laminae in mud, often with low-amplitude climbing ripples
- TI thick mud layer, often with thin convolute silt laminae To thick, basal, lenticular, silt lamina, often with fading-ripple top, microlaminated interior and scoured, load-cast base

S 3-1 Core Geophysics and Age Control Methods

Core Geophysics

The cores collected offshore Sumatra (**Fig. 3-2**) were scanned at sea with a GEOTEK Multi Sensor Core Logger (MSCL), obtaining P-wave velocity, gamma ray density, resistivity, and loop magnetic susceptibility (MS) at 0.5 cm spaced intervals in 1.5-m length sections. Split cores were imaged with a high resolution line-scan digital camera and the lithostratigraphy was described. High resolution point MS data were collected using a Bartington MS2E point sensor at 0.5 cm spacing. The cores were imaged with the Oregon State University Aquilion 64 slice X-ray Computed Tomography (CT) system with a nominal voxel size of 0.5 mm.

Age Control Methods

Age control for stratigraphy is provided by Accelerator Mass Spectrometer (AMS) ^{14}C and ^{210}Pb radiometric techniques. ^{14}C data is based on decay with a half-life of 5,730 years and is useful for strata between ~300 - ~35,000 years old (Stuiver and Braziunes, 1993). ^{210}Pb data, based on a shorter half-life of 22 years (Noller, 2000), provides information about sedimentary deposition for the past ~150 years. We use ^{210}Pb age data to constrain the timing of deposition for the most recently deposited sediments.

To estimate ages of the turbidites using radiocarbon, we extract the calcium carbonate shells of planktic foraminifers preserved in the hemipelagic sediment below each turbidite to provide a maximum limiting age. We utilized planktic foraminiferid species as they most closely represent the age of the youngest sea water, the surface water that is most closely in ^{14}C equilibrium with the atmosphere. We sample below each turbidite because this is the sediment closest in age to the turbidite. We do not use the age of the sediment above the turbidite because the boundary between the top of the turbidite tail and the hemipelagic sediment is difficult to identify reliably and bioturbation is concentrated at this boundary. These methods are outlined in Goldfinger et al. (2012).

Trench core sites were deeper than the Carbonate Compensation Depth (CCD), the depth below which foraminiferid $CaCO_3$ tests dissolve faster than they are deposited. Therefore foraminiferid abundance was nil in trench core sediments, so ^{14}C age control applies only to the slope cores.

Sediment samples were removed from the cores while avoiding the 0.5 cm of material nearest the core walls to avoid visible or undetected deformation and friction drag along the core walls. In some cases, highly irregular turbidite bases resulted in sampling an interval below the basal irregularities, and applying a correction to the hemipelagic thickness called the “gap.” Hemipelagic sediment samples were freeze dried to separate clay particles to

improve rinsing through a sieve, washed in a dilute sodium hexametaphosphate solution to keep the fine particles in suspension, sieved through a 125 µm stainless steel sieve, then dried in a warm oven. Typically 25-50 individual planktic foraminifers (depending on size/weight) were identified then removed from this dried > 125 µm size fraction using a fine sable brush moistened with distilled water. Foraminiferal sample ages were determined using Accelerator Mass Spectrometry (AMS) methods at the Keck AMS facility at University of California, Irvine in collaboration with John Southon.

The primary sources of radiocarbon error include variation of the age in surface and near surface sea water, the sedimentation rate, the level of atmospheric radiocarbon in the atmosphere, and the basal erosion during turbidite emplacement. There does not yet exist sufficient prehistoric benthic-planktic age pairs with which to construct an age model in this region, so the reservoir correction is probably the largest source of error in this study and we have no way to evaluate this source of epistemic error. Because of the small number of cores collected at any given core site, we cannot evaluate basal erosion, and

Supplemental Table 3-1.

Sample Number	Lab Sample Number [1]	Sample Name	Core Number	Depth (cm)	Lab Age [2]	Lab Age Error	Cal. Age [3]	Cal. Age Error	Hemi Sed Rate (cm ka^{-1})[4]	Sed Rate Error
SUM-145	77175	RR0705_79PC_307_309_SUM-145	79PC	308	4650	20	4860	60	18	1
SUM-227	107808	RR0705_96PC_206_208_SUM-227	96PC	207	480	20	30	30	1	1
SUM-228	107806	RR0705_96PC_222_224_SUM-228	96PC	223	1150	20	670	40	11	1
SUM-089	65300	RR0705_96PC_287.5_289.5_SUM-089	96PC	288.5	5920	20	6280	60	18	1
SUM-090	65301	RR0705_96PC_374_376_SUM-090	96PC	375	2430	20	2040	80	22	1
SUM-232	107809	RR0705_96PC_399_401_SUM-232	96PC	400	2410	20	2010	90	18	1
SUM-177	76991	RR0705_103TC_012.5_014.5_SUM-177	103TC	13.5	1310	20	840	70	2	1
SUM-178	76992	RR0705_103TC_036_038_SUM-178	103TC	37	1890	20	1400	80	3	1
SUM-179	76993	RR0705_103TC_039_041_SUM-179	103TC	40	2070	20	1610	80	5	1
SUM-180	76994	RR0705_103TC_079_081_SUM-180	103TC	79.5	2990	20	2750	60	5	1
SUM-084	65297	RR0705_103PC_020_022_SUM-084	103PC	21	1230	20	740	70	11	1
SUM-054	54323	RR0705_103PC_049_051_SUM-054	103PC	50	1940	30	1450	80	24	1
SUM-085	65298	RR0705_103PC_092_094_SUM-085	103PC	93	2710	20	2350	70	11	1
SUM-055	54324	RR0705_103PC_111_113_SUM-055	103PC	112	2990	20	2720	60	8	1
SUM-087	65299	RR0705_103PC_174_176_SUM-087	103PC	175	3930	20	3770	90	11	1
SUM-050	54306	RR0705_103PC_209_211_SUM-050	103PC	210	4360	20	4480	80	11	1
SUM-052	54322	RR0705_103PC_277_279_SUM-052	103PC	278	5100	20	5430	110	16	1
SUM-053	65528	RR0705_103PC_300.5_302.5_SUM-053	103PC	301.5	5360	30	5720	110	13	1
SUM-224	107805	RR0705_103PC_324_326_SUM-224	103PC	325	5580	30	5890	80	20	1
SUM-253	107804	RR0705_103PC_383_385_SUM-253	103PC	384	6020	30	6350	90	26	1
SUM-176	77107	RR0705_104TC_011_013_SUM-176	104TC	12	710	20	290	70	2	1
SUM-175	77106	RR0705_104TC_047.5_049.5_SUM-175	104TC	48.5	1220	20	740	70	1	1
SUM-060	65529	RR0705_104PC_049.5_051.5_SUM-060	104PC	50.5	1070	20	600	60	11	1
SUM-062	54325	RR0705_104PC_067.5_069.5_SUM-062	104PC	68.25	1270	20	790	80	11	1
SUM-061	65530	RR0705_104PC_122_124_SUM-061	104PC	123	1630	50	1150	110	12	1
SUM-082	65531	RR0705_104PC_158_160_SUM-082	104PC	159	2040	20	1590	80	11	1
SUM-115	65532	RR0705_104PC_207_209_SUM-115	104PC	208	2420	220	2080	550	18	1
SUM-235	107807	RR0705_104PC_326_328_SUM-235	104PC	327	3000	40	2760	70	20	1
SUM-080	65294	RR0705_108PC_039_041_SUM-080	108PC	40	2020	20	1530	80	17	1
SUM-081	65295	RR0705_108PC_132.5_134.5_SUM-081	108PC	133.5	3040	20	2790	60	13	1

1. Radiocarbon samples were analyzed at the Keck Carbon Cycle Accelerator Mass Spectroscopy Facility at Earth System Science Dept., UC Irvine.

2. Lab-reported age errors reported to 2 standard deviations.

3. Calibrated age (in calendar years) ranges before A. D. 1950 according to Stuiver and Reimer[2] calculated using marine reserevior correction (ΔR = 16) errors reported with 95% error.

4. Hemipelagic Sedimentation rate is calculated from dividing unit thickness by the calibrated age.

- Radiocarbon concentrations are given as fractions of the Modern standard, $D^{14}C$, and conventional radiocarbon age, following the conventions of Stuiver and Polach[1].

- Size-dependent sample preparation backgrounds have been subtracted, based on measurements of ^{14}C-free calcite.

- All results have been corrected for isotopic fractionation according to the conventions of Stuiver and Polach[1], with $\delta^{13}C$ values measured on prepared graphite using the AMS spectrometer. These can differ from $\delta^{13}C$ of the original material, if fractionation ocurred during sample graphitization or the AMS measurement, and are not shown.

- Inverted age in trigger cores (in gray) represent repeated section not shown in Figure 2 nor in Supplemental Document 1.

there will likely be undetected erosion in these data. Sedimentation rates are calculated using ^{14}C age estimates and thickness of hemipelagic sediment. Sedimentation rates are used to calculate ages for turbidites that have no direct age.

The "lab" radiocarbon ages are reported in years before present (BP, measured from 1950) with a 2 standard deviation lab error (Stuiver et al., 1998). ^{14}C ages are calibrated (Stuiver and Polach, 1977) and a marine reservoir correction of 16±11 years is made using the Marine09 database (Reimer et al., 2009). Only two delta R values are available for the Sumatra area, and while constraints are few on this correction, we here are correlating marine sites to other nearby marine sites, thus the local correlations are valid while absolute ages may contain additional uncertainty. One additional correction we make to the calibrated age is the sediment gap thickness correction (thickness of sediment between the turbidite and the sample; see OxCal code below). For individual ages, we propagate these uncertainties using RMS (root mean square) calculations using estimates of the uncertainties at each step. This calculation includes the lab uncertainties and results in the final reported 2σ range for each radiocarbon age. In later sections of the paper, we calculate region wide mean event ages. For these, we average the ages (using the combine function in OxCal), and again apply RMS calculations to the averaged error ranges to produce 95% RMS error range for each averaged age. No lab multipliers were applied to the data.

Some stratigraphy in trench cores has been correlated with deposits in slope cores. Based on these correlations (turbidites and a tephra deposit), the ages from the slope cores are plotted on the trench core figures (**Figures 3-8 and 3-10**). The turbidites in cores 03PC, 05PC, and 107TC are correlated using geophysical wiggle matching (techniques in Goldfinger et al., 2012) with turbidites in core 108PC, 104PC, and 103PC. The tephra in 38GC and 41GC is correlated using electron microprobe and Inductively Coupled Plasma Mass Spectrometry, ICPMS (Salisbury et al., 2012)

Appendix S 3-4 Sumatra core RR0705-96PC

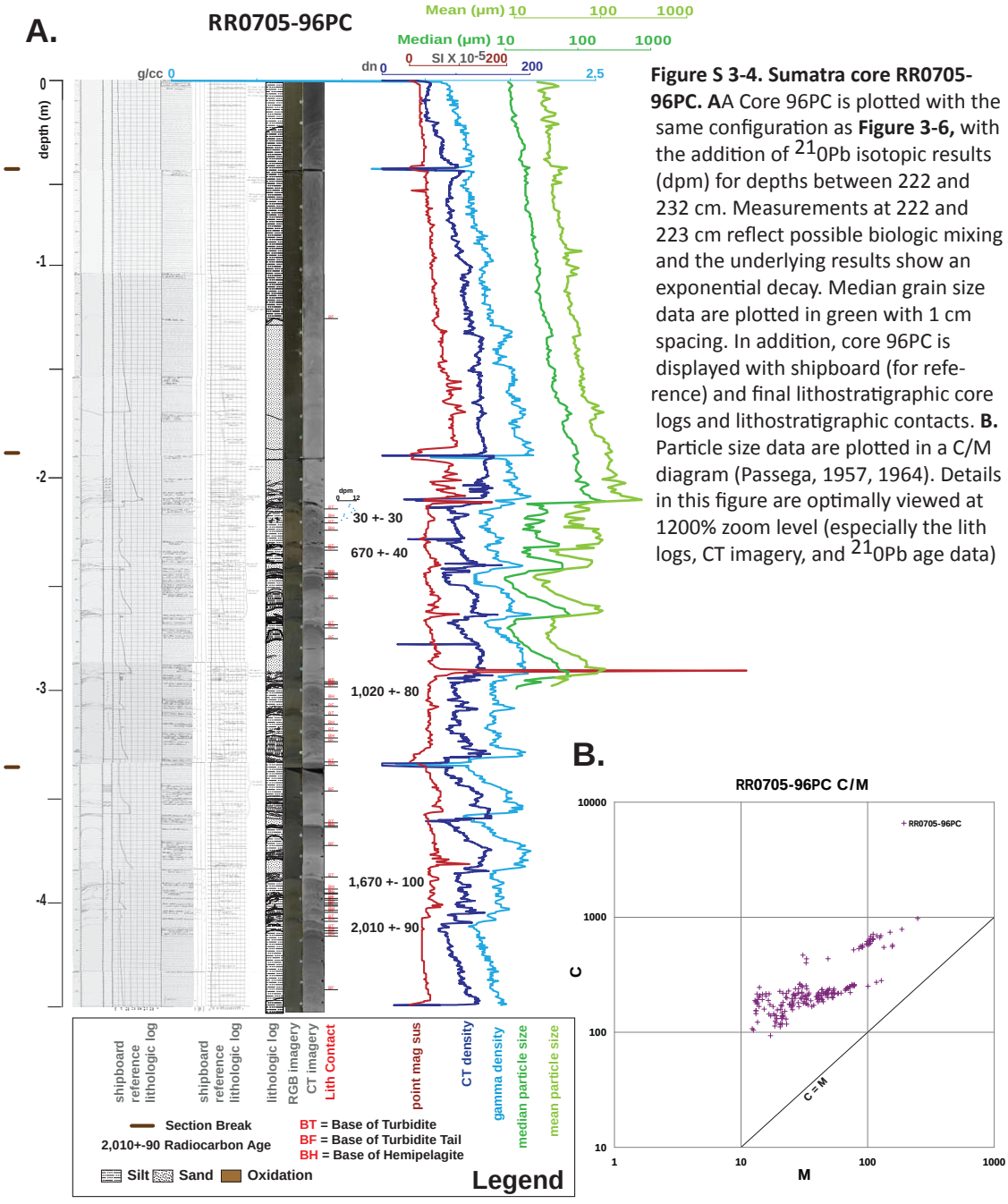

Figure S 3-4. Sumatra core RR0705-96PC. AA Core 96PC is plotted with the same configuration as **Figure 3-6,** with the addition of ^{21}0Pb isotopic results (dpm) for depths between 222 and 232 cm. Measurements at 222 and 223 cm reflect possible biologic mixing and the underlying results show an exponential decay. Median grain size data are plotted in green with 1 cm spacing. In addition, core 96PC is displayed with shipboard (for reference) and final lithostratigraphic core logs and lithostratigraphic contacts. **B.** Particle size data are plotted in a C/M diagram (Passega, 1957, 1964). Details in this figure are optimally viewed at 1200% zoom level (especially the lith logs, CT imagery, and ^{21}0Pb age data)

Appendix 4-1

Parameter Selection and SLIDE settings

We discuss the parameters and their selected values and ranges of values used in this paper. Settings used for each analysis, along with the results for each site, are listed in **Appendix 4-2**.

Cohesion is determined by combining the results of several studies (Hempel, 1985; Sultan et al., 2009; Johnson et al., 2012). Hempel (1985) used sediment from Kasten Cores collected offshore Washington and Oregon on the continental slope. Hempel (1985) conducted shear strength measurements using a motorized shear vane device inserted normal to bedding planes. Sultan et al. (2009) collected cores from the base of the continental slope and trench offshore Sumatra and provide geotechnical data for cores MD05-2972 and MD05-2975. Johnson et al. (2012) conducted in situ analysis of tensile fracture toughness (measuring the stress required to cause tensile failure of sediments) and these data are correlated with shear strength. We combined the data from in the uppermost sediments from these three studies.

Angle of Internal Friction

was determined from undrained triaxial strength testing conducted at the MIT (Cambridge, Massachusetts, USA) geotechnical laboratory using the reference standards ASTM D4767 (ASTM International, 2003). These tests were conducted on sediment collected from whole core samples from the Ocean Drilling Program Site 1244, Hydrate Ridge, Cascadia continental margin. We use the mean peak angle of internal friction for the uppermost sediments that are not remolded nor resedimented.

Sediment Weight

Unit Weight, γ, γ_{sat}, γ_{dry}, γ', kN/m^3 is expressed as a force per unit volume.

When all the voids are filled with water, the bulk unit weight is identical to the saturated unit weight, γ_{sat}, and when all the voids are filled with air, the bulk unit weight is identical with the dry unit weight, γ_{dry}.

Pore Water Pressure

Excess pore pressure refers to a sudden increase in pore pressure within sediment due to rapidly loading conditions, commonly referred to as “undrained loading.” We consider excess pore pressure from two sources: that imparted due to the change in stress from the overlying sediment mass and that imparted due to seismic loads. SLIDE software uses the B-bar coefficient in their calculations of excess pore pressure (Skempton, 1954; Rocscience, 2012)

Excess pore pressure is related by the following equation:

$\Delta u = \text{B-bar} * \Delta\sigma_v$

Where σ_v is the change in vertical stress. B-bar relates directly to the percent to which the sediment is saturated. We assume the sediment is completely saturated, so we set B-bar = 1.

Deterministic Safety Factor

Safety Factor calculated for the global minimum slip surface, from the regular (non-probabilistic) analysis.

Mean Safety Factor

The mean Safety Factor obtained from probabilistic analysis. Average safety factor, of all the safety factors calculate for the Global Minimum slip surface. This should be close to the value of the deterministic safety factor. For sufficiently large samples, the two values should be nearly equal.

Probability of Failure

The Probability of Failure is the number of analyses with safety factor < 1, divided by the total Number of Samples. PF = number failed/number samples X 100%

For PF = 11%, 110 out of 1000 samples have FS < 1

Reliability Index

The Reliability Index is an indication of the number of standard deviations which separate the Mean Safety Factor from the critical safety factor (= 1).

A Reliability Index of at least 3 is usually recommended, as a minimal assurance of a safe slope design. For this example, RI = 1.24, which indicates an unsatisfactory level of safety for the slope.